Sebastian Oberst
Benjamin Halkon
Jinchen Ji
Terry Brown *Editors*

Vibration Engineering for a Sustainable Future

Numerical and Analytical Methods to Study Dynamical Systems, Vol. 3

Springer

Vibration Engineering for a Sustainable Future

Sebastian Oberst • Benjamin Halkon • Jinchen Ji
Terry Brown
Editors

Vibration Engineering for a Sustainable Future

Numerical and Analytical Methods to Study Dynamical Systems, Vol. 3

Springer

Editors
Sebastian Oberst
Centre for Audio, Acoustics and Vibration
Faculty of Engineering and IT
University of Technology Sydney
Sydney, NSW, Australia

Benjamin Halkon
Centre for Audio, Acoustics and Vibration
Faculty of Engineering and IT
University of Technology Sydney
Sydney, NSW, Australia

Jinchen Ji
School of Mechanical and Mechatronic
Engineering, Faculty of Engineering and IT
University of Technology Sydney
Sydney, NSW, Australia

Terry Brown
School of Mechanical and Mechatronic
Engineering, Faculty of Engineering and IT
University of Technology Sydney
Sydney, NSW, Australia

ISBN 978-3-030-46465-3 ISBN 978-3-030-46466-0 (eBook)
https://doi.org/10.1007/978-3-030-46466-0

This Springer imprint is published by the registered company Springer Nature Switzerland AG
The registered company address is: Gewerbestrasse 11, 6330 Cham, Switzerland

Preface

These proceedings, presented in three volumes, contain a selection of papers presented at the 18th Asia-Pacific Vibration Conference (APVC 2019), held at the University of Technology Sydney (UTS) in Sydney, Australia from 18–20 November 2019. Vibration and associated phenomena are all around us every day but are often overlooked and/or not fully understood. However, it is of fundamental importance to the engineering of the systems we continually interact with in our daily lives. This conference enabled experienced vibration engineering researchers and practitioners, along with the experts of the future, to come together to present and discuss their latest interests and activities in the domain. Additionally, five international leaders in the field from across the region and beyond presented keynote plenary sessions.

The APVC is a long-standing technical conference with a proud history. It was first held in Japan in 1985 and since then every two years in several different countries including Korea, China, Australia, Malaysia, Singapore, New Zealand, Hong Kong and Vietnam. At APVC 2019 we had 219 delegates from 15 different countries including some from outside the region (Germany, Great Britain, France, Czech Republic, Brazil, United Arab Emirates).

Thank you to all the APVC 2019 sponsors whose financial support and presence in the exhibition area helped us to deliver a vibrant and successful event. We especially acknowledge our Platinum and Gold sponsors: Polytec GmbH, Warsash Scientific Pty Ltd, Bestech Australia Pty Ltd and Siemens Digital Industries Software. We also thank UTS for hosting the conference and UTS Tech Lab for its generous support.

The papers presented in these proceedings encompass fundamental and applied research, theoretical approaches, computational methods and simulation, and experimentation in vibration engineering. The authors, from 18 different countries, are researchers and practitioners, including: professors, students, engineers and

scientists from academia and industry. The three volumes, each with papers organized into sections aligned with the conference oral presentation technical sessions, are:

Vol. 1 – Active and Passive Noise and Vibration Control
Vol. 2 – Experiments, Materials and Signal Processing
Vol. 3 – Numerical and Analytical Methods to Study Dynamical Systems

Contributions were invited from across the region and beyond with a total of 245 extended abstracts submitted with the local organizing committee accepting 183 after review, representing a rejection rate of 25%. Authors of accepted extended abstracts were then invited to submit full papers with a maximum length of six pages. A total of 183 full papers were submitted and 145 were selected (21% rejection rate) for the proceedings following a rigorous review process involving world-leading experts in their fields as external reviewers. At least two reviewers considered each paper. Selected reviewers were active researchers in the relevant fields and we sincerely thank them for providing their expert opinion, valuable time and effort. The Local Organizing Committee compiled the reviews and sent them to authors to assist them with refining and improving their papers before final submission and editorial approval. We would also like to thank all authors for their excellent work and significant contribution.

Finally, we would like to thank Springer for their support in producing and publishing these proceedings.

Sydney, NSW, Australia

Sebastian Oberst
Benjamin Halkon
Jinchen Ji
Terry Brown

Acknowledgements

On behalf of the Scientific Steering Committee, I would like to express my sincere gratitude to the Local Organizing Committee for their greatest contribution to the APVC 2019. The LOC has been organized by Prof. Jinchen (JC) Ji and Prof. Benjamin (Ben) Halkon in UTS. I also would like to sincerely thank UTS students and staff, session chairs, and external sponsors and exhibitors, who worked extremely hard to deliver an excellent event. I also thank the Steering Committee for its contribution. In delivering APVC 2019, many firsts were achieved, including: invitations and participants specifically extended to beyond the Asia-Pacific region; engineers from industry actively engaged with the conference; the APVC conference financially supported by a government department (the New South Wales Government through the Office of the Chief Scientist and Engineer); best student paper awards rigorously panel reviewed; and peer-reviewed selected papers officially published in three volumes by international publisher, Springer.

Tokyo Metropolitan University, Hachioji, Tokyo, Japan Takuya Yoshimura

Organization

Local Organizing Committee

Jinchen (JC) Ji	University of Technology Sydney, Australia (Chair)
Benjamin (Ben) Halkon	University of Technology Sydney, Australia (Chair)
Sebastian Oberst	University of Technology Sydney, Australia (Technical Chair)
Terry Brown	University of Technology Sydney, Australia (Program Chair)
Liya Zhao	University of Technology Sydney, Australia (Ordinary Member)
Philippe Blanloeuil	University of New South Wales, Australia (Ordinary Member)
Paul Walker	University of Technology Sydney, Australia (Ordinary Member)
Yancheng Li	University of Technology Sydney, Australia (Ordinary Member)
Hamed Kalhori	University of Technology Sydney, Australia (Ordinary Member)

Steering Committee

Takuya Yoshimura	Tokyo Metropolitan University, Japan (Chairman)
Shigehiko Kaneko	University of Tokyo, Japan
Toshihiko Komatsuzaki	Kanazawa University, Japan
Youngjin Park	Korea Advanced Institute of Science and Technology, Korea
No-Cheol Park	Yonsei University, Korea
Haiyan Hu	Beijing Institute of Technology, China

Li Cheng	Hong Kong Polytechnic University, Hong Kong
Jinhao Qiu	Nanjing University of Aeronautics and Astronautics, China
Zhichao Hou	Tsinghua University, China
Tianran (Terry) Lin	Qingdao University of Technology, China
M. Salman Leong	University of Technology, Malaysia
Zaidi Mohd Ripin	University of Science, Malaysia
Nguyen Van Khang	Hanoi University of Science and Technology, Vietnam
Stefanie Gutschmidt	University of Canterbury, New Zealand
Ian Howard	Curtin University, Australia
Jinchen Ji	University Technology Sydney, Australia
Benjamin Halkon	University of Technology Sydney, Australia
Oshihiro Narita (Honourable)	Hokkaido University, Japan
Hong Hee Yoo (Honourable)	Hanyang University, Korea
Athol J. Carr (Honourable)	University of Canterbury, New Zealand
Ban Chun Wen (Honourable)	Northeastern University, China

Scientific Committee

Richard Markert	Technical University Darmstadt, Germany
Xiaojun Qiu	University of Technology Sydney, Australia
Rodney Entwistle	Curtin University, Australia
Yong-Hwa Park	Korea Advanced Institute of Science and Technology, Korea
Con Doolan	University of New South Wales, Australia
Benjamin Cazzolato	University of Adelaide, Australia
Jaspreet Singh	The University of Auckland, New Zealand
Pietro Borghesani	University of New South Wales, Australia
Tamas Kalmar-Nagy	Budapest University of Technology and Economics, Hungary
Mohammad Fard	Royal Melbourne Institute of Technology, Australia
Guilin Wen	Hunan University, China
Jin Zhou	Shanghai University, China
CW Lim	City University of Hong Kong, Hong Kong
Dongping Jin	Nanjing University of Aeronautics and Astronautics, China
Xinwen Wang	China University of Mining and Technology, Beijing
Jian Xu	Tongji University, China
Shaopu Yang	Shijiazhuang Tiedao University, China
Hu Ding	Shanghai University, China
Qinsheng Bi	Jiangsu University, China
Hailin Wang	South China Agricultural University, China

Qingyun Wang	Beihang University, China
Jie Huang	Beijing Institute of Technology, China
Jie Yang	Royal Melbourne Institute of Technology, Australia
Haiping Du	University of Wollongong, Australia
Linke Zhang	Wuhan University of Technology, China
Sam Han	ActronAir, Australia

UTS Support Staff and Volunteers

Abbasnejad, Behrokh	Ho, Ngoc Thao Han (Sophie)	Ni, Qing	Zhang, Ying
Böni, Alison	Huynh, Timothy	Pereira, Kyle	Zheng, Jingyang
Chong, Hong Kit	Li, Wenjie	Sansom, Travers	
Darwish, Abdel	Lu, Shuixiu	Xiao, Tong	
Hayati, Hasti	Lym, Martin	Ye, Kan	

Reviewers

Abdrrahim, Houmat	Huang, Dongmei	Matsuzaki, Kenichiro	Walker, Paul
Abu Bakar, Abdul Rahim	Hui, Kar Hoou	Matthews, David	Wang, Shuping
Adams, Christian	Huston, Dryver	Melnikov, Anton	Wang, Yuxing
Adams, George G.	Inoue, Tsuyoshi	Min, Cheonhong	Wang, Xu
Agoston, Katalin	Irvine, Tom	Mitchell, Sean	Wang, Feng
Aihara, Tatsuhito	Ishikawa, Satoshi	Moreau, Danielle Joy	Wang, Qiang
Alkmim, Mansour	Ito, Atsuhiro	Morishita, Shin	Wang, Yuning
Bai, Shipeng	Iwamoto, Hiroyuki	Nakano, Yutaka	Wang, Kuoting
Baydoun, Suhaib Koji	Ji, Jinchen	Nakashima, Itsuki	Wang, Shiliang
Bi, Kaiming	Jin, Dongping	Nerse, Can	Wantanabe, Seiji
Bianciardi, Fabio	Jung, Hyung-Jo	Ng, Alex	Watterson, Peter
Biswal, Deepak Kumar	Kalhori, Hamed	Ning, Donghong	Wen, Hao
Blanloeuil, Phillipe	Kang, Hooi Siang	Nitzschke, Steffen	Wen, Guilin
Bonneau, Oliver	Karimi, Hamid Reza	Oberholster, Abrie	Woschke, Elmar
Borghesani, Pietro	Karimi, Mahmoud	Oberst, Sebastian	Wu, Lifu
Brown, Terry	Kawamura, Shozo	Ota, Shinichiro	Wu, Helen
Buchwald, Patrick	Kessissoglou, Nicole	Papangelo, Antonio	Xiao, Tong
Butlin, Tore	Shen, Jianwei	Patnaik, S Srikant	Xiao, Tong
Carpenter, Harry	Kawamura, Shozo	Pradhan, Somanath	Xu, Jian
Cazzolato, Benjamin	Kessissoglou, Nicole	Prasad, Marehalli	Xu, Daolin
Cheer, Jordon	Kil, Hyun Gwon	Qiu, Xiaojun	Yabui, Shota
Chen, Tong	Kim, Dong Joon	Qu, Jiao	Yamada Keisuke

Chiang, Yan Kei	Kim, Dong Hyeon	Rahnejat, Homer	Yamamoto, Hiroshi
Choudhury, Madhurjya Dev	Kingan, Micheal Joseph	Rose, Francis	Yamazaki, Toru
Christie, Matthew	Komatsu, Tadashi	Rudorf, Martin	Yamazumi, Mitsuhiro
Dai, Wei	Komatsuzaki, Toshihiko	Ruppert, Michael	Yan, Han
Daniel, Christian	Kondo, Eiji	S, Bala Murugan	Yang, Jian
Darwish, Abdel	Kondou, Takahiro	Saeed, Omear	Yang, Guidong
Davy, John	Koo, Bonsoo	Saito, Takashi	Yao, JianChun
De Ryck, Laurent	Koutsovasillis, Panagiotis	Sanliturk, Kenan Y.	Ye, Kan
Denimal, Enora	Krueger, Timm	Sasaki, Takumi	Yonezawa, Heisei
Dhupia, Jaspreet Singh	Kundu, Pradeep	Seering, Warren	Yoo, Hong Hee
Ding, Qian	Kurihara, Kai	Shah, JayKumar	Yoshida, Tatsuya
Ding, Hu	Kuroda, Katsuhiko	Shangguan, Wenbin	Yue, Xiaole
Dong, Xufeng	Lai, Joseph	Shiiba, Taichi	Zhang, Hua
Dubbini, Janet L	Lee, Doo Ho	Shin, Eung-Soo	Zhang, Xiaoxu
Dubey, Manish Kumar	Lee, Chan	Smith, Wade	Zhang, Xiaozhu
Fard, Mohammad	Lei, Jiazhen	Sowa, Nobuyuki	Zhang, Guoqiang
Fisher, Joeffrey	Lei, Gang	Spannan, Lars	Zhang, Linke
Forrier, Bart	Li, Weihua	Stender, Merten	Zhang, Kai
Fowler, Deborah	Li, Huan	Stone, Brian	Zhao, Sipei
Fujita, Satoshi	Li, Wei	Su, Zhu	Zhao, Feng
Furuya, Kohei	Lidfors Lindqvist, Anna	Sueda, Miwa	Zhao, Liya
Geng, Xiaofeng	Lin, Susanna	Sun, Xiuting	Zheng, Minyi
Gong, Sanpeng	Liu, Pengfei	Taji, Shoichi	Zhong, Jiaxin
Hahn, Eric	Logan, Patrick	Tao, Jiancheng	Zhou, Jiaxi
Han, Tian	Lu, Shuixiu	Terashima, Osamu	Zhou, Yulong
Halkon, Benjamin	Lu, Yun	Terumichi, Yoshiaki	Zhou, Shilei
Hansen, Kristy	Luo, Liang	Tian, Fangbao	Zhou, Liangqiang
Hauret, Patrice	Luo, Quantian	Tomoda, Akinori	Zhu, Qiaoxi
Hayati, Hasti	Luo, Lin	Tsuchida, Takahiro	Zhu, Chendi
Hirano, Yakashi	Lv, Ling	Tsujiuchi, Nobutaka	Zou, Kun
Hisano, Shotaro	Maheo, Lauret	Ura, Kentaro	Zou, Hai-Shan
Hosoya, Naoki	Makki Alamdari, Mehrisadat	Vahidi, Ardalan	
Hossain, Mahbub	Mao, Xin	Veidt, Martin	
Hou, Zhichao	Matsuyama, Marin	Vio, Gareth	

Organiser APVC 2019

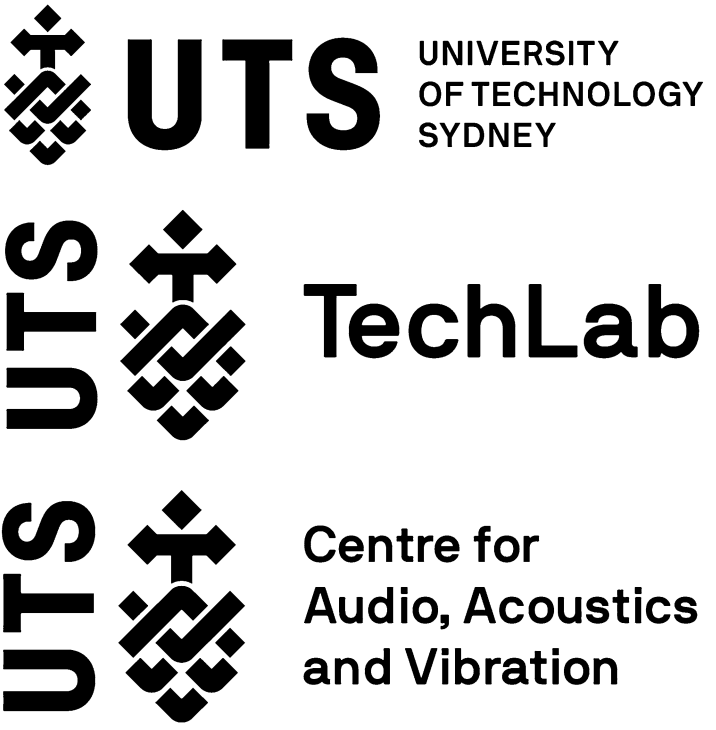

Sponsors and Exhibitors, APVC 2019

Polytec has been bringing light into the darkness for 50 years. With more than 400 employees worldwide, we develop, produce and distribute optical measurement technology solutions for research and industry. Our quality innovative products have an excellent reputation internationally among the expert community. We find solutions tailored to our customers' requirements.

The development and production of innovative measurement systems, especially for our core technology Laser Doppler Vibrometry (LDV), has kept our customers and us at the forefront of dynamic characterization. The implementation of LDV extends from basic vibration measurement tasks to advanced modal analysis/FE correlation. Ultimately, our solutions are meant to help companies to assert and build upon their technological leadership. The effective use of the laser technology allows a non-contact, non-invasive test method for vibration which is widely appreciated across industries such as Automotive, Aerospace, Semiconductor, Consumer Electronics, etc.

The decades of experience have allowed Polytec to expand the technology and our product line-up which could be generally summarized as follows:

Micro to macro sample dimensions
Single-point or full-field scanning
1D or 3D axis data
FRF, transient, mode and operational deflection shape analysis capable

Max frequency BW up to 2.5 GHz
Max distance up to 300 m
Sub-pm resolution

Together with Warsash Scientific, our long-standing partner in the ANZ region for over 40 years, Polytec would welcome visitors to inspect the latest Polytec VibroFlex series range of research grade single point laser Doppler vibrometers at the APVC 2019 exhibition. The modular concept of VibroFlex combines the versatility of a universal front-end with a selection of special sensor heads, tailored to the needs of your measuring task, including the latest Xtra IR sensor head option.

For more information please visit www.polytec.com.

BESTECH
Sensors & Teaching Equipment

Bestech Australia, an ISO9001 certified company, supplies state-of-the-art test and measurement sensors for measurement of physical parameters, data acquisition systems as well as technical teaching equipment from world leading manufacturers. Our constantly expanding product portfolio is suitable for university research, teaching and R&D laboratories as well as for demanding high precision measuring applications in industrial environments. We are proud to complement this with our own manufacture.

We offer full local technical support throughout the entire product lifecycle including product specification, commissioning, training and repair. This is delivered by our team of factory trained application engineers and product specialists. We pride in delivering excellent service for ultimate customer satisfaction.

SIEMENS
Ingenuity for life

Digitization is rapidly gaining ground. Today's manufacturers develop new product architectures and material types, offer consumers customization options and massively introduce smart functionalities. These innovations are enabled by capabilities such as mechatronics, additive manufacturing, and concepts like cloud or the internet of things. Engineers need to master this additional complexity, which is often related to an ever-increasing demand for energy efficiency, while still dealing with classic performance requirements, such as noise, vibrations and durability.

This evolution urges companies to dramatically transform their classical verification-centric development processes. Instead, the Digital Twin paradigm is on a rise. In this new approach, manufacturers associate every individual product to a set of ultra-realistic, multi-physics models and data, that stay in-sync, and can predict its real behavior throughout the lifecycle, starting from the very early stages.

To achieve this, simulation needs to gain realism to become capable of taking up a predictive role, while the combination of increased validation workload and the exploration of uncharted design territories requires more productive and innovative testing methodologies. On top of that, manufacturers will need to deploy an infrastructure that helps them remove the traditional barriers between departments, even letting product development continue after delivery. That is exactly the core business of Siemens Digital Industries Software.

Siemens Digital Industries Software offers manufacturers across the various industries a comprehensive environment that helps their engineering departments create and maintain a Digital Twin. Within this offering, the Simcenter™ solutions portfolio focuses on performance engineering. Simcenter uniquely integrates physical testing with system simulation, 3D CAE and CFD, and combines this with design exploration and data analytics. Simcenter helps engineers accurately predict vehicle performance, optimize designs and deliver innovations faster and with greater confidence.

Brüel & Kjær

At Brüel & Kjær, we help our customers solve sound and vibration challenges and develop advanced technology for measuring and managing sound and vibration. We ensure component quality, optimize product performance and improve the environment. Founded in 1942, Brüel & Kjær Sound & Vibration Measurement A/S has grown to become the world's leading supplier of advanced technology for measuring and managing the quality of sound and vibration.

The sound and vibration challenges facing our customers are diverse, including vibration in car engines; evaluation of building acoustics; mobile telephone sound quality; cabin comfort in passenger airplanes; production quality control; wind turbine noise; and much more. Our innovative and highly practical solutions have made us the first choice of engineers and designers from around the world. Many of our researchers and developers are recognized as world experts, who aid the scientific community and teach at renowned centres. By applying their thorough knowledge and experience, we can help you at every stage of your product's life cycle: ensuring quality from design to manufacture, and efficiency throughout deployment and operations.

Brüel & Kjær maintains a network of sales offices and representatives in 55 countries. That means local-language help is always at hand during office hours. A global group of engineering specialists supports our local teams. They can advise on and help solve all manner of sound and vibration measurement, analysis and management problems. To further support our customers worldwide, we regularly hold courses and road-shows, and participate in sound and vibration focused trade shows and conferences worldwide.

MathWorks is the leading developer of mathematical computing software. MATLAB, the language of engineers and scientists, is a programming environment for algorithm development, data analysis, visualization, and numeric computation. Simulink is a block diagram environment for simulation and Model-Based Design for multidomain dynamic and embedded engineering systems. Engineers and scientists worldwide rely on these product families to accelerate the pace of discovery, innovation, and development in automotive, aerospace, electronics, financial services, biotech-pharmaceutical, and other industries. MATLAB and Simulink are also fundamental teaching and research tools in the world's universities and learning institutions.

Accelerate Discovery with the NI Platform

Researchers are driving time-critical, ambitious innovation while addressing grand engineering challenges in the broad areas of transportation, wireless communications, medicine, energy and climate change. Across each of these application areas, researchers need to easily acquire measurements, scale to complex multidisciplinary systems, and rapidly prototype a scalable solution. For more than 40 years, NI is central to accelerating researcher innovation by providing the technology and support to prototype systems, publish findings and secure funding from 5G Wireless and Communications all the way to Autonomous and Electrical Vehicles.

John Morris Scientific was founded In April 1956 to service consumables and instrumentation throughout the South Pacific Science industry. Today we employ over 85 talented sales and service professionals across 12 key locations – to ensure you receive unrivalled customer service in your location. John Morris Group offers technical/application advice to Laboratory, R&D, Nano-Fabrication, High Energy Physics, Synchrotron, Industrial, Process and Food/Packaging users. Although we have the largest range we believe "It's not about the box" and we look forward to delivering your team with solutions that add value to your process. As you face increasing pressures (budget, time and results), the success of our offering is based

on more than just supplying you with the “box” or its price. At John Morris Group we focus on satisfying your end-to-end needs … today and over the longer term.

Special Sessions

Topic: Recent Advances on Vibration Control of Engineering Structures

Organizers:

Dr. Yancheng Li, University of Technology Sydney, Australia,
email: Yancheng.li@uts.edu.au
Dr. Kaiming Bi, Curtin University, Australia, email: Kaiming.bi@curtin.edu.au
A/Prof Xufeng Dong, Dalian University of Technology, China,
email: dongxf@dlut.edu.cn

Topic: Active Noise Control for a Quieter Future

Organizers:

Dr Sipei Zhao, University of Technology Sydney, Australia,
email: sipei.zhao@uts.edu.au
Dr Shuping Wang, University of Technology Sydney, Australia,
email: shuping.wang@uts.edu.au
Associate Professor Lifu Wu, Nanjing University of Information Science & Technology, email: wulifu@nuist.edu.cn

Topic: Noise, Vibration and Their Applications in Electricity Power Systems

Organizers:

A/Professor Linke Zhang, Wuhan University of Technology, China,
email: lincol@whut.edu.cn

A/Professor Yuxing Wang, Zhejiang University, China,
email: wangyuxing@zju.edu.cn
Professor Tianran Lin, Qingdao University of Technology, China,
email: trlin@qut.edu.cn

Topic: Applications and Advances in Laser Doppler Vibrometry

Organizers:

Dr Ben Halkon, University of Technology Sydney, Australia,
email: Benjamin.Halkon@uts.edu.au
Dr Philippe Blanloeuil, University of New South Wales, Australia,
email: p.blanloeuil@unsw.edu.au
Prof. Enrico Primo Tomasini, Universita Polytecnica delle Marche, Italia,
email: aivela@univpm.it

Contents

Part VIII Human Body Vibration

Part I
Computational Methods of Vibrations

Simulative Determination of Ideal Fluid Properties for an Automatic Ball Balancer Under Different Run-up Scenarios

Lars Spannan, Christian Daniel, and Elmar Woschke

1 Introduction

In pursue of material reducing and lightweight centrifugal rotor systems for medical purposes, the use of carbon-reinforced plastic (CRP) is an interesting concept. However, due to the reduced weight, the impact of operation induced unbalances, i.e. unevenly positioned samples, and consequently the rotor deflections during operation are increased. The integration of ABB units in the design of centrifugal rotors has the potential to counteract the increased susceptibility to unbalance by means of a passive working principle, therefore avoiding the necessity of sensors, actuators or control units. In this study, a CRP rotor for medical centrifuges is equipped with a prototype of an ABB, and the balancing capabilities are evaluated in a test rig presented in Sect. 2. Throughout the design of an ABB, the eccentricity of the ball orbit and the friction between the balancing balls and the cavity walls need to be minimized, while the balancing masses and the orbit radii, limited by the available space, must be maximized to obtain an efficient ABB, as indicated in [1] and [2]. In contrast, the damping effect of the environing fluid is to be neither maximized nor minimized, and an optimal choice is sought [3]. During the transient phase prior to the rotor reaching the final operating speed and the balls adopting their final stationary resting positions relative to the rotor system, the movement of the balls is strongly dependent on the fluid in the cavity. From gaseous environments to highly viscous oils, a wide scope is available to design the ABB properties regarding the fluid damping. In order to demonstrate the influence of the chosen viscous fluid in the ABB on the system behaviour and transient vibrations, different run-up accelerations and fluid properties, i.e. density and viscosity, are considered. Section 3 presents a multibody simulation approach with which the effect of the

L. Spannan (✉) · C. Daniel · E. Woschke
Otto von Guericke University, Magdeburg, Germany
e-mail: lars.spannan@ovgu.de; christian.daniel@ovgu.de; elmar.woschke@ovgu.de

S. Oberst et al. (eds.), *Vibration Engineering for a Sustainable Future*,
https://doi.org/10.1007/978-3-030-46466-0_1

fluid on the balancing masses is modelled by solving the Navier-Stokes equations in the annular cavity and issuing a velocity-dependent drag relation. By comparing the balancing mass movement in the experiments and the simulation model, the suitability to use the simulation in order to identify ideal fluid properties, i.e. density and kinematic viscosity, for the design of ABBs is evaluated.

2 Experimental Test-Rig

The CRP rotor under consideration is depicted in Fig. 1 on the left. An ABB is mounted underneath in a pre-existing cavity. It consists of an aluminium housing, containing the balancing masses and the viscous fluid, which is closed by a transparent acrylic lid in order to visually determine the position of the balancing masses. The rotor system is mounted at the end of an elastic shaft, which is lead from above, mounted in two radial bearings and powered by a belt drive; see Fig. 1 on the right. The rotation is recorded by an encoder, and the deflection of the shaft near the CRP rotor is measured with a laser triangulation sensor, respectively. Due to the low stiffness of the shaft in relation to the rotor mass, the first critical angular frequency of the system is at $\omega_{0,1} = 21.4\,\mathrm{rad\,s^{-1}}$. After an initial conventional balancing of the system in two planes of the CRP rotor, a well-defined additional unbalance is introduced in the balancing plane of the ABB. Due to simplicity, only one balancing ball is considered in the study, while two balls are necessary to counterbalance arbitrary unbalance in the ABB plane. Because the chosen ball is not capable of counterbalancing the additional unbalance completely, the ideal ball position is still easily determined. It is located directly across the additional unbalance with respect to the rotor system. Due to this simplification, the influences of ball collision and drag reduction, caused by slipstream effects of balls close to each other, are avoided.

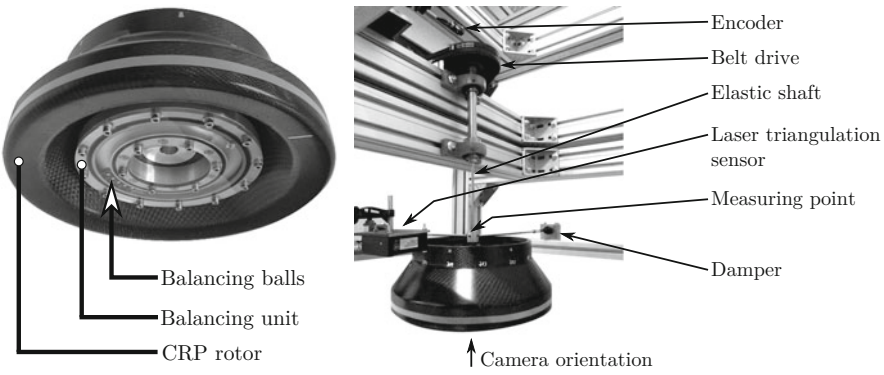

Fig. 1 CRP centrifuge rotor with balancing unit attached (left). Test rig with belt driven elastic shaft (right)

Table 1 Properties of selected silicone oils (polydimethylsiloxane)

$\nu_{25\,°C}$ [mm^2 s^{-1}]	0.65	1.0	3.0	4.0	5.0	10	20	50
$\rho_{25\,°C}$ [kg m^{-3}]	745	795	871	935	893	913	921	942

2.1 Run-up Scenarios

The rotor is accelerated linearly to a nominal speed of 37.7 rad s^{-1}. Depending on the time until the first critical speed is surpassed, a suitable fluid damping, inherently depending on the density and viscosity, is required in order to avoid the unfavourable positioning of the balancing masses at sub-critical speeds as presented in [3] for example. By increasing the run-up time from 5 to 15 s, this relation is highlighted.

2.2 Fluid Properties

The cavity in the ABB system is filled with transparent silicone oil commonly available in a wide range of viscosities. The densities and viscosities for a selection of low viscous silicone oils are presented in Table 1. By exchanging the ABB fluid, the influence on the balancer efficiency under different run-up conditions is examined.

3 Simulation Model

Using a multibody simulation model, the possibility to determine ideal fluid properties a priori in the design stage is evaluated. Representing the system from Sect. 2, the shaft is modelled with a Timoshenko beam, and the deflection and rotation of the upper end are constrained by a bushing force element. The CRP rotor is assumed to be rigid and therefore represented as additional inertia in the system of equations.

The balancing mass is modelled as a rigid sphere with the freedom to move inside the ABB cavity. If contact with the raceway of the cavity is detected, normal forces F_N are induced on a penalty-based approach. Rolling friction $F_R = \mu\, F_N$ and adhesion $F_{\mathrm{Adh,max}} = \mu_0\, F_N$ are considered, also influencing the transient ball position and the final resting position at stationary rotor speed. A possible setup to estimate the coefficient μ is presented in [4].

The flow velocity-dependent drag forces on the balancing balls are not modelled linearly as presented in [3] or [5], for example, but by solving the Navier-Stokes equations for the axisymmetric domain and evaluating a non-linear relationship between the resulting Reynolds number and the drag force

$$F_{\text{Drag}} = \frac{1}{2}\,\rho\,\bar{A}\,C_D(\text{Re})\,v_{\text{flow}}^2, \quad \text{with Re} = \frac{v\,d_{\text{ball}}}{v_{\text{flow}}}\,.$$

Based on an empirical equation linking the drag coefficient C_D and the Reynolds number Re of the flow (see [4]), a more sophisticated model of the fluid structure interaction in ABBs is anticipated [6]. Beneficial of this approach is the description of fluid damping based on quantifiable properties such as density ρ and kinematic viscosity ν of the fluid and the geometry. Widely used linear drag force formulations need to collate mentioned properties in a single damping parameter.

4 Results

In a first comparison, a rotor run-up within 5 s and two different fluids with kinematic viscosities of 3 and 5 $\text{mm}^2\,\text{s}^{-1}$ is considered. An unbalance of magnitude above the compensation capability of the balancing ball is added to the rotor. Its angular position is serving as the reference position. The initial position of the balancing ball is equal to this reference position. Consequently, the ideal position of the balancing ball to have a maximum positive effect on the rotor unbalance and resulting deflections is at π rad.

As can be seen from Fig. 2, the ball environed in the silicone oil with a kinematic viscosity of $\nu = 5\,\text{mm}^2\,\text{s}^{-1}$ settles in its final resting position earlier than the configuration with $\nu = 3\,\text{mm}^2\,\text{s}^{-1}$. Both configurations settle in the vicinity of π rad but show slight differences which are attributed to the effects of friction.

In a second comparison, the acceleration time for the configuration with $\nu = 5\,\text{mm}^2\,\text{s}^{-1}$ is increased from 5 to 15 s; see Fig. 3. Due to the decreased acceleration, the ball, driven by the viscous fluid, shows no significant lag of its orbit velocity compared to the rotor speed. Therefore the ball finds its resting position during

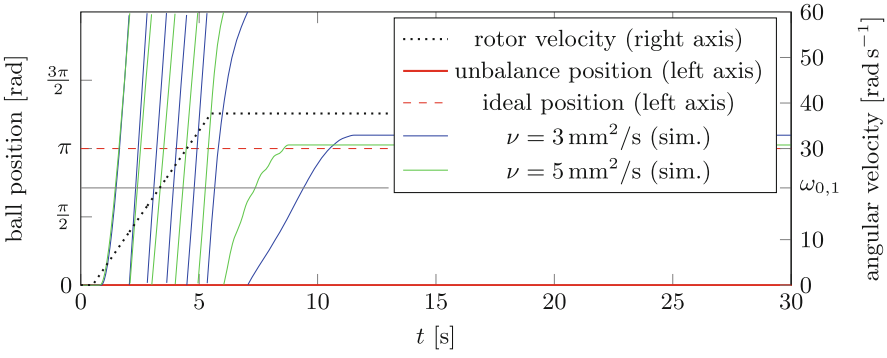

Fig. 2 Ball position with respect to the rotor during run-up for different environing fluids. The additional unbalance is positioned at 0 rad

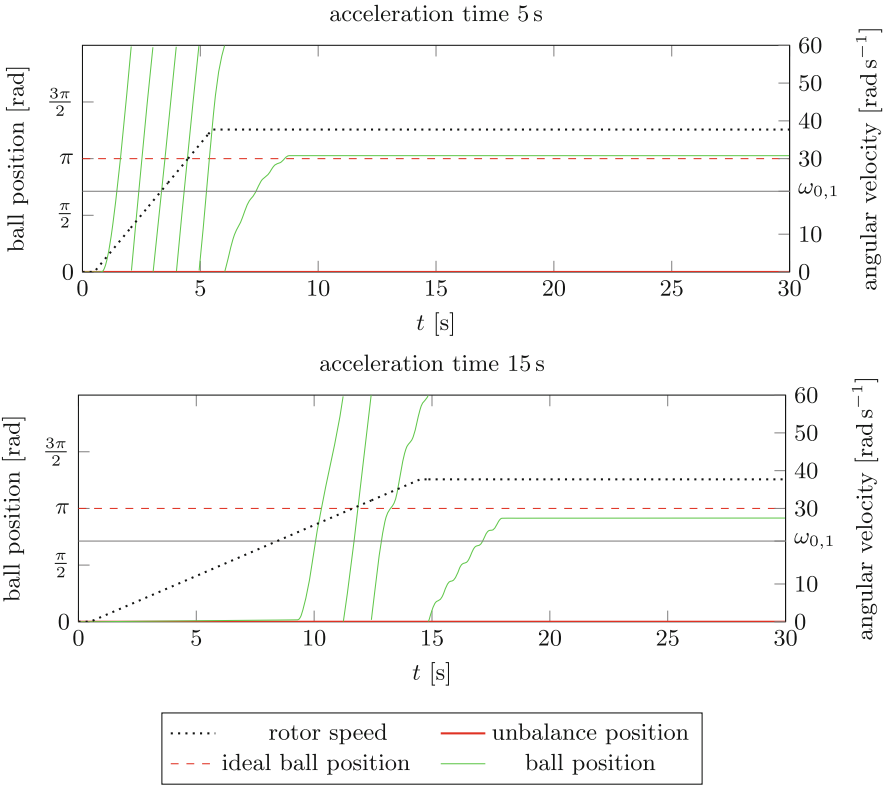

Fig. 3 Simulated ball position with respect to the rotor during run-up for different accelerations. Silicone oil with a kinematic viscosity of $\nu = 5\,\mathrm{mm^2\,s^{-1}}$ is used. The additional unbalance is positioned at 0 rad

sub-critical operation at the undesired location of the primary unbalance, causing increased unbalance excitation of the rotor. After the first critical speed $\omega_{0,1}$ is surpassed at $t \approx 8.5\,\mathrm{s}$, the desired automatic balancing effect can occur. Due to the phase shift of the rotor deflection, the balancing ball is now driven to its optimal resting position at π rad causing a nearly balanced system for $t > 18\,\mathrm{s}$.

5 Conclusion and Outlook

As can be seen from the conducted run-up simulations of different ABB configurations, the influence of fluid damping on the positioning process of the balancing balls is confirmed. In further investigations, the ball movement will be extracted from recordings of the experimental tests, and a comparison to the simulation model can be conducted leading to an evaluation of the presented modelling approach.

By modelling the drag with a velocity-dependent relation based on the solution of the Navier-Stokes equations, only quantifiable properties of the fluid and ABB geometry are required, and the determination of an elusive damping coefficient is avoided. Nevertheless, the a priori determination of suitable friction coefficients still requires experimental studies or experience from ABBs of similar design.

In order to delimit feasible fluid characteristics for a given run-up process in future considerations, the conducted simulations are rerun with different initial positions of the balancing ball. As a result the influence of fluid properties can be distinguished from influences of initial conditions. For future models, the ABB has to be equipped with more than one ball in order to include occurring collision and slipstream effects.

References

1. Ishida, Y., Matsuura, T., Zhang, X.L.: Efficiency improvement of an automatic ball balancer. J. Vib. Acoust. **134**(2), 021012 (2012). https://doi.org/10/fxxtw2
2. Bykov, V.G., Kovachev, A.S.: Dynamics of a rotor with an eccentric ball auto-balancing device. Vestnik St. Petersburg Univ.: Math. **47**(4), 173–180 (2014). https://doi.org/10/ggcdsn
3. Ryzhik, B., Sperling, L., Duckstein, H.: The influence of damping on the efficiency of autobalancing devices for rigid rotors. In: Proceedings of the Second International Symposium on Stability Control of Rotating Machinery ISCORMA-2003, Gdańsk, pp. 104–113 (2003)
4. Spannan, L., Daniel, C., Woschke, E.: Experimental study on the velocity dependent drag coefficient and friction in an automatic ball balancer. Technische Mechanik **37**(1), 62–68 (2017). https://doi.org/10/gf3s8h
5. Green, K., Champneys, A., Friswell, M.: Analysis of the transient response of an automatic dynamic balancer for eccentric rotors. Int. J. Mech. Sci. **48**(3), 274–293 (2006). https://doi.org/10/bgff3w
6. Spannan, L., Daniel, C., Woschke, E.: Simulation of the ball kinetic in ball-type automatic balancing devices by solving the axisymmetric Navier-Stokes equations in annular cavities. In: Proceedings of the 10th International Conference on Rotor Dynamics – IFToMM, vol. 4, pp. 109–118. Springer (2018). https://doi.org/10/gf3s8f

Structural-Acoustic Coupled Analysis by Concentrated Mass Model

S. Hisano, S. Ishikawa, S. Kijimoto, and H. Iwamoto

1 Introduction

FEM is often used as an effective analysis method for vibroacoustic coupling problems. Craggs [1] gave equations of motion in FEM for the structural-acoustic coupled problem. However, eigenvalue analysis requires a long computational time because the mass and stiffness matrices of the equation of motion are asymmetric. Although many methods for symmetrizing these matrices have been proposed, problems with spurious solution and zero eigenvalue occur due to the increase of extra degrees of freedom [2, 3]. From the above background, we are studying an analysis method that has few extra degrees of freedom and symmetric coefficient matrices. In our previous study [4], we proposed a CMM of quadrilateral elements for two-dimensional acoustic space. This model consists of mass points and connecting springs and has variable displacement in its acoustic space. Also, mass points are placed on the edge of each element. This model has symmetric mass and stiffness matrices and does not generate spurious modes and zero eigenvalues. Therefore, structural-acoustic coupled analysis can be performed efficiently. The effectiveness of the CMM was shown in the past for an acoustic space-membrane vibration coupled system. In this paper, we propose the CMM of arbitrary element shape in structural-acoustic coupled analysis. Furthermore, we propose a coordinate transformation method that improves the calculation speed by reducing the degree of freedom. In this way, the coordinates become the sound pressure of the acoustic

S. Hisano (✉) · H. Iwamoto
Seikei University, Musashino-shi, Tokyo, Japan
e-mail: s.hisano@st.seikei.ac.jp; hiroyuki-iwamoto@st.seikei.ac.jp

S. Ishikawa · S. Kijimoto
Kyushu University, Nishi-ku, Fukuoka, Japan
e-mail: ishikawa@mech.kyushu-u.ac.jp; kiji@mech.kyushu-u.ac.jp

S. Oberst et al. (eds.), *Vibration Engineering for a Sustainable Future*,
https://doi.org/10.1007/978-3-030-46466-0_2

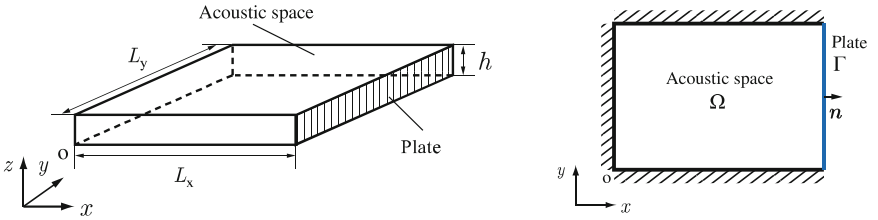

Fig. 1 Analytical target model

space and the displacement of the structure as in the typical FEM, but the symmetry of the coefficient matrices is preserved.

2 Proposed Method

The acoustic space of analysis target is bounded by a flat plate and three rigid walls as in Fig. 1. Each side of the acoustic space is L_x, L_y, h ($h \ll L_x, L_y$), and the thickness of the flat plate is b. The element shapes are arbitrary.

2.1 Equation of Motion of Vibroacoustic System

Deriving the equation of motion by the FEM with the displacement of the acoustic space and the plate as the state quantity, we obtain the following equation [5].

$$\left.\begin{aligned} &\mathbf{M}\ddot{\mathbf{w}}(t) + \mathbf{K}\mathbf{w}(t) = \mathbf{0} \\ &\mathbf{M} = \begin{bmatrix} \mathbf{M}_{aa} & \mathbf{0} & \mathbf{0} \\ \mathbf{0} & \mathbf{M}_{ss} & \mathbf{0} \\ \mathbf{0} & \mathbf{0} & \mathbf{0} \end{bmatrix}, \quad \mathbf{K} = \begin{bmatrix} \mathbf{K}_{aa} & \mathbf{0} & \mathbf{K}_{ap} \\ \mathbf{0} & \mathbf{K}_{ss} & \mathbf{K}_{sp} \\ \mathbf{K}_{pa} & \mathbf{K}_{ps} & \mathbf{0} \end{bmatrix}, \quad \mathbf{w}(t) = \begin{bmatrix} \mathbf{x}_a(t) \\ \xi(t) \\ \mathbf{p}_b(t) \end{bmatrix} \end{aligned}\right\} \tag{1}$$

where $\mathbf{x}_a(t), \xi(t)$ are a displacement vector of the acoustic space and the flat plate and $\mathbf{p}_b(t)$ is a sound pressure vector acting perpendicular to the coupled boundary. $\mathbf{M}$ and $\mathbf{K}$ are mass matrix and Stiffness matrix; both matrices are symmetric.

2.2 Coordinate Transformation

In this section, the extra degrees of freedom of Eq. (1) are reduced by performing coordinate transformation. The internal and boundary elements Ω, Γ of the coupled system are separated as follows:

$$\left.\mathbf{x}_{\mathrm{a}} = \begin{bmatrix} \mathbf{x}_{\mathrm{a}}^{\Omega} \\ \mathbf{x}_{\mathrm{a}}^{\Gamma} \end{bmatrix},\ \xi = \xi^{\Gamma} \right\} \tag{2}$$

Ω, Γ represent an element corresponding to the inner area or the boundary area, respectively. Assuming that the acoustic space element is a primary element for simplicity, the following equation holds:

$$\left.\mathbf{K}_{\mathrm{pa}}^{\Gamma}\mathbf{x}_{\mathrm{a}}^{\Gamma} + \mathbf{K}_{\mathrm{ps}}^{\Gamma}\xi^{\Gamma} = \mathbf{0} \ \Rightarrow\ \mathbf{x}_{\mathrm{a}}^{\Gamma} = \mathbf{Z}\xi^{\Gamma},\ \mathbf{Z} = -\left(\mathbf{K}_{\mathrm{pa}}^{\Gamma}\right)^{-1}\mathbf{K}_{\mathrm{ps}}^{\Gamma} \right\} \tag{3}$$

From Eqs. (2) and (3), Eq. (1) can be modified as follows:

$$\begin{bmatrix} \mathbf{M}_{\mathrm{aa}}^{\Omega\Omega} & \mathbf{M}_{\mathrm{aa}}^{\Omega\Gamma}\mathbf{Z} \\ \mathbf{Z}^{\mathrm{T}}\mathbf{M}_{\mathrm{aa}}^{\Gamma\Omega} & \mathbf{Z}^{\mathrm{T}}\mathbf{M}_{\mathrm{aa}}^{\Gamma\Gamma}\mathbf{Z}+\mathbf{M}_{\mathrm{ss}}^{\Gamma\Gamma} \end{bmatrix} \begin{bmatrix} \ddot{\mathbf{x}}_{\mathrm{a}}^{\Omega} \\ \ddot{\xi}^{\Gamma} \end{bmatrix} + \begin{bmatrix} \mathbf{K}_{\mathrm{aa}}^{\Omega\Omega} & \mathbf{K}_{\mathrm{aa}}^{\Omega\Gamma}\mathbf{Z} \\ \mathbf{Z}^{\mathrm{T}}\mathbf{K}_{\mathrm{aa}}^{\Gamma\Omega} & \mathbf{Z}^{\mathrm{T}}\mathbf{K}_{\mathrm{aa}}^{\Gamma\Gamma}\mathbf{Z} + \mathbf{K}_{\mathrm{ss}}^{\Gamma\Gamma} \end{bmatrix} \begin{bmatrix} \mathbf{x}_{\mathrm{a}}^{\Omega} \\ \xi^{\Gamma} \end{bmatrix} = \begin{bmatrix} \mathbf{0} \\ \mathbf{0} \end{bmatrix} \tag{4}$$

The sound pressure vector $\mathbf{p} = [dp_{\mathrm{ae},1}\ \ dp_{\mathrm{ae},2}\ \cdots\ dp_{\mathrm{ae},N}]^{\mathrm{T}}$ is defined using the i-th element average sound pressure $dp_{\mathrm{ae},i}$. The sound pressure vector $\mathbf{p}$ and the displacement vector $\mathbf{x}_{\mathrm{a}}$ have the following relation:

$$\begin{bmatrix} \mathbf{p} \\ \xi^{\Gamma} \end{bmatrix} = \begin{bmatrix} \mathbf{T}^{\Omega} & \mathbf{T}^{\Gamma}\mathbf{Z} \\ \mathbf{0} & \mathbf{I} \end{bmatrix} \begin{bmatrix} \mathbf{x}_{\mathrm{a}}^{\Omega} \\ \xi^{\Gamma} \end{bmatrix} \tag{5}$$

where $\mathbf{T}^{\Omega}$, $\mathbf{T}^{\Gamma}$ are transformation matrices. The total potential energy of the coupled system $U_{\mathrm{c}}(t)$ is expressed as follows using sound pressure vector $\mathbf{p}$:

$$U_{\mathrm{c}}(t) = \frac{1}{2}\mathbf{p}^{\mathrm{T}}\alpha\mathbf{I}\mathbf{p} + \frac{1}{2}\xi^{\mathrm{T}}\mathbf{K}_{\mathrm{ss}}\xi = \frac{1}{2}\begin{bmatrix} \mathbf{x}_{\mathrm{a}}^{\Omega} \\ \xi^{\Gamma} \end{bmatrix}^{\mathrm{T}} \begin{bmatrix} \mathbf{T}^{\Omega} & \mathbf{T}^{\Gamma}\mathbf{Z} \\ \mathbf{0} & \mathbf{I} \end{bmatrix} \begin{bmatrix} \alpha\mathbf{I} & \mathbf{0} \\ \mathbf{0} & \mathbf{K}_{\mathrm{ss}} \end{bmatrix} \begin{bmatrix} \mathbf{p} \\ \xi^{\Gamma} \end{bmatrix} \tag{6}$$

where $\alpha = V_{\mathrm{ae}}/\rho_{\mathrm{a}}c_{\mathrm{a}}^2$, ρ_{a} is density of air, c_{a} is speed of sound, and V_{ae} is the element volume of the acoustic space. On the other hand, the potential energy $U_{\mathrm{c}}(t)$ can also be expressed as follows using displacement vector $\mathbf{x}_{\mathrm{a}}$:

$$U_{\mathrm{c}}(t) = \frac{1}{2}\mathbf{x}_{\mathrm{a}}^{\mathrm{T}}\mathbf{K}_{\mathrm{aa}}\mathbf{x}_{\mathrm{a}} + \frac{1}{2}\xi^{\mathrm{T}}\mathbf{K}_{\mathrm{ss}}\xi = \frac{1}{2}\begin{bmatrix} \mathbf{x}_{\mathrm{a}}^{\Omega} \\ \xi^{\Gamma} \end{bmatrix}^{\mathrm{T}} \begin{bmatrix} \mathbf{K}_{\mathrm{aa}}^{\Omega\Omega} & \mathbf{K}_{\mathrm{aa}}^{\Omega\Gamma}\mathbf{Z} \\ \mathbf{Z}^{\mathrm{T}}\mathbf{K}_{\mathrm{aa}}^{\Gamma\Omega} & \mathbf{Z}^{\mathrm{T}}\mathbf{K}_{\mathrm{aa}}^{\Gamma\Gamma}\mathbf{Z} + \mathbf{K}_{\mathrm{ss}} \end{bmatrix} \begin{bmatrix} \mathbf{x}_{\mathrm{a}}^{\Omega} \\ \xi^{\Gamma} \end{bmatrix} \tag{7}$$

The following equation is obtained from Eqs. (6) and (7):

$$\begin{bmatrix} \mathbf{T}^{\Omega} & \mathbf{T}^{\Gamma}\mathbf{Z} \\ \mathbf{0} & \mathbf{I} \end{bmatrix} \begin{bmatrix} \alpha\mathbf{I} & \mathbf{0} \\ \mathbf{0} & \mathbf{K}_{\mathrm{ss}} \end{bmatrix} \begin{bmatrix} \mathbf{p} \\ \xi^{\Gamma} \end{bmatrix} = \begin{bmatrix} \mathbf{K}_{\mathrm{aa}}^{\Omega\Omega} & \mathbf{K}_{\mathrm{aa}}^{\Omega\Gamma}\mathbf{Z} \\ \mathbf{Z}^{\mathrm{T}}\mathbf{K}_{\mathrm{aa}}^{\Gamma\Omega} & \mathbf{Z}^{\mathrm{T}}\mathbf{K}_{\mathrm{aa}}^{\Gamma\Gamma}\mathbf{Z} + \mathbf{K}_{\mathrm{ss}}^{\Gamma\Gamma} \end{bmatrix} \begin{bmatrix} \mathbf{x}_{\mathrm{a}}^{\Omega} \\ \xi^{\Gamma} \end{bmatrix} \tag{8}$$

Coordinate transformation of Eq. (4) is performed using Eqs. (5) and (8). As a result, the following equation of motion is obtained:

$$\left.\begin{aligned} &\ddot{\mathbf{p}}_{\mathrm{s}} + \mathbf{A}_{\mathrm{p}}\mathbf{B}_{\mathrm{p}}\mathbf{p}_{\mathrm{s}} = \mathbf{0} \\ &\mathbf{A}_{\mathrm{p}} = \mathbf{T}_{\mathrm{p}}\mathbf{M}_{\mathrm{c}}^{-1}\mathbf{T}_{\mathrm{p}}^{\mathrm{T}},\ \mathbf{T}_{\mathrm{p}} = \begin{bmatrix} \mathbf{T}^{\Omega} & \mathbf{T}^{\Gamma}\mathbf{Z} \\ \mathbf{0} & \mathbf{I} \end{bmatrix},\ \mathbf{M}_{\mathrm{c}} = \begin{bmatrix} \mathbf{M}_{\mathrm{aa}}^{\Omega\Omega} & \mathbf{M}_{\mathrm{aa}}^{\Omega\Gamma}\mathbf{Z} \\ \mathbf{Z}^{\mathrm{T}}\mathbf{M}_{\mathrm{aa}}^{\Gamma\Omega} & \mathbf{Z}^{\mathrm{T}}\mathbf{M}_{\mathrm{aa}}^{\Gamma\Gamma}\mathbf{Z} + \mathbf{M}_{\mathrm{ss}}^{\Gamma\Gamma} \end{bmatrix} \\ &\mathbf{B}_{\mathrm{p}} = \begin{bmatrix} \alpha\mathbf{I} & \mathbf{0} \\ \mathbf{0} & \mathbf{K}_{\mathrm{ss}} \end{bmatrix},\ \mathbf{p}_{\mathrm{s}} = \begin{bmatrix} \mathbf{p} \\ \xi^{\Gamma} \end{bmatrix} \end{aligned}\right\} \tag{9}$$

Equation (9) has reduced degrees of freedom compared to Eq. (1), and the coefficient matrix $\mathbf{A}_{\mathrm{p}}$and $\mathbf{B}_{\mathrm{p}}$ are symmetrical. Therefore, eigenvalue calculation can be performed efficiently. Inverse matrix operations $\mathbf{M}_{\mathrm{c}}^{-1}$ are less computationally costly than eigenvalue analysis because $\mathbf{M}_{\mathrm{c}}$ is a sparse and symmetric matrix. Furthermore, when formulating elements as a lumped mass model, $\mathbf{M}_{\mathrm{c}}$ is simplified as follows:

$$\mathbf{M}_{\mathrm{c}} = \begin{bmatrix} \mathbf{M}_{\mathrm{aa}}^{\Omega\Omega} & \mathbf{0} \\ \mathbf{0} & \mathbf{Z}^{\mathrm{T}}\mathbf{M}_{\mathrm{aa}}^{\Gamma\Gamma}\mathbf{Z} + \mathbf{M}_{\mathrm{ss}}^{\Gamma\Gamma} \end{bmatrix} \tag{10}$$

where $\mathbf{M}_{\mathrm{aa}}^{\Omega\Omega}$ and $\mathbf{M}_{\mathrm{ss}}^{\Omega\Omega}$ are diagonal matrices. By using Eq. (10), the matrix $\mathbf{A}_{\mathrm{p}}$ becomes sparse matrix, and inverse matrix operation and eigenvalue operation become more efficient. This method can also be used for large-scale calculations.

3 Eigenvalue Analysis

Eigenvalue analysis is performed to confirm the effectiveness of the proposed method. As the proposed method, the eigenvalue analysis method is shown for the model of Eq. (9), and the eigenvalue analysis method of the two-dimensional acoustic space one-dimensional plate coupled system by FEM is shown for comparison. We compare the results of the eigenvalue analysis with the proposed method and conventional FEM. The calculation accuracy and calculation speed of the proposed method are evaluated by the analysis results.

3.1 Proposed Eigenvalue Analysis

Assuming harmonic vibration in Eq. (9), we obtain the asymmetric general eigenvalue problem that can be expressed by the following equation:

$$\mathbf{A}_{\mathrm{p}}\mathbf{B}_{\mathrm{p}}\mathbf{P} = \omega^2\mathbf{P} \tag{11}$$

where both $\mathbf{A}_\mathrm{p}$ and $\mathbf{B}_\mathrm{p}$ are symmetric. Equation (11) can be converted to a symmetric standard eigenvalue problem using Cholesky decomposition. $\mathbf{B}_\mathrm{p} = \mathbf{L}_\mathrm{p}\mathbf{L}_\mathrm{p}^\mathrm{T}$ is decomposed using the lower triangular matrix $\mathbf{L}_\mathrm{p}$. Substituting $\mathbf{B}_\mathrm{p} = \mathbf{L}_\mathrm{p}\mathbf{L}_\mathrm{p}^\mathrm{T}$ into Eq. (11) and multiplying $\mathbf{L}_\mathrm{p}^\mathrm{T}$ from left to both sides gives the standard eigenvalue problem of the symmetric matrix as follows:

$$\left.\mathbf{L}_\mathrm{p}^\mathrm{T}\mathbf{A}_\mathrm{p}\mathbf{L}_\mathrm{p}\tilde{\mathbf{P}} = \omega^2\tilde{\mathbf{P}},\ \tilde{\mathbf{P}} = \mathbf{L}_\mathrm{p}^\mathrm{T}\mathbf{P}\right\} \tag{12}$$

3.2 Eigenvalue Analysis by Craggs

The eigenvalue analysis method by Craggs [1] is shown as a comparison object of the proposed method. We can obtain the following asymmetric Eq. (1):

$$\left.\begin{aligned}&\tilde{\mathbf{M}}\ddot{\mathbf{u}} + \tilde{\mathbf{K}}\mathbf{u} = \mathbf{0}\\ &\tilde{\mathbf{M}} = \begin{bmatrix}\tilde{\mathbf{M}}_{\mathrm{aa}} & \tilde{\mathbf{M}}_{\mathrm{as}}\\ \mathbf{0} & \tilde{\mathbf{M}}_{\mathrm{ss}}\end{bmatrix},\ \tilde{\mathbf{K}} = \begin{bmatrix}\tilde{\mathbf{K}}_{\mathrm{aa}} & \mathbf{0}\\ \tilde{\mathbf{K}}_{\mathrm{sa}} & \tilde{\mathbf{K}}_{\mathrm{ss}}\end{bmatrix},\ \mathbf{u} = \begin{bmatrix}\tilde{\mathbf{p}}\\ \tilde{\xi}\end{bmatrix}\end{aligned}\right\} \tag{13}$$

where $\tilde{\mathbf{p}}$ is the sound pressure vector at the element node position and $\tilde{\xi}$ is the displacement vector of the plate. $\tilde{\mathbf{M}}$, $\tilde{\mathbf{K}}$ are mass matrix and stiffness matrix. From Eq. (13), both matrices $\tilde{\mathbf{M}}$, $\tilde{\mathbf{K}}$ have asymmetry. Assuming harmonic vibration in Eq. (13) to perform eigenvalue analysis, we obtain the following equation:

$$\tilde{\mathbf{M}}^{-1}\tilde{\mathbf{K}}\mathbf{U} = \omega^2\mathbf{U} \tag{14}$$

Equation (14) is an asymmetric standard eigenvalue problem.

3.3 Numerical Calculation

Eigenvalue analysis of a coupled system is performed using rectangular elements as shown in Fig. 2, where x_{ei}, y_{ei} are the displacement of the air in the direction x, y, w_{ei}, θ_{ei} are the bending displacement and bending angle at both ends, p_{be} is a sound pressure acting to the coupled boundary of element, and l_x, l_y are the element length. Orange dots indicate displacement of acoustic space, and blue dots indicate displacements of structures. Figure 3 shows the node arrangement by the quadrilateral element where the division number of the acoustic space in the x, y directions is $N_\mathrm{x} = 4$, $N_y = 3$. Table 1 shows the analytical condition used for analysis. Table 2 shows the comparison results of the natural frequency obtained by the CMM (Eq. (12)) and conventional FEM (Eq. (14)). In eigenvalue analysis, "eigs function" of Matlab 2018a is used. $\tilde{\mathbf{M}}^{-1}$ in Eq. (14) is calculated in advance, and the calculation time is not included in the evaluation. The division number of the

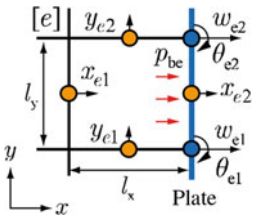

Fig. 2 Element definition

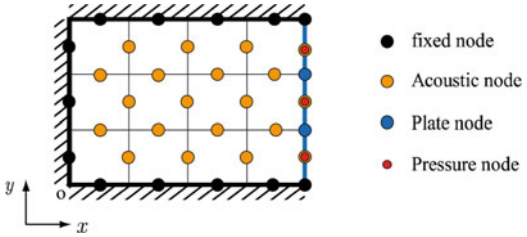

Fig. 3 Node position in rectangular element

Table 1 Analytical conditions

(L_x, L_y) [m]	(0.5, 0.4)
(h, b) [m]	(0.02, 0.001)
p_0 [kPa]	101.3
c_a [m/s]	334.2
(ρ_a, ρ_s) [kg/m^3]	(1.27, 2700)
γ	1.4
E [GPa]	68.3

Table 2 Comparison of natural frequency

Modal number	Natural frequency [Hz]	
	CMM	FEM
1	51.83	51.83
2	87.23	87.23
3	172.96	172.96
4	285.07	285.09
5	340.16	340.22

acoustic space in the x, y directions is $N_x = 75$, $N_y = 60$. Five natural frequencies from the lower order of the coupled system are indicated. The natural frequencies calculated by CMM and FEM agree well. Therefore, eigenvalue analysis by the proposed method is valid. Table 3 shows the degrees of freedom and the calculation time by each method. Degrees of freedom by CMM and FEM are about the same although two division numbers are shown. The proposed method can perform eigenvalue analysis faster than FEM because the asymmetry of the FEM eigenvalue problem significantly slows down the calculation of the eigenvalues.

Table 3 Comparison of calculation time

N_x	N_y	CMM (Eq. (12))		FEM (Eq. (14))	
		DOF	Time [s]	DOF	Time [s]
25	20	538	0.04	584	0.43
75	60	4618	8.52	4754	69.22

4 Conclusion

In this study, an analysis method using a lumped mass model was shown in order to develop an efficient analysis method for vibroacoustics. We proposed a method to reduce the extra degrees of freedom by coordinate transformation of the equation of motion. This method preserves the symmetry of the coefficient matrix after transformation. Eigenvalue analysis was performed by the proposed method and the conventional FEM. Proposed method is faster than the conventional FEM in the analysis.

References

1. Craggs, A.: The transient response of a coupled plate-acoustic system using plate and acoustic finite elements. J. Sound Vib. **15**, 509–528 (1971)
2. Bermudez, A., et al.: Computational Acoustics of Noise Propagation in Fluids – Finite Element Methods. Springer, Berlin (2008)
3. Sigrist, J.: Fluid-Structure Interaction. Willey, Southampton (2015)
4. Ishikawa, S., Matsuo, A., Akayama, Y., Kijimoto, S.: Coupled analysis of two-dimensional acoustic and membrane vibration by concentrated mass model. Adv. Mech. Eng. **9**(12), 1–13 (2017)
5. Bermudezs, A., Hervella-Nieto, L.: Finite element computation of three-dimensional acoustic and membrane vibration by concentrated mass model. J. Sound Vib. **219**(2), 279–306 (1999)

Evaluation of Isolated Dynamic Properties of the Component Connected with Main Structure

Shunsuke Takada, Takuya Yoshimura, and Kohei Furuya

1 Introduction

At present, computer-aided engineering (CAE) analysis is utilized in dynamic design to predict performance in various industrial fields. However, if numerical modeling is not accurate, CAE cannot predict properties correctly. When complex structures having a large number of parts are targeted, it is not easy to identify which part has lack of accuracy [1]. For solving this problem, there would be a direct approach for comparing properties of the component; frequency response functions (FRFs) are evaluated in an isolated situation after removing the interest component from the assembly. However, this approach is time consuming and inefficient. Hence, it is necessary to develop a method that can evaluate vibration characteristics of components in an isolated condition without removing.

We had proposed *a nodal constraint method* [2]. It extracts the vibration characteristics of the target subcomponent alone when the boundary elements are under constraints. By this method, it is possible to identify the factor of FRF difference between models efficiently. However, in the case of components connected with many degrees of freedom, the effects of noise such as measurement errors are magnified, making it difficult to compare models. In this study, we propose more noise-effective method than the original approach. In order to reduce the noise effect, we propose a method that reduces degrees of freedom at the connecting part using singular value decomposition [3–5].

S. Takada (✉) · T. Yoshimura
Department of Mechanical Systems Engineering, Tokyo Metropolitan University, Hachioji-shi, Tokyo, Japan
e-mail: takada-shunsuke1@ed.tmu.ac.jp; yoshimu@tmu.ac.jp

K. Furuya
Department of Mechanical Engineering, Gifu University, Gifu-shi, Gifu-ken, Japan
e-mail: furuya@gifu-u.ac.jp

S. Oberst et al. (eds.), *Vibration Engineering for a Sustainable Future*,
https://doi.org/10.1007/978-3-030-46466-0_3

2 Derivation of the Nodal Constraint Method

In this section, we explain the nodal constraint method. We consider a structure shown in Fig. 1. In this structure, a main system and a subcomponent r are connected at a connecting part U that has m degrees of freedom.

The relationship between input and output in Fig. 1 is written as

$$\begin{Bmatrix} \boldsymbol{X_r} \\ \boldsymbol{X_U} \end{Bmatrix} = \begin{bmatrix} \boldsymbol{G_{rr}} & \boldsymbol{G_{rU}} \\ \boldsymbol{G_{Ur}} & \boldsymbol{G_{UU}} \end{bmatrix} \begin{Bmatrix} \boldsymbol{F_r} \\ \boldsymbol{F_U} \end{Bmatrix} \tag{1}$$

where $\boldsymbol{G}$ is a FRF matrix between subscript and $\boldsymbol{F}$ and $\boldsymbol{X}$ are excitation force and displacement indicated by a subscript, respectively. Assuming that the displacement of the connecting part is zero: $\boldsymbol{X_U} = 0$ and substituting this in the second row of Eq. (1) gives

$$\boldsymbol{F_U} = -\boldsymbol{G_{UU}}^{-1}\boldsymbol{G_{Ur}}\boldsymbol{F_r}, \tag{2}$$

Equation (2) is substituted into the first row of Equation (1) and divided by the excitation force $\boldsymbol{F_r}$. We obtain

$$\boldsymbol{G_{rr}}^{*} = \boldsymbol{G_{rr}} - \boldsymbol{G_{rU}}\boldsymbol{G_{UU}}^{-1}\boldsymbol{G_{Ur}}. \tag{3}$$

Equation (3) is a driving point FRF at the evaluation point r when the connecting part U is constrained. It gives the nodal constraint method, by which we can extract and evaluate vibration characteristics of a single component without removing from main structure. However, according to Eq. (3), the method requires the inverse $\boldsymbol{G_{UU}}$ matrix, which is prone to be affected by measurement errors.

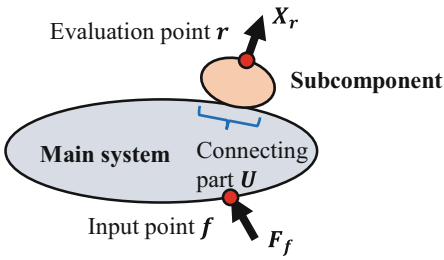

Fig. 1 Schema of structure

3 Formulation of the Reduction Method of Degrees of Freedom at the Connecting Part

We propose an improved nodal constraint method in order to suppress the influence of measurement error expansion caused by inverse matrix calculation. It is attained by reduction of degrees of freedom at the connecting part using singular value decomposition. Formulation of the proposed method is described.

As in Chap. 2, we consider the structure shown in Fig. 1. Let frequency range of interest be $\omega_1, \ldots, \omega_k$ and arrange FRF $\boldsymbol{G}_{\boldsymbol{UU}}^{\boldsymbol{\omega}}$ at the connecting part $\boldsymbol{X}_{\boldsymbol{U}}$. It gives

$$\boldsymbol{G}_{\boldsymbol{UU}}^{\boldsymbol{\omega}} = \begin{bmatrix} G_{u1u1}(\omega_1), \ldots, G_{u1u1}(\omega_k) & G_{u1u2}(\omega_1), \ldots, G_{u1u2}(\omega_k) & \cdots & G_{u1um}(\omega_1), \ldots, G_{u1um}(\omega_k) \\ G_{u2u1}(\omega_1), \ldots, G_{u2u1}(\omega_k) & G_{u2u2}(\omega_1), \ldots, G_{u2u2}(\omega_k) & \cdots & G_{u2um}(\omega_1), \ldots, G_{u2um}(\omega_k) \\ \vdots & \vdots & \ddots & \vdots \\ G_{umu1}(\omega_1), \ldots, G_{umu1}(\omega_k) & G_{umu2}(\omega_1), \ldots, G_{umu2}(\omega_k) & \cdots & G_{umum}(\omega_1), \ldots, G_{umum}(\omega_k) \end{bmatrix} \tag{4}$$

This is separated into real and imaginary parts to create a matrix $\boldsymbol{R}$, which is factorized by the singular value decomposition. It can be expressed as

$$\boldsymbol{R} = \left[\operatorname{Re}\left[\boldsymbol{G}_{\boldsymbol{UU}}^{\boldsymbol{\omega}}\right], \operatorname{Im}\left[\boldsymbol{G}_{\boldsymbol{UU}}^{\boldsymbol{\omega}}\right] \right] = \boldsymbol{P}\,\boldsymbol{D}\,\boldsymbol{Q}^{T} \tag{5}$$

where $\boldsymbol{P}$ and $\boldsymbol{Q}$ are orthogonal matrices and $\boldsymbol{D}$ is a diagonal matrix expressed as

$$\boldsymbol{D} = \left[\operatorname{diag}\left(d_1, d_2, \ldots, d_m | 0_{m\times(n-m)}\right) \right] \tag{6}$$

The nonnegative real values $\{d_i \geq 0\}_{i=1}^{m}$ of $\boldsymbol{D}$ are called singular values of matrix $\boldsymbol{R}$. The reason for separating the matrix into real and imaginary parts and performing singular value decomposition is that the elements of $\boldsymbol{P}$ are real. Here, assuming that $d_{t+1} = \ldots = d_m \simeq 0$, the orthogonal basis vectors of the columns of $\boldsymbol{R}$ are $\boldsymbol{p_1}, \ldots, \boldsymbol{p_t}$ which are the column components of $\boldsymbol{P}$, and these are put together to obtain

$$\boldsymbol{P_t} = \left[\boldsymbol{p_1}, \ldots, \boldsymbol{p_t}\right] \tag{7}$$

By evaluating cumulative contribution ratio for $\boldsymbol{R}$, approximation in an appropriate range becomes possible. The cumulative contribution ratio s when the matrix is approximated by the rank t is given by

$$\mathrm{s} = \frac{\sum_{i=1}^{t} {d_i}^2}{\sum_{i=1}^{m} {d_i}^2} \tag{8}$$

Secondly, the displacement $\boldsymbol{X_U}$ and the excitation force $\boldsymbol{F_U}$ of the connecting part are reduced to t dimensions as follows:

$$\boldsymbol{P}_t^T \boldsymbol{X}_U = \boldsymbol{P}_t^T \boldsymbol{G}_{Ur} \boldsymbol{F}_r + \boldsymbol{P}_t^T \boldsymbol{G}_{UU} \boldsymbol{F}_U \tag{9}$$

$$\boldsymbol{F}_U = \boldsymbol{P}_t \boldsymbol{F}_t \tag{10}$$

Using the Eqs. (9) and (10), we obtain

$$\boldsymbol{F}_t = -\left(\boldsymbol{P}_t^T \boldsymbol{G}_{UU} \boldsymbol{P}_t\right)^{-1} \boldsymbol{P}_t^T \boldsymbol{G}_{Ur} \boldsymbol{F}_r \tag{11}$$

by considering the restraint force ($\boldsymbol{P}_t^T \boldsymbol{X}_U = 0$) acting on the connecting part. Substituting Eqs. (10) and (11) into the first row of Eq. (1), we obtain

$$\boldsymbol{G}_{rr}{}^{**} = \boldsymbol{G}_{rr} - \boldsymbol{G}_{rU} \boldsymbol{P}_t \left(\boldsymbol{P}_t^T \boldsymbol{G}_{UU} \boldsymbol{P}_t\right)^{-1} \boldsymbol{P}_t^T \boldsymbol{G}_{Ur} \tag{12}$$

by dividing both sides by the excitation force $\boldsymbol{F}_r$ at the evaluation point. This is the nodal constraint method in which degrees of freedom of the connecting part is reduced to t degrees of freedom.

4 Application of Reduced Nodal Constraint Method to Automotive Parts

4.1 Model Outline and Experiment Conditions

In this research, we examined a cut body which is separated from an automobile body (see Fig. 2); Fig. 2a is an experimental model, and Fig. 2b is a numerical model. A battery with a supporting stay shown in Fig. 2 is a target component. The connecting part between the battery and the connecting structure has three translational degrees of freedom from ① to ④ except for the z-axis direction of ② and ③, and measurement was performed with 10 degrees of freedom. An evaluation point is ⑤ that is at the top of the battery; a driving point FRF at ⑤ is estimated by the proposed method.

4.2 Experimental Result and Consideration

Figure 3 shows the results of comparing driving point FRFs (y-axis direction) of the battery between the models in the state of being attached to the cut body. As can be seen from this figure, plural peaks can be observed in this condition, and the natural modes due to the coupled vibration with the main structure are excited. This is because the substructure of the battery is not be isolated from the main structure.

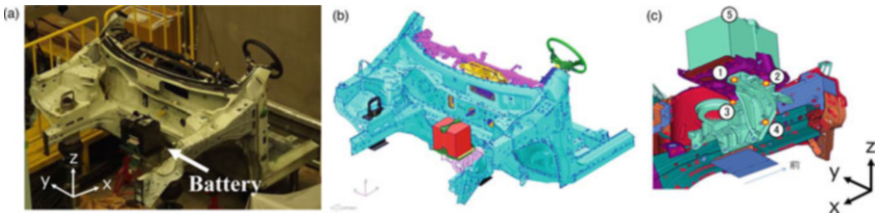

Fig. 2 Target models. (**a**) Experimental model. (**b**) Numerical model. (**c**) Battery

Fig. 3 Comparison of driving point FRFs

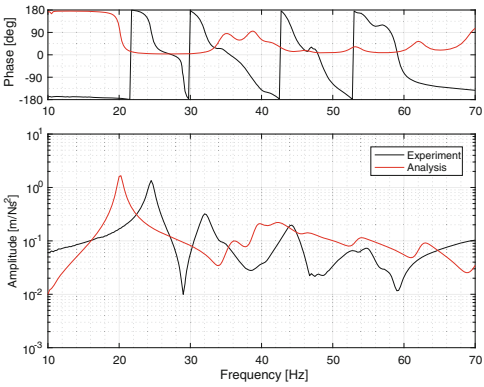

Figure 4 shows driving point FRFs (y-axis direction) using the conventional method. From this figure, it can be seen that the effects of noise appear prominently in the FRFs, making it difficult to compare the vibration characteristics between the models. In addition, the amplitudes of the FRFs show large discrepancy. As a result, we found that the FRF matrix between each degree of freedom of the coupling part ($\boldsymbol{G_{UU}}$ in Eq. (12)) in the numerical model is ill-conditioned. These FRF matrices are calculated at each frequency step, and the maximum values of the condition numbers are 6.6×10^3 and 2.8×10^7 in the experimental and numerical models, respectively. Therefore, the difference of amplitudes is greatly expanded when the inverse matrix calculation is performed. Ill-conditioning of the FRF matrix means that the behavior of the each FRF in the coupling degrees of freedom is not fully independent.

Secondly, we applied the reduction method proposed in this research. First, singular value decomposition is applied on the FRF matrix at the coupling degrees of freedom of the connecting part (see Fig. 5). The magnitude of the tenth singular value is clearly smaller than that of the first one. By evaluating the cumulative contribution rate, it is confirmed that more than 0.99 of the original matrix can be expressed even if the singular values are adopted up to five major ones. Therefore, we judged that the matrix can be reduced to five degrees of freedom.

Based on the above examination, driving point FRFs are compared between the models (see Fig. 6). From this figure, we confirmed that the influence of noise is significantly reduced and the peaks are compared more easily than the conventional

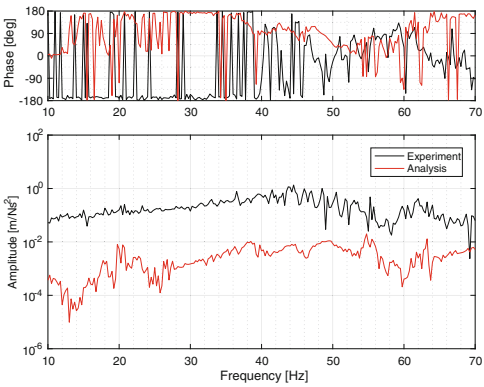

Fig. 4 Application of conventional method

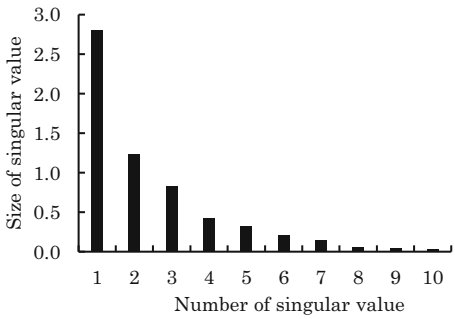

Fig. 5 Result of singular value decomposition

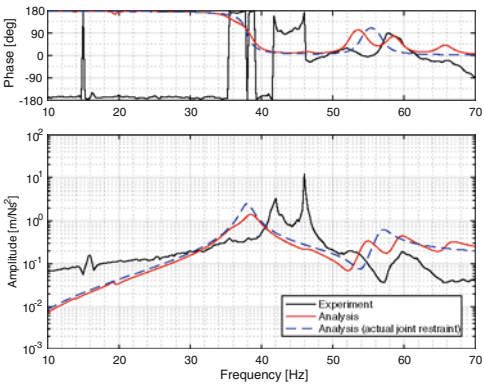

Fig. 6 Application of proposed method

method shown in Fig. 4. In both models, there are two dominant peaks at around 40 Hz and 60 Hz. From the shift of these peaks, we confirmed that the discrepancy exists between the models; we found that the vibration characteristics could be easily compared between the models by using the proposed approach. Figure 6 also shows a driving point FRF of the numerical model when three degrees of freedom for each of the five connecting part are actually constrained. It can be concluded that the driving point FRFs is properly estimated by the proposed approach.

5 Conclusion

In this paper, we proposed a method to reduce the noise effect in the nodal constraint method. Moreover, we examined the validity of the method by conducting the vibration experiment on an automobile component.

For the automotive component, we confirmed that the influence of noise in the conventional method can be significantly reduced by decreasing the coupling degrees of freedom at the connecting part. Furthermore, the number of degrees of freedom necessary for describing the FRF at the connecting part can be determined by applying the singular value decomposition to the FRF matrix.

References

1. Ishinabe, Y., et al.: Investigation of parts with insufficient accuracy for prediction of noise and vibration by sensitivity analysis. Dyn. Des. Conf. **2016**, 364 (2016)
2. Kimura, Y., et al.: Identification of contributing factors to difference of FRFs between finite element model and actual structure: (theory of nodal constraint method and application to a simple model). Dyn. Des. Conf. **2017**, 433 (2017)
3. Takada, S., et al.: Validity check of the numerical model by applying reduction approach. Mech. Eng. Congress. **243**, G1000806 (2018)
4. van der Seijs, M.V., et al.: Validation of current state Frequency Based Substructuring Technology for the characterization of Steering Gear – Vehicle Interaction. In: Topics in Experimental Dynamic Substructuring, vol. 2, pp. 253–266. Springer, New York (2014)
5. Mirza, W.I., et al.: Frequency based substructuring for structure with double bolted joints: a case study. Int. J. Automot. Mech. Eng. **16**, 6188–6199 (2019)

Modeling of Complex Modes with Wave-Based Scaling

C. Nerse and S. Wang

1 Introduction

In the literature, complex modes are subject of applications that range from composites to rotating machineries [1, 2]. Complex modes have been shown to exhibit wave characteristics, and its composition with respect to traveling wave and standing wave was introduced [3]. Complex modes that result from non-uniform distribution of damping have been studied. Eigensolution and sensitivity analyses were undertaken to estimate the variation with respect to system parameters. For lightly damped systems, approximation methods were developed to obtain the complex eigenvectors from undamped modal parameters [4]. These advancements have widened the perspective in which we view the complex modes. In a more recent work, a new approach was proposed to model complex modes with a waveguide, for a simple non-proportional damping configuration [5]. It was shown that complex modes can be estimated without solving the eigenvalue problem. Complex modes can be scaled such that the imaginary part is minimized. This scaling technique was used to produce performance indices with respect to damping non-proportionality [6]. In this study, we show a wave-based scaling method on a non-proportionally damped system. It extends a previously made observation corresponding to a complex mode formation scheme [7]. It was shown that the difference between a complex mode and a real normal mode can be expressed by propagating patterns that behave like waves. Thereby, these patterns are refracted as they cross an intersection that divides damping medium. This relationship is described Snell's law. In this work we show that a beam structure that has a partially applied constrained layer damping has complex modes that behave according to the predictions. Case studies

C. Nerse · S. Wang (✉)
School of Mechanical Engineering, Gwangju Institute of Science and Technology, Gwangjugwangyeogshi, Republic of Korea
e-mail: can@gm.gist.ac.kr; smwang@gist.ac.kr

S. Oberst et al. (eds.), *Vibration Engineering for a Sustainable Future*,
https://doi.org/10.1007/978-3-030-46466-0_4

were conducted with respect to different damping configurations. In Sect. 2, we outline the theory of the method. Then, in Sect. 3, we show a comparison of the numerical and experimental results and give our conclusions.

2 Methods

Similar to a light beam that gets refracted at the boundary of two media, it can be argued that the complex mode featuring wave characteristics can also be represented with a similar perspective. In this regard, consider a structure with simply supported boundary conditions. Analytically, the deflection patterns for a real normal mode of beam can be expressed by a sine function, where m corresponds to the spatial wavenumber on x coordinate and L_x is the length of the beam, as shown in Eq. (1):

$$\mathrm{W}_m(x) = \sin\left(m\pi x/L_x\right) \tag{1}$$

When the system is proportionally damped, these deflection patterns retain the same shape. However, if the damping is non-uniformly distributed, as in the case of partially applied damping layer on a plate, the mode shapes are complex-valued. It is argued that the difference between a complex mode and the respective normal mode can be described propagating wave-like patterns as shown in Fig. 1. When the system is proportionally damped, the net sum of the patterns is zero, while, when the system is non-proportionally damped, we observe refraction at the individual intersections of damping. For a typical non-proportional damping configuration, the summation of patterns is a non-zero variation. Thereby, they contribute to the imaginary part of the complex mode.

As shown in Fig. 1c, the left propagating pattern is refracted at the damping intersections. This relationship is governed by Snell's law:

$$\frac{\sin\left(\theta_2\right)}{\sin\left(\theta_1\right)} = \frac{k_{m,1}}{k_{m,2}} = \frac{d_1}{d_2} \tag{2}$$

where d_1 and d_2 correspond to the refractive indices of damping regions D_1 and D_2, respectively.

3 Results and Discussion

To verify the numerical predictions, an experimental setup was prepared. A steel beam of 3 mm thickness was clamped at both ends. Shaker excitation was used at an end node to excite the beam, and uniaxial accelerometers were attached. Measurement nodes were selected so that they are equally spaced. Figure 2 shows the dimensions of the setup and locations of the transducers. Note that in the method

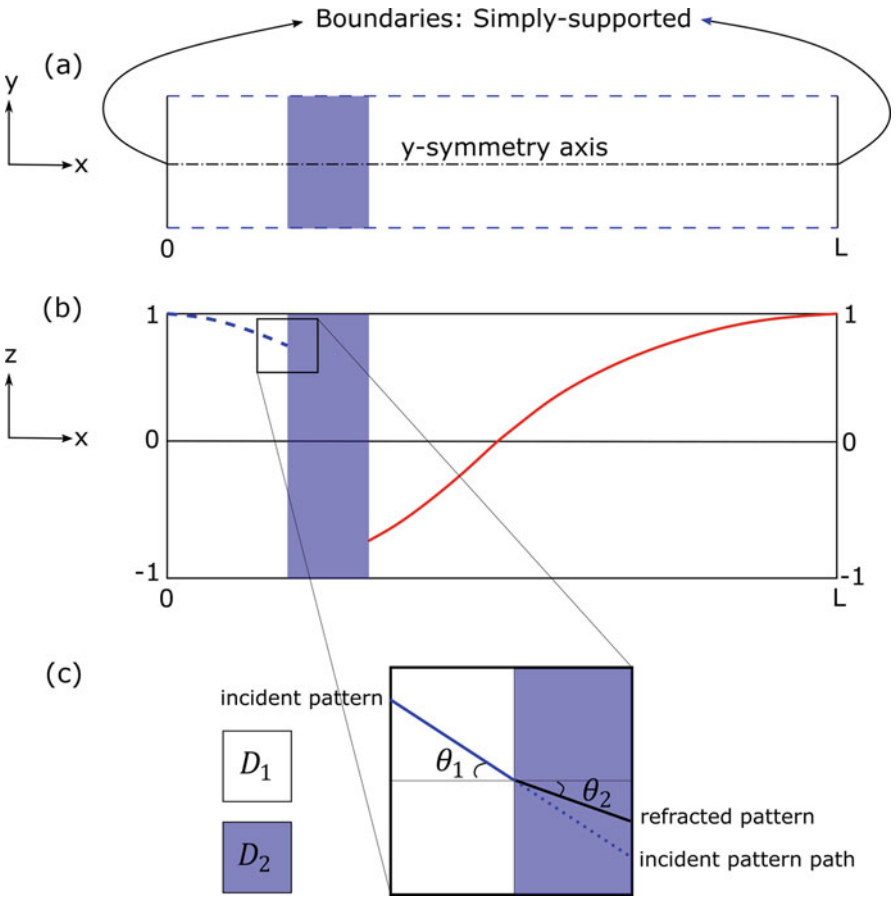

Fig. 1 Overview of the complex mode formation framework. (**a**) (x–y) section view of beam structure with a non-proportional damping patch. (**b**) Propagating patterns from the boundaries of the structure, blue dash line: left propagating pattern, red solid line: right propagating pattern. (**c**) Refraction of the propagating pattern at a damping intersection

section we described the boundary conditions to be simply supported. Simply supported boundary conditions are the most simplistic form for analytical solution [8]. However, in an experiment setup, it is not easy to achieve it. Therefore, generally, clamped boundary conditions are used. Comparing both boundary conditions, it was shown that although the modal frequencies are higher for clamped boundary condition due to increase in overall stiffness, the mode shapes are very similar to that of simply supported boundary condition [8, 9]. Hence, in the experiments we used clamped boundary conditions.

Partial damping treatment was applied by attaching three layers of 3M damping foil [10] on the bottom surface of the beam (see Fig. 2). We have tested three different cases, i.e., Q1, Q2, and H1, that refer to quarter or half size of the beam

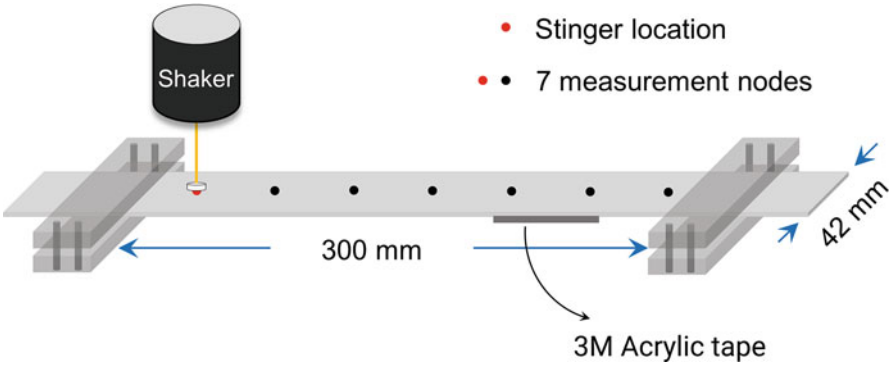

Fig. 2 Experimental setup showing the exciter and transducer locations

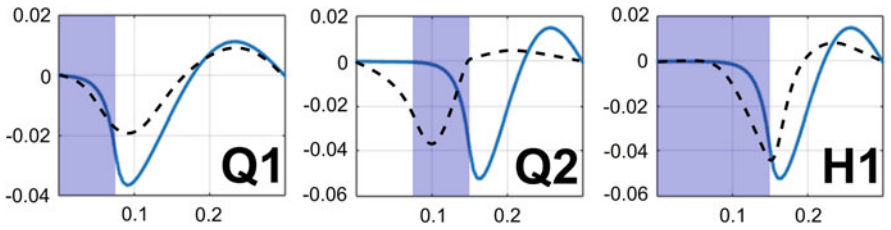

Fig. 3 Comparison of the imaginary values of the normalized first mode with respect to numerical approximation and the experiment. Blue solid line: method, black dash line: experiment

in the longitudinal direction. The complex modes that were obtained from the experiments are compared to the numerical predictions in Fig. 3.

Numerical predictions and the experiment have been shown to be similar; in particular, Q1 and H1 configurations. This has valuable implications for practical applications. One such benefit can be attained for benchmarking of the existent method, such that for cases where finite element modeling is not feasible an experimental procedure can be done for verification. In addition, in industrial applications where damping treatments are used for noise and vibration control, such approximation method can be utilized for preliminary decisions regarding the optimum location for the damping layer attachment. In the future studies, the present method can also be implemented into structural-acoustic coupling problems.

Acknowledgments This study was supported by a National Research Foundation of Korea (NRF) Grant funded by the Korean government (NRF-2017R1A2A1A05001326).

References

1. Meirovitch, L.: A new method of solution of the eigenvalue problem for gyroscopic systems. AIAA J. **12**(10), 1337–1342 (1974)
2. Parthasarathy, G., Reddy, C.V.R., Ganesan, N.: Partial Coverage of Rectangular Plates by Unconstrained Layer Damping Treatments. J. Sound Vib. **102**(2), 203–216 (1985)
3. Feeny, B.F.: A complex orthogonal decomposition for wave motion analysis. J. Sound Vib. **310**, 77–90 (2008)
4. Adhikari, S.: Rates of change of eigenvalues and eigenvectors in damped dynamic system. AIAA J. **37**, 1452–1458 (1999)
5. Unruh, O.: Parametric study of sound radiation properties of complex vibration patterns in rectangular plates using an analytical model. Acta Acust United Acust. **101**, 701–712 (2015)
6. Liu, K., Kujath, M.R., Zheng, W.: Quantification of non-proportionality of damping in discrete vibratory systems. Comput. Struct. **77**, 557–569 (2000)
7. Nerse, C., Wang, S.: On the formation of complex modes in non-proportionally damped systems. J. Sound Vib. **463**, 114978 (2019)
8. Leissa, A.: Vibrations of plates. Acoust. Soc. Am. **13**(10), (1993)
9. Xiao, H., Sheng, M., et al.: The study on free vibration of elastically restrained beams carrying various types of attachments with arbitrary distributions. Shock. Vib. **20**, 369–383 (2013)
10. 3M damping foil 2552, 3M company (2012)

Structure Optimization of Noise and Vibration Performance using FRF Baseline

Hironori Shiga, Takuya Yoshimura, Koji Saito, and Akira Suto

1 Introduction

At present, CAE is widely used for mechanical structures, and complex dynamic analysis using the finite element method (FEM) is highly realized. However, when performing dynamic analysis, the mode density increases as the frequency increases, so the analysis method is to be chosen according to the target frequency range. In the low-frequency range, modal analysis is generally used widely. In the high-frequency range, statistical energy analysis (SEA) is used. However, focusing on the mid-frequency range, several methods (e.g., methods combining FEM and SEA [1–3]) have been proposed, but effective methods have not been established yet. Therefore, as a new approach for the mid-frequency range, it is examined to grasp the tendency of the global frequency response of the frequency region rather than treating the modes individually.

H. Shiga (✉) · T. Yoshimura
Tokyo Metropolitan University, Hachioji-shi, Tokyo, Japan
e-mail: shiga-hironori@ed.tmu.ac.jp; yoshimu@tmu.ac.jp

K. Saito · A. Suto
HONDA R&D Co. Ltd., Wako-shi, Saitama, Japan
e-mail: koji_02_saito@n.t.rd.honda.co.jp; akira_suto@n.t.rd.honda.co.jp

S. Oberst et al. (eds.), *Vibration Engineering for a Sustainable Future*,
https://doi.org/10.1007/978-3-030-46466-0_5

2 Theory

2.1 Baseline

The baseline is expressed by adding virtual damping to the FRF [4]. An example of baseline is shown in Fig. 1. Compared to the FRF used for conventional noise and vibration evaluation, it is expected to evaluate vibration level in a more global frequency band than observing individual peaks.

2.2 Sensitivity Analysis Theory with Mass Addition

Sensitivity analysis for the FRF or baseline with mass addition theory [5] is to consider how the point r response under point f vibration changes with the addition of mass to the point i as shown in Fig. 2.

First, the acceleration after mass addition is expressed as follows:

$$\begin{Bmatrix} \ddot{x}_r^* \\ \ddot{x}_f^* \\ \ddot{x}_i^* \end{Bmatrix} = \begin{bmatrix} H_{rr} & H_{rf} & H_{ri} \\ H_{fr} & H_{ff} & H_{fi} \\ H_{ir} & H_{if} & H_{ii} \end{bmatrix} \begin{Bmatrix} 0 \\ f \\ f_{add} \end{Bmatrix} \tag{1}$$

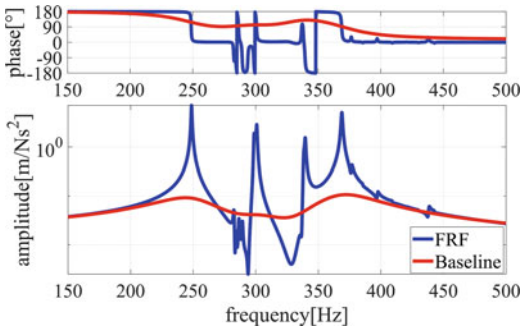

Fig. 1 Examples of FRF and baseline

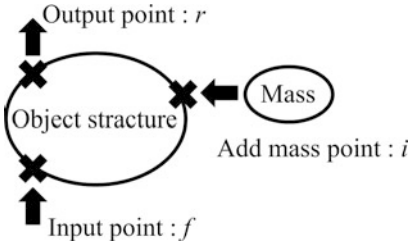

Fig. 2 Mass addition model

Here, $\ddot{x}$ is acceleration. "*" indicates that the mass is added. H_{ba} is FRF at point b response under point a vibration. f is force. f_{add} is force generated by added mass. FRF after adding mass can be expressed with the design variable m as follows:

$$H_{rf}^{*} = \frac{\ddot{x}_r^{*}}{f} = H_{rf} - \frac{H_{ri} H_{if}}{H_{ii} + {}^{1}\!/_{m}} \tag{2}$$

FRF sensitivity with mass addition S can be expressed as follows by partially differentiating H_{rf}^{*}:

$$S = \frac{\partial H_{rf}^{*}}{\partial m}\bigg|_{m=0} = -H_{ri} H_{if} \tag{3}$$

Next, we formulate sensitivity analysis of FRF sum of squares in the frequency band. The FRF sum of squares P is expressed as follows:

$$P = \sum_{\omega_{low}}^{\omega_{high}} H_{rf}(\omega) \bullet H_{rf}^{conj}(\omega) = \sum_{\omega_{low}}^{\omega_{high}} \left| H_{rf}(\omega) \right|^2 \tag{4}$$

At this time, FRF sum of squares sensitivity with mass addition S' is expressed as follows, where $\frac{\partial H_{rf}}{\partial m}$ is S:

$$S' = \frac{\partial P}{\partial m} = \sum_{\omega_{low}}^{\omega_{high}} \left(H_{rf} \bullet \frac{\partial H_{rf}^{conj}}{\partial m} + \frac{\partial H_{rf}}{\partial m} \bullet H_{rf}^{conj} \right) = \sum_{\omega_{low}}^{\omega_{high}} 2\mathrm{Re}\left(H_{rf}^{conj} \frac{\partial H_{rf}}{\partial m} \right) \tag{5}$$

3 Numerical Analysis

3.1 Analysis Condition

The simplified structure model used this time is a rectangular solid with dimensions of 0.2 [m] × 2 [m] × 2.0 [m] with beams on 12 sides. Young's modulus E is 206 [GPa], and density ρ is 7860 [kg/m^3]. The node of input point is #4, and the node of output point is #73. The directions of input point and output point are z. The proportional viscous damping is assumed. The virtual damping is equivalent to $\zeta = 0.03$~0.05. This model is shown in Fig. 3. Mass of this model is about 25 [kg].

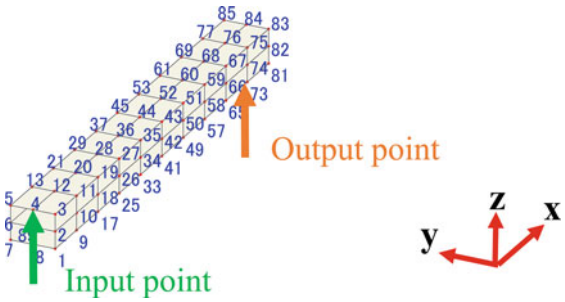

Fig. 3 Simplified structure model

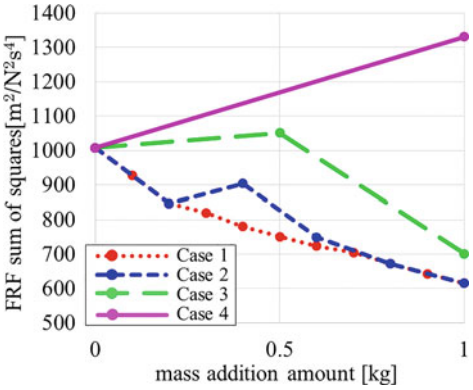

Fig. 4 Transition to mass addition by FRF method

3.2 Comparing the Reduction of the FRF Sum of Squares Between FRF Method and Baseline Method

The purpose of this analysis is to enable structural changes that reduce vibration level from a viewpoint of global optimization using the baseline.

Sensitivity analysis and mass addition based on it were performed alternately and repeated until the total mass addition reached 1 kg. The amount of mass addition per one time was varied in four ways of 0.1 [kg] (case1), 0.2 [kg] (case2), 0.5 [kg] (case3), and 1 [kg] (case4). The above was tried by both FRF method and baseline method. Here, FRF method means structure change based on FRF sum of squares sensitivity. Similarly, baseline method means structure change based on baseline sum of squares sensitivity. Figures 4 and 5 show the transition of FRF sum of squares to mass addition in each case and method.

According to Fig. 4 using FRF method, FRF sum of squares continues to decrease when the amount of mass addition per 1 time is small. However, if the amount of mass per 1 time is large, FRF sum of squares decreases poorly or gets worse. According to Fig. 5 using baseline method, FRF sum of squares continues to decrease regardless of amount of mass per 1 time.

The results for the FRF method and the baseline method were compared. In the case of amount of mass addition per 1 time is small, FRF sum of squares is reduced

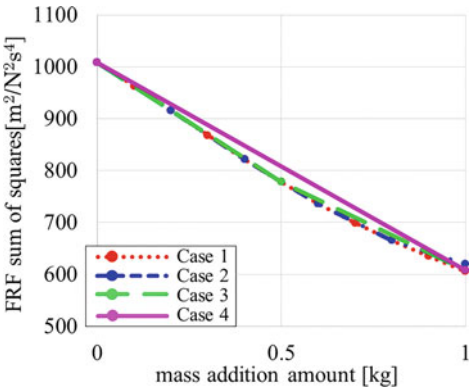

Fig. 5 Transition to mass addition by baseline method

in a similar way between two methods. On the other hand, in the case of amount of mass addition per 1 time is large, using the baseline method reduces FRF sum of squares, even if using the FRF method worsens FRF sum of squares. Here it is observed that the reduction in baseline method is not always the best but relatively good regardless of amount of mass addition at one time.

3.3 Comparing the Structure Change Between FRF Method and Baseline Method

The difference between the simplified structure models after mass addition was compared between the FRF method and the baseline method. Figure 6 shows the structures change by mass addition at 1 kg in total in each case and method. The added mass is expressed as a sphere, and the volume of the sphere is displayed in proportion to the amount of mass addition.

The results for the FRF method and the baseline method were compared. In the case of the FRF method, mass tends to be added to various points each time, but in the case of the baseline method, mass is added only around the output point consistently. Furthermore, in the case of the baseline method, FRF sum of squares is well reduced. Here it is observed that the mass addition points are more concentrated near the input point or the output point in the baseline method than in the FRF method.

4 Conclusion

In this study, the structural modification was applied to a simple structure in order to reduce the FRF sum of squares in a certain frequency range. The optimization result by the baseline was compared with that by the conventional approach by

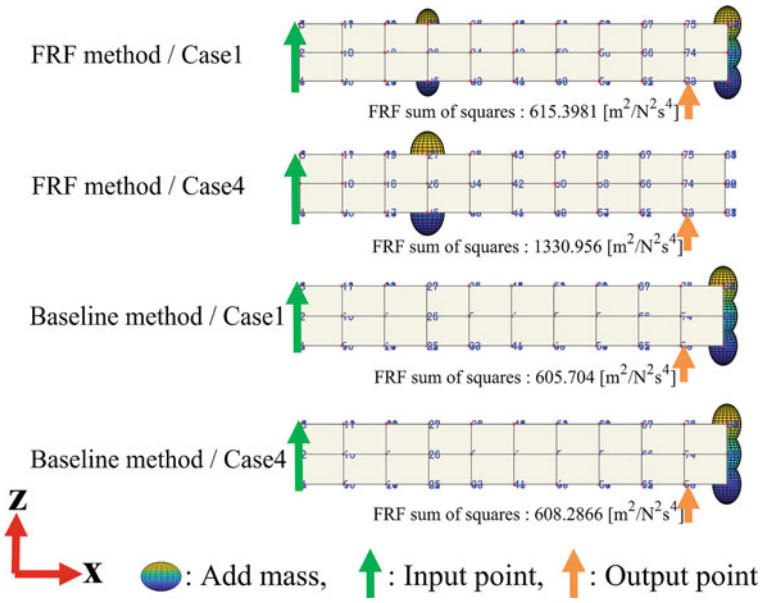

Fig. 6 Schematic representation of structural changes

the FRF. The following two can be claimed. First, the reduction of FRF sum of squares in baseline method is not always the best but relatively good regardless of amount of mass addition at one time. Second, the mass addition points are more concentrated near the input point or the output point in the baseline method than in the FRF method. From the above, it is concluded that the baseline method can reduce vibration level from a viewpoint of global optimization rather than local optimization. In a future work, we would like to explore a method that combines the baseline method and the FRF method, by which the global and the local optimization are both implemented.

References

1. Yan, H., Parrett, A., Nack, W.: Statistical energy analysis by finite elements for middle frequency vibration. Finite Elem. Anal. Des. **35**(4), 297–304 (2000)
2. Fahy, F.J., Mohammed, A.D.: A study of uncertainty in applications of sea to coupled beam and plate systems, part I: computational experiments. J. Sound Vibr. **158**(1), 45–67 (1992)
3. Steel, J.A., Craik, R.J.M.: Statistical energy analysis of structure-borne sound transmission by finite element methods. J. Sound Vib. **178**(4), 553–561 (1994)
4. Kawabata, R., Yoshimura, T.: Development of dynamic design method by utilizing frequency response function expanded to s-plane. The Japan Society of Mechanical Engineers The Proceedings of Conference of Kanto Branch, 19G22 (2019)
5. Urushiyama, Y., Noguchi, H., Tobita, T.: Sensitivity analysis using frequency response function in NVH analysis. Honda R&D Tech. Rev. **1**, (1989)

Snowboard Simulation with Distinct Element Method and Finite Element Method

Tatsuya Yoshida, Fumiyasu Kuratani, and Shogo Nakamura

1 Introduction

Snowboard and ski manufacturers generally develop new products by a trial-and-error process. In this process, test riders evaluate the prototype boards and provide individual and subjective opinions of the performances of the boards. The designers then attempt to correct the mechanical properties and the board shapes based on these evaluations. The relationships between the mechanical properties of skis and snowboards and their performance have been investigated in several analytical and experimental studies [1, 2]. However, the test conditions are often different between prototype and field testing. This renders quantitative evaluation and efficient redesign difficult.

One approach used to evaluate the performance of a prototype is the development of numerical simulations. Although some studies [3, 4] have represented snow as a continuous body using the finite element method (FEM), these simulations lacked consideration of the discrete behaviors and large deformations when the deformation of snow surfaces increase. The nonlinearity of the force acting on the bottom of the board, which relates to the board's penetration of the snow surface, frequent shear fracture, and slip of the fracture surface, is enhanced as the tilt angle of the board increases [5]. Therefore, models based on a continuum, such as the FEM, are not suitable for representing snow and for maintaining the calculation times within a reasonable limit for the design.

In our previous study, we developed a simulation model to reproduce the discrete behavior of snow with the distinct element method and examined the influence of board shapes on turning motion [6]. The previous study focused on the shapes of

T. Yoshida (✉) · F. Kuratani · S. Nakamura
Department of Mechanical Engineering, University of Fukui, Fukui, Japan
e-mail: t-yoshi@u-fukui.ac.jp; kuratani@u-fukui.ac.jp; jm190378@u-fukui.ac.jp

S. Oberst et al. (eds.), *Vibration Engineering for a Sustainable Future*,
https://doi.org/10.1007/978-3-030-46466-0_6

rigid body snowboards. Herein, we reproduce the deformation of the board with the FEM and examine the influence of both board shape and stiffness on the turning motions and overall characteristics of the board.

2 Mechanism of Snowboard Turn

Figure 1 shows a snowboard in the early stage of a turn. The attack angle, which is shown in Fig. 1a, is the angle formed between the traveling direction and the board's centerline. Snowboarders form the attack angle by twisting their body. Because the component of the reaction force acting in the direction opposite to the traveling direction affects the lateral direction of the board, the attack angle allows a snowboard turn. Figure 1b shows the snowboard during the turn as seen from the traveling direction. The edge angle is the angle between the snow surface and the snowboard. As the edge angle increases, the direction of the reaction force acting on the board changes. The reaction force can be decomposed into one in the direction parallel to the snow surface and one that is perpendicular to it. This parallel force also allows the snowboard to turn. Furthermore, the sidecut, which is the curved part on the side of the board, also affects the movement of the snowboard. The sidecut penetrates the snow surface by increasing the edge angle, and the groove formed by the penetration constrains the motion of the board. Therefore, the curvature of the sidecut influences the curvature of the turn, and boards with smaller sidecut radii have the tendency to produce smaller turn radii.

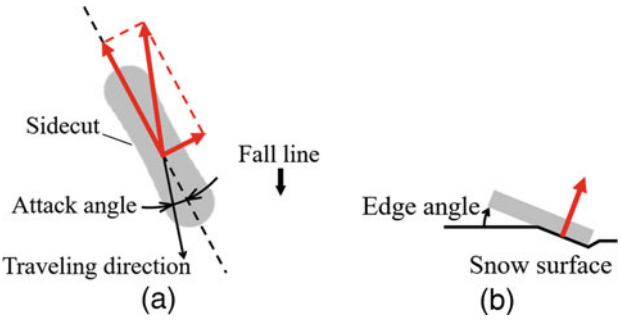

Fig. 1 Mechanism of snowboard turn. (**a**) Top view. (**b**) Front view

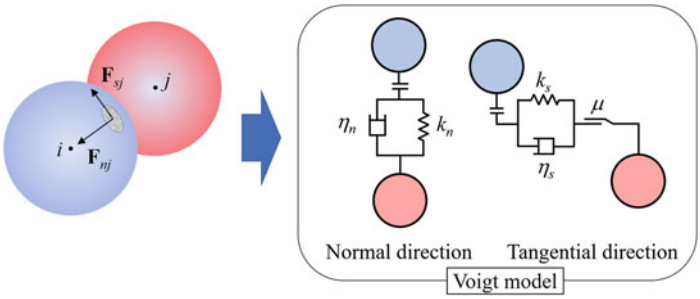

Fig. 2 Snow modeling with distinct element method [6]

3 Simulation Method

3.1 Snow Model [6]

In this simulation, snow is modeled as particle elements. The particle behavior is calculated using the distinct element method (DEM). Based on the Voigt model, shown in Fig. 2, the DEM calculates the contact forces between the snow particles. In Fig. 2, k is the spring coefficient, η is the damping coefficient, and μ is the friction coefficient. The subscript n indicates the normal direction, and the subscript t indicates the tangential direction. The motion equation for particle i is shown in the following equation and is solved numerically with Euler's algorithm.

$$m_i \frac{d2\mathbf{x}_i}{dt2} = m_i \mathbf{g} + \sum \mathbf{F}_{nj} + \sum \mathbf{F}_{tj} \tag{1}$$

In the above equation, m_i is the mass of the particle i, $\mathbf{x}_i$ is the position vector of particle i, and $\mathbf{g}$ is the gravitational acceleration vector. $\mathbf{F}_{nj}$ and $\mathbf{F}_{tj}$ are the contact force vectors due to particle j in the normal and tangential directions.

3.2 Snowboard Model

The deformation of the snowboard is reproduced with the FEM, and the rigid-body translational and rotational motions of the snowboard are reproduced by numerically solving these motion equations with six degrees of freedom. The force acting on the board model is calculated by detecting the contacts between the finite element (FE) meshes and particles. When the board slides and deforms, the meshes are also displaced, and the contacts with the particle elements at each time step are considered via the displacements of the nodes. The interaction force is then determined by the DEM, as shown in the previous section. This calculated force is considered to be the external force acting on the board, and the contact points and

force vectors between the FE mesh and particles are thus calculated in detail. The board was modeled in the FEM software ANSYS with Shell181 which is a four-node shell element with six degrees of freedom for each node. The time history response of board deflection was calculated by the modal superposition method with an analytical target frequency range of less than 5 kHz. The modal damping ratio was set to 1% for all modes. The Newmark-β method was used as the time integration method, with the time interval for both the board and snow model set to 1.0×10^{-5} s.

4 Simulation Conditions

4.1 Shape and Mechanical Properties of Snowboard

The snowboard models were constructed to evaluate the influence of sidecut radius and board stiffness. Two snowboard shape configurations were modeled: one with a sidecut radius of 8 m and another with a straight sidecut. The modeled boards are shown in Fig. 3 with local coordinate systems (x', y', z') located at the center of each board. The x' axis is set along the longitudinal direction of the board, the y' axis is along the width of the board, and the z′ axis is perpendicular to the board surface. The board dimensions, mass, and inertial moment are shown in Table 1. To examine the influence of board stiffness, the boards were tested with elastic moduli of 5 GPa, 7.5 GPa, 15 GPa, and 30 GPa, and the board was modeled as a rigid body. These values were determined on the basis of the natural frequencies of typical snowboards (from 15 to 20 Hz), which approximately corresponds to between 7.5 GPa and 15 GPa. Furthermore, to model a rider simply, a concentrated mass of 60 kg was added at (0, 0.05, 0) in the board coordinate system. This load location allows for the retention of the edge, while the board is prevented from turning over by balancing with inertia, reaction force from the slope, and a load torque, as noted in the next subsection.

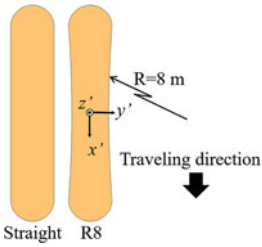

Fig. 3 Shapes of the snowboard

Table 1 Detention and inertia property of the snowboard

Sidecut	Length	Width	Mass	Inertial moment		
				I_{xx}	I_{yy}	I_{zz}
R8	1.5 m	0.3 m	2.91 kg	0.018 kgm^2	0.53 kgm^2	0.54 kgm^2
Straight	1.5 m	0.3 m	3.17 kg	0.023 kgm^2	0.54 kgm^2	0.56 kgm^2

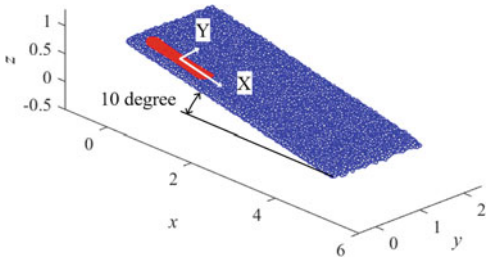

Fig. 4 Slope and initial position of board

4.2 Slope Condition and Load Torque

The simulation slope was tilted at an angle of 10°, as shown in Fig. 4. In the global coordinate system, the x and y axes are located on the horizontal plane, with the z axis pointing in the vertical direction. Moreover, a slope surface coordinate system, which consists of the X–Y axis, was defined to represent snowboard motion on the surface. A total of 11,132 particle elements covered the slope to reproduce granular snow, with the parameters modified to those used by Abe et al. [7].

The initial position of the board was rotated 10° about the y' axis to be parallel to the slope, and the x' axis subsequently matched with the fall line of the slope and the X direction. The boards were then given an initial velocity of 1 m/s along the fall line to slide down the slope. The snowboards were then turned by applying a 30 Nm torque about the x'-axis during sliding. This load torque increases the edge angle and penetration of the inside edge in the snow surface, thus allowing the board to turn.

5 Simulation Results

Figures 5 and 6 show trajectories of the board center on the snow surface coordinate system X–Y for both types of boards. From the results of the R8 board, a decrease in elastic modulus increased the movement in the Y direction. It also increased the deflection of the center of the board, which is shown in Table 2, where the displacement is in the z′ direction of the board coordinate system. The increase in board deflection due to the decrease in elastic modulus alters the contact edge and changes the turning motion.

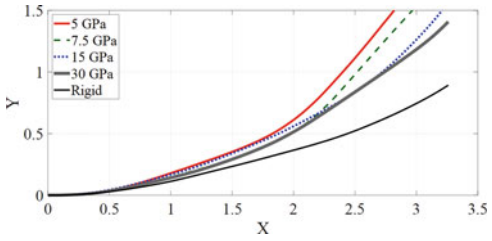

Fig. 5 Trajectories of the R8 board

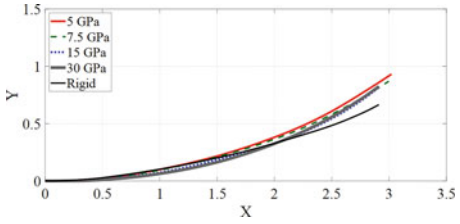

Fig. 6 Trajectories of the straight board

Table 2 Maximum deflections at the centers of the boards

Elastic modulus [GPa]		5	7.5	15	30
Deflection [mm]	Straight	−19.0	−17.1	−9.8	−8.0
	R8	−28.6	−23.1	−20.0	−17.3

Comparing the trajectories of the R8 and straight boards, the straight board was less influenced by the board's elastic modulus than the R8 board and exhibiting similar results between the elastic and inelastic tests. This was due to the stiffness of the straight board being higher than that of the R8 board because of the lack of a sidecut the maximum deflection at the center of the sliding straight board, which is shown in Table 2, was smaller than that of the R8 board. That said, the board deflection still increases with a decrease of elastic modulus for the straight board. From these results, it is suggested that board deflection is not the only aspect affecting trajectory.

Although the edge angle of the R8 board shown in Fig. 7 increased with the decrease in elastic modulus, the effects were less pronounced for the straight board, as shown in Fig. 8. Since the increment of the edge angle increased the component force in the Y direction acting on the board bottom, the movement of the board in the Y direction subsequently increased. From the simulation results, it is suggested that the sidecut and board deflection affect the turn trajectory.

6 Conclusions

We evaluated snowboarding performance quantitively by developing a simulation. The simulation evaluated the influence of board shape and elastic modulus on the characteristics of the turning motion. Although a decrease in the board stiffness with

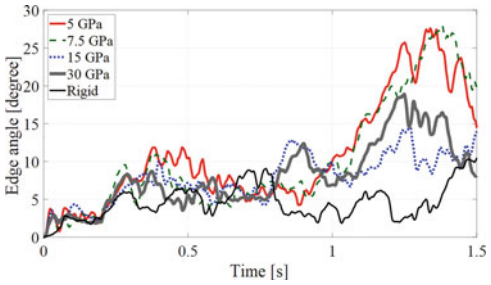

Fig. 7 Edge angle of the R8 board

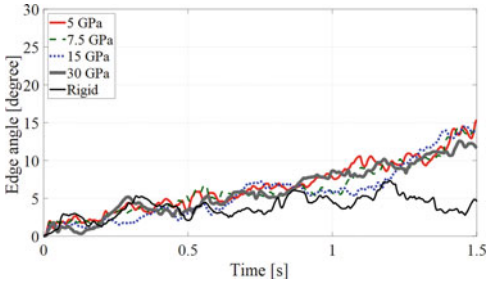

Fig. 8 Edge angle of the straight board

a sidecut increases the magnitude of the turn, the simulations show that a board without a sidecut is hardly affected by the stiffness. These results suggest that the board sliding motion is mainly influenced by the board shape.

Acknowledgment This work was supported by JSPS KAKENHI Grant Number JP17K14614.

References

1. Brennan, S.M., Kollár, L.P., Springer, G.S.: Modelling the mechanical characteristics and on-snow performance of snowboards. Sports Eng. **6**(4), 193–206 (2003)
2. Buffinton, K.W., Shooter, S.B., Thorpe, I.J., Krywicki, J.J.: Laboratory, computational and field studies of snowboard dynamics. Sports Eng. **6**(3), 129–137 (2003)
3. Federolf, P., Lüthi, A., Roos, M., Dual, J.: Parameter study using a finite element simulation of a carving Alpine ski to investigate the turn. Sports Eng. **12**(3), 135–141 (2010)
4. Federolf, P., Roos, M., Lüthi, A., Dual, J.: Finite element simulation of the ski-snow interaction of an alpine ski in a carved turn. Sports Eng. **12**(3), 123–133 (2010)
5. Federolf, P., JeanRichard, F., Fauve, M., Lüthi, A., Rhyner, H.U., Dual, J.: Deformation of snow during a carved ski turn. Cold Regions Sci. Technol. **46**(1), 69–77 (2006)
6. Yoshida, T., Hojo, A., Kuratani, F.: Simulation of snowboarding on snow surface modelled with particle elements. Proceedings of the 6th International Congress on Sport Sciences Research and Technology Support, 23–26 (2018)
7. Abe, M., Fujino, T., Saito, F., Takahata, K., Iwamoto, K.: Three-dimensional dynamic simulation analysis of snow removal characteristics of rotary equipment. J. Syst. Des. Dyn. **5**(5), 982–993 (2011)

Estimation of the Main Transfer Function of Ultrasonic Transducer Array

Min-Jung Sim, Chinsuk Hong, Weui-Bong Jeong, Yub Je, and Yo-Han Cho

1 Introduction

FEM analysis, commonly used for analysing underwater sonar systems, requires high computational resources because of high number of DOF. This paper suggests a method combining BEM and LPM. These two methods are very efficient in reducing the DOF. An application to a planar tonpilz transducer array is presented as an example.

2 Modelling and Analysis

A tonpilz transducer consists of head, piezoelectric element, and tail as shown in Fig. 1. Z_1, Z_2, and Z_3 are the mechanical impedances of head, piezoelectric element, and tail, respectively. Z_E is the electrical impedance, and Z_r is the acoustic radiation impedance. Sherman and Butler [1] explained how to express impedances into matrix representation as shown in Eq. (1) using 'T-Network'.

Unlike any other impedances that can be simply obtained from the LPM, the acoustic radiation impedance, $Z_{r,jk}$ is obtained by BEM analysis. $\tilde{x}_k$ represents velocities and current of kth transducer. $\tilde{F}_k$ represents forces and voltage of j^{th}

M.-J. Sim · W.-B. Jeong
Department of Mechanical Engineering, Pusan National University, Busan, Republic of Korea

C. Hong (✉)
Department of Mechanical Engineering, Ulsan College, Ulsan, Republic of Korea
e-mail: cshong@uc.ac.kr

Y. Je · Y.-H. Cho
Agency for Defense Development, Gyeongsangnam-do, Republic of Korea

S. Oberst et al. (eds.), *Vibration Engineering for a Sustainable Future*,
https://doi.org/10.1007/978-3-030-46466-0_7

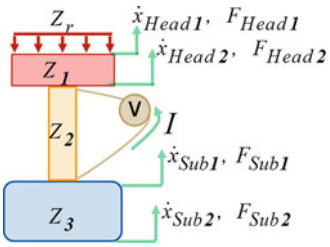

Fig. 1 Free body diagram of a transducer

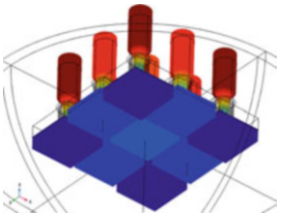

Fig. 2 Array with nine tonpilz transducers

transducer. For the array with n transducers, the impedance matrix equation needs to be expanded as Eq. (4).

$$\begin{bmatrix} Z_{r,jk}+Z_{1,c} & -Z_{1,b} & 0 & 0 & 0 \\ -Z_{1,b} & +Z_{1,c}+Z_{2,c}+N^2Z_E & -Z_{2,b}-N^2Z_E & 0 & -NZ_E \\ 0 & -Z_{2,b}-N^2Z_E & +Z_{2,c}+Z_{3,c}+N^2Z_E & -Z_{3,b} & 0 \\ 0 & 0 & -Z_{3,b} & +Z_{3,c} & +NZ_E \\ 0 & -NZ_E & +NZ_E & 0 & Z_E \end{bmatrix} = \tilde{Z}_{jk} \tag{1}$$

$$\left[\dot{x}_{Head1,k} \;\; \dot{x}_{Head2,k} \;\; \dot{x}_{Sub1,k} \;\; \dot{x}_{Sub2,k} \;\; I_k\right]^T = \tilde{x}_k \tag{2}$$

$$\left[F_{Head1,j} \;\; F_{Head2,j} \;\; F_{Sub1,j} \;\; F_{Sub2,j} \;\; V_j\right] = \tilde{F}_j \tag{3}$$

$$\begin{bmatrix} \tilde{Z}_{11} & \cdots & \tilde{Z}_{1n} \\ \vdots & \ddots & \vdots \\ \tilde{Z}_{n1} & \cdots & \tilde{Z}_{nn} \end{bmatrix} \begin{Bmatrix} \tilde{x}_1 \\ \vdots \\ \tilde{x}_n \end{Bmatrix} = \begin{Bmatrix} \tilde{F}_1 \\ \vdots \\ \tilde{F}_n \end{Bmatrix} \tag{4}$$

3 Numerical Results and Conclusion

In order to verify the validity of suggested method, a planar array composed of nine tonpilz transducers is analysed as shown in Fig. 2. All the transducers have the same driving voltage. In Fig. 3, colour lines are the result of the commercial FEM

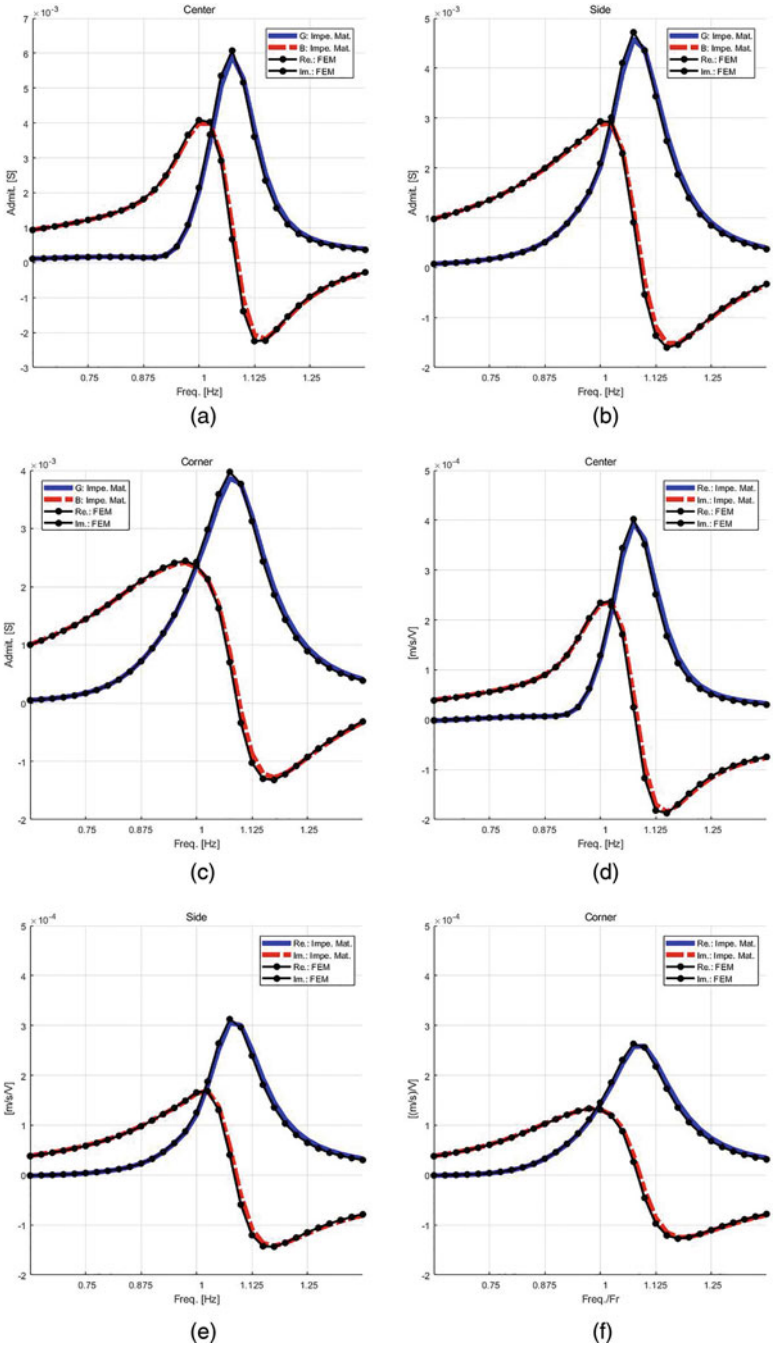

Fig. 3 Responses of each transducer: (**a**–**c**) Electrical admittances, (**d**–**f**) head velocities, $\dot{x}_{Head1}$, per unit voltage

software, and black lines are the result of the proposed impedance matrix equation. Figure 3 shows that the proposed method guarantees high accuracy. Unlike when using FEM software, the impedance matrix does not have to be recomputed every time the driving condition changes. Although this paper deals with the simple array, it is expected that it can be extended to more complicated sonar array, allowing more effective sonar system design.

Reference

1. Sherman, C.H., Butler, J.L.: Transducers and Arrays for Underwater Sound. Springer, New York (2007)

Part II
Theoretical Analysis

Bifurcation Analysis of a Doubly Curved Thin Shell Considering Inertial Effects

Martin Rudorf, Sebastian Oberst, Merten Stender, and Norbert Hoffmann

1 Introduction

Space engineering has grown in significance for private companies and the educational sector: The advent of small, compact microsatellites, which use off-the-shelf components, has made space missions affordable. To stowage on the carrier spacecraft, space booms, antennas or solar panels are generally folded or rolled up to then self-deploy once in orbit [1]. However, satellites especially in low Earth orbits are exposed to harsh environmental conditions including aerodynamic drag, changing gravitation, varying temperatures, electromagnetic fluxes and solar radiation pressures [2] – loads which act disturbing and which cause vibrations of thin elastic structures and which can lead to a changed attitude behaviour of the spacecraft.

Studying the nature and extent of these vibration phenomena is difficult, and obtaining direct measurements from satellites would require attaching sophisticated measurement equipment with high temporal and spatial resolution – an extra payload which represents opportunity costs. On-Earth validation of thin, elastic structures is difficult, mainly due to gravity [1, 3]. Numerical modelling of thin structures,

M. Rudorf · M. Stender
Dynamics Group, Hamburg University of Technology, Hamburg, Germany

S. Oberst (✉)
Centre for Audio, Acoustics and Vibration, University of Technology Sydney, Ultimo, NSW, Australia
e-mail: sebastian.oberst@uts.edu.au

N. Hoffmann
Dynamics Group, Hamburg University of Technology, Hamburg, Germany

Department of Mechanical Engineering, Imperial College London, London, UK

S. Oberst et al. (eds.), *Vibration Engineering for a Sustainable Future*,
https://doi.org/10.1007/978-3-030-46466-0_8

modelled via shell elements, is not without obstacles either. Finite element methods tend to easily become numerically ill-conditioned and to run very slowly.

A different approach, which will be followed in this study, is treating the antenna as an open, thin shallow shell [4] using Donnell's theory; results of a 9 degree of freedom (DOF) model based on Amabili's doubly curved, shallow shell model [5] with simply supported boundaries are compared to a mathematical formulation which considers additional inertial terms. Bifurcation diagrams are investigated to discuss the influence of assumptions on the inertia coupling terms on the dynamics.

2 Numerical Modelling

A thin, shallow shell with finite curvilinear dimensions a and b, thickness h and a rectangular base is considered (Fig. 1). $(O; x, y, z)$ is the global coordinate system; $\psi = x/R_x$ and $\theta = y/R_y$ are the angular coordinates with R_x and R_y denoting the radii of curvature in x- and y-direction. The displacements of points on the middle surface are denoted by u, v and w. The displacements in w-direction are considered positive and out-of-plane towards the shell's convex side.

The shell's thickness is assumed to be small compared to spatial dimensions $h \ll a, b$; strains and displacements are so small that higher-order terms in the strain-displacement relations are negligible as are normal stresses relative to the mid-surface ($\sigma_z = \tau_{zx} = \tau_{zy} = 0$); and normal vectors to this mid-surface will not deform [4]. For Donnell's theory the deflection w is of the same order of magnitude as h; the deflections u and v are negligible when compared to w; in-plane and rotary inertia are neglected; and the stress at an arbitrary point inside the shell depends linearly on its distance to the middle surface, i.e. $\epsilon_x = \epsilon_{x,0} + zk_x$, $\epsilon_y = \epsilon_{x,0} + zk_y$, $\gamma_{xy} = \gamma_{xy,0} + zk_{xy}$, with $\epsilon_{x,0}$, $\epsilon_{y,0}$ and $\gamma_{xy,0}$ being the strains on the middle surface and k_x, k_y and k_{xy} denoting changes of curvature and torsion of the mid-surface (no shear deformation). In the following derivations of the kinematic relations, we retain some second-order terms.

The governing equations of motion for u, v and w are derived next using the Lagrange function, and a modal decomposition of discretised displacements is obtained. The Lagrange equations of the second kind for a shell element are written as [4]

$$\frac{d}{dt}\left(\frac{\partial T_\mathrm{S}}{\partial \dot{\mathbf{q}}}\right) - \frac{\partial T_\mathrm{S}}{\partial \mathbf{q}} + \frac{\partial U_\mathrm{S}}{\partial \mathbf{q}} = \mathbf{Q}, \text{ with } \mathbf{Q} = -\frac{\partial F_\mathrm{D}}{\partial \dot{\mathbf{q}}} + \frac{\partial W}{\partial \mathbf{q}} \tag{1}$$

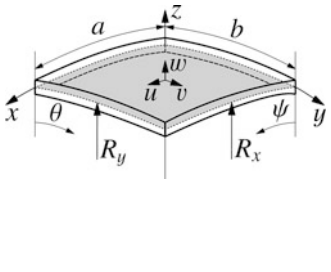

Fig. 1 Doubly curved shell

where the $\mathbf{q}$ and $\dot{\mathbf{q}}$ denote the vectors of generalized DOFs and their derivatives with respect to time. For the shell element under investigation, those represent the continuously distributed displacements of the middle surface u, v and w and the corresponding velocities, which are discretised using modal decomposition. T_S and U_S denote the kinetic and elastic strain energy, respectively. The work done by non-conservative forces (damping F_D, external excitation W) is denoted by $\mathbf{Q}$. Now, $u(x, y, t)$, $v(x, y, t)$ and $w(x, y, t)$ are expanded into Fourier series with time-dependent modal amplitudes and time-invariant, trigonometric shape functions:

$$u = \sum_{m,n=1}^{M,N} u_{m,n} \cos\left(\frac{m\pi x}{a}\right) A,$$

$$v = \sum_{m,n=1}^{M,N} v_{m,n} \cos\left(\frac{n\pi y}{b}\right) B, \text{ and } w = \sum_{m,n=1}^{M_w,N_w} w_{m,n} A B, \tag{2}$$

with $A = \sin\left(\frac{n\pi y}{b}\right)$ and $B = \sin\left(\frac{m\pi x}{a}\right)$. The indices m and n denote the number of half-waves in x- and y-direction, respectively, and $\sum_{m,n=1}^{M,N} = \sum_{m=1}^{M} \sum_{n=1}^{N}$. Owing to the symmetry of the shell element, only odd numbers are considered. The moment and force resultants ($M_{x,y}$, $N_{x,y}$) at the boundaries allow in-plane displacements orthogonal to the edges as well as rotations, but no out-of-plane displacements or displacements parallel to the edges.[1]

The modal expansion has been chosen such that the geometrical BC as well as the constraints on the moment resultants are intrinsically satisfied. To eliminate the force resultants $N_{x,y}$, additional terms $\hat{u}$ and $\hat{v}$ have to be added to the expansions of u and v. They can be obtained by plugging the expressions for the force resultants $N_x = \frac{Eh^3}{1-\nu^2}(\epsilon_{x,0} - \nu\epsilon_{y,0})$, and $N_y = \frac{Eh^3}{1-\nu^2}(\epsilon_{y,0} - \nu\epsilon_{x,0})$ into Eq. (3), which provides, substituting $K_1 = \frac{\partial w}{R_x \partial\psi}\frac{\partial w_0}{R_x \partial\psi}$, $K_2 = \frac{\partial w}{R_y \partial\theta}\frac{\partial w_0}{R_y \partial\theta}$ and $B_1 = \{\psi = 0, a/R_x\}$, $B_2 = \{\theta = 0, b/R_y\}$:

$$\left[\frac{\partial \hat{u}}{R_x \partial\psi} + \left(\frac{\partial w}{4R_x \partial\psi}\right)^2 + K_1 + \frac{\nu \partial \hat{v}}{R_y \partial\theta}\right]_{B_1} = 0$$

$$= \left[\frac{\partial \hat{v}}{R_y \partial\theta} + \left(\frac{\partial w}{4R_y \partial\theta}\right)^2 + K_2 + \frac{\nu \partial \hat{u}}{R_x \partial\psi}\right]_{B_2}. \tag{4}$$

Solving Eq. (4) for $\hat{u}(x, y, t)$ and $\hat{v}(x, y, t)$ gives

[1] $v = w = N_x = M_x = 0$ at $x \in \{0, a\}$, and $u = w = N_y = M_y = 0$ at $y \in \{0, b\}$ (3)

$$-\hat{u} = \sum_{m,n=1}^{M_w,N_w} \frac{m\pi}{a} \left\{ \frac{w_{m,n}(t)}{2} \sin\left(\frac{n\pi y}{b}\right) \sum_{s,k=1}^{M_w,N_w} \frac{s w_{s,k}(t)}{m+s} \sin\left(\frac{k\pi y}{b}\right) \sin\left[\frac{(m+s)\pi x}{a}\right] \right\} \tag{5a}$$

$$-\hat{v} = \sum_{m,n=1}^{M_w,N_w} \frac{n\pi}{b} \left\{ \frac{w_{m,n}(t)}{2} \sin\left(\frac{m\pi x}{a}\right) \sum_{s,k=1}^{M_w,N_w} \frac{k w_{s,k}(t)}{n+k} \sin\left(\frac{s\pi x}{a}\right) \sin\left[\frac{(n+k)\pi y}{b}\right] \right\}. \tag{5b}$$

For a more detailed derivation of these additional terms, see [5]. The modal expansion can now be used to symbolically evaluate the energy expressions in Eq. (1) and to obtain a set of differential equations in the generalized coordinates $\mathbf{q} = \left[u_{m,n},\ v_{m,n},\ w_{m,n}\right]^{\mathrm{T}}$. Here, the expansions are truncated at $M = N = 3$ and $M_w = N_w = 1$ leading to a model with 9 DOFs which still suffices to capture the dynamics of the shell [5].

Using the modal expansions, the algebraic expressions in modal amplitudes for the kinetic energy are derived $T_{\mathrm{S}} = \frac{1}{2}\rho_{\mathrm{S}} h \int_0^a \int_0^b \left(\dot{u}^2 + \dot{v}^2 + \dot{w}^2\right) \mathrm{d}y\, \mathrm{d}x$, where ρ_{S} represents the mass density and rotary inertia has been neglected. However, due to the quadratic terms in $w_{m,n}$ of the additional terms $\hat{u}$ and $\hat{v}$, inertial coupling arises in T_{S}. To illustrate this, a minimal modal expansion that has been set up with $M = N = M_w = N_w = 1$ was used to calculate T_{S}.

$$T_{\mathrm{S}} = \rho_{\mathrm{S}} h \left[\frac{abE_1}{4} + \frac{9(a\pi)^2 E_2 + 9(b\pi)^2 E_2}{64ab} - \frac{4\sqrt{E_2}\left(b\dot{u}_{1,1} + a\dot{v}_{1,1}\right)}{9\pi} \right] \tag{6}$$

using the expressions $E_1 = \dot{u}_{1,1}^2 + \dot{v}_{1,1}^2 + \dot{w}_{1,1}^2$ and $E_2 = w_{1,1}^2 \dot{w}_{1,1}^2$. The first summand of Eq. (6) corresponds to the expression $T_{\mathrm{S}} = \rho_{\mathrm{S}} \frac{abh}{4} \left[\sum_{m=1}^{M} \sum_{n=1}^{N} \left(\dot{u}_{m,n}^2 + \dot{v}_{m,n}^2\right) + \sum_{m=1}^{M_w} \sum_{n=1}^{N_w} \dot{w}_{m,n}^2 \right]$ [5] which is a simplification of Eq. (6).

Next, an expression for the elastic strain energy U_{S} will be derived using the strain-displacement relations according to Donnell's theory and Hooke's law [4]: $\epsilon_{x,0} = \frac{\partial u}{R_x \partial \psi} + \frac{w}{R_x} + \frac{1}{2}\left(\frac{\partial w}{R_x \partial \psi}\right)^2$, $\epsilon_{y,0} = \frac{\partial v}{R_y \partial \theta} + \frac{w}{R_y} + \frac{1}{2}\left(\frac{\partial w}{R_y \partial \theta}\right)^2$, $\gamma_{xy,0} = \frac{\partial u}{R_y \partial \theta} + \frac{\partial v}{R_x \partial \psi} + \frac{\partial w}{R_x \partial \psi}\frac{\partial w}{R_y \partial \theta}$, and $k_x = -\frac{\partial^2 w}{R_x^2 \partial \psi^2}$, $k_y = -\frac{\partial^2 w}{R_y^2 \partial \theta^2}$, and $k_{xy} = \frac{-2\partial^2 w}{R_x R_y \partial \psi \partial \theta}$. Here, $\epsilon_{x,0}$, $\epsilon_{y,0}$ and $\gamma_{xy,0}$ denote again the strain components at an arbitrary point on the middle surface, and k_x, k_y and k_{xy} denote its changes of curvature and torsion.

According to Hooke's law of linear elasticity, the following stress-strain equations hold $\sigma_x = \frac{E(\epsilon_x + \nu\epsilon_y)}{1-\nu^2}$, $\sigma_y = \frac{E(\epsilon_y + \nu\epsilon_x)}{1-\nu^2}$, and $\tau_{xy} = \tau_{yx} = \frac{E\gamma_{xy}}{2(1+\nu)}$, where σ_x and σ_y are the normal stresses in x- and y-direction and τ_{xy} is the shear stress acting along the shell's edges. The general formula for the elastic energy stored in a body during deformation, taking into account the assumptions made by Kirchhoff and Love as well as those for Donnell's theory, reads after using Hook's law:

$$
\begin{aligned}
U_{\mathrm{S}} = & \frac{1}{2}\frac{Eh}{1-\nu^2}\int_0^a\int_0^b\left(\epsilon_{x,0}^2+\epsilon_{y,0}^2+2\nu\epsilon_{x,0}\epsilon_{y,0}+\frac{1-\nu}{2}\gamma_{xy,0}^2\right)\mathrm{d}y\,\mathrm{d}x \\
& +\frac{1}{2}\frac{Eh^3}{12\left(1-\nu^2\right)}\int_0^a\int_0^b\left(k_x^2+k_y^2+2\nu k_x k_y+\frac{1-\nu}{2}k_{xy}^2\right)\mathrm{d}y\,\mathrm{d}x \\
& +\frac{1}{2}\left(\frac{1}{R_x}+\frac{1}{R_y}\right)\frac{Eh^3}{6\left(1-\nu^2\right)}\int_0^a\int_0^b\left(\epsilon_{x,0}k_x+\epsilon_{y,0}k_y\right. \\
& \left.+\nu\epsilon_{x,0}k_y+\nu\epsilon_{y,0}k_x+\frac{1-\nu}{2}\gamma_{xy,0}k_{xy}\right)\mathrm{d}y\,\mathrm{d}x+\mathcal{O}\left(h^4\right).
\end{aligned}
\tag{7}
$$

The first term in Eq. (7) represents the elastic energy resulting from stretching, the second term results from bending, and the third term is due to coupling of the aforementioned. Both coupling and the fourth-order term in h are neglected in Donnell's theory because z/R_x and z/R_y are small with respect to unity.

To model the influence of damping, Rayleigh dissipation function is used [5]:

$$
F_{\mathrm{D}} = \frac{1}{2}c\int_0^a\int_0^b\left(\dot{u}^2+\dot{v}^2+\dot{w}^2\right)\mathrm{d}y\,\mathrm{d}x = \frac{1}{2}\frac{ab}{4}\sum_{m=1}^{M}\sum_{n=1}^{N}c_{m,n}\left(\dot{u}_{m,n}^2+\dot{v}_{m,n}^2+\dot{w}_{m,n}^2\right),
\tag{8}
$$

with the modal damping coefficients $c_{m,n}$ being calculated from the modal damping ratios $\zeta_{m,n}$, which are determined experimentally [5], and the modal masses $\mu_{m,n}$ for which the following relations hold: $\zeta_{m,n} = \frac{c_{m,n}}{2\mu_{m,n}\omega_{m,n}}$ and $\mu_{m,n} = \rho_{\mathrm{S}}h\frac{ab}{4}$, with $\omega_{m,n}$ being the eigenfrequency of mode (m,n). External loading is modelled using virtual work, with $q_{x,y,z}$ denoting distributed forces/unit area: $W = \int_0^a\int_0^b\left(q_x u+q_y v+q_z w\right)\mathrm{d}y\,\mathrm{d}x$. $q_z = f_{\mathrm{N}}\cos\left(\omega_{\mathrm{N}}t\right)\delta\left(x-\tilde{x}\right)\delta\left(y-\tilde{y}\right)$ becomes the distributed load from a concentrated normal force with harmonic time dependence acting on an arbitrary point $(\tilde{x},\tilde{y})$ on the middle surface, where f_{N} is the force's magnitude, ω_{N} is the excitation frequency, and δ denotes the Dirac function which produces eventually $W = f_{\mathrm{N}}\cos\left(\omega_{\mathrm{N}}t\right)w(\tilde{x},\tilde{y},t)$.

3 Numerical Results

A simply supported shell, with 9 DOFs with and without inertial coupling in the kinetic energy [5], is considered.[2] Starting at zero displacement, a harmonically oscillating force is applied to the shell's center, with amplitude variation from 0 to

[2]Symbolic computations via Matlab's Symbolic Toolbox; non-dimensionalised differential equations solved in Julia using the `CVODE_BDF`-algorithm [6]; width, depth, thickness $a = b = 100\,\mathrm{mm}$, $h = 1\,\mathrm{mm}$; principal radii $R_x = R_y = 1\,\mathrm{m}$; Young's modulus, mass density and Poisson's ratio (steel) of 209 MPa, $7800\,\mathrm{kg/m^3}$, $\nu = 0.3$; eigenfrequencies and modal damping coefficients of selected modes were $\omega_{1,1} = 2\pi\cdot 952\,\mathrm{Hz}$, $\omega_{1,3} = \omega_{3,1} = 2\pi\cdot 2575\,\mathrm{Hz}$, $\omega_{3,3} = 2\pi\cdot 4472\,\mathrm{Hz}$ and $c_{1,1} = 0.1486\,\mathrm{kg/s}$, $c_{1,3} = c_{3,1} = 0.4018\,\mathrm{kg/s}$, $c_{3,3} = 0.6977\,\mathrm{kg/s}$.

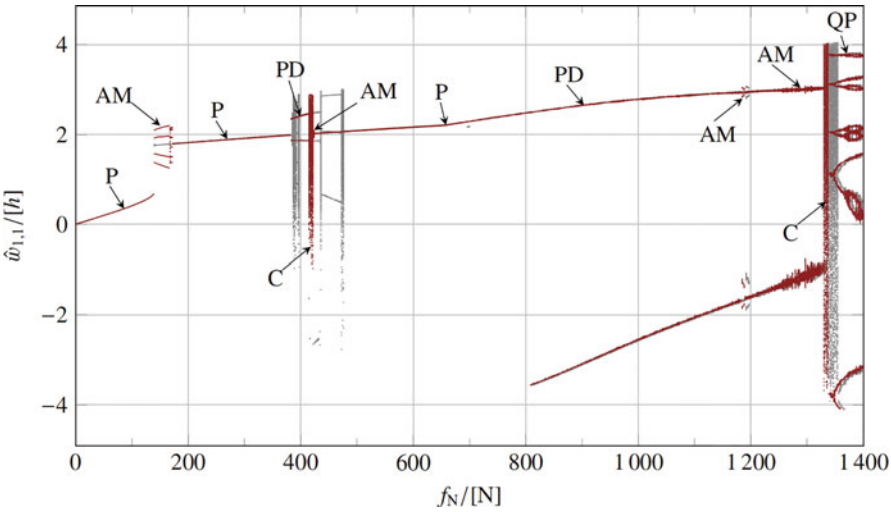

Fig. 2 Orbit diagram for varying levels of harmonic excitation for "IC" (red) and the "w/o IC" model (grey); $\omega_N = 0.8\,\omega_{1,1}$. P period-1, PD period doubling, AM amplitude modulation, QP quasi-periodic, C chaotic

1400 N in steps of 1.75 N and a fixed excitation frequency at $\omega_N = 0.8\,\omega_{1,1}$. Each step is held for 300,000 cycles of the excitation frequency to reach a steady-state solution. Then, all unique amplitudes inside the solution are extracted from the last 1000 cycles per step.

For the simplified model "without inertial coupling" (w/o IC) as well as for the model "with inertial coupling" (IC) at low force magnitudes below 100 N, the deflection amplitude $\hat{w}_{1,1}$ depends linearly on the forcing (Fig. 2) [5]. At $f_N = 138.25$ N, the maximum deflection jumps from $\hat{w}_{1,1} = 0.67$ to 1.77 h, cf. [3]. Beyond this point a multitude of different response types is observed, ranging from periodic over period-doubling and period-tripling motions to quasi-periodic and chaotic dynamics [7]. Noteworthy, qualitative differences between w/o IC and IC include the amplitude modulation after the jump at $f_N = 138.25$ N, where the "w/o IC" only exhibits period-1 oscillations and the chaotic regimes between $f_N \approx 400$ and 500 N and beyond 1300 N. In the first interval, where the "w/o IC" has two chaotic regimes connected by period-doubling behaviour and amplitude modulation, the "IC" shows period-doubling, which coincides with that of the "w/o IC", leading to a single chaotic regime, followed by period-1 solutions coincident with that leading out of the chaotic regime. Beyond 1300 N, the "IC" exhibits chaotic dynamics in the range from $f_N = 1330$ N to $f_N = 1337$ N, whereas the "w/o IC" has a chaotic regime between $f_N = 1335.25$ N and $f_N = 1354.5$ N. The quasi-periodic solutions following the chaotic behaviour, however, are again almost identical.

4 Conclusions

It has been shown how the Lagrange equations for a simply supported shell element can be derived. Fourier series were directly tailored towards the geometrical boundary conditions and the symmetry of the shell. Additional terms had to be added to satisfy also the kinetic boundary conditions. Truncating the series expansions at $M = N = 3$ and $M_w = N_w = 1$ proofed sufficient for obtaining meaningful results agreeing with those presented in [5] for a 22 DOF model. Then, the response to varying levels of harmonic excitation exhibited a large variety of dynamics ranging from simple quasi-harmonic responses over quasi-periodicity to chaos. Neglecting inertial coupling terms might turn to become problematic since dynamic regimes were different for the model with and without the coupling – an effect which may become more pronounced for more compliant, i.e. larger and thinner structures [1, 3].

References

1. Oberst, S., Tuttle, S.L., Griffin, D., Lambert, A., Boyce, R.R.: Experimental validation of tape springs to be used as thin-walled space structures. J. Sound Vib. **419**, 558–570 (2018)
2. Tessler, A.: Structural analysis methods for structural health management of future aerospace vehicles. Key Eng. Mater. **347**, 57–66 (2007)
3. Oberst, S., Tuttle, S.L.: Nonlinear dynamics of thin-walled elastic structures for applications in space. Mech. Syst. Signal Process. **110**, 469–484 (2018)
4. Leissa, A.W.: Vibration of Shells. National Technical Information Service (1973)
5. Amabili, M.: Non-linear vibrations of doubly curved shallow shells. Int. J. Non-Linear Mech. **40**(5), 683–710 (2005)
6. Rackauckas, C., Nie, Q.: Differentialequations.jl – a performant and feature-rich ecosystem for solving differential equations in Julia. J. Open Res. Softw. **5**, 5 (2017)
7. Schuster, H.G., Just, W.: Deterministic chaos. Wiley-VCH, Weinheim, Germany (2005)

Numerical Analysis Method for Flexible Tether with Time-Varying Length Across a Variable Boundary

Kenko Kudo and Yoshiaki Terumichi

1 Introduction

A tethered system is a flexible multibody system that consists of a mothership connected to various equipment items and probes by a flexible tether cable. As a new concept for a tethered system, a marine exploration system with a drone and time-varying length of flexible tether cable is considered. To design such an application with flexible components, the absolute nodal coordinate formulation (ANCF), which is widely used in flexible multibody simulations, is effective [1]. A variable-domain finite element (VFE) approach is also effective for describing the motion of a flexible beam with time-varying length [2, 3]. However, in simulations of the system, it is necessary to consider that the boundary position of the cable fluctuates due to flexibility, the time-varying length of the tether, and fluid forces, such as hydrodynamic drag, buoyancy, and the effect of added mass acting on parts of the cable every moment according to the fluctuation of the sea surface level [4]. Thus, with conventional approaches, the treatment of the fluid effects on each finite element with time-varying length is increasingly complex as time progresses. The aim of this study is to propose a numerical analysis method suitable for dynamics simulation of a flexible tether with large time-varying length and the fluctuation of a boundary position, such as water surface level. Analysis examples are provided to illuminate this fundamental study of numerical analysis with the proposed approach.

K. Kudo (✉) · Y. Terumichi
Sophia University, Chiyoda-ku, Tokyo, Japan
e-mail: k-kenko@eagle.sophia.ac.jp; y-terumi@sophia.ac.jp

S. Oberst et al. (eds.), *Vibration Engineering for a Sustainable Future*,
https://doi.org/10.1007/978-3-030-46466-0_9

2 Analysis Method

In this section, the numerical analysis method for a flexible tether with time-varying length across a variable boundary is presented. The ANCF is applied to a nonlinear finite element method to analyze a flexible tether. A VFE approach is extended to the ANCF, and dimensionless variables are introduced to the equation of motion with the length of the flexible body [5].

2.1 Modeling and Formulation of the VFE-ANCF

In the VFE model applied to the ANCF, a fixed number of elements with time-varying length is considered. The position vector $\mathbf{r}$ in the inertia frame for an arbitrary point on a flexible beam is described using the shape function $\mathbf{S}$, which is constant over time and depends on ξ, and the nodal coordinates $\mathbf{e}$ as follows:

$$\mathbf{r} = \mathbf{S}\mathbf{e}, \tag{1}$$

$$\mathbf{e} = [e_1 \;\; e_2 \;\; e_3 \;\; e_4 \;\; e_5 \;\; e_6 \;\; e_7 \;\; e_8]^{\mathrm{T}}, \tag{2}$$

where $\xi = x/l_e$; x is the coordinate of the point along the beam axis in the deformed configuration; l_e is the length of the element; e_1, e_2, e_5, and e_6 represent the absolute coordinates of the nodes at the left end and right end of the element, respectively; and

$$e_3 = l_e \frac{\partial \mathrm{r}_1\,(x{=}0)}{\partial x},\; e_4 = l_e \frac{\partial \mathrm{r}_2\,(x{=}0)}{\partial x},\; e_7 = l_e \frac{\partial \mathrm{r}_1\,(x{=}l_e)}{\partial x},\; \text{and } e_8 = l_e \frac{\partial \mathrm{r}_2\,(x = l_e)}{\partial x}, \tag{3}$$

in which r_1 and r_2 are the components of the vector $\mathbf{r}$ that defines the global position vector of the arbitrary point described by Eq. (1). The kinetic energy of the element can be defined using the velocity vector derived by differentiating Eq. (1) with respect to time as follows:

$$T_e = \frac{1}{2}\int_{V_e} \rho \dot{\mathbf{r}}^{\mathrm{T}} \dot{\mathbf{r}} dV_e = \frac{1}{2}\rho A l_e \dot{\mathbf{e}}^{\mathrm{T}} \int_0^1 \mathbf{S}^{\mathrm{T}}\mathbf{S} d\xi \dot{\mathbf{e}}, \tag{4}$$

where V_e, ρ, and A are the volume, mass density, and cross-section area of finite element, respectively. In addition, in this paper, the elastic energy is split into two parts, the elastic energy due to the axial strain U_l and the elastic energy due to bending based on the curvature of the deformed beam centerline U_t. Finally, using the Lagrange equation, the equation of motion for an element of the beam is obtained as follows:

$$\mathbf{M}_e\ddot{\mathbf{e}} + \mathbf{Q}_{le} + \mathbf{Q}_{te} = \mathbf{0}, \tag{5}$$

where $\mathbf{M}_e$ is the mass matrix and $\mathbf{Q}_{le}$ and $\mathbf{Q}_{te}$ are the elastic force vector of axial strain and bending, respectively.

2.2 Modeling and Formulation for the Double Flexible Body

To analyze the motion of a flexible body with a variable boundary, the computational analysis model is expressed with double flexible beams, flexible body A and B with n and N elements, respectively, by VFE-ANCF, where both ends of bodies A and B are connected by defining their absolute coordinates and slopes equally. Thus, the generalized coordinates and constraints are defined as follows:

$$\mathbf{q} = \left[\mathbf{e}^{A\mathrm{T}} \ \mathbf{e}^{B\mathrm{T}} \right]^{\mathrm{T}}, \tag{6}$$

$$\mathbf{C} = \begin{bmatrix} e_1^{B(j=1)} - e_5^{A(j=n)} \\ e_2^{B(j=1)} - e_6^{A(j=n)} \\ e_3^{B(j=1)} - e_7^{A(j=n)} \\ e_4^{B(j=1)} - e_8^{A(j=n)} \end{bmatrix} = \mathbf{0}. \tag{7}$$

When the behavior of the flexible body is under holonomic constraints, the system motion is written with an augment method in the following expression:

$$\begin{bmatrix} \mathbf{M} & \mathbf{C_q}^{\mathrm{T}} \\ \mathbf{C_q} & \mathbf{0} \end{bmatrix} \begin{bmatrix} \ddot{\mathbf{q}} \\ \boldsymbol{\lambda} \end{bmatrix} = \begin{bmatrix} \mathbf{Q}_f \\ \boldsymbol{\gamma} \end{bmatrix}. \tag{8}$$

2.3 Introduction of Dimensionless Variables

Dimensionless variables are introduced with $L(t)$ for the each length of the flexible bodies A and B, as in Eq. (9), for the number and length of each element to be dealt with as a constant relative to the each length of flexible bodies A and B independently as time varies:

$$L = LL^*, \ \ l_e = Ll_e{}^*, \ \ x = Lx^*, \ \ t = Tt^*, \ \ \mathbf{e} = L\mathbf{e}^* \tag{9}$$

where $T = L\sqrt{\rho/E}$ is the longitudinal vibration being considered. Using Eq. (9), the equation of motion for an element of the beam in the dimensionless form is obtained as follows:

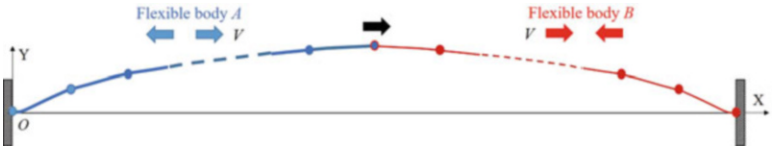

Fig. 1 Double VFE-ANCF model with the proposed method

Table 1 Material parameters

Parameter	Symbol	Units	Value
Length	L	m	1.0
Diameter	D	m	0.001
Modulus of elasticity	E	Pa	1.3×10^9
Density	ρ	kg/m^3	1780

$$\mathbf{M}_e{}^*\ddot{\mathbf{e}}^* + \mathbf{Q}_e{}^* + \mathbf{Q}_{te}{}^* = \mathbf{0}, \tag{10}$$

3 Numerical Simulation

3.1 Comparison of the Proposed Method and ANCF

In this section, a planar motion and vibration analysis for an elastic beam and a comparison between conventional ANCF and double VFE-ANCF, the proposed method, for a numerical simulation of a flexible body with a variable boundary have been carried out. Figure 1 shows the analysis model with double VFE-ANCF. In the initial state, the beam model is located horizontally along the X axis with the natural length, and both end points are fixed. The left end point is attached at the origin of the absolute nodal coordinate system, O-XY. An initial velocity 0.01 m/s is given to the midpoint of the beam in the Y-direction. Material parameters for numerical simulations are listed in Table 1 for a fluorocarbon line.

Numerical analysis with double VFE-ANCF was conducted for the case where the velocity with time-varying length across the boundary position $V = 0.1$ m/s. The length of each finite element has a time-varying value. The modes of the flexible beam with both ANCF and double VFE-ANCF are compared in Fig. 2. The results are in good agreement, indicating that the proposed method is effective in the case of a variable boundary.

3.2 Vibration Analysis with a Variable Boundary

Modeling of planar motion and vibration of a flexible beam with a moving restraint point was carried out, as shown in Fig. 3. Initially, the model is positioned

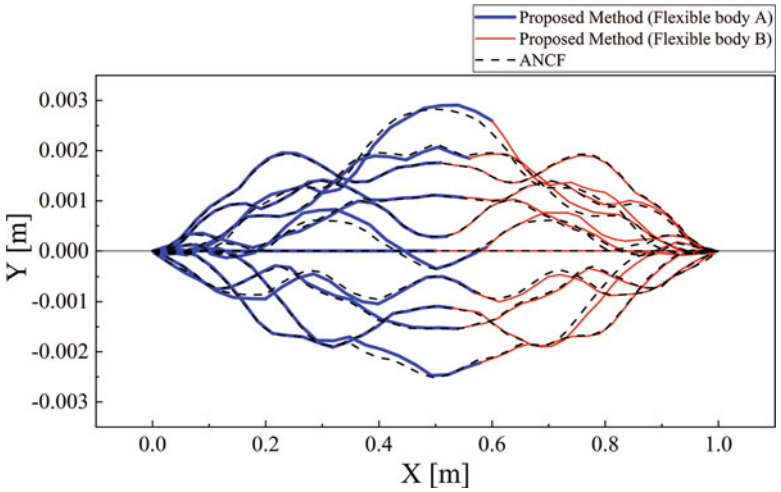

Fig. 2 Modes of the flexible beam

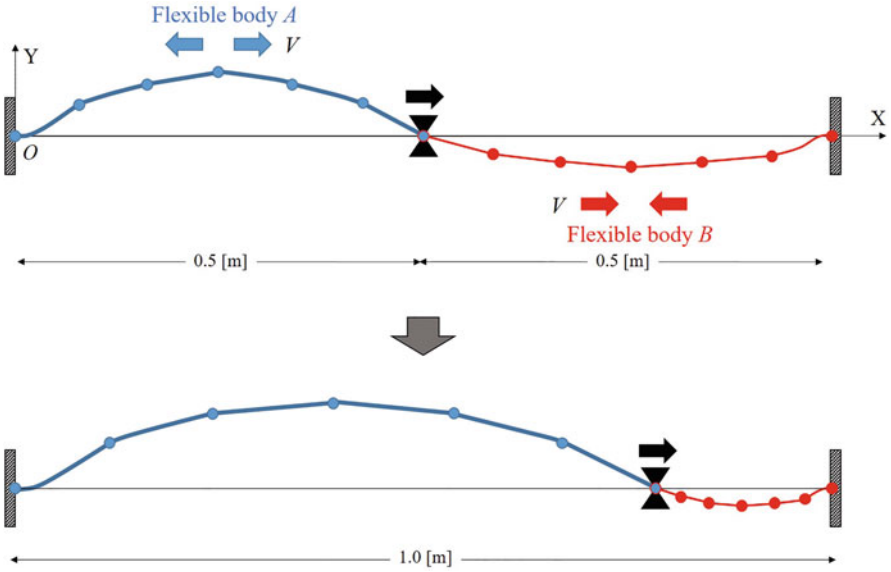

Fig. 3 Analysis model with a variable boundary using the proposed method

horizontally, and the left end point is fixed to the origin of the absolute nodal coordinate system, O-XY. The right end point and vertical direction of the boundary point are also fixed, and an initial velocity is given to the midpoint of flexible body *A* in the Y-direction. The boundary point slid along the X-axis, according to the time-varying length of the flexible bodies *A* and *B* with a constant velocity *V*. The

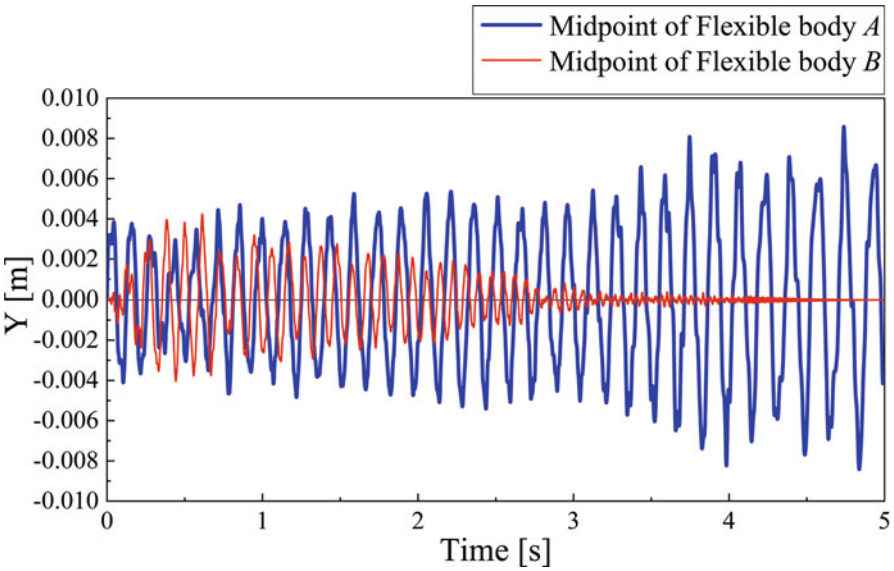

Fig. 4 Displacement of the midpoint of flexible body *A*,*B* in the Y-direction

numerical results, displacement of the midpoint of flexible bodies *A* and *B* in the Y-direction, are shown in Fig. 4. The amplitude of flexible body *A* increases along with the movement of the boundary point, while the amplitude of flexible body *B* decreases. Furthermore, due to the dimensionless formulation, the analysis could be conducted even when the length of the flexible body became quite short as the boundary position slid.

4 Conclusion

A numerical analysis method for a flexible tether with time-varying length across a variable boundary was proposed. A VFE approach was extended to ANCF, and the numerical model was expressed with double flexible beams. Dimensionless variables were also introduced to the equation of motion. The result obtained using the proposed method double VFE-ANCF was compared with the results obtained using the ANCF, and they were in good agreement. In addition, the proposed method is effective even when the length of the flexible body becomes very short as the boundary position slides.

References

1. Shabana, A.: Dynamics of Multibody Systems, 2nd edn. Cambridge University Press, Cambridge (2005)
2. Behdinan, K., Tabarrok, B.: A finite element formulation for sliding beams, Part1. Int. J. Numer. Methods Eng. **43**, 1309–1333 (1998)
3. Kawaguchi, K., Terumichi, Y.: The study of the tether motion with time-varying length using the absolute nodal coordinate formulation with multiple nonlinear time scales. J. Syst. Des. Dyn. **1**(3), 491–500 (2007)
4. Buckham, B., Nahon, M., Seto, M., Zhao, X., Lambert, C.: Dynamics and control of a towed underwater vehicle system, part1: model development. Ocean Eng. **30**, 453–470 (2003)
5. Nayfeh, A., Mook, D.: Nonlinear Oscillations. John Wiley & Sons Inc, New York (1979)

Identification of Modal Properties Using Linear Fit Method with Polynomial Approximation of Residue Term of Frequency Response Function

Daiki Tajiri, Shinsuke Takehara, Masami Matsubara, and Shozo Kawamura

1 Introduction

As a technique to understand vibration characteristics, experimental modal analysis is used to identify modal properties, such as the natural frequency, damping characteristics, and residue from vibration tests. In the identification methods of modal properties in the frequency domain, it is necessary to determine the analysis frequency range and the number of degrees of freedom (DOFs) in the frequency response function (FRF). However, they are often part of the phenomena of actual structures with infinite DOFs. Therefore, mode components that lie outside of the analysis frequency range adversely affect the identification accuracy. As a countermeasure for this, there is a method of modeling it by a quadratic function as residual mass and residual rigidity to improve the identification accuracy of the mode to be analyzed [1]. In this conventional method, it is assumed that the modes corresponding to the residual terms have components only in the real part and that it is sufficiently far from the analysis frequency range. However, if a mode that lies outside of this range is near the boundaries, it is difficult to approximate it with a quadratic function, and the influence is also apparent in the imaginary part, so approximation by the conventional method is inappropriate.

Therefore, in this study, an approximate method is proposed that both the real part and the imaginary part of the FRF of the mode components lie outside the analysis frequency range with a cubic function. The natural frequency and damping

D. Tajiri · S. Takehara (✉) · M. Matsubara · S. Kawamura
Toyohashi University of Technology, Department of Mechanical Engineering, Toyohashi-shi, Aichi, Japan
e-mail: tajiri@dynamics.me.tut.ac.jp; s185107@edu.tut.ac.jp; mm018@edu.imc.tut.ac.jp; kawamura@me.tut.ac.jp

S. Oberst et al. (eds.), *Vibration Engineering for a Sustainable Future*,
https://doi.org/10.1007/978-3-030-46466-0_10

characteristics of the mode are identified by the linear fit method (LFM) of the FRF [2, 3]. To verify the validity of the proposed method, modal properties are identified of the second to ninth modes of the FRF in a 10-DOF system.

2 Theory of Proposed Identification Method

A method is proposed to identify modal properties by approximating the method of the mode components that lie outside the analysis frequency range with a cubic function for the real part and for the imaginary part and by separating each mode. The theory of the proposed method is explained here.

Now, accelerance which is a format for the FRF with a hysteretic damping system is considered for the vibration system of n-DOF. Let $H_{r,e}$ be the FRFs with single-input-single-output with input point e and reference point r. If the mode components corresponding to e or r in the p-th mode are $\phi_{e,p}$ and $\phi_{r,p}$, then $H_{r,e}$ for an arbitrary angular frequency ω is as follows. The modal properties are the p-th mode natural angular frequency ω_{np} ($=2\pi f_{np}$, natural frequency f_{np}), structural damping coefficient g_p, and residue $(\phi_{r,p}\phi_{e,p})/k_p$.

$$H_{r,e}(\omega) = \frac{X_r}{F_e} = \sum_{p=1}^{n} \frac{-\omega^2 \left(\phi_{r,p}\phi_{e,p}\right)/k_p}{1 - \left(\omega/\omega_{np}\right)^2 + j g_p} \tag{1}$$

The LFM is a single-DOF method that constructs a linear equation whose natural angular frequency and damping characteristics are unknowns from the theoretical expressions of the real part and imaginary part of the FRF, and it identifies unknowns by the least squares method using measurement data obtained experimentally [2–4]. In the range where the p-th mode is dominant, the mode components that lie outside the analysis frequency range are approximated by a cubic function, and the real part and the imaginary part are as follows:

$$\begin{aligned}
\mathrm{Re}\left\{H_{r,e}^{p}(\omega)\right\} &= \frac{-\omega^2(\phi_{r,p}\phi_{e,p})/k_p\left\{1-(\omega/\omega_{np})^2\right\}}{\left\{1-(\omega/\omega_{np})^2\right\}^2+g_p^2} + c_1\omega_q^3 + c_2\omega_q^2 + c_3\omega_q + c_4 \\
\mathrm{Im}\left\{H_{r,e}^{p}(\omega)\right\} &= \frac{-\omega^2(\phi_{r,p}\phi_{e,p})/k_p(-g_p)}{\left\{1-(\omega/\omega_{np})^2\right\}^2+g_p^2} + d_1\omega_q^3 + d_2\omega_q^2 + d_3\omega_q + d_4
\end{aligned} \tag{2}$$

In Eq. (2), the cubic function parts are identified at the same time as the residue, so neglecting now and further deleting the residue term and simplifying, the basic equation of the LFM is as follows:

$$\mathrm{Im}\left\{H_{r,e}^{p}(\omega)\right\}\omega^2\frac{1}{\omega_{np}^2} - \mathrm{Re}\left\{H_{r,e}^{p}(\omega)\right\}g_p = \mathrm{Im}\left\{H_{r,e}^{p}(\omega)\right\} \tag{3}$$

If z is the number of data points included in the analysis frequency range to which the LFM is applied, Eq. (1) is z simultaneous equations. If the damping characteristics are large, the more one adopts the data far from the resonance peak in the analysis frequency range, the more likely it is that the mode components that lie outside of the analysis frequency range will have a bad influence on the identification of modal properties. Therefore, the natural angular frequency and the structural damping coefficient are identified by the weighted least-squares method, shown as follows, using the weighting function $\mathbf{W}$ that emphasizes the data near the resonance peak. The diagonal component w_{pm} of the weighting function $\mathbf{W}$ is a function in the form of the imaginary part of the FRF, which is calculated from the estimated natural angular frequency $\omega_{n\alpha}$ of focusing on the p-th mode and structural damping coefficient g_β. To reduce the influence of mode components that lie outside the analysis frequency range, the value of g_β corresponding to the structural damping coefficient is set to 0.001 [5].

$$
\begin{aligned}
&\mathbf{x} = \left(\mathbf{A}^{\mathrm{T}}\mathbf{W}\mathbf{A}\right)^{-1}\mathbf{A}^{\mathrm{T}}\mathbf{W}\mathbf{B} \qquad (q = 1, 2, \cdots, z)\\
&\mathbf{A} = \begin{bmatrix} H_I\left(\omega_{p1}\right)\omega_{p1}^2 & H_R\left(\omega_{p1}\right) \\ H_I\left(\omega_{p2}\right)\omega_{p2}^2 & H_R\left(\omega_{p2}\right) \\ \vdots & \vdots \\ H_I\left(\omega_{pz}\right)\omega_{pz}^2 & H_R\left(\omega_{pz}\right) \end{bmatrix} \quad \mathbf{x} = \begin{Bmatrix} \frac{1}{\omega_{np}^2} \\ -g_p \end{Bmatrix} \quad \mathbf{B} = \begin{Bmatrix} H_I\left(\omega_{p1}\right) \\ H_I\left(\omega_{p2}\right) \\ \vdots \\ H_I\left(\omega_{pz}\right) \end{Bmatrix} \\
&\mathbf{W} = \begin{bmatrix} w_{p1} & 0 & 0 & 0 \\ 0 & w_{p2} & 0 & 0 \\ 0 & 0 & \ddots & 0 \\ 0 & 0 & 0 & w_{pz} \end{bmatrix}, \quad w_{pq} = \left|\mathrm{Im}\left\{\frac{1}{1-\left(\omega_q/\omega_{n\alpha}\right)^2+jg_\beta}\right\}\right|
\end{aligned}
\tag{4}
$$

The parameters obtained from the LFM are inserted in the following equation of the real part of the FRF (Eq. (5)). The residue of the mode to be analyzed and the coefficients of the cubic functions of representing the real part of the mode components that lie outside the analysis frequency range are identified by the least-squares method. Furthermore, the parameters of the identified modal properties are inserted in the following equation of the imaginary part of the FRF (Eq. (6)), and the coefficients of the cubic function representing the imaginary part of the mode components that lie outside the analysis frequency range are identified.

From the above, the initial values of the parameters required to reconstruct the FRF in the analysis frequency range are obtained. Subsequently, the initial values are updated by the mode separation method. This single-DOF method is performed for each mode to be analyzed to identify each modal property.

$$
\begin{aligned}
&\mathbf{Y}_{\mathrm{Re}} = \left(\mathbf{C}_{\mathrm{Re}}^{\mathrm{T}}\mathbf{C}_{\mathrm{Re}}\right)^{-1}\mathbf{C}_{\mathrm{Re}}^{\mathrm{T}}\mathbf{D}_{\mathrm{Re}} \qquad (q = 1, 2, \cdots, z)\\
&\mathbf{Y}_{\mathrm{Re}} = \begin{Bmatrix} \left(\varphi_{r,p}\varphi_{e,p}\right)/k_p \\ c_1 \\ c_2 \\ c_3 \\ c_4 \end{Bmatrix}, \quad \mathbf{C}_{\mathrm{Re}} = \begin{bmatrix} e_{p1} & {\omega_{p1}}^3 & {\omega_{p1}}^2 & \omega_{p1} & 1 \\ e_{p2} & {\omega_{p2}}^3 & {\omega_{p2}}^2 & \omega_{p2} & 1 \\ \vdots & \vdots & \vdots & \vdots & \vdots \\ e_{pz} & {\omega_{pz}}^3 & {\omega_{pz}}^2 & \omega_{pz} & 1 \end{bmatrix},\\
&\mathbf{D}_{\mathrm{Re}} = \begin{bmatrix} \mathrm{Re}\left\{H_{r,e}^{p}\left(\omega_{p1}\right)\right\} \\ \mathrm{Re}\left\{H_{r,e}^{p}\left(\omega_{p2}\right)\right\} \\ \vdots \\ \mathrm{Re}\left\{H_{r,e}^{p}\left(\omega_{pz}\right)\right\} \end{bmatrix}, e_{pq} = \frac{\left\{1-\left(\omega_q/\omega_{np}\right)^2\right\}}{\left\{1-\left(\omega_q/\omega_{np}\right)^2\right\}^2+g_p^2}
\end{aligned}
\tag{5}
$$

$$
\begin{aligned}
&\mathbf{Y}_{\mathrm{Im}} = \left(\mathbf{C}_{\mathrm{Im}}^{\mathrm{T}}\mathbf{C}_{\mathrm{Im}}\right)^{-1}\mathbf{C}_{\mathrm{Im}}^{\mathrm{T}}\mathbf{D}_{\mathrm{Im}} \qquad (q = 1, 2, \cdots, z)\\
&\mathbf{Y}_{\mathrm{Im}} = \begin{Bmatrix} d_1 \\ d_2 \\ d_3 \\ d_4 \end{Bmatrix}, \quad \mathbf{C}_{\mathrm{Im}} = \begin{bmatrix} {\omega_{p1}}^3 & {\omega_{p1}}^2 & \omega_{p1} & 1 \\ {\omega_{p2}}^3 & {\omega_{p2}}^2 & \omega_{p2} & 1 \\ \vdots & \vdots & \vdots & \vdots \\ {\omega_{pz}}^3 & {\omega_{pz}}^2 & \omega_{pz} & 1 \end{bmatrix},\\
&\mathbf{D}_{\mathrm{Im}} = \begin{bmatrix} \mathrm{Im}\left\{H_{r,e}^{p}\left(\omega_{p1}\right)\right\} - l_{p1}\left(\varphi_{r,p}\varphi_{e,p}\right)/k_p \\ \mathrm{Im}\left\{H_{r,e}^{p}\left(\omega_{p2}\right)\right\} - l_{p2}\left(\varphi_{r,p}\varphi_{e,p}\right)/k_p \\ \vdots \\ \mathrm{Im}\left\{H_{r,e}^{p}\left(\omega_{pz}\right)\right\} - l_{pz}\left(\varphi_{r,p}\varphi_{e,p}\right)/k_p \end{bmatrix}, l_{pq} = \frac{-g_p}{\left\{1-\left(\omega_q/\omega_{np}\right)^2\right\}^2+g_p^2}
\end{aligned}
\tag{6}
$$

3 Identification of Modal Properties by Numerical Examples

In this study, the modal properties of eight-DOF systems from a 10-DOF system that has two modes that lie outside of the analysis frequency range are identified. In the FRF, there are natural frequencies of every 10 Hz between 10 and 100 Hz for each mode, the structural damping coefficients are 5.000×10^{-2} for all modes uniformly, and the residues are set to arbitrary values for each mode. The analysis frequency range is the interval from the antiresonance formed between the first and second modes of the FRF to the antiresonance formed between the ninth and tenth modes. The frequency resolution is 0.25 Hz, and the FRF contains no noise.

Modal properties are identified for the above verification model. Table 1 shows the true values of the structural damping coefficient and the values of identification by the proposed and the conventional methods. The values of identification by the proposed method, shown in Table 1, are close to the true values, and the maximum relative error is approximately 0.7% in the ninth mode. However, the values of identification by the conventional method have a large difference from the true

Table 1 Identified values of structural damping

Mode order	g_p of true value	g_p by proposed method	g_p by conventional method
2	5.000×10^{-2}	5.002×10^{-2}	5.017×10^{-2}
3	5.000×10^{-2}	5.004×10^{-2}	5.001×10^{-2}
4	5.000×10^{-2}	5.006×10^{-2}	4.933×10^{-2}
5	5.000×10^{-2}	5.008×10^{-2}	4.988×10^{-2}
6	5.000×10^{-2}	5.011×10^{-2}	4.990×10^{-2}
7	5.000×10^{-2}	5.016×10^{-2}	5.008×10^{-2}
8	5.000×10^{-2}	5.028×10^{-2}	5.056×10^{-2}
9	5.000×10^{-2}	5.036×10^{-2}	5.637×10^{-2}

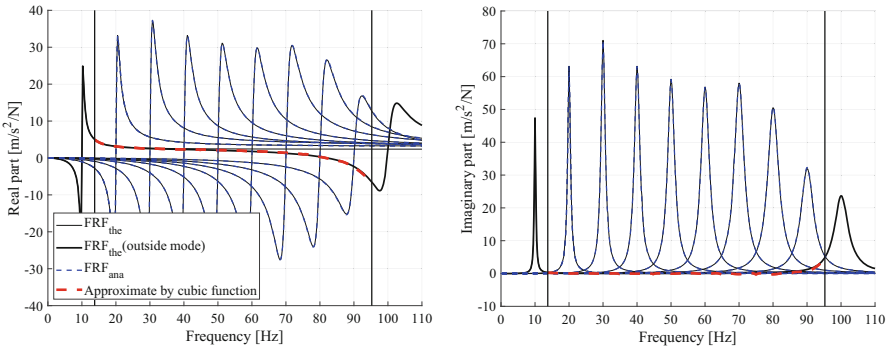

Fig. 1 Synthesis function drawn by the identification result of the proposed method

value, and the maximum relative error is approximately 12% in the ninth mode; thus, it is clear that the identification accuracy is poor. This is thought to be because, in the conventional method, only the real part of the mode components that lie outside the analysis frequency range is approximated by the quadratic function, and the imaginary part of the mode components is ignored. Also, Fig. 1 shows a comparison of the original FRF and the synthesis function reconstructed by the proposed method in the real and the imaginary parts. The vertical lines indicate the top and bottom of the analysis frequency range, the black solid lines indicate the original FRF, the blue broken lines indicate the synthesis function, and the red broken line indicates the approximation result. Figure 1 shows that the synthesis functions of the real and imaginary parts are in good agreement with the original FRF. This is because the mode components that lie outside the analysis frequency range can be approximated appropriately. This high identification accuracy of the proposed method is maintained even if the antiresonance frequency that lies outside of the analysis frequency range is included in the analysis frequency range.

The above shows that the modal properties can be identified with high accuracy only from the data of the analysis frequency range for the FRF of the multi-DOF system by the proposed method.

4 Discussion and Conclusion

In this study, a method was proposed to identify modal properties by approximating the influence of the modes that lie outside the analysis frequency range with a cubic function for each of the real and imaginary parts of the FRF. In this method, modal properties can be identified with high accuracy, and it is understood that the synthesis function is in good agreement with the original FRF. However, the mode components that lie outside of the analysis frequency range cannot be approximated appropriately by the conventional method; therefore, in the higher-order modes of the modes to be identified, the identification accuracy is low.

The above shows that the proposed method has significance as a multi-DOF method for accurately identifying the modal properties in a specific frequency range in the FRF where the modes are close to the boundaries. There are two differences between the proposed method and the conventional method in that the mode components that lie outside of the analysis frequency range are approximated using a cubic function and the imaginary part is approximated. However, in this study, it has not been researched which differences are more effective for the results. This investigation will be a future subject.

References

1. Ewins, D.J.: Modal Testing, Theory, Practice, and Application, 2nd edn, pp. 422–427. Research Studies Press Ltd, Baldock (2000)
2. Kawamura, S., Kita, M., Matsubara, M., Ise, T.: Study of the effect of specimen size and frequency on the structural damping property of beam. Mech. Eng. J. **3**(6), 16-00446 (2016)
3. Matsubara, M., Kawamura, S., Ise, T.: Application of modal properties identification to multi-degree-of-freedom system using simultaneous equations of the real and imaginary parts of frequency response function. Trans. JSME. **84**(860), 17–00540 (2018)
4. Matsubara, M., Tajiri, D., Takehara, S., Kawamura, S.: Linear fit method for modal parameter estimation using the real and imaginary parts of frequency response function (Identification accuracy improvement based on weighted least square method). Trans. JSME. **85**(873), 012011 (2019)
5. Tajiri, D., Matsubara, M., Kawamura, S.: Identification of modal parameters in a lightly damped system based on impact vibration testing: application of exponential window and removal of its effect. J. Phys. **1264**(1), 18–00433 (2019)

Analysis of Transient Response Moment of a SDOF System Under Non-Gaussian Random Excitation by the Equivalent Non-Gaussian Excitation Method

Takahiro Tsuchida and Kohei Kanno

1 Introduction

Stochastic response analysis of mechanical and structural systems subjected to random excitation has been carried out widely for many decades. In many cases, the random excitation has been assumed to be a Gaussian process. However, some random excitations (e.g., road roughness [1], shallow water waves [2]) possess highly non-Gaussianity. The response of a system under non-Gaussian excitation is generally non-Gaussian, and the response characteristics are quite different from those in the case of Gaussian excitation. Therefore, response analysis in consideration of the non-Gaussianity of random excitation is significant. It's also important to analyze transient response under random excitation because the transient response often exceeds stationary response.

In recent years, the equivalent non-Gaussian excitation method was presented to obtain the response moments of non-Gaussian randomly excited systems [3]. It was demonstrated that this method provides accurate results of the stationary response moments up to the fourth order for non-Gaussian random excitation with a wide range of probability distributions and bandwidth of power spectrum. However, the effectiveness of the method in transient analysis has not been verified yet.

In this study, we analyze the transient response of a SDOF linear system subjected to non-Gaussian random excitation by the equivalent non-Gaussian excitation method. In the analysis, in order to derive a closed set of moment equations for the system response, the diffusion coefficient in a stochastic differential equation ruling the excitation is replaced by an equivalent one, which is expressed by a quadratic polynomial.

T. Tsuchida (✉) · K. Kanno
Tokyo Institute of Technology, Meguro, Japan
e-mail: ttsuchida@sc.e.titech.ac.jp; kanno@k.sc.e.titech.ac.jp

S. Oberst et al. (eds.), *Vibration Engineering for a Sustainable Future*,
https://doi.org/10.1007/978-3-030-46466-0_11

In numerical examples, the analytical method will be applied to a SDOF system subjected to non-Gaussian excitation with the generalized Gaussian distribution.

2 System and Non-Gaussian Random Excitation

Consider a single-degree-of-freedom linear system described by

$$\ddot{X} + 2\zeta \dot{X} + X = U(t) \tag{1}$$

where X denotes the displacement, ζ is the damping ratio, and $U(t)$ is a zero-mean stationary non-Gaussian random excitation.

The non-Gaussian random excitation $U(t)$ is prescribed by both its first-order probability density function $p_U(u)$ and power spectral density $S_U(\omega)$. Various non-Gaussian distributions are taken into account for $p_U(u)$. The power spectrum $S_U(\omega)$ is given by

$$S_U(\omega) = \frac{\alpha \mathrm{E}[U^2]}{\pi(\omega^2 + \alpha^2)} \tag{2}$$

where α is the bandwidth parameter. $S_U(\omega)$ is shown in Fig. 1 (Left).

The excitation $U(t)$ can be described by the following one-dimensional Itô stochastic differential equation [4]

$$dU = -\alpha U dt + D(U) dB(t) \tag{3}$$

where α is the bandwidth parameter in Eq. (2), $B(t)$ is a Wiener process, and the diffusion coefficient $D(u)$ is expressed by

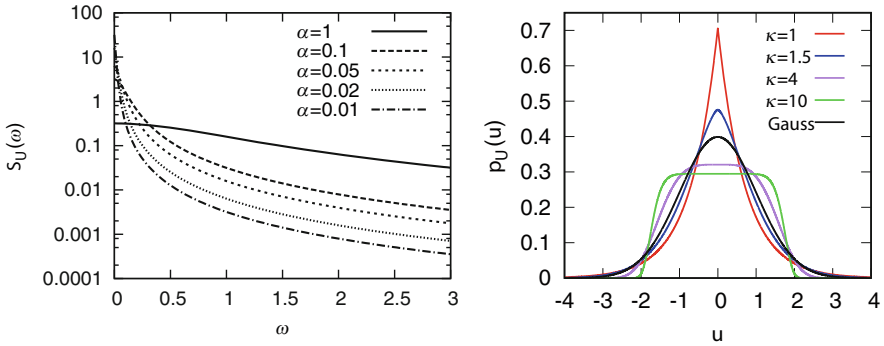

Fig. 1 Left: Power spectrum. Right: Generalized Gaussian distribution. ($\mathrm{E}[U] = 0$, $\mathrm{E}[U^2] = 1$)

$$D^2(u) = -\frac{2\alpha}{p_U(u)} \int_{-\infty}^{u} p_U(s) \cdot s \, ds \tag{4}$$

3 Equivalent Non-Gaussian Excitation Method

A set of Itô stochastic differential equations consisted of the governing equations for the system (1), and the excitation (3) is described by

$$dX = \dot{X} dt \tag{5}$$

$$d\dot{X} = (-2\zeta \dot{X} - X + U)dt \tag{6}$$

$$dU = -\alpha U dt + D(U) dB(t) \tag{7}$$

Using the Itô's formula [5] to Eqs. (5), (6), and (7), moment equations for the system response can be derived. However, the moment equations are generally not closed due to the nonlinearity of $D^2(u)$ given by Eq. (4).

In the equivalent non-Gaussian excitation method, the diffusion coefficient $D(U)$ in Eq. (7) is replaced with the equivalent one $D_{\text{eq}}(U)$. $D_{\text{eq}}^2(U)$ is expressed by a quadratic polynomial.

$$D_{\text{eq}}^2(U) = A_{\text{eq}} U^2 + B_{\text{eq}} U + C_{\text{eq}} \tag{8}$$

where the coefficients A_{eq}, B_{eq}, and C_{eq} are adjusted by minimization of the mean square error $\text{E}[e^2]$ between $D^2(U)$ and $D_{\text{eq}}^2(U)$.

$$\text{E}[e^2] = \text{E}[(D^2(U) - D_{\text{eq}}^2(U))^2] = \text{E}[(D^2(U) - A_{\text{eq}} U^2 - B_{\text{eq}} U - C_{\text{eq}})^2] \tag{9}$$

Minimization of $\text{E}[e^2]$ is realized when the following three conditions hold:

$$\frac{\partial \text{E}[e^2]}{\partial A_{\text{eq}}} = 0, \quad \frac{\partial \text{E}[e^2]}{\partial B_{\text{eq}}} = 0, \quad \frac{\partial \text{E}[e^2]}{\partial C_{\text{eq}}} = 0 \tag{10}$$

Solving Eq. (10) with respect to A_{eq}, B_{eq} and C_{eq} leads to

$$\begin{aligned} A_{\text{eq}} = & \frac{(\text{E}[U^2] - \text{E}[U]^2)(\text{E}[U^2 D^2(U)] - \text{E}[U^2]\text{E}[D^2(U)])}{(\text{E}[U^4] - \text{E}[U^2]^2)(\text{E}[U^2] - \text{E}[U]^2) - (\text{E}[U^3] - \text{E}[U]\text{E}[U^2])^2} \\ & - \frac{(\text{E}[U^3] - \text{E}[U]\text{E}[U^2])(\text{E}[U^2 D^2(U)] - \text{E}[U^2]\text{E}[D^2(U)])}{(\text{E}[U^4] - \text{E}[U^2]^2)(\text{E}[U^2] - \text{E}[U]^2) - (\text{E}[U^3] - \text{E}[U]\text{E}[U^2])^2} \end{aligned} \tag{11}$$

$$B_{\mathrm{eq}} = \frac{(\mathrm{E}[U^4] - \mathrm{E}[U^2]^2)(\mathrm{E}[U\,D^2(U)] - \mathrm{E}[U]\mathrm{E}[D^2(U)])}{(\mathrm{E}[U^4] - \mathrm{E}[U^2]^2)(\mathrm{E}[U^2] - \mathrm{E}[U]^2) - (\mathrm{E}[U^3] - \mathrm{E}[U]\mathrm{E}[U^2])^2} - \frac{(\mathrm{E}[U^3] - \mathrm{E}[U]\mathrm{E}[U^2])(\mathrm{E}[U^2 D^2(U)] - \mathrm{E}[U^2]\mathrm{E}[D^2(U)])}{(\mathrm{E}[U^4] - \mathrm{E}[U^2]^2)(\mathrm{E}[U^2] - \mathrm{E}[U]^2) - (\mathrm{E}[U^3] - \mathrm{E}[U]\mathrm{E}[U^2])^2} \tag{12}$$

$$C_{\mathrm{eq}} = \mathrm{E}[D^2(U)] - A_{\mathrm{eq}}\mathrm{E}[U^2] - B_{\mathrm{eq}}\mathrm{E}[U] \tag{13}$$

The second-, third-, and fourth-order moment equations for the excitation $U(t)$ are

$$-2\alpha\mathrm{E}[U^2] + \mathrm{E}[D^2(U)] = 0 \tag{14}$$

$$-3\alpha\mathrm{E}[U^3] + 3\mathrm{E}[u D^2(U)] = 0 \tag{15}$$

$$-4\alpha\mathrm{E}[U^4] + 6\mathrm{E}[U^2 D^2(U)] = 0 \tag{16}$$

From Eqs. (11), (12), (13), (14), (15), and (16), A_{eq}, B_{eq}, and C_{eq} are evaluated by $\mathrm{E}[U^n]$ $(n = 1, 2, 3, 4)$, which can be calculated from $p_U(u)$.

By replacing $D(U)$ in Eq. (7) with $D_{\mathrm{eq}}(U)$, the stochastic differential equation governing the equivalent non-Gaussian excitation can be obtained as

$$dU = -\alpha U dt + \sqrt{A_{\mathrm{eq}}U^2 + B_{\mathrm{eq}}U + C_{\mathrm{eq}}}\,dB(t) \tag{17}$$

Since the three coefficients are determined by the moments $\mathrm{E}[U^n]$ $(n = 1, 2, 3, 4)$, the equivalent non-Gaussian excitation given by Eq. (17) retains the same moments up to the fourth order as those of the original excitation [3].

Finally, the moment equations are derived from Eqs. (5), (6), and (17).

$$\begin{aligned}\frac{d}{dt}\mathrm{E}[X^i \dot{X}^j U^k] =& i\mathrm{E}[X^{i-1}\dot{X}^{j+1}U^k] - j\mathrm{E}[X^{i+1}\dot{X}^{j-1}U^k] \\ &+ \left(-2j\zeta - k\alpha + \frac{1}{2}k(k-1)A_{\mathrm{eq}}\right)\mathrm{E}[X^i\dot{X}^j U^k] \\ &+ j\mathrm{E}[X^i\dot{X}^{j-1}U^{k+1}] + \frac{1}{2}k(k-1)B_{\mathrm{eq}}\mathrm{E}[X^i\dot{X}^j U^{k-1}] \\ &+ \frac{1}{2}k(k-1)C_{\mathrm{eq}}\mathrm{E}[X^i\dot{X}^j U^{k-2}]\end{aligned} \tag{18}$$

4 Numerical Examples

The equivalent non-Gaussian excitation method will now be applied to the system (1) under non-Gaussian excitation with the zero-mean generalized Gaussian distribution, which is expressed as [6]

$$p_U(u) = \frac{\kappa}{2a\Gamma(1/\kappa)} \exp\left(-\frac{|u|^\kappa}{a^\kappa}\right) \tag{19}$$

where $\Gamma(\cdot)$ is the gamma function and $\kappa(>0)$ represents the shape parameter. a is the scale parameter. In this study, a is adjusted so that $\sigma^2 = 1$. In Fig. 1 (Right), the generalized Gaussian distributions for four types of κ are shown.

The diffusion coefficient $D^2(u)$ corresponding to Eq. (19) is given as

$$D^2(u) = \frac{2\alpha a^2}{\kappa}\Gamma\left(\frac{2}{\kappa}, \frac{|u|^\kappa}{a^\kappa}\right) \exp\left(\frac{|u|^\kappa}{a^\kappa}\right) \tag{20}$$

where $\Gamma(\cdot, \cdot)$ is the upper incomplete gamma function. Since Eq. (20) is complicated nonlinear, $D(U)$ is replaced with the equivalent one $D_{\mathrm{eq}}(U)$. The moments of the generalized Gaussian distribution are given as follows:

$$\mathrm{E}[U^n] = a^n \Gamma\left(\frac{n+1}{\kappa}\right)\Gamma\left(\frac{1}{\kappa}\right)^{-1} \quad (n = 2, 4), \quad \mathrm{E}[U] = \mathrm{E}[U^3] = 0 \tag{21}$$

Using Eqs. (11), (12), (13), (14), (15), (16), and (21), A_{eq}, B_{eq}, and C_{eq} can be calculated. Then, the closed moment equations (18) are derived and solved to obtain the response moments.

Parameters are given as follows:

$\zeta = 0.05$
$\alpha = 0.01$ $(\alpha/\zeta = 0.2)$, $\alpha = 0.05$ $(\alpha/\zeta = 1)$, $\alpha = 1$ $(\alpha/\zeta = 20)$
$\kappa = 1$ (kurtosis $= 3$), $\kappa = 10$ (kurtosis $= -1.11584$)

Assume that initial conditions of the system are $X(0) = 0$ and $\dot{X}(0) = 0$, and the excitation is added to the system at $t = 0$.

The results of the transient displacement kurtosis are shown in Fig. 2. The analytical results are in good agreement with Monte Carlo simulation results, which were calculated by 2×10^7 direct numerical integration of Eqs. (1) and (3). These results illustrate the effectiveness of the equivalent non-Gaussian excitation method for transient response analysis.

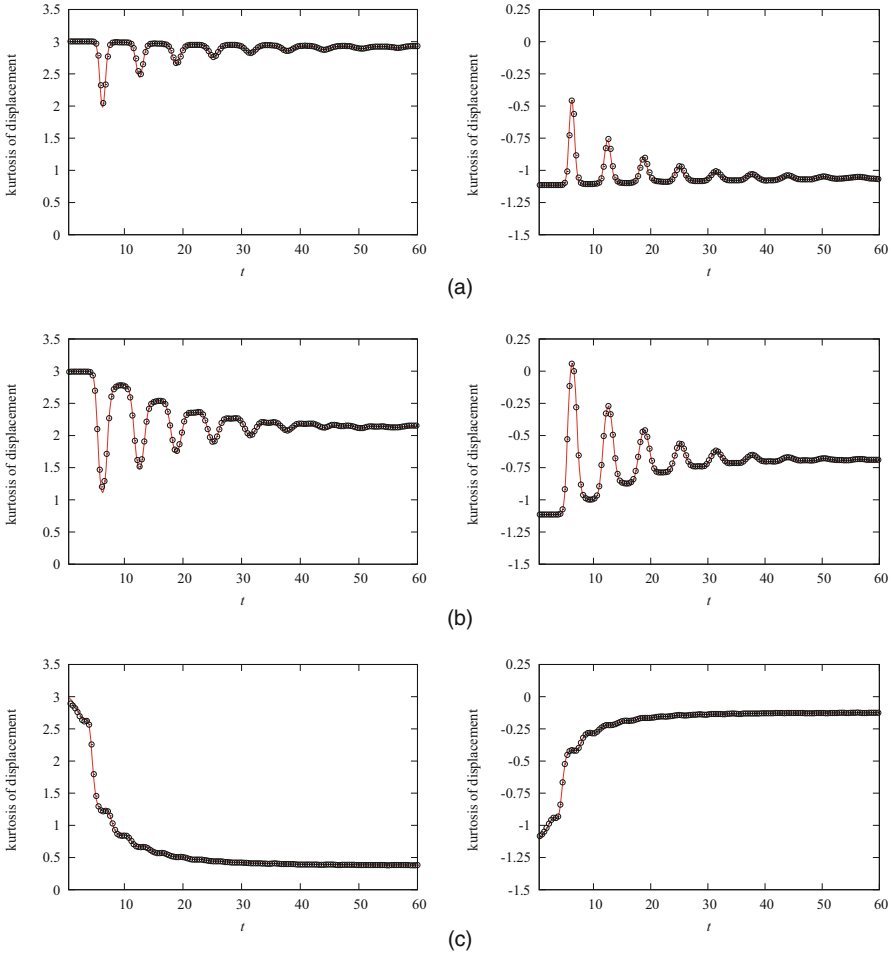

Fig. 2 Kurtosis of displacement response, left: $\kappa = 1$, right: $\kappa = 10$, solid line : equivalent non-Gaussian excitation method, $\odot$: Monte Carlo simulation. (**a**) $\alpha = 0.01$. (**b**) $\alpha = 0.05$. (**c**) $\alpha = 1$

5 Conclusions

Transient response analysis has been performed for a SDOF linear system under non-Gaussian random excitation using the equivalent non-Gaussian excitation method. The non-Gaussian random excitation is prescribed by both its probability density function and power spectrum and is described by a stochastic differential equation. In the analytical method, in order to derive a closed set of moment equations for the system response, the diffusion coefficient in the governing equation for the excitation is replaced by an equivalent one.

In numerical examples, a SDOF system under non-Gaussian excitation with the generalized Gaussian distribution has been analyzed. The analytical results were in good agreement with simulation results in all cases considered.

References

1. Grigoriu, M.: Applied Non-Gaussian Processes: Examples, Theory, Simulation, Linear Random Vibration, and MATLAB Solutions. Prentice Hall, Englewood Cliffs (1995)
2. Ochi, M.K.: Non-Gaussian random processes in ocean engineering. Probabilist. Eng. Mech. **1**(1), 28–39 (1986)
3. Tsuchida, T., Kimura, K.: Response moments of dynamic systems under non-Gaussian random excitation by the equivalent non-Gaussian excitation method. In: 12th International Conference on Recent Advances in Structural Dynamics, Southampton, p. 2168 (2016)
4. Cai, G.Q., Lin, Y.K.: Generation of non-Gaussian stationary stochastic processes. Phys. Rev. E. **54**(1), 299–303 (1996)
5. Gardiner, C.: Stochastic Methods: A Handbook for the Natural and Social Sciences, 4th edn. Springer, Berlin/Heidelberg (2009)
6. Sharifi, K., Leon-Garcia A.: Estimation of shape parameter for generalized Gaussian distributions in subband decompositions of video. IEEE Trans. Circ. Syst. Video **5**(1), 52–56 (1995)

Study of the Effect of Shape Processing of a Specimen on the Modal Properties

Shozo Kawamura, Go Kikuchi, and Masami Matsubara

1 Introduction

When the dynamic design of a structure is carried out by using finite element method, the dynamic characteristics of the member of the structure have to be identified in advance. The natural frequencies of the complex shaped member can be obtained when we apply the properties, such as Young's modulus and density and so on, of the simple shaped member to the complex shaped member. Furthermore, the damping property of the actual complex shaped member is sometimes assumed to be the same as the one of a simple shaped member with the same material. The damping properties often become a function of the frequency; thus, the damping property of the complex shaped member may not be obtained when we apply the damping property of the simple shaped member to the complex one. In this study, a beam specimen made of steel is adopted, and the modal properties of both uniform shaped specimen and L-shaped one are identified; then the influence of the shape processing is investigated on the damping property.

To identify the modal properties such as the natural frequency and the modal damping ratio, the "experimental modal analysis" has been established [1–4]. In this study, the specimen with low damping property is treated, so we adopt the linear fit method proposed by authors [5]. The method is as follows. First we derive the coupled equation of real and imaginary part of the frequency response function (FRF). The equation has the natural frequency and modal damping ratio as unknown parameters, and the modal parameters are identified by the least square method. It is proved that this method can identify the low damping property with high accuracy [5]. Furthermore, we identify the modal parameters of the specimen of

S. Kawamura · G. Kikuchi (✉) · M. Matsubara
Toyohashi University of Technology, Toyohashi, Aichi, Japan
e-mail: kawamura@me.tut.ac.jp; kikuchi@dynamics.me.tut.ac.jp; matsubara@me.tut.ac.jp

S. Oberst et al. (eds.), *Vibration Engineering for a Sustainable Future*,
https://doi.org/10.1007/978-3-030-46466-0_12

free supported condition, so the effect of the rigid body mode must be considered. Therefore, we will construct the linear fit method considering the rigid body mode. Using the identification method, we obtain the modal parameters of plain and L-shaped specimen, and the relationship between the natural frequency and the modal damping ratio is constructed, and the influence of the shape processing is investigated on the damping property.

2 Identification Method Considering Rigid Body Mode

Equation of motion of multi-degree-of-freedom system having mass matrix **M** and stiffness matrix **K** and damping matrix **C** is expressed as follows:

$$\boldsymbol{M\ddot{x}} + \boldsymbol{C\dot{x}} + \boldsymbol{Kx} = \boldsymbol{F}e^{j\omega t} \tag{1}$$

Here the modal matrixes are normalized as follows:

$$\boldsymbol{\Phi}^{\boldsymbol{T}}\boldsymbol{M}\boldsymbol{\Phi} = \boldsymbol{I} \tag{2}$$

$$\boldsymbol{\Phi}^{\boldsymbol{T}}\boldsymbol{K}\boldsymbol{\Phi} = \boldsymbol{\omega}_{\boldsymbol{r}}^{\boldsymbol{2}} \tag{3}$$

where ω_r is the natural angular frequency of the r-th mode, and $\boldsymbol{\omega}_{\boldsymbol{r}}^{\boldsymbol{2}}$ is the diagonal matrix composed of ω_r^2 (r=1,⋯,N). Damping matrix **C** is assumed to be proportional viscous damping expressed as follows by using modal damping ratio ζ_r and natural angular frequency ω_r

$$\boldsymbol{\Phi}^{\boldsymbol{T}}\boldsymbol{C}\boldsymbol{\Phi} = \boldsymbol{2\zeta_r\omega_r} \tag{4}$$

where $\boldsymbol{2\zeta_r\omega_r}$ is the diagonal matrix composed of $2\zeta_r\omega_r$ (r=1,⋯,N). Assuming harmonic excitation $\mathbf{x} = \mathbf{X}e^{j\omega t}$, the response **X** is expanded by natural vibration mode

$$\boldsymbol{X} = \sum_{r=1}^{N} q_r\boldsymbol{\varphi}_r = \boldsymbol{\Phi q} \tag{5}$$

Substituting Eq. (5) into Eq. (1), and using the orthogonality of natural vibration mode, the equation of the r-th mode is written as follows:

$$\left\{-\omega^2 + j\omega\left(2\zeta_r\omega_r\right) + \omega_r^2\right\} q_r = \boldsymbol{\varphi}_{\boldsymbol{r}}^{\boldsymbol{T}}\boldsymbol{F} \tag{6}$$

Modal displacement can be obtained from Eq. (6), and the response **X** is expressed as follows:

$$\boldsymbol{X} = \sum_{r=1}^{N} q_r \boldsymbol{\varphi_r} = \sum_{r=1}^{N} \frac{\boldsymbol{\varphi_r} \boldsymbol{\varphi_r^T} \boldsymbol{F}}{\omega_r^2 \text{-} \omega^2 + j\omega\,(2\zeta_r \omega_r)} \tag{7}$$

In the actual experiment, we measure the acceleration, so the FRF is the accelerance. The accelerance A_l/F_i is expressed as follows:

$$\frac{A_l\,(\omega)}{F_i\,(\omega)} = \frac{-\omega^2 X_l\,(\omega)}{F_i\,(\omega)} = \sum_{r=1}^{N} \frac{-\phi_{rl}\phi_{ri}(\omega/\omega_r)^2}{1-(\omega/\omega_r)^2 + j\,(2\zeta_r \omega/\omega_r)} \tag{8}$$

To identify the modal properties, we use the linear fit method proposed by the authors [5]. In the method [5], the rigid body mode is not considered, while in this study, its effect must be considered because the relatively lower elastic mode is treated. We separate Eq. (8) into rigid body modes and the r-th elastic mode.

$$\frac{A_l\,(\omega)}{F_i\,(\omega)} = \sum_{s=1}^{N_R} \phi_{sl}\phi_{si} + \frac{-\phi_{rl}\phi_{ri}(\omega/\omega_r)^2}{1-(\omega/\omega_r)^2 + j\,(2\zeta_r \omega/\omega_r)} = C + \frac{-\phi_{rl}\phi_{ri}(\omega/\omega_r)^2}{1-(\omega/\omega_r)^2 + j\,(2\zeta_r \omega/\omega_r)} \tag{9}$$

Real part and imaginary part of accelerance are set as $R(\omega)$ and $I(\omega)$, respectively. Then, the real and imaginary parts of Eq. (9) are expressed as follows:

$$R\,(\omega) = C + \frac{-\phi_{rl}\phi_{ri}(\omega/\omega_r)^2 \left\{1-(\omega/\omega_r)^2\right\}}{\left\{1-(\omega/\omega_r)^2\right\}^2 + (2\zeta_r \omega/\omega_r)^2} \tag{10}$$

$$I\,(\omega) = \frac{\phi_{rl}\phi_{ri}(\omega/\omega_r)^2\,(2\zeta_r \omega/\omega_r)}{\left\{1-(\omega/\omega_r)^2\right\}^2 + (2\zeta_r \omega/\omega_r)^2} \tag{11}$$

Coupling these equations, we obtain the next equation:

$$\omega^2 I\,(\omega)\left(\frac{1}{\omega_r^2}\right) - 2\omega R\,(\omega)\left(\frac{\zeta_r}{\omega_r}\right) + 2\omega\left(\frac{\zeta_r C_r}{\omega_r}\right) = I\,(\omega) \tag{12}$$

In Eq. (12), $1/\omega_r^2$, ζ_r/ω_r, and $\zeta_r C_r/\omega_r$ are unknown parameters. Simultaneous equation is obtained by using accelerance around the natural frequency of the r-th vibration mode.

$$\begin{bmatrix} \omega_{m1} I\,(\omega_{m1}) & -2\omega_{m1} R\,(\omega_{m1}) & 2\omega_{m1} \\ \omega_{m2} I\,(\omega_{m2}) & -2\omega_{m2} R\,(\omega_{m2}) & 2\omega_{m2} \\ \vdots & \vdots & \vdots \\ \omega_{mn} I\,(\omega_{mn}) & -2\omega_{mn} R\,(\omega_{mn}) & 2\omega_{mn} \end{bmatrix} \begin{Bmatrix} 1/\omega_r^2 \\ \zeta_r/\omega_r \\ C\zeta_r/\omega_r \end{Bmatrix} = \begin{Bmatrix} I\,(\omega_{m1}) \\ I\,(\omega_{m2}) \\ \vdots \\ I\,(\omega_{mn}) \end{Bmatrix} \tag{13}$$

where the angular frequency ω_{mk} is the k-th measured one. There are three unknown parameters, so simultaneous equation is built by more than three measured data. Solving this equation using least square method, the natural angular frequency ω_r, modal damping ratio ζ_r, and effect of rigid body mode C of the r-th mode can be obtained.

In addition, if damping property is modeled by proportional hysteresis damping as follows:

$$\mathbf{C} = \frac{1}{\omega}\left(\alpha_s \mathbf{M} + \beta_s \mathbf{K}\right), \tag{14}$$

then damping property term is

$$j\left(\alpha_s + \beta_s {\omega_r}^2\right) = j\omega\left(2\zeta_r \omega_r\right) \tag{15}$$

and then g_r is as follows:

$$g_r = \frac{\alpha_s}{{\omega_r}^2} + \beta_s = 2\zeta_r \frac{\omega}{\omega_r} \to 2\zeta_r \quad (\omega \to \omega_r) \tag{16}$$

In this study, g_r is called as the structural damping coefficient of the r-th mode.

3 Identification of Modal Parameters

3.1 Specimen and Experiment Method

Two types of specimen of SPCC steel beam are adopted, which are the plain beam specimen and L-shaped beam specimen. In the case of plain beam specimen, its width is 35 mm, thickness is 1.6 mm, while the length l is 400 mm, 500 mm, or 600 mm. In the case of L-shaped beam specimen, the beam whose size is the same as the plain beam specimen is processed to L-shaped at $(1/3)l$ location as shown in Fig. 1b.

In the experiment, the accelerometer (PCB 352A73) is attached on the specimen and impact at the opposite side of the specimen. The location is $0.47l$ for the plain specimen and $0.25l_1$ for the L-shaped one. These locations are determined such as not to be nodes for the interested vibration mode.

In order to realize the free support condition, these specimens are suspended from the rigid frame by Kevlar string. In the plain specimen, the supporting location is the node for the interested vibration mode, while in the L-shaped specimen, it is the corner point as shown in Fig. 1b.

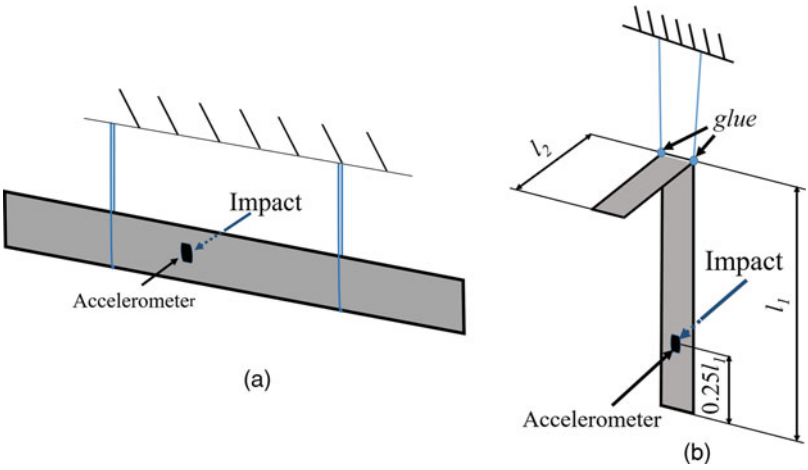

Fig. 1 Experimental conditions. (**a**) Plain beam specimen. (**b**) L-shaped beam specimen

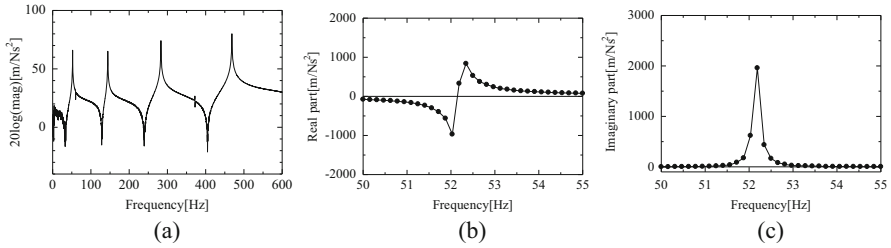

Fig. 2 Measured FRF of 400 mm plain beam specimen. (**a**) Magnitude. (**b**) Real part. (**c**) Imaginary part

3.2 Measured FRF

As an example of the measured result, Figs. 2 and 3 show the FRFs of 400 mm plain and L-shaped specimen, which are the magnitude, real part, and imaginary part around the 1-st mode.

As shown in Fig. 3b, we can observe that the real part of the FRF approaches a finite value, not zero, i.e., the influence of the rigid body mode. Therefore, the identification method considering the rigid body mode described in Chap. 2 is effective for identification of modal parameters.

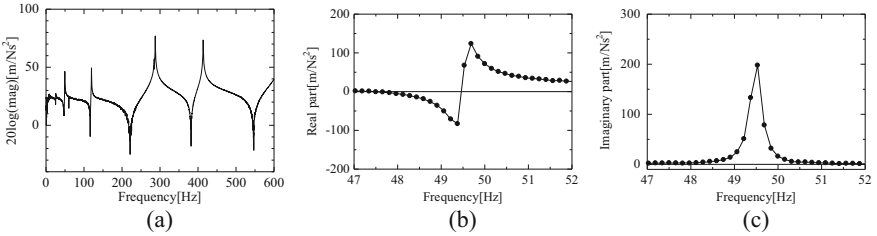

Fig. 3 Measured FRF of 400 mm L-shaped beam specimen. (**a**) Magnitude. (**b**) Real part. (**c**) Imaginary part

Table 1 Identification results of modal properties of 400 mm plain beam specimen

	Natural frequency [Hz]	Structural damping coefficient
1st mode	52.172	0.00135
2nd mode	144.16	0.00072
3rd mode	283.05	0.00051
4th mode	468.57	0.00048

Table 2 Identification results of modal properties of 400 mm L-shaped beam specimen

	Natural frequency [Hz]	Structural damping coefficient
1st mode	49.446	0.00373
2nd mode	119.60	0.00132
3rd mode	287.39	0.00058
4th mode	413.45	0.00069

Fig. 4 Relation between the natural frequency and the structural damping in the case of 400 mm specimen

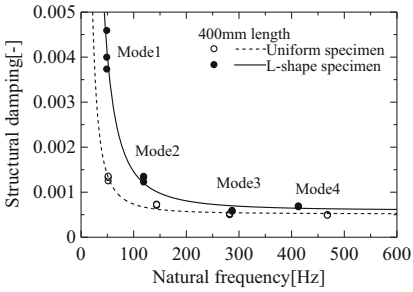

3.3 Identification Results

We show the identification results of 400 mm plain in Table 1 and L-shaped specimen in Table 2, respectively. In these tables, the natural frequency and the structural damping coefficient are shown.

The relation between the natural frequency and the structural damping coefficient is shown in Fig. 4.

As shown in Fig. 4, the damping properties of both specimens are almost the same at the frequency range over 300 Hz, while at the lower frequency range, a significant difference can be observed.

Moreover, the parameters α_s and β_s, which are the coefficients of the proportional hysteresis damping, are identified by using Eq. (16); the results are as follows:

$$\text{Plain beam specimen} \quad \alpha_s = 85.6, \quad \beta_s = 5.17 \times 10^{-4}$$

$$\text{L-shaped beam specimen} \quad \alpha_s = 340, \quad \beta_s = 5.93 \times 10^{-4}$$

The parameter β_s is almost the same between the plain and the L-shaped specimen, while a significant difference in the parameter α_s is shown. It is recognized that the parameter α_s is important for the lower-frequency range.

4 Conclusions

In this study, a beam specimen made of steel is adopted, and the modal properties of both uniform-shaped specimen and L-shaped one are identified; then the influence of the shape processing is investigated on the damping property.

As a result, it is recognized that the damping property is high in the low-frequency band and low constant in the high-frequency band. Furthermore, the damping property of the L-shaped specimen is higher in the low-frequency band than the case of uniform specimen, while it is almost the same in the higher-frequency band.

The damping property of a simple beam is often used in case of a more complex shaped beam, but we concluded that it was not adequate in the low-frequency band.

Acknowledgment This work was supported by JSPS KAKENHI Grant Number JP18K04019.

References

1. Ewins, D.J.: Modal Testing, Theory, Practice, and Application. Wiley, New Jersey (2000)
2. Jimin, H., Zhi-Fang, F.: Modal Analysis. Butterworth Heinemann, Oxford (2001)
3. Editorial committee: Modal analysis handbook. Corona (in Japanese), Tokyo (2000)
4. Nagamatsu, A.: Modal Analysis. Baifukan, (in Japanese), Tokyo (1985)
5. Kawamura, S., et al.: Bulletin of the JSME. Mech. Eng. J. **3**(6), 16-00446 (2016). https://doi.org/10.1299/mej.16-00446

Identification of Statistical Characteristics of Random Excitation Acting on Machines or Structures

Shozo Kawamura, Takuo Henmi, and Masami Matsubara

1 Introduction

Abnormality diagnosis of structures is a very important technology to realize the sustainable society, which means the safety- and security-based society. Generally, abnormality diagnosis is conducted by continuous monitoring of vibration of the structure and evaluating changes of measured value such as response. Furthermore, the diagnosis will be carried out when the magnitude of vibration exceeds the threshold level. However, the changes of the vibrations may occur by the change of excitation or by the changes of the structural parameters. Therefore, it is very important to identify the excitation acting on the structure in order to judge whether there is an abnormality from vibration of the structure. There are many studies about force identification [1–4]. The authors, also, have published some studies [5, 6]. Most of them treat the steady-state vibration base on the frequency response function (FRF), while the actual excitation such as wind or earthquake has random characteristics. In this study, we proposed a method to identify statistical characteristics of random excitation acting on a structure by using a measured response. First, the FRF of the structure is identified in advance, and the power spectrums of the system are obtained. Moreover, the power spectrum of the response is gotten by performing FFT to the time history of measured one; the power spectrum of the excitation is identified using power spectrums of both the response and the system. The validity of the proposal method is confirmed by numerical simulation to a single-degree-of-freedom model. After that, this method is expanded to a multi-degree-of-freedom vibration system, and the identification method of the random excitation is established.

S. Kawamura · T. Henmi (✉) · M. Matsubara
Toyohashi University of Technology, Toyohashi, Aichi, Japan
e-mail: kawamura@me.tut.ac.jp; henmi@dynamics.me.tut.ac.jp; matsubara@me.tut.ac.jp

S. Oberst et al. (eds.), *Vibration Engineering for a Sustainable Future*,
https://doi.org/10.1007/978-3-030-46466-0_13

2 Proposal Method

We consider a system acting on a random excitation. Since the system irregularly vibrate by the random input, the output of the system is also irregularly. The response of the system is observed as an output depended on time. However, non-periodic random vibrations cannot be analytically solved as equations in the time domain. Then, the proposal method describes the system input/output relation in the frequency domain. The system input/output relation in the frequency domain is

$$B\left(j\omega\right) \cdot X\left(j\omega\right) = F\left(j\omega\right) \tag{1}$$

where $B(j\omega)$, $X(j\omega)$, and $F(j\omega)$ are the frequency characteristic of the system, the response, and the excitation, respectively. Thus, the equation can be analytically solved by representing the non-periodic random vibration as the time-independent frequency characteristics. Further, when the FRF of the system is identified in advance, the frequency characteristics of the random excitation can be identified by performing FFT to the time history of measured random response and obtaining its frequency characteristics.

The frequency characteristics of vibrations are classified into the magnitude and phase of the vibration. In order to apply the magnitude of a response of a structure acting on a random excitation to abnormality diagnosis, the proposal method treats power spectrums showing the magnitude of the vibration as the frequency characteristics. The power spectrum of the response $\Phi_x(\omega)$ is expressed as follows:

$$\Phi_x\left(\omega\right) = X^*\left(j\omega\right) \cdot X\left(j\omega\right) \tag{2}$$

where * means complex conjugate. As can be seen from Eq. (2), the power spectrum has no phase information because it is defined as a real number, and its magnitude is equal to the square of the vibration amplitude. In addition, in the case of the multi-degree-of-freedom system acting on some excitation, the correlation of the response and the excitation of each objects must be considered. When the frequency characteristics of the response of the object r and s are $X_r(\omega)$, $X_s(\omega)$, respectively, the correlation between both of them is expressed as a cross spectrum $\Phi_{x_r x_s}\left(j\omega\right)$ as follows:

$$\Phi_{x_r x_s}\left(j\omega\right) = {X_r}^*\left(j\omega\right) \cdot X_s\left(j\omega\right) \tag{3}$$

As an example, we consider a two-degree-of-freedom system, which the number of measured responses and the number of excitations are equal. When each power and cross spectrum are described as one matrix, the system input/output relation is

$$\begin{Bmatrix} \Phi_{x_1x_1} \\ \Phi_{x_1x_2} \\ \Phi_{x_2x_1} \\ \Phi_{x_2x_2} \end{Bmatrix} = \begin{bmatrix} G_{11}{}^*G_{11} & G_{11}{}^*G_{12} & G_{12}{}^*G_{11} & G_{12}{}^*G_{12} \\ G_{11}{}^*G_{21} & G_{11}{}^*G_{22} & G_{12}{}^*G_{21} & G_{12}{}^*G_{22} \\ G_{21}{}^*G_{11} & G_{21}{}^*G_{12} & G_{22}{}^*G_{11} & G_{22}{}^*G_{12} \\ G_{21}{}^*G_{21} & G_{21}{}^*G_{22} & G_{22}{}^*G_{21} & G_{22}{}^*G_{22} \end{bmatrix} \begin{Bmatrix} \Phi_{f_1f_1} \\ \Phi_{f_1f_2} \\ \Phi_{f_2f_1} \\ \Phi_{f_2f_2} \end{Bmatrix} \tag{4}$$

The four terms on the left side can be obtained from the measured response. The coefficient matrix on the right side is also obtained from the mathematical model of the system built in advance. Therefore, it is possible to identify four unknowns about the characteristics of the excitation on the right side. Since Eq. (4) is a four-dimensional simultaneous linear equation, the excitation is uniquely determined. When the number of excitations is less than the number of the measured responses, or the excitation has no correlation between other excitations, the characteristics of the excitation are identified by using the least square method.

3 Numerical Simulation for Single-Degree-of-Freedom System

In order to conduct numerical simulation, firstly we generate a random excitation. The characteristics of a random excitation are classified into the wideband process (e.g., wind) and narrow band process (e.g., earthquake). In this study, these characteristics of the excitations are generated from random number. The normally distributed random number, whose average value is 0 and standard deviation is 0.5, is generated. The frequency characteristic of the generated random number is white noise. The output according to the frequency characteristic of the system can be obtained as time history by acting the random number as input to an arbitrary second-order lag system. This output is used as a random excitation in numerical simulation. The parameters of second-order lag system in this simulation are ω_n=35 Hz and ζ=0.25, which is equivalent to wide band process. Figure 1 shows the time history and power spectrum of the generated excitation.

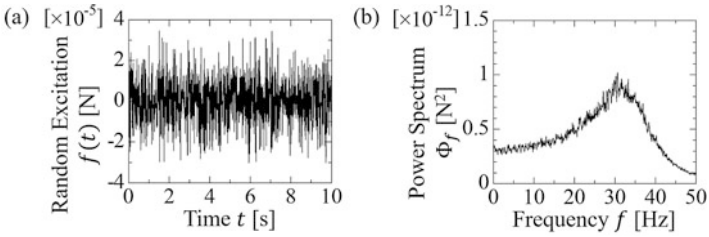

Fig. 1 (**a**) The time history and (**b**) power spectrum of the generated excitation

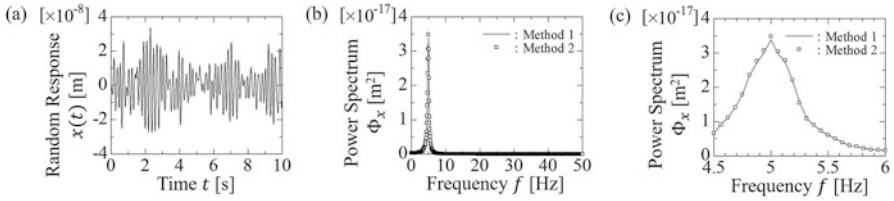

Fig. 2 (**a**) The time history and (**b**, **c**) power spectrum of the random excitation

We consider the single-degree-of-freedom system, which is $\omega_n = 5$ Hz and $\zeta = 0.05$. When the previous described random excitation acts on this system, the equation of motion in the frequency domain is expressed as follows:

$$\left({\omega_n}^2 - \omega^2 + j \cdot 2\zeta\omega_n\omega\right) X(j\omega) = F(j\omega) \tag{5}$$

The results of the numerical simulation carried out under the conditions of 1024 times averaging process with a time resolution of 7.8125 ms and a frequency resolution of 0.0625 Hz are shown in Fig. 2. Method 1 obtains the frequency characteristics of the response by acting the time history of the generated excitation (shown in Fig. 1) to the system and performing FFT to the time history of the calculated response. Also, Method 2 means calculating directly the frequency characteristics of the response by substituting the frequency characteristics of the generated excitation into the right side of Eq. (5). The power spectrum of the obtained response is almost zero in the high-frequency band, the characteristics in the high-frequency band of the excitation are suppressed, and the frequency characteristics of the system are emphasized. Also, the response (Method 1) obtained by performing FFT to the time history is almost equal to the response (Method 2) calculated directly from the frequency characteristics of the system and the excitation in the frequency domain.

The power spectrum of the excitation acting on the system is identified using the power spectrum of the response (Method 1). The result of comparing the power spectrum of the identified excitation with the power spectrum of the excitation generated from the random number in advance is shown in Fig. 3. In the high frequency, the power spectrum of the excitation after identification is less than the excitation before identification. The characteristics of the system are concentrated around 5 Hz, and the power spectrum in the other frequency bands is almost zero. The power spectrum of the obtained response is emphasized small value in the high-frequency band of the system because the wide band excitation also affects the high-frequency band of the system. Thus, the excitation identified by using this response may be emphasized the error in the high-frequency band. On the other hand, the identification result in the low-frequency band is significant because the power spectrum of the system has certain value in low-frequency band.

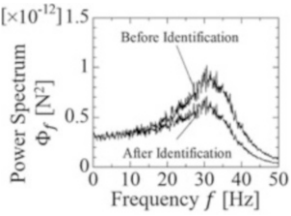

Fig. 3 Identification result of the random excitation

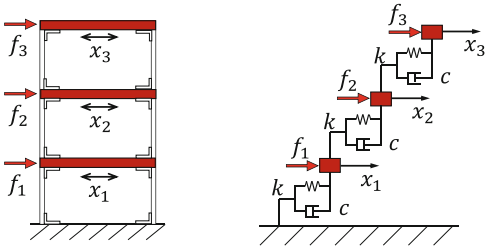

Fig. 4 The modeled multi-degree-of-freedom vibration system

Therefore, the validity of the proposal method in the single-degree-of-freedom system is confirmed because the power spectrum of the excitation after identification is almost equal to the power spectrum of the excitation before identification in the low-frequency band.

4 Numerical Simulation for Three-Degree-of-Freedom System

Since the validity of the proposal method was confirmed in Sect. 3, in this section, we establish the identification method of the random excitation by expanding the proposal method to a multi-degree-of-freedom vibration system. We consider a three-degree-of-freedom model shown in Fig. 4, in which random excitations act on each layer. This is modeled a three-layered structure receives wind as random excitations. Each excitation has almost the same characteristics by changing the initial value of the random number. The natural frequencies of this system are 5.166 Hz, 14.331 Hz, and 20.421 Hz. The equation of motion in the frequency domain is expressed as follows:

$$\left([K] - \omega^2 [M] + j \cdot \omega [C]\right) \{X(j\omega)\} = \{F(j\omega)\} \tag{6}$$

The simulation was carried out under the same conditions as Sect. 3. The power spectrum (Method 1) of the response obtained by numerical integration and the power spectrum (Method 2) of the response calculated directly from the Eq. (6) are shown in Fig. 5a, b. There is a difference between the response

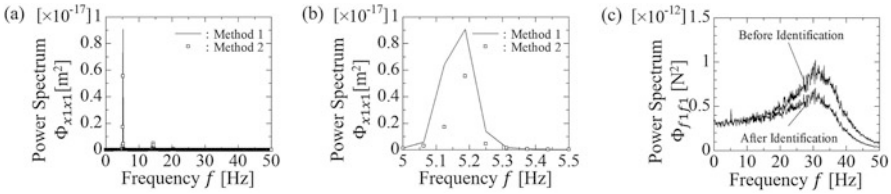

Fig. 5 (**a**, **b**) The power spectrum of the random response of the first layer. (**c**) Identification result of the random excitation acting on the first layer

(Method 1) obtained by performing FFT to the time history and the response (Method 2) calculated directly from the frequency characteristics of the system and the excitation in the frequency domain. The result of comparing the power spectrum of the identified excitation with the power spectrum of the excitation generated from the random number in advance is shown in Fig. 5c. There is a slight difference between each excitation at the first-order natural frequency because of the difference of the response shown in Fig. 5a, b. However, the excitation is identified with almost the same accuracy as the identification result of the single-degree-of-freedom system in all frequency bands. Therefore, the proposal method is also valid to the multi-degree-of-freedom system, and the excitation can be identified with enough accuracy. More improvement of identification accuracy may be achieved by analyzing the correct response.

5 Conclusions

In this research, we proposed a method to identify statistical characteristics of random excitation acting on a structure by using a measured response. First, the FRF of the structure was identified in advance, and the power spectrums of the system were obtained. Further, the power spectrum of the response was gotten by performing FFT to the time history of measured one; the power spectrum of the excitation was identified by using power spectrums of both the response and the system.

The validity of the proposal method in the single-degree-of-freedom system was confirmed by numerical simulation. In the case of the multi-degree-of-freedom system, the response has a difference around the natural frequencies; however, the excitation was identified with enough accuracy as in the single-degree-of-freedom system.

Acknowledgment This work was supported by JSPS KAKENHI Grant Number JP18K04019.

References

1. Stevens, K.K.: Force identification problems: an overview. In Proceedings of the 1987 SEM Spring Conference on Experimental Mechanics. Houston, TX, USA (1987)
2. Shih, C.Y., Zhang, Q., Allemang, R.J.: Force identification by using principle and modal coordinate transformation method. ASME Publ. DE. **18**(4), 303–309 (1989)
3. Karlsson, S.E.: Identification of external structural loads from measured harmonic responses. J. Sound Vib. **196**(1), 59–74 (1996)
4. Sanchez, J., Benaroya, H.: Review of force reconstruction techniques. J. Sound Vib. **333**, 2999–3018 (2014)
5. Kawamura, S., Hori, S., Minamoto, H.: Identification of external force acting on a machine or a structure in the case of unknown force location. J. Environ. Eng. **4**(2), 422–430 (2009)
6. Kawamura, S., Ise, T., Matsubara, M.: Identification of external force acting on a machine or a structure in the case of unknown excitation points. J. Eng. Res. Appl. **8**(6), 12–19 (2018)

Consideration of Traveling Waves Using Superposition of Vibration Modes

Keisuke Yamada

1 Introduction

When a continuous body is excited by an impulsive force at one point, a wave propagates concentrically from that point regardless of boundary conditions. This phenomenon can be observed even if we use the modal analysis for simulations. The modal analysis uses superposition of vibration modes [1]. In many cases, these vibration modes are equal to the standing waves of the continuous body. However, the modal analysis can express the wave phenomenon because the modal analysis is just a kind of coordinate transformation. This is the base of the proposed method. In addition, we propose a method to install arbitrary mechanical impedances at boundaries using the substructure elimination method [2]. First, partial structures are eliminated from the original structure, and second, arbitrary mechanical impedances are installed at the new boundaries. In this paper, the governing equations when the arbitrary mechanical impedances are installed at the boundaries are derived using the substructure elimination method. In addition, the formulations to extract the traveling waves are derived. The traveling waves of the continuous bodies that are surrounded by nonreflective boundaries are extracted using the proposed method in the simulations because the exact traveling waves can be theoretically derived under this condition.

K. Yamada (✉)
Kansai University, Suita-shi, Osaka, Japan
e-mail: yamadak@kansai-u.ac.jp

S. Oberst et al. (eds.), *Vibration Engineering for a Sustainable Future*,
https://doi.org/10.1007/978-3-030-46466-0_14

2 Theoretical Analysis

Only the harmonic excitation and steady state are considered in this study. The acoustic field and bending vibration of the beam and plate are described as representatives.

2.1 Acoustic Field

Analytical models for the one-dimensional and two-dimensional acoustic fields are shown in Fig. 1. The surrounding acoustic fields are substructures to be eliminated in Fig. 1. Springs are installed at the new boundaries in the analytical model for one-dimensional acoustic field, whereas elastic bodies are installed in the analytical for two-dimensional acoustic field. These springs and elastic bodies provide the arbitrary mechanical impedances at the new boundaries. Instead of springs and elastic bodies, dashpots and viscous bodies can be used; however, springs and elastic bodies are advantageous in terms of the computational load of the eigenvalue analysis. The density and bulk modulus of the air are given as ρ_{A} and κ_{A}, respectively, whereas the density and bulk modulus of the air in the eliminated area are given as ρ_{B} and κ_{B}, respectively. The left-hand end of the acoustic tube represents the origin of x coordinate system in the analytical model for one-dimensional acoustic field. The positive direction of x-axis is the right-hand direction.

The wave equation for the one-dimensional acoustic field is expressed as

$$\rho(x)\frac{\partial^2\psi}{\partial t^2} + \rho_{\mathrm{AB}}\left(H\left(x-x_{\mathrm{B}}\right)\left.\frac{\partial^2\psi}{\partial t^2}\right|_{x=x_{\mathrm{B}}} - H\left(x-x_{\mathrm{C}}\right)\left.\frac{\partial^2\psi}{\partial t^2}\right|_{x=x_{\mathrm{C}}}\right) - \frac{k_{\mathrm{s}}}{S}\left(H\left(x_{\mathrm{B}}-x\right)\left.\frac{\partial\psi}{\partial x}\right|_{x=x_{\mathrm{B}}} - H\left(x-x_{\mathrm{C}}\right)\left.\frac{\partial\psi}{\partial x}\right|_{x=x_{\mathrm{B}}}\right) = \kappa(x)\frac{\partial^2\psi}{\partial x^2} + \kappa_{\mathrm{A}}\frac{w_{\mathrm{p}}}{d}H_{\mathrm{p}} \tag{1}$$

$$\rho(x) = \rho_{\mathrm{A}} + \rho_{\mathrm{AB}}\left(H\left(x_{\mathrm{B}}-x\right) + H\left(x-x_{\mathrm{C}}\right)\right), \quad \rho_{\mathrm{AB}} = \rho_{\mathrm{B}} - \rho_{\mathrm{A}}, \tag{2, 3}$$

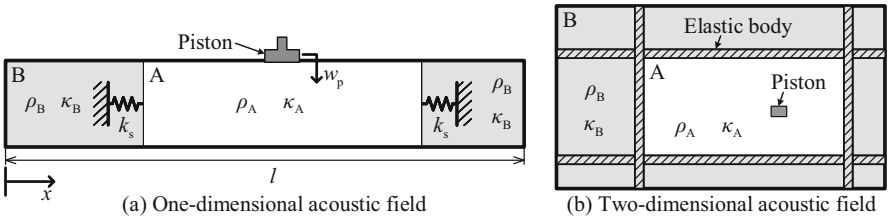

Fig. 1 Analytical models for the one-dimensional and two-dimensional acoustic field

$$\kappa(x) = \kappa_{\mathrm{A}} + \kappa_{\mathrm{AB}} \left(H\left(x_{\mathrm{B}} - x\right) + H\left(x - x_{\mathrm{C}}\right) \right), \quad \kappa_{\mathrm{AB}} = \kappa_{\mathrm{B}} - \kappa_{\mathrm{A}}, \tag{4, 5}$$

$$H_{\mathrm{p}} = H\left(x - x_{\mathrm{pL}}\right) - H\left(x - x_{\mathrm{pR}}\right) \tag{6}$$

where ψ is the displacement potential, t is time, H is the Heaviside step function, k_{s} is the spring constant of the springs, S is the cross-sectional area of the acoustic tube, w_{p} is the displacement of the piston, d is the height of the acoustic tube, x_{B} and x_{C} are the x coordinates of the two springs, respectively, and x_{pL} and x_{pR} are the x coordinates of the left-hand and right-hand ends of the piston. The displacement potential is expressed by the superposition of the vibration mode of the acoustic field before the substructures are eliminated.

$$\psi(x, t) = \sum_{\mathrm{h}=0}^{\infty} \Psi_{\mathrm{h}}(x)\xi_{\mathrm{h}}(t), \quad \Psi_{\mathrm{h}}(x) = A_{\mathrm{h}} \cos\left(k_{\mathrm{h}} x\right), \quad k_{\mathrm{h}} = \frac{\mathrm{h}\pi}{l} \tag{7, 8, 9}$$

where $\Psi_{\mathrm{h}}(x)$ is the eigenfunction of the displacement potential, ξ_{h} is the modal displacement, the subscript h denotes the mode order, k_{h} is the wave number, A_{h} is the arbitrary constant, and l is the length of the acoustic tube. From Eqs. (1) and (7), the equation of motion with respect to the i-th vibration mode can be derived [2]. The sound pressure in the acoustic tube can be derived by the left-hand side of Eq. (1).

The wave equation of the analytical model for the two-dimensional acoustic field can be derived in the same manner as the one-dimensional acoustic field [2].

To make nonreflective boundaries at the new boundaries, the mechanical impedances of the springs and elastic bodies should be equal to the characteristic impedance of the air [3]. Therefore, the spring constant of the springs and spring constant per unit area of the elastic bodies should be respectively given as

$$k_{\mathrm{s}} = \mathrm{j}\omega\sqrt{\rho_{\mathrm{A}}\kappa_{\mathrm{A}}}S, \quad \beta = \mathrm{j}\omega\sqrt{\rho_{\mathrm{A}}\kappa_{\mathrm{A}}}, \tag{10, 11}$$

where ω is the excitation angular frequency and j is the imaginary unit. Using Eq. (11) and substructure elimination method, obliquely incident sound waves are also completely absorbed because the elastic bodies function only in the normal direction.

2.2 Bending Vibration

Analytical models for the beam and plate are shown in Fig. 2. The surrounding areas are substructures to be eliminated in Fig. 2. Springs and elastic bodies are installed at the new boundaries as well as the case of the acoustic field; however, rotational springs are additionally required to make arbitrary impedances at the new

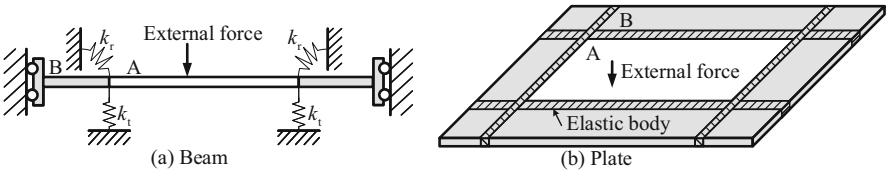

Fig. 2 Analytical models for the beam and plate

boundaries. The elastic bodies function in the direction of rotation as well as in the translational direction in the analytical model for the plate. The equations of motion of the models can be derived using the substructure elimination method [2].

To make nonreflective boundaries at the new boundary, the mechanical impedances of the translational and rotational springs and elastic bodies should be equal to the characteristic impedance of the beam and plate [4, 5]. Therefore, the spring constants of the springs and spring constants per unit length of the elastic bodies should be given as

$$k_{\mathrm{t}} = \mathrm{j}\omega\sqrt{\omega}\sqrt[4]{\mu^3 EI}, \quad k_{\mathrm{r}} = \frac{\mathrm{j}\omega\sqrt[4]{\mu(EI)^3}}{\sqrt{\omega}}, \quad \beta_{\mathrm{t}} = \mathrm{j}\omega\sqrt{\omega}\sqrt[4]{\sigma^3 D}, \quad \beta_{\mathrm{r}} = \frac{\mathrm{j}\omega\sqrt[4]{\sigma D^3}}{\sqrt{\omega}} \tag{12, 13, 14, 15}$$

where k_{t} and k_{r} are the spring constants of the translational and rotational springs, respectively; β_{t} and β_{r} are the spring constants per unit length of the elastic body in the translational and rotational directions, respectively; μ is the line density; E is the Young's modulus of the beam; I is the second moment of area of the beam; σ is the area density of the plate; and D is the flexural rigidity of the plate. A beam is a specific case of a plate. Therefore, Eqs. (14) and (15) can be derived using Eqs. (12) and (13) without inconsistencies.

2.3 *Extraction of Traveling Waves*

When the equation of motion is given as the wave equation, the vibration of a continuous body consists of the forward and backward traveling waves. As an example, the displacement potential in the one-dimensional acoustic field is defined as

$$\psi(x,t) = \left(C_{\mathrm{F}} e^{-\mathrm{j}kx} + C_{\mathrm{B}} e^{\mathrm{j}kx}\right) e^{\mathrm{j}\omega t}, \quad k = \frac{\omega}{c_{\mathrm{A}}}, \quad c_{\mathrm{A}} = \sqrt{\frac{\kappa_{\mathrm{A}}}{\rho_{\mathrm{A}}}} \tag{16, 17, 18}$$

where k is the wave number, c_{A} is the speed of sound, and C_{F} and C_{B} are the constants of the forward and backward traveling waves, respectively. In case of the

modal analysis, the displacement potential is expressed by the superposition of the vibration modes as given in Eq. (7). In addition, the gradient of the displacement potential gives the particle displacement. Because the displacement potentials and their gradients are respectively equal, the following equations can be derived:

$$C_{\mathrm{F}}e^{-\mathrm{j}(kx-\omega t)},\, C_{\mathrm{B}}e^{\mathrm{j}(kx+\omega t)} = \sum_{\mathrm{h}=0}^{\infty} \frac{A_{\mathrm{h}}}{4}\left[\left(1 \pm \frac{k_{\mathrm{h}}}{k}\right)e^{-\mathrm{j}k_{\mathrm{h}}x} + \left(1 \mp \frac{k_{\mathrm{h}}}{k}\right)e^{\mathrm{j}k_{\mathrm{h}}x}\right]\xi_{\mathrm{h}} \tag{19}$$

Using Eq. (19), the forward and backward traveling waves can be extracted. Traveling waves can be derived in the same manner even in the multidimensional cases.

In the same manner as the case of a wave equation, traveling waves and evanescent waves can be derived using the modal analysis even in the case of bending vibrations. As an example, the deflection of a beam can be given as

$$w = \left(C_{\mathrm{F}}e^{-\mathrm{j}kx} + C_{\mathrm{B}}e^{\mathrm{j}kx} + C_{\mathrm{L}}e^{-kx} + C_{\mathrm{R}}e^{kx}\right)e^{\mathrm{j}\omega t} = \sum_{\mathrm{h}=0}^{\infty} W_{\mathrm{h}}\xi_{\mathrm{h}}, \quad k = \sqrt[4]{\frac{\mu}{EI}}\sqrt{\omega} \tag{20, 21}$$

where C_{F} and C_{B} are the constants of the forward and backward traveling waves, respectively; C_{L} and C_{R} are the constants of the left and right evanescent waves, respectively; W_{h} is the eigenfunction of the deflection; and ξ_{h} is the modal displacement. Because the deflection, slope, bending moment, and shear force are respectively equal, four kinds of waves can be derived. As an example, in the case where the deflection of the beam is given by the Fourier cosine series using the modal analysis, the traveling waves and evanescent waves are respectively derived as

$$C_{\mathrm{F}}e^{-\mathrm{j}(kx-\omega t)},\, C_{\mathrm{B}}e^{\mathrm{j}(kx+\omega t)} = \sum_{\mathrm{h}=0}^{\infty} \frac{A_{\mathrm{h}}}{8}\left(1+\frac{k_{\mathrm{h}}^2}{k^2}\right)\left[\left(1 \pm \frac{k_{\mathrm{h}}}{k}\right)e^{-\mathrm{j}k_{\mathrm{h}}x} + \left(1 \mp \frac{k_{\mathrm{h}}}{k}\right)e^{\mathrm{j}k_{\mathrm{h}}x}\right]\xi_{\mathrm{h}} \tag{22}$$

$$C_{\mathrm{L}}e^{-kx+\mathrm{j}\omega t},\, C_{\mathrm{B}}e^{kx+\mathrm{j}\omega t} = \sum_{\mathrm{h}=0}^{\infty} \frac{A_{\mathrm{h}}}{8}\left(1-\frac{k_{\mathrm{h}}^2}{k^2}\right)\left[\left(1 \pm \mathrm{j}\frac{k_{\mathrm{h}}}{k}\right)e^{-\mathrm{j}k_{\mathrm{h}}x} + \left(1 \mp \mathrm{j}\frac{k_{\mathrm{h}}}{k}\right)e^{\mathrm{j}k_{\mathrm{h}}x}\right]\xi_{\mathrm{h}} \tag{23}$$

where A_{h} is the arbitrary constant of the eigenfunction and k_{h} is the wave number of the h-th vibration mode. Traveling waves and evanescent waves can be derived in the same manner even in the case of plates.

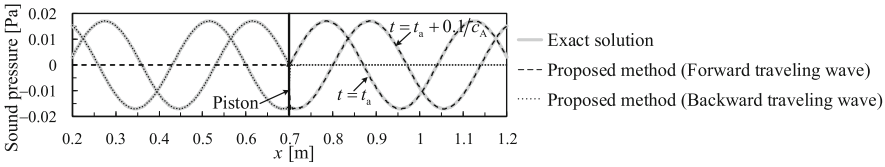

Fig. 3 Simulation results of the sound pressure in the one-dimensional acoustic tube

Table 1 Material properties used in the simulation of the one-dimensional acoustic field

ρ_A	1.2	kg/m^3	ρ_B	$\rho_A \times 10^{-6}$	kg/m^3	x_B	0.2	m
κ_A	138720	Pa	κ_B	$\kappa_A \times 10^{-6}$	Pa	x_C	1.2	m
S	0.015	m^2	l	1.4	m	x_{pL}	0.699	m
d	0.1	m	W_p	1	μm	x_{pR}	0.701	m

3 Simulation

In this simulation, nonreflective boundaries were installed at the new boundaries using the substructure elimination method. The simulation results were obtained using the equations of motion using modal coordinates [2]. Only the simulation results of the one-dimensional acoustic field were shown in this paper as an example because of the limitation of pages. The length of the piston was sufficiently short compared to the wavelength as the piston can be regarded as a point sound source.

The simulation results of the sound pressure in the acoustic tube are shown in Fig. 3. The forward and backward traveling waves at certain times t_a and $t_a + 0.1/c_A$ are shown in Fig. 3. The material properties used in this simulation are listed in Table 1. Here, W_p is the amplitude of w_p. From zeroth to 500th vibration modes were used. The excitation frequency was 1000 Hz. Because the superposition of the vibration modes is a kind of series, the Gibbs phenomena can be observed near the excitation point by the piston. The simulation results agree well with the exact solutions. The installation of arbitrary boundaries using the substructure elimination method and the extraction of the traveling waves using the modal analysis are effective.

4 Conclusion

The method to install arbitrary mechanical impedances including the nonreflective boundaries at the boundaries of continuous bodies using the substructure elimination method was described. In addition, the formulations to extract the traveling waves and evanescent waves using the superposition of vibration modes were also derived theoretically. The effectiveness of the proposed methods was verified through the comparison of the simulation results with the exact solutions.

References

1. Nagamatsu, A.: Modal analysis. Baifukan, Tokyo (1985). (in Japanese)
2. Yamada, K.: Vibration analysis using substructure change and elimination methods. In Proceedings of the 25th international Congress on Sound and Vibration, USB memory 485. Hiroshima (2018)
3. Kinsler, L.E., Frey, A.R., Coppens, A.B., Sanders, J.V.: Fundamentals of Acoustics. John Wiley & Sons, California (1982)
4. Iwaya, Y., Suzuki, Y., Sakata, M., Sone, T.: Influence of the terminating impedance of a semi-infinite beam on the reflection of bending wave and vibration intensity. J Acoust. Soc. Jpn. **56**(4), 243–248 (2000). (in Japanese).
5. Kido, I., Matsumura, Y., Wakida, Y.: A proposal on wave propagation analysis with non-reflection boundary for profound comprehension of vibration transmission. In: Proceedings of ISMA 2012-USD 2012, pp. 17–20, Leuven (2012)

Part III
Rotor Dynamics

Rotordynamic Force Coefficients for Open and Shrouded Impellers

Pascal Jolly, Olivier Bonneau, and Mihai Arghir

1 Introduction

Rocket engine turbopumps are very complex rotating machines with a very low mass-to-power ratio. This power concentration requires designers to continuously improve the performance and the reliability of the mechanical components composing the turbopumps, including impellers. Indeed, the principle of impeller operation requires the use of gaps – flow paths – where leaks affect both the efficiency of the turbopump and its stability. In the case of a LH_2 turbopump, the pressure rise provided by each compressor stage must be of several MPa, while the shaft has to cross critical speeds to reach the operating speed. Therefore, design of LH_2 turbompump requires a rigorous rotordynamic characterization in its whole [1] by providing rotordynamic force coefficients for the rotating parts, among which bearings, seals, and impellers. Among the available solutions to reduce the cost of turbopumps, an open (face) impeller can be used instead of a shrouded impeller [2]. The present paper aims to compare experimental rotordynamic force coefficients produced by both type of impellers, as well as the performance curves.

2 Tested Impellers

The measurements were carried out using the BALAFRE test rig which is dedicated to the identification of dynamic force coefficients of thin fluid film components. The test rig, as well as the method used to identify rotordynamic force coefficients,

P. Jolly (✉) · O. Bonneau · M. Arghir
Institut Pprime, CNRS – Université de Poitiers – ISAE ENSMA, Poitiers, France
e-mail: pascal.jolly@univ-poitiers.fr

S. Oberst et al. (eds.), *Vibration Engineering for a Sustainable Future*,
https://doi.org/10.1007/978-3-030-46466-0_15

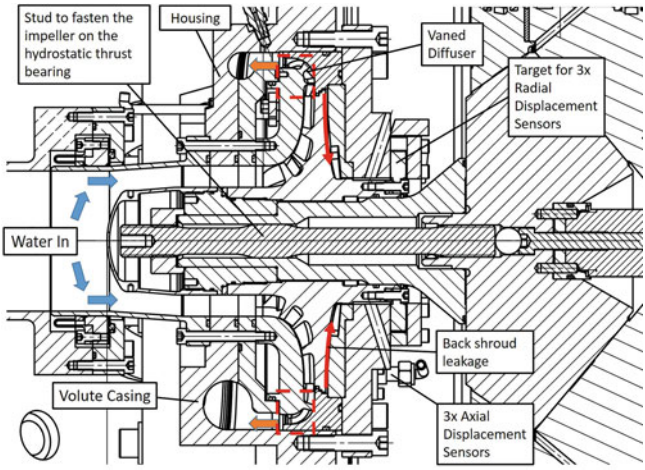

Fig. 1 Schematic view of the test section with an open impeller

has been described in a previous work [3], so only few details will be given hereafter. The test facility is mainly composed of a test cell, an electric motor (180 kW, 6000 rpm max), a hydraulic closed circuit with hot water (50 °C max) pressurized at 0.5 MPa (with various pumps and tanks), and a programmable logic controller associated with a DAQ device. The maximum pressure differential is 4.5 MPa. The tested component can have a nominal diameter up to 350 mm. In many works, known orbiting motions are imposed to the impeller (whirling motion is produced by an eccentric drive mechanism), and resulting hydrodynamic forces are measured [4–6]. In [7], measurements are performed using a hydraulic exciter to impose transient excitations (up to 50 Hz) to the impeller in one direction of motion (vertical translation). In the present work, the impeller is fixed on the rotor of a double conical hydrostatic thrust bearing (cf. Fig. 1) that transmits the dynamic displacements applied by 8 piezoelectric shakers, mounted 4 by 4 in its forward and rear planes. The volute casing is fixed on a rigid part which is mounted on the frame of the test cell via three piezoelectric force transducers which constitute a force balance.

Two types of centrifugal impellers were tested: open (unshrouded) and closed (front shrouded). Although the impellers were designed to work with a cryogenic fluid, water was used as working fluid. All the tests were conducted with a vaned diffuser. The flowrate of water passing through the diffuser is measured by a Venturi flowrate meter located at the outlet of the volute. Since the inlet flowrate is also measured, the leakage between the back shroud and the casing is also estimated. The open impeller has been tested first in order to set the pressure loss to install downstream of the volute casing to reach a given flow rate at 4000 rpm (Best

Table 1 Tested Combinations of eye-packing seal and front casing

Configuration name	Eye packing seal	Front casing
Open	No seal/no shroud	Smooth
AS-S	Annular seal	Smooth
FS-S	Face seal	Smooth
LS-S	Labyrinth seal	Smooth
AS-T	Annular seal	Textured
FS-T	Face seal	Textured
LS-T	Labyrinth seal	Textured

Efficiency Point – BEP).[1] Then, the closed impeller has been tested with the pressure loss obtained previously and by combining three types of eye-packing seal and two types of front casing (smooth and textured), as listed in Table 1. For all the tests, the flow coefficient ϕ is of the order of 0.15.

The volute casing is equipped with six eddy current proximity probes which are positioned three by three, for measuring radial and axial displacements of the impeller relatively to the casing, respectively. Before each test, a dedicated part is used to calibrate in situ and simultaneously the response (gain and offset) of these sensors. The tests are performed by imposing only two translation degrees of freedom, from a centered position and without misalignment. For each rotor speed Ω, experimental data (displacements, forces, pressures, flowrates, temperatures, torque) are recorded for steady-state static case and dynamic excitations. The tests conditions are:

- Rotor speed Ω: 2000, 3000, 4000 and 5000 rpm
- Excitations frequencies ω: 20, 30, 40, 50, 60, 70, 80, 90 and 110 Hz
- Water supply pressure P_s: 0.6 MPa

3 Results and Discussion

3.1 Performance Curves

Figure 2 shows the performance curves, for each combination listed in Table 1, where the pressure rise (differential head) is defined as the difference between the inlet pressure of the impeller and the outlet pressure of the diffuser. Pressure and flowrate at BEP are used to normalize the corresponding data.

Experimental points for the open impeller are the closer from the computed efficiency curve (reference), except at 5000 rpm where the measured pressure rise is lower than predicted. The shrouded impeller configurations $LS-T$ and $AS-T$

[1] Ariane Group has proceeded to many CFD simulations, using FINE/Turbo, in order to define the theoretical performance curves.

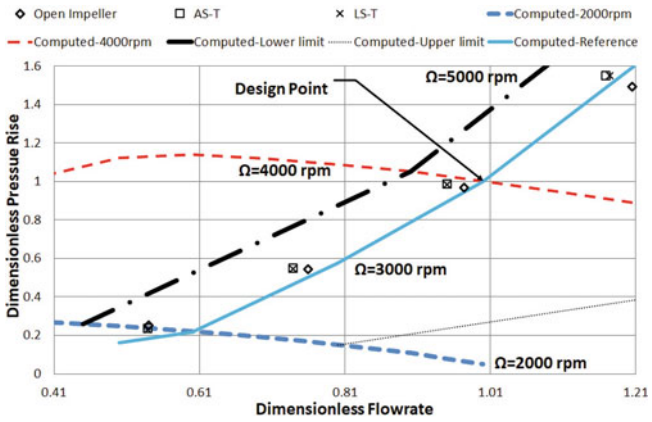

Fig. 2 Performance curves in centered position for the two types of impellers

better fit the reference curve. In the next section, only these two configurations for the shrouded impeller will be used.

3.2 *Experimentally Identified Rotordynamic Force Coefficients*

According to Childs [8], and as mentioned in [9], the present experimental dynamic force coefficients of impellers are made nondimensional as follows:

$$\begin{aligned} &\text{Dimensionless stiffness coefficients} \quad K_{ij}^{*} = \frac{K_{ij}}{\pi \rho b_2 r_2^2 \Omega^2} \\ &\text{Dimensionless damping coefficients} \quad C_{ij}^{*} = \frac{C_{ij}}{\pi \rho b_2 r_2^2 \Omega} \end{aligned} \tag{1}$$

where ρ = mass density of pumped liquid, r_2 = impeller outer (discharge) radius, and b_2 = impeller discharge width including impeller side plate. For various shaft speeds, Fig. 3 shows the evolution of the four terms K_{ij}^{*} of the stiffness matrix for the three configurations mentioned above (open impeller, shrouded impeller $LS-T$ and $AS-T$). The open impeller produces the lower stiffness coefficients, with negative values of K_{xx}^{*} for the three rotating speed, while they are positive for the shrouded impeller equipped with an annular seal. For both types of impellers, present experimental results do not provide equal values for the direct stiffness coefficients while the assumption $K_{xy}^{*} = -K_{yx}^{*}$ is almost verified. The amplitude of the latter, as well as K_{yy}^{*}, decrease with increasing Ω while the amplitude of K_{xx}^{*} increase with increasing Ω.

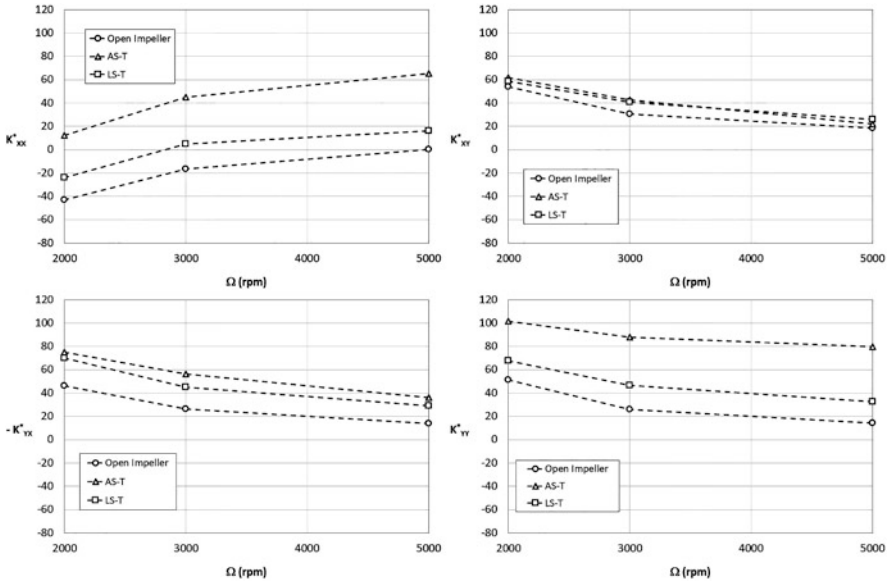

Fig. 3 Dimensionless identified stiffness coefficients K_{ij}^{*} for the open impeller and two configurations of shrouded impeller

For open and closed impellers, the normalized damping coefficients (Fig. 4) are almost constant in the range of rotating speeds, while the cross-coupled damping coefficients are of the same order. The open impeller produces the lower direct damping coefficients.

The shrouded impeller provides higher direct stiffness and damping coefficients than the open impeller because of the eye packing seal (or wear ring seal) that is mounted on its front side.

4 Conclusion

A test rig dedicated to the identification of rotordynamic force coefficients of thin fluid film components is used for testing two types of impellers: open and shrouded. An open impeller, which is less expensive to manufacture with respect to the front shrouded type, would produce lower direct stiffness and direct damping coefficients compared to the latter, which is fitted with an eye-packing seal. Stiffness and damping cross-coupled coefficients are almost the same for both types of impellers.

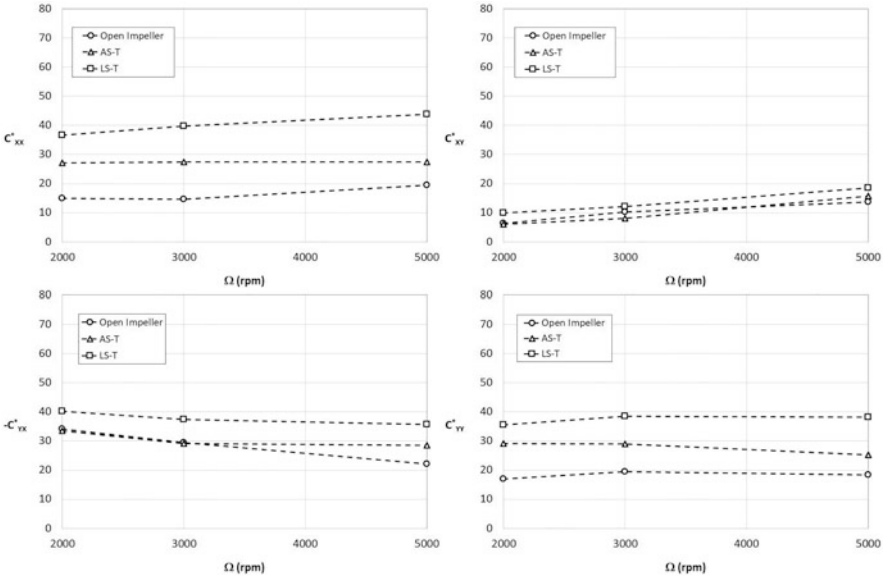

Fig. 4 Dimensionless identified damping coefficients C^*_{ij} for the open impeller and two configurations of shrouded impeller

Acknowledgments The authors are grateful to Centre National d'Etudes Spatiales (CNES) and to ARIANE GROUP for using the BALAFRE test rig and for their agreement to present this experimental work. This work was partially funded by the French Government "Investments for the Future" program (EQUIPEX GAP, PIA, ANR-11-EQUIPEX-0018).

References

1. Jeon, S.M., Kwak, H.D., Yoon, S.H., Kim, J.: Rotordynamic analysis of a turbopump with the casing structural flexibility. J. Propuls. Power **24**(3), 433–436 (2008)
2. Fayolle, P., Lambert, P.-A., Gelain, P., Fonteyn, P., Olofsson, H., Ore, S., Supie, P., Dehouve, J.: Major achievements reached through TPX LH2-Turbopump demonstration program. In: 47th AIAA/ASME/SAE/ASEE Joint Propulsion Conference & Exhibit, San Diego, July 2011
3. Jolly, P., Arghir, M., Bonneau, O., Hassini, M.: Experimental and theoretical rotordynamic coefficients of smooth and round-hole pattern water-fed annular seals. ASME. J. Eng. Gas Turbines Power **140**(11), 112501–112508 (2018)
4. Yoshida, Y., Tsujimoto, Y., Yokoyama, D., Ohashi, H., Kano F.: Rotordynamic fluid force moments on an open-type centrifugal compressor impeller in precessing motion. Int. J. Rotating Mach. **7**(4), 237–251 (2001)

5. Uchiumi, M., Nagao, N., Yoshida, Y., Eguchi, M.: Comparison of rotordynamic fluid forces between closed impeller and open impeller. In: Proceedings of ASME. Fluids Engineering Division Summer Meeting, Rio Grande, 8–12 July 2013
6. Valentini, D., Pace, G., Pasini, A., Torre, L., Hadavandi, R., d'Agostino, L.: Analyses of hydrodynamic radial forces on centrifugal pump impellers. Eur. J. Mech. B/Fluids **61**, 336–345 (2017)
7. Bolleter, U., Wyss, A., Welte, I., Sturchler, R.: Measurement of hydrodynamic interaction matrices of boiler feed pump impellers. ASME. J. Vib. Acoust. **109**(2), 144–151 (1987)
8. Childs, D.W.: Turbomachinery Rotordynamics: Phenomena, Modeling and Analysis. Wiley, New York (1993)
9. Corbo, M.A., Malanoski, S.B.: Pump rotordynamics made simple. In: Proceedings of the Fifteenth International Pump Users Symposium, Turbomachinery Laboratory Texas A M University, College Station, pp. 167–204 (1998)

Vibration Force Transmissibility of a Rotor-Stator System with Potential Rub-Impact

Wei Dai and Jian Yang

1 Introduction

There have been wide applications of high-speed rotating machineries such as aero-engines and electric generators. In many practical designs, there is always a need of reducing the clearance between the rotor and the stator, which subsequently increases the possibility of rub-impact between these two components during the operation. It has been previously shown that rub-impacts within rotordynamic system may lead to unwanted vibrations, components wear, or even severe safety problems for the system [1]. Therefore, it is necessary to investigate the rub-impact mechanism within rotary machinery system to achieve enhanced design. It is also important to understand vibration transmission characteristics of rotordynamic systems with possible rub-impact for operation monitoring or fault diagnosis. It has been shown in previous studies that stiffness and damping nonlinearities can largely affect the vibration transmission characteristics within the subsystems of an integrated structure [2–4]. Understanding the vibration force and power flow transmission characteristics can contribute to dynamic designs of vibration suppression systems to achieve enhanced performance [5–9]. The current paper attempts to address this problem by establishing the system model firstly. Different methods are then employed to obtain the force transmissibility and to examine the effects of system parameters such as contact stiffness, contact friction coefficient, and mass eccentricity, on the vibration transmission between rotor and stator.

W. Dai · J. Yang (✉)
Department of Mechanical, Materials and Manufacturing Engineering, University of Nottingham Ningbo China, Ningbo, People's Republic of China

W. Dai
Key Laboratory of More Electric Aircraft Technology of Zhejiang Province, University of Nottingham Ningbo China, Ningbo, People's Republic of China
e-mail: wei.dai@nottingham.edu.cn

S. Oberst et al. (eds.), *Vibration Engineering for a Sustainable Future*,
https://doi.org/10.1007/978-3-030-46466-0_16

2 Nonlinear Rotordynamic Modeling with Rub-Impact

The rotordynamic model is shown in Fig. 1. An eccentric rotor with mass m is mounted on a rigid shaft which is supported by two identical deep groove ball bearings. The rotor mass center C is of a distance of e to its geometric center O', resulting in an out-of-balance excitation force as the vibration source. Its displacements are denoted by x and y, along OX and OY orthogonal axes, respectively. The radial displacement is thus represented by $r = \sqrt{x^2 + y^2}$. The motion of the rotor along the shaft (i.e., OZ-axis) is not considered. The stator is assumed to be rigidly supported on the ground, and it is concentric with the rotor when the system is in the static equilibrium position.

Based on the classical rub-impact model [1, 10, 11], the impact contact between the rotor and stator is assumed to be elastic, and the interaction force is acting in the line of OO' shown in Fig. 1. The Coulomb-type friction force model is used to represent the tangential rub force which is perpendicular to the line of OO'. It is noted that the friction heat is assumed to be negligible. The rub-impact forces are expressed as

$$f_x = \frac{k_c\,(r-\delta_c)\,U\,(r-\delta_c)}{r}\,(x-\mu y)\,,\; f_y = \frac{k_c\,(r-\delta_c)\,U\,(r-\delta_c)}{r}\,(y+\mu x)\,, \tag{1a, 1b}$$

acting on the stator in the directions of OX and OY, respectively, where k_c is the rotor-stator contact stiffness, μ is the contact friction coefficient, δ_c is the clearance width between rotor and stator in the static position, and

$$U(s) = \begin{cases} 0, \text{ when } s \le 0, \\ 1, \text{ when } s > 0. \end{cases} \tag{2}$$

The governing equations of the system are

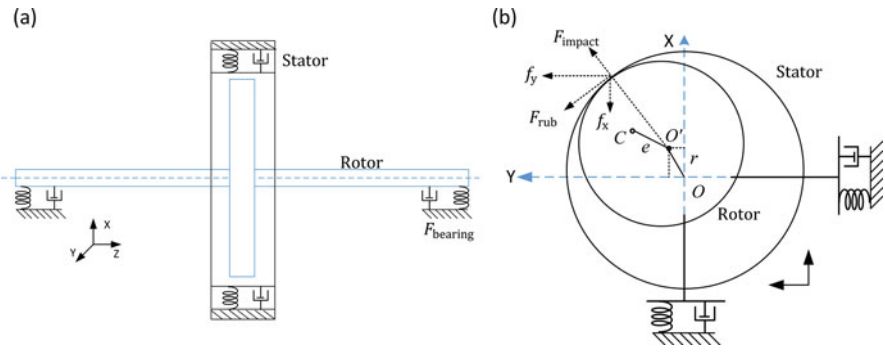

Fig. 1 A schematic representation of the rotordynamic model

$$m\ddot{x} + c\dot{x} + kx + f_x = me\omega^2 \cos \omega t, \tag{3a}$$

$$m\ddot{y} + c\dot{y} + ky + f_y = me\omega^2 \sin \omega t, \tag{3b}$$

where k and c are the stiffness and damping coefficients of rotor-bearing system, respectively. To facilitate later derivations, the following non-dimensional parameters are introduced:

$$\omega_1 = \sqrt{\frac{k}{m}}, \quad \zeta_1 = \frac{c}{2m\omega_1}, \quad E_c = \frac{e}{\delta_c}, \Omega = \frac{\omega}{\omega_1}, \lambda = \frac{k_c}{k}, \quad X = \frac{x}{\delta_c}, Y = \frac{y}{\delta_c},$$
$$R = \frac{r}{\delta_c}, \tau = \omega_1 t,$$

where ω_1 and ζ_1 are the undamped natural frequency and the damping ratio of the rotor system, respectively; E_c and Ω are the mass eccentric ratio and the dimensionless excitation frequency, respectively; λ is the contact stiffness ratio; X and Y are the dimensionless displacement amplitudes in the directions of OX and OY, respectively; R is the dimensionless displacement amplitude in the radial direction; and τ is the dimensionless time. Using these parameters and variables, Eqs. (3a) and (3b) is transformed into

$$X'' + 2\zeta_1 X' + X + F_X = E_c \Omega^2 \cos(\Omega\tau), \tag{4a}$$

$$Y'' + 2\zeta_1 Y' + Y + F_Y = E_c \Omega^2 \sin(\Omega\tau), \tag{4b}$$

where the primes denote differentiation operations with respect to the nondimensional time τ, F_X and F_Y are the dimensionless rub-impact forces

$$F_X = \frac{\lambda(R-1)U(R-1)}{R}(X - \mu Y), \quad F_Y = \frac{\lambda(R-1)U(R-1)}{R}(Y + \mu X), \tag{5a, 5b}$$

acting on the stator decomposed in the directions of OX and OY, respectively. The nondimensional nonlinear equation can be solved by first-order harmonic balance method approximations with alternating frequency time (HB-AFT) scheme with numerical continuation [11–13] or the fourth-order Runge-Kutta numerical integration method to obtain the steady-state response of the system. For the current system, the dimensionless transmitted force from the rotor to the stator has identical amplitude with the resultant rub-impact force act on the rotor. So the force transmissibility is

$$TR = \frac{\max\left(\left|\sqrt{F_X^2 + F_Y^2}\right|\right)}{F_0 \Omega^2}. \tag{6}$$

3 Results and Discussions

Figures 2, 3, and 4 investigate the effects of system parameters including rotor-stator contact stiffness ratio, mass eccentric ratio, and contact friction coefficient on the steady-state response of the rotor as well as the force transmissibility from rotor to stator. The system damping ratio is set as $\zeta_1 = 0.01$. The first-order HB-AFT results are represented by different lines, while the numerical integration results are obtained by using the fourth-order Runge-Kutta (RK) method and denoted by symbols. Figure 2 examines the influence of contact stiffness ratio by keeping the mass eccentric ratio and contact friction coefficient to be fixed with $E_c = 0.1$ and $\mu = 0$, respectively. Three different values of contact stiffness ratio are considered with $\lambda = 0$, 1, and 2. It is shown in Fig. 2a that the introduction of the rotor-stator contact bends the peak of steady-state response curve to the high-frequency range. Multiple solutions can be observed near resonance frequency of the rotor, indicating the sensitivity of the response to the initial conditions. The peak value of the displacement response in radial direction R_{max} increases slightly as the contact stiffness ratio increases. Figure 2b shows that the increase of contact stiffness ratio has hardening effect on the force transmissibility curves and results in higher peak value at higher rotational speed.

Figure 3 studies the influence of the mass eccentric ratio by keeping the contact stiffness ratio and contact friction coefficient to be fixed with $\lambda = 1$ and $\mu = 0$, respectively. Three different values of mass eccentric ratio are considered with $E_c = 0.1$, 0.2, and 0.3. Figure 3a shows that the increase of mass eccentric ratio can enlarge the response amplitude in a wide range of rotational speed of the rotor. Figure 3b shows that as the mass eccentric ratio increases, the force transmissibility curves bend to the high frequencies. However, there is very small change in the

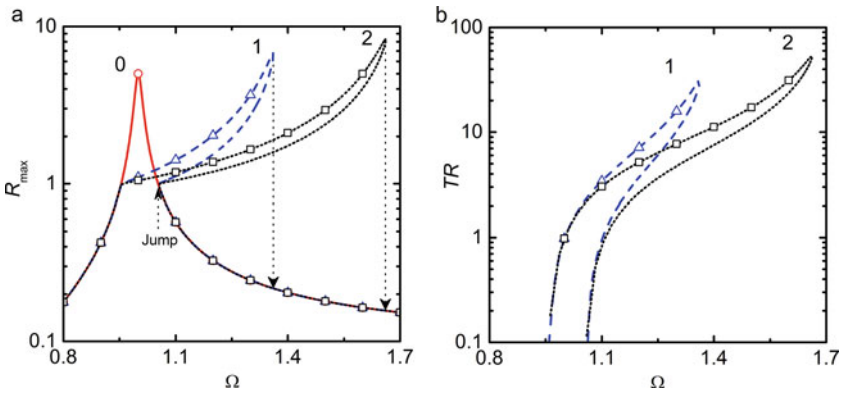

Fig. 2 Effects of contact stiffness ratio on the (**a**) steady-state maximum displacement R_{max}, (**b**) force transmissibility *TR*. The solid, dashed, and dotted lines for $\lambda = 0$, 1, and 2, respectively. Triangles and squares: RK results for $\lambda = 1$ and 2, respectively

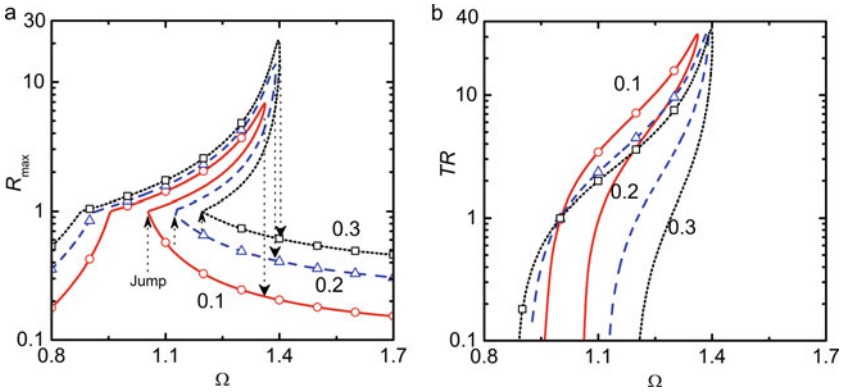

Fig. 3 Effects of mass eccentric ratio on the (**a**) steady-state maximum displacement $R_{\max}$, (**b**) force transmissibility *TR*. The solid, dashed, and dotted lines for $E_c = 0.1$, 0.2, and 0.3, respectively. Circles, triangles, and squares: RK results for $E_c = 0.1$, 0.2, and 0.3, respectively

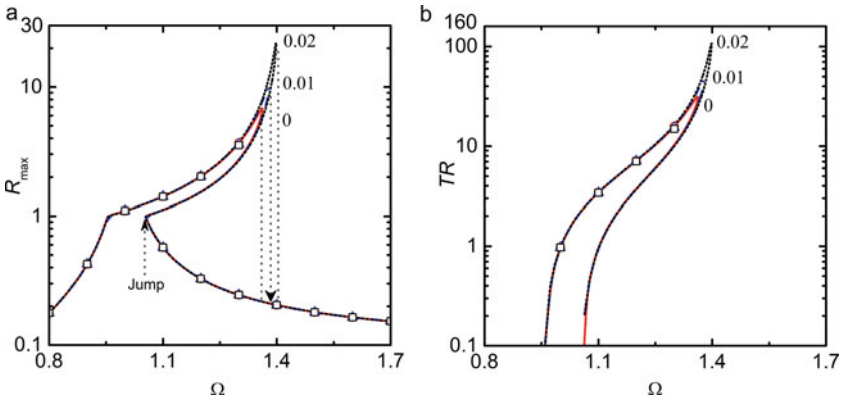

Fig. 4 Effects of contact friction coefficient on the (**a**) steady-state maximum displacement $R_{\max}$, (**b**) force transmissibility *TR*. The solid, dashed, and dotted lines for $\mu = 0$, 0.01, and 0.02, respectively. Circles, triangles, and squares: RK results for $\mu = 0$, 0.01, and 0.02, respectively

peak value. There may be larger force transmissibility when rotor speed locates from $\Omega \approx 0.875$ to $\Omega \approx 1.05$ but lower value of *TR* from $\Omega \approx 1.05$ to $\Omega \approx 1.40$.

Figure 4 studies the effects of contact friction coefficient by using fixed values of the contact stiffness ratio and mass eccentric ratio with $\lambda = 1$ and $E_c = 0.1$. Three different values of contact friction coefficient are considered with $\mu = 0, 0.01$, and 0.02. It shows that with the rise of contact friction coefficient, the peak values of the maximum displacement $R_{\max}$ and the force transmissibility both increase substantially.

4 Conclusion

This paper investigated the force transmissibility between rotor and stator with possible rub-impact based on a modified Jeffcott rotor model. The governing equations of the rotor system excited by mass eccentricity were constructed and solved by HB-AFT approximation and numerical integration method. The effects of contact stiffness, mass eccentricity, and contact friction coefficient on the dynamic response of the rotor and force transmissibility to the stator were investigated. It was shown that a higher contact stiffness has hardening effect on the steady-state response as well as force transmissibility. It may increase the peak values of the rotor displacement response and the peak force transmissibility. It was also shown that the increase of mass eccentricity would lead to a larger vibration response, but the force transmissibility value may become lower at certain rotor speed. It was also found that a higher contact friction coefficient may increase the vibration response as well as the force transmission to the stator.

References

1. Hou, L., Chen, H.Z., Chen, Y.S., Lu, K., Liu, Z.S.: Bifurcation and stability analysis of a nonlinear rotor system subjected to constant excitation and rub-impact. Mech. Syst. Signal Process. **125**, 65–78 (2019)
2. Yang, J., Xiong, Y.P., Xing, J.T.: Nonlinear power flow analysis of the Duffing oscillator. Mech. Syst. Signal Process. **45**(2), 563–578 (2014)
3. Yang, J., Shi, B.Y., Rudd, C.: On vibration transmission between interactive oscillators with nonlinear coupling interface. Int. J. Mech. Sci. **137**, 238–251 (2018)
4. Shi, B.Y., Yang, J., Rudd, C.: On vibration transmission in oscillating systems incorporating bilinear stiffness and damping elements. Int. J. Mech. Sci. **150**, 458–470 (2019)
5. Yang, J., Xiong, Y.P., Xing, J.T.: Dynamics and power flow behaviour of a nonlinear vibration isolation system with a negative stiffness mechanism. J. Sound Vib. **332**(1), 167–183 (2013)
6. Yang, J., Xiong, Y.P., Xing, J.T.: Power flow behaviour and dynamic performance of a nonlinear vibration absorber coupled to a nonlinear oscillator. Nonlinear Dyn. **80**(3), 1063–1079 (2015)
7. Dai, W., Yang, J., Shi, B.Y.: Vibration transmission and power flow in impact oscillators with linear and nonlinear constraints. Int. J. Mech. Sci. **168**, 105234 (2020). https://doi.org/10.1016/j.ijmecsci.2019.105234
8. Shi, B.Y., Yang, J.: Quantification of vibration force and power flow transmission between coupled nonlinear oscillators. Int. J. Dyn. Control. **8**(2), 418–435 (2019)
9. Yang, J., Xiong, Y.P., Xing, J.T.: Vibration power flow and force transmission behaviour of a nonlinear isolator mounted on a nonlinear base. Int. J. Mech. Sci. **115-116**, 238–252 (2016)
10. Chu, F., Zhang, Z.: Bifurcation and chaos in a rub-impact jeffcott rotor system. J. Sound Vib. **210**(1), 1–18 (1998)
11. Von Groll, G., Ewins, D.J.: The harmonic balance method with arclength continuation in rotor/stator contact problems. J. Sound Vib. **241**(2), 223–233 (2001)
12. Dai, W., Yang, J.: Vibration analysis of a rotordynamic system with nonlinear bearing supports. In: 26th International Congress on Sound and Vibration, Montréal, Canada (2019)
13. Dai, W., Yang, J.: Rotordynamic analysis of a permanent magnet synchronous motor considering nonlinear unbalanced magnetic pull. In: 22nd International Conference on Electrical Machines and Systems, Harbin, China (2019)

The Vibration and Forces Control During the Rotor Rubbing by Application of Magnetically Sensitive Fluids Lubricating the Rotor Bearings

Jaroslav Zapoměl and Petr Ferfecki

1 Introduction

To enable operation of rotors mounted in hydrodynamic bearings (HDB) at high angular speed, HDBs are inserted in squeeze film bearings. A simple dynamical analysis shows that to achieve their optimum performance, their damping effect must be adaptable to the current operating speed [1]. This leads to a proposal and investigation of a new design of a rotor support element that is intended for machines working in a wide range of running velocities. The element is formed by an HDB inserted in a semiactive controllable magnetorheological (MR) squeeze film damper.

The effect of the proposed coupling element on the rotor vibration attenuation and the force transmission at normal operation conditions was studied in [2]. This article deals with its influence on the rotor behavior in the case of collisions occurring between the disc and the stationary part. The results of the computational simulations show that adapting the damping in the rotor supports to the current operating speed makes it possible to reduce the rubbing force acting between the disc and the stationary part.

J. Zapoměl (✉)
VSB – Technical University of Ostrava, Department of Applied Mechanics, Ostrava-Poruba, Czech Republic

Institute of Thermomechanics, Prague, Czech Republic
e-mail: jaroslav.zapomel@vsb.cz; zapomel@it.cas.cz

P. Ferfecki
VSB – Technical University of Ostrava, Department of Applied Mechanics, Ostrava-Poruba, Czech Republic

VSB – Technical University of Ostrava, IT4Innovations National Supercomputing Center, Ostrava-Poruba, Czech Republic
e-mail: petr.ferfecki@vsb.cz

S. Oberst et al. (eds.), *Vibration Engineering for a Sustainable Future*,
https://doi.org/10.1007/978-3-030-46466-0_17

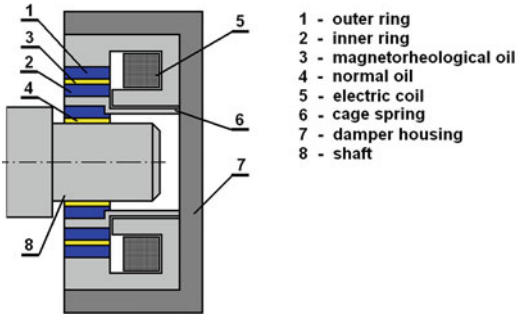

Fig. 1 Drawing of the support element

2 The Proposed Support Element

The proposed support element (Fig. 1) represents a combination of an MR squeeze film damper and an HDB. The main parts of the damper are two concentric rings separated by a thin film of MR oil. The rotor journal is inserted in the inner damper ring, which is coupled with the damper housing by a cage spring and is designed as a bushing of the HDB.

The relations for the pressure distribution in the individual oil layers can be found in [3], and the details on solving the corresponding equations, calculation of the hydraulic forces, and distribution of the magnetic field in the damping device are reported in [4, 5]. Validation of the developed mathematical model of the studied support element is reported in [2].

3 The Simulated Rotor System

The analyzed rotating machine (Fig. 2) consists of a flexible rotor, to which one rigid disc placed in an opening of a square shape is attached. The rotor angular speed is constant. During the operation, the rotor is loaded by its weight and is excited by the unbalance and collisions of the disc. The cage springs are prestressed to eliminate their stationary deflection. In the computational model, the rotor is represented by a Jeffcott one. The friction in the contact areas is considered to be of a Coulomb type.

Lateral vibration of the rotor is governed by a set of six differential equations

$$\begin{aligned} &m\ddot{y}_D + (b_P + b_M)\,\dot{y}_D - b_M\dot{y}_J + k_S y_D - k_S y_J + \dot{\vartheta} b_M z_D - \dot{\vartheta} b_M z_J \\ &\quad = m e_T \dot{\vartheta}^2 \cos\vartheta + F_{cony} \end{aligned} \tag{1}$$

$$\begin{aligned} &m\ddot{z}_D + (b_P + b_M)\,\dot{z}_D - b_M\dot{z}_J + k_S z_D - k_S z_J - \dot{\vartheta} b_M y_D + \dot{\vartheta} b_M y_J \\ &\quad = m e_T \dot{\vartheta}^2 \sin\vartheta - mg + F_{conz} \end{aligned} \tag{2}$$

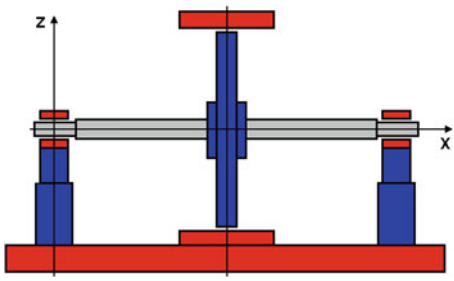

Fig. 2 Scheme of the simulated rotor system (axis y is perpendicular to axes x and z)

Table 1 Notation of the used quantities

Symbol	Name	Symbol	Name
m	The disc mass	y_J, z_J	The journal displacements
b_P	Coefficient of the disc environment damping	y_R, z_R	The ring displacements
b_M	Coefficient of the shaft material damping	F_{hdy}, F_{hdz}	The HDB force
k_S	The shaft bending stiffness	F_{mry}, F_{mrz}	The MR damping force
k_R	The cage spring stiffness	F_{psy}, F_{psz}	The prestress force
e_T	Eccentricity of the disc centre	F_{cony},F_{conz}	The impact force acting on disc
g	The gravity acceleration	ϑ	Angle of the rotor rotation
y_D, z_D	The disc displacements	$\dot{(\cdot)}$, $\ddot{(\cdot)}$	Notation of the first and second time derivatives

$$-b_M\dot{y}_D + b_M\dot{y}_J - k_S y_D + k_S y_J - \dot{\vartheta} b_M z_D + \dot{\vartheta} b_M z_J = F_{hdy} \tag{3}$$

$$-b_M\dot{z}_D + b_M\dot{z}_J - k_S z_D + k_S z_J + \dot{\vartheta} b_M y_D - \dot{\vartheta} b_M y_J = F_{hdz} \tag{4}$$

$$k_R y_R = -F_{hdy} + F_{mry} + F_{psy} \tag{5}$$

$$k_R z_R = -F_{hdz} + F_{mrz} + F_{psz} \tag{6}$$

Notation of the individual quantities used in the governing equations is summarized in Table 1.

The governing Eqs. (1, 2, 3, 4, 5, and 6) are nonlinear as components of the hydraulic and contact forces depend on displacements and velocities of the rotor journal and of the disc.

The impact forces acting on the disc in the horizontal and vertical directions consist of two components. The normal component induced by elastic deformation of the disc and the stationary part in the vicinity of the contact area is always orientated toward the disc center, and the tangential component caused by the dry friction is always directed against the disc rotation. The corresponding relations for the elastic and friction forces can be found in [6].

4 Results of the Simulations

The principal technological and operation parameters of the investigated rotor system can be found in Table 2.

The dynamical analysis, which for simplicity assumes that stiffness of the HDB is very high, shows that the critical speed of the rotor system can be approximately expected for two limit cases (no damping produced by the dampers, overdamped regime of the dampers) in the interval of 115–200 rad/s. The simulations were focused on two velocities of the rotor rotation, 100 rad/s, which is close to the lower bound of the rotor critical speed, and 400 rad/s, which is sufficiently high above its upper bound.

In Figs. 3, 4, and 5, the disc center trajectories, time history of the force transmitted to the stationary part through the support element, and the force acting on the disc during rubbing are depicted. The results are related to the velocity of 100 rad/s. Application of the current reduces the size of the orbit and changes its character from chaotic to periodic. Increased damping reduces magnitude of the impact force.

Table 2 The principal technological parameters of the studied rotor system

Value	Name	Value	Name
450 kg	The rotor mass	0.3 Pas	The MR oil dynamic viscosity not effected by magnetic field
20 MN/m	The shaft stiffness	150 mm	The damper diameter
5 MN/m	The cage spring stiffness	40 mm	The damper length
110 mm	The HDB diameter	50 μm	Eccentricity of the disc center
60 mm	The HDB length	1 GN/m	The contact stiffness
0.2 mm	The bearing clearance	0.2	The friction coefficient
0.01 Pas	The bearing oil dynamic viscosity		

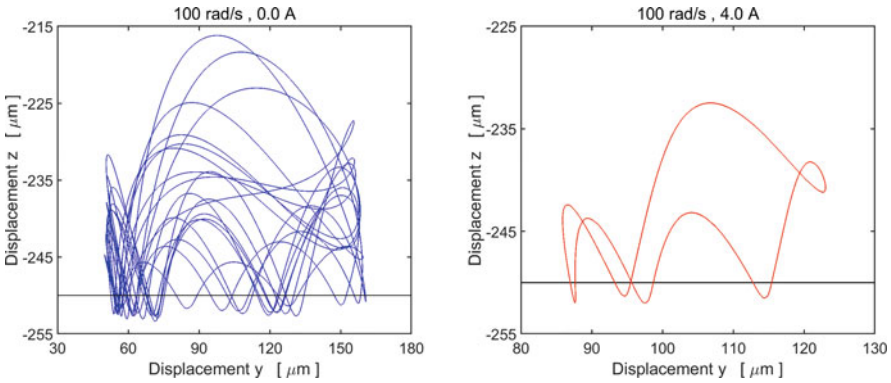

Fig. 3 Trajectory of the disc center (100 rad/s, current 0.0 A; 4.0 A)

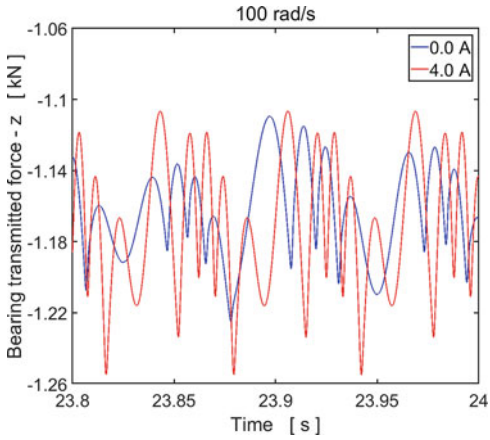

Fig. 4 Bearing force time history (100 rad/s)

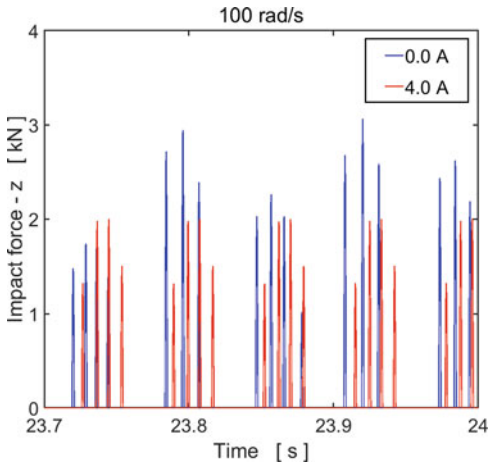

Fig. 5 Impact force time history (100 rad/s)

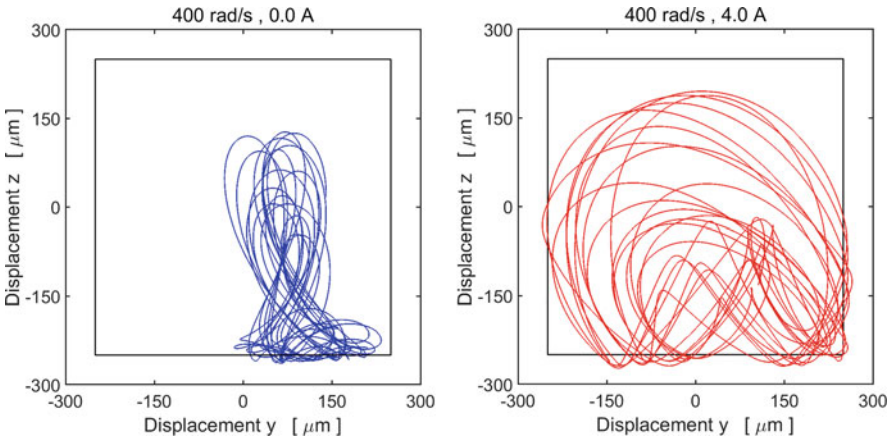

Fig. 6 Trajectory of the disc center (400 rad/s, current 0.0 A; 4.0 A)

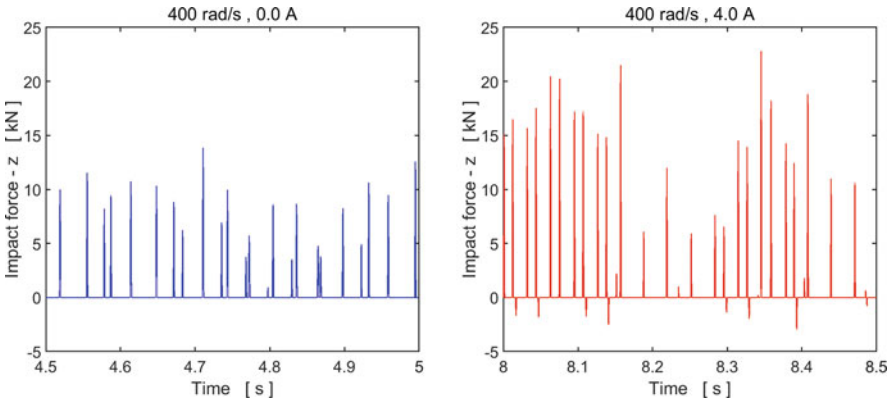

Fig. 7 Time history of the impact force in the z direction (400 rad/s, current 0.0 A; 4.0 A)

Figures 6 and 7 show results of the simulations related to the speed of the rotor rotation of 400 rad/s. It is evident that the rotor behaves in a different way. The trajectory of the disc center indicates that the rotor motion is chaotic. Application of the current does not change the character of the vibration, increases its amplitude, and leads to increase in the impact force acting between the disc and the stationary part.

The results imply that suitable adaption of the damping effect in the rotor supports makes it possible to reduce the magnitude of the impact forces acting between the disc and the stationary part.

5 Summary and Conclusions

The main objective of the study presented in this paper is a new semiactive coupling element that consists of a HDB inserted in an MR squeeze film damper. The results show that adapting the damping effect to the current operating speed makes it possible to minimize the rubbing force in a wide interval of operating speeds. The control of damping in the rotor supports is simple as the damping element is semiactive and the controller can work only in the on/off regime. This is a great technological advantage.

Acknowledgement This work was supported by the Czech Science Foundation (grant project 19-06666S) and by the National Programme of Sustainability (NPU II, project LQ1602 – IT4Innovations excellence in science).

References

1. Zapoměl, J., Ferfecki, P., Kozánek, J.: Determination of the transient vibrations of a rigid rotor attenuated by a semiactive magnetorheological damping device by means of computational modelling. Appl. Comput. Mech. **7**, 223–234 (2013)
2. Zapoměl, J., Ferfecki, P., Forte, P.: A new mathematical model of a short magnetorheological squeeze film damper for rotordynamic applications based on a bilinear oil representation – derivation of the governing equations. Appl. Math. Modell. **52**, 558–575 (2017)
3. Zapoměl, J., Ferfecki, P., Kozánek, J., Savin, L.: Controllable magnetically sensitive rotor support element for reducing oscillation and force transmission. In: Uhl, T. (ed.) Advances in Mechanism and Machine Science, pp. 3385–3394. Springer, Krakow (2019)
4. Ferfecki, P., Zapoměl, J., Kozánek, J.: Analysis of the vibration attenuation of rotors supported by magnetorheological squeeze film dampers as a multiphysical finite element problem. Adv. Eng. Softw. **104**, 1–11 (2017)
5. Zapoměl, J., Ferfecki, P., Kozánek, J.: Modelling of magnetorheological squeeze film dampers for vibration suppression of rigid rotors. Int. J. Mech. Sci. **127**, 191–197 (2017)
6. Zapoměl, J., Ferfecki, P.: A computational investigation of the disk-housing impacts of accelerating rotors supported by hydrodynamic bearings. J. Appl. Mech. **78**, 1–13 (2011)

Influence of Unbalance Angle and Eccentricity on the Vibration of a Cracked Rotor

Joseph Patrick Spagnol and Helen Wu

1 Introduction

Early detection of fatigue cracks in rotating machinery can be difficult to achieve with minimal disruption to normal operation due to their imperceptibility. Failure to detect and remedy cracks in rotating shafts will eventually result in catastrophic mechanical failure [1]. Cracked shafts exhibit a nonlinear reduction in bending stiffness that causes anomalous vibration characteristics. The nonlinearity is the result of the shaft becoming stiffer in bending when loads periodically cause the crack to partially or fully close. This concept is known as "crack breathing."

The proximity between the bending load direction and the crack is essential for describing the breathing behavior of a crack [2]. Existing cracked rotor models in the literature, known as weight-dominant models (such as in [3]), assume the influence of dynamic loads such as rotating imbalance is negligible when considering the breathing of a crack. In particular, in these models the crack smoothly transitions from a completely open to completely closed state and vice versa. However, dynamic loads may impact the breathing behavior of a crack potentially causing it to erratically change states or remain within one state indefinitely [2, 4].

J. P. Spagnol (✉) · H. Wu
Western Sydney University, Kingswood, NSW, Australia
e-mail: j.spagnol@westernsydney.edu.au; helen.wu@westernsydney.edu.au

S. Oberst et al. (eds.), *Vibration Engineering for a Sustainable Future*,
https://doi.org/10.1007/978-3-030-46466-0_18

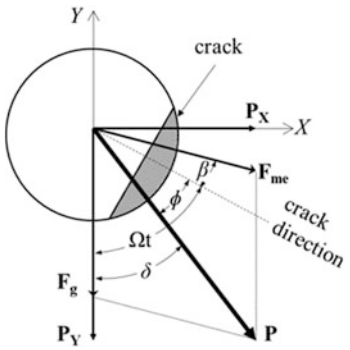

$$\phi(t) = \Omega t - \tan^{-1}\left[\frac{\sin(\Omega t + \beta)}{\cos(\Omega t + \beta) + \eta}\right]$$

Fig. 1 Cracked shaft cross section showing unbalance and weight loading

2 Crack Breathing Model

2.1 Influence of Unbalance on Crack Breathing

In weight-dominant models, static loads (such as rotor weight) are the only contributors to the bending of the shaft resulting in an unchanging bending direction. However, rotating imbalance causes the bending direction to constantly change, and therefore, the proximity between the bending load and the crack also changes.

As represented in Fig. 1, the authors of [5] (and similarly in [6]) show that the angle between the bending direction P and the crack direction (called proximity angle ϕ herein) is an important factor in the breathing mechanism of a shaft crack when rotating imbalance is present. It is dependent on the unbalance angle β, shaft rotation angle Ωt, and the ratio of the weight force F_g to rotating unbalance force F_{me} known as the load ratio η and is numerically equal to $mg/m_e d\Omega^2$, where m is the mass of the rotor, g is the acceleration due to gravity, $m_e \bullet d$ is the eccentricity amount, and Ω is the rotor speed. With this model, if η approaches infinity, then the rotor becomes increasing weight-dominant. The proximity angle equation is included in Fig. 1.

2.2 Stiffness Changes in Cracked Shaft

The authors of [7] showed that the reduction in area moment of inertia of the cracked cross section can be used to model the change in stiffness of a shaft due to a breathing crack. The time-varying area moments of inertia derived in [3] in the vertical and horizontal centroidal directions, $I_{\overline{X}}$ and $I_{\overline{Y}}$, are given as

$$I_{\overline{X}}(t) = \left(I - \overline{I}_1\right) f_1(t) + \overline{I}_1, \tag{1}$$

$$I_{\overline{Y}}(t) = \left(2I - \overline{I}_1 - \overline{I}_2\right) f_2(t) - \left(I - \overline{I}_1\right) f_1(t) + \overline{I}_2 \tag{2}$$

where $I = \pi R^4/4$ and $f_1(t)$ and $f_2(t)$, known as breathing functions, are shape functions that reflect the change in area moment of inertia over time and are given as

$$f_1(t) = 1 - \frac{1}{2^p}\left[\binom{p}{p/2} + 2\sum_{j=1}^{(p/2)}\binom{p}{j-1}\cos\left((p-2(j-1))\frac{\Omega t}{2}\right)\right], \tag{3}$$

$$f_2(t) = 1 - \left(\frac{\theta_1 + \theta_2}{2\pi}\right) + \frac{2}{\pi(\theta_2 - \theta_1)}\sum_{j=1}^{p}\frac{\cos(j\theta_2) - \cos(j\theta_1)}{j^2}\cos(j\Omega t) \tag{4}$$

Readers should consult the original source for the values of $\bar{I}_1$, $\bar{I}_2$, θ_1, and θ_2.

To account for the unbalance effect on the crack breathing behavior, the proximity angle ϕ is substituted into Eqs. (3) and (4). In Fig. 2 the time-varying area moment of inertia based on the unbalance angle β and crack depth μ is shown, where $\mu = h/R$, h is the depth of the crack and R is the shaft radius. A force ratio of $\eta = 0.5$ is used, which means the unbalance force is two times larger than the weight force. As β approaches 180°, i.e., the unbalance mass is gradually placed opposite to the crack direction, the overall area moment of inertia increases towards

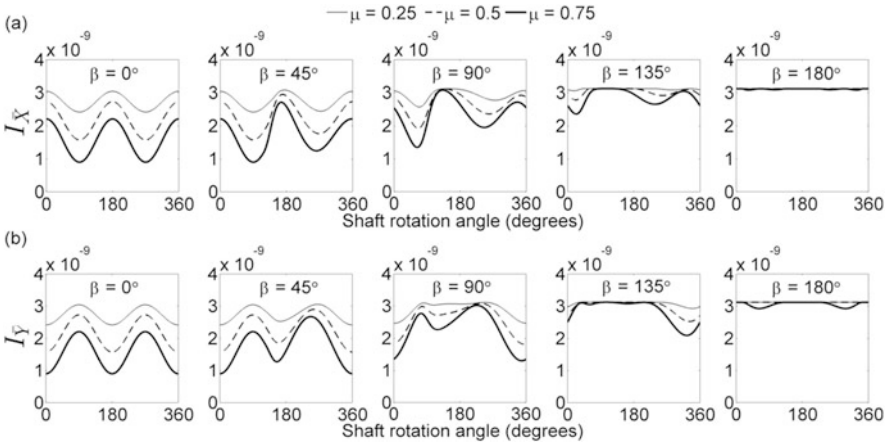

Fig. 2 Change in area moment of inertia of the cracked cross section due to rotating unbalance for $R = 7.94$ mm, $\eta = 0.5$ about the (**a**) centroidal X axis and (**b**) centroidal Y axis for $p = 10$

the maximum value ($\pi R^4/4$), therefore meaning that the crack becomes less open and almost does not open at all.

3 Vibration of a Cracked Rotor Using the Proposed Model

3.1 Rotor Model

The eight element rotor ($N = 8$) seen in Fig. 3 will be used to examine the influence of unbalance eccentricity and angle on the vibration of a cracked rotor. The rotor features a disk at its mid-span (node 5) and a fatigue crack at element 5. Also, the rotor is supported by bearings at its ends. The same rotor and bearing specifications in [5] are used.

3.2 Equations of Motion

The dynamic response of the rotor was obtained using the MATLAB ode15s function which is an adaptive step solver for stiff problems. The use of ode15s requires the equations of motion to be written as a first-order system as in Eq. (5)

$$\left\{\dot{Q}\right\} = [A]\{Q\} + [B]\{F\}, \tag{5}$$

where Q is the $8(\mathrm{N}+1) \times 1$ vector of nodal displacements and velocities. The matrices $[A]$ and $[B]$ are given as.

$$[A] = \begin{bmatrix} [Z] & [I] \\ -[M]^{-1}[K_{ce}] & -[M]^{-1}[G] \end{bmatrix}; \quad [B] = \begin{bmatrix} [Z] \\ [M]^{-1} \end{bmatrix} \tag{6}$$

where $[Z]$ is a $4(\mathrm{N}+1) \times 4(\mathrm{N}+1)$ matrix of zeros, $[I]$ is a $4(\mathrm{N}+1) \times 4(\mathrm{N}+1)$ identity matrix, $[M]$ is the global mass matrix, $[G]$ is the global damping/gyroscopic matrix, and $[K_{ce}]$ is the global cracked element matrix. The global matrices can

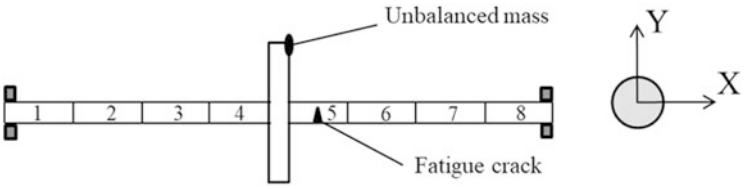

Fig. 3 Cracked rotor with centrally mounted disk supported by rolling-element bearings. The fifth element is the location of the crack, and the disk supports an unbalanced mass

be assembled using standard finite element modeling procedures [8]. The cracked element matrix is given in [5]; however, the $I_{\overline{X}}$ and $I_{\overline{Y}}$ values should be calculated via the methodology outlined in Sect. 2.2.

3.3 Dynamic Response of Cracked Rotor

Figure 4 shows the effect of increasing the unbalance angle β on the first critical speed value and resonant peak radial amplitude as predicted by the proposed model and weight-dominant model from [3]. It is detailed in [2] that the presence of a fatigue crack in a shaft shifts the rotor critical speed leftward (towards zero) when compared to an undamaged shaft and may increase the resonant amplitude. This idea explains the plateauing of critical speed and peak amplitude for the proposed model when the unbalance mass is placed 120–180° as the crack remains mostly closed, and therefore, the shaft behaves as if it were undamaged. This plateauing phenomenon can also be inferred from [6]. The plateauing of the critical speed and peak amplitude is not seen in the weight-dominant model.

In Fig. 5, the frequency plot of the disk's (node 5) vertical amplitude for the proposed model and the weight-dominant model is presented. In Fig. 5a, $\beta = 180°$, $\Omega = 780$ RPM, and $m_e \cdot d = 0.01$ result in $\eta = 0.63$ for the proposed model. Since $\eta < 1$, the unbalance force has an appreciable effect on the crack behavior, and the two models significantly differ. As such, the proposed model shows the disappearance of the $2\times$ and $3\times$ frequencies (which are typical indicators for the presence of a crack) suggesting that the rotor is behaving as if it were undamaged. However, in Fig. 5b, β is also 180°, but there is still an appreciable $2\times$ component relative to the $1\times$ component for both models highlighting the existence of the crack. Since $\Omega = 780$ RPM and $m_e \cdot d = 0.001$, the ratio $\eta = 6.31$, so the proposed model is quite weight-dominant; and consequently, there is a strong similarity between the

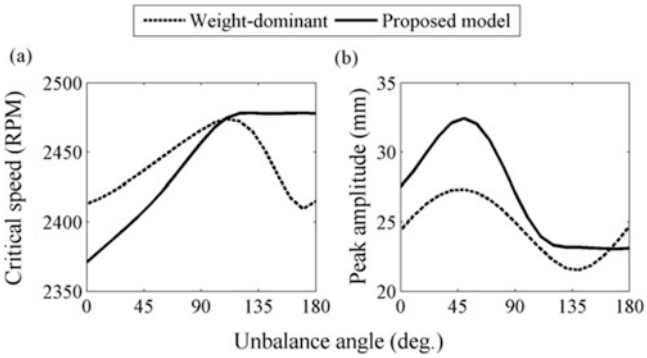

Fig. 4 Change in (**a**) critical speed value and (**b**) resonant peak amplitude of the cracked rotor ($\mu = 0.3$) due to a change in unbalance angle

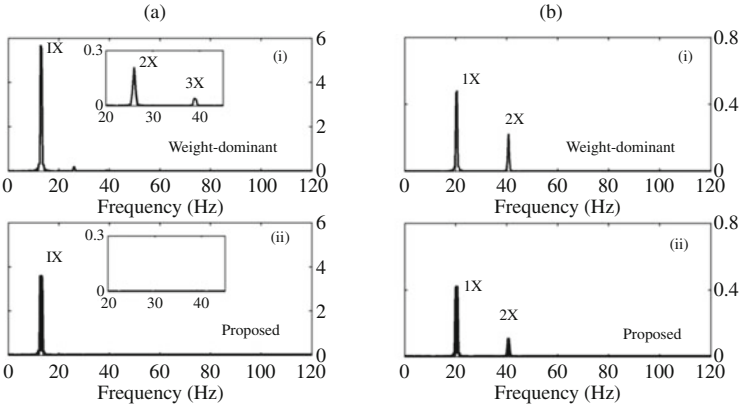

Fig. 5 Frequency amplitude plot of the disk in the vertical direction where $\beta = 180°$ and $\Omega = 780$ RPM with (**a**) $\eta = 0.63$ and (**b**) $\eta = 6.31$ for both the (i) weight-dominant model and (ii) proposed model

two models. This means that the unbalance angle placed opposite to the crack is not sufficient enough to cause the shaft to behave as if it were undamaged and that the η value must be considered.

4 Conclusion

This study examined the effects of unbalance angle and eccentricity on the breathing behavior of a fatigue crack. The proposed model shows that placement of the unbalance mass placed between approximately 120° and 180° causes the critical speed and peak amplitude to plateau as the crack remains fully closed or almost fully closed; thus the rotor behaves as if it were undamaged. Frequency analysis of the disk's vertical amplitude using the proposed breathing model showed the disappearance of the $2\times$ and $3\times$ frequency amplitudes with a low weight-to-unbalance force ratio ($\eta = 0.63$), i.e., a poorly balanced rotor, once again suggesting that the shaft behaves as if it were undamaged when $\beta = 180°$. However, the proposed model predicts an appreciable $2\times$ amplitude when the rotor is decently balanced ($\eta = 6.31$) despite placing the unbalance mass at 180°, and therefore, the presence of the crack remains comprehensible. Since the amplitude of the $2\times$ and $3\times$ frequency components is typically used for the detection of cracks, the balancing procedure of rotors should aim for an unbalance angle between 0° and 90° in addition to reducing the weight-to-unbalance ratio.

Acknowledgments The support given by Dr. Keqin Xiao is greatly appreciated.

References

1. Sekhar, A., Prabhu, B.: Transient analysis of a cracked rotor passing through critical speed. J. Sound Vib. **173**(3), 415–421 (1994)
2. Bachschmid, N., Pennacchi, P., Tanzi, E.: Cracked Rotors: A Survey on Static and Dynamic Behaviour Including Modelling and Diagnosis. Springer, Berlin Heidelberg (2010)
3. Al-Shudeifat, M.A., Butcher, E.A.: New breathing functions for the transverse breathing crack of the cracked rotor system: approach for critical and subcritical harmonic analysis. J. Sound Vib. **330**(3), 526–544 (2011)
4. Rubio, L., Muñoz-Abella, B., Rubio, P., Montero, L.: Quasi-static numerical study of the breathing mechanism of an elliptical crack in an unbalanced rotating shaft. Lat. Am. J. Solids Struct. **11**(13), 2333–2350 (2014)
5. Spagnol, J.P., Wu, H., Xiao, K.: Dynamic response of a cracked rotor with an unbalance influenced breathing mechanism. J. Mech. Sci. Technol. **32**(1), 57–68 (2018)
6. Ishida, Y., Liu, J., Inoue, T., Kondo, H.: Detection of a rotor crack using nonstationary response (change of maximum amplitude in nonstationary vibration due to the direction of unbalance). Nippon Kikai Gakkai Ronbunshu C Hen. Trans. Jpn. Soc. Mech. Eng. **18**(2), 316–323 (2006)
7. Gasch, R.: A survey of the dynamic behaviour of a simple rotating shaft with a transverse crack. J. Sound Vib. **160**(2), 313–332 (1993)
8. Ishida, Y., Yamamoto, T.: Linear and Nonlinear Rotordynamics: A Modern Treatment with Applications. Wiley-VCH, Weinheim (2013)

Synchronous Blade Vibration Analysis Using Blade Tip Timing Method

Y. Oh, H. H. Yoo, and Y. Kim

1 Introduction

Blade tip timing (BTT) method analyzes the vibration characteristics of compressor and turbine blades using noncontact sensors. BTT sensors measure the time of arrivals (TOA) of each blade when it passes the sensors [1]. TOAs are converted to the blade tip displacements compared to the theoretical passing time had it not been any vibration in the system. BTT method requires a complicated signal processing algorithm because it generates a non-uniform undersampled signal, so the various studies for developing the BTT data processing methods have been recently carried out [2–5]. The vibration response that occurs in a blade-disk system is classified into two independent forms, synchronous and asynchronous [2]. Synchronous vibration is induced by an excitation frequency corresponding to a multiple of the rotating speed by an integer [3, 4], while asynchronous vibration is induced by an excitation frequency, mainly due to aerodynamic instability such as rotating stall and flutter [5], corresponding to a multiple of the rotating speed by non-integer.

There have been some studies on the vibration analysis methods for blade tip timing data. Dimitriadis [3] compared three analysis methods by applying and formulating the simulation data to the tip timing problem. All of the methods they compared satisfy the reliable accuracy with quite low noise. However, the results were highly dependent on the noise levels. Rigosi [4] modified the existing two parameter plot methods that extract vibration results from data obtained by at least two sensors.

Y. Oh · H. H. Yoo (✉)
Department of Mechanical Engineering, Hanyang University, Seoul, Republic of Korea
e-mail: hhyoo@hanyang.ac.kr

Y. Kim
Korea Electric Power Research Institute, Daejeon, Republic of Korea

S. Oberst et al. (eds.), *Vibration Engineering for a Sustainable Future*,
https://doi.org/10.1007/978-3-030-46466-0_19

In this study, a new algorithm which makes use of given blade tip timing data to characterize the synchronous blade vibration is provided. First, curve fitting of data in the target RPM section of each sensor and each blade is made by the curve defined according to single degree of freedom (SDOF) theory. This gives the instantaneous amplitude, the resonant frequency, the oscillation phase, and the Q factor of the individual blades at the peak point. The engine order is then estimated using the phase information obtained above. Theoretically, dividing the phase difference of each sensor by the sensor angle difference determines the engine order. However, for real signals, it is impossible to estimate the engine order in this way due to various circumstances. Lastly, the newly proposed engine order estimation method is carried out through this study. Even though each sensor observes the blades passing time at different locations, while they measure different phases, they are actually the same at the reference point. An integer value that minimizes the difference between phases at the reference point for each sensor determines the engine order estimate.

2 Blade Vibration Analysis Method

The proposed method consists of five major stages: acquisition of raw data measured by sensors fixed to the casing, deriving the timing data of the blades from the pulse data, deriving the dynamic or static displacement every moment of arrival, smoothing the displacement data, and identifying various vibration parameters reflecting the vibration characteristics of the blade-disc system. In this study, the identification methods of blade vibration parameters are proposed and applied. The proposed method performs curve fitting around the point where the vibration displacement is particularly large, that is, the point where resonance sweeping is assumed, in the smoothed blade tip displacement versus RPM diagram. Generally, it is desirable to select the 500RPM region around the RPM where the resonance sweeping occurs. The vibration characteristics of the blades can be obtained by the proposed model.

Figure 1 shows the bladetip timing measurement system. When the blades are rotating, they pass the static sensors attached to the case. Then the TOAs of all blades can be obtained from the sensors as shown in Fig. 2. The red lines indicate the real measured time with vibration, while the blue dot lines indicate the theoretical time without vibration. The theoretical TOAs can be defined by the following equation:

$$\tilde{T}_n = \frac{\sum_{k=1}^{N} T_k + \left(n - \frac{N+1}{2}\right)/\omega}{N} \tag{1}$$

where T_k is the measured TOAs, $N$is the number of blades, and ω is the rotor speed. The gap between two TOAs which determine how much the blades vibrate is converted to the tip displacement data. Then the displacement data is smoothed by applying the moving average and median filtering techniques. When the blade

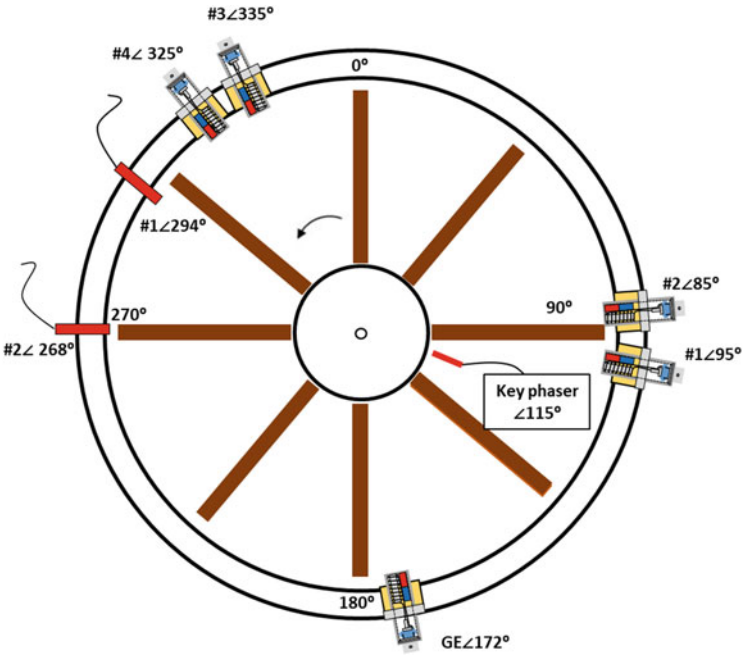

Fig. 1 Blade tip timing measurement system

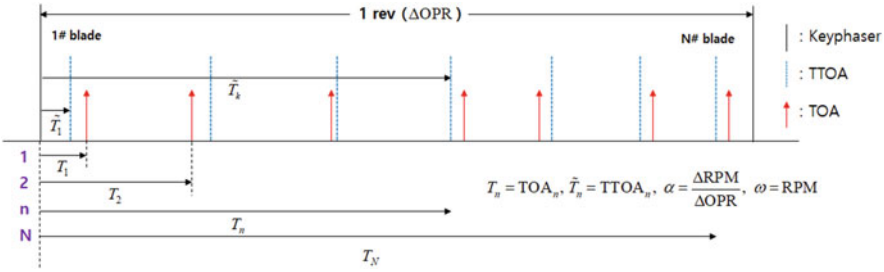

Fig. 2 Time of arrival data obtained from the sensors

resonates, the smoothed data around peak points is represented by fitting curve. The method follows the theory of nonlinear curve fitting. For nonlinear curve fitting, one needs to specify the initial values of each parameter. The fitting result is very sensitive depending on which value is specified as the initial value. The proposed method generates one analysis result for each sensor in the start section. Assuming that theoretically there is an infinite number of sensors, enveloping the measured data from them will have the same result as the actual time trend. When the data values of one sensor are connected based on the single degree of freedom (SDOF) theory, it becomes a curved shape, which is defined as the SDOF regression curve. The regression curve is a nonlinear regression curve with four parameters. In other

words, it is the core of this method to obtain the four fitting parameters when the blades resonate. Vibration amplitudes, phase angles, resonant rotor speeds, and damping factors are the main four parameters.

3 Numerical Results and Discussions

Figure 3 shows the results of fitting between proposed method and commercial software. The vibration data near resonance RPM measured by four eddy current sensors shows the same resonance RPM. It is clear that the results between the proposed method and commercial software have good agreement. The vibration parameters such as amplitude, phase, resonance RPM, and Q-factor are tabulated in Table 1. Only sensor #2 shows the quite low amplitude compared to the other sensors. It is presumed that the difference is due to an error in the gap measurement between the sensor and the blade. Differences between phase angles for sensors are so nature that they can be applied to determine the system engine order. Theoretically, the engine orders have the same value for each sensor, so the proposed method determines the estimated engine order when there is an integer value that minimizes the sum of the difference between the reference point phase values of the sensors for an integer value. We can determine the specific engine order by selecting the mode from the estimated values from all blades.

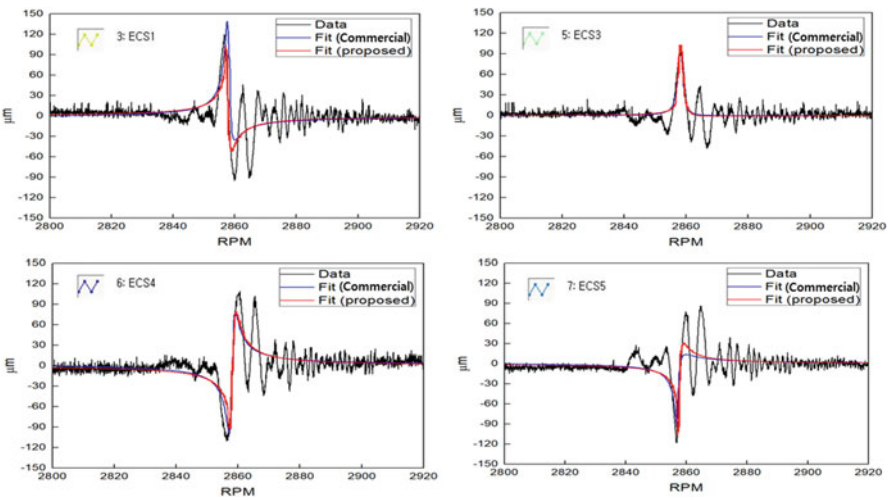

Fig. 3 Blade displacement and fitting curve

Table 1 Vibration parameters obtained by the proposed method

Sensors	Amplitude (μm)	Phase (deg)	Resonance (RPM)	Q-factor
#1	80.2	319	2855	995
#2	47.7	10	2855	1022
#3	85.2	107	2855	1046
#4	83.2	164	2855	1026

4 Conclusion

In this study, the synchronous vibration analysis method was developed based on the curve fitting theory. Nonlinear curve fitting based on single degree of freedom vibration model was applied to the measured tip timing data of rotating blades. The proposed method was validated by comparing the fitting graphs to those obtained by the commercial software. Various blade parameters such as the amplitude, the resonant frequency, the oscillation phase, and the Q factor of the individual blades were obtained at the peak point. The engine order was then estimated using the phase information obtained above. The proposed method can be applied to the vibration monitoring system.

References

1. Heath, S., Imregun, M.: An improved single-parameter tip-timing method for turbomachinery blade vibration measurements using optical laser probes. Int. J. Mech. Sci. **38**(10), 1047–1058 (1996)
2. Zielinski, M., Ziller, G.: Noncontact vibration measurements on compressor rotor blades. Meas. Sci. Technol. **11**, 847–856 (2000)
3. Dimitriadis, G., Carrington, I.B., Wright, J.R., Copper, J.E.: Blade-tip timing measurement of synchronous vibrations of rotating bladed assemblies. Mech. Syst. Signal Process. **16**(4), 599–622 (2002)
4. Liu, C., Jiang, D.: Improved blade tip timing in blade vibration monitoring with torsional vibration of the rotor. J. Phys. Conf. Ser. **364**, 012136 (2012)
5. Yue, L., Liu, H., Zang, C., Wang, D., Hu, W., Wang, L.: The parameter identification method of blade asynchronous vibration under sweep speed excitation. J. Phys. Conf. Ser. **744**, 012051 (2016)

Output Reachable Set Estimation for Singular Seat Suspension Systems

Wenxing Li, Haiping Du, Zhiguang Feng, Donghong Ning, and Weihua Li

1 Introduction

Seat suspensions play a very important role to improve the driving comfort for vehicle drivers [1]. Different spring stiffness and damping coefficients have different effects on the performance of seat suspensions. Therefore, how to choose appropriate seat suspension parameters is a worthy study topic for seat suspension designers.

The reachable set estimation aims to derive some closed bounded set of the states of dynamic systems from the origin by bounded input peak values [2]. During the past decades, a lot of studies about reachable set estimation have been investigated in different areas, such as the reachable set estimation [3] and the output reachable set estimation [4, 5].

In this paper, the singular seat suspension system is defined where the seat deflection, relative velocity, and the upper seat acceleration are defined as systems states. The deflection of the seat suspension and the acceleration of the upper seat suspension are defined as the system output because they have a close relationship with the seat suspension performance and are easily measured in practice [6]. Then, the singular seat suspension system is established, and the output reachable set is estimated.

W. Li (✉) · H. Du · D. Ning
School of Electrical, Computer and Telecommunications Engineering, University of Wollongong, Wollongong, NSW, Australia
e-mail: wl898@uowmail.edu.au

Z. Feng
College of Automation, Harbin Engineering University, Harbin, China

W. Li
School of Mechanical, Material, Mechatronic and Biomedical Engineering, University of Wollongong, Wollongong, NSW, Australia

S. Oberst et al. (eds.), *Vibration Engineering for a Sustainable Future*,
https://doi.org/10.1007/978-3-030-46466-0_20

Some simulation results are given to show the effectiveness of the proposed output reachable set estimation method. Different system parameters (drivers' masses, spring stiffness, and damping coefficients) have a great effect on the results of the output reachable set estimation. According to the output reachable set estimation and different requirements of different vehicle seat suspensions, seat suspension designers can choose proper seat suspension parameters, which can give them theoretical support to reduce the cost of the suspension design and test.

Notation The notation used throughout this paper is standard. $\mathbb{R}^n$ represents the n-dimensional Euclidean space. $P > 0$ denotes that P is a real symmetric and positive definite matrix; * represents the symmetric terms in a symmetric matrix; sym(A) means $A + A^T$; $\mathbb{R}_{\geq 0}$ denotes the fields of natural numbers; diag$\{\cdots\}$ stands for a block-diagonal matrix.

2 Singular Seat Suspension Model and the Output Reachable Set Estimation

As shown in Fig. 1, a simplified passive seat suspension model is given. Based on Newton's second law, the dynamic passive seat suspension model can be written as

$$m\ddot{z}_s + F_k + F_c = 0 \tag{1}$$

where $m \in [m_{\min}, m_{\max}]$ is the unsprung mass, which can be different values among different drivers; F_k and F_c are the forces of the spring and the damper of the seat suspension, respectively; z_s and z_v are the displacements of the upper suspension and the external excitation, respectively. F_k and F_c are nonlinear mostly, but to simplify the study problem, we assume the expressions of these two forces as follows:

$$F_k = f_k\left(z_s - z_v\right), F_c = f_c\left(\dot{z}_s - \dot{z}_v\right),$$

where f_k and f_c are the assumptive spring stiffness and damping coefficient, respectively, which may vary in some range.

Then, we define the state variables as follows:

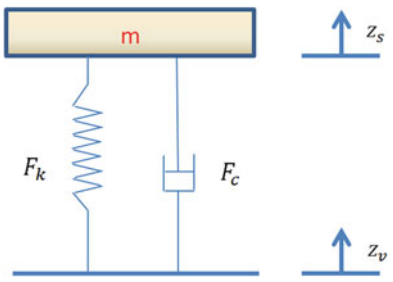

Fig. 1 Vibration model of the seat suspension system

$$x_1 = z_s - z_v, x_2 = \dot{z}_s - \dot{z}_v, x_3 = \ddot{z}_s,$$

where x_1 is the suspension deflection; x_2 is the relative seat velocity; x_3 is the acceleration of the upper suspension. Define the state vector as $x = [x_1 \ x_2 \ x_3]$ and $\ddot{z}_v$ is considered as the disturbance ω which satisfies

$$\omega^T(t)\omega(t) \leq \overline{\omega}^2 \tag{2}$$

where $\overline{\omega}$ is a real constant.

Then the dynamic equation of the seat suspension system can be described as

$$E\dot{x}(t) = Ax(t) + B\omega(t),$$

$$y(t) = Cx(t), \tag{3}$$

where

$$E = \begin{bmatrix} 1 & 0 & 0 \\ 0 & 1 & 0 \\ 0 & 0 & 0 \end{bmatrix}, A = \begin{bmatrix} 0 & 1 & 0 \\ 0 & 0 & 1 \\ f_k & f_c & m \end{bmatrix}, B = \begin{bmatrix} 0 \\ -1 \\ 0 \end{bmatrix}, C = \begin{bmatrix} 1 & 0 & 0 \\ 0 & 0 & 1 \end{bmatrix}.$$

The state of the singular seat suspension system is $x(t) \in \mathbb{R}^3$ and the initial condition x_0 belongs to a bounded ellipsoid

$$x_0 \in \mathcal{X}_0 \triangleq \mathcal{E}(\mathcal{R}_0) \tag{4}$$

and $y(t) \in \mathbb{R}^2$ is the output.

The output reachable set of the system (3) is defined as

$$\mathcal{R}_y \triangleq \left\{ y(t) \in \mathbb{R}^2 | \omega(t), x(t), y(t), x_0 \text{ satify (2), (3), (4)}, t \in \mathbb{R}_{\geq 0} \right\} \tag{5}$$

If the disturbance is not considered, the singular seat suspension system can be described as

$$E\dot{x}(t) = Ax(t) \tag{6}$$

Definition 1 [7]

1. The pair (E, A) is called to be regular if det $(sE - A)$ is not identically zero.
2. The pair (E, A) is called to be impulse free if deg (det$(sE - A)) =$ rank (E).
3. The pair (E, A) is called to be stable if all the roots of det $(sE - A)$ have negative real parts.
4. The singular system (6) is called to be regular, impulse free, and stable if the pair (E, A) is regular, impulse free, and stable.
5. The singular system (6) is called to be admissible if it is regular, impulse free, and stable.

Lemma 1 [3, 4] Define a Lyapunov function $V(x)$ for the system (3) satisfying $V(0) = 0$ and $V(x) > 0$. If there exists a scalar $\alpha > 0$, such that

$$\dot{V} + \alpha V \dot{x}(t) - \frac{\alpha}{\overline{\omega}^2} \omega^T(t)\omega(t) \leq 0, \tag{7}$$

$$V\ (x_0) \leq x_0^{\mathrm{T}} \mathcal{R}_0 x_0, \tag{8}$$

$$x^T(t) C^T \mathcal{R}_y C x(t) \leq V\ (x(t)) \tag{9}$$

then we can get the output reachable set $\mathcal{R}_{\mathrm{y}} \triangleq \mathcal{E}\left(\mathcal{R}_{\mathrm{y}}\right)$.

Theorem 1 Considering the singular seat suspension system (3) under disturbance condition (2) and initial state condition (4) for given conditions $\overline{\omega} > 0, \alpha > 0$, and $\mathcal{R}_0$, if there exist matrices P, $Q > 0$, U, $\mathcal{R}_y > 0$, F, and G with appropriate dimensions, such that

$$E^T P = P^T E \geq 0 \tag{10}$$

$$P^T A + A^T P < 0 \tag{11}$$

$$\Phi = \begin{bmatrix} \Phi_1 & \Phi_2 & F^T B \\ * & -\mathrm{sym}(G) & G^T B \\ * & * & -\frac{\alpha}{\overline{\omega}^2} I \end{bmatrix} < 0 \tag{12}$$

$$C^T \mathcal{R}_y C < Q < \mathcal{R}_0 \tag{13}$$

where $\Phi_1 = \alpha E^T Q E +$ sym $(F^T A)$, $\Phi_2 = (QE + E_0 U)^T - F^T + A^T G$, and E_0 is a full column rank matrix satisfying $E^T E_0 = 0$, then system (3) is admissible and the output reachable set can be obtained as $\mathcal{E}\left(\mathcal{R}_y\right)$.

Proof Firstly, we will prove the regularity and impulse free of the system (3). According to Definition 1, we have $\det(sE - A) = -ms^2 - f_c s - f_k$, which is not identically zero, so the system (3) is regular. Furthermore, because of $m \neq 0$, $\deg(\det(sE - A)) = \text{rank}(E) = 2$, so the system (3) is impulse free.

Then, to prove the stability of the system (3) and get the output reachable set, a Lyapunov function is constructed as

$$V_1(x(t)) = x^T(t)P^T Ex(t) \tag{14}$$

If the external disturbance is not considered, the derivative of $V_1(x(t))$ can be obtained as

$$\dot{V}_1(x(t)) = x^T(t)\left(P^T A + A^T P\right)x(t) \tag{15}$$

Based on inequalities (10) and (11), we can get $V_1(x(t)) \geq 0$ and $\dot{V}_1(x(t)) < 0$, so the system (3) is admissible.

Then, to obtain the output reachable set of the system (3), a new Lyapunov function is designed as $V_2(x(t)) = x^T(t)E^T QEx(t)$. The external disturbance is considered,and we can calculate the derivative $V_2(x(t))$ as

$$\dot{V}_2(x(t)) = 2\dot{x}^T(t)E^T(QE + E_0U)x(t). \tag{16}$$

By introducing two free weighting matrices F and G, we can get

$$2\left[x^T(t)F^T + (E\dot{x}(t))^T G^T\right][-E\dot{x}(t) + Ax(t) + B\omega(t)] \equiv 0. \tag{17}$$

We define a state vector as $\xi(t) = \left[x^T(t)\ (E\dot{x}(t))^T\ \omega^T(t)\right]^T$. Then, combining (16) and (17), we have

$$\dot{V}_2(x(t)) + \alpha V_2(x(t)) - \frac{\alpha}{\overline{\omega}^2}\omega^T(t)\omega(t) = \xi^T(t)\Phi\xi(t) < 0 \tag{18}$$

Based on Lemma 1, inequalities (12), (13), and (18), we can get the output reachable set of the system (3) as $\mathcal{E}\left(\mathcal{R}_y\right)$.

3 Simulation Results and Analysis

Some simulation results are given in this section to show the effectiveness of the proposed method to estimate the output reachable set of the singular seat suspension system. The values of the upper-bounded disturbance $\overline{\omega}$, scalar α, and the bounded ellipsoid matrix $\mathcal{R}_0$ are set as $\overline{\omega} = \sqrt{2}$, $\alpha = 0.2$, and $\mathcal{R}_0 = \text{diag}\{50, 6, 0.1\}$.

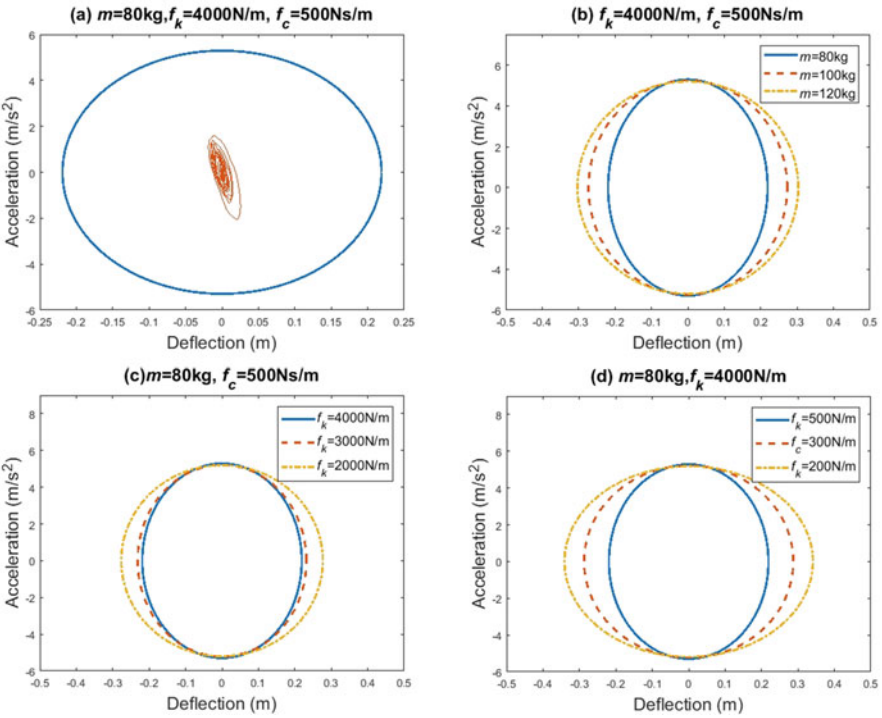

Fig. 2 (**a**) The output reachable set and the system output performance for a random disturbance; (**b**) the different reachable sets for different unsprung masses; (**c**) the different output reachable sets for different spring stiffness; (**d**) the different output reachable set for different damping coefficients

Figure 2 shows the different output reachable set estimation performance for different situations. The blue ellipsoid in (a) is the output reachable set for seat suspension system ($m = 80\text{kg}, f_k = 4000\text{N/m}, f_c = 500\text{Ns/m}$), and inside red curve is the simulated system output performance for a random disturbance, where we can see that the system output is bounded in the output reachable set. Figures (b)–(d) show the different output reachable sets when we only change one of the three parameters (unsprung mass for (b), spring stiffness for (c), and damping coefficient for (d)). Here, we can find that the output reachable set gets smaller when the unsprung mass gets smaller and the spring stiffness or damping coefficients get larger. Therefore, when engineers design seat suspensions for different vehicles, the proposed method can help them to choose springs and dampers within a reasonable parameter range for seat suspensions according to different designing requirements.

4 Conclusion

In this paper, the output reachable set estimation problem for singular seat suspension systems is studied. With the help of two Lyapunov functions, the singular seat suspension system is proved to be admissible, and the output reachable set can be bounded by a set of bounding ellipsoids. Simulation results show the influence of different parameters on the output reachable set estimations, which is helpful for seat suspension designers to choose appropriate parameters according to different requirements of different vehicle seat suspensions. Designing a method to combine the different reachable set estimations of different parameters to meet some certain requirements will be our future work.

References

1. Deng, H., et al.: Design and verification of a seat suspension with variable stiffness and damping. Smart Mater. Struct. **28**(6), 065015 (2019)
2. Liu, G., et al.: New insight into reachable set estimation for uncertain singular time-delay systems. Appl. Math. Comput. **320**, 769–780 (2018)
3. Feng, Z., Lam, J.: On reachable set estimation of singular systems. Automatica. **52**, 146–153 (2015)
4. Xiang, W., Tran, H.-D., Johnson, T.T.: Output reachable set estimation for switched linear systems and its application in safety verification. IEEE Trans. Autom. Control. **62**(10), 5380–5387 (2017)
5. Xiang, W., Tran, H.-D., Johnson, T.T.: Output reachable set estimation and verification for multilayer neural networks. IEEE Trans. Neural Netw. Learn. Syst. **29**(11), 5777–5783 (2018)
6. Ning, D., et al.: Vibration reduction of seat suspension using observer based terminal sliding mode control with acceleration data fusion. Mechatronics. **44**, 71–83 (2017)
7. Xu, S., Lam, J.: Robust Control and Filtering of Singular Systems, vol. 332. Springer (2006)

Transient Simulation of a Rotor Supported in Partially Filled Herringbone Grooved Journal Bearings Using the Narrow Groove Theory: Boundary Conditions

Steffen Nitzschke, Elmar Woschke, Christian Daniel, and Thorsten Sporbeck

1 Introduction

A HGJB is a special case of journal bearing with groove-ridge pairs in the surface, which are arranged in a herringbone pattern. Additionally to the circumferential fluid transport of a plain journal bearing this configuration causes a fluid transport towards the bearings centerline.

This kind of bearing is mainly used in hard disk and optical drives (CD, DVD) [1] and for miniature fan motors [2]. Furthermore they are applied in medical devices, e.g., as support of the rotating anode inside an X-ray tube [3], because the bearings are able to run without external fluid supply [4]. This is necessary, because due to thermal reasons liquid metal serves as bearing fluid here. For rotor dynamic research of such a rotating anode, the transient bearing forces and, thus, the pressure distribution in the fluid film have to be known. For this sake, in case of plain bearings, usually the Reynolds partial differential equation (R-PDE) is solved numerically via finite difference- [5, 6], finite volume- [1], or finite element method [7, 8]. These can here also be utilized, but this leads due to the groove-ridge pairs necessarily to a fine mesh with a high number of unknowns and a large computational effort.

Another approach is given by the NGT, which enables a possibility to calculate a mean pressure over a groove-ridge pair if a sufficient number of such pairs exists [9, 10]. Therefore, the R-PDE can be reformulated in terms of the averaged pressure, which afterward has also to be solved numerically, but on a considerable coarser

S. Nitzschke (✉) · E. Woschke · C. Daniel
Otto von Guericke University, Magdeburg, Germany
e-mail: steffen.nitzschke@ovgu.de; elmar.woschke@ovgu.de; christian.daniel@ovgu.de

T. Sporbeck
Siemens Healthcare GmbH, Erlangen, Germany
e-mail: thorsten.sporbeck@siemens-healthineers.com

S. Oberst et al. (eds.), *Vibration Engineering for a Sustainable Future*,
https://doi.org/10.1007/978-3-030-46466-0_21

mesh. Subsequently, this approach can be integrated as an online method into a transient rotordynamic simulation in order to calculate bearing forces as well as torques [11]. If additionally cavitational effects are taken into account, e.g., via the regularized Elrod algorithm [12, 13], the film fraction can be investigated.

2 Narrow Groove Theory and Equations of Motion

Since for rotor dynamics the bearing forces are of interest more than the local pressure p, which is varying over a groove ridge pair, it is convenient to introduce

$$p_0 = \lim_{\bar{b}\to 0} \frac{1}{\bar{b}} \int_{-\bar{b}/2}^{+\bar{b}/2} p \, \mathrm{d}\zeta \qquad \text{with} \quad b = b_r + b_g \tag{1}$$

as the pressure averaged over a groove-ridge pair. Following the approach from [10], p_0 can be determined directly from a modified R-PDE taking into account the groove geometry, which is described by the functions A, B, C and F, G depending on the local film height $h_r(\varphi, s, t)$, cf. Fig. 1. Considering partial filling in the gap can be handled, e.g., using the Elrod algorithm, which is demonstrated in [11]. Finally, the R-PDE reads

$$\begin{aligned} &\frac{\partial}{\partial\varphi}\left(\frac{(\Delta R)^3}{12\eta_{liq}}\left(\frac{A}{r}\frac{\partial p_0}{\partial\varphi} + B\frac{\partial p_0}{\partial s}\right) - \frac{1}{2}\vartheta\,\omega\, r\,\Delta R\, F\right) + \\ &r\frac{\partial}{\partial s}\left(\frac{(\Delta R)^3}{12\eta_{liq}}\left(\frac{B}{r}\frac{\partial p_0}{\partial\varphi} + C\frac{\partial p_0}{\partial s}\right) - \frac{1}{2}\vartheta\,\omega\, r\,\Delta R\, G\right) = r\,\frac{\partial(\vartheta\, h_r)}{\partial t} \end{aligned} \tag{2}$$

with the complementary unknowns avg. pressure p_0 and film fraction ϑ: In regions where $p_0 > p_{\mathrm{cav}}$, the gap is completely filled, which is equivalent to $\vartheta = 1$; otherwise $p_0 = p_{\mathrm{cav}}$ holds and the film fraction varies $0 < \vartheta < 1$.

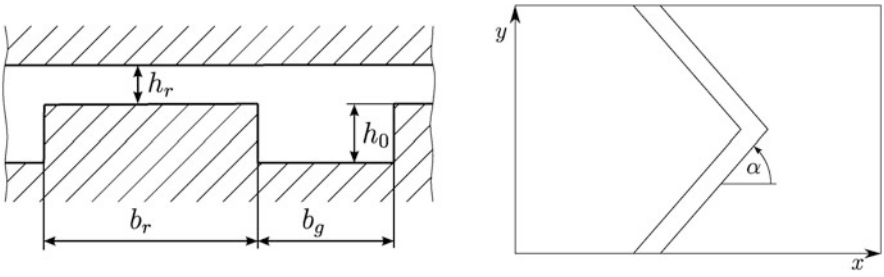

Fig. 1 Geometry of herringbone profile: Definition of groove-ridge pair (left) and orientation angle (right) [11]

Equation (2) builds together with an appropriate set of boundary conditions an initial boundary value problem with elliptical character, which has due to the partial derivatives no closed analytical solution. Hence, a numerical method like the finite volume method according to [14] is used to derive a system of equations for the complementary unknowns. For this sake, the fluid film is discretized with a 2-D mesh in circumferential and axial direction with a number of volumes n. Due to the mixed derivatives, a nine-point stencil results from the discretization procedure. In the pressure region, central differences are suitable, while in the cavitation region upwinding is necessary, which leads to backward differences there. Finally, a nonlinear system of n equations

$$\underline{\underline{A}}(\underline{u})\,\underline{u} = \underline{r} \tag{3}$$

for the n complementary unknowns, gathered in vector $\underline{u}$, results. Details concerning the nonlinearity and how the obtain a fast and reliable solution are given in [12, 13]. Additionally the validation of the procedure (including NGT) against literature is documented in [11].

3 Boundary Conditions

Initially the fluid film is assumed to be fully filled (film fraction is 100%), but during operation some amount of fluid is squeezed out of the film. In order to study the behavior of the rotor-bearing system with partially filled films, the axial boundary conditions (AXBC) have to be revised. It is only allowed, that fluid is *leaving* the bearing at ambient pressure p_{amb}, which can only occur in pressure regions

$$p_0\Big|_{s=\pm b/2} = p_{\mathrm{amb}} \quad \text{if} \quad q_{\mathrm{amb}} > 0\,. \tag{4}$$

Reentering of fluid in cavitation regions is not permitted, leading to

$$\frac{\partial \vartheta}{\partial s}\Big|_{s=\pm b/2} = 0 \qquad \text{if} \qquad \vartheta < 1\,, \tag{5}$$

where s denotes the axial direction. Since the cavitation region is not known a priori, it has to be determined using the Elrod algorithm in an iterative process. Hence, one of the above equations has to be chosen accordingly. During the iteration it may occur that the Dirichlet condition Eq. (4) is applied in the cavitation region, which would lead to a volume flow q_{amb} entering the bearing. Then, the AXBC has locally to be switched to Eq. (5). On the opposite, this condition applied in the pressure region leads to boundary pressures $p_0 > 0$, which means, that fluid is prevented from leaving the bearing. In this case, the AXBC has to be switched back to Eq. (4). The final solution shows a converged apportionment concerning both regions and the appropriate AXBC.

4 Transient Solution Process

Finally, the procedure is embedded into a time integration scheme, which solves the rotor-bearing-system's equation of motion (EQM) and the transient part of the R-PDE. Without limitation to the generality, the EQM may be written as

$$\underline{\underline{M}}\,\underline{\ddot{x}} + \underline{h}_{\omega}(\underline{\dot{x}}, \underline{x}) + \underline{h}_{\mathrm{el}}(\underline{\dot{x}}, \underline{x}) + \underline{f}_{\mathrm{bearing}}(\underline{\dot{x}}, \underline{x}) = \underline{f}_{\mathrm{ext}}(t)\,, \tag{6}$$

wherein $\underline{\underline{M}}$ denotes the rotor's mass matrix. The vectors $\underline{h}_{\omega}$ and $\underline{h}_{\mathrm{el}}$ represent the gyroscopic, centrifugal as well as the corriolis forces and the elastic forces of the shaft, respectively. Starting from initial conditions $(\underline{\dot{x}}, \underline{x})\big|_{t=0}$, Eq. (6) is used to calculate the current accelerations $\underline{\ddot{x}}$, which are then integrated w.r.t. time by an appropriate ODE solver.

During the time integration process, the transient part of Eq. (2)

$$\frac{\partial(\vartheta\, h_r)}{\partial t} = \vartheta\, \frac{\partial h_r}{\partial t} + h_r\, \frac{\partial \vartheta}{\partial t} = \vartheta\, \dot{h}_r + h_r\, \frac{\partial \vartheta}{\partial t} \tag{7}$$

has to be considered. While $\dot{h}_r$ is directly linked to the rotor's translational velocity, the transient development of the film fraction needs to be discretized w.r.t. time, e.g., by a backward difference

$$h_r\, \frac{\partial \vartheta}{\partial t} = h_r\Big|_t\, \frac{\vartheta_t - \vartheta_{t-\Delta t}}{\Delta t} \tag{8}$$

for each finite volume i. The FVM process requires the integration of Eq. (8), which on the 2d grid with mesh size $\Delta\varphi \times \Delta s$ results in

$$\iint\limits_{\Omega_i} h_r\, \frac{\partial \vartheta}{\partial t} r\, d\varphi ds = h_r\Big|_t\, \frac{r\,\Delta\varphi\Delta s}{\Delta t}\, \vartheta_t - h_r\Big|_t\, \frac{r\,\Delta\varphi\Delta s}{\Delta t}\, \vartheta_{t-\Delta t}\,. \tag{9}$$

While the last term enters in the right-hand side $\underline{r}$ of Eq. (3), the first one applies to the diagonal of $\underline{\underline{A}}$. Since Δt is a rather small value, Eq. (9) serves as a kind of penalty formulation between the current and the past film fraction, which avoids its timeless change. Furthermore, this relation ensures the positive definiteness of $\underline{\underline{A}}$, which allows a unique solution, even if no explicit fluid supply is present, which is usually the case in HGJBs, cf (Fig. 2).

5 Application and Conclusion

The rotor described in Table 1 was investigated for different initial film fraction values ($\vartheta_{\mathrm{init}} = 99\%, 90\%, 80\%, 60\%$) under gravity and unbalance. The rotor starts at the bearing center and after some time finds a stationary orbit, cf. Fig. 3 left.

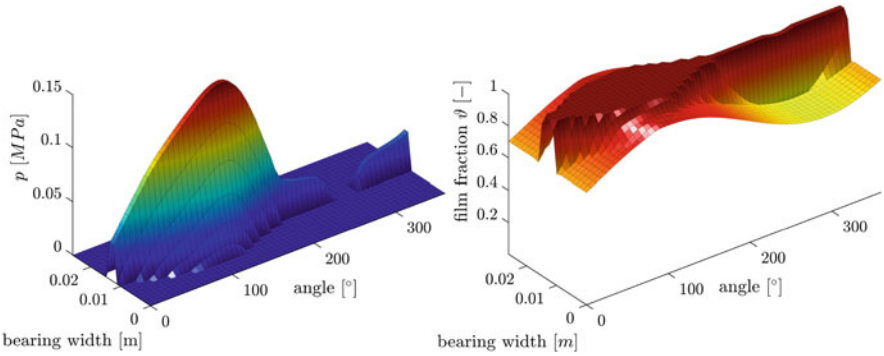

Fig. 2 Pressure distribution (left) and film fraction (right) in a partial filled HGJB (initial film fraction 80%) calculated with NGT

Table 1 Parameters of rotor and bearing

Parameter	Value	Unit	Parameter	Value	Unit	Parameter	Value	Unit
B	0,026	$[m]$	$r_{\text{unbalance}}$	0.0001	$[m]$	$\Delta R/R$	0.001	$[-]$
D	0,024	$[m]$	ω	500	$[rad/s]$	$h_0/\Delta R$	1.166	$[-]$
m_{rotor}	5	$[kg]$	g_y	−9,81	$[m/s^2]$	η	0,0015	$[Pa\,s]$

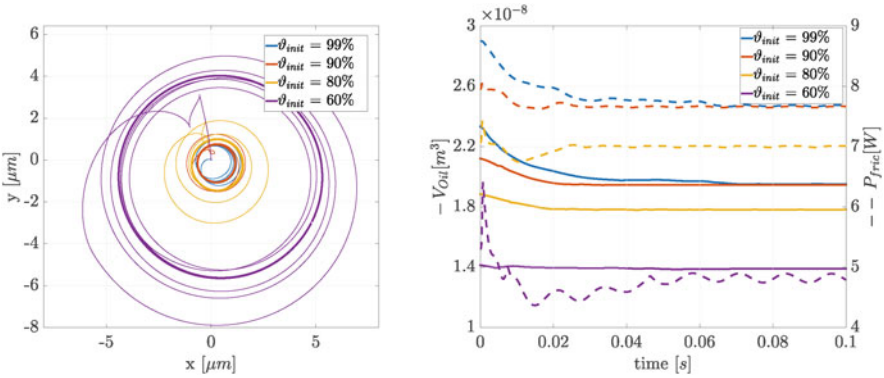

Fig. 3 Rotor orbit (left) and fluid volume in gap (right, solid) as well as friction power (right, dashed) for different initial values of film fraction. Distribution of pressure and film fraction is shown in Fig. 2 for $\vartheta_{\text{init}} = 80\%$

Due to the rotor motion, redundant fluid is squeezed out of the bearing until the orbit becomes stationary, cf. Fig. 3 right. As expected, the orbit size increases with decreasing initial film fraction. Subsequently, the question how much the bearing has initially to be filled can be investigated, if different initial conditions of film fraction are compared concerning rotor amplitude, minimal film width, power loss, heat transfer capacity, etc.

Acknowledgments The results were partially generated in the framework of the project WO 2085/2 "Numerische Analyse des transienten Verhaltens dynamisch belasteter Rotorsysteme in Gleit- und Schwimmbuchsenlagern unter Berücksichtigung kavitativer Effekte," which is supported by the DFG (Deutsche Forschungsgemeinschaft/German Research Foundation). This support is gratefully acknowledged.

References

1. Jang, G.H., Chang, D.I.: Analysis of a hydrodynamic herringbone grooved journal bearing considering cavitation. J. Tribol **122**, 103–109 (2000). https://doi.org/10.1115/1.555333
2. Chen, C.Y., Liu, C.S., Li, Y.C.: Design and characterization of miniature fluid dynamic bearing using novel multi-step elliptical grooves. Microsyst. Technol. **21**(1), 91 (2015). https://doi.org/10.1007/s00542-013-2023-5
3. Dössel, O.: Bildgebende Verfahren in der Medizin. Springer Vieweg, Berlin/Heidelberg (2016). https://doi.org/10.1007/978-3-642-54407-1
4. Muijderman, E.A.: Fettgeschmierte Spiralrillenlager – neue hydrodynamische Gleitlager. In: Bartz, W.J. (ed.) Selbstschmierende und wartungsfreie Gleitlager, pp. 86–133. Expert Verlag, Ehningen bei Böblingen (1993)
5. Lee, T.S., Liu, Y.G., Winoto, S.H.: Analysis of liquid-lubricated herringbone grooved journal bearings. Int. J. Numer. Methods Heat Fluid Flow **14**(3), 341–365 (2004). https://doi.org/10.1108/09615530410517995
6. Chao, P., Huang, J.: Calculating rotordynamic coefficients of a ferrofluid-lubricated and herringbone-grooved journal bearing via finite difference analysis. Tribol. Lett. **19**(2), 99 (2005). https://doi.org/10.1007/s11249-005-5087-2
7. Bonneau, D., Absi, J.: Analysis of aerodynamic journal bearings with small number of herringbone grooves by finite element method. J. Tribol. **116**, 698–704 (1994). https://doi.org/10.1115/1.2927320
8. Zirkelback, N., San Andrés, L.: Finite element analysis of herringbone grooved journal bearings: a parametric study. J. Tribol. **120**, 234–240 (1998). https://doi.org/10.1115/1.2834415
9. Hirs, G.G.: The load capacity and stability characteristics of hydrodynamic grooved journal bearings. ASLE Trans. **8**, 296–305 (1965). https://doi.org/10.1080/05698196508972102
10. Bootsma, J.: Liquid-lubricated spiral-groove bearings. Ph.D. thesis, Technische Hogeschool Delft (1975)
11. Nitzschke, S., Woschke, E., Daniel, C., Sporbeck, T.: Transient simulation of a rotor supported in partially filled herringbone grooved journal bearings using the narrow groove theory. In: Santos, I. (ed.) Proceedings of the 13th International Conference Dynamics of Rotating Machinery – SIRM, Copenhagen (2019). ISBN 978-87-7475-568-5
12. Nitzschke, S., Woschke, E., Schmicker, D., Strackeljan, J.: Regularised cavitation algorithm for use in transient rotordynamic analysis. Int. J. Mech. Sci. **113**, 175–183 (2016). https://doi.org/10.1016/j.ijmecsci.2016.04.021
13. Nitzschke, S., Woschke, E., Daniel, C.: Application of regularised cavitation algorithm for transient analysis of rotors supported in floating ring bearings. In: Cavalca, K.L., Weber, H.I. (eds.) Proceedings of the 10th ICoVP – IFToMM, pp. 371–387. Springer (2019). https://doi.org/10.1007/978-3-319-99272-3_26
14. Patankar, S.: Numerical Heat Transfer and Fluid Flow. Hemisphere Publishing Corp. (1980). https://doi.org/10.1201/9781482234213

Suppression of Friction-Induced Vibration in Rotary Sliding System Using Lateral Spin Sliding

Chiharu Tadokoro, Yuto Aso, Takuo Nagamine, and Ken Nakano

1 Introduction

Friction-induced vibration is a self-excited vibration that arises due to the instability of system around the equilibrium point of a sliding system owing to the velocity-weakening properties of the frictional force. In case of rotary sliding systems, such as the brake and clutch of an automobile, the friction-induced vibration could lead to serious issues that reduce the mechanical performances and user's comfort.

The friction-induced vibration can be reduced by enhancing the frictional properties of the sliding system through modification of the sliding components such as material, surface roughness, and lubricant. Recently, Kado et al. proposed that a "yaw angle misalignment (YAM)" between the direction of the drive and the driven translational motions in a translational sliding system generates a positive damping effect to stabilize the sliding system without any additional damping mechanism [1, 2]. This was proposed on the basis of the structural design of the translational sliding system. Tadokoro et al. demonstrated that the YAM method can be applied to a rotary sliding system using a parallel misalignment between the drive and the driven rotational axes [3].

This study aims to determine the effectiveness of the lateral spin sliding method to prevent the friction-induced vibration as an alternative to application of YAM to a rotary sliding system.

C. Tadokoro (✉) · Y. Aso · T. Nagamine
Saitama University, Saitama, Japan
e-mail: Tadokoro@mail.saitama-u.ac.jp

K. Nakano
Yokohama National University, Yokohama, Japan

S. Oberst et al. (eds.), *Vibration Engineering for a Sustainable Future*,
https://doi.org/10.1007/978-3-030-46466-0_22

2 Principle

Figure 1 shows the model that describes the principle for suppressing friction-induced vibration using a lateral spin sliding in a rotary sliding system. The model consists of a drive part (lower side in the side view) and a driven part (upper side in the side view). In the drive part, a rigid disc is rotated at a constant angular velocity. In the driven part, a rigid ball (mass: m) is supported by a linear spring (stiffness: k) attached to a stationary rigid wall. The ball contacts the disc under a constant normal load. Let x be the displacement of the ball from the origin. The direction of x corresponds to the tangential direction of the rotation of the disc. The ball is rotated about the x axis. The rotation of the ball is termed as the lateral spin. The sliding velocity, V, is the relative velocity between the velocities, V_{drive} and V_{spin}, of the disc and the ball at the contact position. The lateral spin velocity, V_{spin}, generates a yaw angle misalignment, φ, between the sliding velocity, V, and the ball's translational velocity, $\dot{x}$. The relative velocity, V_{rel}, between them is as follows:

$$V_{\text{rel}} = V - \dot{x} \tag{1}$$

$$\varphi = \tan^{-1} \frac{V_{\text{spin}}}{V_{\text{drive}}} \tag{2}$$

where ($\dot{}$) is the time derivative. The equation of motion of the ball is written as

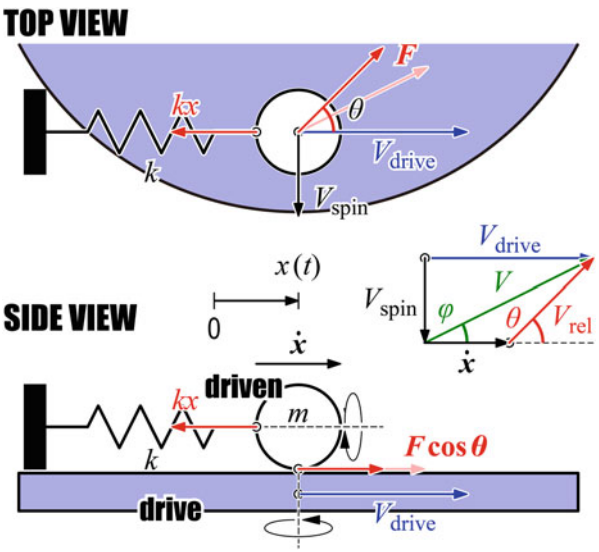

Fig. 1 Theoretical model of rotary sliding system with lateral spin sliding

$$m\ddot{x} + kx = F\left(V_{\text{rel}}\right)\cos\theta \tag{3}$$

$$V_{\text{rel}} = \sqrt{V^2 - 2V\dot{x}\cos\varphi + \dot{x}^2} \tag{4}$$

$$\cos\theta = \frac{V\cos\varphi - \dot{x}}{V_{\text{rel}}} \tag{5}$$

where θ is the direction of V_{rel} from the x axis. Linearizing these equations around $V_{\text{rel}} = V$, we obtain the following equation:

$$m\ddot{x} + (c_1 + c_2)\,\dot{x} + kx = F(V)\cos\varphi \tag{6}$$

The two coefficients, c_1 and c_2, in the second term on the left-hand side of this equation are the effective damping coefficients arising from the friction force, defined as

$$c_1 = F'(V)\cos^2\varphi \tag{7}$$

$$c_2 = \frac{F(V)\sin^2\varphi}{V} \tag{8}$$

When the slope $F(V)$ is negative, c_1 is also negative, which gives a negative damping that causes friction-induced vibration. On the other hand, the additional coefficient, c_2, is always positive, which gives a positive damping that suppresses friction-induced vibration. When V_{spin} is large, φ becomes large and the friction-induced vibration can be suppressed.

3 Details of Experiment

Figure 2 depicts the experimental apparatus, which involves a point contact between the stainless-steel roller (diameter: 50 mm, thickness: 10 mm, and radius of curvature: 5 mm) and the phenol-resin disc (diameter: 120 mm and thickness: 20 mm). The roller and the disc were rotated independently using the stepping motors A and B. The direction of the sliding velocity of the roller, V_{spin}, was orthogonal to the direction of the sliding velocity of the disc at the point contact, V_{drive}. The roller and the stepping motor (B) were placed on a plate, which was supported by parallel leaf springs. The deformation direction of the parallel leaf springs corresponds to the tangential direction of the rotation of the disc. The normal load, W, was applied using dead weight. During the experiment, when the disc was rotated at $V_{\text{drive}} = 50$–300 mm/s and $W = 30$ N, the deformation, X, of the parallel leaf springs was measured using a displacement sensor.

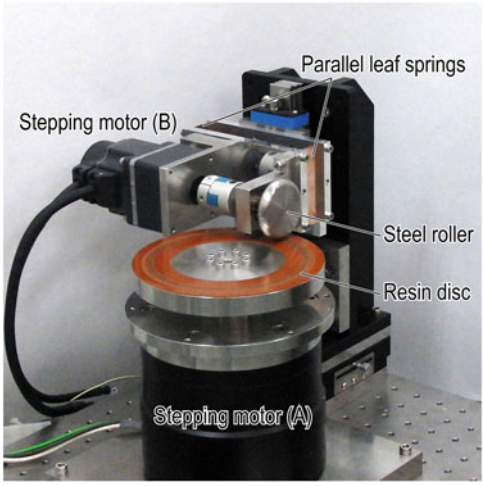

Fig. 2 Photograph of experimental apparatus

4 Results and Discussion

Figure 3 illustrates the result of displacement measurements that depict the effect of the lateral spin sliding on the friction-induced vibration. When the roller was not rotating ($V_{\text{spin}} = 0$ mm/s), it lead to the generation of friction-induced vibration. The amplitude of the vibration was 1 mm, and the frequency of the vibration was 28 Hz, which is equivalent to the natural frequency of the roller unit, i.e., 29 Hz. It was observed that when V_{spin} was increased, the amplitude of the vibration decreased. Over $V_{\text{spin}} = 200$ mm/s, the friction-induced vibration disappeared completely. Hence, it was found that application of lateral spin sliding to the sliding contact suppresses friction-induced vibration.

5 Conclusion

Friction test was conducted using a homemade apparatus to demonstrate the effectiveness of lateral spin sliding method on decreasing the friction-induced vibration. It was observed that when the velocity of the lateral spin sliding was sufficiently high, the friction-induced vibration was completely suppressed. The experimental results show that the lateral spin sliding provides a positive-damping effect in the rotary sliding system.

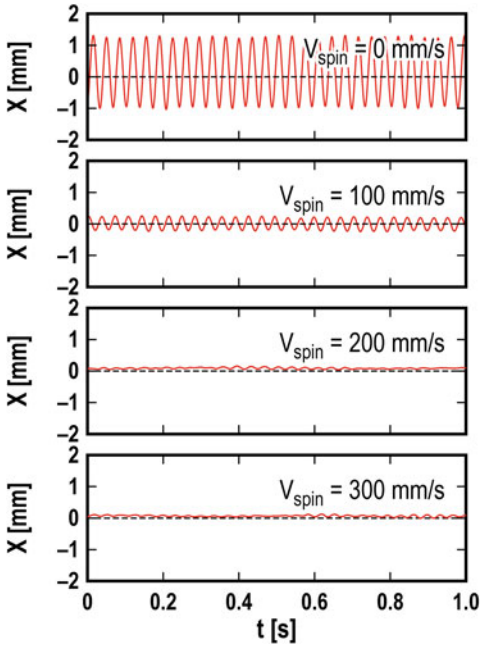

Fig. 3 Temporal changes in X ($V_{\text{drive}} = 200$ mm/s)

References

1. Kado, N., Tadokoro, C., Nakano, K.: Measurement error of kinetic friction coefficient generated by frictional vibration. Trans. J. Soc. Mech. Eng. Part C. **79**, 2635–2643 (2013)
2. Kado, N., Tadokoro, C., Nakano, K.: Kinetic friction coefficient measured in tribotesting: influence of frictional vibration. Tribol. Online. **9**(2), 63–70 (2014)
3. Tadokoro, C., Nagamine, T., Nakano, K.: Stabilizing effect arising from parallel misalignment in circular sliding contact. Tribol. Int. **120**, 16–22 (2018)

Experimental Estimation of Friction Characteristic of Annular Plain Seal

K. Ura, T. Inoue, and S. Yabui

1 Introduction

Hir's bulk flow analysis [1, 2] has been used to analyze the rotor dynamic (RD) fluid force acting on the seal. Recently, Yamada et al. [3] extended the analytical capacity of the static eccentricity. Blasius model [1, 2] is widely used for a friction factor of shear stress in bulk flow analysis. The friction coefficients in this model have been generally determined experimentally. Yamada's experimentally estimated coefficients [4] are well known and often used. Iwatsubo [5] derived different friction coefficients experimentally. Childs [6] estimated the friction coefficient of the stator wall experimentally using the Yamada's friction coefficients [4] for rotor wall. Arghir [7] estimated four friction coefficients by experiment and analysis. San Andres [8] obtained four friction coefficients using computational fluid dynamics (CFD). There are other important literatures on the influence of elasto-hydrodynamic conditions. In these previous researches, the friction coefficients are determined as constant values which are uniquely determined by the structure of the machine, but these values were different from each other. In this paper, friction coefficients of Blasius model in annular plain seal are estimated by experiment, and their characteristics are investigated. Seal surfaces were assumed to be smooth. In both steady and unsteady conditions, friction coefficients were estimated not in a form of constant values but as values which hold functional relationship. This functional expression representation could explain the conventionally obtained various friction coefficients in the literature.

K. Ura · T. Inoue (✉) · S. Yabui
School of Mechanical Engineering, Nagoya University, Nagoya, Aichi, Japan
e-mail: ura.kentaro@d.mbox.nagoya-u.ac.jp; inoue.tsuyoshi@nagoya-u.jp; yabui@nuem.nagoya-u.ac.jp

S. Oberst et al. (eds.), *Vibration Engineering for a Sustainable Future*,
https://doi.org/10.1007/978-3-030-46466-0_23

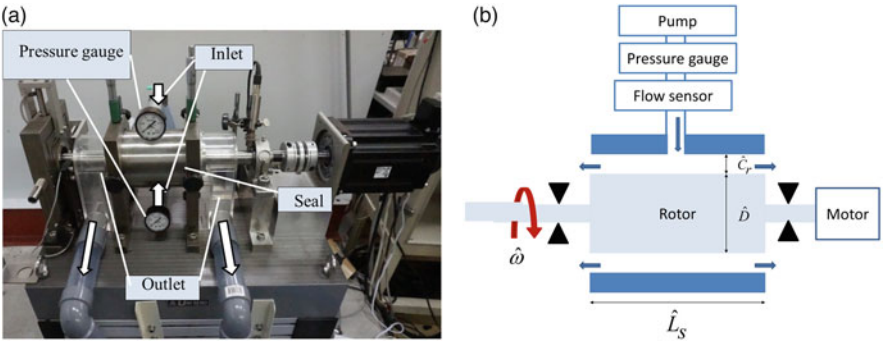

Fig. 1 Experimental system. (**a**) Experimental apparatus. (**b**) Rotor and fluid flow in experiment

2 Experiment

Figure 1 shows the experimental setup used in this paper. In the experiment, shaft's rotational speed and inlet pressure were set as the operating condition and measured. The used fluid was water, and the flow rate at seal inlet was measured and recorded as the result for the condition. A total 535 cases of experiments were conducted.

For the unsteady-state case, Kanki's experimental results [9] were used. Static eccentricity was $\hat{q}_s = 0.05454$ mm, and the following 10 coefficients were used as reference:

$$RD_{\mathrm{exp}eriment}{}^{\mathrm{T}} = \left[\begin{array}{cccccccccc} \hat{M}_{xx} & \hat{M}_{yy} & \hat{C}_{xx} & \hat{C}_{yy} & \hat{C}_{xy} & \hat{C}_{yx} & \hat{K}_{xx} & \hat{K}_{yy} & \hat{K}_{xy} & \hat{K}_{yx} \end{array} \right] \tag{1}$$

$$-\left\{ \begin{array}{c} \hat{F}_x \\ \hat{F}_y \end{array} \right\} = \left[\begin{array}{cc} \hat{M}_{xx} & 0 \\ 0 & \hat{M}_{yy} \end{array} \right] \left\{ \begin{array}{c} \ddot{\hat{x}} \\ \ddot{\hat{y}} \end{array} \right\} + \left[\begin{array}{cc} \hat{C}_{xx} & \hat{C}_{xy} \\ \hat{C}_{yx} & \hat{C}_{yy} \end{array} \right] \left\{ \begin{array}{c} \dot{\hat{x}} \\ \dot{\hat{y}} \end{array} \right\} + \left[\begin{array}{cc} \hat{K}_{xx} & \hat{K}_{xy} \\ \hat{K}_{yx} & \hat{K}_{yy} \end{array} \right] \left\{ \begin{array}{c} \hat{x} \\ \hat{y} \end{array} \right\} \tag{2}$$

Experiment conditions of this paper and Kanki's data [9] are shown in Table 1. $\hat{L}_s$ is seal length, $\hat{D}$ is shaft diameter, $\hat{C}_r$ is clearance, $\hat{\omega}$ is rotational speed, $\hat{P}_{in}$ is inlet pressure, and $\hat{q}_s$ is static eccentricity. Experimental result in concentric steady state is shown in Fig. 2. Rotational speed $\hat{\omega}$ and inlet pressure $\hat{P}_{in}$ are on the horizontal axes, and flow rate $\hat{Q}$ is on the vertical axis. Result shows that flow rate depends on the inlet pressure strongly, but hardly depends on the rotational speed.

3 Theoretical Analysis

3.1 Governing Equations in Bulk Flow Model

Governing equation of annular plain seal is shown in Eqs. (3), (4), and (5):

Table 1 Conditions of experiment

	Steady state	Unsteady state (Kanki [9])
$\hat{L}_s$	70 mm	200 mm
$\hat{D}$	70 mm	200 mm
$\hat{C}_r$	0.2 mm	0.5 mm
$\hat{\omega}$	300 rpm ~ 200 rpm (7 cases)	2000 rpm
$\hat{P}_{in}$	0.02 MPa ~ 0.2 MPa (30 cases)	0.98 MPa
$\hat{q}_s$	0	0.05454 mm

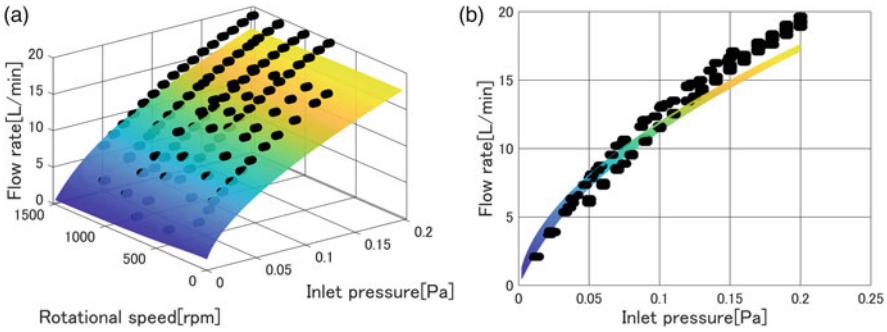

Fig. 2 Comparison of analytical and experimental results (steady state). (**a**) Flow rate vs operational condition. (**b**) Flow rate vs Inlet pressure

$$\frac{\partial \hat{h}}{\partial \hat{t}} + \frac{\partial \left(\hat{u}_z \hat{h}\right)}{\partial \hat{z}} + \frac{1}{\hat{r}} \frac{\partial \left(\hat{u}_\theta \hat{h}\right)}{\partial \theta} = 0 \tag{3}$$

$$-\hat{h} \frac{\partial \hat{p}}{\partial \hat{z}} = \hat{\rho} \hat{h} \left(\frac{\partial \hat{u}_z}{\partial \hat{t}} + \hat{u}_z \frac{\partial \hat{u}_z}{\partial \hat{z}} + \frac{\hat{u}_\theta}{\hat{r}} \frac{\partial \hat{u}_z}{\partial \theta} \right) + \hat{\tau}_{sz} + \hat{\tau}_{rz} \tag{4}$$

$$-\frac{\hat{h}}{\hat{r}} \frac{\partial \hat{p}}{\partial \theta} = \hat{\rho} \hat{h} \left(\frac{\partial \hat{u}_\theta}{\partial \hat{t}} + \hat{u}_z \frac{\partial \hat{u}_\theta}{\partial \hat{z}} + \frac{\hat{u}_\theta}{\hat{r}} \frac{\partial \hat{u}_\theta}{\partial \theta} \right) + \hat{\tau}_{s\theta} + \hat{\tau}_{r\theta} \tag{5}$$

$\hat{h}$ is gap. Shear stress is defined as follows:

$$\begin{aligned} \hat{\tau}_{rz} &= \tfrac{1}{2} \hat{\rho} f_r \hat{u}_z \hat{U}_r, \quad & \hat{\tau}_{r\theta} &= \tfrac{1}{2} \hat{\rho} f_r \left(\hat{u}_\theta - \hat{r}\omega\right) \hat{U}_r \\ \hat{\tau}_{sz} &= \tfrac{1}{2} \hat{\rho} f_s \hat{u}_z \hat{U}_s, \quad & \hat{\tau}_{s\theta} &= \tfrac{1}{2} \hat{\rho} f_s \hat{u}_\theta \hat{U}_s \end{aligned} \tag{6}$$

The subscripts of r, s indicate rotor and stator walls, and the subscripts of θ, z indicate the circumferential and axial directions. The friction factors f_r, f_s in Blasius model [1, 2] are defined as follows:

Table 2 Analytical and experimental rotor-dynamic coefficients

	Experiment [9]	*Analysis*	*Error*
$\hat{M}_{xx}$, $\hat{M}_{yy}$ [kg]	234.42, 223.87	321.4, 321.33	0.37, 0.44
$\hat{C}_{xx}$, $\hat{C}_{yy}$ [kNs/m]	154.50, 150.99	176.82, 176.82	0.14, 0.17
$\hat{C}_{xy}$, $\hat{C}_{yx}$ [kNs/m]	57.4, −54.82	55.9, −56.16	0.026, 0.025
$\hat{K}_{xx}$, $\hat{K}_{yy}$ [MN/m]	3.35, 3.98	5.57, 5.62	0.66, 0.41
$\hat{K}_{xy}$, $\hat{K}_{yx}$ [kNs/m]	10.23, −11.35	6.55, −6.55	0.36, 0.42

$$f_* = n*\left(\frac{2\rho\hat{h}\hat{U}*}{\mu}\right)^{m_*} \quad * = r, s \tag{7}$$

Here, $\hat{U}_r$, $\hat{U}_s$ are the fluid velocities relative to the rotor and stator walls. Yamada's friction coefficients [4], $mr = ms = -0.25$, $nr = ns = 0.079$, were used as reference.

It is noted that only viscous friction is taken into account in this paper, and no direct contact of rough surfaces is considered.

3.2 Steady-State Flow Analysis

Flow rate $\hat{Q} = 2\pi\hat{r}\hat{C}_r\hat{u}_{z0}$ was calculated from axial flow velocity $\hat{u}_{z0}$. Figure 2 shows the flow rate $\hat{Q}$ for rotational speed $\hat{\omega}$ and inlet pressure $\hat{P}_{in}$. This result shows that the error between analytical and experimental results increases for inlet pressure.

3.3 Unsteady-State Flow Analysis

Table 2 shows analytical RD coefficients for the Kanki's experiment condition [9]. For example, the error for $\hat{M}_{xx}$ is $Error = |(234.42 - 321.4)/234.42| = 0.37$.

4 Estimation of Friction Coefficients

4.1 Concentric Steady State

In some cases, the friction coefficients on the rotor and the stator have been assumed to be equal ($mr = ms, nr = ns$) [4, 5]. In this paper, the same assumption is used. Then, the error defined in the following equation is used as evaluation function:

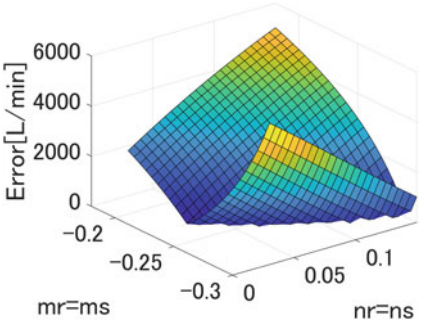

Fig. 3 Error for friction coefficients m, n

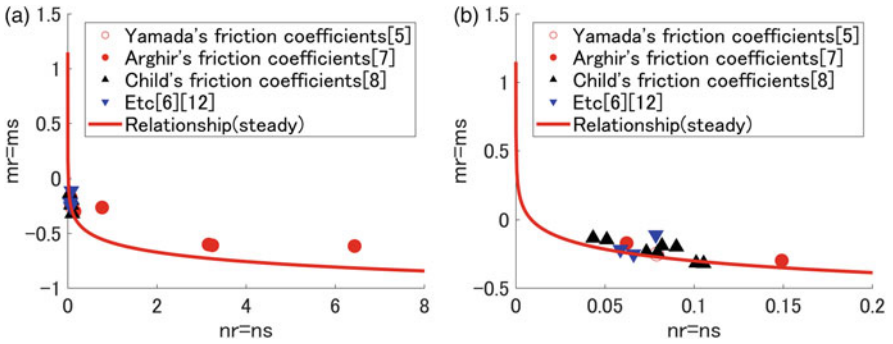

Fig. 4 Relationship of friction coefficients (steady state condition). (**a**) Whole ranges used for estimation. (**b**) Enlarged illustration

$$Error = \sum_{i}^{535} \left| \frac{\hat{Q}_{\text{experiment}}(i) - \hat{Q}_{\text{simulation}}(i)}{\hat{Q}_{\text{experiment}}(i)} \right| \tag{8}$$

The error of Eq. (8) for m, n is shown in Fig. 3. As shown in Fig. 3, the minimum error condition is not obtained as a point, but is obtained as a functional relationship of m, n. Figure 4 shows this functional relationship of the friction coefficients.

The friction coefficients of literature [4–7] are also shown. The coefficients of literature close to the functional relationship are obtained in this paper. Especially, they agree well in the small value range of n as shown in Fig. 4b.

4.2 Unsteady State

The friction coefficients m, n were estimated using the sum of errors in Table 2 as the evaluation function. Here, it is noted that the direct inertia terms are considered with a weight of 1/10 because their measurement was difficult and may contain errors.

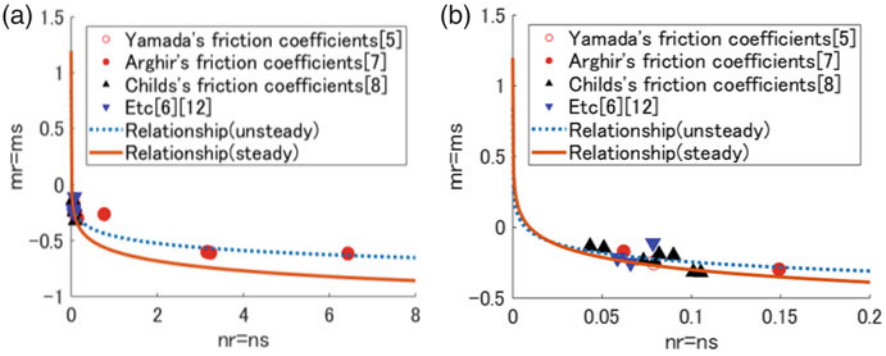

Fig. 5 Relationship of friction coefficients (unsteady state). (**a**)Whole ranges used for estimation. (**b**) Enlarged illustration

Figure 5 shows the functional relationship of the friction coefficients obtained for the unsteady-state results. The functional relationship of steady state, shown in Fig. 5, is also shown for the comparison. The friction coefficients of unsteady state (dashed line) show the similar characteristics of the one for steady state (solid line) in Fig. 5. Furthermore, both functional relationships agree well with the friction coefficients in the literature. The estimation results for the unsteady state were closer to the friction coefficient of the literature than the steady-state results.

4.3 Discussion

The steady-state condition was in the transition range from laminar to turbulent, and unsteady-state condition was in the turbulent range, but the functional relationship of friction coefficients obtained from these conditions were similar. Particularly, when m is large and n is small, these functional relationships agree. The friction coefficients in the literature [4–7] were different from each other; however, these values can be supported from the result of Figs. 4 and 5. The results for steady and unsteady states show small discrepancy, especially in the large value range of n. One of the causes for this discrepancy is because the former is in the transition condition from laminar to turbulent flow, while the latter is in the turbulent flow condition.

5 Conclusion

In this paper, the friction coefficients of Blasius model were estimated and considered. Coefficients of the rotor and stator walls are assumed to be equal ($mr = ms, nr = ns$). In both steady and unsteady conditions, the functional

relationships of the friction coefficients are obtained. These functional relationships can explain the values of friction coefficients obtained in the literature.

Further improvement of the friction coefficients estimation may be possible by estimating all four coefficients. However, the representation and physical explanation using simple functional relationships may be difficult for such case. Moreover, the current work assumed isothermal conditions in the analysis, but thermal effects should be taken into account in more high speed rotating situation.

Acknowledgment The authors would like to acknowledge the support of Mr. Yamada in the analytical analysis and Mr. Tachibana in developing the experimental system used in this work.

References

1. Hirs, G.G.: A bulk-flow theory for turbulence in lubricant films. ASME J. Lubr. Technol. **95**(2), 137–146 (1973)
2. Childs, D.W.: Dynamic analysis of turbulent annular seals based on Hirs' lubrication equation. J. Lubrication Technol. **105**(3), 429–436 (1983). https://doi.org/10.1115/1.3254636
3. Yamada, K., Ikemoto, A., Uchiumi, M., Inoue, T.: Nonlinear analysis of rotordynamic fluid forces in the annular plainseal by using extended bulk-flow analysis: influence of static eccentricity and whirling amplitude. J. Eng. Gas Turbines Power. **141**(2), 021017 (2018). https://doi.org/10.1115/1.4041128
4. Yamada, Y.: Resistance of flow through an annulus with an inner otating cylinder. Bull. JSME. **5**(18), 302–310 (1962)
5. Iwatsubo, T.: Calculation of dynamic force of parallel annular seal with eccentricity. JSME Trans. Ser. C. **60**(580), 4136–4141 (1994). https://doi.org/10.1299/kikaic.60.4136
6. Childs, D., Fayolle, P.: Test results for liquid 'damper' seals using a round-hole roughness pattern for the stators. ASME J. Tribol. **121**(1), 42–49 (1999)
7. Arghir, M., Billy, F., Pineau, G., Frene, J., Texier, A.: Theoretical analysis of textured "damper" annular seals. J. Tribol. **121**(1), 669–678 (2007). https://doi.org/10.1115/1.2738072
8. San Andres, L., Wu, T., Maeda, H., Ono, T.: A computational fluid dynamics modified bulk-flow analysis for circumferentially shallow grooved liquid seals. J. Eng. Gas Turbines Power. **140**(1), 012504 (2018)
9. Kanki, H., Kawakami, T.: Experimental study on the dynamic characteristics of pump annular seals. IMechE Int. Conf. on VIRM, 1984-10, 159–166, England (1984)

Part IV
Energy Harvesting Systems

Enhanced Vibration Energy Harvesting Using Mechanical Stoppers and Parametric Resonances

Y. Fan, M. H. Ghayesh, and T. Lu

1 Introduction

Vibration-based energy harvesting techniques, with the capability to convert everyday unwanted kinetic energy into electrical energy, have attracted increasing numbers of researchers. In recent years, in the field of remote sensing and wireless controlling, an inevitable drawback has been raised up; the consumption of battery impacts the functionality of these devices, even though the required energy levels are in small scales. Alternatively, vibration-based energy harvesting techniques (VEH) have the capability to transfer those undesirable kinetic energy sources into electrical energy and hence reimburse the essential power needed by wireless sensors and actuators.

In order to harvest more energy, VEH techniques are desired to operate at resonance regime, such that an optimal level of kinetic energy can be harvested. However, in the ambient environment, the surrounding frequency sources generally are time-varying, random, and able to jump over a wide-frequency spectrum; based on this, nonlinear vibration-based energy harvesting techniques, which apply internally or externally induced nonlinearities to the harvesting devices, can form relatively wider resonance regimes compared to linear counterpart such that the kinetic energy sources in real environment can be amassed more effectively.

Among nonlinear VEH techniques, piecewise-linear energy harvesters utilize externally induced nonlinearities (i.e., mechanical stoppers) to further increase the operational bandwidth. For the sake of demonstration, consider a cantilever beam-based energy harvester, under base excitation, due to large deflection, the beam engages with mechanical stoppers which locate at both sides of the beam; as the boundary condition is being suddenly changed, the system exhibits large stiffness

Y. Fan (✉) · M. H. Ghayesh · T. Lu
School of Mechanical Engineering, University of Adelaide, Adelaide, SA, Australia
e-mail: yimin.fan@adelaide.edu.au

S. Oberst et al. (eds.), *Vibration Engineering for a Sustainable Future*,
https://doi.org/10.1007/978-3-030-46466-0_24

which results an instantly higher resonance; a hardening frequency response can be observed, and hence a wider resonance regime can be achieved. Soliman et al. [1] presented the first paper of piecewise-linear energy harvester; Liu et al. [2] proposed an energy harvester with a curve fixture; Fan et al. [3] studied a monostable energy harvester with two-side mechanical stopper.

One of the main goals of VEH is utilizing the resonance regime of the designed devices in order to increase the harvested energy level; in addition to applying nonlinearities into designing, multimode and multi-degree of freedom (DOF) energy harvesters are another broadband VEH approach. The performance of multimode and multi-DOF energy harvesters has been carried out by researchers [4–7]. Different from conventional multimode and multi-DOF VEH techniques, consider an imperfectly excited (when the base excitation direction is not perpendicular to the beam length) cantilever-based energy harvester, a principle parametric resonance can be observed at twice the fundamental resonance, which can be considered as another mode of the core element. Abdelkefi et al. [8] investigated a parametrically excited energy harvester theoretically.

In this paper, an energy harvester using mechanical stoppers and parametric resonances is presented; mechanical stoppers induced a strongly hardening frequency response to form a wider frequency bandwidth compared to its linear counterpart; to further increase the operational bandwidth, under parametric excitation, the primary and parametric resonances were merged together due to the externally induced nonlinearity by mechanical stoppers, hence an increase of 388% in frequency bandwidth.

2 Device Configuration

The system shown in Fig. 1 is the proposed energy harvester with two-side mechanical stoppers. An aluminum cantilever beam (115 mm × 9.1 mm × 0.5 mm) with a coupled magnetic tip mass of 6 gram (3 gram per side) is under clamped-free condition; a two-side mechanical stopper is located at 66 mm distance along the beam length from the clamped position, while the gap distance between the stoppers and the beam is 1.97 mm per side; a 16 turns coil structure is fixed onto a support structure as a transducer. The orientation angle between the direction of the base excitation and the beam length is set to be 30°; both forward and backward frequency sweeps with 1 KHz sampling rate are conducted to the experiment; a constant base acceleration 0.5 g is maintained for all experiments.

3 Results and Discussion

Figure 2a shows the frequency-displacement response curve for no stopper and two-side stopper configurations. Under base excitation, the no stopper configuration indicated that the system had a fundamental resonance at 6.7 Hz and parametric resonance at 13.7 Hz; a slightly softening response can be observed from the fun-

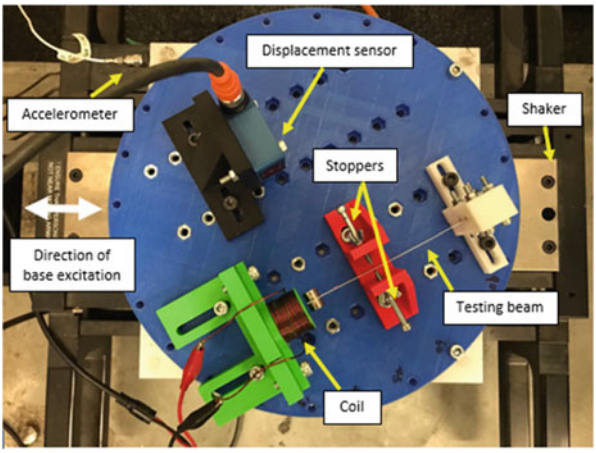

Fig. 1 The proposed energy harvester with mechanical stopper

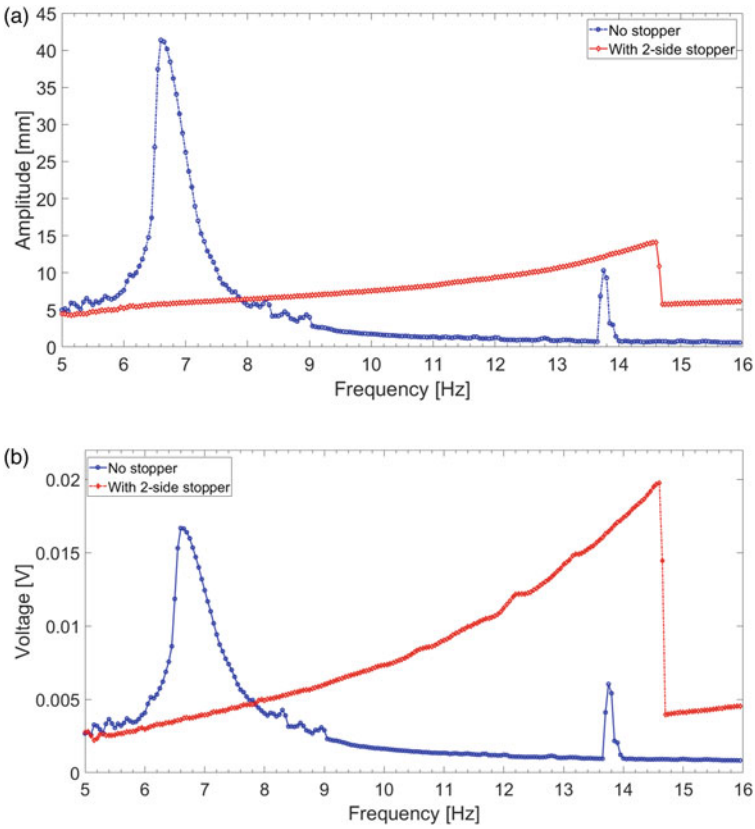

Fig. 2 Frequency response curve for no stopper and two-side stopper configurations: (**a**) frequency-displacement curve; (**b**) frequency-voltage curve

damental resonance, while the behavior of parametric resonance was approximately linear; with two-side mechanical stopper engagement, the deflection of the beam was limited by the obstacle; the peak deflection was decreased from 41.14 mm to 14.1 mm; the two-side stopper configuration exhibited a strongly hardening frequency response which merged the primary and parametric resonances together. Figure 2b shows the frequency-voltage curve for no stopper and two-side stopper configurations. Different from the frequency-displacement curve, two-side stopper configuration had higher peak voltage of 0.0197 V than no stopper configuration of 0.0167 V. In addition to peak voltage, the no stopper configuration had an overall effective bandwidth of 1.6 Hz with 0.006 V reference voltage level, while the two-side stopper configuration had 6.6 Hz continuous bandwidth. Figures 3 and 4 show the time trace, phase plane diagram, and fast Fourier transform (FFT) for no stopper and two-side stopper configurations, respectively.

Figure 5a, b shows the forward and backward frequency sweeps of no stopper and two-side stopper configurations, respectively. In Fig. 5a, it is evident that the amplitude of parametric resonance was doubled in backward frequency sweep while the fundamental frequency remained at same level; compared to no stopper configuration, two-side stopper configuration exhibited a bifurcation at 8.9 Hz during backward frequency sweep; with the mechanical stopper engagements, the system underwent strongly hardening responses during both forward and backward frequency sweeps, which implied the instantly effective primary resonances were altered to higher values; however, for backward frequency sweep case, because the experimental beam could not be activated to resonance status, the deflection of the

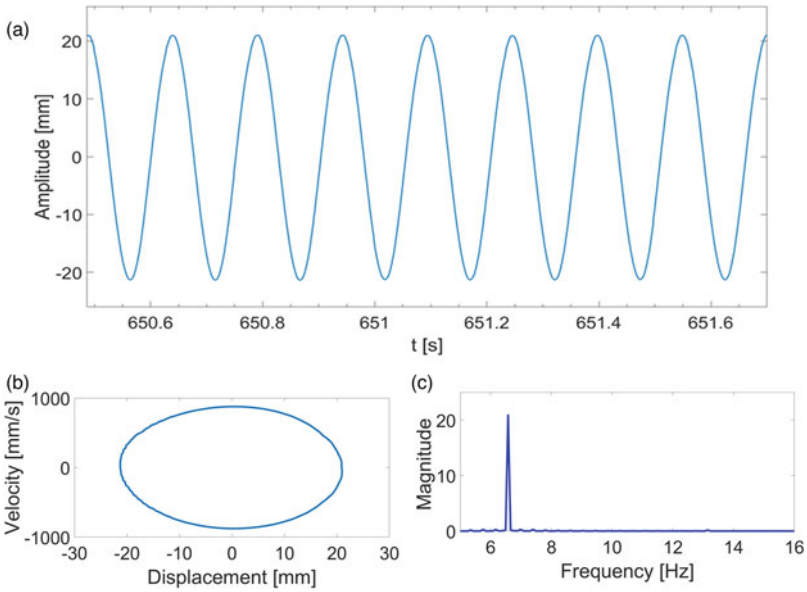

Fig. 3 No stopper configuration: (**a**) time trace; (**b**) phase plane diagram; (**c**) FFT

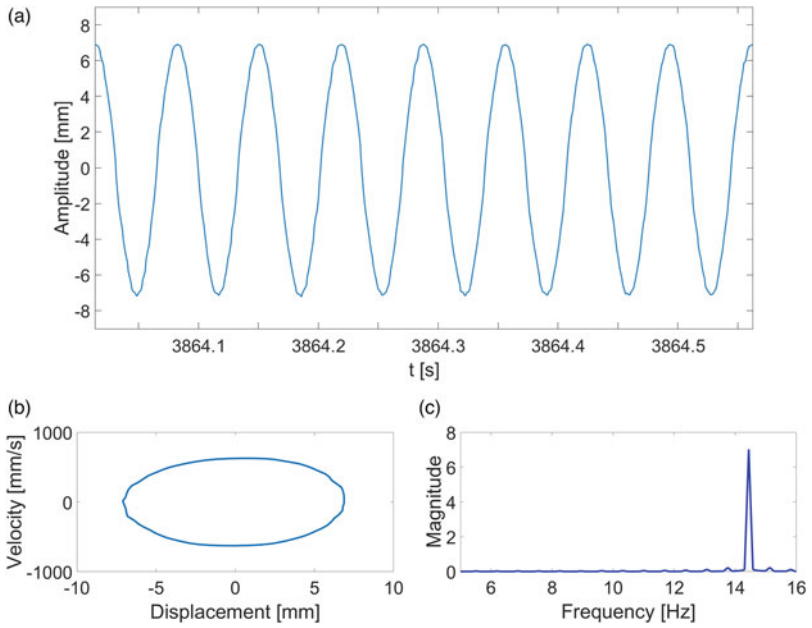

Fig. 4 Two-side stopper configuration: (**a**) time trace; (**b**) phase plane diagram; (**c**) FFT

beam was not able to interact with the stoppers until the base excitation was 8.9 Hz; the system behavior of the two-side stopper configuration was similar to no stopper configuration from 16 Hz to 8.9 Hz (see Fig. 5b).

The gap distance between the stopper and the core element (i.e., a beam) decides the changing in system's inherent stiffness as well as the peak amplitude of the beam deflection, where the inherent stiffness determines the level of the hardening frequency response and the amplitude of the beam deflection decides the level of collected voltage such that there is a certain trade-off between the peak voltage level and the operational bandwidth. For the design parameter selections, a core element with lower primary resonance is more accessible to merge primary and parametric resonances together and form a continuous frequency bandwidth, while a core element with higher primary resonance is capable to have a wider overall frequency bandwidth.

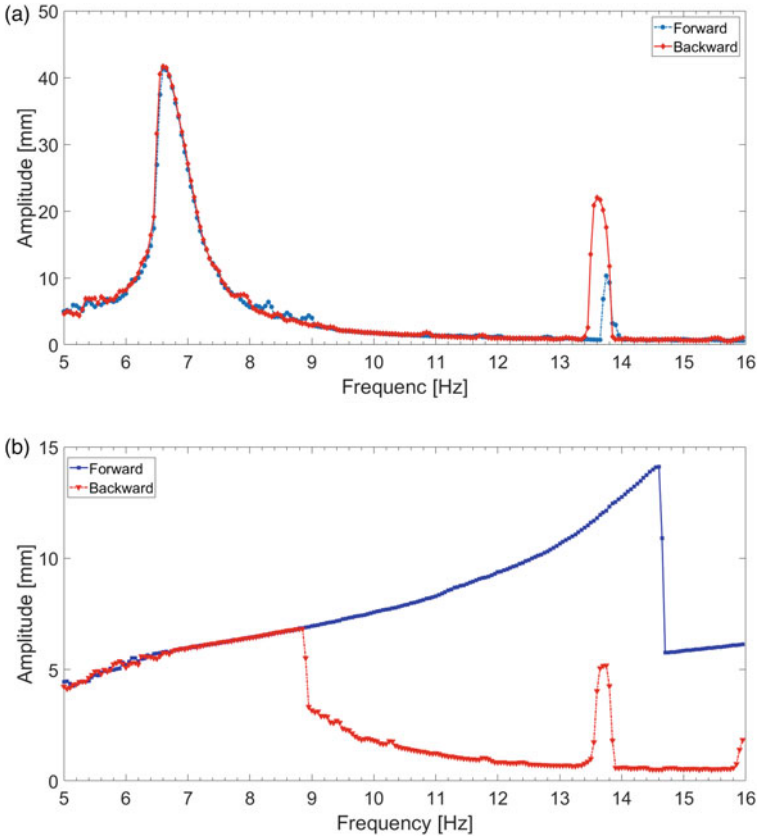

Fig. 5 Frequency-displacement response curve for both forward and backward frequency sweeping: (**a**) no stopper configuration; (**b**) two-side stopper configuration

4 Conclusion

The main goal of this paper is to design and experimentally test a wideband energy harvester using mechanical stoppers and parametric resonances. In order to harvest more kinetic energy from ambient environment and encounter with random and time-varying frequency sources, nonlinear energy harvesting techniques have the merit of broadening the operational frequency bandwidth, such as externally induced nonlinearity – mechanical stoppers; with two-side stopper configuration, the proposed energy harvester exhibited a strongly hardening frequency response, which increased by 350% compared to linear counterpart; in addition to mechanical stoppers, combing parametric excitation with mechanical stoppers, the primary and parametric resonances can be merged together in the presence of mechanical stoppers; hence, a continuously effective bandwidth can be formed with a 388% increase in the overall frequency bandwidth.

References

1. Soliman, M.S.M., Abdel-Rahman, E.M., El-Saadany, E.F., Mansour, R.R.: A wideband vibration-based energy harvester. J. Micromech. Microeng. **18**(11), 115021 (2008)
2. Liu, W., Liu, C., Ren, B., Zhu, Q., Hu, G., Yang, W.: Bandwidth increasing mechanism by introducing a curve fixture to the cantilever generator. Appl. Phys. Lett. **109**(4), 043905 (2016)
3. Fan, K., Tan, Q., Zhang, Y., Liu, S., Cai, M., Zhu, Y.: A monostable piezoelectric energy harvester for broadband low-level excitations. Appl. Phys. Lett. **112**(12), 123901 (2018)
4. Roundy, S., Leland, E.S., Baker, J., Carleton, E., Reilly, E., Lai, E., Otis, B., Rabaey, J.M., Wright, P.K., Sundararajan, V.: Improving power output for vibration-based energy scavengers. IEEE Pervas. Comput. **4**(1), 28–36 (2005)
5. Tadesse, Y., Zhang, S., Priya, S.: Multimodal energy harvesting system: piezoelectric and electromagnetic. J. Intell. Mater. Syst. Struct. **20**(5), 625–632 (2009)
6. Kim, I.-H., Jung, H.-J., Lee, B.M., Jang, S.-J.: Broadband energy-harvesting using a two degree-of-freedom vibrating body. Appl. Phys. Lett. **98**(21), 214102 (2011)
7. Deng, H., Du, Y., Wang, Z., Zhang, J., Ma, M., Zhong, X.: A multimodal and multidirectional vibrational energy harvester using a double-branched beam. Appl. Phys. Lett. **112**(21), 213901 (2018)
8. Abdelkefi, A., Nayfeh, A.H., Hajj, M.R.: Global nonlinear distributed-parameter model of parametrically excited piezoelectric energy harvesters. Nonlinear Dyn. **67**(2), 1147–1160 (2012)

Two Configurations of Using a Tuned Mass Damper to Harvest Vehicle Vertical Vibration Energy

S. P. Bai and Z. C. Hou

1 Introduction

Vehicle vertical vibration energy dissipation is an important part of vehicle energy waste and is mainly dissipated through suspension and tire. Many scholars have studied how to directly harvest the energy dissipated through these two parts [1–3], while some scholars proposed an idea of using "additional systems" for energy harvesting [4, 5]. The additional device can be seen as tuned mass damper (TMD) and seems to have good potential in vibration energy harvesting due to its flexible layouts and parameter selections. However, limited research has been done on the use of TMDs in vehicle vibration energy harvesting. In this paper, the authors try to systematically explore the applicability of using a TMD to harvest vehicle vibration energy while focusing on questions as follows: (1) what is the impact of the introduced TMDs to vehicle dynamic performances? (2) how much energy can be harvested by the TMDs at most?

2 Dynamics Modeling

For a vehicle traveling on a straight road, its vertical dynamic behavior is usually described as a quarter car model without tire damping. Considering the TMD working principles and to harvest energy dissipated by the tire, we added tire damping to a quarter car model, as shown in Fig. 1. This model will be used as a basis for comparison, thus termed as the reference model. Two new models

S. P. Bai · Z. C. Hou (✉)
Tsinghua University, Beijing, P. R. China
e-mail: houzc@tsinghua.edu.cn

S. Oberst et al. (eds.), *Vibration Engineering for a Sustainable Future*,
https://doi.org/10.1007/978-3-030-46466-0_25

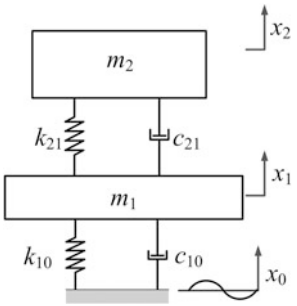

Fig. 1 The reference model

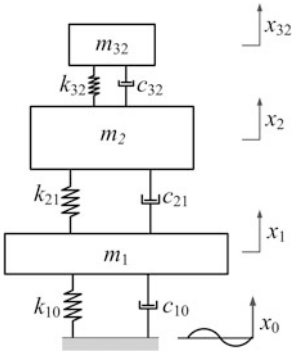

Fig. 2 The S-TMD model

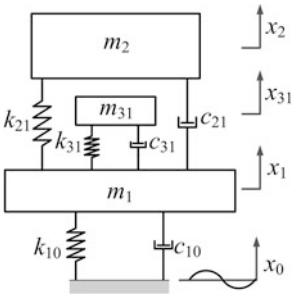

Fig. 3 The U-TMD model

are built by introducing one TMD to the sprung mass and the unsprung mass of the reference model. The two TMDs are named as "sprung TMD" and "unsprung TMD," respectively, and the corresponding models are termed for short as the S-TMD model and the U-TMD model, as shown in Figs. 2 and 3.

In Figs. 1, 2, and 3, m_1 and m_2 are the unsprung mass and the sprung mass, respectively, k_{10} and k_{21} the stiffness factors of the tire and suspension spring, and c_{10} and c_{21} the damping coefficients of the tire and suspension damper. Correspondingly, x_1 and x_2 are the displacements of the unsprung mass and the sprung mass, while x_0 is the road surface profile. In Figs. 2 and 3, m_{32}, k_{32}, c_{32} are the mass, spring stiffness factor, and damper damping coefficient of the sprung TMD, and m_{31}, k_{31}, c_{31} are those of the unsprung TMD, with x_{32}, x_{31} the

displacements of the sprung TMD and unsprung TMD, respectively. Here, c_{31} and c_{32} are used to harvest vibration energy, but the mechanical damping and circuit damping are neglected as previous researches have done with suspension damping.

Applying the Newton's second law, the dynamic equations of the models can be deduced.

Road input is usually built as white noise in terms of velocity in frequency domain and is expressed as [1].

$$S_{\mathrm{vel}}(\omega) = 2\pi G_{\mathrm{r}} V \tag{1}$$

It is clear that $S_{\mathrm{vel}}(\omega)$ is only related to road roughness coefficient G_{r} and vehicle speed V.

3 Performance Evaluation

To understand the benefits of using a TMD to harvest vehicle vertical vibration energy, some indices are defined based on energy dissipation.

For a single damper c_{ij}, the energy dissipation during a unit time or the dissipated power is

$$P_{\mathrm{ij}} = c_{\mathrm{ij}}\left(\dot{x}_{\mathrm{j}} - \dot{x}_{\mathrm{i}}\right)^2 \tag{2}$$

Here, subscripts i, j (= 0,1,2,3 and $i \neq j$) represent the road input and degrees of freedom (DOFs) of the unsprung mass, the sprung mass, and the TMD, respectively. $\dot{x}_{\mathrm{j}} - \dot{x}_{\mathrm{i}}$ is the relative velocity between two damper ends.

For the aforementioned road random velocity excitation, the above equation can be deduced as

$$P_{\mathrm{ij}} = \frac{c_{\mathrm{ij}}}{2\pi}\int_{\omega_1}^{\omega_2} 2\pi G_{\mathrm{r}} V \left| H(\omega)_{\left(\dot{x}_{\mathrm{j}} - \dot{x}_{\mathrm{i}}\right)\sim\dot{x}_0} \right|^2 \mathrm{d}\omega \tag{3}$$

with $H(\omega)_{\left(\dot{x}_{\mathrm{j}} - \dot{x}_{\mathrm{i}}\right)\sim\dot{x}_0}$ the frequency response function from $\dot{x}_0$ to $\left(\dot{x}_{\mathrm{j}} - \dot{x}_{\mathrm{i}}\right)$.

Based on Eqs. (2) and (3), four indices are defined as follows.

Total energy dissipation is defined as the sum of energy dissipated by all dampers in a model and can be calculated by

$$P = \sum P_{\mathrm{ij}} \tag{4}$$

TMD energy harvesting potential, or the TMD dissipated energy, is the upper limit of energy that could be harvested by a TMD.

Vehicle dissipated energy reduction is defined as the difference between the reference model and a quarter car model with a TMD, in terms of energy dissipation of the suspension and tire. The calculation can be deduced as

$$\Delta P_{\mathrm{st}} = \left(P_{21}^{1} - P_{21}^{\mathrm{k}}\right) + \left(P_{10}^{1} - P_{10}^{\mathrm{k}}\right) \tag{5}$$

Here, superscript 1 represents the reference model, and subscript k (=2, 3) represents the S-TMD model or the U-TMD model. The right hand of Eq. (5) is suspension and tire dissipated energy difference between the reference model and the models with a TMD.

Tire proportion in vehicle dissipated energy reduction is defined as

$$\Delta R_{10} = \frac{P_{10}^{1} - P_{10}^{\mathrm{k}}}{\Delta P_{\mathrm{st}}} \times 100\% \tag{6}$$

This index is proposed to evaluate the portion tire part takes, in vehicle dissipated energy reduction.

Three indices, namely, body acceleration $\ddot{x}_2$, suspension deflection f_{d}, and tire relative dynamic load F_{d}/G, are selected to evaluate vehicle dynamic performances [6].

The TMD dynamic deflection is defined to check necessary space for a vehicle to host a TMD.

4 TMD Parameter Selection

To a primary system of multiple DOFs, if the ratio of any two adjacent natural frequencies is larger than 2.0 [7], a DVA can be designed separately for each mode. Furthermore, if a dominant DOF exists in a given mode, the design of a DVA to this mode can be simply performed on a 1-DOF system that contains only the dominant DOF in the physical space, without having much inaccuracy [8].

For the quarter car model of a typical passenger car, the ratio of the two natural frequencies is usually around 10, and each mode contains a dominant DOF [6]. As a result, the design of a DVA to either mode can be accomplished by regarding the mode as a dominant-DOF-only 1-DOF system in the physical space as shown in Figs. 4 and 5.

For the systems shown in Figs. 4 and 5, the parameters of the matched TMDs are selected by applying H_2 optimization method for a damped primary system under base excitation [9]. In this method, mass ratio between the TMD and the primary

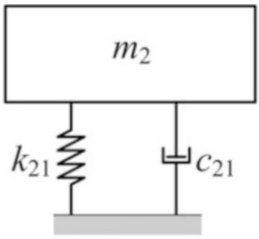

Fig. 4 Equivalent 1-DOF system for mode 1

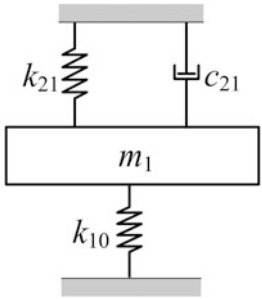

Fig. 5 Equivalent 1-DOF system for mode 2

system is determined in advance, and the stiffness factor and damping coefficient of the TMD can then be calculated.

5 Model Comparison

In this section, the two models with a TMD are simulated using as much as 1/4 of the real full-car parameters and compared with the reference model.

In Ref. [1], a quarter car model without tire damping was employed. Based on the parameters used in this reference and with reference to parameters in Ref. [10–12], a tire vertical damping coefficient of 300 N·s/m is selected. The parameters of either TMD are then calculated in accordance to Ref. [9]. D-class and E-class roads are selected, and vehicle speed range u is set based on commonly used vehicle speeds.

Figures 6, 7, and 8 give the defined energy-related indices calculation results.

Figure 6 depicts the total energy dissipation of the three models under two different classes of road. It is clear that the total energy dissipations of the three models are identical when the road class is the same. In another word, the introduction of a TMD has no impact to the overall energy dissipation. It would be safe to predict that the harvestable energy by a TMD should come from the reduced energy dissipation of the suspension and the tire.

Figure 7 presents the TMD energy harvesting potential. Another calculation shows that the vehicle dissipated energy reduction of either of the two models with a TMD is identical to TMD energy harvesting potential. This proves the aforementioned prediction that the TMD energy harvesting potential in either of the models with a TMD equals to the reduced energy dissipated by the suspension and the tire.

Figure 8 shows the variation of the tire proportion in vehicle dissipated energy reduction of the two models with a TMD. It can be found from calculation that only 0.2% of the TMD energy harvesting potential comes from tire for the S-TMD model. For the U-TMD model, the percentage is higher than the S-TMD model. It is more than 16% at all speeds and even above 17% when the vehicle speed exceeds 30 km /h.

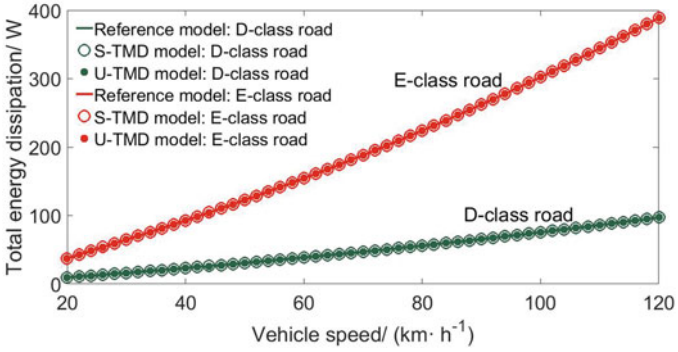

Fig. 6 Total energy dissipation of the three models

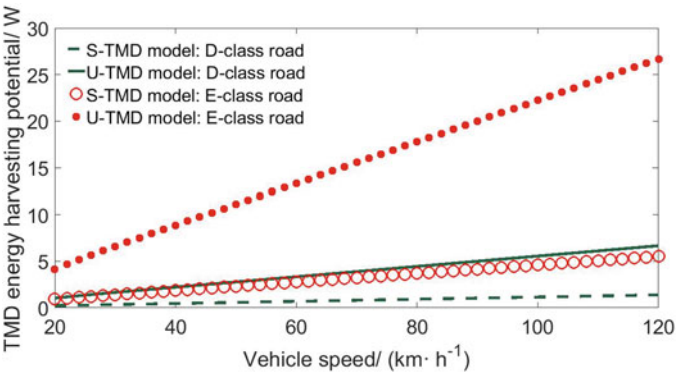

Fig. 7 TMD energy harvesting potential of the models with a TMD

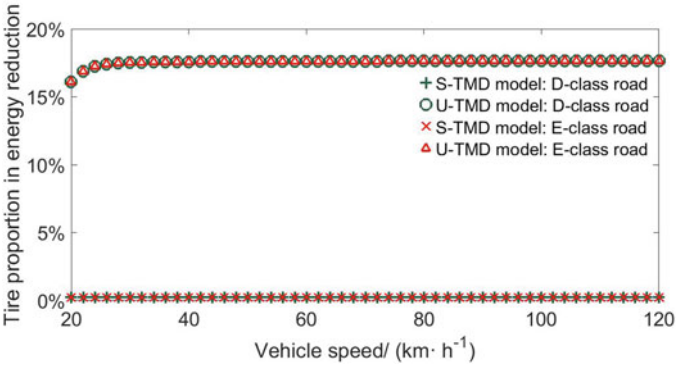

Fig. 8 Tire proportion in vehicle dissipated energy reduction of the models with a TMD

The above analysis demonstrates that a TMD can be used to harvest vehicle vertical vibration energy, and the U-TMD model has bigger advantage in this regard.

Further calculation shows TMD can help improve vehicle dynamic performances, and in addition, S-TMD model is better in this respect. What's more, calculation results also show TMDs do not require large space.

6 Conclusions

In this paper, applicability of using a tuned mass damper to harvest vehicle vibration energy is studied. The main conclusions are as follows:

1. Either configuration of TMDs can be used to harvest vehicle vertical vibration energy, and the TMD matched to the unsprung mass has better performance in it than the TMD matched to the sprung mass. The introduced TMDs do not change the total energy dissipation, but change the energy distribution.
2. Either configuration of the TMDs will improve vehicle ride comfort, handling, and safety at the same time in terms of body acceleration, suspension dynamic deflection, and tire relative dynamic load. The TMD matched to the sprung mass is better in this regard.
3. For either configuration, the TMD's deflection is very small, not asking for much space for installing.

References

1. Zuo, L., Zhang, P.: Energy harvesting, ride comfort, and road handling of regenerative vehicle suspensions. J. Vib. Acoust. **135**(1), 011002 (2013)
2. Casavola, A., Iorio, F., Tedesco, F.: A multi-objective H_∞ control strategy for energy harvesting in regenerative vehicle suspension systems. Int. J. Control. **91**(4), 741–754 (2018)
3. Jackson, N., O'Keeffe, R., Waldron, F., et al.: Evaluation of low-acceleration MEMS piezoelectric energy harvesting devices. Microsyst. Technol. **20**(4–5), 671–680 (2014)
4. Mapelli, F., Sabbioni, E., Tarsitano, D.: Structural Dynamics and Renewable Energy. Springer, New York (2010)
5. Yang Y.: A Method and Device to Improve Kinetic Energy Generation Efficiency (in Chinese). China Patent, CN103267000A (2013)
6. Yu, Z.: Automobile Theory (in Chinese), 5th edn. China Machine Press, Beijing (2009)
7. Wu, L., Gu, Z., Zhang, A.: A further investigation of using dynamic vibration absorber to reduce vibration (in Chinese). J. Vib. Shock. **1**, 1–7 (1994)
8. Zhang X., Wu P.: Study on suspensions with dynamic absorbers (in Chinese). J. Jiangsu Univ. (Natural Science Edition) (5), 389–392 (2004)
9. Asami, T., Nishihara, O.: Analytical solutions to H_∞ and H_2 optimization of dynamic vibration absorbers attached to damped linear systems. J. Vib. Acoust. **124**(2), 284–295 (2002)
10. Ji, X.: The dynamic stiffness and damping characteristics of the tire (in Chinese). Automot. Eng. **5**, 315–320 (1994)
11. Luo, Y., Tan, D.: A research on the hub-motor driven wheel structure with a novel built-in mounting system (in Chinses). Automot. Eng. **35**(12), 1105–1110 (2013)
12. Zhang, F., Feng, D., Ling, X., et al.: Vertical coupling dynamics model of heavy truck-pavement-subgrade (in Chinese). China J. Highw. Transp. **28**(4), 1–12 (2015)

Galerkin Analyses of Cantilevered Piezoelectric Energy Harvesting Based on Superharmonic Resonances

G. C. Zhang, J. Y. Chen, and B. Zhang

1 Introduction

Harvesting mechanical energy in a range of low excitation frequencies is of great interest [1, 2]. Two superharmonic resonances will be discussed as the resonant frequency is only one third or half of the natural frequency. The considered electromechanical system is a piezoelectric cantilever with a tip magnet at its free end [3–5], as shown in Figs. 1 and 2. Due to the coupled electrical components, the mathematical model is an integro-partial differential equation [6, 7]. The tip magnet is assumed to be repelled by an external magnet, and the magnetic force serves nonlinear boundary conditions at the right end.

The aim of this paper is to develop Galerkin method to deal with the nonlinear boundary conditions. The conventional Galerkin method is effective to treat a partial differential equation with linear boundary conditions. It requires choosing an appropriate family of trial functions which satisfy all linear boundary conditions. The solution is expressed in the form of a weighted sum of trial functions. However, the current problem describes a cantilever beam with nonlinear boundary conditions. Even though, in a family of trial functions, each spatial function satisfies the nonlinear boundary condition, a combination of these trial functions will generally not do so. The present initial-boundary value problem could be circumvented by exchanging two original steps of Galerkin method [8].

The trick is now to choose weight functions as the first step, instead of trial functions. Combined with the nonlinear boundary condition, a list of identities can be obtained by weighted integrals of the governing equation. Then, the Galerkin truncation is used to treat two superharmonic resonances. The second and third

G. C. Zhang (✉) · J. Y. Chen · B. Zhang
Hainan University, Haikou, P. R. China
e-mail: gczhang@hainanu.edu.cn

S. Oberst et al. (eds.), *Vibration Engineering for a Sustainable Future*,
https://doi.org/10.1007/978-3-030-46466-0_26

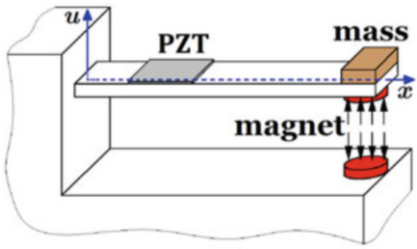

Fig. 1 The cantilevered piezoelectric energy harvester

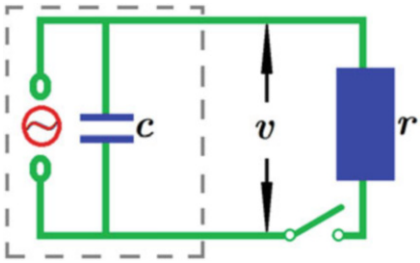

Fig. 2 The coupling electric circuit

superharmonic resonances may occur in the electromechanical system having quadratic and cubic nonlinearities.

2 Application of Galerkin Method into Governing Equation

The application of the Euler-Bernoulli beam theory yields the governing equation

$$\ddot{u} + u'''' + \alpha \dot{u}'''' = \theta v \left[\delta'(x - x_2) - \delta'(x - x_1)\right], c\dot{v} + \frac{v}{r} = \theta \int_{x_1}^{x_2} \dot{u}'' dx \tag{1}$$

where c represents the equivalent capacitance, θ represents the electromechanical coupling coefficient, $v(t)$ represents the voltage across the resistive load r at the time of t, α stands for the viscosity coefficient, $u(x, t)$ is the transversal displacement of the cantilever whose clamped end is the original point, the superscript prime represents the (partial) derivative of the preceding function taken with respect to its spatial variable x, and the overdot denotes the (partial) derivative over the time variable t. The boundary conditions are simplified as

$$\begin{aligned} u(0, t) = \beta \sin(\omega t), u'(0, t) = u''(1, t) = 0, \eta \ddot{u}(1, t) \\ = u'''(1, t) + \alpha \dot{u}'''(1, t) + F(d - \beta \sin(\omega t) + u(1, t)) \end{aligned} \tag{2}$$

where η is the ratio of the tip point mass to mass of the cantilever and d is the initial distance between the two cylindrical magnets in Fig. 1. The magnetic force $F(d)$ is a fractional function of magnet spacing d [3, 4, 9].

$$F(d) = c_0\left[d^{-2} + (d+2h)^{-2} - 2(d+h)^{-2}\right] \tag{3}$$

where c_0 is the magnetic coefficient and h is the length of each cylindrical magnet.

The equilibrium position is

$$\underline{u}(x) = A_{\mathrm{e}}\left(1.5x^2 - 0.5x^3\right) \tag{4}$$

where A_{e} satisfies

$$F\left(d + A_{\mathrm{e}}\right) = 3A_{\mathrm{e}} \quad (|A_{\mathrm{e}}| \le d) \tag{5}$$

The standard governing equation of the relative motion is

$$\begin{aligned} &\dot{z} + z'' + \dot{z}'''' + \alpha\dot{z}'''' = \theta v\left[\delta'\left(x - x_2\right) - \delta'\left(x - x_1\right)\right] + \beta\omega^2\sin(\omega t), \\ &c\dot{v} + \frac{v}{r} = \theta\int_{x_1}^{x_2}\dot{z}''\mathrm{d}x \end{aligned} \tag{6}$$

where

$$z(x,t) = u(x,t) - \underline{u}(x) - \beta\sin(\omega t) \tag{7}$$

The corresponding boundary conditions are

$$\begin{aligned} &z(0,t) = z'(0,t) = z''(1,t) = 0, \;\; z'''(1,t) + \alpha\dot{z}'''(1,t) \\ &\quad = \eta\ddot{z}(1,t) - \eta\beta\omega^2\sin(\omega t) + \sum_{j=1}^{+\infty}\left[c_j z^j(1,t)\right] \end{aligned} \tag{8}$$

where $j = 1, 2, 3, 4\ldots$

$$c_j = c_0(j+1)(-1)^{j+1}\left[(d+A_{\mathrm{e}})^{-2-j} + (d+A_{\mathrm{e}}+2h)^{-2-j} - 2(d+A_{\mathrm{e}}+h)^{-2-j}\right] \tag{9}$$

The modal function of the unperturbed linear system is in the form of

$$\begin{aligned} &\phi_k(x) \\ &= \frac{\left(\sin\sqrt{\omega_k} + \mathrm{sh}\sqrt{\omega_k}\right)\left[\cos\left(x\sqrt{\omega_k}\right) - \mathrm{ch}\left(x\sqrt{\omega_k}\right)\right] + \left(\cos\sqrt{\omega_k} + \mathrm{ch}\sqrt{\omega_k}\right)\left[\mathrm{sh}\left(x\sqrt{\omega_k}\right) - \sin\left(x\sqrt{\omega_k}\right)\right]}{2\left(\cos\sqrt{\omega_k}\,\mathrm{sh}\sqrt{\omega_k} - \sin\sqrt{\omega_k}\,\mathrm{ch}\sqrt{\omega_k}\right)} \end{aligned} \tag{10}$$

where ω_k satisfies

$$\sqrt{\omega_k^3}\left(1+\cos\sqrt{\omega_k}\mathrm{ch}\sqrt{\omega_k}\right)=\left(c_1-\eta\omega_k^2\right)\left(\cos\sqrt{\omega_k}\mathrm{sh}\sqrt{\omega_k}-\sin\sqrt{\omega_k}\mathrm{ch}\sqrt{\omega_k}\right) \tag{11}$$

Now Galerkin method is developed to treat the nonlinear boundary conditions. We first choose many a modal function as weight functions to give a weighted average of Eq. (6) by integrating it with respect to x over [0,1]. Performing the integral over the closed interval [0,1] leads to

$$\begin{aligned}\int_0^1 \ddot{z}\phi_k \mathrm{d}x+\int_0^1 \phi_k z''''\mathrm{d}x+\alpha\int_0^1 \phi_k \dot{z}''''\mathrm{d}x=\beta\omega^2\sin(\omega t)\int_0^1 \phi_k \mathrm{d}x\\ +\theta v\int_0^1\left[\delta'(x-x_2)-\delta'(x-x_1)\right]\phi_k \mathrm{d}x\end{aligned} \tag{12}$$

According to the nonlinear boundary conditions (8), it becomes

$$\begin{aligned}v\theta_k+\int_0^1 \ddot{z}\phi_k \mathrm{d}x+\alpha\omega_k^2\int_0^1 \dot{z}\phi_k \mathrm{d}x+\left(\eta\omega_k^2-c_1\right)\alpha\dot{z}(1,t)+\omega_k^2\int_0^1 z\phi_k \mathrm{d}x+\\ \left(\eta\omega_k^2-c_1\right)z(1,t)+\eta\ddot{z}(1,t)+\sum_{j=1}^{+\infty}\left[c_j z^j(1,t)\right]=\eta_{1k}\beta\omega^2\sin(\omega t)\end{aligned} \tag{13}$$

where

$$\theta_k=\theta\left[\phi_k'(x_2)-\phi_k'(x_1)\right] \text{ and } \eta_{nk}=\eta+\int_0^1 \phi_k^n(x)\mathrm{d}x \tag{14}$$

The second step is to choose appropriate trial functions. In general, it is convenient to expand the displacement in terms of the linear free-oscillation modes.

$$z(x,t)=\sum_{n=1}^{+\infty}\left[\phi_n(x)q_n(t)\right] \tag{15}$$

To perform calculations, N-term truncation that has a finite number of terms is used. Then, the electrical component of Eq. (6) becomes

$$c\dot{v}+\frac{v}{r}=\theta\sum_{n=1}^{N}\left[\dot{q}_n\int_{x_1}^{x_2}\phi_n''(x)\mathrm{d}x\right]=\sum_{n=1}^{N}(\theta_n\dot{q}_n) \tag{16}$$

Meanwhile, the mechanical counterpart (13) is given as follows:

$$\left(\ddot{q}_k + \alpha\omega_k^2\dot{q}_k + \omega_k^2 q_k\right)\eta_{2k} - \alpha c_1 \sum_{n=1}^{N}\dot{q}_n + \sum_{j=2}^{\infty} c_j \left(\sum_{n=1}^{N} q_n\right)^j + v\theta_k = \omega^2\beta\eta_{1k}\sin(\omega t) \tag{17}$$

In the following, the one-term truncated system will be used to analyze the steady-state response. Based on Eqs. (16) and (17), the governing equation is

$$\begin{aligned}&\left(\ddot{q}_1 + \alpha\omega_1^2\dot{q}_1 + \omega_1^2 q_1\right)\eta_{21} - \alpha c_1\dot{q}_1 + v\theta_1 \\ &\quad + \sum_{n=2}^{\infty} c_n q_1^n = \omega^2\beta\eta_{11}\sin(\omega t), \quad c\dot{v} + \frac{v}{r} = \theta_1\dot{q}_1(t)\end{aligned} \tag{18}$$

3 Two Superharmonic Resonances

The method of two time scales can be employed to solve the second superharmonic resonance when 2ω approaches ω_1. To the first-order approximation, the steady-state motion at the free end is given by

$$z(1,t) \approx a_1\sin(\omega t) - a_2\sin\left(2\omega t - \arctan\frac{2\sigma_2\eta_{21}}{\alpha\omega_1^2\eta_{21} - \alpha c_1}\right) \tag{19}$$

where

$$\sigma_2 = 2\omega - \omega_1, \quad a_1 = \frac{\omega^2\beta\eta_{11}}{\eta_{21}\left(\omega_1^2 - \omega^2\right)} \text{ and } a_2 = \frac{|c_2|\,a_1^2}{2\omega_1\sqrt{4\sigma_2^2\eta_{21}^2 + \alpha^2\left(\omega_1^2\eta_{21} - c_1\right)^2}} \tag{20}$$

At the steady state, the voltage output is approximately predicted by

$$\begin{aligned}v(t) \approx\ & b_1\sin\left(\omega t + \arctan\frac{1}{cr\omega}\right) \\ & - b_2\sin\left(2\omega t + \arctan\frac{\alpha\omega_1^2\eta_{21} - \alpha c_1 - 2cr\sigma_2\omega_1\eta_{21}}{\alpha cr\omega_1^3\eta_{21} - \alpha cr c_1\omega_1 + 2\sigma_2\eta_{21}}\right)\end{aligned} \tag{21}$$

where

$$b_1 = \frac{r\omega\theta_1 a_1}{\sqrt{1 + c^2r^2\omega^2}} \text{ and } b_2 = \frac{r\omega_1\theta_1 a_2}{\sqrt{1 + c^2r^2\omega_1^2}} \tag{22}$$

When 3ω approaches ω_1, the third superharmonic resonance occurs due to the cubic nonlinearity. The steady-state response can be approximately obtained by the method of three time scales. The second-order approximation to the time history of displacement can be expressed as

$$z(1,t) \approx a_1 \sin(\omega t) + a_3 \cos(3\omega t - \varphi) - \frac{c_2\left(a_1^2+a_3^2\right)}{2\eta_{21}\omega_1^2} + \frac{c_2 a_1 a_3}{\eta_{21}\left(2\omega\omega_1-\omega^2\right)} \sin(2\omega t - \varphi) + \frac{c_2 a_1^2}{2\eta_{21}\left(\omega_1^2-4\omega^2\right)} \cos(2\omega t) + \frac{c_2 a_3^2}{6\eta_{21}\omega_1^2} \cos(6\omega t - 2\varphi) + \frac{c_2 a_1 a_3}{\eta_{21}\left(\omega^2+2\omega\omega_1\right)} \sin(4\omega t - \varphi) \tag{23}$$

The amplitude a_3 satisfies

$$\boldsymbol{\Lambda}_1^2 a_3^2 + \left(2\omega_1\eta_{21}\sigma_3 - \boldsymbol{\Lambda}_2 - \boldsymbol{\Lambda}_3 a_3^2\right)^2 a_3^2 = \boldsymbol{\Lambda}_4^2 \tag{24}$$

where

$$\sigma_3 = 3\omega - \omega_1 \tag{25}$$

and

$$\begin{aligned} \boldsymbol{\Lambda}_1 &= \alpha\omega_1\left(\omega_1^2\eta_{21} - c_1\right) + \frac{r\theta_1^2\omega_1}{1+c^2r^2\omega_1^2}, \quad \boldsymbol{\Lambda}_4 = \frac{a_1^3}{4\eta_{21}}\left(c_3\eta_{21} + \frac{2c_2^2}{4\omega^2-\omega_1^2}\right) \\ \boldsymbol{\Lambda}_2 &= \frac{cr^2\theta_1^2\omega_1^2}{1+c^2r^2\omega_1^2} + \left(\frac{3}{2}c_3\eta_{21} + \frac{2c_2^2}{\omega^2-4\omega_1^2} - \frac{c_2^2}{\omega_1^2}\right)\frac{a_1^2}{\eta_{21}}, \quad \boldsymbol{\Lambda}_3 = \frac{9c_3\eta_{21}\omega_1^2-10c_2^2}{12\eta_{21}\omega_1^2} \end{aligned} \tag{26}$$

The phase φ satisfies

$$\boldsymbol{\Lambda}_1 \tan\varphi = 2\omega_1\eta_{21}\sigma_3 - \boldsymbol{\Lambda}_2 - \boldsymbol{\Lambda}_3 a_3^2 \tag{27}$$

The analytical response (23) is stable if and only if

$$\boldsymbol{\Lambda}_1^2 + \left(2\omega_1\eta_{21}\sigma_3 - \boldsymbol{\Lambda}_2 - 2\boldsymbol{\Lambda}_3 a_3^2\right)^2 > \boldsymbol{\Lambda}_3^2 a_3^4 \tag{28}$$

The stability boundary is

$$\boldsymbol{\Lambda}_1^2 + \left(2\omega_1\eta_{21}\sigma_3 - \boldsymbol{\Lambda}_2 - 2\boldsymbol{\Lambda}_3 a_3^2\right)^2 = \boldsymbol{\Lambda}_3^2 a_3^4 \tag{29}$$

At the steady state, the voltage output is

$$v(t) \approx b_1 \sin\left(\omega t + \arctan\frac{1}{cr\omega}\right) + b_3 \cos\left(3\omega t - \varphi + \arctan\frac{1}{cr\omega_1}\right) \tag{30}$$

where

$$b_3 = \frac{r\omega_1\theta_1 a_3}{\sqrt{1 + c^2 r^2 \omega_1^2}} \tag{31}$$

4 Results and Discussions

The considered parameters are listed in Table 1 [3, 4]. Their dimensionless values are $x_1 = 0$, $x_2 = 1$, $c_0 = 0.508394$, $d = 0.15$, $h = 0.004167$, $\eta = 0.02$, $c = 0.000001$, $r = 1000\,000$, $\theta = 0.0002$, and $\omega_1 = 4.048371$ [9].

When $\beta = 0.001$, Fig. 3 (or 4) illustrates the effect of viscosity coefficient on the primary-harmonic amplitude a_1 (or the second-order superharmonic amplitude a_2) with $\alpha = 0.001$, 0.002, and 0.003. It is remarked that the primary-harmonic amplitude is independent of viscosity coefficient. However, the superharmonic amplitude decreases with increased viscosity damping.

Table 1 The considered physical parameters [3, 4, 9]

Description	Values	Description	Values
Mass of the cantilever	25.6 g	The tip point mass	0.512 g
Length of the cantilever	480 mm	Length of the magnet	2 mm
Moment of inertia	0.36 mm^4	Radius of the magnet	4 mm
Young's modulus	3.81×10^{10}Pa	Residual flux density	1.1 T
Capacitance	5.9531×10^{-8}F	Permeability of air	1.256×10^{-6}H·m^{-1}
Resistive load	7,631,732 Ω	Acceleration of gravity	9.8067 m·s^{-2}
Electromechanical coupling coefficient	1.1906×10^{-5} N·V^{-1}	Initial distance between two magnets	338.5 mm

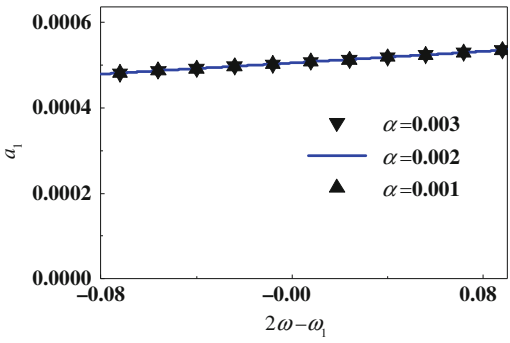

Fig. 3 The primary-harmonic amplitude

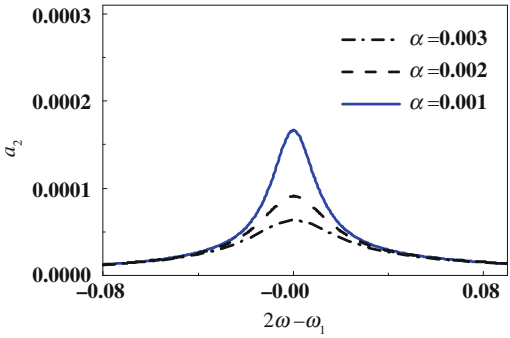

Fig. 4 The second superharmonic amplitude

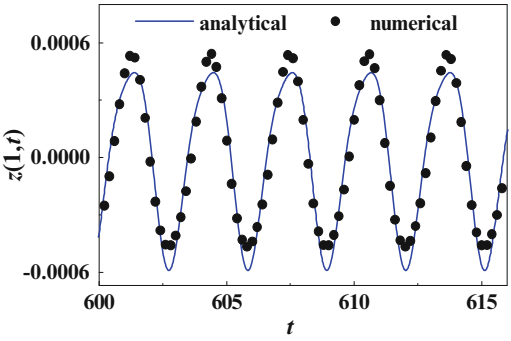

Fig. 5 The time history at $\omega = 2.03$

When $\alpha = 0.001$, $\beta = 0.001$, and $\omega = 2.03$, the time history of Eq. (18) can be computed out from the classical fourth-order Runge-Kutta method. Figure 5 illustrates the comparison between the numerical steady-state motion (dots) and the analytical results (line) based on Eq. (19). They qualitatively coincide with each other on the second-order superharmonic resonance.

Figure 6 shows the analytical steady-state motion (23) and those numerical results on the third-order superharmonic resonance where $\alpha = 0.001$, $\beta = 0.1$, and $\omega = 1.37$. It can be seen that these values are almost the same because three time scales are used here, instead of two time scales. In addition, it is obvious that the superharmonic and primary-harmonic amplitudes both grow with increased excitation amplitude.

Figures 7 and 8 illustrate the effects of viscosity on a_1 and a_3, respectively, where $\beta = 0.1$. The solid, dashed, and dashed-dotted lines stand for the analytical results (24), and the dotted line is their stability boundaries. An evident resonance occurs when 3ω approaches ω_1. The third superharmonic resonance can be employed to harvest energy at a low frequency. However, the resonant frequency is always larger than one third of the first natural frequency attributing to the electromechanical coupling.

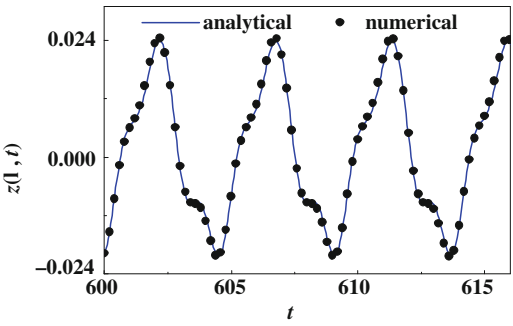

Fig. 6 The time history at $\omega = 1.37$

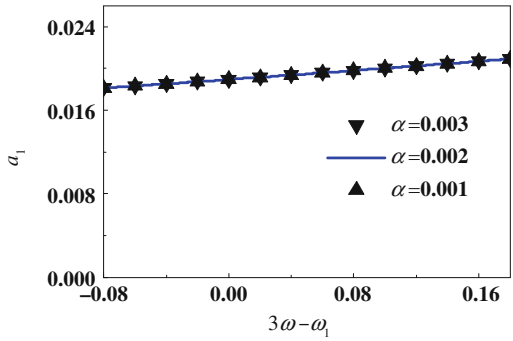

Fig. 7 The primary harmonic amplitude

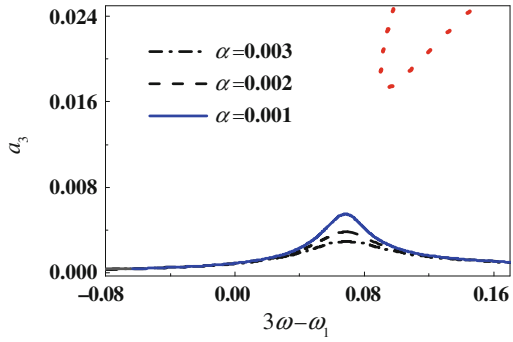

Fig. 8 The third superharmonic amplitude

5 Conclusions

This paper provides a way to solve an integro-partial differential equation with nonlinear boundary conditions. Galerkin method is developed to convert it into a set of ordinary differential equations. Weight functions are chosen at first, prior to trial functions. Then, the truncated governing equation can be computed by the numerical Runge-Kutta method and the analytical method of multiple time scales.

The proposed methodology is used to solve a cantilevered piezoelectric energy harvester. The second- and third-order superharmonic resonances are both ana-

lyzed. Their primary-harmonic amplitudes are independent of damping, while the superharmonic amplitudes both decrease with increased viscosity coefficient. In general, a small damping along with large excitation amplitude leads to an obvious superharmonic resonance.

Acknowledgments The work was supported by Hainan Provincial Natural Science Foundation (No. 118QN183) and the National Natural Science Foundation of China (No. 11602131).

References

1. Masana, R., Daqaq, M.F.: Energy harvesting in the super-harmonic frequency region of a twin-well oscillator. J. Appl. Phys. **111**(4), 044501 (2012)
2. Abdelkefi, A., Barsallo, N.: Comparative modeling of low-frequency piezomagnetoelastic energy harvesters. J. Intel. Mater. Syst. Str. **25**(14), 1771–1785 (2014)
3. Challa, V.R., Prasad, M.G., Shi, Y., Fisher, F.T.: A vibration energy harvesting device with bidirectional resonance frequency tunability. Smart Mater. Struct. **17**(1), 015035 (2008)
4. Challa, V.R., Prasad, M.G., Fisher, F.T.: Towards an autonomous self-tuning vibration energy harvesting device for wireless sensor network applications. Smart Mater. Struct. **20**(2), 025004 (2011)
5. Tang, L.H., Yang, Y.W.: A nonlinear piezoelectric energy harvester with magnetic oscillator. Appl. Phys. Lett. **101**(9), 094102 (2012)
6. Abdelkefi, A., Barsallo, N.: Nonlinear analysis and power improvement of broadband low-frequency piezomagnetoelastic energy harvesters. Nonlinear Dynam. **83**(1–2), 41–56 (2016)
7. Kim, P., Yoon, Y.J., Seok, J.: Nonlinear dynamic analyses on a magnetopiezoelastic energy harvester with reversible hysteresis. Nonlinear Dynam. **83**(4), 1823–1854 (2016)
8. Sedighi, H.M., Shirazi, K.H.: A new approach to analytical solution of cantilever beam vibration with nonlinear boundary condition. J. Comput. Nonlin. Dyn. **7**(3), 034502 (2012)
9. Zhang, G.C., Chen, L.Q., Ding, H.: Forced vibration of tip-massed cantilever with nonlinear magnetic interactions. Int. J. Appl. Mech. **6**(2), 1450015 (2014)

Study on Operational Energy Model Construction

Katsuhiko Kuroda

1 Introduction

Automotive industry required for improving the fuel consumption is lighting the weight of car. Accordingly, vibro-acoustic analysis to the high frequency is desired by using high stiffness thin plate which is thinner than conventional one. For systems with many resonant modes, the dynamic response is often analyzed using statistical energy analysis (SEA) [1]. We have developed a structural design process on the basis of experimental SEA for reducing structure-borne sound [2], the efficiency of which has been verified by applying it to various machines. The process identifies which internal loss factors (ILFs) or coupling loss factors (CLFs) should be changed to reduce the noise radiating from the machinery. However, problems such as devices are difficult to perform an excitation experiment and time-consuming experimental test, and the input is different between the excitation experiment and the actual operation. So, in this paper, we propose an operational energy model that does not require excitation experiments in the stationary state of the device and conduct basic studies by numerical analysis using FEM-based experimental SEA with three series coupled plates and compare it with the results of the conventional process described above. Furthermore, the effectiveness of the proposed method was examined by applying them to an actual handheld vacuum cleaner and comparing it with the results of the conventional method as well.

K. Kuroda (✉)
Nagasaki Institute of Applied Science, Nagasaki, Japan
e-mail: kuroda_katsuhiko@nias.ac.jp

S. Oberst et al. (eds.), *Vibration Engineering for a Sustainable Future*,
https://doi.org/10.1007/978-3-030-46466-0_27

2 Basic Theory

2.1 SEA Power Balance Equation

In SEA, a system is regarded as an assembly of subsystems, and consideration of the power balance between them leads to a basic set of SEA eqs. [1], $\mathrm{P} = \omega\,\mathbf{LE}$. Here, ω is the center angular frequency of the band, **E** is a vector containing the subsystem energies, and **P** is the external input power vector. The loss factor matrix, **L**, comprises internal loss factors (ILFs), $\eta_{i,i}$, and coupling loss factors (CLFs), $\eta_{i,j}$. Estimation of the ILFs and CLFs is referred to as the construction of the SEA model.

2.2 Structural Design Process for Reducing Structure-Borne Sound

The structural design process for reducing structure-borne sound developed by the authors [2] follows this procedure: (i) constructing an SEA model, (ii) identifying the external input power during operation, (iii) specifying the loss factors which should be changed in order to reduce the noise radiated from the machinery, and (iv) examining the structural design in order to realize the desired SEA parameters.

3 Proposal of Operational Energy Model

3.1 Identification of Input Power and Operational Energy Model Construction

Identification of input power and model construction on the operational energy model proposed by the author are the same as in the conventional method described in Sect. 2.2. After measuring the subsystem energy in the actual operation on the each subsystem, (1) the operating input power is predicted from the basic eq. $\mathbf{P} = \omega\mathbf{LE}$ with setting the value of ILF. Furthermore, (2) the CLF is predicted from Eq. (1) by APIM [3] from the measured operating subsystem energy normalized by predicted operating input power. (3) Predict the sensitivity and variation value due to the fluctuation of each loss factors for reducing the target vibrational energy, which are evaluated as in the conventional method [2], using the perturbation method.

$$\eta_{i,j} = \frac{E_{ij}/P_i}{\omega E_{ii}/P_i \times E_{jj}/P_j} \tag{1}$$

where E_{ij} is the energy of subsystem j when subsystem i is excited and P_i is the input power of subsystem i.

3.2 *Test Structure and Experimental Outline by Numerical Analysis*

The target structure to be compared with the conventional method is a three series coupled plate with a plate thickness of 3 mm, which is relatively close to the shape of the handheld vacuum cleaner shown in Fig. 3. All the edges of the plate were free supported. Fig. 1 (*a*) shows the common operational test of the conventional method and the proposed method. An excitation experiment was performed at two locations per subsystem since it is desirable to excite several different locations in order to excite all vibration modes in Fig. 1 from (*b*) to (*g*). The purple circle in Fig. 1 denotes the excitation location, and the magnitude of the excitation force in the conventional method in Fig. 1 from (*b*) to (*g*) is to set to be a unit force. Rotational frequencies of two motors are only known (the magnitude is unknown) from the measurement results of the vacuum cleaner of the real machine, and the magnitude of the excitation force on subsystem 2 is set to be 5 N from 440 Hz to 460 Hz and 1 N in other frequencies as an input of the main motor, and the magnitude of the excitation force on subsystem 3 is set to be 1 N from 45 Hz to 55 Hz as an input for the suction motor. The blue circles (five responses per subsystem) in Fig. 1 denote the response location. The material properties of the plate are as follows: Young's modulus $E = 3.5$ G Pa, material density $\rho = 1270$ kg/m^3, and Poisson's ratio $\nu = 0.36$. The mass of subsystems 1, 2, and 3 are 0.057 kg, 0.114 kg, and 0.038 kg, respectively. The velocity of the response is calculated for the range between 10 Hz and 800 Hz at 1 Hz steps, and the one-third octave band frequencies from 40 Hz to 630 Hz is calculated. The size of each element in the mesh is about 20 mm × 20 mm, which is sufficient to contain six nodes per bending wavelength up to 1.25 k Hz. The ILF is assumed to be 1% for all modes. The first natural frequency is estimated by FEM as 16.8 Hz except for the rigid mode.

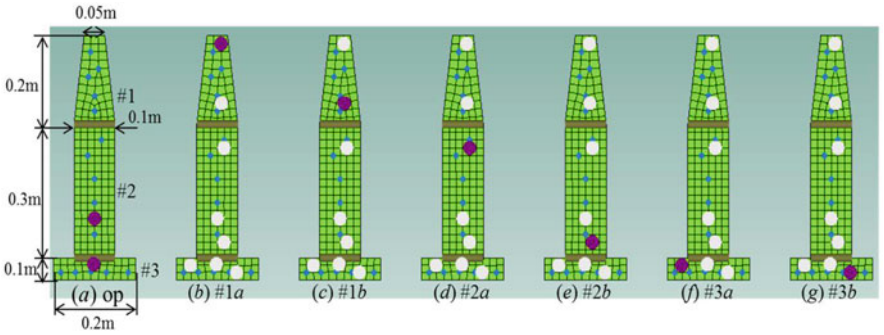

Fig. 1 Test-plate three series subsystem structure: points marked "•" are response points, and "•" are excitation points

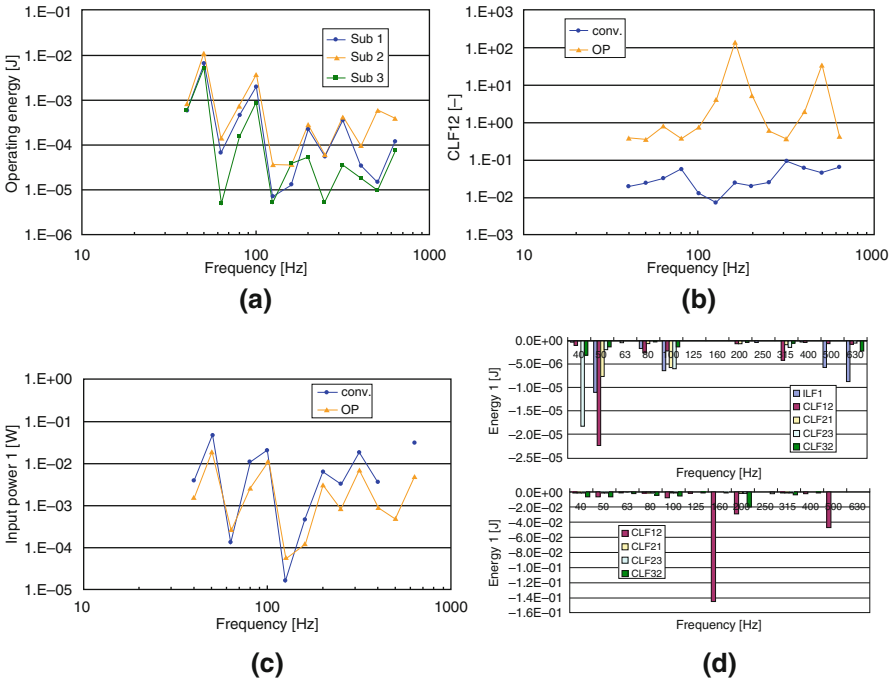

Fig. 2 Example of comparison results between the conventional method and the proposed method by analytical model. (**a**) Operating subsystem energy. (**b**) Coupling loss factor 12. (**c**) Input power of subsystem 1. (**d**) Variation value of subsystem 1 due to the fluctuation of loss factors (upper is conventional, lower is proposed)

Comparison Results Between the Proposed Method and Conventional Method

Figure 2 shows a comparison between the conventional method and the proposed method as to the vibration energy of subsystems in machine operation, the coupling loss factor, the input power, and the variation value of subsystem 1 for the operating energy due to the fluctuation of loss factors. The coefficient of variation of the loss factor was 10%. As a result of operating subsystem energy from Fig. 2a, a large peak is seen at 50 Hz, and it can be seen that the effect of the suction motor of subsystem 3 appears in all subsystems. In the comparison results of CLF 12 in Fig. 2b, the value of proposed method becomes relatively large compared to the conventional method, a reverse trend is obtained at several frequencies, which is left as a problem for future investigation. The comparison results of vibration input power of subsystem 1 in Fig. 2c show that they are almost consistent quantitatively, and the conventional method shows negative values, and there are unidentifiable frequencies. In the comparison results of variation value of subsystem 1 in Fig. 2d, in the conventional method, focusing on 50 Hz related to the suction motor of subsystem 3, the results of ILF 1 and CLF 12 show minus, and assuming that the original value of each loss factor is increased by 10%, this indicates that the result

of the operating energy of subsystem 1 decreases, and the result is considered to be appropriate. On the other hand, in the proposed method, the variation value of subsystem 1 is also reduced by increasing the value of CLF12.

3.3 Actual Test Structure and Experimental Outline by Real-World Operations

As shown in Fig. 3, the target structure is actual handheld vacuum cleaner in which three subsystems were connected in series. The experimental SEA model is constructed by using impulse hammers (Dytran; 5800SL) and accelerometers (PCB; 3524A, four responses per subsystem). The number of impulses (two excitations per subsystem) for constructing.

SEA model is set to 5, and the time for actual operation is set to 20 seconds, and the arithmetic mean of the power spectrum is calculated using a rectangular window function. The mass of subsystems 1, 2, and 3 are 0.3 kg, 1.745 kg, and 0.555 kg, respectively. The acceleration of the response is calculated for the range between 0 Hz and 2 k Hz at 1.25 Hz steps, and the one-third octave band frequencies from 40 Hz to 1.6 k Hz are calculated. The ILF is assumed to be 0.15% for all modes.

Comparison Results Between the Proposed Method and Conventional Method
Figure 4 shows an example results in real-world machine operation. The coefficient of variation of the loss factor was 10%. As a result of operating subsystem energy from Fig. 4a, a large peak is seen at 50 Hz, and it can be seen that the effect of the suction motor of subsystem 3 appears in all subsystems. At 500 Hz, the influence of the main motor of subsystem 2 appears not only in subsystem 2 but also in subsystem 1. In the comparison results of CLF 12 in Fig. 4b, the value of proposed method becomes relatively large compared to the conventional method. The comparison results of vibration input power of subsystem 1 in Fig. 4c show that the value of the proposed method appears relatively large to be similar to those of CLF. In the comparison results of variation value of subsystem 1 in Fig. 4d,

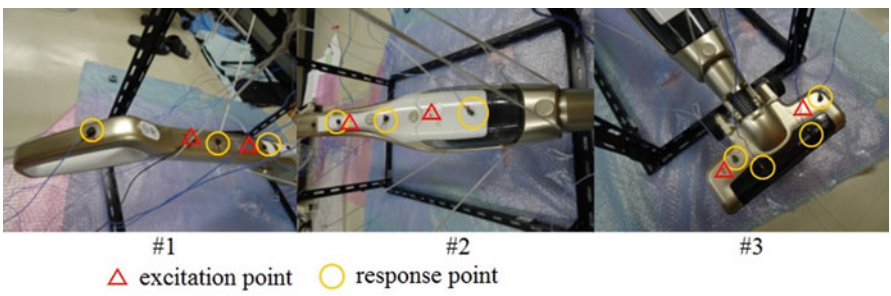

Fig. 3 Test cleaner

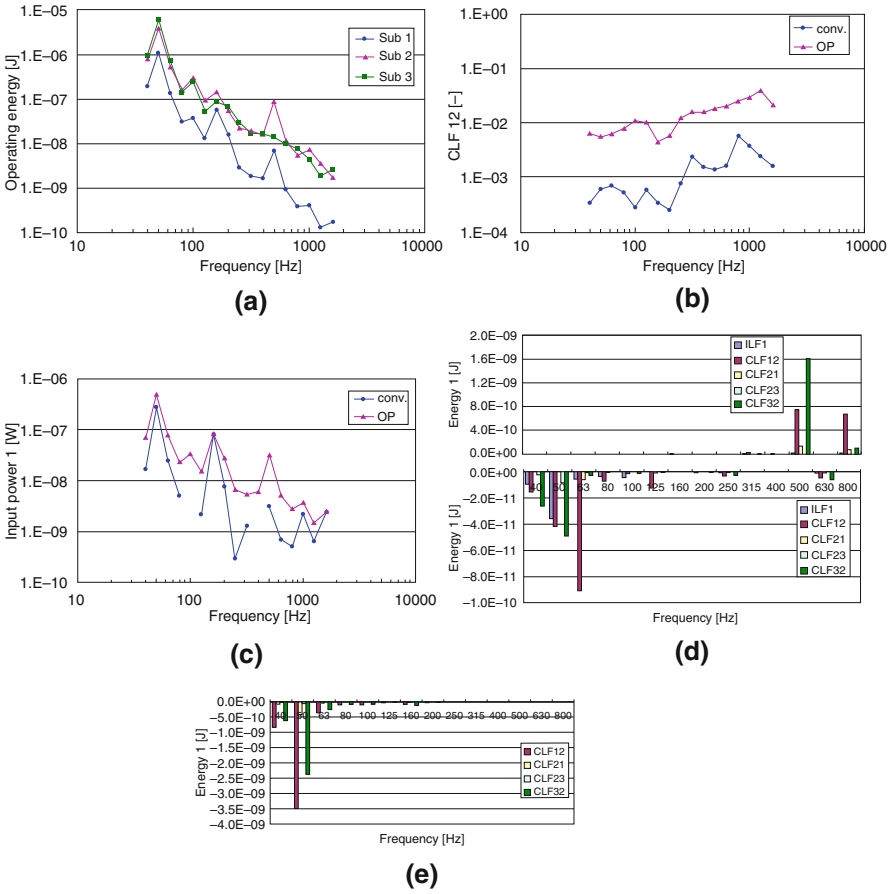

Fig. 4 Example of comparison results between the conventional method and the proposed method by experimental model. (**a**) Operating subsystem energy. (**b**) Coupling loss factor 12. (**c**) Input power of subsystem 1. (**d**) Variation value of subsystem 1 due to the fluctuation of loss factors by conventional method. (**e**) Variation value of subsystem 1 due to the fluctuation of loss factors by proposed method

the results of ILF 1 and CLF 12 are negative at 50 Hz; the results are reasonable. The result of CLF32 is positive at 500 Hz, and decreasing the value of CLF32 indicates that the result of operating energy of subsystem 1 decreases, and the result is considered to be appropriate. On the other hand, in the proposed method in Fig. 4e, the same tendency as the conventional method is shown at 50 Hz.

4 Conclusions

In this paper, we propose an operational energy model that does not require excitation experiments in the stationary state of the device and conduct basic studies and compare the conventional method by numerical analysis using FEM-based experimental SEA with simple three series coupled plates. Furthermore, the effectiveness of the proposed method was examined by applying them to an actual handheld vacuum cleaner and comparing it with the results of the conventional method as well. Although there is a problem in case of the device whose ILF value is unknown, the effectiveness of the proposed method is shown.

Acknowledgments This research was supported by SUZUKI Foundation and Nagasaki Institute of Applied Science of Institute for Innovative Science and Technology. We thank them for their assistance.

References

1. Lyon, R.H.: Statistical Energy Analysis of Dynamical Systems Theory and Application. MIT Press (1975)
2. Yamazaki, T., Kuroda, K.: The method of application of SEA in structural design process for reducing structure-borne noise in machinery Part1: general procedure. Mechanics. **28**(3), 69–75 (2009)
3. Lalor N.: Practical Considerations for the Measurement of Internal and Coupling Loss Factors on Complex Structures, ISVR Technical Report No.182, (1990)

Vibration-Based Uniform Curvature Piezoelectric Energy Harvester

Sinwoo Jeong and Hong Hee Yoo

1 Introduction

A vibration-based piezoelectric energy harvester (PEH) is known as one of the promising technologies for realizing self-powered wireless sensor nodes. As shown in Fig. 1a, the sensor node is usually installed on a surface of vibrating sources, and the sensor node anatomy is as Fig. 1b. As can be seen in Fig. 1b, an allowed space for the energy harvester is not sufficient. Therefore, the harvester has to be as compact as possible, and the allowed design space is defined as a cuboid having a size of $D_{width} \times D_{length} \times D_{height}$ in this study (Fig. 1c).

In this study, a uniform curvature PEH (UCPEH) is proposed. The main feature of the UCPEH is that it is deflected with a uniform curvature, whereas the conventional cantilever-shaped PEH (CCPEH) shows a high curvature near a fixed-end and an almost zeros curvature at a tip. Therefore, the UCPEH could have much better durability due to its lower maximum stress than that of the CCPEH. In other words, the UCPEH could have much higher power generation performance when both UCPEH and CCPEH are in the same maximum stress condition. For the purpose of numerical analyses, mathematical models for both UCPEH and CCPEH are developed based on the Ritz method [1, 2] for beams, and performance comparisons are conducted in this study.

S. Jeong · H. H. Yoo (✉)
Department of Mechanical Convergence Engineering, Hanyang University, Seoul, South Korea
e-mail: hhyoo@hanyang.ac.kr

S. Oberst et al. (eds.), *Vibration Engineering for a Sustainable Future*,
https://doi.org/10.1007/978-3-030-46466-0_28

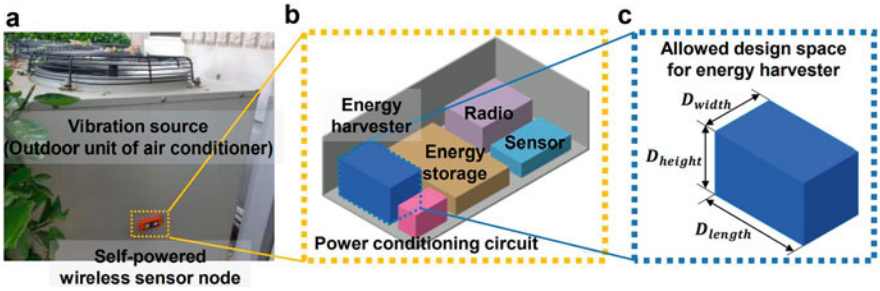

Fig. 1 (**a**) Outdoor unit of air conditioner as a vibration source and wireless sensor node, (**b**) wireless sensor node anatomy, and (**c**) allowed design space for energy harvester

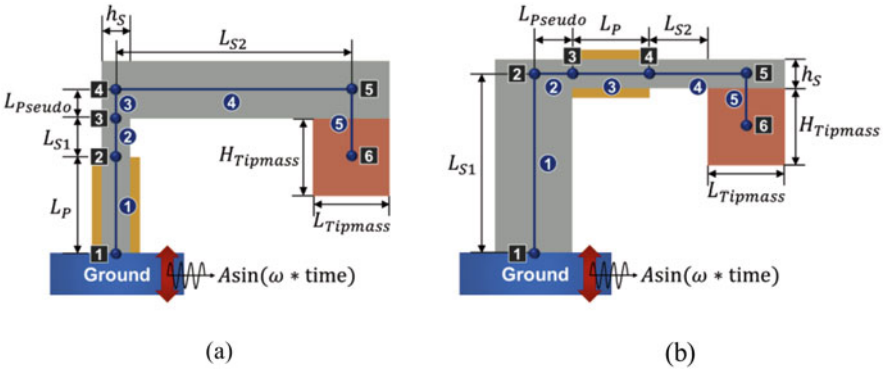

Fig. 2 Configurations of (**a**) UCPEH and (**b**) CCPEH

2 Mathematical Modeling

The structures are mathematically modeled with the 2D Euler beam elements, and a piezoelectric effect is mathematically modeled based on the process given in the previous paper [3–6]. It is assumed that the ground undergoes transverse vibration as a sinusoidal function having a magnitude of 2 m/s^2 and frequency of ω. Here, a range of ω is usually under 200 Hz in a real life.

The configurations of the UCPEH and CCPEH are shown in Fig. 2. In the figure, the yellow, gray, and red parts are piezoelectric material, substrate, and tip mass. The numbers in black squares and blue circles denote node and element numbers, respectively. Here, we have seven design variables: L_P, L_{S1}, L_{Pseudo}, L_{S2}, $H_{Tipmass}$, h_S, and R which are a load resistance connected to the piezoelectric plates. Other properties including $L_{Tipmass}$, material, and piezoelectric properties have constant values that correspond to the values of lead (for tip mass), polylactic acid (for substrate), and PZT-5H (for piezoelectric material).

One thing that should be noted in this model is that the elements 2 and 5 are pseudo parts such that they only rigidly connect the two side nodes of the elements,

and it is assumed that the elements have almost zero density and infinite Young's modulus. Additionally, for the purpose of modeling the tip mass, mass and mass moment of inertia properties are assign to node 6 when deriving the equations of motion.

3 Numerical Examples

In this study, it is assumed that the allowed design space, mass, volume of the piezoelectric material, and maximum stress at piezoelectric material are $10\times40\times40$ mm^3, 10 g, 100 mm^3, and 28 MPa. Each UCPEH and CCPEH were designed using the optimization algorithm under the given constraints. As a result, frequency response functions for the power and maximum stress are given in Fig. 3a, b, respectively.

As expected in the start of this paper, the UCPEH shows much higher power response in the entire frequency region (Fig. 3a). In the stress results (Fig. 3b), it should be noted that the stress constraint is not active in both results. It could mean that both systems have room for accepting more loads, i.e., higher magnitude of the input acceleration or heavier tip mass. However, the former is not a design variable, and the latter would be not desirable in some cases.

4 Conclusions

In this study, a new configuration of vibration-based piezoelectric energy harvester, so called UCPEH, is developed in this study. Due to the special feature of proposed configuration, the higher curvature is allowed in the UCPEH without exceeding the upper limit of the maximum stress value. As a result, the power generation

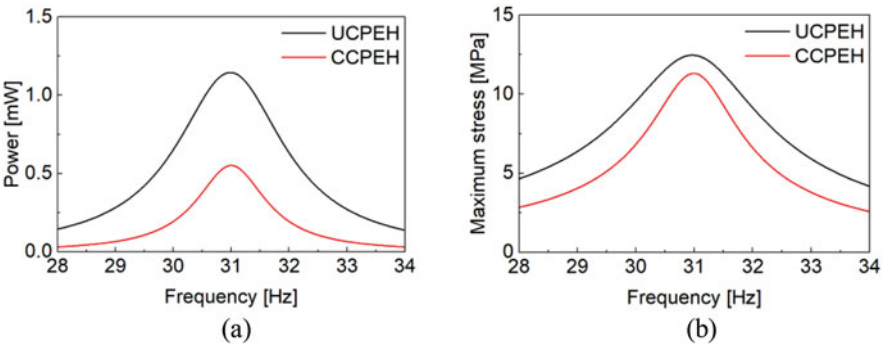

Fig. 3 Frequency response functions for (**a**) power and (**b**) maximum stress

performance of the proposed UCPEH is about 107% higher than that of the CCPEH under the same conditions.

References

1. Jeong, S., et al.: Electromechanical modeling and power performance analysis of a piezoelectric energy harvester having an attached mass and a segmented piezoelectric layer. Smart Mater. Struct. **26**(3), 035035 (2017)
2. Jeong, S., Yoo, H.H.: Flexibility modeling of a beam undergoing large deflection using the assumed mode method. Int. J. Mech. Sci. **133**, 611–618 (2017)
3. Jeong, S., Yoo, H.H.: Nonlinear structural analysis of a flexible multibody system using the classical Rayleigh–Ritz method. Int.J.of Nonlin. Mech. **110**, 69–80 (2019)
4. Erturk, A., Inman, D.J.: A distributed parameter electromechanical model for cantilevered piezoelectric energy harvesters. J. Vib. Acoust. **130**(4), 041002 (2008)
5. Erturk, A., Inman, D.J.: Issues in mathematical modeling of piezoelectric energy harvesters. Smart Mater. Struct. **17**(6), 065016 (2008)
6. Erturk, A., Inman, D.J.: On mechanical modeling of cantilevered piezoelectric vibration energy harvesters. J. Intell. Mater. Syst. Struct. **19**(11), 1311–1325 (2008)

Effect on Rocking Vibration Due to Characteristics Uncertainty of Three-Dimensional Seismic Isolation System

Cocoro Seo, Satoshi Fujita, and Shigeki Okamura

1 Introduction

Many earthquakes have occurred in Japan. The seismic design is one of the important matters to be considered in the safety design of the structures. High safety is necessary for the important structures such as nuclear facilities and so on. The seismic isolation system in the horizontal direction has been investigated, because the seismic loading on the structures can be reduced by seismic isolation systems. However, seismic conditions in Japan are changing, and the vertical seismic conditions have become more severe. As a result, the vertical seismic loading on the structures has been increased. For example, fast reactor, next-generation reactor, has internal device that is sensitive to the vertical vibration.

For that reason, in order to secure earthquake resistance in the next-generation nuclear power plants, the adoption of the three-dimensional seismic isolation system is being considered [1, 2]. The adoption of the three-dimensional seismic isolation system is effective to decrease the seismic force not only horizontally but also vertically. When the vertical frequency with the three-dimensional isolation system is low, the rocking vibration occurs [3]. In the case of about 3 Hz in vertical frequency, the response in vertical direction is reduced, and rocking vibration is

C. Seo (✉)
Department of Mechanical Engineering, Graduate School of Tokyo Denki University, Tokyo, Japan
e-mail: 18kmk16@ms.dendai.ac.jp

S. Fujita
Department of Mechanical Engineering, Tokyo Denki University, Tokyo, Japan
e-mail: sfujita@cck.dendai.ac.jp

S. Okamura
Department of Mechanical Engineering, Toyama Prefectural University, Toyama, Japan
e-mail: okamura@pu-toyama.ac.jp

S. Oberst et al. (eds.), *Vibration Engineering for a Sustainable Future*,
https://doi.org/10.1007/978-3-030-46466-0_29

negligible [4]. However, rocking vibration also occurs due to the deviation of the center of gravity and the center of stiffness, which is the central point of the vertical stiffness. The vertical stiffness of the three-dimensional seismic isolation system varies due to manufacturing tolerances and so on. For that reason, the rocking vibration probably occurs due to uncertainty of characteristics of the vertical stiffness of the three-dimensional seismic isolation system. This paper describes the effect on rocking vibration due to uncertainty of vertical characteristics of three-dimensional seismic isolation system.

2 Analytical Method

In this section, the analysis model and the analysis method will be explained. In this study, the effect on rocking vibration and isolation performance of structure is investigated in terms of probabilistic by Monte Carlo simulation. The analysis model assumes a nuclear power plant. Because a nuclear power plant is bilateral symmetrical, the center of gravity is the center of figure. The vertical stiffness is varied to confirm the effect on rocking vibration. Thus, the vertical stiffness is probabilistically varied. The rocking vibration and seismic isolation performance are investigated by repeating the analysis.

2.1 Analytical Model

The analysis model is a one mass point model as shown in Fig. 1. The model has three degree of freedom: horizontal X, vertical Z, and rotation θ. Table 1 shows analysis model parameters. The parameters were set with reference to the research on nuclear power plants [5]. The number of seismic isolation devices is 25. The seismic isolation devices are arranged at uniform intervals within the left end to the right end in the horizontal direction (X). Equations (1)–(3) show the equation of motion. Here, M is mass, K_h is horizontal stiffness, K_v is vertical stiffness, C_h is horizontal damping, C_v is vertical damping, l_n is the distance from the center of gravity position to the seismic isolation device, and h_1 is the height of the center of gravity position.

$$M\ddot{x}+\sum_{i=1}^{n} C_{hi}\left(\dot{x}+h_1\dot{\theta}\right)+\sum_{i=1}^{n} K_{hi}\left(x+h_1\theta\right)=-M\ddot{Z}_H \tag{1}$$

$$M\ddot{z}+\sum_{i=1}^{n} C_{vi}\left(\dot{z}+l_i\dot{\theta}\right)+\sum_{i=1}^{n} K_{vi}\left(z+l_i\theta\right)=-M\ddot{Z}_V \tag{2}$$

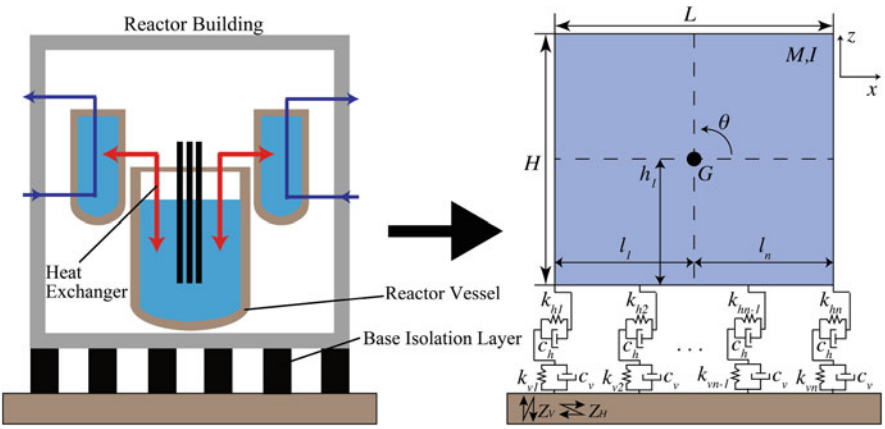

Fig. 1 Analytical model

Table 1 Analytical model parameters

Natural period horizontal [s]	3.4
Natural frequency of vertical [Hz]	3
Mass: M [kg]	5.11×10^8
Structure height: H [m]	100
Structure width: L [m]	100
Height of center of gravity: h_I [m]	50

$$I\ddot{\theta}+\sum_{i=1}^{n}C_{hi}\dot{x}h_1+\sum_{i=1}^{n}K_{hi}xh_1+\sum_{i=1}^{n}C_{vi}\dot{z}l_i+\sum_{i=1}^{n}K_{vi}zl_i + \left(\sum_{i=1}^{n}C_{hi}h_1^2+\sum_{i=1}^{n}C_{vi}l_i^2\right)\dot{\theta}+\left(\sum_{i=1}^{n}K_{hi}h_1^2+\sum_{i=1}^{n}K_{vi}l_i^2\right)\theta=0 \quad (3)$$

2.2 Input Seismic Wave

A Kobe NS/UD wave shown in Fig. 2 is used as input seismic wave [6]. In this seismic wave, the maximum velocity in the horizontal direction was normalized to 1.0 m/s, and the maximum velocity in the vertical direction was normalized to 0.5 m/s. This seismic wave assumes a large seismic wave.

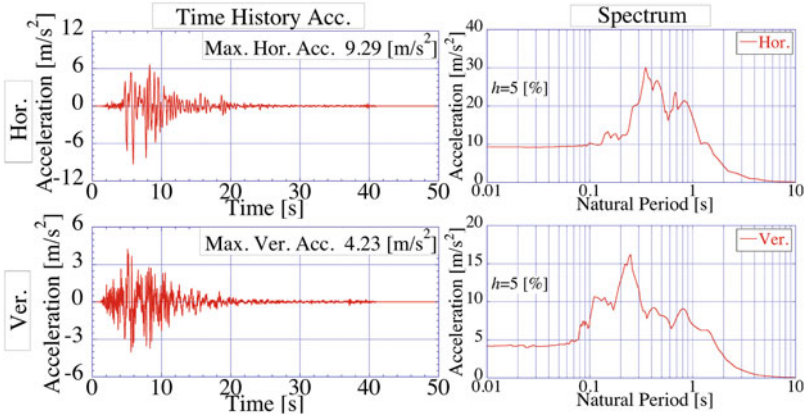

Fig. 2 Input seismic wave

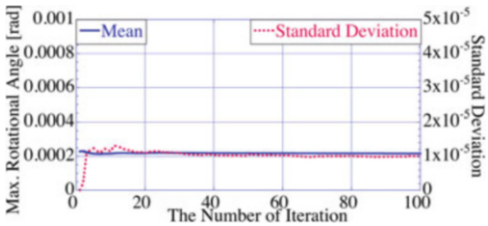

Fig. 3 Convergence of mean and standard deviation max. Response of rotation angle

2.3 Parametric Condition

Vertical Stiffness of the Seismic Isolation System As the uncertainty of the characteristics of the seismic isolation system, the variation is added to the vertical stiffness of each seismic isolation system. The variation of the vertical stiffness of the rubber bearing is about 20% from the reference value, and the variation is normal distribution [7]. For that reason, in this paper, it is assumed that the variation of vertical stiffness is normally distributed. The vertical stiffness is determined by coefficient of variation from 0.1 to 0.4 in 0.1 steps. In addition, the total value of vertical stiffness is set constant.

Determination of Number of Analysis In this study, the vertical stiffness is optionally set based on coefficient of variation. For that reason, we investigate the number of analyses, for which the average and the standard deviation of the maximum rotation angle *of structure* converges. Figure 3 shows the state of convergence of the maximum rotation angle when the coefficient of variation is 0.4. The horizontal axis shows the number of analysis, and the vertical axis shows the average and standard deviation of the maximum rotation angle. In Fig. 3, the mean and the standard deviation of the analysis result are both converge at more than 60 iterations. For that reason, in this paper, the number of analysis is set to 60 iterations.

3 Analysis Result

3.1 Maximum Rotation Angle

Figure 4 shows the maximum rotation angle and its average when the coefficient of variation of the vertical stiffness of the seismic isolation device is 0.1–0.4. In addition, the range of 1σ to 3σ of the maximum rotation angle is shown. Furthermore, the result of nominal condition that does not change the stiffness of the seismic isolation system is shown. In Fig. 4, as the coefficient of variation of the vertical stiffness of the seismic isolation system increases, the dispersion of the rocking vibration increases. However, the effect on the structure is considered to be small, because the order of the maximum rotation angle is about 10^{-4}.

3.2 Maximum Response Acceleration

Figure 5 shows the horizontal and the vertical maximum response acceleration and its average when the coefficient of variation of the vertical stiffness of the seismic isolation device is 0.1–0.4. In addition, the range of 1σ to 3σ of the maximum rotation angle is shown. Furthermore, the result of nominal condition that does not change the stiffness of the seismic isolation system is shown. In the horizontal results shown in Fig. 5, as the coefficient of variation of the vertical stiffness of the seismic isolation system increases, the dispersion of horizontal maximum response acceleration increases. The variation of the response is less than 2%, when compared to the result of 3σ with the result of nominal condition. For the reason, the effect on the horizontal acceleration due to the rocking vibration is small. In the vertical results shown in Fig. 5, as the coefficient of variation of the vertical stiffness of the seismic isolation system increases, the dispersion of vertical maximum response acceleration increases. The variation of the response is less than 1%, when compared to the result of 3σ with the result of nominal condition. For the reason, the effect on the vertical acceleration due to the rocking vibration is small.

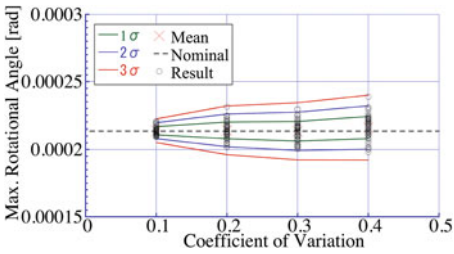

Fig. 4 Max. response of rotation angle due to uncertainty of vertical stiffness

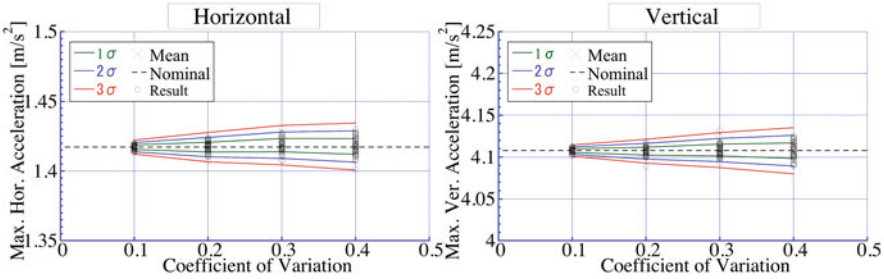

Fig. 5 Max. response of acceleration due to uncertainty of vertical stiffness

4 Conclusion

In this paper, we investigated the effect on rocking vibration due to uncertainty of vertical stiffness of three-dimensional seismic isolation system. As the result, as the uncertainty of the vertical stiffness increases, the response of the structure increases. However, even with the uncertainty of vertical stiffness, the effect on the response of the structure is small. Therefore, the effect of the uncertainty of the vertical stiffness on the structure is negligible.

References

1. Fujita, S., et al.: Shake Table Test on Three-Dimensional Vibration Isolation System Comprising Rubber Bearing and Coil Springs, Eleventh World Conference on Earthquake Engineering, Paper No.276 , 1996
2. Miyagawa, T., et al.: Research and Development of Three-Dimensional Seismic Isolation System Part1 Development Program and Design Requirement for Three- Dimensinal Seismic Isolation System, AIJ Annual Meeting, 2018. [in Japanese]
3. Fujita, S., Minagawa, K., Kodaira, T.: Required Properties of Seismic Isolation System for Nuclear Power Plants, ASME 2010 Pressure Vessels & Piping Division, PVP2010-25409, July 18–28, 2010
4. Miyagawa, T, et al.: Research and Delevopment of Three Dimensional Seismic Isolation System Utilized Coned-Disc-Springs with Rubber Bearings, ASME 2017 Pressure Vessels & Piping Conference, PVP2017-65549, July 16–20, 2017
5. Fukasawa, T., et al.: Research and Development of Three-Dimensional Isolation System for Sodium-Cooled Fast Reactor (PART 1) Proposal of Analytical Models Based on Loading Tests, Proceedings of the ASME 2018 Pressure Vessels and Piping Conference, 2018
6. Japanese Meteorological Agency Homepage.: https://www.data.jma.go.jp/svd/eqev/data/kyoshin/jishin/hyogo_nanbu/index.html. Last accessed 01 Nov 2019
7. The Japan Society of Seismic Isolation.::[sekkeishanotameno menshin seishinkozohan-dobukku], Asakura Publishing Co., Ltd., Tokyo, 127-128, ISBN978-4-254-26642-9, 2014. [in Japanese]

Part V
Multibody Dynamics

A Study on Coupled Vibration Between Flexible Body and Rigid Body in Tethered System

Daiki Ishihsra, Yoshiaki Terumichi, and Shoichiro Takehara

1 Introduction

A tethered system that connects multiple apparatus by a flexible body, such as a cable, has high utility for exploration activity and work in extreme environments out of the normal reach of people, such as the deep ocean and space. In these environments, where the cost of conveying equipment is high, it is possible to reduce costs with miniaturization and weight reduction. However, experiments need to be conducted over a long period of time with sufficient verification to ensure that the dynamics analysis by computers is effective in terms of predictive control and design development. In a tethered system, because the rigid bodies and the flexible body with large deformation interact with each other through joints between them, the whole system shows complicated behavior. Therefore, to elucidate motion in a coupled system, it is necessary to understand the movement of the whole system, including coupled movement between flexible and rigid bodies. Because of this, it is modeled as a problem of flexible multibody dynamics with large deformation.

Toward the elucidation of the motion mechanism of a coupled multibody system with both flexible and rigid bodies, the purpose of this study was to model and formulate a tethered system as a coupled system and to consider coupling vibration between flexible and rigid bodies according to the numerical results.

D. Ishihsra (✉)
Division of Mechanical Engineering, Graduate School of Science and Technology, Sophia University, Tokyo, Japan
e-mail: hrdn25@eagle.sophia.ac.jp

Y. Terumichi · S. Takehara
Department of Engineering and Applied Sciences, Sophia University, Tokyo, Japan

S. Oberst et al. (eds.), *Vibration Engineering for a Sustainable Future*,
https://doi.org/10.1007/978-3-030-46466-0_30

2 Modeling and Formulation

In this paper, the analytical model for the tethered system is a flexible body connecting two rigid bodies. The flexible body is modeled by an absolute nodal coordinate formulation (ANCF) [1, 2], which is a nonlinear finite element method. Moreover, the motion of the tethered system was evaluated using numerical simulation and fast Fourier transform analysis.

2.1 Absolute Nodal Coordinate Formulation (ANCF)

In this section, we describe the formulation of planar motion of the flexible body with large deformation by using ANCF. This approach can express motion of the flexible body with high precision in an absolute coordinate system by using global slopes that are obtained as the derivatives of the absolute displacements.

The global displacement of an arbitrary element i on the flexible body is written as

$$\mathbf{r^i} = \begin{bmatrix} r_1^{\mathrm{i}} & r_2^{\mathrm{i}} \end{bmatrix}^{\mathbf{T}} = \mathbf{S^i q^i} \tag{1}$$

where $\mathbf{r^i}$ is the global position vector for an arbitrary point on the flexible element, $\mathbf{S^i}$ is the element shape function, and $\mathbf{q^i}$ is the vector of the absolute nodal coordinates and slopes of the element.

The kinetic energy of the element is defined as

$$T = \frac{1}{2}\int_{\mathrm{V}} \rho \dot{\mathbf{r}}^{\mathbf{T}} \dot{\mathbf{r}} dV \tag{2}$$

where ρ is the mass density and V is the volume of the element. The kinetic energy of the element is written as

$$T = \frac{1}{2}\dot{\mathbf{q}}^{\mathbf{i}\mathbf{T}} \mathbf{M^i} \dot{\mathbf{q}}^{\mathbf{i}} \tag{3}$$

where $\mathbf{M^i}$ is the constant mass matrix of the element. The elastic energy of the element is defined as

$$U = \frac{1}{2}\int_0^1 \left\{ \mathrm{EA}\left(\frac{\partial u_{\mathrm{l}}}{\partial x}\right)^2 + \mathrm{EI}\left(\frac{\partial^2 u_{\mathrm{t}}}{\partial x^2}\right)^2 \right\} \mathrm{dx} \tag{4}$$

where u_{l} and u_{t} are the horizontal and vertical deformation of the arbitrary point in the object coordinate system, respectively. The elastic force on the element $\mathbf{Q_k^i}$ is written as

$$\mathbf{Q}_{\mathbf{k}}^{\mathbf{i}} = \left(\frac{\partial U}{\partial \mathbf{q}^{\mathbf{i}}}\right)^{\mathrm{T}} \tag{5}$$

The above relations can be used to write the motion equation for all elements of the flexible body as

$$\mathbf{M}_{\mathbf{t}}\ddot{\mathbf{q}}_{\mathbf{t}} = \mathbf{Q}_{\mathbf{t}} \tag{6}$$

where $\mathbf{M_t}$ is the mass matrix, $\mathbf{q_t}$ is the vector for nodal coordinate, and $\mathbf{Q_t}$ is the vector for the elastic force, including the elastic force.

2.2 Modeling and Formulation of the Coupled System

The tethered system is assumed to be as follows:

- Two rigid bodies are coupled by a tether.
- The boundary condition at both ends of the fixed beam is given between the tether and the rigid bodies.
- The rigid bodies have rotary springs around their centers of gravity.

To take the constraint force into consideration, the motion equation is written as

$$\mathbf{M}\ddot{\mathbf{q}} + \mathbf{C}_{\mathbf{q}}^{\mathbf{T}}\boldsymbol{\lambda} = \mathbf{Q} \tag{7}$$

The governing equation, including boundary conditions of the whole system, is written as follows by using an augmented formulation [3] that is the basic solution of the multibody system:

$$\begin{bmatrix} \mathbf{M} & \mathbf{C}_{\mathbf{q}}^{\mathbf{T}} \\ \mathbf{C}_{\mathbf{q}} & \mathbf{0} \end{bmatrix} \begin{bmatrix} \ddot{\mathbf{q}} \\ \boldsymbol{\lambda} \end{bmatrix} = \begin{bmatrix} \mathbf{Q} \\ \boldsymbol{\gamma} \end{bmatrix} \tag{8}$$

where $\mathbf{M}$ is the mass matrix, $\mathbf{q}$ is the vector of nodal coordinate, $\mathbf{C}$ is the boundary condition, $\boldsymbol{\lambda}$ is the Lagrange multiplier, $\mathbf{Q}$ is the vector of the elastic force and external force of the whole system, and $\boldsymbol{\gamma}$ is defined as

$$\boldsymbol{\gamma} \equiv \mathbf{C}_{\mathbf{q}}\ddot{\mathbf{q}} = -\left(\mathbf{C}_{\mathbf{q}}\mathbf{q}\right)_{\mathbf{q}}\mathbf{q} - 2\mathbf{C}_{\mathbf{qt}}\mathbf{q} - \mathbf{C}_{\mathbf{tt}} \tag{9}$$

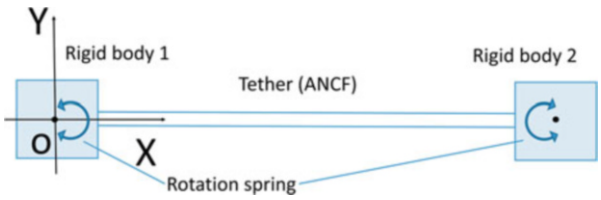

Fig. 1 Analytical model of the coupled system

Table 1 Numerical conditions for simulation

Component	Property	Case 1	Case 2
Tether	Material	Rubber	Polyethylene
	Young's modules [N/m^2]	5.0×10^6	1.3×10^9
	Density [kg/m^3]	960	
	Mass Mt [kg]	0.08	
	Length [m]	1	
	Diameter [m]	0.01	
Rigid body	Mass Mr [kg]	0.1	
	Height [m]	0.2	
	Width [m]	0.2	
	Rotary spring constant [Nm/rad]	10	
	Moment of inertia [kg $\cdot$ m^2]	5.0×10^{-4}	

3 Numerical Simulation and Discussion

In this section, the characteristics of the coupled system are discussed by solving the governing equation. At first, we will show two cases in which the states of coupled motion become significantly different when different tether stiffnesses are assumed.

Table 1 shows the analysis conditions for the two cases. Figures 2 and 3 show the frequency spectrum for rigid body rotation (red curve) and tether deflection (blue curve) for cases 1 and 2, respectively. The curves formed with short dashes are the natural frequency of the beam fixed at both ends. The vertical line shows the natural frequency of the rigid body and rotary spring model. In case 1, the frequencies of the tether deflection and rigid body rotation in the coupling model are almost equal to each of the natural frequencies. In contrast, in case 2, the frequencies in the coupling model are different from each of the natural frequencies. When the tether has high stiffness, the coupling effect between each element is strengthened; consequently, the frequencies in the tethered system should be considered as peculiar to the coupled system.

For the following discussion, to consider the coupling effect, the numerical results use the following conditions:

- The stiffness of the tether is low (stiffness of rubber is assumed).
- Initial velocity v_0 is small; in other words, the tether deflection is infinitesimal.

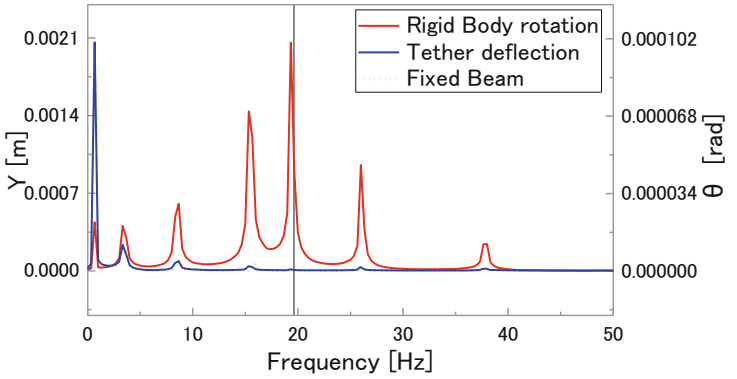

Fig. 2 Frequency spectrum for case 1

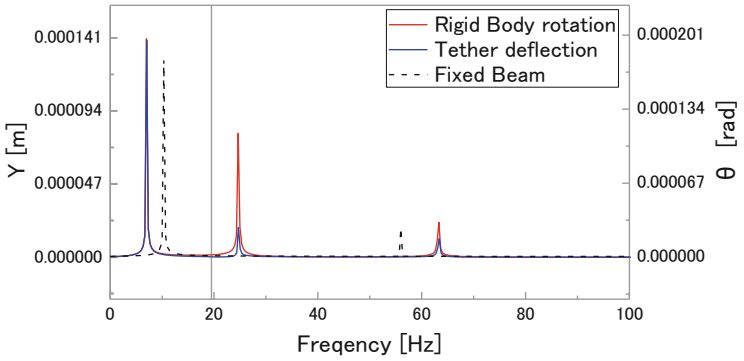

Fig. 3 Frequency spectrum for case 2

The parameter μ is defined as the mass ratio between the tether and rigid body. Other than the mass of the rigid bodies, the analysis conditions are the same as in case 1.

Figure 4 shows the frequency spectra of the rigid body rotation (solid curves) and tether deflection (short dashed curves) in each case. The vertical dashed lines show the natural frequencies of the rigid body-rotary spring model where the mass of the rigid bodies is the same. Examination of the rigid body rotation in the coupled system reveals vibration components with large amplitudes close to the natural frequencies of the rigid body and rotary spring model. In other words, there is a feature that significantly enhances the vibration mode of the tether having a frequency close to the natural frequency of the rigid body and rotary spring model.

Figure 5 shows the frequency spectra for rigid body rotation. The vertical axis indicates the amplitude of the vibration, and the horizontal axis indicates $f_n - f_r$, which is the frequency range centered about the natural frequencies of the rigid body-rotary spring model. At the rigid body rotation, the vibration components having frequencies close to f_r are excited.

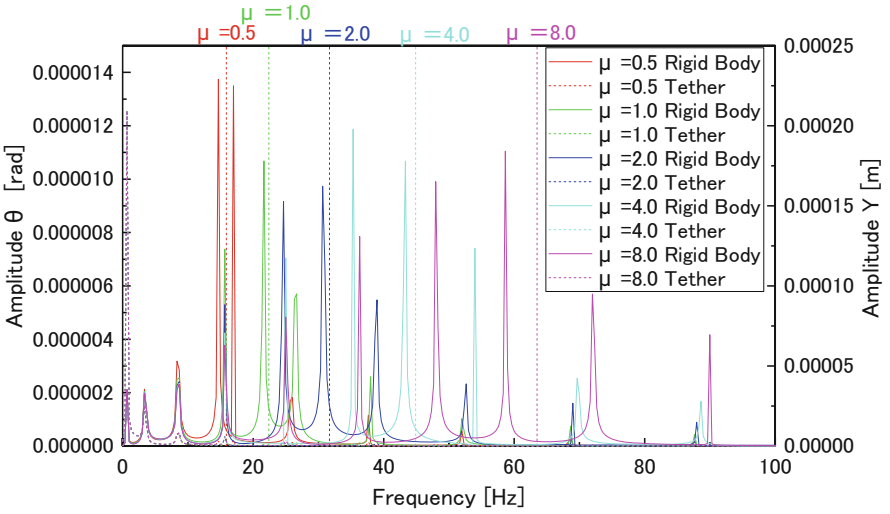

Fig. 4 Frequency spectra

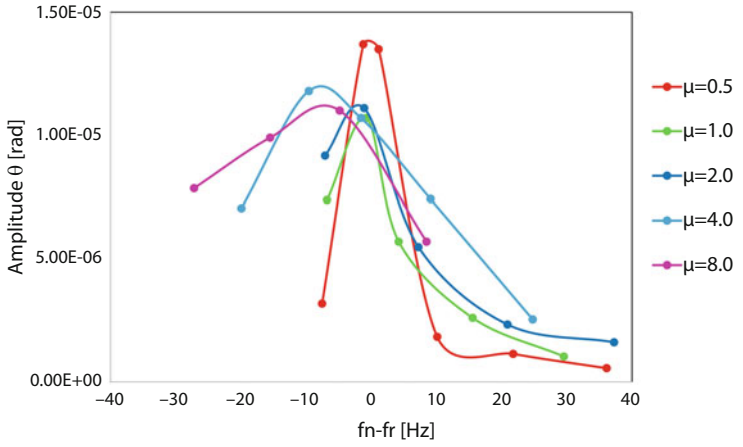

Fig. 5 Frequency spectra of rigid body having vertical axis $f_n - f_r$

4 Conclusion

This study numerically evaluated the coupled vibration between a flexible and rigid bodies. The strength of coupling between a flexible tether and rigid bodies depends on the elasticity of the tether. In the case where the tether has low stiffness, the frequencies of the flexible body and rigid bodies in the coupled system correspond approximately to each of the natural frequencies. In addition, rigid body rotation

has a feature that significantly enhances the vibration mode of the tether having a frequency close to the natural frequency of the rigid body-rotary spring model.

References

1. Michel Géradin, A.C.: Flexible Multibody Dynamics: A Finite Element Approach. Wiley, Liège, Belgium (2001)
2. Shabana, A.A.: Dynamics of Multibody Systems, 2nd edn. Cambridge University Press, Boca Raton, FL (1988)
3. Shabana, A.A.: Computational Dynamics, 2nd edn. John Wiley, Boca Raton, FL (2001)

Vibration Model for an Infant-Carriage System

Shinichiro Ota and Ryo Ota

Notation

z, θ	:	Linear vertical and rotational coordinates of the carriage
x_1, z_1, θ_1	:	Linear horizontal and vertical, and rotational coordinates of the infant's head
z_2	:	Linear vertical coordinate of the infant's torso
m, I, θ	:	Mass, moment of inertia, and pitch angle of the carriage
k_f, k_r, c_f, c_r	:	Spring constants and damping coefficients of the front and rear wheels
k_s, c_s	:	Spring constants and damping coefficients between the seat cushion and the infant
l_f, l_r	:	Distance from the front and rear wheels to the centroid of the carriage
l_1	:	Distance between the neck joint and the centroid of the head
l_2	:	Distance between the torso and the centroid of the baby carriage
m_1, I_1, m_2	:	Mass and moment of inertia of the head and torso
k_θ, c_θ	:	Spring constants and damping coefficients for the neck tilt
w_f, w_r	:	Vertical displacements from the front- and rear-wheel contact points to the road

S. Ota (✉)
Faculty of Computer Science and Systems Engineering, Okayama Prefectural University, Okayama, Japan
e-mail: ota@ss.oka-pu.ac.jp

R. Ota
Graduate School of Computer Science and Systems Engineering, Okayama Prefectural University, Okayama, Japan
e-mail: sk619004@ss.oka-pu.ac.jp

S. Oberst et al. (eds.), *Vibration Engineering for a Sustainable Future*,
https://doi.org/10.1007/978-3-030-46466-0_31

1 Introduction

An infant-carrying vehicle transmits mechanical vibrations from the road surface to the infant. Excessive vibrations have been observed on an infant dummy placed on a vehicle seat [1, 2]. Infants are particularly sensitive to mechanical motions owing to their large head-to-body mass ratio compared to adults [3], and because their joints are relatively underdeveloped. Excessive vibrations can therefore be a major safety concern. Reducing vibrations becomes an important issue [4], which depends significantly on the properties of the seat cushion. There are effective ways to study the seat characteristics relevant for infants. Theoretical parameters describing a seat cushion can be investigated by isolating the vibration characteristics associated with the infant passenger and constructing a theoretical model that reproduces the vibration phenomenon.

The purpose of this study is to develop a model describing the vibrations experienced by an infant seated in a carriage. We performed measurements in which a carriage carrying an infant passed over a bump and over a random surface. We also designed a vibration model and simulated the infant-carriage system. The model and simulation calculations were validated by comparisons with the experiments.

2 Measurement

Figure 1 shows the location of the measurement equipment on the carriage. The equipment consists of acceleration sensors, an analog-to-digital (AD) converter, a power supply for the AD converter, and a mobile computer. The acceleration sensors were placed on the axels of the front and rear wheels and on the seat, the head, and the torso. The subject was a 5-year-old boy weighing 16 kg and measuring 102 cm.

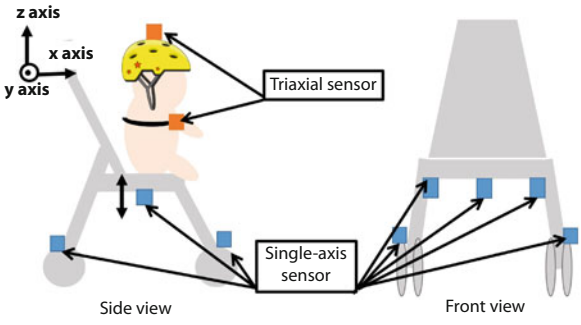

Fig. 1 The measurement system comprising acceleration sensors

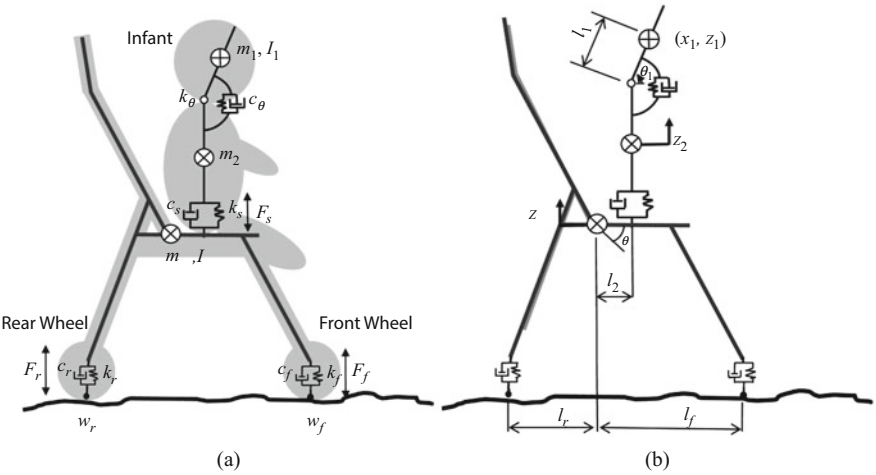

Fig. 2 Vibration model of the infant-carriage system, with its four degrees of freedom. (**a**) Mechanical properties. (**b**) Coordinate system

2.1 Vibration Analysis

We developed a customized model to investigate the vibrations experienced by an infant seated in the carriage system. Figure 2a and b depict the mechanical vibration model and its associated coordinate system and dimensions, respectively.

2.1.1 Infant-Carriage System

The infant-carriage system consists of front and rear wheels and the main frame structure. The wheels are modeled as springs coupled with a damper. The vehicle frame was also considered as a rigid body with its mass and moment of inertia located at its centroid. The equation of motion of the carriage system is

$$\begin{aligned} m\ddot{z} &= F_f + F_r - F_s \\ I\ddot{\theta} &= F_f l_f - F_r l_r - F_s l_2 \end{aligned} \tag{1}$$

$$\begin{aligned} F_f &= k_f\{w_f - (x - l_f\theta)\} + c_f\{\dot{w}_f - (\dot{x} - l_f\dot{\theta})\} \\ F_r &= k_f\{w_r - (x + l_r\theta)\} + c_r\{\dot{w}_r - (\dot{x} + l_r\dot{\theta})\} \\ F_s &= k_s\{(x + l_2\theta) - x_2\} + c_s\{(\dot{x}_1 + l_2\dot{\theta}) - \dot{x}_2\} \end{aligned} \tag{2}$$

Table 1 Mechanical properties, dimensions, and initial angles describing the infant's body

Mass	Dimension	Spring constant
$m = 3.2\,\mathrm{kg}$	$l_f = 0.34\,\mathrm{m}$	$k_f = 22.7\,\mathrm{kN/m}$
$m_1 = 13.7\,\mathrm{kg}$	$l_r = 0.26\,\mathrm{m}$	$k_r = 22.7\,\mathrm{kN/m}$
$m_2 = 1.9\,\mathrm{kg}$	$l_1 = 0.06\,\mathrm{m}$	$k_\theta = 3.88\,\mathrm{N{\cdot}m/rad}$
	$l_2 = 0.096\,\mathrm{m}$	
Inertia moment	Initial angle	Viscosity coefficient
$I = 0.288\,\mathrm{kg{\cdot}m^2}$	$\theta = 0.0°$	$c_f = 52.3\,\mathrm{N{\cdot}s/m}$
$I_1 = 0.00684\,\mathrm{kg{\cdot}\,m^2}$	$\theta_1 = 80.0°$	$c_r = 52.3\,\mathrm{N{\cdot}s/m}$
		$c_\theta = 0.0129\,\mathrm{Nm{\cdot}s/rad}$

2.1.2 Infant System

The parameters describing the body of the 5-year-old infant are the segment mass, the segment centroid, and the segment moment of inertia, as specified in Table 1.

Tilting about the neck region was modeled using a spring and a damping system. The equations of motion of the infant system are thus given by

$$\left.\begin{aligned} \ddot{\theta_1} &= A_1/A_3 \\ \ddot{z_2} &= A_2/A_3 \\ A_1 &= -m_1 l_1 \cos\theta \left(-k_f\left(z_2 - (z + \theta l_2)\right) - c_f\left(\dot{z_2} - (\dot{z} + \dot{\theta} l_2)\right)\right) \\ A_2 &= m_1 l_1 \cos\theta_1 \left(-k_\theta(\theta_1 - \theta_{1,0}) - c_\theta \dot{\theta_1}\right) \\ A_3 &= m_1 m_2 {l_1}^2 + {m_1}^2 {l_1}^2 \sin^2\theta_1 \end{aligned}\right\} \tag{3}$$

2.2 Analytical Condition

The four simultaneous second-order ordinary differential equations describing the infant-carriage system as a whole were solved using the Runge-Kutta-Gill method.

2.2.1 Transient Response

A single sinusoidal wave (amplitude 12 mm, wavelength 60 mm) was applied to the front and rear wheels as input. A numerical analysis was performed to determine the response to the input. The governing equations were solved 20,000 times with a step size of 0.001 s for an assumed carriage velocity of 0.8 m/s.

2.2.2 Frequency Response

The characteristics of the frequency response were examined by applying sinusoidal waveforms in the frequency range of 1 to 20 Hz. The total amplitude and the discrete

points of the frequency were 0.005 m and 50, respectively. The calculation was repeated 10,000 times with a step size of 0.001 s. The root mean square (RMS) values were calculated by the acceleration at each time step and used to represent the values of each frequency.

2.3 *Results and Discussion*

Figure 3 illustrates the vibrations experienced by the infant and by the carriage seat. The measurement in Fig. 3a shows a peak in the seat acceleration occurring around 0.01 s, after which the acceleration of the infant increases. This pattern corresponds to the front wheels passing over the bump at 0 s. There is a delay in the transmission of the vibration from the front wheels to the seat and from the seat to the infant. The body vibrates again at 0.8 s, after the initial vibrations in the infant, resulting from the rear wheels going over the bump.

The numerical analysis results in Fig. 3b show the peak in the seat acceleration occurring at approximately 0.01 and 0.8 s. The simulated behavior agrees with the measurements in showing the delayed vibration in the infant. However, the minimum simulated value for the acceleration is less than the measured value because the contact between the tire and the road surface was modeled as a spring-damper system, whereas this contact is in fact very intermittent in the real system. The simulated transient response shows consistency with the measurements.

Figure 4 displays the experimental and analytical results for the frequency response. The horizontal and vertical axes represent the frequency and the vertical acceleration ratio, respectively. The acceleration ratio of the infant equals the acceleration of the infant divided by that of the seat. Figure 4a shows some resonances in the infant measurement, with peaks at 2.3 and 7.6 Hz in the trace representing the horizontal head vibration. The horizontal vibration of the torso

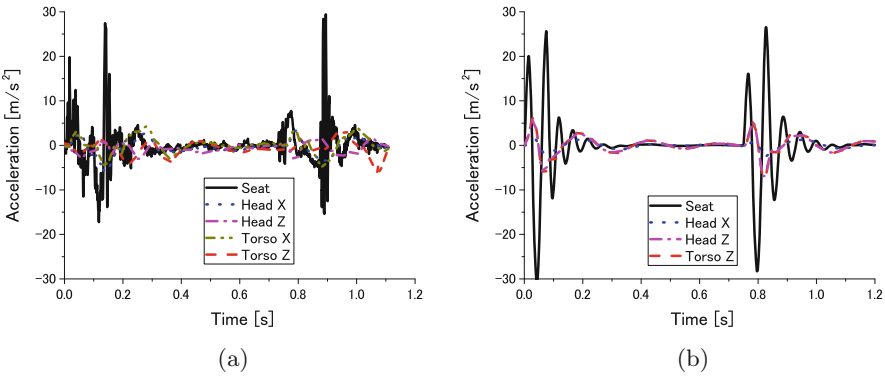

Fig. 3 Waveforms of the vehicle body and of the infant in the transient response. (**a**) Measurement. (**b**) Numerical analysis

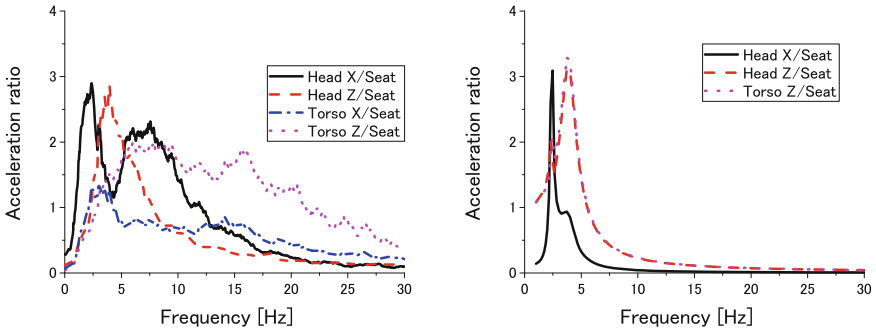

Fig. 4 Acceleration ratios in the frequency response of the infant's motion. (**a**) Measurement. (**b**) Numerical analysis

displays a local peak at 2.9 Hz. This peak presumably represents the same vibration mode in the head and the torso, given the agreement between the first peak of the head trace and the local peak of the torso trace. The peaks at 3.9 and 5.9 Hz indicate a resonance in the vertical vibrations in the head and torso traces.

On the other hand, the analysis results of Fig. 4b do not reproduce the second resonance in the longitudinal direction for the head motion, despite showing agreement with regard to the first resonance. This may be due to the horizontal motion of the torso not being fully considered. The amplitude magnification at the resonance in the torso was also found to differ from the measured value. As this factor, the torso vibrates vertically and horizontally by the vertical vibration transmitted from the vehicle body in measurement, but it is considered that a model considering only the vertical direction is used.

The above results suggest that, although the theoretical model reproduces the first resonance, it is less successful in reproducing the second resonance. In future work, we plan to develop the theoretical model to take into account the horizontal motion of the torso.

3 Conclusions

Resonances were observed between 1.5 and 8.0 Hz in the head and torso motions of the 5-year-old infant. The resonance frequencies are consistently displayed in the measurements and simulations. The numerical analysis therefore agreed with the measurements in terms of the transient response and the frequency response, thereby validating the vibration model.

References

1. Ota, S., Nishiyama, S., Shinohara T.: Vibration analysis system for a bicycle with a rider and two infant seats. In: ASME 2014 IMECE, IMECE2014-36224, Montreal, 14–20 Nov 2014
2. Ota, S., Nishiyama, S., Shinohara T.: Effect of a structure on occupants in a bicycle with a rider and two infant seats. In: International Congress of Sound and Vibration 22th, T11.RS02, Florence, 12–16 July 2015
3. Stratz, C.H.: Der Körper des Kindes und seine Pflege für Eltern, Erzieher, Ärzte und Künstler. Ferdinand Enke, Stuttgart (1909)
4. Griffin, M.J.: Handbook of Human Vibration. Academic, San Diego (1994)

Dynamic Simulation of Baby Carriage Under Running Condition: Analyzing Force Given to Driver's Arm

Chihiro Kamio, Tatsuhito Aihara, and Gaku Minorikawa

1 Introduction

A lot of parents use baby carriages to transport babies because it is easier than carrying babies. The development of baby carriages has improved significantly by modern implementation of technology [1]. Furthermore, the safety of baby carriage is investigated in various fields [2, 3]. The factors related to the safety and comfort of a baby carriage include the vibration and the impact force generated by a rough road surface or obstacle. These cause stress for the baby and negatively affect operability for the operator [4]. Previous research has clarified that 80% of its operators mostly feel stress when passing over a level difference [5]. One of the methods to make operation of a baby carriage comfortable is the reduction of the force given to the driver's arm.

In this study, to reduce the impact force generated by passing the carriage over a level difference, experiments with a human pushing carriages were conducted to clarify the received force in an actual environment. Additionally, a simulation model was developed to perform design and performance evaluation efficiently. The accuracy of the developed simulation model was verified by comparison of simulation results and experimental ones. Moreover, this study analyzed the case of adding damping elements to frames of a baby carriage based on the developed simulation model.

C. Kamio (✉) · T. Aihara · G. Minorikawa
Hosei University, Tokyo, Japan
e-mail: chihiro.kamio.5y@stu.hosei.ac.jp; tatsuhito.aihara@hosei.ac.jp; minori@hosei.ac.jp

S. Oberst et al. (eds.), *Vibration Engineering for a Sustainable Future*,
https://doi.org/10.1007/978-3-030-46466-0_32

2 Measurement of Force Given to Driver's Arm

2.1 Experimental Environment

Figure 1 shows the baby carriage, the level difference, and measurement points used in experiments. A standard baby carriage was used, and a ferrous plate was placed on the ground as a level difference. The mass was put on the carriage seat to replicate the weight of a baby. The driving speed was controlled to be 1000 mm/s by limiting the step size of the operator and controlling step timing using a metronome. The received force of driver's arm was measured attaching load cell on the carriage handle. The load cell was placed at the center of the hands pushing the carriage (Fig. 2). To subject the force to one point, the load cell was covered with plates. Additionally, the vibration transferred directly from the road surface was measured attaching accelerometer on the front leg as a reference.

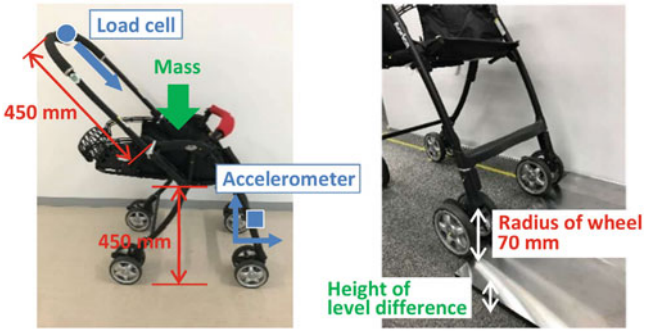

Fig. 1 Baby carriage, level difference, and measurement points used in experiments

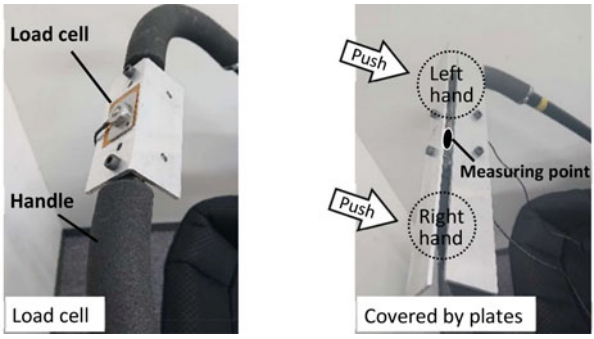

Fig. 2 Load cell and covering plates used to measure the received force of driver's arm

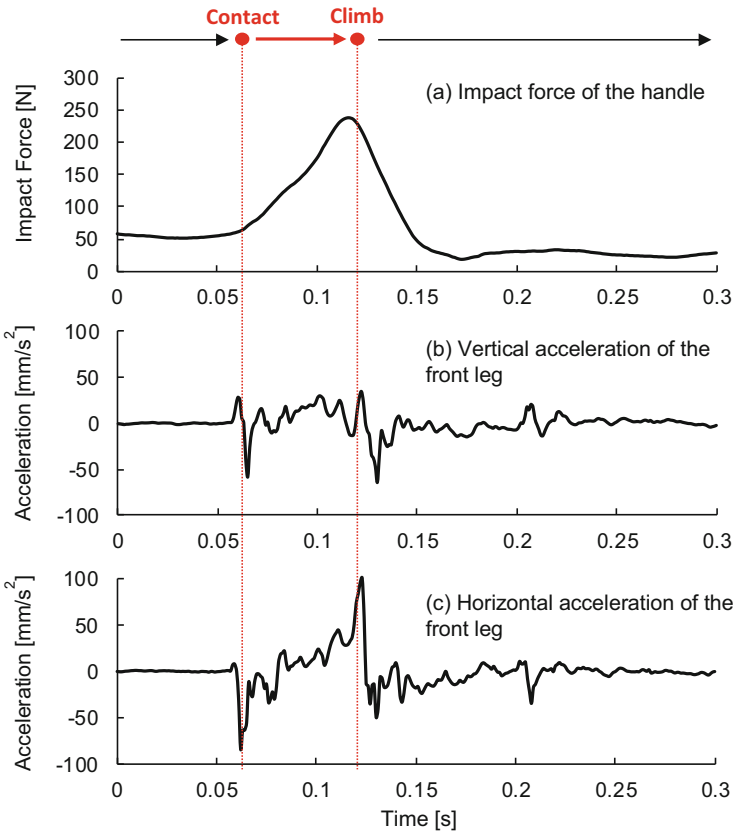

Fig. 3 Experimental result of the impact force and accelerations of two directions at measurement points (in Fig. 1) when the carriage front legs pass over the level difference. The weight of mass is 10 kg, and the height of level difference is 15 mm

2.2 Experimental Results

This study focused the impact force and the vibration (acceleration) when the carriage front legs pass over the level difference. One of experimental results are shown in Fig. 3 when the weight of mass is 10 kg, and the height of level difference is 15 mm. There are two large vibration peaks (at approximately 0.06 and 0.12 s). They can be assumed that the first large peak was generated by contact with the level difference, and the second peak was generated when climbing the level difference. By contrast, there is only one peak in the impact force. It is clarified that the force given to driver's arm is the largest when the carriage climbs on a level difference after contact with a level difference (i.e., the operator needs the largest force of pushing the carriage at this time).

3 CAE Analysis

3.1 Simulation Model

This study developed a simulation model to perform design and performance evaluation efficiently considering the environment under operating conditions. It is necessary to consider the combination of multiple conditions in a system with many parts, such as a baby carriage. Therefore, multibody dynamics that can analyze how the mechanism systems move under the influence of forces was used [6, 7].

Figure 4 shows the comprehensive view of the developed simulation model containing a baby carriage and road. The baby carriage was simply modeled referring the actual structure. This model includes some elastic elements. Translational springs are attached between wheels and legs as suspensions. To model some clearance between parts that introduce additional vibration, joints around legs are connected by rotational springs. Furthermore, this study simulated the elastic deformation of front legs by connecting multiple rigid bodies using springs to reduce analysis time. Front legs were divided into fifths, which were connected by translational and rotational springs. Driver's arms holding and pushing the carriage handle were modeled using translational spring because the spring can model the elastic movement of elbow joints when a baby carriage impact a level difference. The force given to this spring corresponds to the impact force given to driver's arm. The massless object was placed at the tips of the spring and applied translational motion equivalent to 1000 mm/s of driving speed the same as experiments. The weight of mass and the height of level difference can change to any value.

3.2 Validity Verification of Simulation Model

To verify the validity of the developed simulation model, results of simulations and experiments were compared. Figure 5 shows influences on the maximum value of impact force in the weight of mass and the height of level difference. The simulation

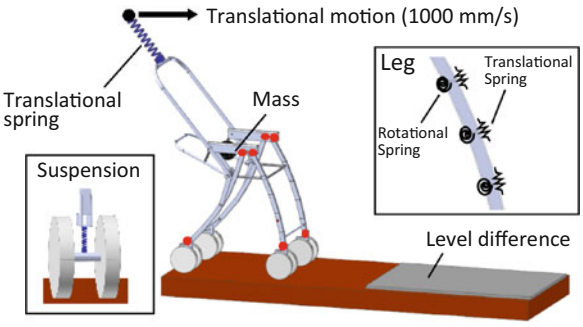

Fig. 4 The comprehensive view of the simulation model and the structure of baby carriage model

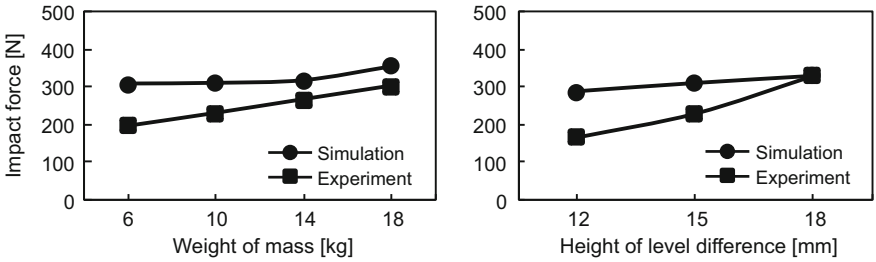

Fig. 5 Influences on the maximum value of impact force in the weight of mass and the height of level difference

model was able to provide the trend similar to experiments in both cases. Therefore, this simulation model is appropriate to analyze the impact force of a baby carriage passing over a level difference.

4 Shock Absorption Mechanism

For the purpose of development of shock absorption mechanism, this study analyzed the case of adding damping elements to frames of a baby carriage. Figure 6 shows the structure of the shock absorption mechanism proposed in this study. It can suppose that springs or air suspensions are used as damping elements. In this study, to model damping elements easily, springs were added into front legs. Figure 7 shows simulation results of maximum value of impact force when the baby carriage model containing the shock absorption mechanism proposed in this study passes over the level difference. One can see that the impact force given to the driver's arm was reduced due to adding these parts. It is assumed that the shock absorption mechanism proposed in this study can alleviate both the vertical and horizontal impact forces because damping elements (springs) are attached obliquely to the road surface.

5 Conclusion

The aim of this study is to reduce the impact force given to the driver's arm generated by passing the carriage over a level difference. For that purpose, this study conducted experiments with a human pushing carriages to clarify the received force. Furthermore, the simulation model is developed to perform design and performance evaluation efficiently. The key points of this study can be summarized as follows:

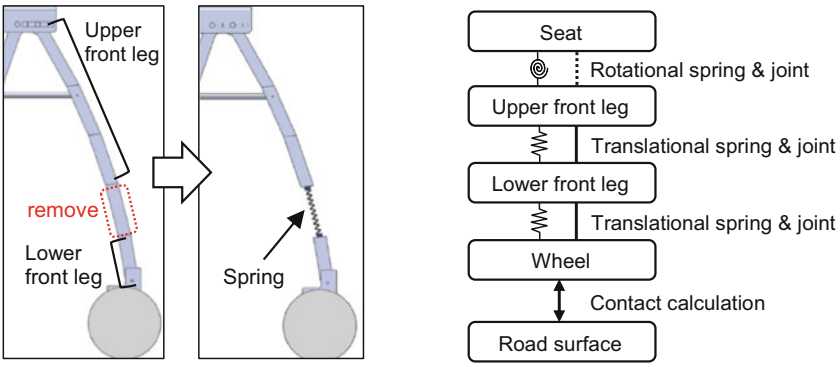

Fig. 6 Structure of the shock absorption mechanism adding damping elements into front legs proposed in this study

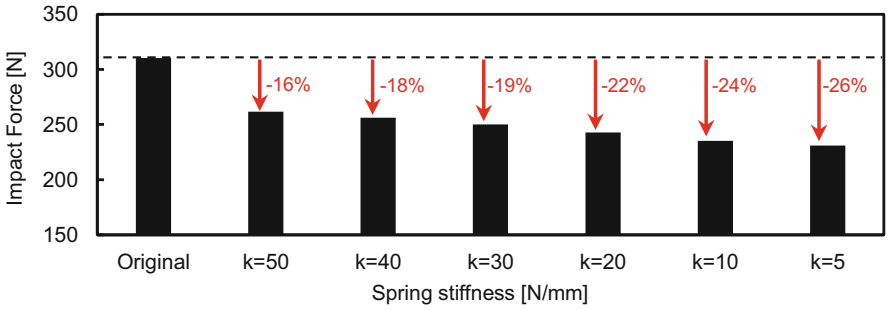

Fig. 7 Simulation results of maximum value of impact force when the baby carriage model containing the shock absorption mechanism proposed in this study pass over the level difference

1. The impact force given to the driver's arm and the vibration of the carriage front leg were measured in experiments. The impact force is the largest when the carriage climbs on the level difference after contact with the level difference.
2. The simulation model including the driver's arm modeled by translational spring was developed. Its validity was verified to compare with experimental results when changing the weight of mass and the height of level difference.
3. The case of adding damping elements into front legs of a baby carriage is based on the developed simulation model. In simulation results, it is clarified that the impact force given to the driver's arm can be reduced by this mechanism.

References

1. Koh, B.X., Nirmal, U., Yuhazri, M.Y.: Developments on baby strollers over the last decade. Curr.J.Appl.Sci.Technol. **33**(6), 1–25 (2019)

2. Dols, J., Pons, V., Alcalá, E., Valles, B., Martín, Á.: Analysis of dynamic behavior and safety of baby carriages in public transportation buses. Transp. Res. A Policy Pract. **49**, 1–9 (2013)
3. Fowler, E., Kobe, C., Roberts, K.J., Collins, C.L., McKenzie, L.B.: Injuries associated with strollers and carriers among children in the United States, 1990 to 2010. Acad. Pediatr. **16**(8), 726–733 (2016)
4. Muraki, S., Saito, S., Ookura, M.: Physical strain and risk during stroller locomotion on cross and combined slopes. Adv. Eng. Forum. **10**, 43–50 (2013)
5. Pigeon News (in Japanese).: https://www.pigeon.co.jp/news/assets/pdf/141209_2.pdf. Last accessed 17 July 2019
6. Schiehlen, W.: Multibody system dynamics: roots and perspectives. Multibody Syst. Dyn. **1**, 149–188 (1997)
7. RecurDyn Online Help.: https://functionbay.com/documentation/onlinehelp/default.htm#!Documents/introduction.htm . Last accessed 17 July 2019

Part VI
Dynamics of Transport Systems

Non-destructive Technologies for Stress-Free Temperature Measurement of Continuous Welded Rails

Ralph (Wei) Zhang, Helen Wu, and Chunhui Yang

1 Introduction

Continuous welded rails (CWRs) significantly strengthen railway track, and they provide the foundation for high-speed and heavy haul railway revenue. However, by eliminating rail joints and gaps between rail sections, as the ambient temperature changes during a year from extremely cold winter to hot summer, high thermal stress may exist and change within welded rails. In some circumstances, if the CWR structure is combined with poor track maintenance, it may cause catastrophic disasters such as track buckling, broken rails, and/or derailment [1, 3]. To ensure the CWR track is in stable, longitudinal stress (neutral temperature of CWR) measurement via measuring and monitoring stress-free temperature (SFT) is the "Holy Grail" of the CWR track maintenance [1, 3, 4]. Using the non-destructive method to measure and monitor the longitudinal thermal stress in CWR tracks is one of key efforts for railway track engineers and researchers for decades. In recent years, several relatively "matured" technologies have been applied in the field of non-destructive measurement of the neutral temperature of CWR. In the last decade in Australia, three types of non-destructive technologies were approved by the railway infrastructure authorities for neutral temperature in-field measurement. These include the magnetic Barkhausen noise (TRACKSAFE RELEASE or RailScan), mechanical method (VERSE® and A-Frame), and vibration method (D'Stresen) [1–7].

R. (Wei) Zhang (✉) · H. Wu · C. Yang
School of Computing, Engineering and Mathematics, Western Sydney University, Penrith, NSW, Australia
e-mail: WEI.ZHANG@transport.nsw.gov.au; R.Yang@westernsydney.edu.au; Helen.Wu@westernsydney.edu.au

S. Oberst et al. (eds.), *Vibration Engineering for a Sustainable Future*,
https://doi.org/10.1007/978-3-030-46466-0_33

2 Magnetic Barkhausen Noise Method

The magnetic Barkhausen noise technology [1] is equipped within a smartly designed machine – TRACKSAFE RELEASE system – to carry out the measurement of longitudinal stress distribution in the CWR track. Based on the micro-magnetic theory, every part of ferromagnetic materials contributes to the uniform magnetization. The TRACKSAFE RELEASE system is designed based on magneto-elastic principle to measure the stress distribution and the neutral temperature of continuously welded rails (CWRs) [1, 2]. The device operates by means of noncontact gauging and allows fast measurement and documentation of the actual neutral temperature of rails. The longitudinal stress and the neutral temperature are determined by measurement of characteristic magnetic values [2]. The TRACKSAFE RELEASE system consists of a manually operated railcar, a central unit, and a pair of probe as shown in Fig. 1.

The central unit contains the computer-operated measuring electronics. A separate battery provides the power supply for the equipment. The probe consists of two yokes that are pressed around the railhead. The rail temperature is measured by integral infrared thermometer. The rail is magnetized by the application of an alternating magnetic field. Interaction of the magnetic field with the magnetic microstructure is orientation dependent and can be measured with an appropriate probe. The measured signal contains the pulses generated in the rail and has a noise-like spectrum. The amplitude of this termed magnetic Barkhausen noise (MBN) depends significantly on the longitudinal stress in the rail. Tension increases the

Fig. 1 The TRACKSAFE RELEASE unit

amplitude of the MBN, while compression leads to its decrease. The higher the longitudinal stress, the higher the signal amplitude for the MBN.

After completing the measurement, the raw data are downloaded to a laptop for further evaluation. The final results are obtained by evaluating and plotting the measured values of the magnetic parameter and rail temperature vs. the longitudinal coordinate and measuring point number and further by depicting the load stress determined by means of the averaged magnetic parameters and calibration curve.

3 Mechanical Method: VERSE®

The mechanical method with its device – VERSE® – is a technology patented by Vortok International. This technology is commercialized for CWR neutral temperature measurement by using the equipment of VERSE®. It is based on the beam-column bending theory, in which the axial load affects the vertical force required to lift a rail [3]. The principle is to assume that the rail can be schematized as a simply supported beam – Euler-Bernoulli beam – under concentrated loading to estimate the longitudinal stress in the track (Fig. 2).

VERSE® claimed that it can measure the CWR neutral temperature with an accuracy of 0.2 °C and a standard deviation of 1.3 °C. The method can be adapted to different kinds of rails and get instant result of CWR neutral temperature. As the method can be applied to tracks in tension, the ambient temperature must be lower than the true CWR neutral temperature.

Fig. 2 VERSE® equipment used on CWR track

4 D'Stresen Vibration Method

D'Stresen system has the potential of estimating the neutral temperature condition quickly and non-destructively. System components include a variable speed shaker, a tune bar (TB) with an accelerometer, a magnetic rail temperature probe, and a data acquisition system. Figure 3 shows the D'Stresen motorized shaker and the tune bar (TB). The shaker contains an eccentric weight which operates over a speed range of 65–80 hertz (Hz) (3900–4800 rpm). The shaker is clamped to a railhead via mechanical cams. The tune bar which is a cantilever beam and the accelerometer, vibrates sympathetically, due to the shaker's rotation when clamped to the railhead nearby. After installation, a computer controls the motor through a narrow sweep encompassing the cantilever's first bending resonance and then records the largest resulting peak-to-peak velocity signal.

According to the manufacturer, this velocity can be related to the existence of longitudinal load in the rail. Roughly stated, the velocity is largest for a rail without longitudinal stress and is reduced in a predictable fashion as either tensile or compressive thermal stress exists.

4.1 Magnetic Barkhausen Noise Method

The magnetic Barkhausen noise method [1, 5] has a significant limitation of applicability when it is used on Australian mainline track. This is because there are significant asset management differences between the continental European railway (including the Chinese, Japanese, and Russian Railways) and the English-speaking countries' railways. That is, the non-English speaking countries usually have a fixed interval of rail changing policy; this can be based either on the years after

Fig. 3 D'Stresen system mounted on CWR track

installation or million gross tons of traffic passed. However, the English-speaking countries usually utilize the "condition-based rail changing policy," and as a result, defected rails that are found by the inspection will be replaced. Hence, after many years of traffic revenue, within one CWR module, it may be consisted of many rails made in different years, by using different manufacture methods, with different head-hardened way, etc., although their profiles are the same or very similar. For example, in Melbourne Metro, for the rails in one CWR module over the main line, it can consist of up to five types of AS 53 kg/m profile rails. These rails can be mixed in one CWR module, and their calibration curves are significantly different.

To understand the amount of the curvature-bending moment effect to the longitudinal thermal stress, a finite element model was created to carry out a numerical study. In brief, a finite element model was created for a 10-m length rail (the length is the same as the 10 m chord for versine measurement), and applied the side pressure on the rail, making the displacement in the middle of the 10 m rail equal to the versine (10 m chord) of a specified rail radius. Hence, the bending stress in the longitudinal direction that is caused by the curvature of curved track can be obtained from the model, as shown in Fig. 4. Comparing the results from TRACKSAFE RELEASE's in-field measurement and numerical study, it is found that the difference is minimal ($\leq$3%).

A significant advantage of the MBN method is that its measurement results are only based on the stress condition of the rails. It has the capability/potential to be used to measure the neutral temperature of CWR on sharp curves, non-ballast girder bridge, and turnout area (stock rails and closure rails).

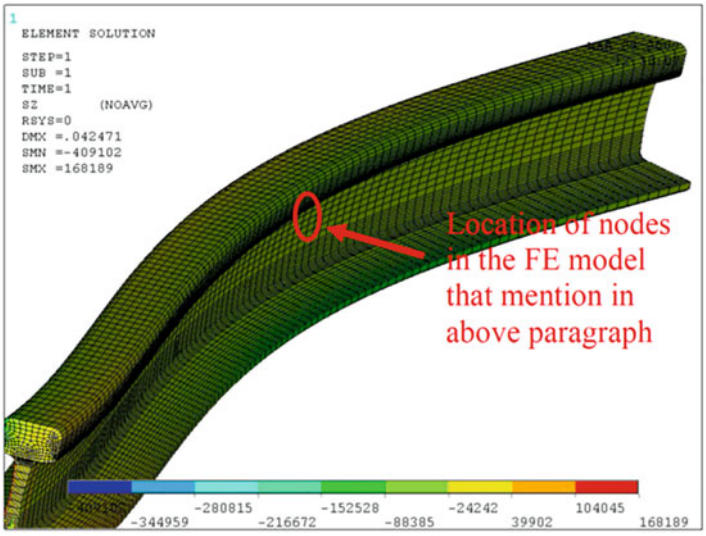

Fig. 4 Z-component stress distribution and its deformation shape of the convex rail's FE model

4.2 Mechanical Method: VERSE®

Because of simple physical background and easy of operation, ***VERSE®*** was acknowledged as the most reliable device and can provide accuracy results. It has been approved by all the major railway authorities in Australia and has been included into the technical standards of CWR stability management. Major shortcomings for this device include:

- Low productivity: VERSE® testing needs to unclip and re-clip the fasteners for at least 20–30 m track in length. At least three labors are required, including an operator, P.O., and labors for unclip and re-clip fasteners. The measurement process needs about 40 minutes.
- Limitation of locations: VERSE® cannot be used on curved tracks, which have a radius of equal or less than 700 m, non-ballast bridges, and locations close to fix points.
- Ambient limitation: VERSE® is the device that only can be used to measure the neutral temperature of CWR when it is in the tension, e.g., VERSE® cannot be used when rail temperature is reached to the designed neutral temperature (in Australia 38 °C or higher, e.g., ambient temperature is 33 °C).
- High cost: About $ 6000–7000 per working day.

4.3 D'Stresen Vibration Method

The D'Stresen method provides some good results at some verification trial and in-field measurement services. However, it still does not have a quick in-field calibration/verification process to ensure its reliability and the accuracy of their results. Before further improvement can be achieved, it cannot be used as a stable technology to carry out day-to-day CWR measurements. Based on its physical theory, it has the capability to be used to measure the neutral temperature of CWR on sharp curves, but no evidences showed that it has the potential to be used on non-ballast girder bridge and turnout area.

5 Conclusion

A large number of neutral temperature results of CWR track measured by the magnetic Barkhausen noise, mechanical method, and vibration method have shown that all of these three methods have the capability to carry out the CWR neutral temperature measurement. However, some further improvements are required for TRACKSAFE RELEASE and D'Stresen methods to ensure that they are suitable for

Australian track conditions, i.e., TRACKSAFE RELEASE to automatically shift the calibration curves when it measures different type of rails within one CWR module, and a more reliable calibration method is required for the D'Stresen method.

References

1. Zhang, R., Wu, H.: Using magnetic barkhausen noise technology and finite element method to study the condition of continuous welded rails on the Darwin-Alice springs line. J. Civ. Eng. Archit. **5**(7), 596–605 (2011)
2. Chikazumi, S.: Physics of Magnetism. Wiley, New York (1964)
3. Kerr, A.: Fundamentals of Railway Track Engineering. Simmons-Boardman Books Inc., Omaha (2003)
4. Kish, A.: Guidelines to Best Practices for Heavy Haul Railway Operations – Infrastructure Construction and Maintenance Issues. International Heavy Haul Associations, Virginia Beach (2009)
5. Moller, R. Radmann, P. Zhang, R.: Using magnetic Barkhausen noise technology and numerical method to study the condition of continuous welded rails on Australian heavy axle track. In: 9th International Heavy Haul Conference, Shanghai (2009)
6. Wegner, A.: Non-destructive Determination of the Stress Free Temperature in CWR Tracks. International Rail Forum, Madrid (2004)
7. Wegner, A.: Prevention of track buckling and rail fracture by non-destructive testing of the neutral temperature in cw-rails. In: 8th International Heavy Haul Conference on "High Tech in Heavy Haul", Kiruna (2007)

Study on Rail Corrugation Development Mechanisms

Kyohei Katada and Yoshiaki Terumichi

1 Introduction

On railway tracks, the corrugation that frequently occurs on the inner rails of sharp curves often results in noise and vibration, and it is even possible that such corrugation could lead to severe accidents [1]. Therefore, it is necessary to clarify the mechanisms of rail corrugation development. However, there are currently no widely accepted theories on the evolution of such corrugation, nor countermeasures to prevent it, so numerous railway transportation companies must continue to extend significant amounts of time and money on the maintenance and replacement of corrugated rails [2]. In this study, a numerical analysis is conducted to reveal some of the mechanisms of rail corrugation. In particular, focusing on a two-axle bogie that runs on a rail with elasticity, this paper aims to numerically clarify the mechanisms of rail corrugation development in terms of the phase relationships between rail corrugation, contact pressure, and slip rate.

2 Modeling and Formulation

2.1 Bogie-Track Model

A 1/10 scale bogie-track model that consists of a two-axle bogie is used to simulate an actual subway, as shown in Fig. 1. This model expresses 2D motion. The wheels and bogie are supported in the vertical and horizontal directions by a spring-damper

K. Katada (✉) · Y. Terumichi
Sophia University, Chiyoda-ku, Tokyo, Japan
e-mail: k-katada-6sh@eagle.sophia.ac.jp

S. Oberst et al. (eds.), *Vibration Engineering for a Sustainable Future*,
https://doi.org/10.1007/978-3-030-46466-0_34

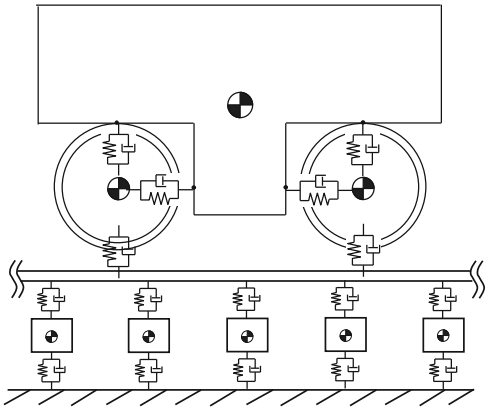

Fig. 1 Bogie-track model

system. The track model consists of rails, sleepers, and a foundation. The rails and sleepers and the sleepers and foundation are supported vertically by a spring-damper system. In this analysis, the absolute nodal coordinate formulation is applied to a formulation for the rail model as a flexible beam with elasticity.

2.2 Wear Development Model

To express rail wear, a finite number of monitoring points are set on the rail model, and wear depth is calculated at each point. The wear development model is shown in Fig. 2. The monitoring points are set at equal intervals and do not move in the X direction, as shown in Fig. 2i. When the contact point between the wheel and the rail passes over the monitoring points, the wear depth is calculated based on the wear rule of Archard, as shown in Fig. 2ii [3], using:

$$Z = c\,|\zeta|\,p, \tag{1}$$

where Z is the wear depth, c is the wear coefficient that is unique to the material, ζ is the slip rate, and p is the contact pressure between the wheels and the rail. To express the continuous shape of the rail, the monitoring points are connected with a spline function, as shown in Fig. 2iii [4, 5]. The process is carried out every time the front and rear wheels ran on the rail. Furthermore, since the bogie repeatedly runs over the same track, the front wheel runs on a rail that possesses wear caused by the rear wheel in the previous lap, and the rear wheel runs on a rail that possesses wear caused by the front wheel just moment before.

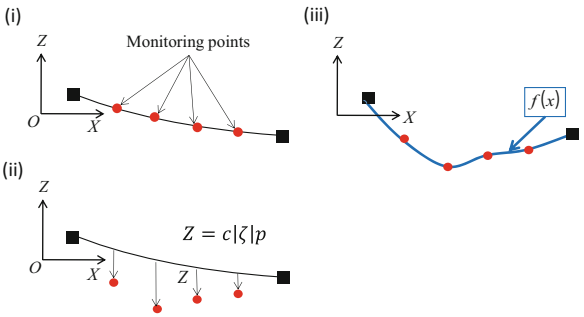

Fig. 2 Wear calculation process

2.3 Formulation

In this model, the equation of motion for the bogie is given as:

$$\mathbf{M}^{\mathrm{B}}\ddot{\mathbf{q}}^{\mathrm{B}} = \mathbf{Q}_{\mathrm{F}}^{\mathrm{B}} + \mathbf{Q}_{\mathrm{g}}^{\mathrm{B}}, \tag{2}$$

where $\mathbf{M}^{\mathrm{B}}$ is the mass matrix for the bogie, $\ddot{\mathbf{q}}^{\mathrm{B}}$ are generalized coordinates, $\mathbf{Q}_{\mathrm{F}}^{\mathrm{B}}$ is the force vector between the bogie and the wheels, and $\mathbf{Q}_{\mathrm{g}}^{\mathrm{B}}$ is the gravity vector on the bogie. The equation of motion for the front wheel is:

$$\mathbf{M}^{\mathrm{WF}}\ddot{\mathbf{q}}^{\mathrm{WF}} = \mathbf{Q}_N^{WF} + \mathbf{Q}_T^{WF} + \mathbf{Q}_M^{WF} + \mathbf{Q}_g^{WF} + \mathbf{Q}_F^{WF}, \tag{3}$$

in which $\mathbf{M}^{\mathrm{WF}}$ is the mass matrix for the front wheel, $\ddot{\mathbf{q}}^{\mathrm{WF}}$ are generalized coordinates, and $\mathbf{Q}_N^{WF}$, $\mathbf{Q}_T^{WF}$, $\mathbf{Q}_M^{WF}$, $\mathbf{Q}_g^{WF}$, and $\mathbf{Q}_F^{WF}$ are the elastic force vector due to elastic contact between the front wheel and the rail, the tangential force vector on the front wheel, the moment vector due to the tangential force, the gravity vector on the front wheel, and the force vector between the bogie and the front wheel, respectively. The equation of motion for the rear wheel is obtained similarly. The equation of motion for the rail is:

$$\mathbf{M}^{R}\ddot{\mathbf{q}}^{R} = \mathbf{Q}_N^{R} + \mathbf{Q}_T^{R} + \mathbf{Q}_e^{R} + \mathbf{Q}_g^{R} + \mathbf{Q}_k, \tag{4}$$

where $\mathbf{M}^{R}$ is the mass matrix for the rail, $\ddot{\mathbf{q}}^{R}$ are the generalized coordinates, and $\mathbf{Q}_N^{R}$, $\mathbf{Q}_T^{R}$, $\mathbf{Q}_e^{R}$, $\mathbf{Q}_g^{R}$, and $\mathbf{Q}_k$ are the elastic force vector on the rail, the tangential force vector on the rail, the external force vector from the sleepers, the gravity vector on the rail, and the elastic force vector due to the deformation of the rail, respectively. The equation of motion for the sleepers is:

$$m_s\ddot{q}^{sk} = \left\{k_R\left(e_2^k - q^{sk}\right) + c_R\left(\dot{e}_2^k - \dot{q}^{sk}\right)\right\} + \left(-k_s q^{sk} - c_s q^{sk}\right) - m_s g, \tag{5}$$

in which k_R and c_R are the rigidity and attenuation of the supporting rail, respectively, and k_s and c_s are the rigidity and the attenuation of the supporting sleeper, respectively.

3 Numerical Results and Discussion

3.1 Rail Corrugation Development

In this section, the development of rail corrugation is discussed. Figure 3 shows that rail corrugation with a wavelength of 1.0 mm is generated after ten laps and subsequently grows. The frequency of this corrugation is calculated using Eq. (6):

$$v = f\lambda \tag{6}$$

where $v = 4$ km/h, which is the bogie speed, and $\lambda = 1.0$ mm, which is the above wavelength. As a result, $f = 1111$ Hz is obtained. An eigenvalue analysis was conducted to reveal this frequency. The result is shown in Fig. 4 and compared with the frequency calculated in Eq. (6). Since the modes near 1111 Hz are determined by the elastic force between the rail and the wheels, it is assumed that these factors are relevant to the rail corrugation phase.

Furthermore, Eq. (1) shows that the wear depth depends on the contact pressure and slip rate. The wear depth, contact pressure, and the slip rate after running 20 laps are shown in Fig. 5. Here, it can be seen that the wear depth and the slip rate have opposite phases. This indicates that the phase relationship between the rail corrugation and the slip rate is the primary mechanism for rail corrugation development.

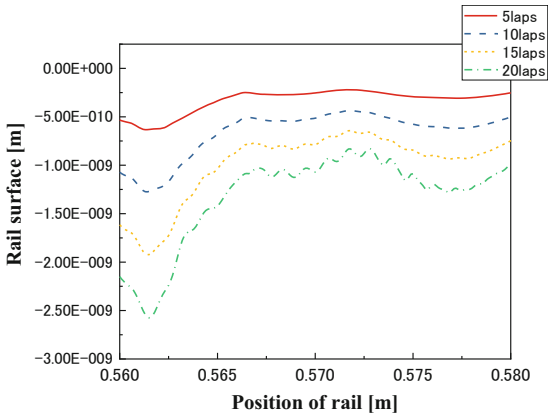

Fig. 3 Rail surface (5–20 laps)

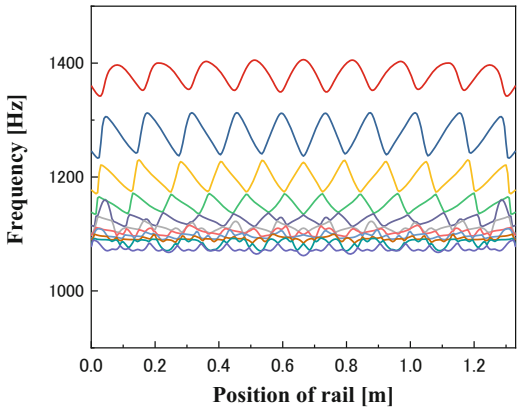

Fig. 4 Eigenvalue analysis

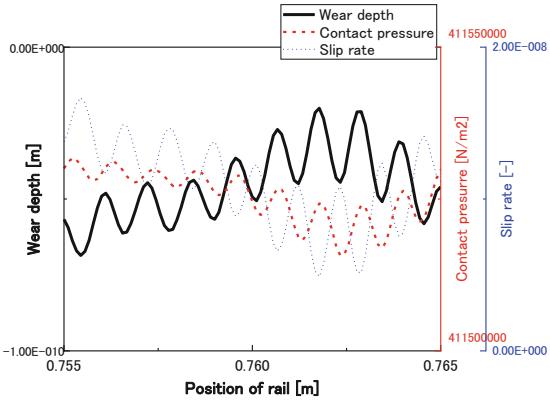

Fig. 5 Wear depth, contact pressure, and slip rate

3.2 Effect of Distance Between Axles on Rail Corrugation Development

In this section, the effect of the axle distance on rail corrugation development is discussed in terms of bogies with different natural frequencies running on a rail with corrugation. To alter the natural frequencies, the distance between axles was changed. Initially, a two-axle bogie with a constant axial distance of 0.19 m ran on the track for 24 laps, after which the axial distance was changed from 9/10 to 11/10. The rail surface after 40 laps and the results of an eigenvalue analysis are shown in Figs. 6 and 7, respectively.

From Fig. 6, it can be seen that difference in the distance between the axles and the rail position results in the different wear depth. It is assumed that the rail corrugation that develops under the phase conditions for the first 24 laps would be similar to the slip rate phase that occurs from 25 laps onward. The phase of the slip rate depends on the natural frequency, which is shown in Fig. 7.

Fig. 6 Rail surface

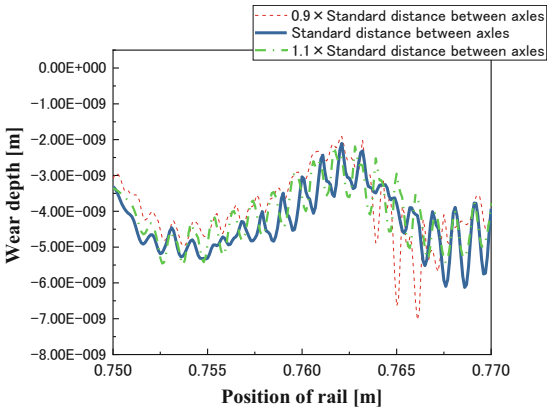

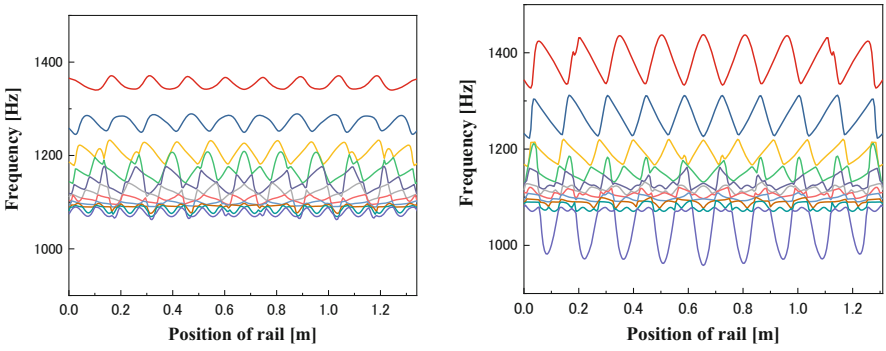

Fig. 7 Eigenvalue analysis: (**a**) distance between axles ×0.9 and (**b**) ×1.1

4 Conclusion

In this study, the mechanisms governing rail corrugation development were clarified in terms of the phase relationships between the rail corrugation, contact pressure, and the slip rate. When a two-axle bogie runs under constant conditions, rail corrugation is generated, the frequency of which corresponds to the natural frequency of the mode determined by the elastic force between the rail and the wheels. Therefore, we conclude that the phase relationships between the rail corrugation and the contact pressure and/or slip rate are the main factors governing rail corrugation development.

To discuss the effect of natural frequencies on rail corrugation development, bogies with different natural frequencies were operated on a rail with corrugation. Since we found that rail corrugation develops when the phase relationships between the rail corrugation and the slip rate are similar, it can be concluded that the primary mechanism governing rail corrugation development has been clarified.

References

1. Suda, Y.: Experimental study on mechanism of rail corrugation using corrugation simulator. Wear. **253**, 162–171 (2002)
2. Grassie, S.L.: Rail corrugation: characteristics, causes, and treatments. Proc. Inst. Mech. Eng. Part F. **207**(16), 57–68 (1993)
3. Archard, J.F.: Contact and rubbing of flat surfaces. J. Appl. Phys. **24**(8), 981–988 (1953)
4. Shabana, A.A.: Numerical procedure for the simulation of wheel/rail contact dynamics. J. Dyn. Syst. Meas. Control. **123**(2), 168 (2001)
5. Shikin, E.V., Plis, A.I.: Handbook on Splines for the User. CRC press, Boca Raton (1995)

Simulation of Cooperative Objects' Transportation System Controlled by the Network of Swarm

Ryota Ishidu and Shin Morishita

1 Introduction

Insects such as ants, bees, or termites are said to have some sociality and tend to form a flock living in colonies. While each insect in a colony seems to act with their own intentions, the insect colony looks highly organized. It is understood that these insects can achieve difficult tasks that cannot manage solely by swarming. This system has been called "swarm intelligence" [1]. The swarm intelligence may be characterized by the robustness, the fault tolerance, and the scalability: the robustness means the ability to maintain its function regardless of changing environmental conditions, and the fault tolerance is the ability of continuation of function even when individual elements fail. Further, the scalability means the ability to handle the growing number of agents. In such insect colonies, the acquisition of new activities and the adaptation to their surroundings may be performed in the closed systems. On the contrary, the artificial swarm robot systems controlled by artificial intelligence such as artificial neural networks still depend on some controllers placed outside of the swarm to get control of rules for each robot. This makes impossible for these systems to adapt to environmental changes without some outside control systems. Thus, the artificial swarm should have the ability that may correct and acquire its behavior by itself. It is also well known that an artificial neural network, which is one of the information processing methods, has learning

R. Ishidu (✉)
Graduate School of Environment and Information Sciences, Yokohama National University, Yokohama, Japan
e-mail: ishidu-ryota-gf@ynu.jp

S. Morishita
Faculty of Yokohama National University, Yokohama, Japan
e-mail: morishita-shin-xf@ynu.ac.jp

S. Oberst et al. (eds.), *Vibration Engineering for a Sustainable Future*,
https://doi.org/10.1007/978-3-030-46466-0_35

ability. The learning ability, which is the ability to adapt to changes in the external environment, is realized by adjusting the parameters in networks.

In this paper, the Boids model [2], which is an early work of artificial life research, was used to reproduce the flocking behavior. The learning algorithm in artificial neural networks was applied to the swarm of Boid network, and the task of transporting objects of different sizes to the proper goals according to the size of the objects was simulated. It was shown that the swarm acquired how to decide on appropriate goals for given objects through many transportation trials. After learning, the Boid units could sense the size of objects and transport to proper goals the given objects.

2 Cooperative Transportation Task

The cooperative transportation is performed in various natural systems and has been a prescribed task for studying the degree of cooperation in multirobots [3]. In this study, the extended version of this task was given to a swarm. As shown in Fig. 1, the transportation goals are located at three points, and circular-shaped object is set at the center position. Each goal has a range of acceptable size of objects to be transported; the acceptable ranges for goal 1, 2, and 3 are from 200 mm to 400 mm in radius, 400 mm to 600 mm, and 600 mm to 800 mm, respectively. If an object having the size within the acceptable range is transported to a goal, this transportation is defined as "successful," and otherwise it is defined as "failed."

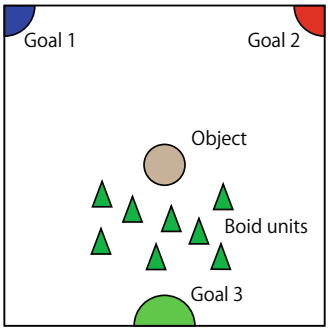

Fig. 1 Transportation task

3 Proposed Transportation System

3.1 Boids Model

There may be numerous kinds of modeling technique to simulate and understand the natural systems. Cellular automata (CA) is one of the discrete modeling methods proposed by von Neumann and Ulam in the 1940s. CA was originally proposed from the attempt to create a self-replicating machine [4] and attracted much interest of many scientists and researchers in the field of artificial life from the 1970s to 1990s. They tried to simulate the natural life by attempting to abstract the fundamental dynamical principles underlying phenomena and recreating these dynamics in computers and other physical media [5]. As one of these researches, Reynolds succeeded in simulating flocking behavior of birds [2], which was called "Boids." In the Boids model, the flocking behavior was reproduced from simple interactions among the Boid units.

3.2 Goal Decision and Learning Method

As shown in Fig. 2, the swarm of Boid units surrounds the target object at nearly equal intervals, and each Boid unit measures the distance to the nearest unit and the angle between the direction to the nearest units and the direction to the object.

Taking the distance d and angle θ as input, each Boid unit calculates state values $\boldsymbol{s} = (s_1, s_2, s_3)$, which are used to determine its own destination, by following equation:

$$\boldsymbol{s} = \boldsymbol{w_o} \varsigma \left(w_1 d + w_2 \theta + b \right) \tag{1}$$

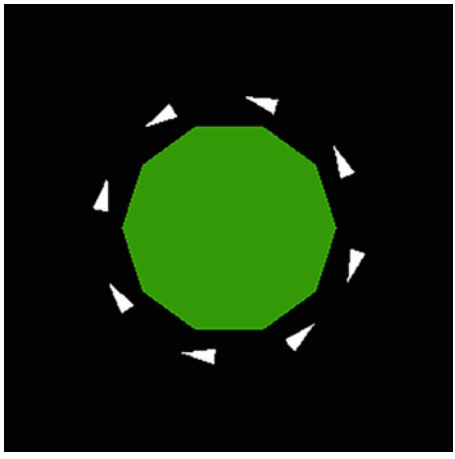

Fig. 2 Snapshot of Boid units surrounding an object. White triangles and a green circle denote Boid units and the object, respectively

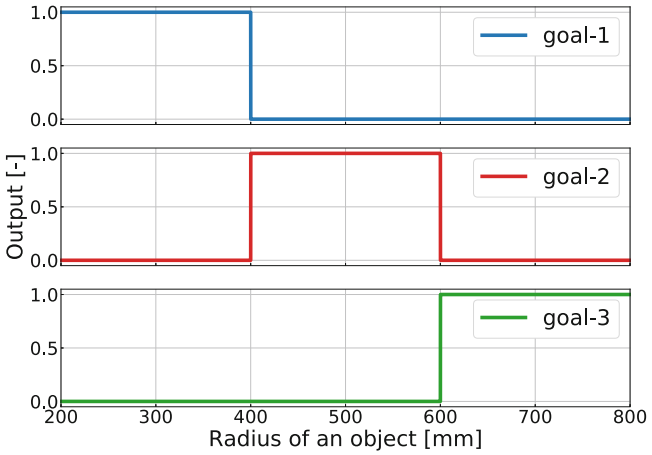

Fig. 3 Example of teaching signals to three different goals corresponding to the size of object

where, w_1, w_2, b, and $\boldsymbol{w}_O$ are parameters possessed by each Boid unit which correspond to the weights and thresholds of artificial neural networks. Also, $\varsigma(x)$ denotes the sigmoid function generally used as a mapping function of artificial neural networks. Each Boid unit calculates the weight vector of goals $\boldsymbol{g} = (g_1, g_2, g_3)$ and the transport destination from its state values $\boldsymbol{s}$ and the position of goals $\boldsymbol{p}_1$, $\boldsymbol{p}_2, \boldsymbol{p}_3$:

$$\boldsymbol{g} = \varsigma(\boldsymbol{s}) \tag{2}$$

$$\boldsymbol{p}_{dest} = g_1\boldsymbol{p}_1 + g_2\boldsymbol{p}_2 + g_3\boldsymbol{p}_3 \tag{3}$$

During the transporting procedure, each Boid unit communicates the state values with its nearby units and updates its state values to the average values with its neighbors. After this communication, the state values converge to a certain value, and the destinations of all Boid units are unified. This procedure corresponds to constructing a three-layered neural network, where its middle layer is composed of Boid units.

In this paper, a judge was introduced outside of the swarm in the teaching procedure and decided the output from the network whether the object was transported to the appropriate goal or not. As shown in Fig. 3, the teaching signals given to the Boid network by the judge were composed of the mapping from the input to output, the radius of object as input and numerical digit from 0 to 1 as output. Regarding the swarm of Boid units as a three-layered neural network, the parameters included in the network were updated by the conventional learning algorithm of back propagation method [6]. As the parameters in the Boid network were updated by the teaching signals, the correct goals will become more likely to be chosen.

4 Numerical Simulations

4.1 Simulation Conditions

The simulation was performed with 8 Boid units and one object at each time. The radius of objects is chosen in the interval [200, 800] in mm. The transportation of various-sized objects by the swarm of Boid units was performed repeatedly, and the Boid network learned to convey the object to the proper destination; learning coefficient was 0.5, initial values of weights and thresholds are random from −0.001 to 0.001, and transportation was repeated up to 1,000,000 times. The accuracy rate of transportation was estimated from the past 1000 transports. Moreover, in every 5000 transports, the weight vector of goals, $\boldsymbol{g}$, was measured to evaluate its classification performance. The radii of object were prepared 50 patterns from 200 mm to 800 mm for evaluation, and trials of each object's size pattern were performed ten times. During this evaluation, the parameters in the Boid network were not updated.

4.2 Results and Discussion

Figure 4 shows the snapshots that were taken after 1,000,000 times of learning. From Fig. 4a, b, it is confirmed that the Boid units have the ability to transport the different size of objects toward the appropriate goals.

The transition of the accuracy rate is shown in Fig. 5. As shown in Fig. 5, the accuracy rate increased along the learning process and approached about 90% after learning. Figure 6 shows the converged weight vector of goals in the Boid network at

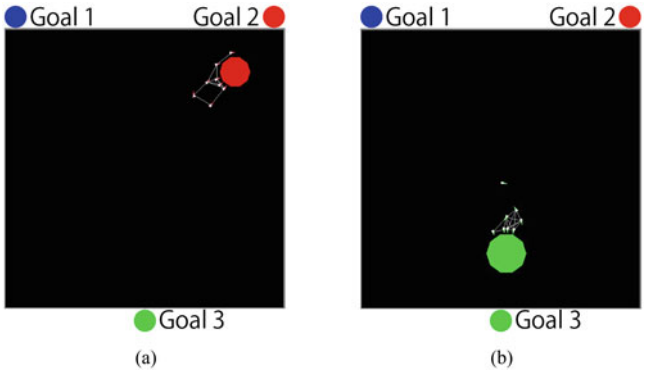

Fig. 4 Snapshots of object transportation. Triangles and circle indicate Boid unit and the object, respectively. The colors of objects denote their appropriate goals, and the colors of units denote their transportation destinations

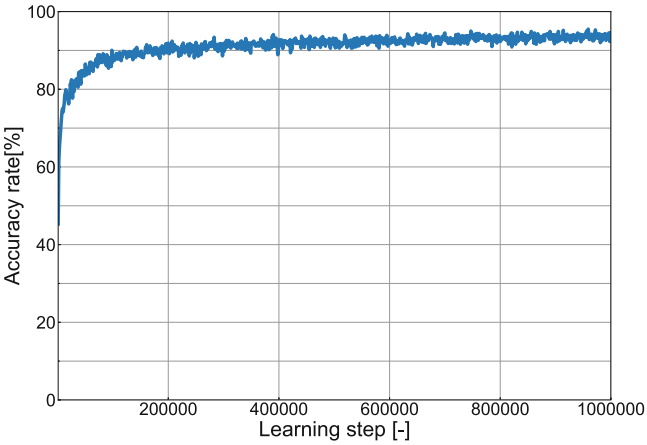

Fig. 5 Learning process curve. Each accuracy rate was measured from the past 1000 times trials of transportation

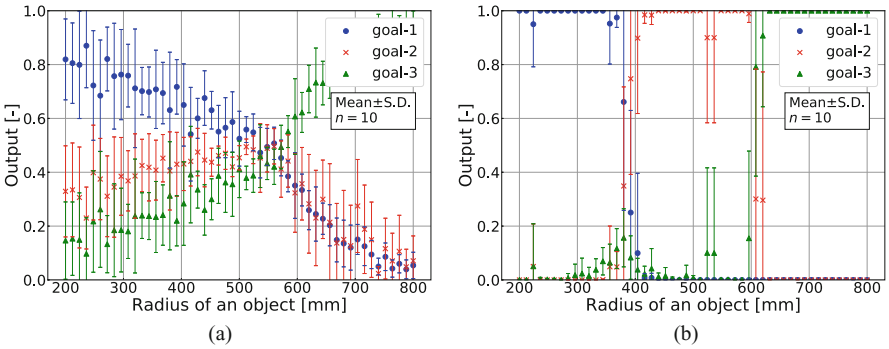

Fig. 6 Size of objects vs. converged outputs form the Boid network. (**a**) Learning time: 5000. (**b**) Learning time: 1,000,000

5000 and 1,000,000 times of learning. In reference to the teaching signals shown in Fig. 3, it is confirmed that the weight vector of goals after 1,000,000 learning steps was closer to the teaching signals than that after 5000 steps. From the viewpoint of statistics, the variance of the weight vector of goals after 1,000,000 steps was far smaller than that after 5000 steps, except in the case of object radius of around 400 mm and 600 mm, which were quite near to the boundary values of radius ranges to each goal. By repeating the transportation trials, the swarm of Boid units might learn to estimate the size of objects from the geometrical information of neighbor units and determine the appropriate transportation destinations based on the size of objects.

5 Conclusions

In this paper, the learning ability of a swarm composed of the Boid units was studied through the cooperative transportation task. The learning ability of the swarm was created by introducing weight parameters in transmission of information between Boid units referring to artificial neural networks. As a result, it is shown that a swarm of Boid units could learn to transport objects to appropriate goals, which are varied to the size of the objects, from the positional relationship with their neighboring units.

Although the swarm intelligence is originally generated in a closed swarm, it is inevitable at present that a certain judge should be placed outside the swarm. In this sense, the teaching signals are necessary for learning. In the future, in order to reduce the contribution of judgment placed outside the swarm, some improvements may be required such that the skilled workers may teach new workers what they have learned.

References

1. Bonabeau, E., Dorigo, M., Theraulaz, G.: Swarm Intelligence: from Natural to Artificial Systems, 1st edn. Oxford University Press, New York (1999)
2. Reynolds, C.W.: Flocks, herds and schools: a distributed behavioral model. ACM SIGGRAPH Comput. Graphics. **21**, 25–34 (1987). https://doi.org/10.1145/37402.37406
3. Groß, R., Dorigo, M.: Evolution of solitary and group transport behaviors for autonomous robots capable of self-assembling. Adapt. Behav. **16**(5), 285–305 (2008). https://doi.org/10.1177/1059712308090537
4. Schiff, J.L., (Translated by Umeo, H., Peper, F., Adachi, S., Isokawa, T., Imai, K., Komatsuzaki, T., Jia, L.): Cellular Automata: A Discrete View of the World (in Japanese). 1st edn. Kyoritsu Shuppan, Tokyo, Japan (2011)
5. Langton, C.G., Taylor, C., Farmer, J.D., Rasmussen, S.: Artificial Life II, 1st edn. Addison-Wesley Publishing Company, Redwood City (1991)
6. Rumelhart, D.E., Hinton, G.E., Williams, R.J.: Learning representations by back-propagating errors. Nature. **323**(9), 533–536 (1986). https://doi.org/10.1038/323533a0

Effect of a Carrier Block Shape on the Speed Fluctuation in a Cable Transport System

K. S. Kim and E. S. Shin

1 Introduction

Power cables of moving equipment are transported by a carrier system that can support the weight of the cables and convert from straight to curved depending on the location of the equipment [1]. Polygon blocks connected by pin joints can meet the requirements of the carrier system by providing lateral stiffness as well as limited rotation. One of the problems in the system is the speed fluctuation due to switching from straight to curved, which might lead to instability and cable wear. Although many studies [2, 3] have been conducted on the behavior of chain drive systems, few are found on the block drive systems. In this work, a simplified model is proposed for the kinematic analysis of the block drive system, and the effect of the block length on the speed fluctuation is investigated.

2 Simplified Kinematic Modeling of a Cable Transport System

2.1 Two-Phase Motion of a Carrier System

As shown in Fig. 1, the carrier system consists of two straight sections, a curved section, and two switching blocks between them. Each block has two revolute joints and multiple contact surfaces, but no rotation occurs between the blocks in the

K. S. Kim · E. S. Shin (✉)
Chungbuk National University, Chungbuk, South Korea
e-mail: esshin@cbnu.ac.kr

S. Oberst et al. (eds.), *Vibration Engineering for a Sustainable Future*,
https://doi.org/10.1007/978-3-030-46466-0_36

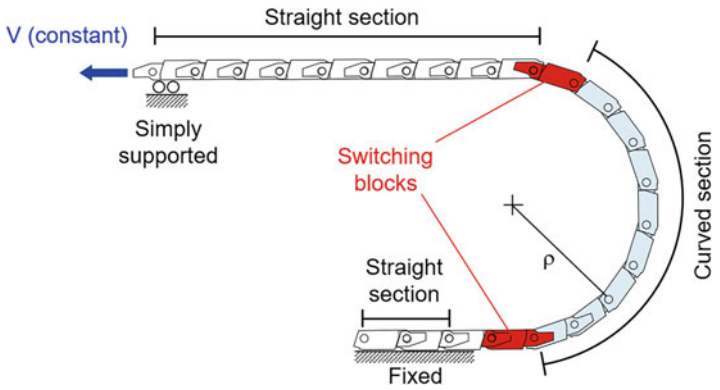

Fig. 1 Schematic of a cable carrier system

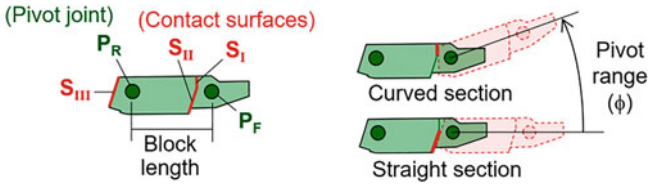

Fig. 2 Block configuration and its rotation

straight and curved sections. Only the switching blocks rotate around their pin joints, which leads to the transition from the straight to the curved or vice versa.

The lower switching block always pivots around the rear joint P_R in Fig. 2, but the upper experiences two phases of rotation. It starts the rotation around the front joint P_F until it reaches the pivot limit ϕ, and this is defined as phase 1. Given the block length L and the radius of curvature ρ,ϕ can be determined as:

$$\phi = \cos^{-1}\left[1 - \frac{1}{2}\left(\frac{L}{\rho}\right)^2\right] \tag{1}$$

Next, the upper switching block starts to rotate about P_R which is called phase 2. The transition characteristics are significantly changed from phase 1 to phase 2.

2.2 *Derivation of a Loop Equation*

Figure 3 shows a simplified kinematic modeling of the carrier system. A single vector is used for each of the two straight and curved sections, respectively, and two vectors are introduced for the two switching blocks. Thus, a loop equation of the system can be written as:

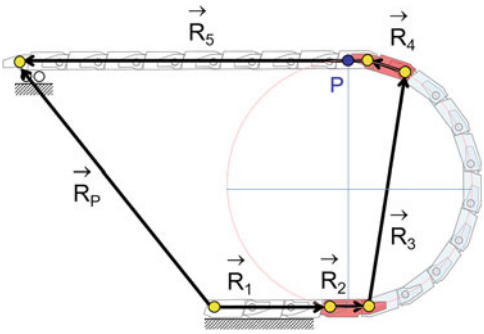

Fig. 3 Kinematic modeling for deriving a loop equation

Table 1 Variables of the loop equation

Vector	Phase 1	Phase 2
2	θ_2 (variable)	θ_2 (variable)
3	$\theta_2 + \frac{C_n+1}{2}\phi$	$\theta_2 + \frac{C_n+1}{2}\phi$
4	$\theta_2 + (C_n + 1)\phi$	θ_4 (variable)
5	θ_5 (variable)	θ_4

$$\overrightarrow{R_1} + \overrightarrow{R_2} + \overrightarrow{R_3} + \overrightarrow{R_4} + \overrightarrow{R_5} = \overrightarrow{R_p} \tag{2}$$

Once the pivot range ϕ is given, the number of blocks in the curved section, C_n, can be determined, and the magnitude of the corresponding vector can also be obtained:

$$R_3 = \sqrt{2\{1 - \cos(C_n\phi)\}} \tag{3}$$

Before solving Eq. (2), the two-phase of motion should be considered to identify variables that need to be determined. Table 1 shows a summary.

Once Eq. (2) is solved, the motion characteristics at P in Fig. 3 are summarized. Point P is the location on the upper switching block or the straight section, passing through the center of the circle that includes the curved section.

3 Results and Discussions

3.1 Axial and Lateral Behavior of the Carrier Versus Block Length

A parameter study was performed by varying the block length, and the motion characteristics around the upper switching block were obtained as illustrated in Fig. 4. The motion characteristics change significantly when switching occurs from phase 1 to phase 2. The axial motion changes its direction at the time of switching, and the lateral motion varies linearly in phase 1 and sinusoidally in phase 2. Some sudden changes not related to the phase shift occur when P in Fig. 3 moves to the

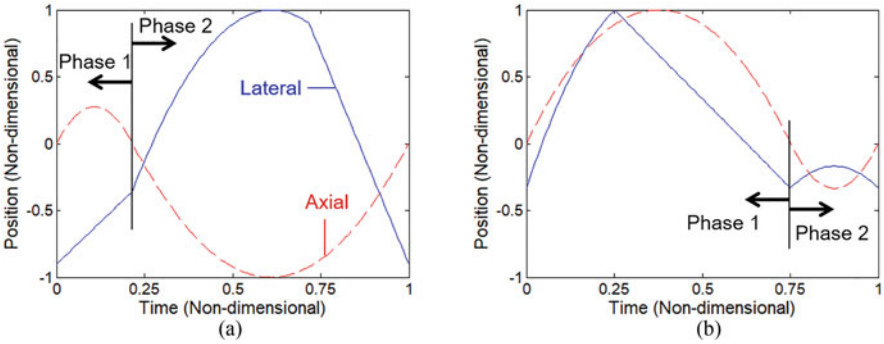

Fig. 4 Position variation at transition: (**a**) $L = 21.4$ mm and (**b**) $L = 22.4$ mm

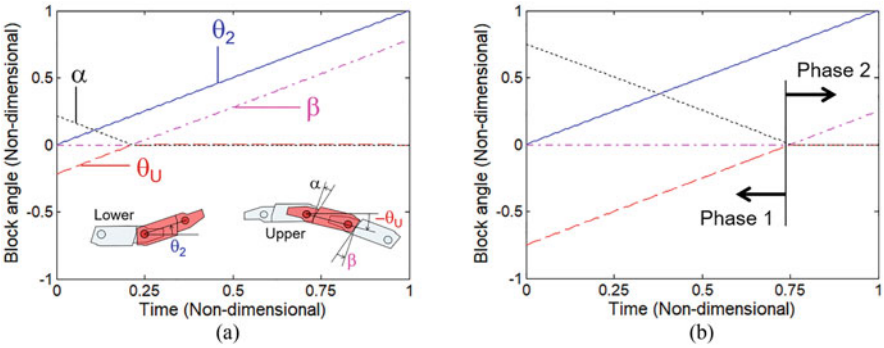

Fig. 5 Angular motion of the switching blocks: (**a**) $L = 21.4$ mm and (**b**) $L = 22.4$ mm

switching block from the straight section. Figure 5 shows the relationship between the two-phase motion and the orientation of the upper switching block.

Figure 6 shows the speed fluctuation in the axial and lateral directions with respect to the variation of the block length. It is found that periodic patterns appear in both the axial and lateral directions and a big difference exists between the maximum and minimum fluctuations.

In the axial direction, the speed variation is minimized when the interval of phase 2 is near zero. In the lateral direction, however, it becomes minimum when the interval is approximately 40% of the period. Furthermore, the block length corresponding to a minimum fluctuation in the axial direction is almost the same as that corresponding to a maximum fluctuation in the lateral direction as summarized in Table 2.

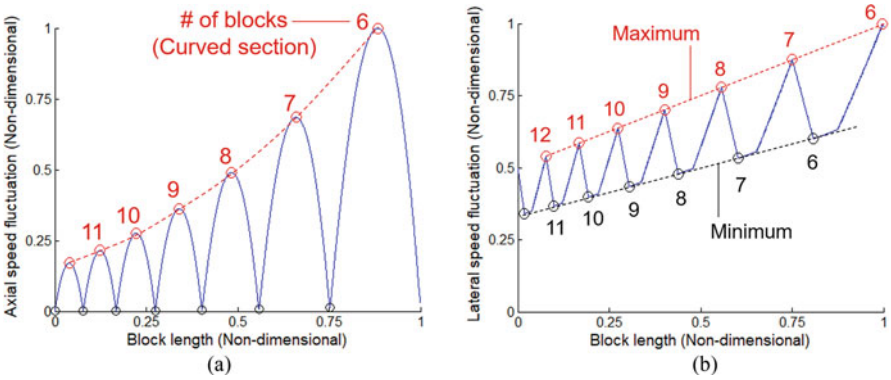

Fig. 6 Speed fluctuation vs. block length: (**a**) axial and (**b**) lateral

Table 2 Axial and lateral fluctuations vs. the block length

	Axial (mm)		Lateral (mm)	
C_n	max	min	max	min
12	16.1	15.6	15.7	15.1
11	17.4	16.8	16.9	16.3
10	18.8	18.2	18.3	17.5
9	20.6	19.9	20.0	19.1
8	22.7	21.8	22.0	20.9
7	25.3	24.3	24.3	23.0
6	28.6	27.2	27.2	25.7

3.2 Comparison of Results with the Multibody Dynamics

A multibody dynamics analysis using ADAMS is performed to consider the inertia and gravity of the carrier block as shown in Fig. 7, and its results are compared with those from the simplified kinematic analysis in Fig. 8. Firstly, the periodicity is observed in the kinematic analysis, but two blocks are added to the straight section at the end of the simulation in the multibody dynamic analysis, and thus the periodicity is broken by the inertia and gravity. Secondly, the lateral position from ADAMS is shifted downward due to the gravity, and the phase 2 motion starts faster than that of the kinematic analysis. This is also caused by the deflection of the block due to the gravity and enlarge the difference between the two approaches.

Similarly, the axial position from ADAMS is shifted to the positive direction, which means that the carrier with inertia effects moves more slowly to the left than in the kinematic approach.

In addition, big differences observed in Fig. 8a, b are caused by normalizing the results for better understanding of its characteristics. If the differences are nondimensionalized by a single period of the traveling distance, $2\,L$, a maximum error in the axial direction is only 0.23%, and an error in the lateral is 1.92%.

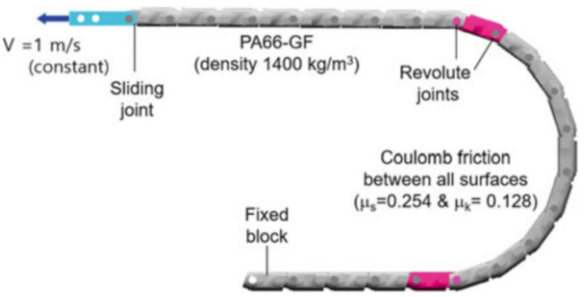

Fig. 7 Multibody dynamics modeling of a cable carrier (ADAMS)

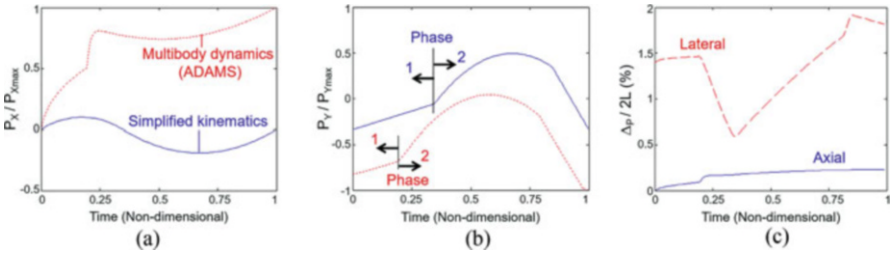

Fig. 8 Comparison between the kinematics and multibody dynamics: (**a**) axial, (**b**) lateral, and (**c**) differences

4 Conclusions

This study investigated the effect of a block length of the carrier system on its speed fluctuation. The kinematic analysis using a simplified modeling was performed, and the motion characteristics of the switching block are obtained. It is found that the speed fluctuation has a repetitive pattern as the block length changes and its magnitude decreases as the length is reduced. It is also observed that the block length corresponding to a minimum fluctuation in the axial direction is almost the same as that corresponding to a maximum fluctuation in the lateral direction. Consequently, an optimal block length can be determined through further consideration of the carrier system in future research.

References

1. Igus, T.: Basics of cable carriers. Mach. Des. 1–4 (2013)
2. Pereira, K., Ambroisio, A., Ramalho, I.: A methodology for generation of planar models for multibody chain drives. Multibody Sys. Dyn. **24**, 303–324 (2010)
3. Fuglede, N., Thomsen, J.: Kinematics of roller chain drives – exact and approximate analysis. Mech. Mach. Theory. **100**, 17–32 (2016)

Hydraulic Control Design for Digging Trajectory Tracking of Scale Model Excavator

T. Hirano, Atsuhiro Ito, N. Tsujiuchi, Akihito Ito, T. Yoshida, F. Kuratani, and H. Andou

1 Introduction

In our previous study, we developed automatic digging algorithms that reproduce the high-efficiency digging work of a skilled operator by combining two digging modes: raking and lift-up [1]. We built a dynamic model of an excavator and a soil model for the computer simulation. These simulations evaluated the payload and consumed energy generated in the digging work designed by our algorithms. However, we have not conducted verification experiments using a real excavator because of the high cost, low safety, and lack of locations. Therefore, to flexibly conduct verification, we retrofitted a scale model radio-controlled hydraulic excavator, the "1/14 Scale RTR Earth Digger 360L," shown in Fig. 1a. It has a hydraulic circuit, shown in Fig. 1b, consisting of hydraulic cylinders, a pump, and servo valves. It also has the same hydraulic problems, such as oil leakage and response delay, as a real excavator. In this hydraulic system, it is comparatively easy to control the actuation of only one cylinder. When simultaneously actuating multiple cylinders, the valves should be controlled so that hydraulic oil is adequately distributed to each cylinder. This is because the pump output is constant and, when simply controlling valves according to the target actuation velocity of each cylinder, oil flows from a high-pressure zone

T. Hirano · A. Ito (✉) · N. Tsujiuchi · A. Ito
Department of Mechanical Engineering, Doshisha University, Kyotanabe, Japan
e-mail: cyjb1501@mail4.doshisha.ac.jp; ctwd0528@mail4.doshisha.ac.jp; ntsujiuc@mail.doshisha.ac.jp; aito@mail.doshisha.ac.jp

T. Yoshida · F. Kuratani
Department of Mechanical Engineering, University of Fukui, Fukui, Japan
e-mail: t-yoshi@u-fuki.ac.jp; kuratani@mech.u-fukui.ac.jp

H. Andou
Caterpillar Japan LLC, Akashi, Japan
e-mail: andou_hiroaki@cat.com

S. Oberst et al. (eds.), *Vibration Engineering for a Sustainable Future*,
https://doi.org/10.1007/978-3-030-46466-0_37

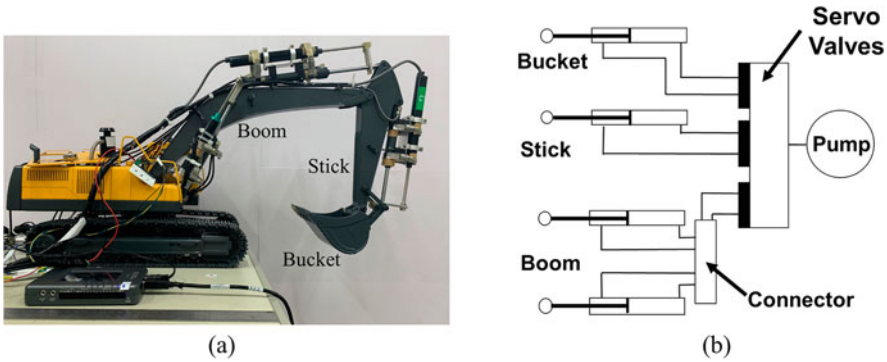

Fig. 1 Scale model and hydraulic circuit. (**a**) 1/4-scale model experimental excavator. (**b**) Hydraulic circuit of scale model

to a low-pressure zone. Thus, it is necessary to compensate each valve opening rate while considering each cylinder velocity in order to simultaneously actuate all cylinders. Because of this, the hydraulic circuit is a strong nonlinearity system, and hydraulic control is more difficult than electrical one.

In this study, we design hydraulic circuit controllers for the scale model so that the tracking accuracy is improved by controlling the valves to distribute an appropriate oil flow to each cylinder.

2 Generate the Target Digging Trajectory [1]

The bucket tip position at time point t is defined by Eqs. (1) and (2) [1]. The target digging trajectory is determined with the initial bucket angle, the rotation velocity of the bucket, and other parameters, which are defined in Fig. 2. The required variations of each cylinder length are calculated from the target bucket tip positions [2–4], and the target velocities of each cylinder actuation are calculated by the inverse kinematics. The target trajectory and target velocity in this study are shown in Fig. 3.

$$x_E = \int_0^t |v| \cos\{(1 - d\psi/d\varphi)\,\varphi_i - \psi_0 + \dot{\varphi}\,(1 - d\psi/d\varphi)\,t - \pi\}\,dt \tag{1}$$

$$y_E = \int_0^t |v| \sin\{(1 - d\psi/d\varphi)\,\varphi_i - \psi_0 + \dot{\varphi}\,(1 - d\psi/d\varphi)\,t - \pi\}\,dt \tag{2}$$

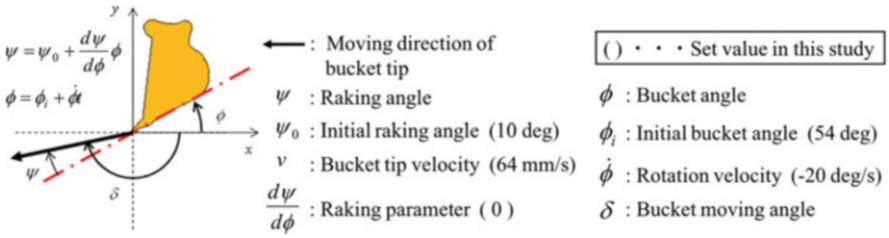

Fig. 2 Definitions of parameters of the digging trajectory

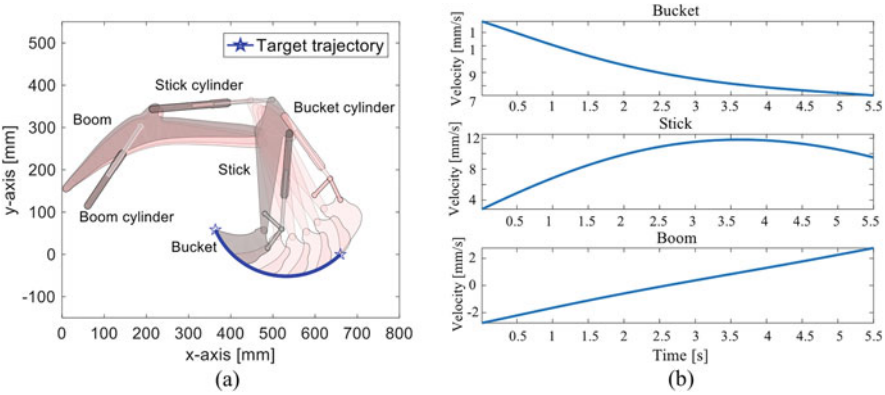

Fig. 3 Target trajectory and target velocity of each cylinder

3 Control Method for the Scale Model

Each cylinder actuation creates bucket motion. To control the cylinder actuation, we need to control the oil flow rate with servo valves. Expanding the valve opening area increases the cylinder actuation velocity. In this study, we designed controllers that control the bucket tip position and bucket angle by controlling each cylinder's actuation velocity. Servo motor rotation changes the valve opening rate, and the servo motors are controlled by the pulse width modulation (PWM). Stroke sensors are attached to each cylinder to measure the actuation length and velocity.

We designed these controllers based on PID control method. The target value input to the PID controller is the target cylinder velocity. The PID controller calculates the control output according to the error between the target velocity and the actual velocity and determines the duty cycle, which determines the rotation angle of the servo motor in PWM. The parameters of the PID method were experimentally decided for each cylinder according to these actual responses because the mathematical model of this scale excavator had not been developed yet and the parametric study had not been conducted.

In this study, PID parameters are used as fixed values in order to evaluate effects of compensation methods that adjust the valve opening rate and control the oil flow distribution for each cylinder. The controller simply consisted of only PID feedback loop is called Ver. 1. Three improvement points explained in the following section were added to the controller Ver. 1.

4 Controller Improvement and Evaluations of Tracking Results

4.1 Evaluation Method of Measurement Trajectories

The measurement trajectory is kinematically calculated from the measurement cylinder displacement. To quantitatively evaluate the measurement trajectories, average deviations were calculated for each controller by Eq. (3), which uses the mean distance between the target bucket tip position and the actual bucket tip position with respect to each bucket angle. Thus, the average deviation can evaluate the control accuracy of both the bucket tip position and the bucket angle. N is the number of time steps on the trajectory:

$$\overline{D} = \frac{1}{N}\sum_{n=1}^{N}\sqrt{\left(X_{actual,n} - X_{target,n}\right)^2 + \left(Y_{actual,n} - Y_{target,n}\right)^2} \tag{3}$$

We designed five controllers, Ver. 1 through Ver. 5. The average deviations for each controller are shown in Fig. 4a, and the result of Ver. 1 is shown in Fig. 4b.

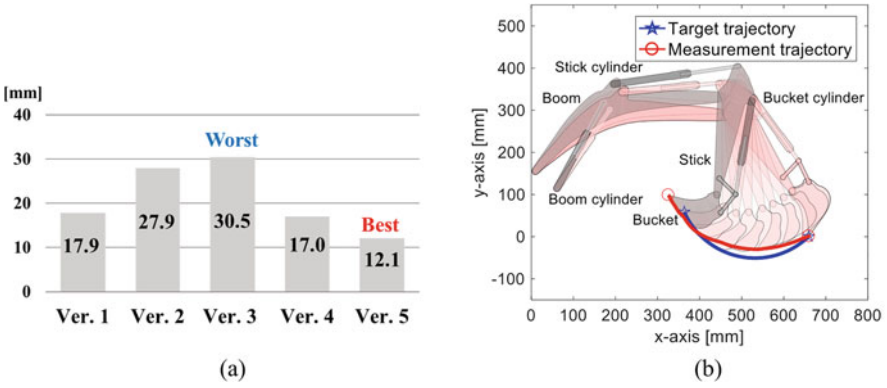

Fig. 4 Average deviations and result of Ver. 1. (**a**) Average deviations. (**b**) Target and measurement trajectory

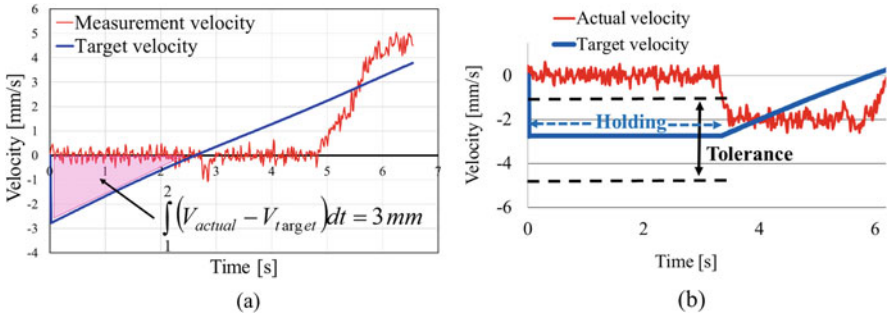

Fig. 5 Velocity of boom cylinder (Ver. 1) and improvement point for Ver. 2. (**a**) Velocity of boom cylinder. (**b**) Holding target initial velocity

4.2 Improvement Point 1: Holding the Target Initial Velocity

The result of Ver. 1 is shallower than the target because the boom cylinder does not retract. As shown in Fig. 5a, the actual velocity of the boom cylinder during the first 5 seconds was zero, and the retraction was insufficient at about 3 mm, which is the integration of the error between the target and the actual velocity during the first approximately 2 seconds (pink area). As a result, the actual bucket tip position is at most 30 mm higher than the target. During digging, a shallower digging trajectory cannot achieve the expected digging payload, so Ver. 1 should be modified.

In the boom-down operation, the opening area of the boom cylinder's valve is squeezed in order to avoid excessively fast boom-down due to the self-weight of the front parts (boom, stick, and bucket). Additionally, Ver.1 was designed without a consideration of the hydraulic response delay. Therefore, the boom-down didn't work insufficiently. In Ver. 2, as seen in Fig. 5b, the target initial velocity value is held until the actual velocity of any one cylinder falls within the tolerance of ± 2 mm/s. Then, subsequent target values begin to be calculated from the target trajectory and input to the controller.

4.3 Improvement Point 2: Preferential Oil Distribution for Boom Cylinders

The result of Ver. 2 was shallower than that of Ver. 1 because the extension of bucket cylinder began at the earliest timing. The bucket's inertia is the smallest of the front parts so the bucket cylinder is more easily actuated. In other words, in case of Ver. 2, the bucket cylinder velocity satisfied the tolerance and became the trigger to start inputting the subsequent target velocity values of each cylinder. However,

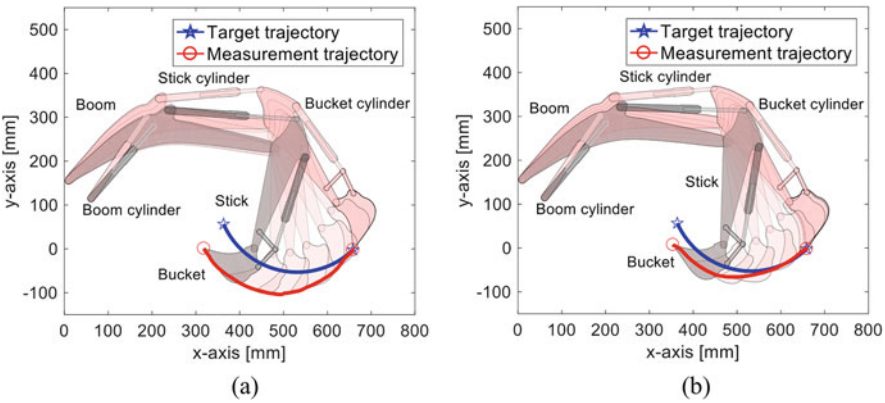

Fig. 6 Results for Ver. 3 and Ver. 5. (**a**) Result of Ver. 3. (**b**) Result of Ver. 5

the average deviation of Ver. 2 was 27.9 mm, and the tracking accuracy was lower than Ver. 1 because the velocity and accuracy to reach the target differ depending on the cylinder load.

In case of Ver. 3, considering that the inertia of the boom cylinder is the largest, the bucket cylinder and the stick cylinder are controlled so as not to actuate; the oil is distributed for only boom cylinders until the boom cylinder velocity satisfies the tolerance, as stated above. The result of Ver. 3 in Fig. 6a was deeper than the target trajectory, but the average deviation was worst at 30.5 mm because the beginning of the stick folding and the bucket rotation were delayed.

4.4 Improvement Point 3: Compensation of Valve Opening Rates

For Ver. 4, to improve the responses of the bucket cylinder and the stick cylinder, these valves are opened only 10% until the velocity of the boom cylinder satisfies the tolerance as shown in Fig. 7a. The average of Ver. 4 was smaller than Ver. 3 and demonstrates improved tracking accuracy.

However, with Ver. 4, the oil flow to boom cylinders decreased slightly because the bucket cylinder's and the stick cylinder's valves were opened. Therefore, in Ver. 5, the valve of the boom cylinder is opened with an additional 50% of the valve opening rate commanded from the PID controller so that the oil flow to boom cylinders is preferred over the other cylinders, as shown in Fig. 7b. The result for Ver. 5 is shown in Fig. 6b, and the average deviation is the smallest of our controllers, so the tracking accuracy was improved through the controller improvement.

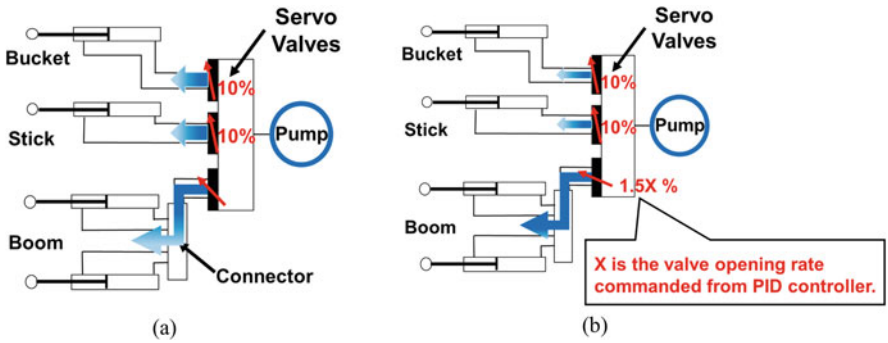

Fig. 7 Valve control method of Ver. 4 and Ver. 5. (**a**) Value control method of Ver. 4. (**b**) Value control method of Ver. 5

5 Conclusion

In this study, compensation methods of the hydraulic control for the digging trajectory tracking were examined. In conclusion, the tracking accuracy was improved by compensating the control output of PID method and adjusting the valve opening rate according to the inertia of each cylinder. The tracking accuracy is further improved by the combination of these compensation methods and the cascade PID control method.

References

1. Hirano, T., Yoshida, T., Tsujiuchi, N., Ito, A., Kuratani, F., Tateishi, M., Andou, H.: Evaluation of automated digging performance for hydraulic excavators. In: #140. The 17th Asian Pacific Vibration Conference (APVC2017), Nanjing, China (2017)
2. Yoshida, T., Koizumi, T., Tsujiuchi, N., Jiang, Z., et al.: Dynamic analysis of an excavator during digging operation. SAE Int. J. Commer. Veh. **6**(2), 419–428 (2013)
3. Chang, P.H., Lee, S.J.: A straight-line motion tracking control of hydraulic excavator system. Mechatronics. **12**(1), 119–138 (2002)
4. Ha, Q.P., Nguyen, Q.H., Rye, D.C., Durrant-Whyte, H.F.: Impedance control of a hydraulically actuated robotic excavator. Autom. Constr. **9**(5–6), 421–435 (2000)

Dynamic Tension Analysis for Governor Rope in Elevator System

Mitsuhiro Yamazumi, Seiji Watanabe, and Nobuyuki Kokawa

1 Introduction

An elevator is a necessary vertical transportation system for building users. Due to vertical movement against the gravity, it requires highly reliable safety mechanisms which activate under abnormal conditions, such as an excess speed or a free fall motion caused by a suspension rope break.

One of the key safety devices that can limit the car speed mechanically is a governor rope system, which consists of a governor pulley, a tension sheave, and a governor rope as shown in Fig. 1. The governor pulley and the tension sheave are installed at the top and the bottom of the elevator shaft, respectively. The governor rope is wrapped around two pulleys as a loop system, and the rope is connected to the elevator car. Hence, the safety system can keep monitoring the car's speed mechanically by the governor pulley's rotational speed.

The tension sheave applies an appropriate tension to the governor rope, so that the governor rope system can achieve a smooth motion in variable car speed conditions. To keep a constant tension in the governor rope, the tension sheave is only suspended by the rope, so that it can move vertically. Due to the unconstrained condition of the sheave, it shows quite complicated dynamic motions while the car is running. In addition to the sheave motion, the inertia force of the governor rope can't be ignored in high-rise buildings [1]. The above inertia force induces other complicated dynamic motions against the governor rope system.

M. Yamazumi (✉) · S. Watanabe
Advanced Technology R&D Center, Mitsubishi Electric Corporation, Amagasaki, Hyogo, Japan
e-mail: Yamazumi.Mitsuhiro@dw.MitsubishiElectric.co.jp;
Watanabe.Seiji@ay.MitsubishiElectric.co.jp

N. Kokawa
Inazawa Works, Mitsubishi Electric Corporation, Inazawa, Aichi, Japan
e-mail: Kokawa.Nobuyuki@ct.MitsubishiElectric.co.jp

S. Oberst et al. (eds.), *Vibration Engineering for a Sustainable Future*,
https://doi.org/10.1007/978-3-030-46466-0_38

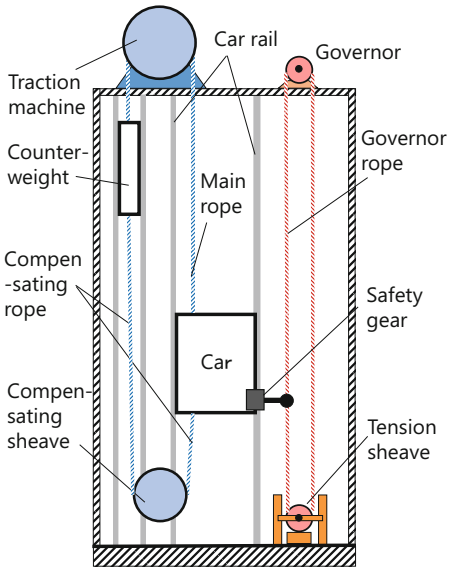

Fig. 1 Governor rope system for elevator

Therefore, several dynamic simulation models of the governor rope system have been studied. Previous researches proposed a rope model as a multibody model [2, 3], or a FEM model [4]. However, it requires a large amount of calculation resources, time, and cost to simulate the dynamic motions against a high-rise building. Therefore a simple model has been required for evaluating the dynamic behavior. For this reason, Fukui focused on the tension sheave vibration and revealed the sheave motion by a simple 1-DOF vibration model [1].

This paper proposes an analytical method for transient motions of the governor rope tension with a 3-DOF model. Firstly, an equivalent rope tension caused by the car acceleration is introduced. Secondly, a distributed rope tension of the governor rope is calculated by a continuous elastic model. The derived model reveals that the dynamics of the governor rope system can be expressed as a function of the car acceleration and position. The proposed model is validated by experiments in an actual elevator system. Finally, dynamic tension behavior while the traction machine is braking is also evaluated by the proposed tension model.

2 Vibration Model

2.1 3-DOF Vibration Model

Figure 2 shows a vibration model of the governor rope system which consists of four elements: a governor rope, a governor pulley, a tension sheave, and a car which is connected to the rope (model variables listed in Table 1).

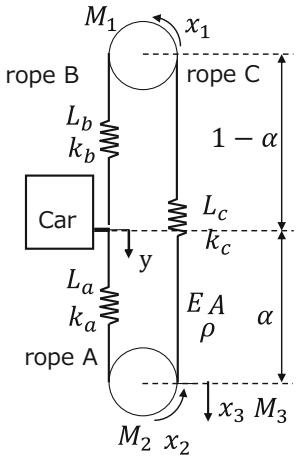

Fig. 2 Vibration model of governor rope system

Table 1 Model variables and parameters

x_1	Governor's rotation	M_1	Governor's mass of inertia
x_2	Tension sheave's rotation	M_2	Tension sheave's mass of inertia
x_3	Tension sheave's translation	M_3	Tension sheave's mass
y	Car's translation	L	Length of rope C
α	Normalized car position by L	ρ	Linear density
	$(0 < \alpha < 1)$	A	Cross-section area
		E	Young's modulus

The governor rope is represented by three parts of a looped rope. The lower part and the upper part of the car side rope are defined as rope A and rope B. The opposite side is defined as rope C. In this model, each rope is defined as a linear spring. The variables x_1 and x_2 are the rotations of the governor pulley and the tension sheave. The variable x_3 is the vertical displacement of the tension sheave. The car displacement y is the system input parameters. In the figure, the positive direction is downward. The parameters M_1 and M_2 are the inertia of the governor pulley and the tension sheave. The parameter M_3 is the mass of tension sheave. Each stiffness of rope A, B, and C is given as k_a, k_b, and k_c in Eq. (1), respectively. Due to its large inertia, the state variable of the car can be neglected from the equation of motion.

A 3-DOF vibration model is newly derived as Eq. (3) by the Euler-Lagrange's equation, and the equation is a function of the relative motion $\boldsymbol{u}$ against the car. In Eq. (3), the damping term is ignored for the sake of simplicity. The state variable vector $\boldsymbol{u}$, the mass matrix $\mathbf{M}$, the stiffness matrix $\mathbf{K}$, and the generalized force vector $\boldsymbol{f}$ are given by Eq. (4) to Eq. (7). In high-rise buildings, the rope mass can't be ignored. Therefore, the mass matrix $\mathbf{M}$ and the force vector $\boldsymbol{f}$ contain the rope inertia and its gravity effect, as shown in Eqs. (5) and (7).

$$k_a = \frac{EA}{L_a}, k_b = \frac{EA}{L_b}, k_c = \frac{EA}{L_c} \tag{1}$$

$$L_a = L\alpha, L_b = L\left(1-\alpha\right), L_c = L \tag{2}$$

$$\mathbf{M}\ddot{\boldsymbol{u}} + \mathbf{K}\boldsymbol{u} = \boldsymbol{f} \tag{3}$$

$$\boldsymbol{u} = \{u_1 \ u_2 \ u_3\}^T = \left\{x_1 - y \ x_2 - y \ x_3\right\}^T \tag{4}$$

$$\mathbf{M} = \begin{bmatrix} M_1 & 0 & 0 \\ 0 & M_2 & 0 \\ 0 & 0 & M_3 \end{bmatrix} + \frac{\rho L}{6}\begin{bmatrix} 2\left(2-\alpha\right) & 1 & -1 \\ 1 & 2\left(1+\alpha\right) & -2\left(1-\alpha\right) \\ -1 & -2\left(1-\alpha\right) & 2\left(1+\alpha\right) \end{bmatrix} \tag{5}$$

$$\mathbf{K} = \begin{bmatrix} k_b + k_c & -k_c & k_c \\ -k_c & k_a + k_c & k_a - k_c \\ k_c & k_a - k_c & k_a + k_c \end{bmatrix} \tag{6}$$

$$\boldsymbol{f} = -\begin{Bmatrix} M_1 + \rho L\left(2-\alpha\right)/2 \\ M_2 + \rho L\left(1+\alpha\right)/2 \\ -\rho L\left(1-\alpha\right)/2 \end{Bmatrix}\ddot{y} + \begin{Bmatrix} -\rho L\alpha/2 \\ -\rho L\left(1-\alpha\right)/2 \\ M_3 + \rho L\left(1+\alpha\right)/2 \end{Bmatrix} g \tag{7}$$

2.2 Equivalent Rope Tension Model

The equivalent rope tension induced by the rope stretch is given by Eq. (8). In the case of constant car acceleration conditions, the stable value of $\overline{\boldsymbol{u}}$ given by Eq. (9) is derived by setting the second derivative of $\boldsymbol{u}$ in Eq. (3) at zero. The vertical displacement of tension sheave is simply identified by Eq. (10), which is the function of the normalized car position α ($=y/L$) and the car acceleration $\ddot{y}$. Substituting Eq. (9) into Eq. (8), the equivalent rope tension $\overline{\boldsymbol{t_1}}$ in constant car acceleration conditions is given by Eq. (11). Equation (11) is also the function of α and $\ddot{y}$:

$$\boldsymbol{t_1} = \left\{t_a \ t_b \ t_c\right\}^T = \begin{bmatrix} 0 & k_a & k_a \\ -k_b & 0 & 0 \\ k_c & -k_c & k_c \end{bmatrix}\boldsymbol{u} \tag{8}$$

$$\overline{\boldsymbol{u}} = \mathbf{K}^{-1}\boldsymbol{f} \tag{9}$$

$$\overline{x}_3 = (M_1 + M_2 + 2\rho L) / (2k_b) \cdot \ddot{y} + (M_3 + \rho L)\, g/2k_c \tag{10}$$

$$\overline{\boldsymbol{t_1}} = \begin{bmatrix} 0 & k_a & k_a \\ -k_b & 0 & 0 \\ k_c & -k_c & k_c \end{bmatrix} \overline{\boldsymbol{u}} = \begin{bmatrix} 0 & k_a & k_a \\ -k_b & 0 & 0 \\ k_c & -k_c & k_c \end{bmatrix} \mathbf{K}^{-1} \boldsymbol{f} \tag{11}$$

2.3 Tension Distribution Model for Each Governor Rope

In high-rise buildings, the rope tension is different from the top to the bottom due to the effect of its rope mass. Therefore tension distribution should be evaluated in each rope. As the rope is a continuous elastic body, the equation of motion for a small part of the rope is given by Eq. (12), where the variable s is the normalized position from top to bottom of each rope, of which the length is l. The variable $\sigma(s)$ is the tension at the position s. We assume that the acceleration of the position s is interpolated by each end acceleration of $\ddot{x}_u$ and $\ddot{x}_l$, as shown in Eq. (13). The distributed tension can be derived by the integration of Eq. (12), as shown in Eq. (14). Equation (14) is the function of the car position α and the car acceleration $\ddot{y}$:

$$\rho l ds \cdot \ddot{x}_r(s) = \sigma\,(s + ds) - \sigma(s) + \rho l ds \cdot g = d\sigma + \rho l ds \cdot g \tag{12}$$

$$\ddot{x}_r(s) = s\ddot{x}_l + (1 - s)\,\ddot{x}_u \tag{13}$$

$$t_2\,(s, \ddot{y}, \alpha) = \int_0^s d\sigma = \int_0^s \rho l \cdot \{\ddot{x}_r(s) - g\}\, ds \tag{14}$$

2.4 Approximate Tension Model

To assume that car's braking deceleration is constant ($\ddot{y} = \beta$), the tensile force at an arbitrary point in the governor rope can be expressed by the equivalent rope tension $\overline{\boldsymbol{t_1}}$ and the distributed tension $\overline{\boldsymbol{t_2}}\,(\boldsymbol{s}) = \left\{ t_2\,(s_a)\ t_2\,(s_b)\ t_2\,(s_c) \right\}^T$, where s_a, s_b, and s_c are the normalized position of rope A, B, and C. The rope tension in Eq. (15) is a function of the car position α and the car acceleration β:

$$\overline{\boldsymbol{t}}\,(\,\boldsymbol{s}, \beta, \alpha\,) = \left\{ \overline{t}_A\ \overline{t}_B\ \overline{t}_C \right\}^{\mathrm{T}} = \overline{\boldsymbol{t_1}}\,(\beta, \alpha) + \overline{\boldsymbol{t_2}}\,(\boldsymbol{s}, \beta, \alpha\,) \tag{15}$$

3 Comparison with Experimental Results

To verify our 3-DOF vibration model, we do several experiments in an actual elevator system. In experiments, we stop the traction machine by the brake while the car is descending, and the governor rope system receives a large step input from the car deceleration.

Figure 3 shows the car acceleration at the middle floor ($\alpha = 0.35$), where the vertical axis is normalized by the deceleration value. Figures 4 and 5 show the rope tension at the connection points between the governor rope and the car. The vertical axis in each figure is normalized by the steady state tension. In each figure, the simulation (the dotted line) matches the experimental result (the real line). Each simulation includes the proportional stiffness damping that is identified by the tension sheave's vibration. The horizontal line in each figure corresponds to Eq. (15), and it matches the experiment. Therefore, our proposed method can simulate the complicated dynamic motion in the governor rope system.

4 Parameter Influence Against Rope Tension

As Eq. (15) is the function of the car position, car acceleration, and the distributed rope position, we can evaluate each parameter's influence against the rope tension behavior. Table 2 shows the tension behavior against each parameter's value change. For example, the second column shows that the tension of rope A while the car is descending (β_2) is smaller than that while the car is running constantly. Conversely, it shows that the tension of rope B while the car is descending is larger than that while the car is running constantly. As the relation of each parameter against the rope tension has been clearly established by Eq. (15), we can make an optimal design against the governor rope system.

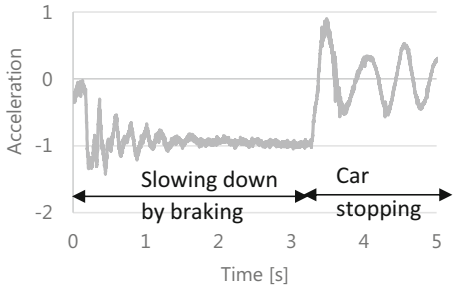

Fig. 3 Car's acceleration at braking

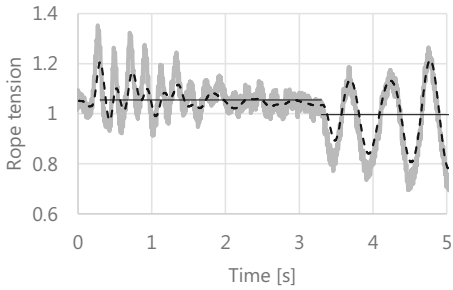

Fig. 4 Tensile force from rope A

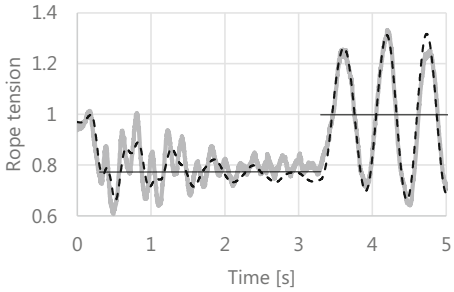

Fig. 5 Tensile force from rope B

Table 2 Influence against rope tension

	Car position: α	Car acceleration: β	Rope position: s
	$\alpha_1 > \alpha_2$	$\beta_1 > 0 > \beta_2$	$s_1 > s_2$
Rope A	$\bar{t}_A(\alpha_1) > \bar{t}_A(\alpha_2)$	$\bar{t}_A(\beta_1) > \bar{t}_A(0) > \bar{t}_A(\beta_2)$	$\bar{t}_A(s_1) < \bar{t}_A(s_2)$
Rope B	$\bar{t}_B(\alpha_1) < \bar{t}_B(\alpha_2)$	$\bar{t}_B(\beta_1) < \bar{t}_B(0) < \bar{t}_B(\beta_2)$	$\bar{t}_B(s_1) < \bar{t}_B(s_2)$
Rope C	$\bar{t}_C(\alpha_1) = \bar{t}_C(\alpha_2)$	$\bar{t}_C(\beta_1) < \bar{t}_C(0) < \bar{t}_C(\beta_2)$	$\bar{t}_C(s_1) < \bar{t}_C(s_2)$

5 Conclusion

This paper proposed a 3-DOF vibration model for the dynamic tension analysis, and we derived a simple but accurate formula which corresponds to the experimental results. Our proposed methods would help to design a more optimal and reliable governor rope system.

References

1. Kotaro, F. et al.: Dynamic analysis for vertical movement of elevator governor tension sheave. In: APVC2015 conference Hanoi, Vietnam (2015)
2. Seiji W., et al: Transient analysis of elevator governor and safety gear mechanism. In: The 2nd Joint International Conference on Multibody System Dynamics (2012)
3. Takayoshi, K. et al: Simulation analysis of governor for elevators by multibody dynamics. In: Proceedings of JSME Conference, pp. 35–38, no. 10–98 (2011) (in Japanese)
4. Ryoichi, T. et al: modelling of governor rope by multibody dynamics with elastic element. In: Proceedings of JSME Conference, pp. 51–54, no. 13–86 (2014) (in Japanese)

Applicability of Automated Digging Algorithm on Sloping Ground for Hydraulic Excavators

T. Hirano, T. Yoshida, N. Tsujiuchi, A. Ito, F. Kuratani, and H. Andou

1 Introduction

In the digging operation of hydraulic excavators, the operator engages two levers simultaneously to control three hydraulic cylinders (boom cylinder, arm cylinder, and bucket cylinder). High-efficiency operation requires high-level skills, so inexperienced operators have lower operational efficiency and consume more time and fuel than skilled experienced operators. One solution for improving efficiency and supporting novice operators is to develop automated excavators. However, excavators have not been completely automated because of the complexity of modeling ground conditions and digging. Excavators need to cope with various operations and operating conditions.

Trajectory tracking control has been proposed as a control strategy, and control systems providing good accuracy have been established [1]. Researchers have derived a trajectory that improves the efficiency of automated digging. Even if efficient trajectories are prepared for different conditions, the desired productivity is not always achieved because of changes in ground conditions: soil properties, variations in ground surface, etc. Therefore, we proposed an automated digging algorithm that robustly determines the digging trajectory by using several parameters [2]. Our algorithm operates by switching between two digging modes: the raking mode for excavating soil and the lift-up mode for reducing cylinder force [3]. The lift-up mode

T. Hirano (✉) · N. Tsujiuchi · A. Ito
Department of Mechanical Engineering, Doshisha University, Kyotanabe, Japan
e-mail: cyjb1501@mail4.doshisha.ac.jp

T. Yoshida · F. Kuratani
Department of Mechanical Engineering, University of Fukui, Fukui, Japan

H. Andou
Caterpillar Japan LLC, Akashi, Japan

S. Oberst et al. (eds.), *Vibration Engineering for a Sustainable Future*,
https://doi.org/10.1007/978-3-030-46466-0_39

reproduces bucket lifting to avoid cylinder stalls by skilled operators. Avoiding cylinder stall is an important factor in realizing efficient, automated digging.

Previous studies performed [2, 3] a parametric analysis to investigate the influence of parameters on the digging performance by digging simulation. A digging simulation model composed of a soil model and the dynamic model of an excavator was used to evaluate the effectiveness of the proposed algorithm. In these studies, a digging simulation was performed on flat ground. On the other hand, the terrain is not always flat in actual digging, so we focus here on digging on a slope. Although our digging algorithm does not need to determine the optimal trajectory, its effectiveness on slopes has not been verified. In this study, the automated digging algorithm for flat ground is applied to a slope, and we verify its effectiveness for the slope and the influence of the parameters.

2 Automated Digging Algorithm [3]

The proposed digging algorithm is shown in Fig. 1. This algorithm restricts the digging reaction force such that it does not increase as high as the cylinder stall pressure while excavating and the cylinder force does not significantly exceed the threshold even at low engine power. A threshold is set in advance for the cylinder force, and the excavator excavates while switching between the two modes in accordance with the value of the cylinder force.

After the digging operation starts, the motion is controlled in accordance with the raking mode algorithm. This mode digs up the soil while the bucket is rotated

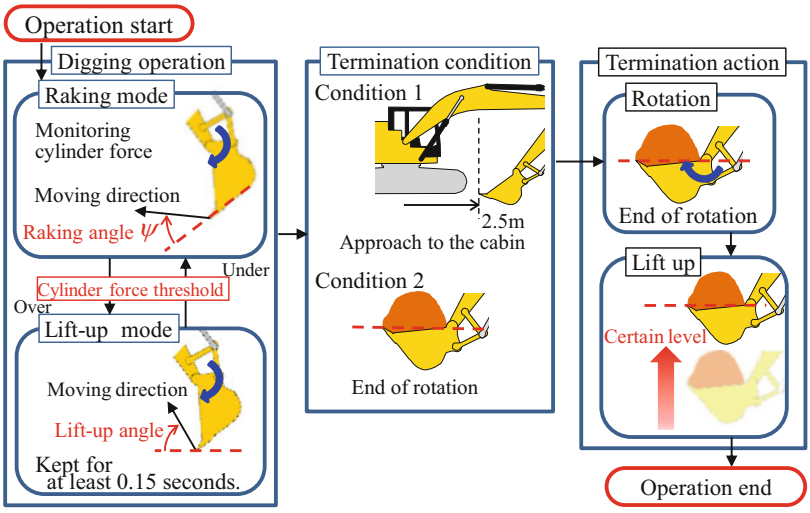

Fig. 1 Automated digging algorithm

at constant velocity. In this mode, the movement of the bucket tip is kept within a specific angle relative to the bottom of the bucket. When the digging reaction force increases and the cylinder force exceeds the preset threshold, the lift-up mode is activated, and the bucket is raised in accordance with the lift-up angle. Activating lift-up results in shallower bucket depths, reducing the digging reaction force. The lift-up mode is held for a period of only 0.15 s after being activated. After cylinder force drops below the threshold, the lift-up mode switches to raking mode.

Digging continues until it reaches one of the two termination conditions while switching between these digging modes. After reaching both termination conditions, the bucket is lifted to the desired level, and the digging is stopped.

3 Simulation Model [4]

The simulation model used in this study does not consider the swing operations of the hydraulic excavator; therefore, it is two-dimensional. The digging simulation model is composed of a soil model and the dynamic model of an excavator.

The soil model is based on the distinct element method (DEM), which calculates the behavior and reaction force of the soil. The DEM allows us to calculate contact forces between particles based on the Voigt model. For all particles, it is possible to calculate the behavior of the soil by numerically integrating the following equation of motion:

$$m_i \frac{d^2 \mathbf{w}_i}{dt^2} = m\mathbf{g} + \sum \mathbf{F}_{nj} + \sum \mathbf{F}_{sj} \tag{1}$$

In this equation, m is the mass of the particle, $\mathbf{w}_i$ is the position vector of particle i, $\mathbf{g}$ is the gravity vector, $\mathbf{F}_{nj}$ is the normal force, and $\mathbf{F}_{sj}$ is the shear force. The bucket is formed out of particle elements. This method enables us to analyze the reaction force on the bucket. In the dynamic model, the reaction force is treated as an external force.

The dynamic model of an excavator is based on kinematics. The driving cylinder force for excavation work is calculated from the equations of motion, by applying the displacement, velocity, and acceleration of the bucket during excavation.

4 Evaluation of Digging Performance

A digging performance is evaluated by payload and energy consumed per digging. In our study, evaluation index is used as an index of the performance and is defined as dividing payload by its consumed energy per one digging as follows:

$$\text{Evaluation index} = \frac{\text{Payload}}{\text{Consumed Energy}} \ [\text{kg/kJ}] \tag{2}$$

The larger the evaluation index, the lower the load and the higher the performance of the digging operation, that is, efficient digging. Considering the energy required for swing motion and soil removal, the payload should preferably be as large as possible. Therefore, to emphasize the payload, the evaluation targets are only those that indicate the payload above the piled bucket capacity. In this study, the excavator model is 20 ton class, and its piled bucket capacity is 0.8 m^3.

5 Simulation Results

5.1 Simulation Conditions

The parameters of the soil model are shown below. Particle radius is 25 mm. Particle density is 1600 kg/m^3. Young's modulus is 6.5 MPa. Poisson's ratio is 0.23. Dumping ratio is 1.0. Friction coefficient is 0.9.

The parameters of the bucket driving parameters are shown below. In the raking mode, the translational velocity and rotational velocity are defined as 0.9 m/s and −20°/s, respectively. When the operation switches to the lift-up mode, the translational velocity is decelerated to 0.54 m/s, and the rotational velocity is decelerated to −4.5°/s for a lift-up angle of 60°.

A bucket angle ϕ_E and a raking angle ψ are defined in Fig. 2. Figure 2 also shows the trajectory of each parameter in raking mode only. In the raking mode, the digging trajectory is determined by an initial bucket angle, a raking parameter $d\psi/d\phi_E$, and velocity parameters. The increase in the initial bucket angle makes the digging trajectory longer and deeper. The increase in the raking parameter $d\psi/d\phi_E$ makes the digging distance extend.

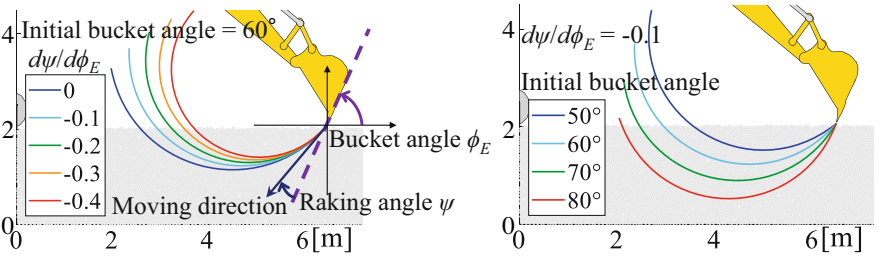

Fig. 2 Trajectory of each parameter in raking mode only

5.2 *Automated Digging on Slopes*

In the case of automated digging on slopes, we do not design an automated digging algorithm for slopes, but we perform automatic digging by applying the algorithm to flat ground. Therefore, we have devised three patterns of automated digging algorithms that are slightly modified from the algorithm for flat ground. The slopes are excavated by each algorithm, and the evaluation indices are compared. Note that the parameters not displayed in graphs have a mechanically impossible posture, do not satisfy termination conditions, or have a payload lower than the piled bucket capacity. The slope angle is 45°. The bucket tip initial position is 1.5 m below the ground where the excavator is located and 7 m away from the swing center of the excavator.

Pattern A: Using the same parameters as the flat ground Lifting the bucket by the lift-up mode of the automated digging algorithm enables digging with the same parameters. The simulation results are shown in Fig. 3.

Since the trajectories are similar regardless of the value of raking parameter $d\psi/d\phi_E$, there is no difference in evaluation index for each raking parameter $d\psi/d\phi_E$. In addition, since the soil was moved by an amount more than the piled bucket capacity at all parameter, the soil was moved too much as the initial bucket angle was larger. As a result, the energy loss increased and the evaluation index decreased.

Pattern B: Using the digging trajectory tilted by the slope angle The bucket angle is the same as the flat ground. The simulation results are shown in Fig. 4.

At pattern B, when raking parameter $d\psi/d\phi_E$ is -0.4, the termination conditions are not satisfied, and the payload is lower than the piled bucket capacity at all parameters except initial bucket angle is 70° and $d\psi/d\phi_E$ is 0. The results are shown in Fig. 4 for reference. In the early phase of digging, the bucket angle is not the angle to rake the soil, so the digging is like scraping the slope. Therefore, the payload decreases, and the evaluation index is low at all parameters.

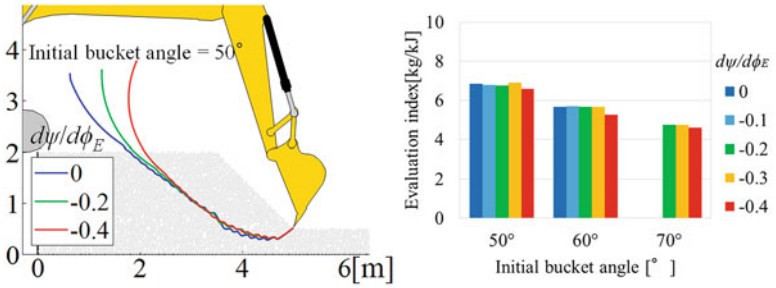

Fig. 3 Simulation result of pattern A (using the same parameters as the flat ground)

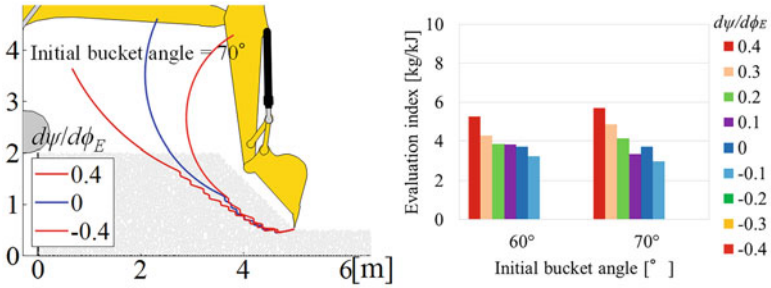

Fig. 4 Simulation result of pattern B (using the digging trajectory tilted by the slope angle)

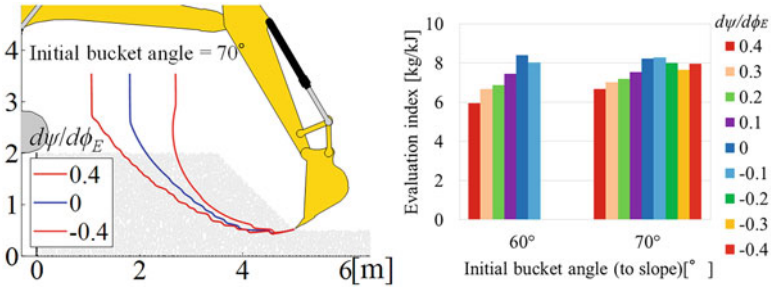

Fig. 5 Simulation results of pattern C (using the initial bucket angle tilted by the slope angle)

Pattern C: Using the initial bucket angle tilted by the slope angle When the bucket is viewed from a slope, it is the same initial angle as the flat ground. The simulation results are shown in Fig. 5.

The energy loss is reduced because the soil is not moved more than necessary. In addition, the number of lift-up mode switches is small. That is, the reaction force is low, and the slope is excavated with low energy. Therefore, the evaluation index is the best among the three patterns devised. The optimum value of the parameters is found to be around 70° at the initial bucket angle and around -0.1 at the raking parameter $d\psi/d\phi_E$.

6 Conclusion

The proposed automated digging algorithm can excavate efficiently on slopes by using the initial bucket angle tilted by the slope angle. In this case, the evaluation index is maximized when the initial bucket angle is around 70° to the slope and raking parameter $d\psi/d\phi_E$ is around -0.1.

References

1. Chang, P.H., Lee, S.J.: A straight-line motion tracking control of hydraulic excavator system. Mechatronics. **12**(1), 119–138 (2002)
2. Hirano, T., Yoshida, T., Tsujiuchi, N., Ito, A., Kuratani, F., Tateishi, M., Andou, H.: Evaluation of automated digging performance for hydraulic excavators. In: The 17th Asian Pacific Vibration Conference, #140, China (2017)
3. Yoshida, T., Tsujiuchi, N., Ito, A., Kuratani, F., Hirano, M., Andou, H.: Simulation-based evaluation of influence on digging performance by control parameters. J. Jpn. Soc. Des. Eng. **51**(11), 821–836 (2016)
4. Yoshida, T., Koizumi, T., Tsujiuchi, N., Jiang, Z., Nakamoto, Y.: Dynamic analysis of an excavator during digging operation. SAE Int. J. Commer. Veh. **6**(2), 419–428 (2013)

Part VII
Dynamics and Control of Networked Systems

Control of Optimal Motion Form of a Bipedal Space Robot Used in the Moon Base by Neural Oscillators

Tadashi Komatsu, Jyun Satou, and Yoshiteru Takahashi

1 Introduction

Recently, some manned moon base projects have been considered in Japan and other countries as the next mission of the International Space Station. And space robots, including humanoid robots, are expected to play an important role in cooperating with astronauts for future lunar exploration [1]. Humanoid robot features have many advantages, such as for interacting with astronauts and the ability to perform human tasks. Particularly, a humanoid robot used in a room of the moon base mainly will do physical work with astronauts in the environment with air and a flat floor as opposed to the Rover. This research investigates the influence of low gravity (1.62 m/s^2) on the motion of the bipedal robot used in a room of the base with low speed for safe movement, for example, walking, running, and jumping, from the viewpoint of energy consumption using dynamic simulations to obtain some data of the control design. On the other hand, the control method of the bipedal robot with high speed has already been studied [1]. By considering the amplitude of joint torque during robot motions, the optimal motion form of a robot was shown. The amplitude of joint torque in running on the moon was almost the same as that in walking on the earth. It means that running is adaptive for a human being on the moon because precise torque control of the legs is difficult. Alternatively, a robot can easily do such precise control with about one-tenth value of the walking torque on the earth. So walking is an optimal motion because of it having small torque and energy saving, unlike astronauts on the moon.

T. Komatsu (✉) · J. Satou
Kanto Gakuin University, Yokohama, Kanagawa, Japan
e-mail: komatsu@kanto-gakuin.ac.jp; satou@kanto-gakuin.ac.jp

Y. Takahashi
Former member of Kanto Gakuin University, Yokohama, Kanagawa, Japan

S. Oberst et al. (eds.), *Vibration Engineering for a Sustainable Future*,
https://doi.org/10.1007/978-3-030-46466-0_40

2 Dynamic Modelling

2.1 Simulation Model

A simulation model was obtained by considering our experimental setup. We applied the Newton-Euler dynamic equation derived by Taga et al. [2]. The system consists of an interconnected chain of rigid links, as shown in Fig. 1. The leg has the joint at the hip and the knee but does not have the joint at the ankle. The model has limited movement in the sagittal plane. *Xi* and *Yi* are inertial coordinates of the center of gravity for each link, θi denotes a joint angle, *Fgi* denotes a reflecting force from the floor in the horizontal and vertical directions, *mi* is the mass of each mass point, and *li* is the length of a link. Nonlinear friction forces are assumed in the hip and knee joints, and elastic forces are assumed in the knee. Here, the floor was modeled as a two-dimensional spring and damper. We also considered a slipping of the foot during locomotion. Each time the ankle touches the ground, the rest position of the spring is reset to the point at which the ankle first touches. The reflecting force *Fgi* is generated by this floor model in both directions.

The general form of dynamics is obtained as follows [2]:

$$\ddot{\mathbf{X}} = \mathbf{P}(\mathbf{X})\left[\mathbf{C}(\mathbf{X})\mathbf{P}(\mathbf{X})\right]^{-1}\left[\mathbf{D}\left(\mathbf{X},\ \dot{\mathbf{X}}\right) - \mathbf{C}(\mathbf{X})\mathbf{Q}\left(\mathbf{X},\ \dot{\mathbf{X}}, \mathbf{T_r}, \mathbf{F_g}\left(\mathbf{X},\ \dot{\mathbf{X}}\right)\right)\right] + \mathbf{Q}\left(\mathbf{X},\ \dot{\mathbf{X}}\ , \mathbf{T_r}, \mathbf{F_g}\left(\mathbf{X},\ \dot{\mathbf{X}}\right)\right) \tag{1}$$

where $\boldsymbol{X}$ is a (14×1) vector of inertia positions and inertial angles of links.

$$\mathbf{X} = (X_1, Y_1, X_2, Y_2, \theta_1, X_4, Y_4, \theta_2, X_3, Y_3, \theta_3, X_5, Y_5, \theta_4)^T \tag{2}$$

$\boldsymbol{P}$ is a (14×8) matrix including mass parameters. $\boldsymbol{C}$ is a (8×14) matrix and $\boldsymbol{D}$ is a (8×1) vector. For example, the following equation is the kinematic constraints:

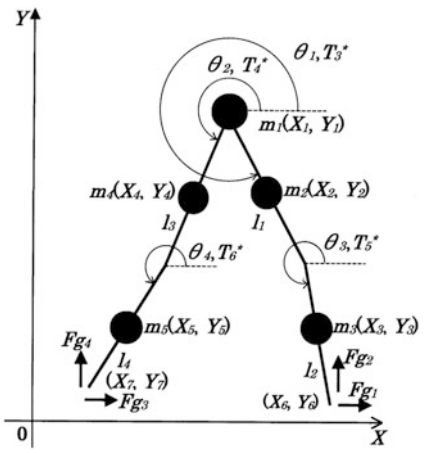

Fig. 1 Simulation model of bipedal space robot

$$X_1 = X_2 - (l_1/2)\cos\theta_1 \tag{3}$$

and we can obtain the following equation by differentiating the above equation twice.

$$\ddot{X}_1 - \ddot{X}_2 - (l_1/2)\sin\theta_1\ddot{\theta}_1 = (l_1/2)\cos\theta_1\dot{\theta}_1^2 \tag{4}$$

By using the following, other constraints:

$$Y_1 = Y_2 - (l_1/2)\sin\theta_1 \tag{5}$$

$$X_1 = X_4 - (l_1/2)\cos\theta_2 \tag{6}$$

$$Y_1 = Y_4 - (l_1/2)\sin\theta_2 \tag{7}$$

$$X_2 + (l_1/2)\cos\theta_1 = X_3 - (l_2/2)\cos\theta_3 \tag{8}$$

$$Y_2 + (l_1/2)\sin\theta_1 = Y_3 - (l_2/2)\sin\theta_3 \tag{9}$$

$$X_4 + (l_3/2)\cos\theta_2 = X_5 - (l_4/2)\cos\theta_4 \tag{10}$$

$$Y_4 + (l_3/2)\sin\theta_2 = Y_5 - (l_4/2)\sin\theta_4 \tag{11}$$

Equations can be written in the compact form as shown in the text:

$$\mathbf{C}(\mathbf{X})\ \ddot{\mathbf{X}} = \mathbf{D}\left(\mathbf{X},\ \dot{\mathbf{X}}\right) \tag{12}$$

$\boldsymbol{Q}$ is a (14 × 1) vector including a constrained force at the knee joint. $\boldsymbol{T}_\mathrm{r}$ is a (4 × 1) vector of joint torques, and $\boldsymbol{F}_\mathrm{g}$ is a (4 × 1) vector of forces on the ankle which depend on the state of the floor.

2.2 H-CPG Control

Hybrid central pattern generator (H-CPG), used in this study, consists of a rhythm generator, a force controller, and an attitude controller. A rhythm generator generates the rhythmical motion of a bipedal robot using CPG. A force controller works

to create a different motion phase, for example, a walking phase and a stepping phase, by controlling forces acting from the leg to the floor. An attitude controller is used for controlling the absolute attitude of the two thighs to be vertical.

2.3 Rhythm Generator

A rhythm generator moves a bipedal robot. We improved the basic model proposed by Matsuoka and applied these improvements to a bipedal robot by Taga et al. [2].

The neural rhythm generator has four unit oscillators as shown in Fig. 2. One unit oscillator consists of two neural oscillators. These unit oscillators consist of inhibitory connections. The two neurons alternately make inputs in the directions of the contraction of the flexor and extensor muscles. Each neural oscillator is interconnected with the others by the inhibitory connections. The connections between hip unit oscillators realize alternate excitations to generate the alternation between the motion of the right and left legs. By using the appropriate connection of relative phases in ipsilateral joints, the extensor neuron of the knee unit oscillator is excited when that of the hip unit oscillator is excited and the foot is leaving the floor. On the other hand, the flexor neuron is excited when the foot is touching the floor. The rhythm generator is obtained by the following differential equations:

$$\tau_i \dot{u}_i = -u_i - \sum_{j=1}^{8} w_{ij} y_i - \beta v_i + u_{0i} + Feed_i \quad (i = 1, 8) \tag{13}$$

$$Feed_i = a_i \, (\theta_1 + \pi/2) \, (-1)^i \quad (i = 1, 2) \tag{14}$$

$$Feed_i = a_i \, (\theta_2 + \pi/2) \, (-1)^i \quad (i = 3, 4) \tag{15}$$

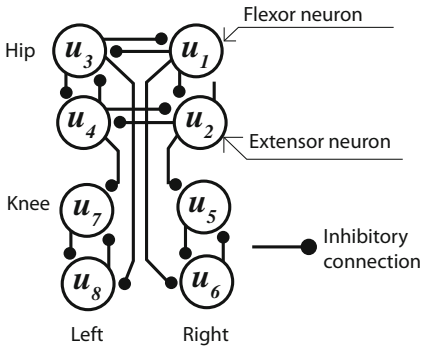

Fig. 2 Neural rhythm generator

$$\tau_i' \dot{v}_i = -v_i + y_i \quad (i = 1, 8) \tag{16}$$

$$y_i = \max(0, u_i) \quad (i = 1, 8) \tag{17}$$

where u_i is the inner state of the ith neuron, y_i is the output of the ith neuron, v_i is a variable representing the degree of the adaptation or self-inhibition effect on the ith neuron, u_{0i} is an external input, and w_{ij} is a connecting weight, respectively. $Feed_i$ is a feedback signal from robot sensors, but $Feed_5$, $Feed_6$, $Feed_7$, and $Feed_8$ are zero. Equations of $Feed_i$ were newly proposed here. τ_i and τ_i' denote time constants of the inner state and the adaptation effect.

Then, for example, an output ${T^*}_{CPGi}$ from this model is obtained by:

$${T^*}_{CPG3} = P_h^f y_1 - P_h^e y_2 \quad \text{(hip/right)} \tag{18}$$

where ${P_h}^f$ and ${P_h}^e$ are control gains.

2.4 Modulation Mechanism

A modulation mechanism realizes precise velocity control of a bipedal robot system. The output $\boldsymbol{T_F}$ of this mechanism is given by the following equation:

$$\boldsymbol{T_F} = \boldsymbol{J}^T (\boldsymbol{F_C} + \boldsymbol{F_V}) \tag{19}$$

where $\boldsymbol{J}^T$ is a transposed Jacobian matrix, which is obtained by kinematic relations between the foot position from the hip and each joint angle. $\boldsymbol{F_C}$ denotes the acting force from the leg to the floor in a support phase. $\boldsymbol{F_V}$ is the virtual force acting to the tip of the leg in a swing phase. To control the walking speed, the driving force of a robot is modulated by $\boldsymbol{F_C}$ through the support phase. Also, the stride length is changed by $\boldsymbol{F_V}$ appropriately.

2.5 Attitude Controller

By using the conventional PD feedback method of a joint angle, a bias input to control the absolute attitudes of the two thighs to be vertical is calculated as follows:

$$T_{Ai} = g_{1i} (\pi/\mathbf{4} - \theta_{i-2}) - g_{2i} \dot{\theta}_{i-2} \quad (i = 3, 6) \tag{20}$$

where g_{1i} and g_{2i} are control gains.

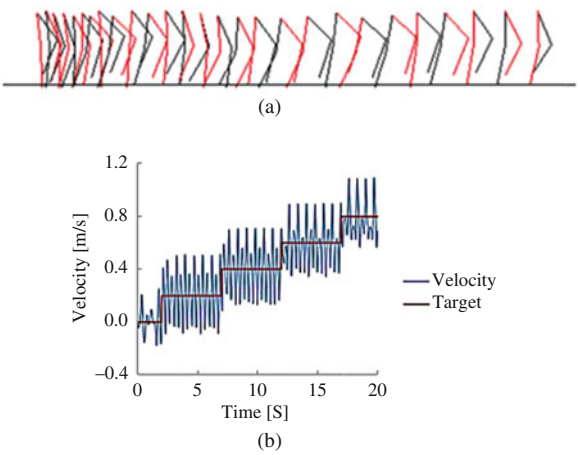

Fig. 3 Walking on the earth. (**a**) The stick figure traced every 0.5 s. (**b**) Velocity versus time

3 Numerical Simulations

The effectiveness of the gravity is demonstrated by numerical simulations. The dynamics for neural oscillators and the motion of a bipedal robot were implemented in C language using the fourth-order Runge-Kutta method for integration with the calculation interval of 2.0×10^{-4} s. Numerical data used in the simulations are summarized as follows: link length l_1, $l_3 = 0.4$ m, l_2, $l_4 = 0.45$ m, pinpoint mass $m_1 = 27$ kg, m_2, $m_4 = 0.2$ kg, m_3, $m_5 = 0.4$ kg, both spring coefficients of floor $k_f = 1.0 \times 10^5$ N/m, both damper coefficients of floor $d_f = 2.24 \times 10^3$ Ns/m, weight coefficients of CPG w_{12},w_{21},w_{34},w_{43},w_{56},w_{65},w_{78},$w_{87} = -2.0$, w_{13},w_{24},w_{31},w_{42},w_{61},w_{83}, w_{52},$w_{74} = -1.0$, others 0, time constant $\tau_i = 0.350$ s, $\tau_i' = 0.250$ s ($i = 1,2,3,4$), $\tau_i = 0.175$ s and $\tau_i' = 0.125$ s ($i = 5,6,7,8$). Simulation results showed that the stable motion was realized (see Fig. 3) and the torque amplitude of running on the moon was almost the same order as that of walking on the ground (see Figs. 4 and 5). Running is a general form for an astronaut, as having been seen in the Apollo Project. It is thought that an astronaut can prevent the decline of an exercise function by using the leg power of the size same as walking on the ground. The torque amplitude of walking on the moon was almost one-tenth of that on the earth at the same speed (see Fig. 6). A robot can easily do precise control of about 10% of the walking torque on the earth. Energy consumptions in the case of Figs. 4, 5, and 6 were 6.8 kJ, 7.0 kJ, and 1.2 kJ. So, by making much of energy saving, walking is an optimal motion for a humanoid robot. The speed should be also reduced compared to walking on the earth with the zero moment point [3].

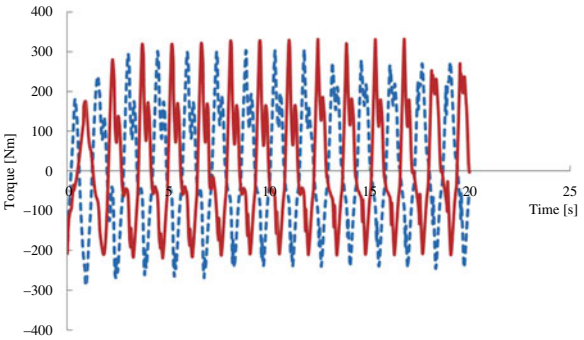

Fig. 4 Knee joint torque of walking on the earth (the solid line denotes the right leg; the dotted line denotes the left leg)

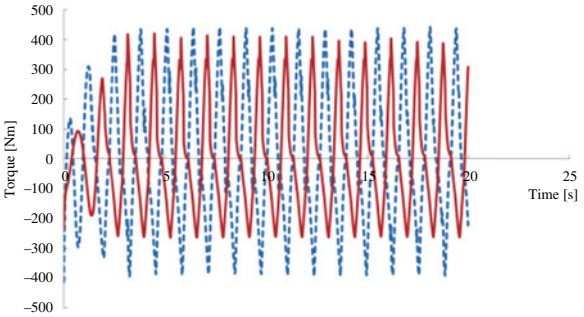

Fig. 5 Knee joint torque of running on the moon (the solid line denotes the right leg; the dotted line denotes the left leg)

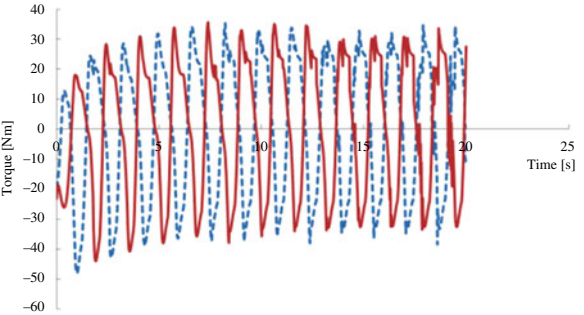

Fig. 6 Knee joint torque of walking on the moon (the solid line denotes the right leg; the dotted line denotes the left leg)

4 Conclusions

In this paper, we investigated the effect of low gravity on bipedal robot motion on the moon, for example, walking, running, and jumping, from the viewpoint of energy consumption using dynamic simulations. By making much of energy saving by suppressing the joint torque, walking is an optimal motion for a humanoid robot. We are now preparing for an experimental setup of a bipedal robot in a lunar simulator.

References

1. Omer, A., Hashimoto, K., Lim, H., Takanishi, A.: Study of bipedal robot walking motion in low gravity: investigation and analysis. Int. J. Adv. Robot Syst. **11**(9), 1–14 (2014)
2. Taga, G., Yamaguchi, Y., Shimizu, H.: Self-organized control of bipedal locomotion by neural oscillators in unpredictable environment. Biol. Cybernetics. **65**, 147–159 (1991)
3. Mineti, A.E.: Walking on other planets. Nature. **409**, 467–468 (2001)

Energetic Consideration on the Occurrence Condition of Self-Synchronization in Two Unbalanced Rotors

M. Sueda, T. Kondou, and H. Mori

1 Introduction

When self-synchronization occurs in a system in which multiple nonlinear self-excited oscillators with different natural frequencies are coupled, all of the oscillators vibrate at one specific frequency due to their interaction. Although several researchers have examined the characteristics of this phenomenon in, e.g., motors [1–4], pendulums [5, 6], and organ pipes [7], the mechanism has not yet been completely clarified.

In order to obtain new insights into the occurrence mechanism, this paper treats a system comprising two counter-rotating unbalanced rotors. The energy integration of the equations of motion yields two equations that describe the conditions on the energy dissipation and the energy transfer required for synchronization. These conditions can be used for analytical prediction of the range of synchronous frequency and the applied voltages at which synchronization occurs. Furthermore, the synchronous frequency and the phase difference can be obtained for given parameters by numerically solving these equations. The validity of the analysis is verified by comparing the results obtained from the two energetic conditions and the shooting method.

M. Sueda (✉)
Department of Mechanical Engineering, Graduate School of Engineering, Kyushu University, Fukuoka-shi, Fukuoka, Japan
e-mail: sueda@mvib.mech.kyushu-u.ac.jp

T. Kondou · H. Mori
Department of Mechanical Engineering, Faculty of Engineering, Kyushu University, Fukuoka-shi, Fukuoka, Japan

S. Oberst et al. (eds.), *Vibration Engineering for a Sustainable Future*,
https://doi.org/10.1007/978-3-030-46466-0_41

2 Analytical Model and Equations of Motion

Figure 1 shows the analytical model considered in this paper. The system comprises two counter-rotating rotors, each of which has unbalanced mass m at distance r from the axis of rotation. The rotors are driven by DC motors that are installed in a rigid body of mass M with their axes of rotation being horizontal and parallel. In the following description, the left- and right-hand motors are denoted as Motor 1 and Motor 2, respectively. The rigid body is supported by springs with spring constants k_x and k_y and dashpots with damping coefficients c_x and c_y and is constrained to move translationally in the vertical plane perpendicular to the motor axes. The horizontal and vertical displacements of the rigid body are denoted by x and y, and the angular displacements of Motor 1 and Motor 2 are denoted by ϕ_1 and ϕ_2, respectively. The positive directions of these variables are defined as shown in Fig. 1. The effect of gravity is ignored.

By using these variables, the equations of motion are derived as follows:

$$\left.\begin{aligned}
&\hat{M}\ddot{x} + c_x\dot{x} + k_x x = mr\left(\ddot{\phi}_1\cos\phi_1 - \dot{\phi}_1^2\sin\phi_1\right) - mr\left(\ddot{\phi}_2\cos\phi_2 - \dot{\phi}_2^2\sin\phi_2\right)\\
&\hat{M}\ddot{y} + c_y\dot{y} + k_y y = -mr\left(\ddot{\phi}_1\sin\phi_1 + \dot{\phi}_1^2\cos\phi_1\right) - mr\left(\ddot{\phi}_2\sin\phi_2 + \dot{\phi}_2^2\cos\phi_2\right)\\
&J\ddot{\phi}_1 + B\dot{\phi}_1 = Ae_1 + mr\left(\ddot{x}\cos\phi_1 - \ddot{y}\sin\phi_1\right)\\
&J\ddot{\phi}_2 + B\dot{\phi}_2 = Ae_2 - mr\left(\ddot{x}\cos\phi_2 + \ddot{y}\sin\phi_2\right)
\end{aligned}\right\} \tag{1}$$

where

$$\hat{M} = M + 2m,\quad J = mr^2 + J_r,\quad A = \frac{K_t}{r_a},\quad B = \frac{K_t K_E}{r_a} \tag{2}$$

in which J_r is the moment of inertia of rotating bodies to which the unbalanced masses are attached, K_t is the torque constant, K_E is the voltage constant, r_a is the armature resistance, e_1 and e_2 are the voltages supplied to Motor 1 and Motor 2, and the overdot symbol indicates differentiation with respect to time. The parameters of the motors are identical, except for voltages e_1 and e_2.

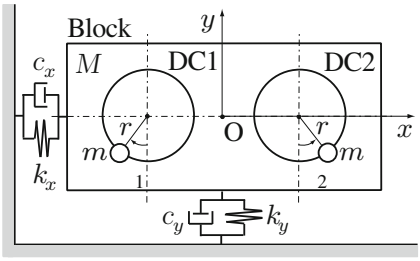

Fig. 1 Analytical model

3 Theoretical Analysis

3.1 Energetic Conditions for Synchronization

In order to derive the conditions for synchronization, the energy integration of Eq. (1) is performed by integrating each equation over one synchronization period after multiplying the equation by the corresponding velocity, $\dot{x}$, $\dot{y}$, $\dot{\phi}_1$, or $\dot{\phi}_2$. Although, for a clear understanding, it is desirable to obtain analytical results rather than numerical results, an exact analysis of Eq. (1) is impossible due to its complexity. Therefore, based on the fact that the time averages of the angular frequencies $\dot{\phi}_1$ and $\dot{\phi}_2$ are entrained into the same value in a synchronized state, it is assumed that the two rotors rotate at the same constant synchronous angular frequency ω with constant phase difference θ. This yields the following analytical solutions for ϕ_1 and ϕ_2:

$$\phi_1 = \omega t, \quad \phi_2 = \omega t + \theta \tag{3}$$

where ω and θ are unknown constants to be determined. Using Eq. (3), the right-hand sides of the first and second equations in Eq. (1) become harmonic functions, and therefore analytical solutions for x and y can also be derived.

By using the analytical solutions for ϕ_1, ϕ_2, x, and y, the energy integration of the third and fourth equations in Eq. (1) over one period $2\pi/\omega$ from initial time t_0 yields the following:

$$2\pi B\omega + \frac{1}{2}E_{cx} + \frac{1}{2}E_{cy} = 2\pi Ae_1 - E_s, \quad 2\pi B\omega + \frac{1}{2}E_{cx} + \frac{1}{2}E_{cy} = 2\pi Ae_2 + E_s \tag{4}$$

where

$$\left.\begin{aligned} E_{cx} &\square\, m\mu\pi r^2\omega^4 \frac{4\zeta_x\omega_x\omega}{\left(\omega_x^2-\omega^2\right)^2+(2\zeta_x\omega_x\omega)^2}\,(-\cos\theta+1) \\ E_{cy} &\square\, m\mu\pi r^2\omega^4 \frac{4\zeta_y\omega_y\omega}{\left(\omega_y^2-\omega^2\right)^2+(2\zeta_y\omega_y\omega)^2}\,(\cos\theta+1) \\ E_s &\square\, -m\mu\pi r^2\omega^4\left[-\frac{\omega_x^2-\omega^2}{\left(\omega_x^2-\omega^2\right)^2+(2\zeta_x\omega_x\omega)^2}+\frac{\omega_y^2-\omega^2}{\left(\omega_y^2-\omega^2\right)^2+(2\zeta_y\omega_y\omega)^2}\right]\sin\theta \end{aligned}\right\} \tag{5}$$

$$\mu = \frac{m}{\hat{M}}, \quad \omega_x = \sqrt{\frac{k_x}{\hat{M}}}, \quad \omega_y = \sqrt{\frac{k_y}{\hat{M}}}, \quad \zeta_x = \frac{c_x}{2\sqrt{\hat{M}k_x}}, \quad \zeta_y = \frac{c_y}{2\sqrt{\hat{M}k_y}} \tag{6}$$

In Eq. (4), the terms $2\pi Ae_1$ and $2\pi Ae_2$ represent the excitation energies supplied by the applied voltages e_1 and e_2, and the term $2\pi B\omega$ represents the energy

Table 1 System parameters

M [kg]	0.57	r [m]	0.013
m [kg]	0.02	r_a [Ω]	8.82
c_x [N·s/m]	1.0	K_t [N·m/A]	13.9×10^{-3}
c_y [N·s/m]	2.0	K_E [V·s/rad]	13.9×10^{-3}
k_x [N/m]	7.28×10^2	J_r [kg·m^2]	2.343×10^{-6}
k_y [N/m]	1.541×10^3		

dissipated by the internal damping of the motor. The remaining terms represent the energy transferred from the rotors to the rigid body. While E_{cx} and E_{cy} in Eq. (4) are parts of such transferred energy, the same expressions are also obtained from energy integration of the damping terms in the first and second equations in Eq. (1) as follows:

$$E_{cx} = \int_{t_0}^{t_0+\frac{2\pi}{\omega}} c_x \dot{x}^2 dt, \quad E_{cy} = \int_{t_0}^{t_0+\frac{2\pi}{\omega}} c_y \dot{y}^2 dt \tag{7}$$

This means that E_{cx} and E_{cy} are, respectively, dissipated by damping coefficients c_x and c_y after transfer to the rigid body. Therefore, E_s is the energy exchanged between the rotors and is hereinafter referred to as the self-synchronized energy.

The two equations in Eq. (4) can be rearranged as follows:

$$4\pi B\omega + E_{cx} + E_{cy} = 2\pi A\,(e_1 + e_2)\,, \quad 2E_s = 2\pi A\,(e_1 - e_2) \tag{8}$$

The first equation indicates that the total excitation energy is consumed as the dissipated energy by damping elements, while the second equation indicates that the self-synchronized energy is exchanged in order to compensate for the gap between the energies supplied by each motor.

The first equation in Eq. (8) contains ω and $\cos\theta$ and therefore determines a certain range of ω (note that $-1 \leq \cos\theta \leq 1$). This gives the range of the synchronous angular frequency ω for which the condition concerning the dissipated energy can be satisfied. On the other hand, the second equation in Eq. (8) contains ω and $\sin\theta$ and similarly gives the range of ω for which the condition concerning the self-synchronized energy can be satisfied. Self-synchronization occurs only when ω is included in both of these ranges.

3.2 Analytical Results

In order to examine the effectiveness of the proposed energy-based analysis, the range of the synchronous frequency $f_{\mathrm{syn}}(=\omega/2\pi)$ was examined using Eq. (8) for the case in which the supplied voltage of Motor 1 was varied, while that of Motor 2 was fixed at $e_2 = 2.0$ V. The parameter values used are shown in Table 1.

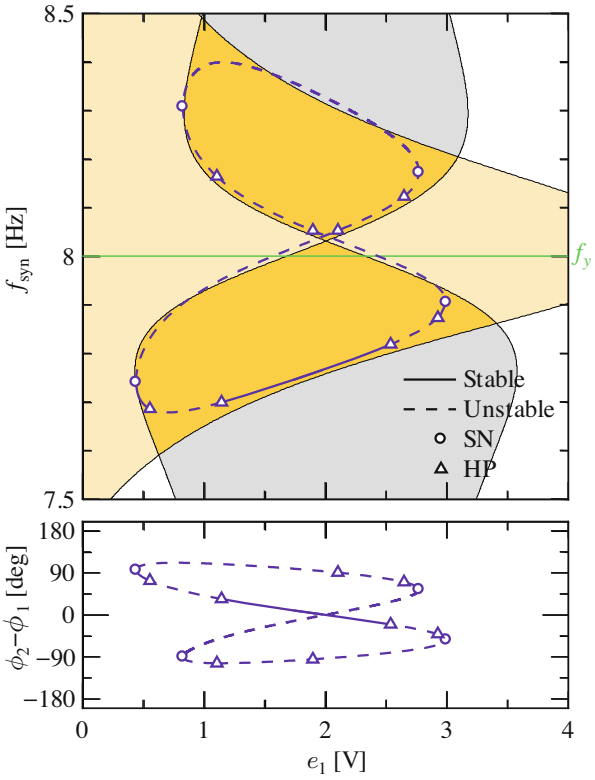

Fig. 2 Calculated results ($e_2 = 2.0$ V)

The results of the proposed analysis suggest that the system in Fig. 1 has three types of synchronized states, one of which is presented in Fig. 2 together with the accurate solution branch obtained by the shooting method. The abscissa is the applied voltage e_1 of Motor 1, and the ordinates are the synchronous frequency f_{syn} and the phase difference $\phi_2 - \phi_1$ between the rotors.

The areas where f_{syn} can satisfy the conditions regarding the dissipated energy and the self-synchronized energy (given by the first and second equations in Eq. (8)) for suitable θ are indicated in beige and gray, and the area where f_{syn} can satisfy both conditions is indicated in orange. The solid and broken lines represent the stable and unstable solutions obtained from the shooting method. The symbols ◯ and Δ on the solution branch denote the saddle-node bifurcation points and Hopf bifurcation points, respectively. The green horizontal line represents the natural frequency $f_y \left(= \sqrt{k_y/\hat{M}}\right)$ obtained from the analytical model with fixed unbalanced masses.

As shown in Fig. 2, the solution branch exists near f_y and is almost included in the orange area, demonstrating that self-synchronization occurs in the area where the

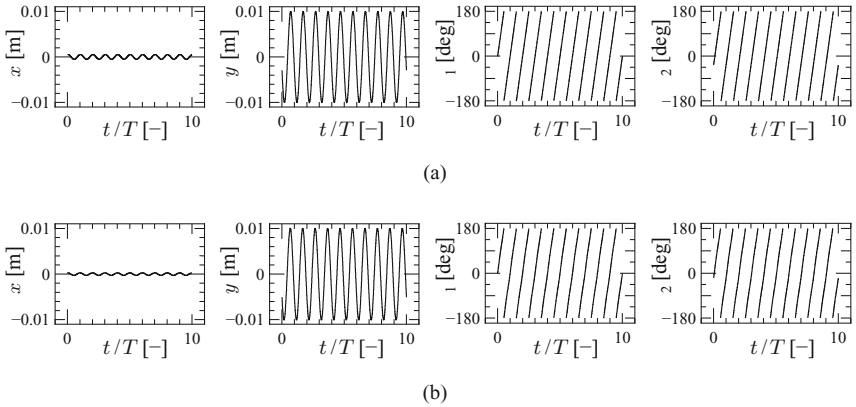

Fig. 3 Results obtained by the proposed method and the shooting method. (**a**) Proposed method. (**b**) Shooting method

two energetic conditions are satisfied. The slight misalignment between the solution branch and the orange area is due to the use of the approximation.

Furthermore, the behavior of the system in a synchronized state is examined by numerically solving Eq. (8) with respect to ω and θ. The result for $e_1 = 2.5$ V and $e_2 = 2.0$ V is shown in Fig. 3 along with the accurate solution obtained by the shooting method. The result of the proposed method is in fairly good agreement with the accurate solution, indicating the validity of the energy-based analysis.

4 Conclusion

The energetic occurrence conditions for self-synchronization have been investigated using a system comprising two counter-rotating unbalanced rotors. The analysis derived two conditions. One condition is that the total energy supplied by the motors must match the dissipated energy consumed by the damping elements, and the other condition is that the gap between the energies supplied by each motor must be within the range in which the energy can be exchanged by the interaction between the rotors through the motion of the rigid body. The derived conditions have been demonstrated to be able to predict the range of synchronous frequency and the applied voltages at which self-synchronization occurs. The behavior of the system in a synchronized state has also been examined by the proposed analysis and exhibits good agreement with the accurate solution.

References

1. Blekhman, I.I.: Synchronization in Science and Technology. ASME Press, New York (1988)
2. Bonkobara, Y., Mori, H., Kondou, T., Ayabe, T.: Self-synchronized phenomena generated in rotor-type oscillators: on the influence of coupling condition between oscillators. J. Syst. Des. Dyn. **2**(3), 861–873 (2008)
3. Nagamine, T., Sato, Y., Kawase, K.: Synchronization and chaos of unbalanced rotors on a flexible structure. J. Syst. Des. Dyn. **2**(1), 45–53 (2007)
4. Paz, M., Cole, J.D.: Self-synchronization of two unbalanced rotors. J. Vib. Acoust. **114**, 37–41 (1992)
5. Pantaleone, J.: Synchronization of metronomes. Am. J. Phys. **70**(10), 992–1000 (2002)
6. Pikovsky, A., Rosenblum, M., Kurths, J.: Synchronization (a Universal Concept in Nonlinear Sciences). Cambridge University Press, Cambridge (2001)
7. Rayleigh, J.W.S.: Theory of Sound, vol. 2. Dover Publications, New York (1945)

Synchronized Behavior of Networked Harmonic Oscillators with Sampled Position States and Input Delays

Hua Zhang, Xiaohui Wu, and Qing Yan

1 Introduction

Coupled harmonic oscillator system is usually regarded as a basic model in describing complex networks and complex systems that involve repetitive movements, i.e., an array of identical LC oscillators in the electrical networks, damper- and spring-coupled pendulums [6], sampling and surveillance [1], and so on. During the past decade, the synchronization of coupled harmonic oscillators has attracted great attentions worldwide, and many important results have been obtained in different views of points; see [1, 6–8] and the references therein for more information.

Recently, we have examined the synchronized cooperative behavior of coupled harmonic oscillators without velocity measurements by using the impulsive control strategy [8], where only the sampled relative position states are used to generate control inputs such that the system achieves synchronization. It is worthy to note that time delays play an important role in many fields such as engineering, physics, or biology [5]. Therefore, it is of great significant importance to study the synchronized behavior of the coupled harmonic oscillators with control input time delays. It is shown that when the largest eigenvalue of the Laplacian matrix of the network topology is equal to or greater than 2, the sampling period should be greater than a threshold [8]. However, the sampling period can be less than the threshold in some cases if a proper time delay is introduced. Moreover, we have found that for some

H. Zhang (✉)
School of Science, Chongqing University of Technology, Chongqing, P. R. China

Tongren University, Tongren, P. R. China
e-mail: zhanghwua@163.com

X. Wu · Q. Yan
School of Science, Chongqing University of Technology, Chongqing, P. R. China
e-mail: 2889719431@qq.com; yantsing@cqut.edu.cn

S. Oberst et al. (eds.), *Vibration Engineering for a Sustainable Future*,
https://doi.org/10.1007/978-3-030-46466-0_42

particular time delays, the coupled harmonic oscillators can always synchronize their motions with all real sampling periods except for those whose products with the frequency are less than 2π and just equal to integer multiples of π.

The rest of this paper is organized as follows. In Sect. 2, some notations, graph theory, and problem formulations are presented. Section 3 gives the main results of this paper. Finally, conclusions are drawn in Sect. 4.

2 Notations and Graph Theory

The following fairly standard notations are used throughout this paper. Let $\mathbb{R}$, $\mathbb{N} = \{1, 2, 3, \ldots\}$, and $\mathbb{R}^{n\times n}$ be the set of real numbers, the set of positive integers, and the set of $n \times n$ real matrices, respectively. $\mathbf{0}_n \in \mathbb{R}^n$ is the vector with all zeros, and $O_n \in \mathbb{R}^{n\times n}$ is a zero matrix. The entries of vector $\mathbf{1}_n \in \mathbb{R}^n$ are all ones, and I_n is an identity matrix of order $n \times n$. The diagonal matrix $\mathrm{diag}(d_1, d_2, \ldots, d_n)$ has entries as d_i , $i = 1, 2, \ldots, n$. For a column vector $\mathbf{p}$, $\mathbf{p}^\top$ denotes its transpose. For matrix $A \in \mathbb{R}^{n\times n}$, $\lambda(A)$ and $\rho(A)$ denote its spectrum and spectral radius, respectively. The symbol $\otimes$ denotes the Kronecker product of two matrices.

Let $\mathcal{G} = (\mathcal{V}, \mathcal{E}, \mathcal{A})$ denote a weighted undirected graph of order n ($n \geq 2$) with a set of nodes $\mathcal{V} = \{1, 2, \ldots, n\}$, a set of edges $\mathcal{E} \subseteq \mathcal{V} \times \mathcal{V}$, and a weighted adjacency matrix $\mathcal{A} = [a_{ij}] \in R^{n\times n}$, which is defined as $a_{ij} \neq 0$ if $(j, i) \in \mathcal{E}$, otherwise $a_{ij} = 0$ for all $i \neq j$, and $a_{ii} = 0$ for all $i = 1, 2, \cdots, n$. An edge of $\mathcal{G}$ is represented by $e_{ij} = (i, j)$, and an undirected path is a sequence of edges. The graph Laplacian with the undirected graph $\mathcal{G}$ is defined as $L = [l_{ij}] \in R^{n\times n}$, where $l_{ii} = \sum_{j=1, j\neq i}^{n} a_{ij}$ and $l_{ij} = -a_{ij}$, $i \neq j$. The undirected graph is called connected if there exists an undirected path between any pair of distinct nodes. If $\mathcal{G}$ is connected, then the Laplacian L is a symmetric semi-definite positive matrix with 0 being the unique eigenvalue and $u_1 = \mathbf{1}_n$ the corresponding eigenvector. There exists a nonsingular matrix $U = [u_1, u_2, \ldots, u_n]$, such that $U^{-1}LU = \mathrm{diag}(0, \lambda_2, \lambda_3, \ldots, \lambda_n) \triangleq J$ and $Lu_i = \lambda_i u_i$, $i = 1, 2, \ldots, n$ and the first row vector of U^{-1} is $\mathbf{1}_n^T/n$ [8].

3 Main Results

Consider a network consisting of n coupled harmonic oscillators described by

$$\dot{r}_i(t) = v_i(t), \quad \dot{v}_i(t) = -\omega^2 r_i(t) + u_i(t), \quad i = 1, 2, \ldots, n, \tag{1}$$

where $r_i(t), v_i(t) \in \mathbb{R}$ represent the position and velocity states of the i-th harmonic oscillator at time t, $u_i(t)$ is the corresponding control input for the i-th oscillator, and $\omega > 0$ denotes the frequency or the position gain of the uncoupled harmonic oscillators.

We have considered the case that the relative velocity states among the oscillators are no longer available, but each oscillator can only obtain its position states relative to its neighbors at a series of sampling instants [8]. In this paper, we consider the following input control protocol for system (1) with input time delays based on the protocol (2) in [8]:

$$u_i(t) = -\sum_{k=1}^{\infty}\left(\sum_{j=1}^{n} a_{ij}\frac{r_{ij}(t-\tau)-r_{ij}(t-T-\tau)}{T}\right)\delta(t-t_k), \tag{2}$$

where $r_{ij}(t-\tau) := r_i(t-\tau) - r_j(t-\tau)$ represents the delayed sampled position state of oscillator i relative to its neighboring oscillator j at time t, the constant $T > 0$ denotes the sampling period, and $0 < \tau < T$ represents the input time delay.

Without loss of generality, we assume that the velocity states of the harmonic oscillators are left continuous at $t = t_k$, that is, $v_i(t_k) = v_i(t_k^-) = \lim_{t\to t_k-} v_i(t)$ and $v_i(t_k^+) = \lim_{t\to t_k+} v_i(t)$. Then, by the impulsive integral characteristic of $\delta(t)$, integrating Eq. (2) at $t = t_k$ yields $v_i(t_k^+) = v_i(t_k) - \sum_{j=1}^{n} a_{ij}\frac{r_{ij}(t_k-\tau)-r_{ij}(t_{k-1}-\tau)}{T}$, which can be regarded as the state updated rule for the velocity states at the discrete instants.

Denote $r(t) = [r_1(t), r_2(t), \ldots, r_n(t)]^\top$ and $v(t) = [v_1(t), v_2(t), \ldots, v_n(t)]^\top$, and notice that the position states of the oscillators are continuous at each time instants, i.e., $r(t_k^+) = r(t_k)$, the system (1) with protocol (2) can be rewritten as the following impulsive differential equations

$$\begin{cases} \begin{bmatrix}\dot r(t)\\ \dot v(t)\end{bmatrix} = \begin{bmatrix} O_n & I_n\\ -\omega^2 I_n & O_n\end{bmatrix}\begin{bmatrix} r(t)\\ v(t)\end{bmatrix},\ t\in(t_{k-1}, t_k],\\ \begin{bmatrix} r(t_k^+)\\ v(t_k^+)\end{bmatrix} = \begin{bmatrix} r(t_k)\\ v(t_k)\end{bmatrix} - \begin{bmatrix} O_n & O_n\\ \frac{1}{T}L & O_n\end{bmatrix}\begin{bmatrix} r(t_k-\tau)-r(t_{k-1}-\tau)\\ v(t_k-\tau)-v(t_{k-1}-\tau)\end{bmatrix}, \end{cases} \tag{3}$$

with the initial states as $r(t_0) = [r_1(t_0), r_2(t_0), \ldots, r_n(t_0)]^\top$ and $v(t_0) = [v_1(t_0), v_2(t_0), \ldots, v_n(t_0)]^\top$. By the transformation

$$x(t) = U^{-1}r(t),\ \ y(t) = U^{-1}v(t), \tag{4}$$

the impulsive differential equation Eq. (3) can be rewritten as

$$\begin{cases} \begin{bmatrix}\dot x(t)\\ \dot y(t)\end{bmatrix} = \begin{bmatrix} O_n & I_n\\ -\omega^2 I_n & O_n\end{bmatrix}\begin{bmatrix} x(t)\\ y(t)\end{bmatrix},\ t\in(t_{k-1}, t_k],\\ \begin{bmatrix} x(t_k^+)\\ y(t_k^+)\end{bmatrix} = \begin{bmatrix} x(t_k)\\ y(t_k)\end{bmatrix} - \begin{bmatrix} O_n & O_n\\ \frac{1}{T}J & O_n\end{bmatrix}\begin{bmatrix} x(t_k-\tau)-x(t_{k-1}-\tau)\\ y(t_k-\tau)-y(t_{k-1}-\tau)\end{bmatrix}. \end{cases} \tag{5}$$

Note that J is in fact a diagonal matrix with the first diagonal entry being 0, and then Eq. (5) can be decomposed into the following $n-1$ subsystems,

$$\begin{bmatrix}\dot{x}_1(t)\\ \dot{y}_1(t)\end{bmatrix}=\begin{bmatrix}0 & 1\\ -\omega^2 & 0\end{bmatrix}\begin{bmatrix}x_1(t)\\ y_1(t)\end{bmatrix}, \tag{6}$$

and

$$\begin{cases}\begin{bmatrix}\dot{x}_\gamma(t)\\ \dot{y}_\gamma(t)\end{bmatrix}=\begin{bmatrix}0 & 1\\ -\omega^2 & 0\end{bmatrix}\begin{bmatrix}x_\gamma(t)\\ y_\gamma(t)\end{bmatrix},\ t\in(t_{k-1},t_k],\\ \begin{bmatrix}x_\gamma(t_k^+)\\ y_\gamma(t_k^+)\end{bmatrix}=\begin{bmatrix}x_\gamma(t_k)\\ y_\gamma(t_k)\end{bmatrix}-\begin{bmatrix}0 & 0\\ \frac{1}{T}\lambda_\gamma & 0\end{bmatrix}\begin{bmatrix}x_\gamma(t_k-\tau)-x_\gamma(t_{k-1}-\tau)\\ y_\gamma(t_k-\tau)-y_\gamma(t_{k-1}-\tau)\end{bmatrix},\ \gamma=2,3,\ldots,n,\end{cases} \tag{7}$$

where $x_1(t)=\mathbf{1}_n^\top r(t)/n\in\mathbb{R}$, $y_1(t)=\mathbf{1}_n^\top v(t)/n\in\mathbb{R}$.

Equation (6) is a system of second-order ordinary differential equations, whose analytical solutions can be easily obtained as

$$\begin{bmatrix}x_1(t)\\ y_1(t)\end{bmatrix}=\Phi(t)\begin{bmatrix}u_1^\top r(t_0)\\ u_1^\top v(t_0)\end{bmatrix}=\begin{bmatrix}\mathbf{1}_n^\top r(t_0)\cos\omega t+\omega^{-1}\mathbf{1}_n^\top v(t_0)\sin\omega t\\ -\omega\mathbf{1}_n^\top r(t_0)\sin\omega t+\mathbf{1}_n^\top v(t_0)\cos\omega t\end{bmatrix}, \tag{8}$$

where the matrix $\Phi(t)=\begin{bmatrix}\cos\omega t & \omega^{-1}\sin\omega t\\ -\omega\sin\omega t & \cos\omega t\end{bmatrix}$ is the Cauchy matrix of the differential ordinary equation of an uncoupled harmonic oscillator, i.e., Eq. (6). The solution of Eq. (7) can be obtained analytically as

$$\begin{aligned}\begin{bmatrix}x_\gamma\left(t_k^+\right)\\ y_\gamma\left(t_k^+\right)\end{bmatrix}&=\begin{bmatrix}x_\gamma(t_k)\\ y_\gamma(t_k)\end{bmatrix}-\begin{bmatrix}0 & 0\\ \frac{\lambda_\gamma}{T} & 0\end{bmatrix}\begin{bmatrix}x_\gamma(t_k-\tau)-x_\gamma(t_{k-1}-\tau)\\ y_\gamma(t_k-\tau)-y_\gamma(t_{k-1}-\tau)\end{bmatrix},\\ &=\Phi(T)\begin{bmatrix}x_\gamma\left(t_{k-1}^+\right)\\ y_\gamma\left(t_{k-1}^+\right)\end{bmatrix}-\begin{bmatrix}0 & 0\\ \frac{\lambda_\gamma}{T} & 0\end{bmatrix}\Phi(T-\tau)\begin{bmatrix}x_\gamma\left(t_{k-1}^+\right)\\ y_\gamma\left(t_{k-1}^+\right)\end{bmatrix}+\begin{bmatrix}0 & 0\\ \frac{\lambda}{T} & 0\end{bmatrix}\\ &\qquad\Phi(T-\tau)\begin{bmatrix}x_\gamma\left(t_{k-2}^+\right)\\ y_\gamma\left(t_{k-2}^+\right)\end{bmatrix}\\ &=\begin{bmatrix}\cos\omega T & \frac{\sin\omega T}{\omega}\\ -\omega\sin\omega T-\frac{\lambda_\gamma\cos\omega(T-\tau)}{T} & \cos\omega T-\frac{\lambda_\gamma\sin\omega(T-\tau)}{\omega T}\end{bmatrix}\begin{bmatrix}x_\gamma\left(t_{k-1}^+\right)\\ y_\gamma\left(t_{k-1}^+\right)\end{bmatrix}\\ &+\begin{bmatrix}0 & 0\\ \frac{\lambda_\gamma\cos\omega(T-\tau)}{T} & \frac{\lambda_\gamma\sin\omega(T-\tau)}{\omega T}\end{bmatrix}\begin{bmatrix}x_\gamma\left(t_{k-2}^+\right)\\ y_\gamma\left(t_{k-2}^+\right)\end{bmatrix}\\ &\triangleq A_\gamma\begin{bmatrix}x_\gamma\left(t_{k-1}^+\right)\\ y_\gamma\left(t_{k-1}^+\right)\end{bmatrix}+B_\gamma\begin{bmatrix}x_\gamma\left(t_{k-2}^+\right)\\ y_\gamma\left(t_{k-2}^+\right)\end{bmatrix},\gamma=2,3,\ldots,n.\end{aligned} \tag{9}$$

with the first two initial conditions of the recursion (8) and (9) are, respectively,

$$\begin{bmatrix} x\,(t_0) \\ y\,(t_0) \end{bmatrix} = \begin{bmatrix} x_0 \\ y_0 \end{bmatrix} \text{ and } \begin{bmatrix} x\left(t_1^+\right) \\ y\left(t_1^+\right) \end{bmatrix} = \left(\Phi(T) \otimes I_n - \begin{bmatrix} O_n & O_n \\ \frac{1}{T} L & O_n \end{bmatrix} \left(\Phi(T-\tau) \otimes I_n - I_n \right) \right) \begin{bmatrix} x_0 \\ y_0 \end{bmatrix}. \tag{10}$$

The states of Eq. (9) at time $t = t_k^+$ with the above two initial conditions are given as

$$\begin{bmatrix} x_\gamma\left(t_k^+\right) \\ y_\gamma\left(t_k^+\right) \end{bmatrix} = \Psi_\gamma^{(k)} \begin{bmatrix} x_\gamma\left(t_1^+\right) \\ y_\gamma\left(t_1^+\right) \end{bmatrix} + \Lambda_\gamma^{(k)} \begin{bmatrix} x_\gamma\,(t_0) \\ y_\gamma\,(t_0) \end{bmatrix}, \tag{11}$$

where $k \geq 2$ and the two lead coefficient matrices $\Psi_\gamma^{(k)}$ and $\Lambda_\gamma^{(k)}$ satisfy $\Psi_\gamma^{(k)} = A_\gamma \Psi_\gamma^{(k-1)} + B_\gamma \Psi_\gamma^{(k-2)}$, $\Lambda_\gamma^{(k)} = \Psi_\gamma^{(k-1)} B_\gamma$ with $\Psi_\gamma^{(0)} = O_2, \Psi_\gamma^{(1)} = I_2$, which implies that $\lim_{k\to\infty} \Lambda_\gamma^{(k)} = O$ if and only if $\lim_{k\to\infty} \Psi_\gamma^{(k)} = O$ for all $\gamma = 2, 3, \ldots, n$.

It is easy to see that both $x_\gamma(t)$ and $y_\gamma(t)$ converge to zero as $\Psi_\gamma^{(k)}$ and $\Lambda_\gamma^{(k)}$ converge to zero given arbitrary initial conditions. Note that the first column of U are all ones and, by Eq. (4), all the states $r_i(t)$ and $v_i(t)$ $(i = 1, 2, \ldots, n)$ in Eq. (3) asymptotically converge to $x_1(t)$ and $y_1(t)$, respectively. Next, we will establish some conditions on which all the states in Eq. (11) converge to zero as k approaches to infinity.

By denoting a matrix $\hat{\Psi}_\gamma^{(k)} = \begin{bmatrix} \Psi_\gamma^{(k)} \\ \Psi_\gamma^{(k-1)} \end{bmatrix} \in R^{4\times 2}$, Eq. (9) can be stacked into the following iterative form

$$\hat{\Psi}_\gamma^{(k)} = \Theta_\gamma \hat{\Psi}_\gamma^{(k-1)}, \text{ with } \Theta_\gamma = \begin{bmatrix} A_\gamma & B_\gamma \\ I_2 & O_2 \end{bmatrix}, \ \gamma = 2, 3, \ldots, n, \quad k = 2, 3, \ldots, \tag{12}$$

which shows that $\lim_{k\to\infty} \Psi_\gamma^{(k)} = 0$ if and only if the spectrum radius of all the leading matrices Θ_γ is less than 1, that is, $\max_\gamma \rho(\Theta_\gamma) < 1$, and hence $\lim_{k\to\infty}[x_\gamma^\top(t_k), y_\gamma^\top(t_k)] = 0$ for all $\gamma = 2, 3, \ldots, n$. The characteristic polynomials of the matrices Θ_γ are given by $P_\gamma(\lambda) = \det\left(\lambda I_4 - \Theta_\gamma\right) = \lambda\phi_\gamma(\lambda)$, where $\phi_\gamma(\lambda) = \lambda^3 + \lambda^2\left(-2\cos\omega T + \lambda_\gamma \frac{\sin\omega(T-\tau)}{\omega T}\right) + \lambda\left(1 + \lambda_\gamma \frac{\sin\omega\tau}{\omega T} - \lambda_\gamma \frac{\sin\omega(T-\tau)}{\omega T}\right) - \lambda_\gamma \frac{\sin\omega\tau}{\omega T}$.

It suffices to show that all the roots of polynomials $\phi_\gamma(\lambda)$ are located in the unit circle, or equivalently, the polynomials $\phi_\gamma(\lambda)$ are Schur stable [3]. Applying the bilinear transformation $s = \frac{z+1}{z-1}$ to $\phi_\gamma(\lambda)$ yields $\phi_\gamma\left(\frac{z+1}{z-1}\right) = \frac{2(1-\cos\omega T)}{(z-1)^3}\varphi_\gamma(z)$, where $\varphi_\gamma(z) = z^3 + \left(1 + \frac{\lambda_\gamma \sin\omega(T-\tau)}{2\omega T \sin^2(\omega T/2)} + \frac{\lambda_\gamma \sin\omega\tau}{2\omega T \sin^2(\omega T/2)}\right)z^2 + \left(\cot^2\frac{\omega T}{2} - \frac{\lambda_\gamma \sin\omega\tau}{\omega T \sin^2(\omega T/2)}\right)z +$

$\cot^2\frac{\omega T}{2} - \frac{\lambda_\gamma \sin\omega(T-\tau)}{2\omega T\sin^2(\omega T/2)} + \frac{\lambda_\gamma \sin\omega\tau}{2\omega T\sin^2(\omega T/2)}$. Then, $\phi_\gamma(\lambda)$ is Schur stable if and only if $\varphi_\gamma(z)$ is Hurwitz stable [4].

Denote $\varphi_\gamma(\mathbf{i}\sigma) = \varphi_{\gamma 1}(\sigma) + \mathbf{i}\varphi_{\gamma 2}(\sigma)$, where the real and image polynomials are, respectively, $\varphi_{\gamma 1}(\sigma) = -\left(1 + \frac{\lambda_\gamma \sin\omega(T-\tau)}{2\omega T\sin^2(\omega T/2)} + \frac{\lambda_\gamma \sin\omega\tau}{2\omega T\sin^2(\omega T/2)}\right)\sigma^2 + \cot^2\frac{\omega T}{2} - \frac{\lambda_\gamma \sin\omega(T-\tau)}{2\omega T\sin^2(\omega T/2)} + \frac{\lambda_\gamma \sin\omega\tau}{2\omega T\sin^2(\omega T/2)}$ and $\varphi_{\gamma 2}(\sigma) = -\sigma^3 + \left(\cot^2\frac{\omega T}{2} - \frac{\lambda_\gamma \sin\omega\tau}{\omega T\sin^2(\omega T/2)}\right)\sigma$. By Theorem 1 in [2], the polynomial $\varphi_\gamma(z)$ is Hurwitz stable if and only if $\varphi_{\gamma 1}(0)\dot{\varphi}_{\gamma 2}(0) - \dot{\varphi}_{\gamma 1}(0)\varphi_{\gamma 2}(0) > 0$ and $\varphi_{\gamma 1}(\sigma)$ and $\varphi_{\gamma 2}(\sigma)$ are interlaced, that is, $c_1' : \omega T\cos^2\frac{\omega T}{2} - \lambda_\gamma\cos\frac{\omega T}{2}\sin\left(\frac{\omega T}{2} - \omega\tau\right) > 0$, $\omega T\sin^2\frac{\omega T}{2} + \lambda_\gamma\sin\frac{\omega T}{2}\sin\left(\frac{\omega T}{2} - \omega\tau\right) > 0$ and $c_2' : \frac{\omega T\cos^2\frac{\omega T}{2} - \lambda_\gamma\cos\frac{\omega T}{2}\sin\left(\frac{\omega T}{2} - \omega\tau\right)}{\omega T\sin^2\frac{\omega T}{2} + \lambda_\gamma\sin\frac{\omega T}{2}\sin\left(\frac{\omega T}{2} - \omega\tau\right)} < \cot^2\frac{\omega T}{2} - \frac{\lambda_n\sin\omega\tau}{\omega T\sin^2(\omega T/2)}$ for all $\gamma = 2, 3, \ldots, n$, which can be equivalently reduced to

$$\begin{aligned} &c_1 : \lambda_n\cos\tfrac{\omega T}{2}\sin\left(\tfrac{\omega T}{2} - \omega\tau\right) < \omega T\cos^2\tfrac{\omega T}{2},\ -\lambda_n\sin\tfrac{\omega T}{2}\cos\left(\tfrac{\omega T}{2} - \omega\tau\right) < \omega T\sin^2\tfrac{\omega T}{2}, \\ &c_2 : \lambda_n\sin\tfrac{\omega T}{2}\cos\left(\tfrac{\omega T}{2} - \omega\tau\right)\sin\omega\tau < \omega T\sin\tfrac{\omega T}{2}\cos\left(\tfrac{\omega T}{2} + \omega\tau\right). \end{aligned} \tag{13}$$

The inequalities in Eq. (13) give the necessary and sufficient condition by which Eq. (3) synchronizes their motions.

Let's revisit Example 2 in [8], where $\omega = 3$ and the largest eigenvalue of the corresponding Laplacian matrix is $\lambda_5 = 5.2968 > 2$. When the time delay $\tau = 0$, the conditions c_1 and c_2 can be reduced to the same condition as that in Theorem 1 in [8]. Since $\lambda_5 > 2$, the sampling period cannot be sufficiently small but be greater than $2\pi/\omega$ in absence of time delay [8]. However, if we set the time delay as $\omega\tau = 3\pi/2$, then $\max_\gamma \rho(\Theta_\gamma)$ are always less than 1 for all sampling periods except those $\omega T = 2k\pi$, $1 \geq k \in \mathbb{N}$, and thus the system can achieve synchronization. Figure 1a visualizes the values of $\max_\gamma \rho(\Theta_\gamma)$ with respect to different sampling periods and fixed time delay $\tau = \pi/2$, where $\omega = 3$. In addition, if we set $\tau = 1.05$ and choose the sampling period as $T = 1.71 < 2\pi/\omega$, the system can still

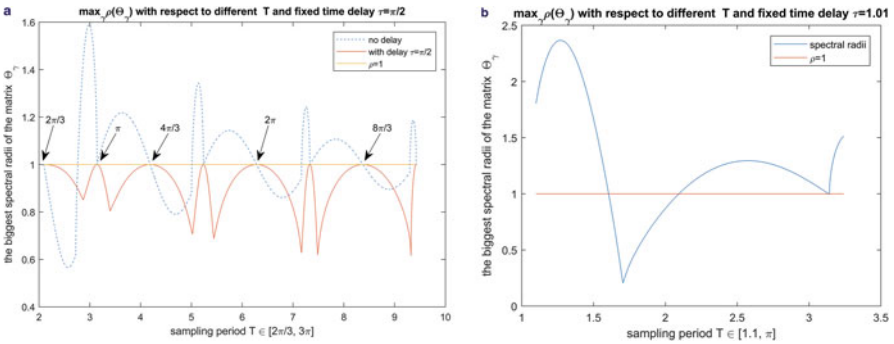

Fig. 1 Maximum spectral radii $\max_\gamma \rho(\Theta_\gamma)$ with respect to T and time delay. (**a**) $2\pi/3 \leq T \leq 3\pi$. (**b**) $1.1 \leq T \leq \pi$

achieve synchronization since $\max_\gamma \rho(\Theta_\gamma) = 0.2243 < 1$; see Fig. 1b. This also implies that the sampling period is sometimes not necessarily greater than $2\pi/\omega$ with an appropriate time delay. As a consequence, time delay is sometimes helpful for achieving synchronization, but not all always.

4 Conclusions

In this paper, we have examined synchronized behavior of coupled harmonic oscillators over an undirected network topology with delayed sampled position states. It is shown that the input time delay sometimes benefits for the synchronization of the coupled harmonic oscillators when the system cannot get synchronized in absence of input delays. For further study, we focus on finding out all the feasible time delays and sampling periods given a fixed network topology and the frequency of the uncoupled harmonic oscillators.

Acknowledgments This work was partially supported by the Natural Science Foundation of Chongqing Science and Technology Bureau (Grant No. cstc2019jcyj-msxmX0020), the National Natural Science Foundation of China (Grant No. 61364003), and the Science and Technology Research Program of Chongqing Municipal Education Commission (Grand No. KJQN201901122).

References

1. Ballard, L., Cao, Y., Ren, W.: Distributed discrete-time coupled harmonic oscillators with application to synchronised motion coordination. IET Control Theory Appl. **4**(5), 806–816 (2010)
2. Huang, L., Wand, L., Hollot, C.: On robust stability of polynomials and related topics. J. Syst. Sci. Complex. **5**(1), 42–54 (1992)
3. Liu, H., Xie, G., Wang, L.: Necessary and sufficient conditions for solving consensus problems of double-integrator dynamics via sampled control. Int. J. Robust Nonlinear Control **20**(15), 1706–1722 (2010)
4. Ogata, K.: Discrete-time control systems, 2 edn. Prentice-Hall, Upper Saddle River (1995)
5. Otto, A., Just, W., Radons, G.: Nonlinear dynamics of delay systems: an overview. Philos. Trans. R. Soc. A: Math. Phys. Eng. Sci. **377**, 20180389 (2019)
6. Tuna, S.E.: Synchronization of harmonic oscillators under restorative coupling with applications in electrical networks. Automatica **75**, 236–243 (2017)
7. Zhang, H., Ji, J.: Group synchronization of coupled harmonic oscillators without velocity measurements. Nonlinear Dyn. **91**(4), 2773–2788 (2018)
8. Zhang, H., Wu, Q., Ji, J.: Synchronization of discretely coupled harmonic oscillators using sampled position states only. IEEE Trans. Autom. Control **63**(11), 3994–3999 (2018)

Bifurcation Analysis and Energy Landscapes of a Synthetic Gene Regulatory Network

Qinghua Zhu and Jianwei Shen

1 Introduction

In recent years, there has been growing interest in gene regulatory networks due to its fundamental role in living organisms [3]. Hence, uncovering the global dynamics of the gene regulatory networks becomes necessary to understand the cellular process. With the development of experimental techniques, it is possible to study cellular functions by designing synthetic gene networks [4]. Gene switches [1] and genetic oscillators [2] have been extensively studied via the design of synthetic gene networks. Here, we will probe the global dynamic characteristics of a synthetic gene regulatory network through bifurcation analysis and energy landscape.

2 Model and Method

In this section, we consider a synthetic biological model proposed by Guantes and Poyatos (2006). Please refer to [2] for detailed information about this model. The corresponding mathematical description is given by:

Q. Zhu
School of Mathematics and Statistics, Zhengzhou University, Zhengzhou, P.R. China
e-mail: zhuqinghua611@163.com

J. Shen (✉)
School of Mathematics and Statistics, North China University of Water Resources and Electric Power, Zhengzhou, China
e-mail: xcjwshen@gmail.com

S. Oberst et al. (eds.), *Vibration Engineering for a Sustainable Future*,
https://doi.org/10.1007/978-3-030-46466-0_43

$$\begin{cases} \frac{dx_1}{dt} = a(m\frac{1+kx_1^2}{1+x_1^2+rx_2^2} - x_1) \\ \frac{dx_2}{dt} = am\phi\frac{1+kx_1^2}{1+x_1^2} - x_2 \end{cases} \tag{1}$$

Here, we utilize the energy landscape proposed by Wang et al. [5] and the bifurcation analysis to investigate the global dynamics of the system. Then, the stability of the stable limit cycles was further investigated through barrier height calculation.

3 Results

In this section, we present the simulation results of the system's dynamics with the help of software Matcont, Xppaut, and Vcell. From Fig. 1, one can see that the system can exhibit rich dynamic properties such as monostability, bistability, and oscillations when taking a set of appropriate system parameters. To have a clear insight into the two-parameter bifurcation in Fig. 1, we plot the corresponding one-parameter bifurcation diagrams with the help of the software Xppaut. Figure 2a shows that there are two Hopf bifurcation points that appear when $a = 10.383491$ and $a = 16.773544$, respectively. And the corresponding first Lyapunov coefficient a_0 is $a_0 = 2.979859 > 0$ and $a_0 = -7.960991 < 0$. Hence, the unstable limit cycle arises from the sub-point when $a = 10.383491$ and disappear when it meets the hc point. With the increases of a, the stable limit cycle is developing until it meets the sup point when $a = 16.773544$. Figure 2c shows that the Z-shape bistable state curve appears when ϕ is relatively large ($\phi = 0.5$). The corresponding phase diagrams of Fig. 2 are plotted in Fig. 3.

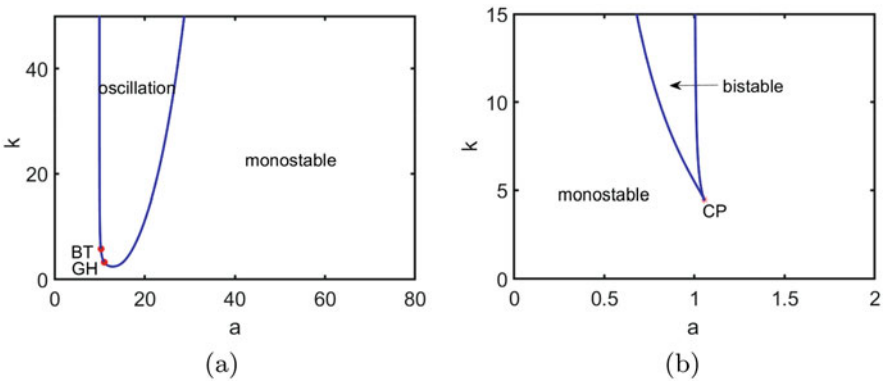

Fig. 1 The two-parameter bifurcation diagrams of the system. (**a**) $m = 1.58, r = 1.0, \phi = 0.05$. (**b**) $m = 1.58, r = 1.0, \phi = 0.5$. The label GH is the generalized Hopf bifurcation, BT is the Bogdanov-Takens bifurcation, and CP is the cusp bifurcation

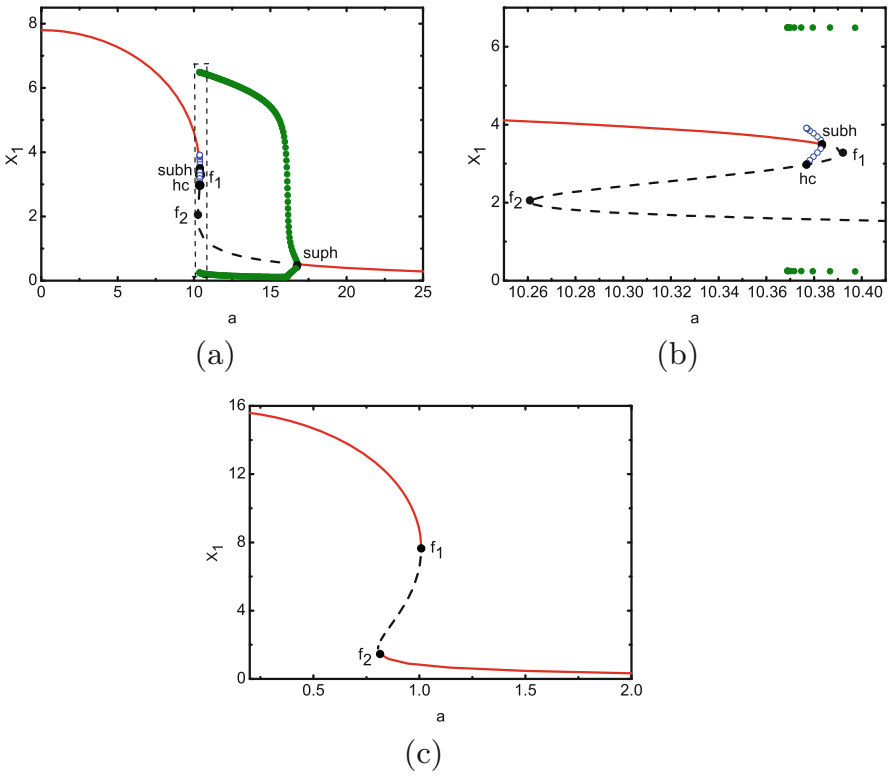

Fig. 2 The one-parameter bifurcation diagrams of x_1 with respect to parameter a. (**a**) (**b**) $m = 1.58, r = 1.0, \phi = 0.05, k = 5.0$. ((**b**) is the enlarged representation of the dashed square in (**a**)). (**c**) $m = 1.58, r = 1.0, \phi = 0.5, k = 3.0$. The red line represents stable equilibrium, and the black-dashed line is the unstable equilibrium. Full green circles represent the maxima and minima of the stable limit cycles, and blue open circles are the maxima and minima of the unstable limit cycles. The solid black circles are the bifurcation points. The labels *suph* and *subh* represent the supercritical Hopf bifurcation points and the subcritical Hopf bifurcation point, respectively. f_i represents the fold bifurcation point, and *hc* represents the homoclinic bifurcation point

From Fig. 3, one can see that there is a single stable steady state when $a = 10.0$ (Fig. 3a). When increasing a to $a = 10.38$, a stable limit cycle appears, which is separated from the stable equilibrium point by an unstable limit cycle (Fig. 3b). Further increasing a to $a = 10.40$, the unstable equilibrium point and the stable equilibrium point collide and then eventually disappear (Fig. 3c). And there are two stable equilibrium points that appear when ϕ increases to $\phi = 0.5$ (Fig. 3d).

In Fig. 4, we plot the energy landscapes which correspond to Fig. 3 to verify these dynamics. From Fig. 4a, the landscape shows that there is a deep funnel with minimum energies, which represents the monostability of the model. In Fig. 4b, the landscape exhibits not only a distinct closed ring valley but also a deep funnel with minimum energies, which indicate that the bistable state (the coexistence of

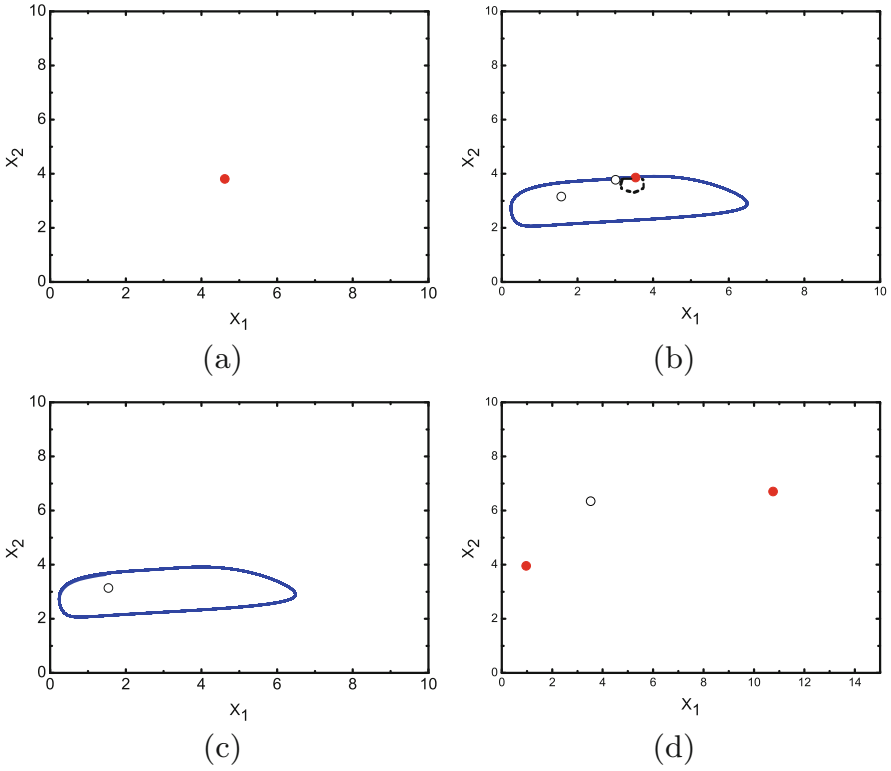

Fig. 3 Phase diagrams of the typical states in one-parameter bifurcation diagrams. Full red circles are stable equilibria, the open black circles are unstable equilibria, the blue line represents stable limit cycle, and the black-dashed line represents unstable limit cycle. (**a**) $a = 10.0, m = 1.58, r = 1.0, \phi = 0.05, k = 5.0$. (**b**) $a = 10.38, m = 1.58, r = 1.0, \phi = 0.05, k = 5.0.$, (**c**) $a = 10.40, m = 1.58, r = 1.0, \phi = 0.05, k = 5.0$. (**d**) $a = 0.9, m = 1.58, r = 1.0, \phi = 0.5, k = 3.0$

a stable state and stable oscillations) emerges. Figure 4c shows that there is only a closed ring valley in the energy landscape, indicating the stable oscillations appear. In Fig. 4c, when increasing ϕ to $\phi = 0.5$, the energy landscape has two deep funnels that correspond to the bistable state(the coexistence of two stable states).

To further investigate the stableness of the stable limit cycles, we introduce the concept of barrier height ($barrier = U_{\max} - U_{\min}$) that is defined in [5]. The simulation results are illustrated in Fig. 5. From Fig. 5, one can see that the barrier heights decrease with the increase of diffusion coefficient. This indicates that the oscillation is more stable under smaller noise.

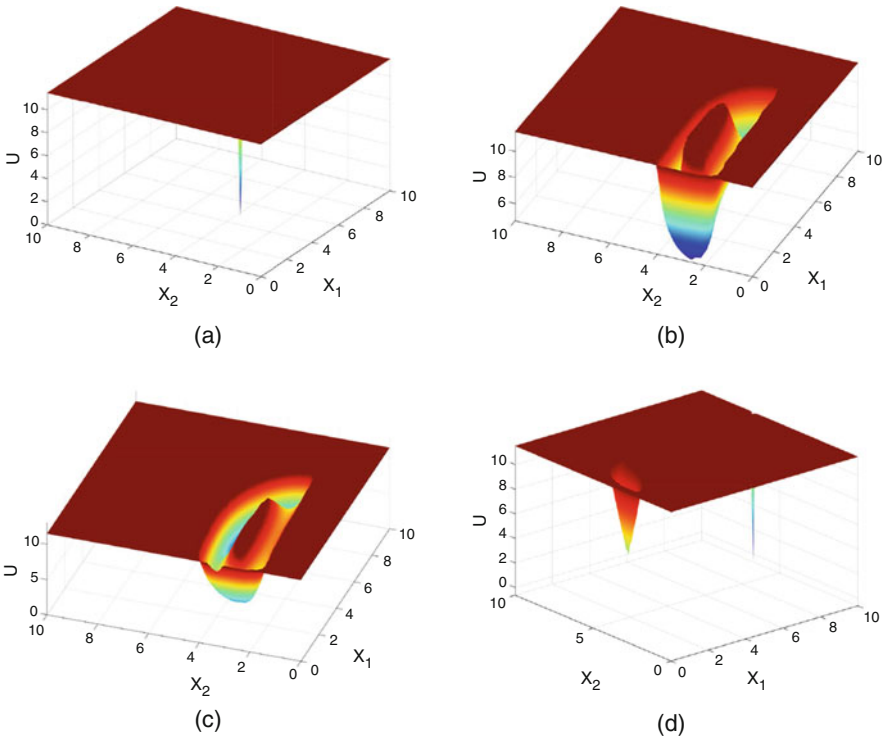

Fig. 4 The energy landscapes corresponding to Fig. 3. The parameters are the same as Fig. 3, and the diffusion coefficient $D = 1.0 \times 10^{-8}$

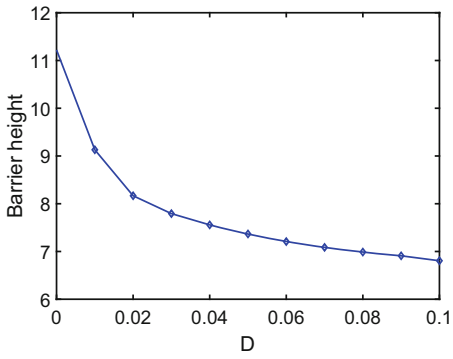

Fig. 5 The barrier heights versus diffusion coefficient D. ($a = 10.40, m = 1.58, r = 1.0, \phi = 0.05, k = 5.0$)

4 Conclusion

In the present paper, we explore the global dynamic properties of a synthetic gene regulatory network by using bifurcation analysis and energy landscape. As the parameters change, the system performed rich dynamics such as monostable state, oscillations, and bistable state (the coexistence of two stable states or the coexistence of a stable state and stable oscillations). And then, these dynamics are demonstrated by energy landscapes. Besides, we provide a method to measure the stability of the stable oscillations and found that smaller noises lead to more stable oscillations. Our method is quite universal and provides a pathway to explore the global dynamics of the complicated gene regulatory systems.

References

1. Gardner, T., Cantor, C., Collins, J.: Construction of a genetic toggle switch in Escherichia coli. Nature **403**, 339–342 (2000)
2. Guantes, R., Poyatos, J.F.: Dynamical principles of two-component genetic oscillators. PLOS Comput. Biol. **2**(3), 1–10 (2006)
3. Sanguinetti, G., Huynh-Thu, V.A.: Gene Regulatory Networks: Methods and Protocols. Springer/Humana Press, New York (2019)
4. Schaerli, Y., Jimnez, A., Duarte, J.M., Mihajlovic, L., Renggli, J., Isalan, M., Sharpe, J., Wagner, A.: Synthetic circuits reveal how mechanisms of gene regulatory networks constrain evolution. Mol. Syst. Biol. **14**(9), e8102 (2018)
5. Wang, J., Xu, L., Wang, E.: Potential landscape and flux framework of nonequilibrium networks: robustness, dissipation, and coherence of biochemical oscillations. Proc. Natl. Acad. Sci. **105**(34), 12271–12276 (2008)

Output Analysis of Neural Oscillator Networks Having Lateral Inhibition Structures

S. Taji, D. Iba, J. Hongu, and I. Moriwaki

1 Introduction

Active mass dampers (AMDs) have been used as anti-vibration devices for high-rise buildings to ensure safety and comfort during small earthquakes or strong winds. However, the control system for the AMDs deactivates the vibration control function when large earthquakes occur. Because the auxiliary mass of the AMDs is limited in the space depending on the installed location, performance degradation happens against parameter variation under the seismic load caused by the major earthquakes.

To solve these problems, we focused on the walking behavior of living things. Recent studies have shown that neural oscillator networks in living things generate walking rhythms and adapt the rhythms to its external environment change. These studies inspired us. We have been developing a new control system for AMDs consisting of the neural oscillators and a position controller [1–3]. This system uses the output of the neural oscillator network synchronizing with the acceleration response of a structure excited by earthquakes. The output of the network provides a rhythmic command to switch the motion direction and stroke amount of the auxiliary mass of the AMDs. Also, to drive the auxiliary mass to the desired value, a PD controller is used as the position controller. In our previous research, it has been confirmed by numerical simulation that the desired displacement for the auxiliary mass was able to be restricted within the stroke limit of the AMD and the oscillator network was able to detect parameter change of the structure. However, the proposed system had one serious disadvantage when used. The proposed system required a

S. Taji (✉) · D. Iba · I. Moriwaki
Department of Mechanical Engineering, Kyoto Institute of Technology, Kyoto, Japan
e-mail: taji@pml.mech.kit.ac.jp

J. Hongu
Department of Mechanical Engineering, Tottori University, Tottori, Japan

S. Oberst et al. (eds.), *Vibration Engineering for a Sustainable Future*,
https://doi.org/10.1007/978-3-030-46466-0_44

large number of neural oscillators to construct the network. Therefore, to implement the new control system into computers, it is necessary to configure a network with fewer neural oscillators than ever before.

In this paper, we propose a new neural oscillation network with lateral inhibition structures. The lateral inhibition is originally found in a vision system. This structure can amplify contrast signals at the edges. Our previous research showed that the swarm of neural oscillators synchronized with external input had similar behavior and the visualized output of the swarm could provide the estimated center frequency of the structural vibration. As a result of the amplification of this property by the lateral inhibition structure, the reduction of the number of neural oscillators can be expected.

2 Control System for AMD

2.1 Target Model

The target model is a one-degree-of-freedom structure with an AMD. The structure mass m_s is supported by the spring k_s and the damper c_s. The mass m_A of the AMD is driven by an actuator which generates the control force u. Where the relative displacement of the structure mass from a reference point on the ground is given as x_s, the relative displacement of the auxiliary mass is given as x_A, and the ground displacement is given as z, the equation of motion of the target model is obtained as Eq. (1):

$$\begin{cases} m_s\ddot{x}_s + c_s\dot{x}_s + k_s x_s = -u - m_s\ddot{z} \\ m_A\ddot{x}_A + m_A\ddot{x}_s = u - m_A\ddot{z} \end{cases} \tag{1}$$

2.2 Neural System

In this study, we use Matsuoka's neural oscillator as the neural oscillator [4]. When the absolute acceleration response of the structure "$\ddot{y}_s = \ddot{x}_s + \ddot{z}$" is given to the neural oscillator as the input, the mathematical model of the oscillator is obtained as Eq. (2):

$$\begin{cases} \tau\dot{x}_{(e,f)} + x_{(e,f)} = -a\max\left(0, x_{(f,e)}\right) + s' - bx'_{(e,f)} + \tau\varepsilon\ddot{y}_s \\ T\dot{x}'_{(e,f)} + x'_{(e,f)} = \max\left(0, x_{(f,e)}\right) \\ s' = s/\left\{1 + \exp\left(-(t-5)\right)\right\} \end{cases} \tag{2}$$

This mathematical model contains two neural cell models that have two first-order lag systems to capture excitation and inhibition properties of the cell and

can establish sustained oscillation with no periodic external force. Generally, these five parameters s, τ, T, b, and a are determined by identification of a neuron, but the specified animate being is not considered in this study. Instead of the usual parameter s, the product of s and a sigmoid function are used to suppress the initial unstable output of the network. The parameters are chosen by a design method to generate the oscillation with a natural frequency and amplitude desired. Here, ε means input gain to the neural oscillator.

3 Neural Oscillator Network

Our previous study showed that the input amplitude to a neural oscillator could be identified by analyzing the energy of the neural oscillator during synchronization with the external input. According to the estimated amplitude of the structure vibration, which is the input to the oscillator, we can generate the desired displacement of the auxiliary mass of the active mass damper and drive it to the aimed place by a position controller such as PD controller. On the other hand, the single neural oscillator can synchronize with the cyclic input in a frequency range, but the range is limited. The oscillator system should cover a broader frequency range than the synchronization band of the single neural oscillator to follow parameter changes due to structural damage by large earthquakes. Therefore, we proposed a network of 36,000 of neural oscillators which had 120 different natural frequencies and 300 different input gains. Extracting the neural oscillators synchronized with the external input from the swarm enables us to realize a robust control system for the AMDs. However, the number of neural oscillators is too much for implementation into a computer. Therefore, it is necessary to reduce its number as much as possible.

In this paper, we propose a new method to reduce the number of the swarm and extract the neural oscillators synchronized with the external input by constructing a new network using lateral inhibition structures.

The lateral inhibition network generates a small output when receiving similar inputs. This network has a three-layer structure, named as an input layer, a first relay station, and a second relay station. The input layer consists of the swarm of the neural oscillators, which have different natural frequencies. The expression of the input layer is shown below:

$$\begin{cases} \dot{x}_i(t) = f_i\left(x_i(t)\right) + \varepsilon p\left(\omega t\right) \\ y_i(t) = g_i\left(x_i(t)\right) \end{cases} \tag{3}$$

Here, x_i $(i = 1, 2, \ldots, n)$ means the state variable of the oscillator, which has four variables of Eq. 2. The subscript i describes i-th neural oscillator. f_i and g_i mean nonlinear function of Matsuoka's neural oscillator. ε and p are the input gain and periodic external force. y_i is the output of Matsuoka's neural oscillator.

In the first relay station, the adjacent outputs of the input layer are combined. Since synchronized neural oscillators have similar outputs, the output of the node in

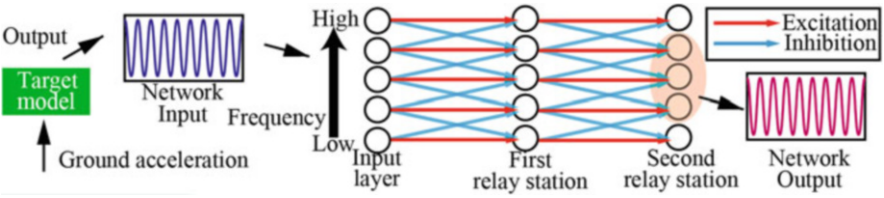

Fig. 1 Neural oscillator network

the station decreases due to the natural property of the lateral inhibition network when the neural oscillators and neighborhoods are synchronized. The combined output in this layer is obtained as follows:

$$v_i(t) = x_i(t) - 0.5\,(x_{i-1}(t) + x_{i+1}(t)) \tag{4}$$

Here, v_i means the output value to the next layer.

In the second relay station, we apply the same process to the output of the first relay station to emphasize the difference between the synchronized and non-synchronized oscillators:

$$w_i(t) = v_i(t) - 0.5\,(v_{i-1}(t) + v_{i+1}(t)) \tag{5}$$

Then, by referring to the output of the second relay station, we determine the neural oscillators synchronized to the external input:

$$z_i(t) = \begin{cases} x_i(t) & \text{if} \quad w_i < \alpha \\ 0 & \text{else} \end{cases} \tag{6}$$

Here, α is the threshold value. Finally, the average value of z_i is used as the output of the neural oscillator network. Figure 1 shows the diagram of the proposed neural oscillator network.

4 Numerical Simulation

In this section, the outputs of the neural network are compared with that of the previous research. Table 1 shows various parameters used in the numerical simulation. The parameters of the neural oscillator are that of the representative oscillator whose natural frequency is 1 Hz, and the amplitude is 1. According to the design method of neural oscillators [2], we defined the time constants τ and T to obtain the desired different natural frequencies. In this simulation, the neural network in the first layer consists of 25 neural oscillators whose natural frequencies are from 0.7 Hz to 1.1 Hz. The step of the frequency is 0.016 Hz. On the other

Table 1 Parameters of target model and neural oscillator

Target model		Neural oscillator	
Parameters	Value	Parameters	Value
m_s	10 kg	s	1.634
k_s	395 N/m	τ	0.0337
c_s	1.244 Ns/m	T	0.405
m_A	0.5 kg	b	2.52
Natural frequency	1.0 Hz	a	2.52

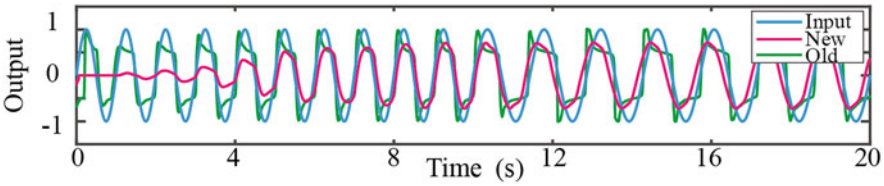

Fig. 2 Comparison of neural oscillator networks with sine wave input

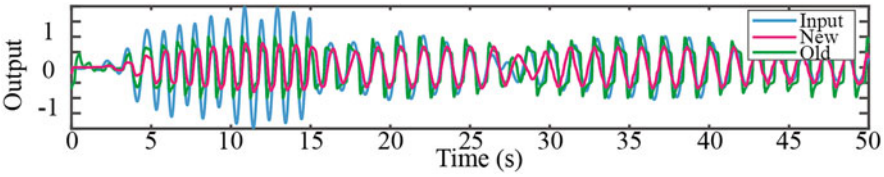

Fig. 3 Comparison of neural oscillator networks with structure's response input

hand, the previous network we proposed had 36,000 neural oscillators whose natural frequency arranged in 0.01 Hz steps from 0.4 Hz to 1.6 Hz, input gain was set from 0.01 to 3.0, and the step size was 0.01. The number of neural oscillators in the proposed network is dramatically reduced.

First, we show the result of numerical simulation whose input is a sine wave. To evaluate the synchronization characteristics to the external input, the frequency of the sine wave used for the input changed from 1.0 Hz to 0.7 Hz at 10 seconds. The amplitude of the input sine wave was 1. Figure 2 shows the input and corresponding network outputs. As can be seen in Fig. 2, the output of the network can follow the input frequency change.

We also evaluated the output of the network, which had earthquake-induced acceleration responses of the structure as the input. The same parameters in Table 1 were used in the numerical simulation. EL_NS wave was used as the input earthquake. The maximum value of the seismic response spectrum was set to the natural frequency of the structure by expanding the time axis. In this simulation, the natural frequency of the structure was changed from 1.0 Hz to 0.7 Hz at 15 seconds. Figure 3 shows the input and corresponding outputs of the network. Figure 4 shows the response frequency measured once every half period each simulation.

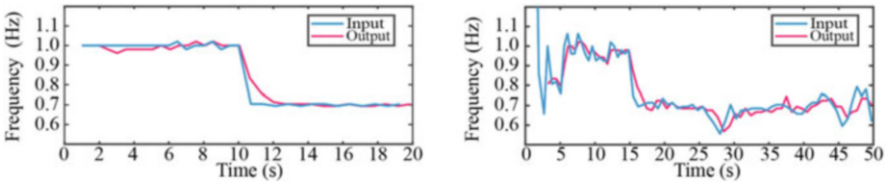

Fig. 4 Transition of frequency of input and output waveform when the sine wave is the input and structure's response is the output

Figures 3 and 4 show that the output of the network also follows the change of the acceleration response of the structure. As can be seen in these figures, when the phase of the acceleration response of the structure was shifted due to the influence of the earthquake wave of 25 seconds to 30 seconds, there was a part where the phase difference between input and output appears. However, after a few seconds, the phase shift was disappeared because of re-synchronization.

5 Conclusion

We introduced a new structure, called a lateral inhibition, into the network of neural oscillators, which were used for controller of active mass dampers for structures. Some numerical simulation results showed that the proposed system was beneficial for the reduction of the number of neural oscillators. Also, we found that the proposed network can identify the frequency of the input waveform in real time, even if the natural frequency of the structure is changed. In the near future, we will develop the control system of the active mass dampers consisting of the neural system and a position controller.

References

1. Architectural Institute of Japan: Active and Semiactive Control for Building –State of the Art, pp. 367–376. Maruyoshi Company (2006)
2. Iba, D., Hongu, J., Sasaki, T., Shima, S., Nakamura, M., Moriwaki, I.: Active mass damper system for high-rise buildings using neural oscillator and position controller: sinusoidally varying desired displacement of auxiliary mass intended foe reduction of maximum control force. In: Proceedings SPIE 10168, Sensors and Smart Structures Technologies for Civil, Mechanical, and Aerospace Systems 2017, 101683F (2017)
3. Tokumura, H., Iba, D., Hongu, J., Taji, S., Moriwaki, I.: Active mass damper operated by CPG and PD controller (Extraction of CPGs synchronized with external input and generation of target displacement for auxiliary mass). In: Dynamics and Design Conference 2018 (2018)
4. Matsuoka, K.: Sustained oscillations generated by mutually inhibiting neurons with adaptation. Biol. Cybern. **52**(6), 367–376 (1985)

Part VIII
Human Body Vibration

Flow-Induced Dynamics of Bifurcated Coronary Arteries

H. J. Carpenter, A. Gholipour, M. H. Ghayesh, A. Zander, and P. J. Psaltis

1 Introduction

As the largest cause of death globally [1] resulting in 18,000 deaths in Australia alone in 2017 [2] and one of the largest global economic burdens [3], cardiovascular diseases pose a significant challenge to global health. Developing an understanding of their initiation and progression is hence critical. While current medical imaging technology is improving rapidly, it is unable to assess the complex interactions and relationships seen in the cardiovascular setting; hence, biomechanical analysis of coronary arteries is crucial for developing a better understanding of cardiovascular diseases.

Of patients who present to emergency with myocardial infraction, artery occlusion caused by atherosclerotic plaque disruption or rupture is often the primary cause [1]; bifurcation regions of the coronary vasculature are the most at-risk areas [4]. A number of investigations were undertaken into the biomechanics of bifurcations [5–8] focusing on developing an understanding of the effects of bifurcation angle, artery diameter [7], and artery curvature [8] on flow patterns. Further investigations assessed three-dimensional reconstruction techniques on shear stresses, an important factor in atherosclerosis initiation and progression, and the relationship between coronary side-branch "steal" and stenosis location. These

H. J. Carpenter (✉) · A. Gholipour · M. H. Ghayesh · A. Zander
School of Mechanical Engineering, University of Adelaide, Adelaide, South Australia, Australia
e-mail: harry.carpenter@adelaide.edu.au

P. J. Psaltis
Vascular Research Centre, Heart Health Theme, South Australian Health & Medical Research Institute (SAHMRI), Adelaide, South Australia, Australia

Department of Medicine, University of Adelaide, Adelaide, South Australia, Australia

S. Oberst et al. (eds.), *Vibration Engineering for a Sustainable Future*,
https://doi.org/10.1007/978-3-030-46466-0_45

investigations made valuable contributions to the field, however, they have not yet considered all the necessary factors, including heart motion.

Heart motion was highlighted as potentially important in atherogenesis [9], and its effect on right coronary artery hemodynamics was previously investigated [10]; however, these investigations were limited by focusing only on computational fluid dynamics (CFD) methods. The development of fluid-structure interaction (FSI) has enabled more accurate biomechanical modelling of coronary arteries; however the effect of varied heart motion on flow-induced dynamics has yet to be investigated.

This paper investigates the impact of including three-dimensional heart motion on the flow-induced artery dynamics in a nonlinear, biomechanical, fluid-structure interaction model. The nonlinear model includes three 45% stenosis, one in each artery branch, as well as all three artery layers, artery taper, hyperelastic and viscoelastic effects, non-Newtonian blood, pulsatile flow, active contraction of the media layer, and lipid pools inside the plaque. It is hoped that these results will contribute to developing accurate and reliable biomechanical models of coronary arteries capable of developing our understanding of atherosclerosis progression and one day predicting its initiation.

2 Investigation Method

A two-way fluid-structure interaction model of the left main bifurcation was assessed using the finite element method. The nonlinear model was adapted from Ref. [11] and included plaque located in each artery section with 45% stenosis, the most at risk of rupture. The intima, media, and adventitia layers were included for a full three-layered artery structure [12] with hyperelastic [13] and viscoelastic effects [14] using the five-parameter Mooney-Rivlin and ANSYS relaxation models, respectively. Artery taper, media layer contraction, and the plaque lipid pool were also considered. Model parameters were implemented from in vitro data assessed from literature.

Due to the importance of wall shear stresses in disease initiation and progression [15], blood flow was modelled as non-Newtonian, turbulent, and incompressible with pulsatile velocity profile included [16]. Reynolds number was assessed as 352, and the three-dimensional heart motion has been included as follows:

Assumed 3D heart motion at inlet:

$$\begin{aligned} x &= 0.08\ \sin(2\pi t/0.8)\ \text{mm}, \\ y &= 0.08\ \sin(2\pi t/0.8)\ \text{mm}, \\ z &= 0.20\ \sin(2\pi t/0.8)\ \text{mm}, \end{aligned} \tag{1}$$

Assumed 3D heart motion at outlets:

$$\begin{aligned} x &= 0.15\ \sin(2\pi t/0.8)\ \text{mm}, \\ y &= 0.15\ \sin(2\pi t/0.8)\ \text{mm}, \\ z &= 0.40\ \sin(2\pi t/0.8)\ \text{mm}, \end{aligned} \tag{2}$$

3 Results and Discussion

Both structural and shear stresses are important in artery biomechanics, disease progression, and plaque/artery failure. Figure 1 illustrates the von Mises stress contour (sub-figure (a)) and wall shear stress contour (sub-figure (b)) at 0.42 s through a single heartbeat which had a full cycle of 0.8 s (75 bpm), the time of maximum inlet velocity. The von Mises stress was highest at the artery bifurcation point and at plaque shoulders, consistent with literature. Wall shear stress was highest across plaques with low wall shear stress regions on the downstream side of plaque buildup, important in plaque growth.

Three-dimensional motion applied at the inlet and outlet (see Eqs. (1) and (2)) resulted in a 150% increase in von Mises stress, as seen in Fig. 2(a), suggesting that artery motion could play an important role in artery or plaque rupture mechanisms.

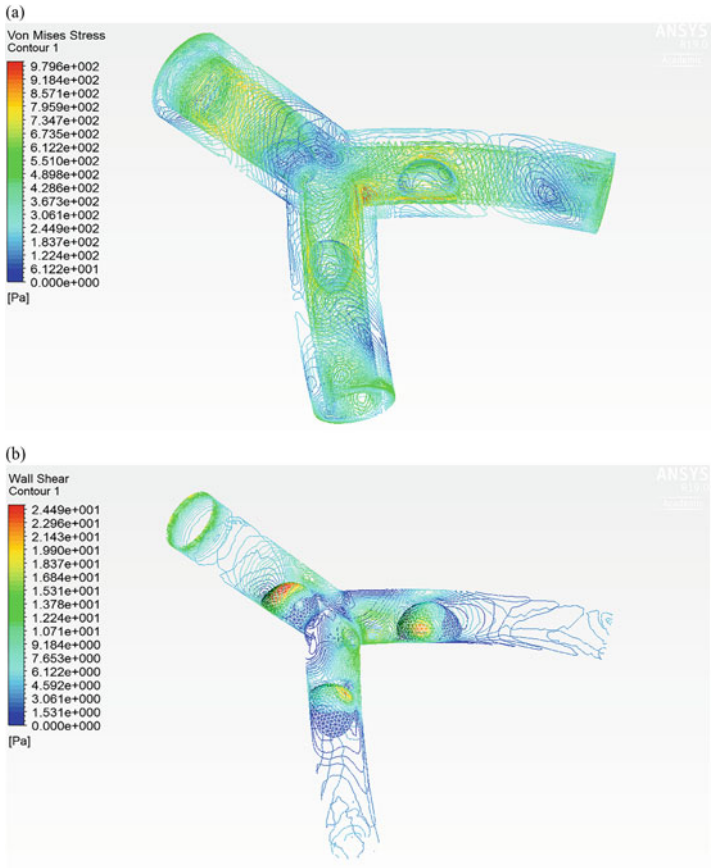

Fig. 1 (**a**) von Mises stress at $t = 0.42$ s and (**b**) wall shear stress at $t = 0.42$ s

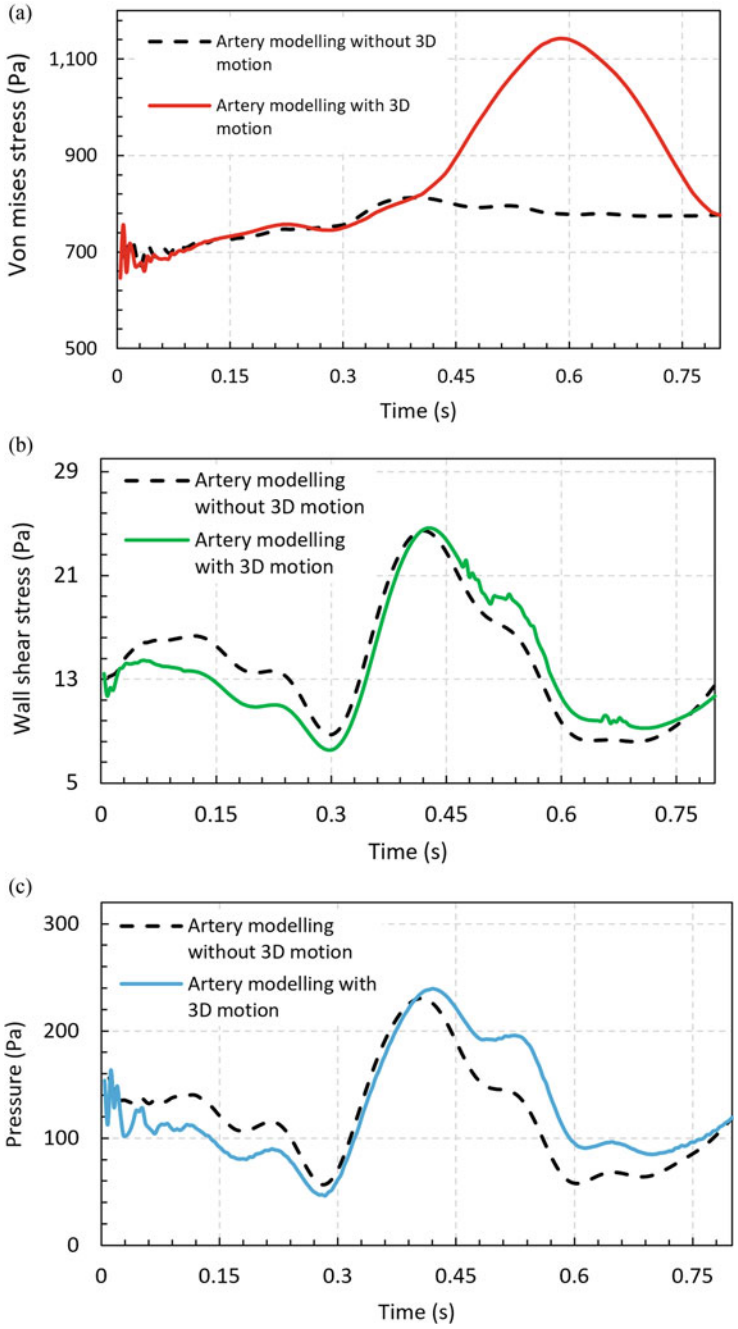

Fig. 2 Comparing simulation of bifurcated coronary artery with and without 3D motion over one heartbeat (0.8 s). (**a**) von Mises, (**b**) shear stress, and (**c**) pressure change

Wall shear stress and pressure magnitude (sub-figure (b) and (c) respectively) were comparable to that without artery motion and followed the pulsatile velocity profile closely (see Ref. [11]).

4 Conclusions

The impact of including the three-dimensional motion of the heart on flow-induced dynamics of the left main coronary artery bifurcation was investigated through fluid-structure interaction. Bifurcations are known atheroprone regions, hence a key location for assessment. The nonlinear biomechanical model included 45% stenosis of each branch, the most at risk of rupture, as well as artery taper, all three artery layers, both hyperelastic and viscoelastic effects, active media layer contraction, pulsatile and non-Newtonian flow, and plaque lipid pools. Three-dimensional motion was applied to the inlet and outlets and assessed using the finite element method. Key conclusions included as follows: (1) Maximum von-Mises stress was increased by 150% with the inclusion of three-dimensional heart motion. (2) Wall shear stress and pressure both showed similar magnitude and distribution with and without motion. (3) Inclusion of three-dimensional heart motion could play a key role in rupture mechanisms. These results are important for developing an accurate and reliable biomechanical model of coronary arteries; eventually this could assist in the prediction of atherosclerosis initiation and progression to combat the increasing number of deaths and economic burden globally.

References

1. Calvert, J.W.: Chapter 5 – ischemic heart disease and its consequences. In: Willis, M.S., Homeister, J.W., Stone, J.R. (eds.) Cellular and Molecular Pathobiology of Cardiovascular Disease, pp. 79–100. Academic Press, San Diego (2014)
2. World Health Organisation, The top 10 causes of death, (2018) https://www.who.int/news-room/fact-sheets/detail/the-top-10-causes-of-death. Last accessed 07 Sept 2019
3. Gheorghe, A., Griffiths, U., Murphy, A., Legido-Quigley, H., Lamptey, P., Perel, P.: The economic burden of cardiovascular disease and hypertension in low-and middle-income countries: a systematic review. BMC Public Health. **18**, 975 (2018)
4. Jahromi, R., Pakravan, H.A., Saidi, M.S., Firoozabadi, B.: Primary stenosis progression versus secondary stenosis formation in the left coronary bifurcation: a mechanical point of view. Biocybern. Biomed. Eng. **39**, 188–198 (2019)
5. Frattolin, J., Zarandi, M.M., Pagiatakis, C., Bertrand, O.F., Mongrain, R.: Numerical study of stenotic side branch hemodynamics in true bifurcation lesions. Comput. Biol. Med. **57**, 130–138 (2015)
6. Gijsen, F.J.H., Schuurbiers, J.C.H., van de Giessen, A.G., Schaap, M., van der Steen, A.F.W., Wentzel, J.J.: 3D reconstruction techniques of human coronary bifurcations for shear stress computations. J. Biomech. **47**, 39–43 (2014)

7. Huo, Y., Finet, G., Lefevre, T., Louvard, Y., Moussa, I., Kassab, G.S.: Which diameter and angle rule provides optimal flow patterns in a coronary bifurcation? J. Biomech. **45**, 1273–1279 (2012)
8. Prosi, M., Perktold, K., Ding, Z., Friedman, M.H.: Influence of curvature dynamics on pulsatile coronary artery flow in a realistic bifurcation model. J. Biomech. **37**, 1767–1775 (2004)
9. Ding, Z., Friedman, M.H.: Dynamics of human coronary arterial motion and its potential role in coronary atherogenesis. J. Biomech. Eng. **122**, 488–492 (2000)
10. Zeng, D., Ding, Z., Friedman, M.H., Ethier, C.R.: Effects of cardiac motion on right coronary artery hemodynamics. Ann. Biomed. Eng. **31**, 420–429 (2003)
11. Gholipour, A., Ghayesh, M.H., Zander, A.: Nonlinear biomechanics of bifurcated atherosclerotic coronary arteries. Int. J. Eng. Sci. **133**, 60–83 (2018)
12. Ferrara, A., Pandolfi, A.: Numerical modelling of fracture in human arteries. Comput. Methods Biomech. Biomed. Engin. **11**, 553–567 (2008)
13. Janela, J., Moura, A., Sequeira, A.: Absorbing boundary conditions for a 3D non-Newtonian fluid–structure interaction model for blood flow in arteries. Int. J. Eng. Sci. **48**, 1332–1349 (2010)
14. Gholipour, A., Ghayesh, M.H., Zander, A., Mahajan, R.: Three-dimensional biomechanics of coronary arteries. Int. J. Eng. Sci. **130**, 93–114 (2018)
15. Huang, X., Yang, C., Zheng, J., Bach, R., Muccigrosso, D., Woodard, P.K., Tang, D.: Higher critical plaque wall stress in patients who died of coronary artery disease compared with those who died of other causes: a 3D FSI study based on ex vivo MRI of coronary plaques. J. Biomech. **47**, 432–437 (2014)
16. Johnston, B.M., Johnston, P.R., Corney, S., Kilpatrick, D.: Non-Newtonian blood flow in human right coronary arteries: transient simulations. J. Biomech. **39**, 1116–1128 (2006)

Effect of Blood Flow Models on the Flow-Induced Vibrations of Coronary Arteries

A. Gholipour, H. J. Carpenter, M. H. Ghayesh, A. Zander, and P. J. Psaltis

1 Introduction

Cardiovascular diseases are the largest cause of death globally [1], resulting in 18,000 deaths in Australia alone in 2017 and over 15 million globally [2]. Of patients presenting with myocardial infarction (heart attack), artery occlusion caused by atherosclerotic plaque disruption is often the primary cause [1]. Wall shear stresses induced by blood flow have been noted as a critical factor in atherosclerosis formation through both experimental and clinical investigations, and hence, a clearer and more consistent approach to modelling the rheological properties of blood flow is needed. Human coronary blood flow has been characterised by many various blood models in literature, resulting in discrepancies and contradictions on the effect of flow-induced vibrations and shear-thinning effects on disease initiation and progression.

One of the major simplifications in fluid-based coronary artery models was the simplification of the blood to a Newtonian fluid [3]; this is despite its shear-thinning nature caused by the suspension and complex microlevel interactions of molecules such as blood cells [4], leucocytes and LDLs [5]. Reasoning used for the simplification was that wall shear effects were only present at low shear rates; as the

A. Gholipour (✉) · H. J. Carpenter · M. H. Ghayesh · A. Zander
School of Mechanical Engineering, University of Adelaide, Adelaide, South Australia, Australia
e-mail: alireza.gholipour@adelaide.edu.au

P. J. Psaltis
Vascular Research Centre, Heart Health Theme, South Australian Health & Medical Research Institute (SAHMRI), Adelaide, South Australia, Australia

Department of Medicine, University of Adelaide, Adelaide, South Australia, Australia

S. Oberst et al. (eds.), *Vibration Engineering for a Sustainable Future*,
https://doi.org/10.1007/978-3-030-46466-0_46

rigid artery conditions used in computational fluid dynamics (CFD) produced shear stresses above the relevant threshold for a non-Newtonian model, fluid was assumed Newtonian.

In physiological conditions, low wall shear stress was correlated to inflammation and particulate build-up leading to atherosclerosis; hence it should not be neglected. Maximum wall shear stress was shown to decrease at the stenosis throat under non-Newtonian flow [6],with increased macromolecule concentration near the stenosis leading to further plaque growth and disease progression compared to Newtonian fluid; further investigations corroborated the importance of using non-Newtonian blood models through direct comparisons [7, 8]. The primary shear-thinning models used to date were the power law [9] and Carreau model [10]; in coronary arteries, wall shear stresses were associated with artery thickening and were shown to impact endothelial cell regulation in atheroprone regions [11], leading to disease initiation. This further highlighted the importance of considering the interaction between the fluid and structure, something not yet investigated when comparing non-Newtonian fluid models in coronary arteries.

This paper investigates, for the first time, the flow-induced effects of differing blood flow models *through fluid-structure interaction* analysis of coronary arteries. The finite element method was used to model a stenosis of 45%, outlined as the most at risk of rupture [12]; the FSI model of the left main coronary artery includes all three artery layers, artery taper, media layer contraction, harmonic heart motion, pulsatile blood flow, plaque lipid pool as well as hyperelastic and viscoelastic effects and was analysed through ANSYS. This has implications for the prediction of the initiation and progression of disease from biomechanical analysis and could contribute to reducing the impact and number of deaths from cardiovascular disease.

2 Investigation Method

Three blood models [7] were assessed through the finite element method [13] using a nonlinear, three-dimensional, two-way fluid-structure interaction model of the left main coronary artery with a 45% stenosis adapted from Ref. [12]. The multilayered artery structure (with intima, media and adventitia) included both nonlinear hyperelastic [14] and viscoelastic effects [15] through the five-parameter Mooney-Rivlin and ANSYS relaxation models, respectively, with in vitro data assessed from literature to define model parameters. Artery taper, media layer contraction, harmonic heart motion and the plaque lipid pool were also considered.

A Newtonian model and the Carreau and power law non-Newtonian models were compared with the power law and Carreau models adapted from Ref. [7] and outlined by Eqs. (1) and (2), respectively:

$$\mu = \mu_0(\dot{\gamma})^{n-1} \tag{1}$$

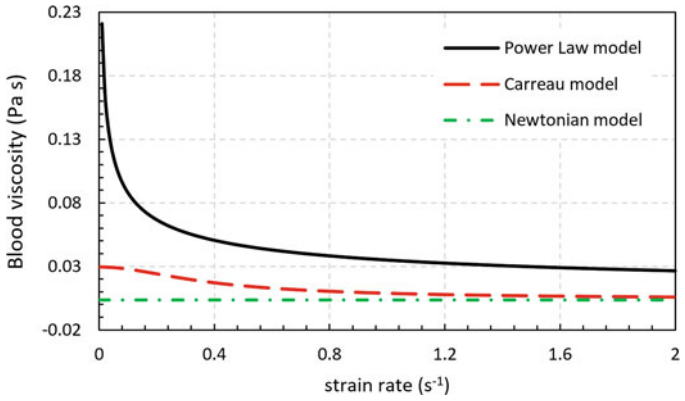

Fig. 1 Blood viscosity versus strain rate for three different blood models: power law model, Carreau model and Newtonian model

$$\mu = \mu_\infty + (\mu_0 - \mu_\infty)\left[1 + (\lambda\dot{\gamma})^2\right]^{(n-1)/2} \tag{2}$$

where μ is viscosity; μ_0 and μ_∞ are viscosity at zero and infinite shear, respectively; $\dot{\gamma}$ is the shear rate; and constants λ, n. The Newtonian model held constant viscosity over all strain rates; blood viscosity vs. strain rate for all three models is outlined in Fig. 1. Flow was also considered incompressible and turbulent and included the physiological pulsation of the blood based on the profile from Ref. [16] with the inlet position fixed to the heart motion and outlet assumed to be free. The flow-induced effects of the variation between blood models were assessed at the stenosis throat.

3 Results and Discussion

Both structural and shear stresses are important in artery biomechanics, disease progression and plaque/artery failure; hence, von Mises and wall shear stresses are assessed at the stenosis throat known as the most vulnerable region. Figure 2 illustrates the velocity streamline (sub-figure(a)) and pressure contour (sub-figure(b)) at 0.42 s through a single heartbeat which had a full cycle of 0.8 s (75 bpm). This time correlated to the peak von Mises stress, wall shear stress and pressure for the power law model outlined in Fig. 3.

The von Mises stress is useful for assessing the failure of the artery/plaque material. The power law model resulted in a peak von Mises stress of approximately 78 kPa, 4.8% higher than the peak stress for the Carreau and Newtonian models and 5.4% higher than at the same time (0.42 s). Sub-figure(a) outlined the von Mises stress profile; the variation showed similarities although the variations were more

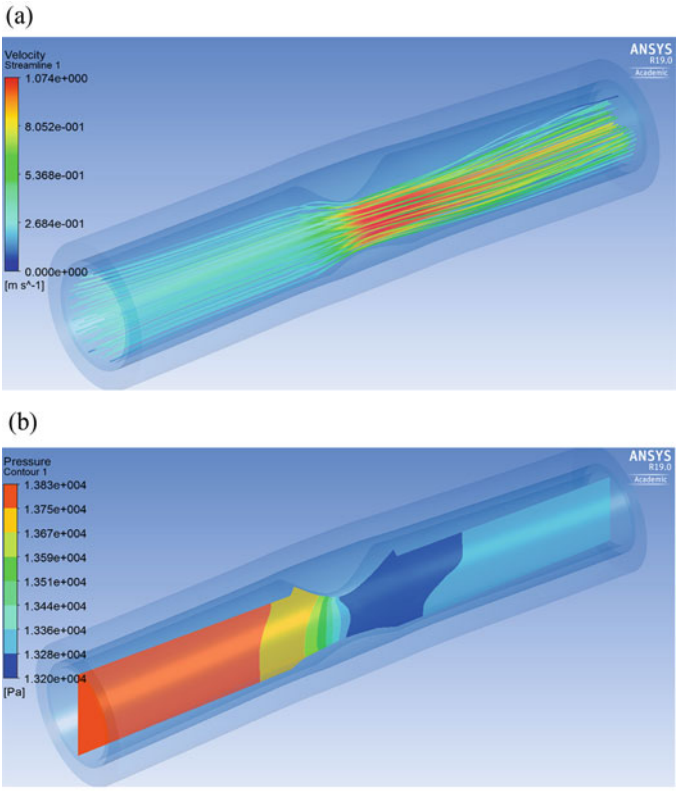

Fig. 2 (**a**) Velocity at $t = 0.42$ s and (**b**) pressure at $t = 0.42$ s

prominent through the power law model with similarities to the case for the wall shear stress (sub-figure(b)). Wall shear stress magnitude increased by over 450%, to 250 Pa using the power law model; this is a significant result due to the role of wall shear stress in atherosclerosis initiation and progression, and considerably larger than earlier investigations which only considered the fluid in their investigation [17]. Pressure (sub-figure(c)) followed a similar trend to wall shear stress albeit with less variation in magnitude (approximately 7% increase).

The Carreau model was further investigated at varied inlet pressure, outlined in Fig. 4. Von Mises stress (sub-figure(a)) and pressure (sub-figure(c)) increased proportionally to the inlet pressure. Wall shear stress showed similarities in distribution; increasing or decreasing pressure from 100 mmHg showed hysteresis from the 100 mmHg distribution and velocity profile as highlighted in sub-figure(b). This shows the importance of considering accurate inlet pressure for stress distribution and blood model for structural and shear stresses as well as artery pressure.

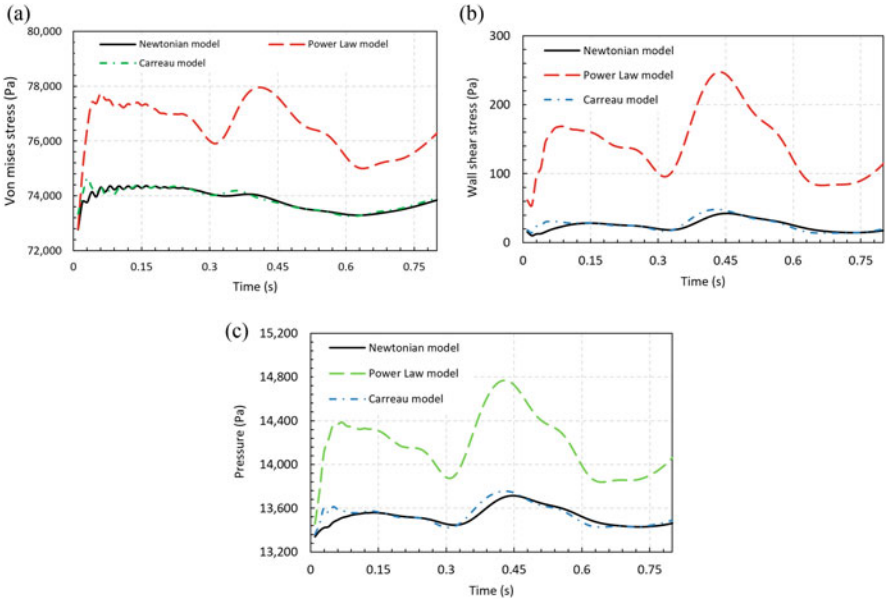

Fig. 3 Stress and pressure field versus time for different blood models (Newtonian, power law and Carreau): (**a**) von Mises, (**b**) shear stress and (**c**) pressure

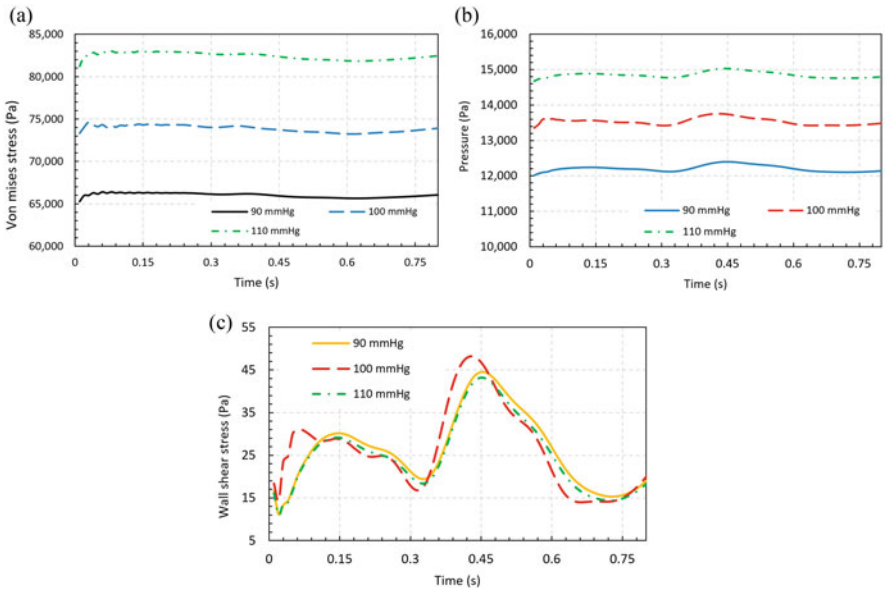

Fig. 4 Stress and pressure field versus time for different blood pressures using the Carreau model: (**a**) von Mises, (**b**) pressure and (**c**) shear stress

4 Conclusions

The impact of different blood flow models in the biomechanical analysis of human coronary arteries was assessed through the development of a FEM, FSI model in ANSYS. The most at-risk stenosis of 45% was analysed including all three artery layers, artery taper, media layer contraction, heart motion, pulsatile blood flow (using Newtonian, Carreau and power law models) and plaque lipid pool as well as hyperelastic and viscoelastic material properties. The following key conclusions resulted and are important in developing our understanding of the flow-induced effects on coronary arteries and plaques which could assist in reducing the global impact of cardiovascular diseases: (1) Blood model greatly affected maximum stress and internal pressure. (2) Maximum von Mises stress increased by 4.8–5.4% in the power law model; the distribution showed similarities but variations were magnified. (3) Wall shear stress magnitude variations of up to 450% were possible when using the power law model. (4) Variations in inlet pressure amplified shear stress hysteresis under the Carreau model.

References

1. Calvert, J.W.: Chapter 5 – ischemic heart disease and its consequences. In: Willis, M.S., Homeister, J.W., Stone, J.R. (eds.) Cellular and Molecular Pathobiology of Cardiovascular Disease, pp. 79–100. Academic Press, San Diego (2014)
2. World Health Organisation, The top 10 causes of death, (2018) https://www.who.int/news-room/fact-sheets/detail/the-top-10-causes-of-death. Last accessed 07 Sept 2019
3. Kachanov, M., Abedian, B.: On the isotropic and anisotropic viscosity of suspensions containing particles of diverse shapes and orientations. Int. J. Eng. Sci. **94**, 71–85 (2015)
4. Zhang, J.-B., Kuang, Z.-B.: Study on blood constitutive parameters in different blood constitutive equations. J. Biomech. **33**, 355–360 (2000)
5. Soulis, J.V., Fytanidis, D.K., Papaioannou, V.C., Giannoglou, G.D.: Wall shear stress on LDL accumulation in human RCAs. Med. Eng. Phys. **32**, 867–877 (2010)
6. Li, X.-y., Wen, G.-b., Li, D.: Computer simulation of non-Newtonian flow and mass transport through coronary arterial stenosis. Appl. Math. Mech. **22**, 409–424 (2001)
7. Johnston, B.M., Johnston, P.R., Corney, S., Kilpatrick, D.: Non-Newtonian blood flow in human right coronary arteries: steady state simulations. J. Biomech. **37**, 709–720 (2004)
8. Katranas, S.A., Antoniadis, A.P., Kelekis, A.L., Giannoglou, G.D.: Insights on atherosclerosis by non-invasive assessment of wall stress and arterial morphology along the length of human coronary plaques. Int. J. Cardiovasc. Imaging. **31**, 1627–1633 (2015)
9. Giannoglou, G.D., Soulis, J.V., Farmakis, T.M., Farmakis, D.M., Louridas, G.E.: Haemodynamic factors and the important role of local low static pressure in coronary wall thickening. Int. J. Cardiol. **86**, 27–40 (2002)
10. Melih Guleren, K.: Numerical flow analysis of coronary arteries through concentric and eccentric stenosed geometries. J. Biomech. **46**, 1043–1052 (2013)
11. Soulis, J.V., Farmakis, T.M., Giannoglou, G.D., Louridas, G.E.: Wall shear stress in normal left coronary artery tree. J. Biomech. **39**, 742–749 (2006)
12. Gholipour, A., Ghayesh, M.H., Zander, A., Mahajan, R.: Three-dimensional biomechanics of coronary arteries. Int. J. Eng. Sci. **130**, 93–114 (2018)

13. Khakalo, S., Balobanov, V., Niiranen, J.: Modelling size-dependent bending, buckling and vibrations of 2D triangular lattices by strain gradient elasticity models: applications to sandwich beams and auxetics. Int. J. Eng. Sci. **127**, 33–52 (2018)
14. Haddad, S.M., Samani, A.: A computational model of the left ventricle biomechanics using a composite material approach. Int. J. Eng. Sci. **111**, 61–73 (2017)
15. Gholipour, A., Ghayesh, M.H., Zander, A.: Nonlinear biomechanics of bifurcated atherosclerotic coronary arteries. Int. J. Eng. Sci. **133**, 60–83 (2018)
16. Chabi, F., Champmartin, S., Sarraf, C., Noguera, R.: Critical evaluation of three hemodynamic models for the numerical simulation of intra-stent flows. J. Biomech. **48**, 1769–1776 (2015)
17. Johnston, B.M., Johnston, P.R., Corney, S., Kilpatrick, D.: Non-Newtonian blood flow in human right coronary arteries: transient simulations. J. Biomech. **39**, 1116–1128 (2006)

Development of Physical Condition Fluctuation Prediction Model Using Trunk Biosignals

Yoshika Nobuhiro, Etsunori Fujita, Ryuichi Uchikawa, Shinichiro Maeda, Shigeyuki Kojima, Yumi Ogura, Tsutomu Kamei, Kohji Murata, Masao Yoshizumi, and Shigehiko Kaneko

1 Introduction

In Japan, drivers of trucks, buses, and taxis tend to keep irregular hours and are therefore more prone to lifestyle diseases such as diabetes and hypertension due to their work practices. Consequently, periodic health checks have shown that the prevalence of such disorders in drivers of business vehicles is higher than in other industries [1] and around 70% of drivers who died were found to have a disease in the brain or cardiovascular system [2]. We are developing systems that can monitor a driver's physical condition, capturing signs of fatigue and entering a sleep phase from biosignals [3, 4]. In this paper, we report on the results of our findings regarding the ability to detect and predict fluctuations in a person's physical state using trunk biosignals.

Y. Nobuhiro (✉) · R. Uchikawa · S. Maeda · S. Kojima · Y. Ogura
Delta Kogyo Co., Ltd., Aki-gun, Hiroshima, Japan
e-mail: nobuhiro-y@deltakogyo.co.jp; uchikawa@deltakogyo.co.jp; maeda@deltakogyo.co.jp; kojima-s@deltakogyo.co.jp; ogu@deltakogyo.co.jp

E. Fujita · M. Yoshizumi
Graduate School of Biomedical and Health Sciences, Hiroshima University, Minami-ku, Hiroshima, Japan
e-mail: gonzo@deltakogyo.co.jp

T. Kamei
Health Promotion and Half Sick (Mibyo) Improvement, Toshima-ku, Tokyo, Japan

K. Murata
Graduate School of Sanyo Gakuen University, Graduate School of Nursing, Naka-ku, Okayama, Japan

S. Kaneko
Faculty of Science and Engineering, Waseda University, Shinjuku-ku, Tokyo, Japan

S. Oberst et al. (eds.), *Vibration Engineering for a Sustainable Future*,
https://doi.org/10.1007/978-3-030-46466-0_47

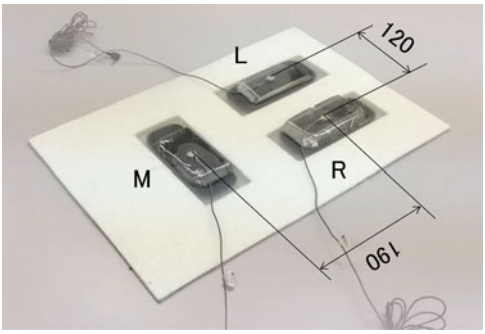

Fig. 1 The 4SR (sound sensing system using stochastic resonance) system

2 Methods

Figure 1 shows the newly developed sound sensing system using stochastic resonance (which we have named 4SR). 4SR is a sensing system comprising of three microphones (L, M, and R) and amplifies the weak acoustic pulse wave (APW) generated in the 5–200 Hz range from the trunk [5]. The L and R microphones are placed 6 cm to the left and right of the chest midline and correspond to the fifth rib, while the M microphone is positioned in the third to fourth lumbar vertebrae area. We extract a pressure waveform (the chest biosignal) derived from the apical beat and the ejection wave to the chest from the L microphone and a pressure waveform (the abdominal biosignal) generated by the abdominal aorta from the M microphone. The APW can thus be captured continuously by bringing the 4SR device into contact with a person's back. In addition, we compared the APW with information obtained from electrocardiogram (ECG) and blood pressure tests.

In order to evaluate significant changes in cardiovascular function, exercise stress tests using a treadmill were performed to collect the necessary data. The subjects were six males ranging in age from their 20s to 40s (average age 33.7, $\pm$7.7 years). We recorded the APW, ECG readings, continuous blood pressure via a fingertip cuff, and upper arm blood pressure. Each subject sat on an automotive seat installed in a room for 20 minutes, ran on a treadmill for about 10 minutes, and then returned to a sitting position again for 60 minutes. While running, we used the Gerkin Protocol Test installed on the treadmill.

In addition, in order to better understand the state of those with impaired cardiovascular function, we performed a resting position experiment for elderly people. The subjects were four older people in their 80s to 90s (a male and three females, average age 88.3, $\pm$2.1 years). We recorded the APW and ECG readings for 6 minutes in the supine position. This measurement was taken in consideration of the subject's condition in the presence of a doctor.

Both experiments were conducted only after approval from the Research Ethics Review Board within Delta Kogyo Co., Ltd., in compliance with the Declaration of Helsinki. Naturally, we explained the purpose and details of the experiments to the subjects before obtaining their agreement to take part.

3 Results and Discussion

Figure 2 shows the results of the time series analysis following the exercise and resting position experiments. Figure 2a shows the results of Subject A, who was in good health, having endurance, and was 26 years old; Fig. 2b shows the results of Subject B, who was a 91 year old patient with chronic atrial fibrillation. Variations in heart rate, LF/HF, and HF [6], which are autonomic nervous activity indicators, were calculated from the ECG readings. Systolic blood pressure (SBP) and diastolic blood pressure (DBP) fluctuations were calculated from the continuous blood pressure waveform. Pressure fluctuations in the chest and abdomen were captured from the peak points of each pressure waveform calculated from the chest and abdominal biosignals. Figure 3 shows Lorenz plots of SBP, the peak points of the thoracic pressure waveform, and the peak points of the abdominal pressure waveform of Subject A. We compared the Lorenz plots every 180 seconds at rest, after the exercise load, and before the end of the measurement. Figure 4 shows the results comparing ECG readings with the thoracic and abdominal pressure waveforms for 5 seconds. Figure 4a shows the waveforms of Subject A at rest; Fig. 4b shows the waveforms of Subject B in the normal state, while Fig. 4c, d show the waveforms displayed at the moment where arrhythmia occurred in Subject B.

As shown in Fig. 2a, the heart rate of Subject A was about 48 bpm at rest and increased to 173 bpm immediately after the exercise load. The heart rate 1980 seconds after the exercise session ended dropped to about 65 bpm, with the heart rate decreasing steadily thereafter. SBP tended to increase rapidly with the start of exercise and decrease again once the exercise load came to an end. By contrast, DBP did not change significantly before or after the exercise load. HF levels were enhanced at rest before the exercise load due to excessive sleepiness. However, both HF and LF/HF were on the same level immediately after the exercise session until to the end of the measurement, and the autonomic nervous activities were in a balanced state. This is supported by the comment made by Subject A following the exercise experiment, who noted that he felt refreshed after the exercise segment and was able to relax that much easier as a result. Pressure waveforms from the chest and abdomen displayed very similar fluctuations. In addition, their waveforms showed a large amount of fluctuation immediately after the end of the exercise load and were similar to the heart rate and SBP variations. The heart rate, SBP, and thoracic and abdominal pressure waveforms showed distinctly different fluctuations before and after the exercise load. We can surmise that the cardiovascular function in Subject A was able to respond to rapid changes in the body due to exercise loads in order to maintain homeostasis and the autonomic nervous system of Subject A was thus functioning properly. These results suggest that the thoracic and abdominal pressure waveforms can capture the change point and degree of change in cardiovascular dynamics, such as heart rate and blood pressure, under load.

As shown in Fig. 3, the Lorenz plots of SBP and the peak points of the thoracic and abdominal pressure waveforms showed the same positional relationship at rest, immediately after the exercise load, and before the end of measurement. In

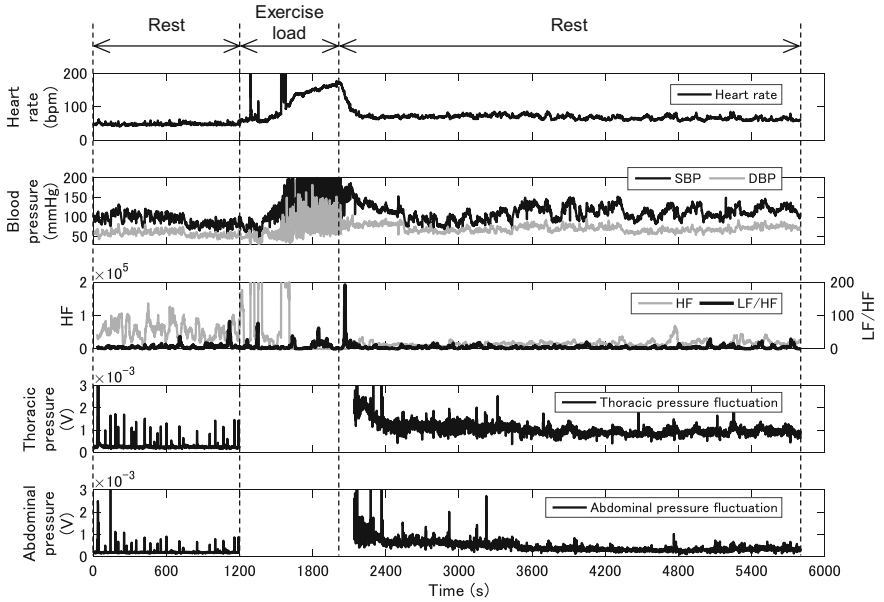

(a) Results of Subject A: heart rate variability, blood pressure variability, autonomic nervous activity, thoracic pressure fluctuation, and abdominal pressure fluctuation are shown.

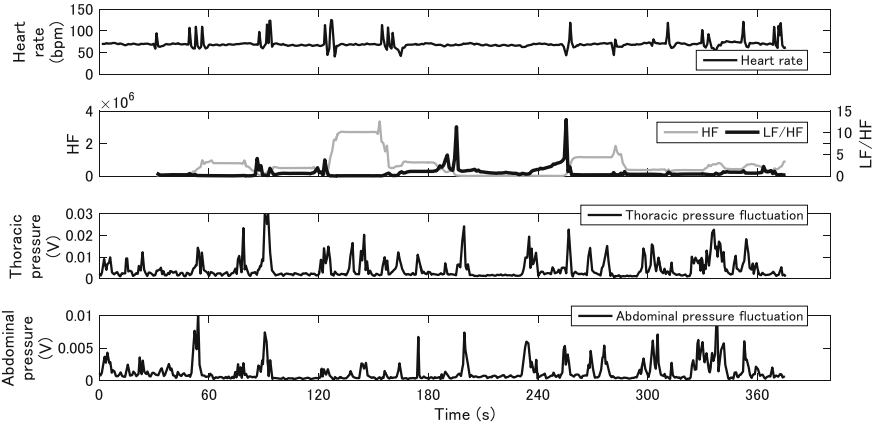

(b) Results of Subject B: heart rate variability, autonomic nervous activity, thoracic pressure fluctuation, and abdominal pressure fluctuation are shown.

Fig. 2 Results of time series analysis. (**a**) Results of Subject A: heart rate variability, blood pressure variability, autonomic nervous activity, thoracic pressure fluctuation, and abdominal pressure fluctuation are shown. (**b**) Results of Subject B: heart rate variability, autonomic nervous activity, thoracic pressure fluctuation, and abdominal pressure fluctuation are shown

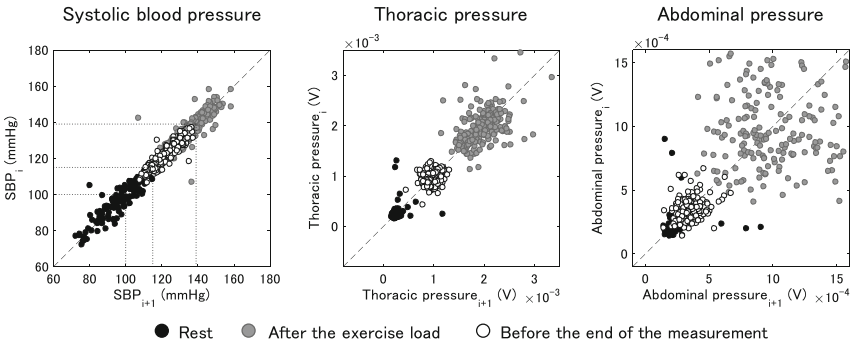

Fig. 3 Lorenz plots of SBP, the peak points of the thoracic pressure waveform, and the peak points of the abdominal pressure waveform of Subject A

particular, the clustering of SBP and chest pressure waveform plots suggests that SBP fluctuation can be estimated from the pressure fluctuations in the chest and abdomen.

Figure 2b shows that the heart rate of Subject B was over 100 bpm on several occasions, indicating that tachycardia occurred. The autonomic nervous activity exhibited a trend that sympathicotonia was caused where tachycardia occurred, with parasympathicotonia following as a result of stroke volume. The pressure variations in the chest and abdomen tended to fluctuate significantly around where tachycardia occurred. Figure 4a, b show that the thoracic and abdominal pressure waveforms of Subject B are to be in tune with the heart rate when in the normal state, as with the waveform of Subject A at rest. However, Fig. 4c shows that both pressure waveforms were disturbed when tachycardia and fluctuations in the ST segment on the ECG occurred. Even though the heart rate was stable between 170 and 250 seconds, sympathetic nerve activity was enhanced rapidly at the 188–196 second mark, and the pressure fluctuations in the chest and abdomen fluctuated significantly at around 210 seconds. As shown in Fig. 4d, disturbances, or arrhythmia, occurred in the ECG waveform between R waves at around 199 seconds. Hence, these results suggest that arrhythmia situations, such as tachycardia, can be deduced and detected from the thoracic and abdominal pressure waveforms.

4 Conclusions

- The degree of change in cardiovascular dynamics, such as heart rate and blood pressure, could be captured via the thoracic and abdominal pressure waveforms.
- Systolic blood pressure fluctuation could be estimated from pressure fluctuations in the chest and abdomen.
- Arrhythmia could be deduced from the thoracic and abdominal pressure waveforms.

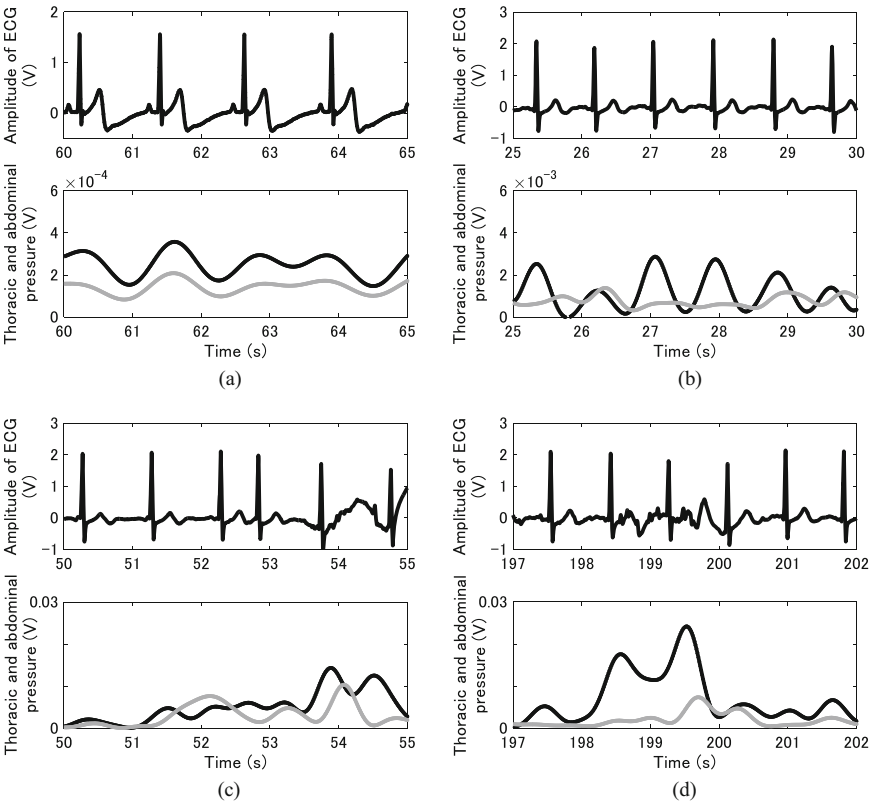

Fig. 4 Comparison of an ECG (upper) and the thoracic and abdominal pressure waveforms (lower), with the thoracic pressure waveform shown in black and the abdominal pressure waveform in gray. (**a**) Rest (Subject A). (**b**) Normal state (Subject B). (**c**) Tachycardia (Subject B). (**d**) Arrhythmia (Subject B)

References

1. Japanese ministry of land, infrastructure, transport and tourism homepage. https://www.mlit.go.jp/jidosha/anzen/subcontents/data/statistics60.pdf. Last accessed 07 Sept 2019
2. Japanese ministry of health, labor and welfare homepage. https://www.mhlw.go.jp/stf/seisakunitsuite/bunya/koyou_roudou/roudoukijun/anzen/toukei.html. Last accessed 07 Sept 2019
3. Fujita, E., Ogura, Y., Ochiai, N., Yasuda, E., Doi, S., Murata, K., Kamei, T., Ueno, Y., Kaneko, S.: Development of simplified appraisal method of fatigue on sitting for extended periods by the data of finger plethysmogram. Jpn. J. Ergon. **40**(5), 254–263 (2004)
4. Fujita, E., Ogura, Y., Ochiai, N., Miao, T., Shimizu, T., Kamei, T., Murata, K., Ueno, Y., Kaneko, S.: Development of the measurement method of the prediction of sleep by finger plethysmogram. Jpn. J. Ergon. **41**(4), 203–212 (2005)

5. Kojima, S., Maeda, S., Uchikawa, R., Nobuhiro, Y., Aoi, K., Ogura, Y., Fujita, E., Murata, K., Kamei, T., Tsuji, T., Yoshizumi, M., Kaneko, S.: Development of a simple system to sense vital signs from the back. J. Jpn. Soc. Des. Eng. **50**(2), 78–88 (2015)
6. Malliani, A., Pagani, M., Lombardi, F., Cerutti, S.: Cardiovascular neural regulation explored in the frequency domain. Circulation. **84**(2), 482–492 (1991)

Contribution of F-actin to Sensing Mechanism of Vibration in Mouse Fibroblastoid Cell

Takumi Nambara and Shin Morishita

1 Introduction

The living body is known to have the functional adaptability to mechanical stimuli from the environment. While the bone density is increased and skeletal muscle fiber tends to be strong by putting stress on the body in exercise or training [1], the calcium in the bone matrix gets out of the body, and muscle fiber may become weak without any stress in the body [2]. The bone architecture may adapt to its mechanical surroundings, which is known as Wolff's law [3]. In the medical field, doctors apply the low-intensity pulsed ultrasound (LIPUS) to the broken bone for the purpose of accelerating its healing [4]. Rehabilitation to patients may be a powerful tool for recovering the wounded body. Though such various effects of mechanical stimuli are closely related to the adaptation mechanism of a living body, the precise procedure has not been clearly revealed yet.

Because a living body consists of various kinds of cells, this adaptation is assumed to be caused by the reaction of each cell. Therefore, it is important to focus on the response of the cell to mechanical stimuli to understand the mechanism of adaptation of a living body. From a viewpoint of mechanical engineering, cells are considered to have autonomous system – sensing the input of mechanical stimuli, controlling its appropriate behavior, and actuating determined behavior. Clarifying the mechanism on how these functions work leads to understanding the response of the cell to mechanical stimuli. If the sensing mechanism of mechanical stimuli in

T. Nambara (✉)
Graduate School of Environment and Information Sciences, Yokohama National University, Yokohama, Japan
e-mail: nambara-takumi-ch@ynu.jp

S. Morishita
Faculty of Yokohama National University, Yokohama, Japan
e-mail: morishita-shin-xf@ynu.ac.jp

S. Oberst et al. (eds.), *Vibration Engineering for a Sustainable Future*,
https://doi.org/10.1007/978-3-030-46466-0_48

cells is clarified, it will be useful to develop some microscale sensors for industrial use. Medical utilization of mechanical stimuli will also become more adequate one by understanding its mechanism.

Lots of experiments regarding mechanosensing have been shown in the literature so far. One of the authors found that the cell density was increased by applying comparatively low-frequency vibration. The cells cultured under some mechanical vibration increased about more than 30% in cell number compared with those without any vibration [5]. After these findings, several studies have focused on the linker of the nucleus and cytoskeleton called LINC complexes [6] and the linker of the cell and extracellular matrix, namely, cell-matrix adhesion by integrin α5β1 and fibronectin. They showed that these structures were essential factors of sensing the applied vibration.

In this study, we hypothesize that cells may sense the applied vibration through the nucleus, F-actin, integrin, and nucleus connectivity. Special interest is focused on the F-actin which binds the nucleus to integrin for sensing vibration. To assess the contribution of F-actin to sensing vibration, one of the metabolites named cytochalasin D (CD) which inhibits actin polymerization is introduced in the medium of cells. Four groups, that is, with CD under static or vibration and without CD under static or vibration, are prepared. The cell number is compared between these groups after confluent concentration state.

2 Materials and Methods

2.1 Cell Culture

There are various kinds of cells in our body, and fibroblasts are known as the major cells responsible for the production of extracellular matrix like collagen, elastin, and fibronectin in connective tissue. Fibroblast cells are easy to handle and often used in experiments in the field of cell biology. In this study, we used fibroblast-like cell line, β1GD25, provided by Dr. Takao Sakai (University of Liverpool, UK). The cell line GD25 was originally produced as a β1integrin-deficient cell line to investigate the role of β1 subunit in cell adhesion, and β1GD25 was transformed by introducing β1 integrin subunit to GD25 [7]. We used this cell line because the connectivity from the nucleus to integrin through actin filament might play some important role for a cell in sensing mechanism of vibration.

Passage number of β1GD25 was 7 to 9 in all experiments. β1GD25 was seeded in 96 multi-well plate (Thermo Fisher Scientific, USA) at 1.0×10^5 cells/well with Dulbecco's Modified Eagle Medium (DMEM, High Glucose-GlutaMAX™-Pyruvate, Gibco, USA) suspended with 10% fetal bovine serum (FBS, Equitech-Bio Inc., USA) and 1% penicillin-streptomycin solution (PS, FUJIFILM Wako Pure Chemical Corporation, JPN). The culture medium of cells was changed once every day. The cells were cultured in the incubator at 37° in the air of 100% humidity and 5% CO_2.

2.2 Addition of Cytochalasin D

The purpose of this research is to find the contribution of actin filament, connected from the nucleus placed deep in the cell to the integrin on the cell membrane, on sensing mechanical vibration. For that reason, the response to mechanical vibration was compared in counting the cell number between the F-actin-inhibited cells and the original cells. It is well known that the actin monomer expressing globular form (G-actin) assembles into polarized filament, which is called as the filamentous actin (F-actin). F-actin is known to support the cellular structure as cytoskeleton.

In the cell biology, it is possible to inhibit the formation of actin filament by adding cytochalasin D (CD), a kind of fungal toxin. CD may bind to the barbed end of actin filament and inhibit the association of subunits. Therefore, a cell cannot organize F-actin when CD is dissolved in the medium at a certain concentration. In this experiment, CD (Cayman Chemical Company, USA) was added to the medium from 1 day before mechanical vibration gave effects on the cultivated cell number.

Too high concentration of CD will inhibit various cell activities and lead cells to die out because F-actin is needed for the cell to survive. In this study, the effect of mechanical vibration on cells was evaluated by comparing the number of cells cultivated in a certain period in incubator. Therefore, the concentration of CD had to set low enough not to affect the cultivated cell number and high enough to inhibit the formation of F-actin partially. Such an appropriate CD concentration was determined as 0.2 μM experimentally.

2.3 Application of Mechanical Vibration

The experimental setup to apply mechanical vibration to cells is shown in Fig. 1. Sinusoidal wave signals produced by a function generator (WF1945A, NF Corporation, JPN) were amplified by power amplifier (Type 2718, Brüel & Kjær, DNK) and input to the electromagnetic exciter (Type 4809, Brüel & Kjær, DNK). Aluminum plate which has enough stiffness not to resonate at vibration frequency of this experiment was fixed on the exciter. Culture plate was attached on this aluminum plate to apply vibration uniformly and vertically to cells.

The exciter was put in the incubator. A sponge was put under the exciter as an isolator not to transfer vibration to incubator. The acceleration amplitude and the frequency of the vibration were set to 0.5 G and 12.5 Hz, which is shown as the most effective one for the increase of cell number according to the previous study [5]. After cells were cultured under static condition for 1 day to have them adhered on the well plate, the vibration was applied to cells all day long during the experiment.

Various physical or chemical phenomena might be induced when the cells are cultured under mechanical vibration. One of them is the sloshing effect of culture medium. The magnitude of sloshing depends on the diameter of culture medium, the height of culture medium in each well, and the viscosity of medium. It was

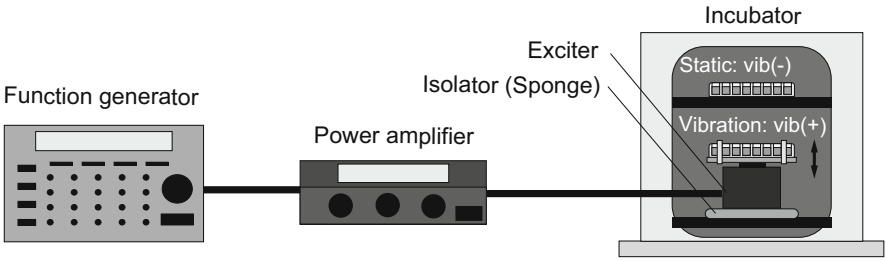

Fig. 1 Experimental setup

reported that the sloshing effect was shown to increase in cell number under some vibration conditions [8]. Then, if the sloshing effect estimated to be not small, it has to be suppressed to investigate the real vibration effect on cells. In the case of this study using 96 multiwell plate, the suppression measures of sloshing were not done because it is confirmed that the sloshing is too small to give effect on cell number.

2.4 Cell Number Count

The effect of vibration on the cultivated cells was indicated by the cell number, at first. The number of living cells was counted by hemocytometer and phase-contrast microscope. The trypan blue solution which dyed only dead cells in blue was used to exclude the dead cells from counting cell number.

2.5 Immunofluorescence

β1GD25 was seeded in 35-mm glass bottom dish (Matsunami Glass Ind., Ltd., JPN) to observe the structure of cells by immunofluorescence. Nucleus antibody, TO-PRO-3 (Molecular Probes, USA), and actin antibody, Alexa Fluor 488 phalloidin (Invitrogen, USA), were used to visualize the structure. After staining, the cell morphology was observed by the inverted-type fluorescence microscope.

2.6 Statistical Analysis

All data was shown in the form of mean ± S.D. The statistical comparisons were performed by Student's *t*-test. A value of $p < 0.05$ was considered significant in all analysis.

3 Result and Discussion

3.1 Result Under Mechanical Vibration with CD

Cell culture experiment under mechanical vibration with CD-included medium was performed at the frequency of 12.5 Hz and the amplitude of 0.5 G. One of the results of cell growth is shown in Fig. 2. The legend vib(+) means the results under vibration and vib(−) under static without vibration. The cells cultured under mechanical vibration without CD increased about 30% in cell number on day 7 and day 8 compared with those under static, as shown in Fig. 2. On the other hand, this increase of cell number was not observed when CD was included in medium. The cells cultivated in the medium included by CD could not sense the applied mechanical vibration under inhibition of F-actin. This result suggested that the organized F-actin was an essential factor of sensing vibration.

3.2 Discussion

F-actin is one of the cytoskeletons and a kind of protein structured inside of living cells. It is known to play important roles in supporting not only cellular structure but also other various functions such as migration or adhesion of cells. This is considered to come from F-actin contractility [9]. F-actin contractility changes the conformation of proteins bound to F-actin. The conformation of proteins is very important in cellular biological signaling because the interaction with other proteins depends on it.

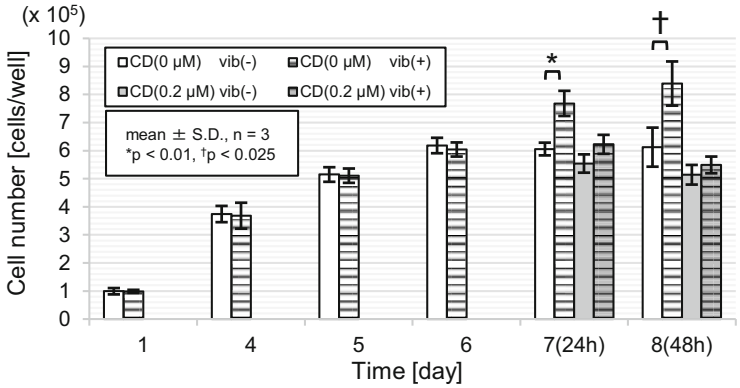

Fig. 2 Cell growth under mechanical vibration with/without CD. Twenty-four hours and 48 h in horizontal axis indicate elapsed time after CD addition. Each mark (* and †) shows significant difference in cell number between static and vibration, cultured at the same CD concentration

The failure of sensing vibration under inhibition of F-actin in this study might suggest that sensing process of vibration also needs F-actin contractility. As described above, the mechanical coupling between the nucleus and F-actin and between integrin α5β1 and fibronectin is needed for sensing vibration. F-actin may connect between these coupling sites and contract each other by its contractility. Focal adhesion is known to consist of many proteins which changed their conformation by tensile force [10]. It is considered that F-actin contractility varies the conformation of proteins in focal adhesion, then mechanical signals are converted to biological signals such as phosphorylation cascades, and finally cells sense mechanical vibration.

4 Conclusions

In this study, we hypothesized that cells might sense the applied vibration through the nucleus, F-actin, integrin, and nucleus connectivity. Special interest was focused on the F-actin which binds the nucleus to integrin for sensing vibration. To assess the contribution of F-actin to sensing vibration, cytochalasin D was introduced in the medium of cells. It was shown experimentally that F-actin is an essential factor of sensing the applied vibration. The sensing process of vibration may need F-actin contractility, but to understand how it contributes to sensing vibration, it may need more experimental investigations.

References

1. Hinton, P.S., Nigh, P., Thyfaulta, J.: Effectiveness of resistance training or jumping-exercise to increase bone mineral density in men with low bone mass: a 12-month randomized, clinical trial. Bone. **79**, 203–212 (2015)
2. LeBlanc, A., Schneider, V., Shackelford, L., West, S., Oganov, V., Bakulin, A., Voronin, L.: Bone mineral and lean tissue loss after long duration space flight. J. Musculoskelet. Nueronal Interact. **1**(2), 157–160 (2000)
3. Wolff, J.: The Law of Bone Remodeling. Springer-Verlag, Cham (1986)
4. Takikawa, S., Matsui, N., Kokubu, T., Tsunoda, M., Fujioka, H., Mizuno, K., Azuma, Y.: Low-intensity pulsed ultrasound initiates bone healing in rat nonunion fracture model. J. Ultrasound Med. **20**(3), 197–205 (2001)
5. Shikata, T., Shiraishi, T., Morishita, S., Takeuchi, R., Saito, T.: Effects of amplitude and frequency of mechanical vibration stimulation on cultured osteoblasts. J. Syst. Des. Dyn. **2**(1), 382–388 (2008)
6. Uzer, G., Thompson, W.R., Sen, B., Xie, Z., Yen, S.S., Miller, S., Bas, G., Styner, M., Rubin, C.T., Judex, S., Burridge, K., Rubin, J.: Cell mechanosensitivity to extremely low-magnitude signals is enabled by a LINCed nucleus. Stem Cells. **33**(6), 2063–2076 (2015)
7. Sakai, T., Zhang, Q., Fässler, R., Mosher, D.F.: Modulation of β1A integrin functions by tyrosine residues in β1 cytoplasmic domain. J. Cell Biol. **141**(2), 527–538 (1998)

8. Yamamoto, T., Morishita, S.: The effect of sloshing of culture medium on cell proliferation. In: Proceedings of the 5th Japan-Korea Joint Symposium on Dynamic & Control, pp. 71–73 (2017)
9. Case, L.B., Waterman, C.M.: Integration of actin dynamics and cell adhesion by a three-dimensional, mechanosensitive molecular clutch. Nat. Cell Biol. **17**(8), 955–963 (2015)
10. Hytönen, V.P., Wehrle-Haller, B.: Mechanosensing in cell–matrix adhesions – converting tension into chemical signals. Exp. Cell Res. **343**, 35–41 (2016)

Vibration Characteristics of Seated Human Body Under Exposure to Vertical Whole-Body Vibration in Wide-Frequency Range

Gen Tamaoki, Koki Sugimoto, Takuya Yoshimura, Yoichiro Kitahara, and Koki Yamashita

1 Introduction

Vibration characteristics of a seated human body exposed to whole-body vibration are important factors in ride comfort of automobiles. There are main resonance frequencies of the human body in a frequency range below approximately 20 Hz. Therefore the vibration characteristics in this frequency range have been discussed in many previous studies [1, 2]. Low-frequency vibration has been known to affect the ride comfort, for example, frequency weighting factors defined in ISO2631-1 [3] and equivalent comfort contours [4]. The equivalent comfort contours show that high-frequency vibration requires larger magnitude in order to feel the same magnitude as low-frequency vibration. It means that human perception of high-frequency vibration is less sensitive than that of low-frequency vibration. This is another reason that the low frequency has been considered an important factor in assessing the ride comfort. As a result of the research on low-frequency vibration and the development of reduction technology of low-frequency vibration, the ride comfort issue seemed to have been achieved. However, the vibration reduction technology of automobiles has made occupants perceive high-frequency vibration. The same thing has happened in electric vehicles that generate less low-frequency vibration. Engineers involved in the development have come to think that high-frequency vibration may have an adverse effect on ride comfort in low vibration or electric cars. Therefore it is necessary to focus on high-frequency vibration for the ride comfort. However the vibration characteristics of a seated human body in

G. Tamaoki (✉) · K. Sugimoto · T. Yoshimura
Tokyo Metropolitan University, Tokyo, Japan
e-mail: tamaoki@tmu.ac.jp; yoshimu@tmu.ac.jp

Y. Kitahara · K. Yamashita
Mazda Motor Corporation, Hiroshima, Japan
e-mail: kitahara.y@mazda.co.jp; yamashita.ko@mazda.co.jp

S. Oberst et al. (eds.), *Vibration Engineering for a Sustainable Future*,
https://doi.org/10.1007/978-3-030-46466-0_49

high-frequency range cannot be said as obvious as that in low-frequency range. The purpose of this study is to examine the vibration characteristics of the seated human body in a wide-frequency range, which means up to 50 Hz beyond 20 Hz that has been previously studied. For the purpose, vibration experiments for the human body with a shaking table and modal analyses of the experimental results are conducted. The goal of this study is to estimate modal characteristics of the human body expressed as the head-spine system in the wide-frequency range. A frequency range below 20 Hz is called the low-frequency range, and a frequency range from 20 Hz to 50 Hz is called the high-frequency range in this study.

2 Human Vibration Experiment

An experiment's schematic diagram is shown in Fig. 1. The coordinate system defined by ISO2631-1 [3] is used in this study (X, fore-and-aft; Y, lateral; and Z, vertical). Subjects sat on a rigid seat fixed on the shaking table (SHINKEN, G-6150-3HT-040) without a backrest and with a footrest that was not attached to the seat and didn't vibrate. The subjects were exposed to vertical vibration only from the seat surface with their back stretched and their feet placed on the footrest. Seat-to-measurement-point acceleration transmissibility was obtained by dividing acceleration of each measurement point of the human body in each direction by acceleration on the seat surface in the excitation direction. The measurement points on the human body were the head; the seventh cervical vertebra; the third and seventh thoracic vertebrae; the first, third, and fifth lumbar vertebrae; and the sacrum. Acceleration in vertical and fore-and-aft directions at each measurement point on the human body except the head was measured with a small lightweight

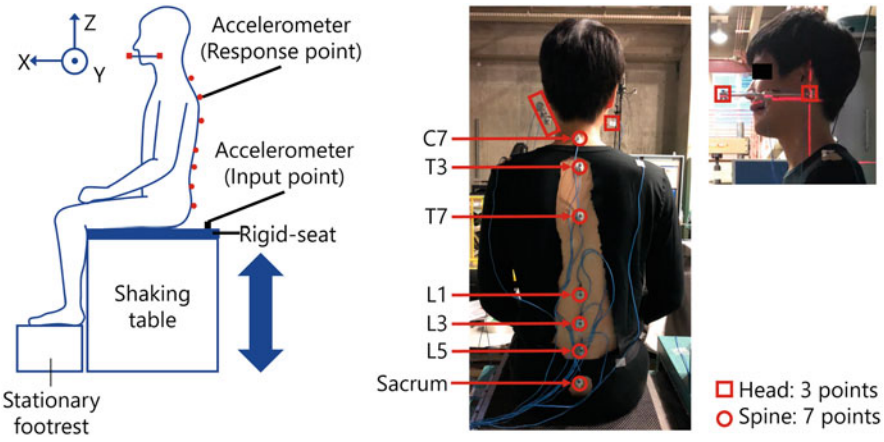

Fig. 1 Experiment schematic diagram and positions of measurement

triaxial accelerometer (1.0 gram, PCB, Type 356A03), which was stuck on a thick paper with double-sided tape and was attached to the skin above each vertebra. The thick paper (10 mm * 10 mm) was used to fix the sensor on the skin tightly. Acceleration in three translational directions of the head was measured with three small lightweight triaxial accelerometers, which were attached to a T-shaped bar bitten by the subject to fix the position of the accelerometers. Seat-to-head transmissibility of six degrees of freedom (three translational and three rotational degrees of freedom) was obtained by calculating nine translational transmissibility measured by these accelerometers, assuming that the head was a rigid body. Acceleration on the seat surface was measured with an accelerometer (PCB, Type 356A32) fixed on the rigid seat. The posture of each subject was measured by using a motion capture system (OptiTrack, Flex13, and Motive Tracker) that the infrared reflective markers were placed at the same positions as the accelerometers. The three-dimensional position coordinates at each position were obtained. The excitation wave was random of a frequency range of under 50 Hz and a magnitude of 0.3 m/s^2 r.m.s. The subjects were five healthy adult males. Their average height was 173 cm (170–178 cm), and average weight was 62 kg (55–75 kg). We conducted the measurements three times for each subject under the same conditions and calculated arithmetic average of three transmissibility.

3 Results and Discussions

Figure 2 shows the transmissibility of each measurement point in z direction for five subjects. The thin lines show the transmissibility of the subjects, and the thick line shows an arithmetic average of the subjects. There were some resonant peaks in the transmissibility of each measurement point. In the low-frequency range, the shape of the peaks was (relatively) steep. There were two peaks at each measurement point above the third lumbar vertebra and three peaks at the fifth lumbar vertebra and the sacrum. The resonant frequencies were almost the same regardless of the subjects, and the average also showed this feature. On the other hand, in the high-frequency range, peaks could not be observed at the head and seventh cervical vertebra though gradual peaks could be observed at other measurement points. The resonant frequencies varied depending on the subjects, and the average didn't show clear peak.

The modal characteristics were estimated from the measured data of the transmissibility by using multi-reference iterative curve fitting technique. Estimated natural frequencies and modal damping ratios are summarized in Table 1. Five modes were estimated in the wide-frequency range. The first, second, and third modes were in the low-frequency range. The fourth and fifth modes were in the high-frequency range. Although variation in the natural frequencies among the subjects was small in the low-order mode, it was greater as the order of the mode was higher. Not only the value but also the variation among the subjects of the modal damping ratio in the high-frequency range seemed to be larger than those in the low-frequency range.

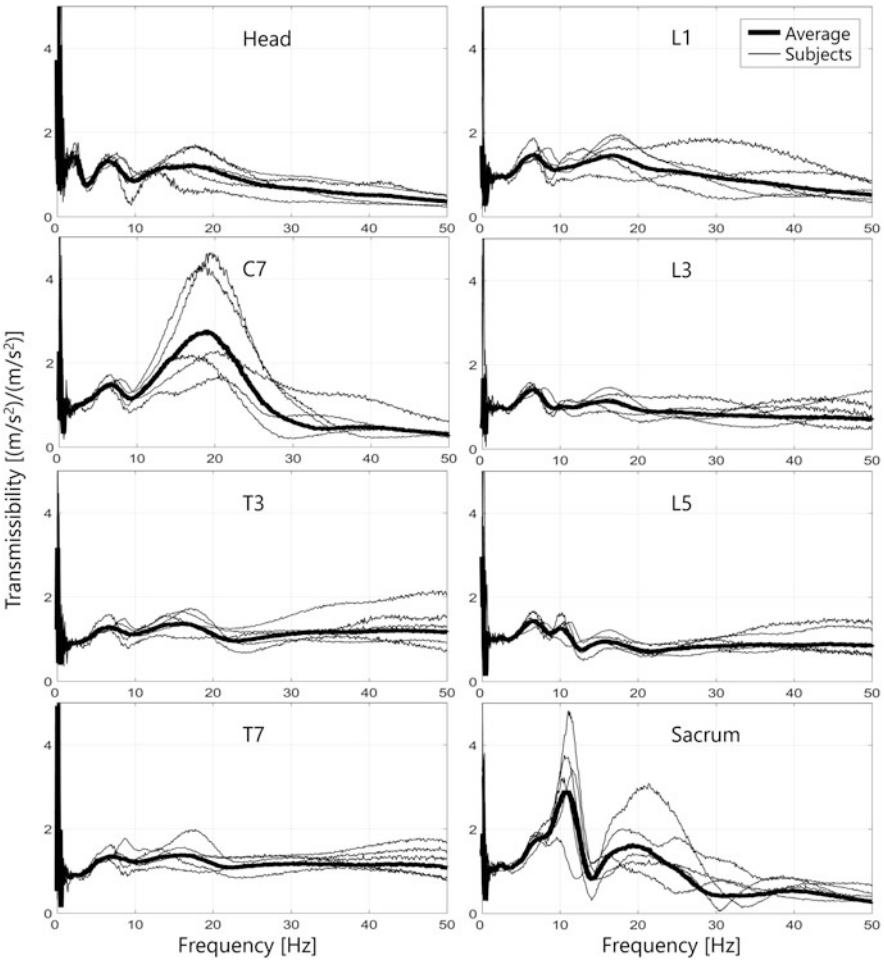

Fig. 2 Transmissibility of each measurement point in z direction for five subjects

Table 1 Identified modal characteristics

Natural frequency [Hz]						Modal damping ration [%]					
	1st	2nd	3rd	4th	5th		1st	2nd	3rd	4th	5th
Sub.1	6.8	11.5	15.4	24.1	33.0	Sub.1	12.9	14.3	28.3	32.6	31.4
Sub.2	7.5	10.2	14.1	28.6	39.5	Sub.2	15.5	16.3	25.8	20.4	49.5
Sub.3	7.9	10.6	17.5	29.0	35.6	Sub.3	15.4	18.2	23.8	35.3	31.7
Sub.4	8.1	11.9	18.0	24.5	42.1	Sub.4	11.9	15.8	23.3	27.6	46.6
Sub.5	7.4	10.8	15.5	29.1	34.7	Sub.5	16.6	16.3	34.4	29.8	71.1
SD	0.5	0.6	1.6	2.5	3.7	SD	2.0	1.4	4.5	5.7	16.3

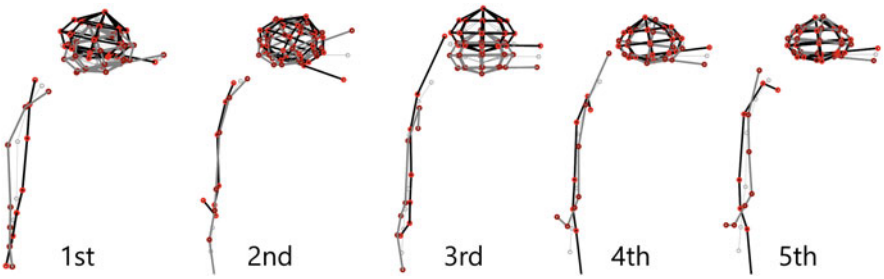

Fig. 3 Mode shape of subject 3

The vibration mode shapes of a typical subject are shown in Fig. 3, since features of the vibration mode shapes of five subjects almost coincide in the low-frequency range. The solid lines show deflections of the mode shape with the phase shifted by 180 degrees, and the broken line shows the neutral position. The first mode was rotation in pitch direction and vertical vibration of the head and bending vibration of the spine. The second mode was pitch rotation of the head and vertical vibration of the buttocks. The third mode was mainly vertical vibration of the cervical vertebra and slightly vertical vibration of the buttocks. The characteristics of the mode shape of these three modes in the low-frequency rage were the same as the results estimated in the previous study for the low-frequency range conducted by Nakai et al. [2]. Therefore, the estimations of this study were thought to be suitable. As to the high-order modes, high-order modes had the following common features, though differences of the features among subjects became large as the order of the mode went high. The mode shapes of some other subjects in the high-frequency range are shown in Fig. 4. The forth mode was vibration of the cervical vertebra and/or the buttocks. The fifth mode was vibration of each part of the spine, and the part mainly vibrated was different depending on the subjects. And in the fourth and fifth modes, depending on the part, some parts may simultaneously vibrate in fore-and-aft direction. From the above, the modal characteristics in the high-frequency range varied depending on the subjects, though the subjects showed similar modal characteristics in the low-frequency range.

4 Conclusions

The vibration experiments for the seated human body were conducted for a wide-frequency range, which is below 50 Hz, and the transmissibility of the human body was obtained. The five natural modes were estimated by using the curve fitting technique. Three modes were in the low-frequency range, and two modes were in the high-frequency range. The vibration mode shapes were obtained as the head-spine system.

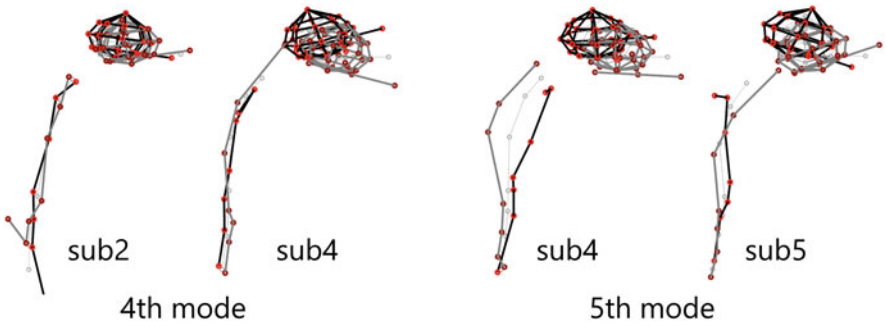

Fig. 4 Examples of fourth and fifth mode shapes of other subjects

The high-frequency vibration could affect the ride comfort because there were two modes in the high-frequency range. Since individual difference in the high frequency may be greater, we will increase the number of the subjects and confirm the validity of the result obtained in this study, and then the relationship between the magnitude of vibration in each points of the body and perception of vibration will be clarified based on the vibration characteristics of seated human body in each frequency range.

Ethical approval: All procedures performed in studies involving human participants were in accordance with the ethical standards of Tokyo Metropolitan University (the ethics committee at Tokyo Metropolitan University, No.H30-102) and with the 1964 Helsinki Declaration and its later amendments or comparable ethical standards.

Informed consent: Informed consent was obtained from all individual participants included in the study.

References

1. Rakheja, S., Dong, R.G.: Biodynamics of the human body under whole-body vibration: synthesis of the reported data. Int. J. Ind. Ergon. **40**(6), 710–732 (2010)
2. Nakai, K., Yoshimura, T., Tamaoki, G.: Experimental modal analysis of human body with the spinal column. J. Environ. Eng. **2**(4), 720–729 (2007)
3. International Organization for Standardization, Mechanical vibration and shock - Evaluation of human exposure to whole-body vibration -. International Standard, ISO 2631-1 (1997)
4. Griffin, M.J.: Handbook of Human Vibration. Academic Press, London (1996)

Changes in Peripheral Circulation and Autonomic Nervous Activity in the Elderly Exposed to Acute Whole-Body Vibration

M. H. Mahbub, Ryosuke Hase, Keiichi Hiroshige, Natsu Yamaguchi, A. N. M. Nurul Haque Bhuiyan, Noriaki Harada, and Tsuyoshi Tanabe

1 Introduction

The method of increasing peripheral circulation by applying vibration seems to be useful for the elderly who are susceptible to aging-related macrovascular and microvascular impairments of the extremities with delayed wound healing or impaired healing of chronic ulcers. However, the published results on WBV-induced changes in peripheral circulation are conflicting [1]. Moreover, those studies usually exposed subjects to high vibration magnitudes frequently exceeding the exposure limit specified in the International Standard ISO 2631–1 [2] and EU Directive 2002/44/EU [3].

A number of the previous studies showed that exposure to WBV, especially at higher frequencies, can have significant effects on the autonomic nervous activity (ANA) and can lead to enhanced vasoconstriction and vibration-induced decrease in peripheral circulation [4, 5]. An intervention modality with exposure to WBV is desirable that would be able to improve peripheral circulation without affecting the

M. H. Mahbub (✉) · R. Hase · N. Yamaguchi · T. Tanabe
Yamaguchi University Graduate School of Medicine, Yamaguchi, Japan
e-mail: hossain@yamaguchi-u.ac.jp; hase@yamaguchi-u.ac.jp; natsu@yamaguchi-u.ac.jp; tanabe@yamaguchi-u.ac.jp

K. Hiroshige
Kyushu Nutrition Welfare University, Fukuoka, Japan
e-mail: hiroshige@knwu.ac.jp

A. N. M. N. H. Bhuiyan
Chittagong Medical College, Chittagong, Bangladesh
e-mail: nislammc@ac.dghs.gov.bd

N. Harada
Junshin Gakuen University, Fukuoka, Japan
e-mail: harada@yamaguchi-u.ac.jp

S. Oberst et al. (eds.), *Vibration Engineering for a Sustainable Future*,
https://doi.org/10.1007/978-3-030-46466-0_50

autonomic nervous system. But till now, no study has investigated the concomitant changes in peripheral circulation and ANA from controlled exposure to WBV with consideration of the exposure limit specified in the relevant standards.

Therefore, the purpose of the current study was to examine the changes in peripheral skin blood flow (SBF) and skin temperature (ST) and also the concomitant responses in ANA induced by acute exposure to WBV, among the elderly, with magnitudes defined according to the International Standard ISO 2631-1 (1997).

2 Subjects and Measurements

Fifteen male (age, median, 73.0 years; interquartile range (IQR), 10.0 years. BMI, median, 25.7 kg/m^2; IQR, 3.2 kg/m^2) and 15 female (age, median, 71.0 years; IQR, 6.0 years. BMI, median, 22.6 kg/m^2; IQR, 5.0 kg/m^2) relatively healthy elderly subjects participated in this study approved by the institutional Human Research Ethics Committee. After entering the experiment room, the subjects acclimatized to the room temperature (25.0 $\pm$ 0.5°C; 15 min) and seated barefoot on a height adjustable chair. This was followed by various measurements included in the experimental protocol (Fig. 1).

While standing barefoot on the side-alternating vibration device, all subjects underwent an intervention (Fig. 1) consisting of any of the following four randomized exposure conditions performed on different days: (1) WBV at 15 Hz, (2) WBV at 20 Hz, (3) WBV at 25 Hz, and (4) control condition (0 Hz). The unweighted and frequency-weighted peak accelerations were 17.75 m/s^2 and 9.64 m/s^2 r.m.s., 31.56 m/s^2 and 14.19 m/s^2 r.m.s., and 49.30 m/s^2 and 17.89 m/s^2 r.m.s. at 15 Hz, 20 Hz, and 25 Hz, respectively; the corresponding A(8) values were 0.76 m/s^2 r.m.s., 1.12 m/s^2 r.m.s., and 1.41 m/s^2 r.m.s., respectively. The peak-to-peak displacement of the vibrating platform was 4 mm. During three bouts (1 min each) of exposure, the participants stood with bent knees at an angle of about 30° (considering a full knee extension of 0°) and lightly grasped the rails of the platform with their hands. Just after the cessation of each bout of exposure, the subjects were asked to stand up quickly but smoothly.

Before				**Intervention**						**After**	
Rest	HRV	VPT	Rest	SBF	Bout 1[1]	Rest	Bout 2[1]	Rest	Bout 3[1]	Rest	SBF
15 min	5 min		≥3 min	(twice)	1 min	1 min	1 min	1 min	1 min	1 min	
					HRV						
					ST						
Seated			Standing								

Fig. 1 Schematic illustration of the experimental protocol. HRV, heart rate variability; SBF, skin blood flow; ST, skin temperature; VPT, vibrotactile perception threshold. [1]SBF was measured immediately after the cessation of each bout of exposure

2.1 Equipment

WBV was produced using a side-alternating vibration device (Galileo 900, Novotec Medical GmbH, Pforzheim, Germany). Left dorsal foot ST and room temperature were measured by digital thermistors (SZL-64, Technol seven, Japan). Right dorsal foot SBF was recorded from an area (260 pixels) proximal to metatarsophalangeal joints, by the noncontact laser speckle flowgraphy system (LSFG-ANW, Softcare Co., LTD., Fukuoka, Japan). Heart rate variability (HRV) data were recorded using a portable battery-operated two-channel heart rate device (CheckMyHeart, DailyCare BioMedical, Inc., Taiwan) connected via electrode cables with disposable Ag/AgCl circular surface electrodes (Bioload SDC-H, GE Healthcare, Japan) placed on ventral forearms. The sampling frequency of HRV was 250 Hz.

2.2 Data Processing and Statistical Analyses

The HRV data were extracted for the real exposure period (total 3 min during three bouts of exposure) and visually inspected for noise or ectopic beats. Then using the fast Fourier transform (FFT) analysis, the following components (in milliseconds squared) were calculated for the detrended values of regular R-R interval data: (1) high-frequency power (HF, 0.15 and 0.40 Hz), (2) low-frequency power (LF, 0.04 to 0.15 Hz), and (3) LF/HF (the ratio of low- to high-frequency power). The values of HF and LF were normalized (expressed in normalized unit or nu) as follows: (1) normalized HF = HF ÷ (total power − VLF) and (2) normalized LF = LF ÷ (total power − VLF), where VLF indicates very low-frequency power (between 0.003 and 0.04 Hz) of HRV. The data were analyzed using Wilcoxon signed-rank test for two-related samples and Friedman test for k-related samples. For multiple comparisons, the adjustments were made by Bonferroni corrections as necessary. Statistical analysis was performed with statistical software package SPSS version 22 for Windows (SPSS Inc., Chicago, IL, USA). Statistical significance was considered at a two-sided P-value of <0.05.

3 Results

The baseline values of SBF under vibration exposure conditions of 15, 20, and 25 Hz did not differ significantly from the values measured under control (0 Hz) condition as shown in Fig. 2. In contrast, during intervention, relative to the control condition, the SBF increased significantly under all three vibration exposure conditions at all three time points ($P < 0.001$). When the comparison was made with the 15 Hz condition, the SBF was significantly greater at all three time points under both 20 Hz and 25 Hz exposure conditions ($P < 0.01$ to 0.001). Also, those increases

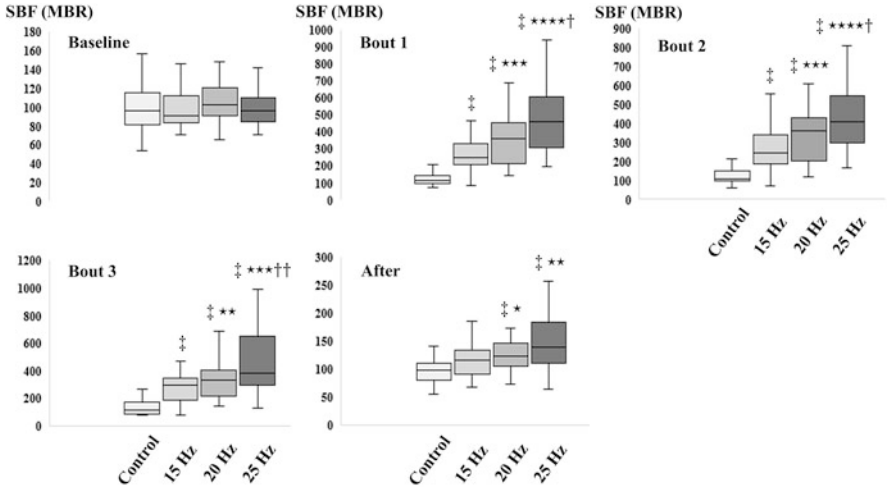

Fig. 2 Boxplots displaying median values of skin blood flow (SBF) (mean blur rate/MBR) with corresponding 25th and 75th percentiles obtained at baseline (before), during (bouts 1, 2, and 3), and after exposure for intervention under four different exposure conditions. Levels of significant differences from the corresponding values by Wilcoxon signed-rank test with adjustments for multiple comparisons by Bonferroni corrections: $^{\ddagger}P < 0.001$; $^{****}P < 0.001$, $^{***}P < 0.005$, $^{**}P < 0.01$, and $^{*}P < 0.05$ versus 15 Hz; $^{\dagger\dagger}P < 0.005$ and $^{\dagger}P < 0.05$ versus 20 Hz

differ significantly between the latter two exposure conditions at those time points ($P < 0.05$ to 0.005). When the analysis was performed with the data after cessation of intervention, compared to the control and 15 Hz conditions, the corresponding SBF remained significantly elevated under 20 Hz ($P < 0.05$ to 0.001) and 25 Hz ($P < 0.005$ to 0.001) exposure conditions; but such increases in SBF did not differ significantly between these two latter conditions.

On the other hand, no significant difference in ST was observed when the values under WBV exposure conditions were compared with the corresponding control values before, during, and after intervention (results not shown).

Compared to the corresponding control condition, the baseline values of LF, HF, or LF/HF for HRV did not show any significant difference under 15 Hz, 20 Hz, and 25 Hz exposure conditions. Also, intervention under three different frequencies with different magnitudes of WBV did not induce any statistically significant change in any of those measured parameters of HRV (Fig. 3).

4 Discussion

For intervention with exposure to WBV, safe and effective vibration parameters like frequency, amplitude, acceleration, etc. have not yet been established. As suggested in ISO 2631-1 [2], subjects should not be exposed to high levels of vibration during

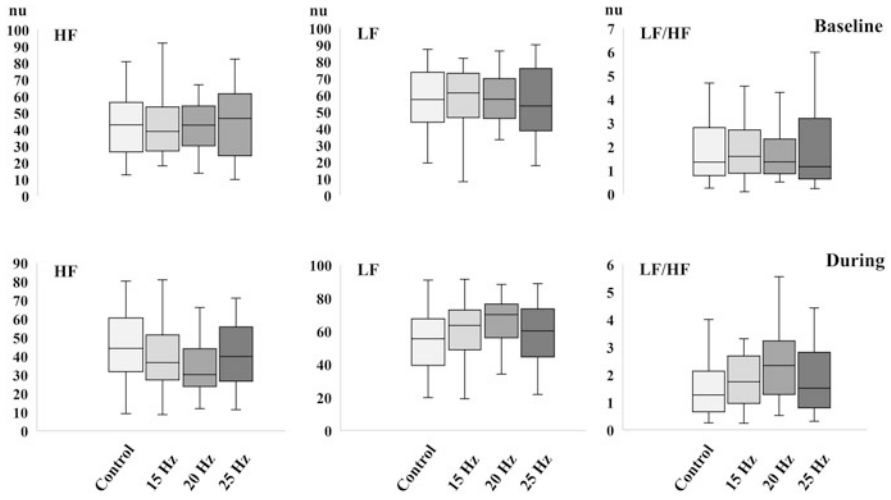

Fig. 3 Boxplots displaying median and 25th and 75th percentiles for the components of HRV under different exposure conditions at baseline (upper panel) and during (lower panel) intervention. Number of subjects included in the analysis: control, $n = 26$; 15 Hz, $n = 25$; 20 Hz, $n = 24$; and 25 Hz, $n = 25$. HF high frequency, *LF* low frequency, *nu* normalized unit

experiments involving human exposure to vibration and shock. According to the EU Directive 2002/44/EU [3], people regularly exposed to WBV in their occupations should not be exposed to a vibration exceeding an A(8) value of 1.15 m/s^2 r.m.s. In line with these, we exposed subjects to WBV to relatively lower frequencies and magnitudes of vibration. However, the same feet posture on the vibration platform and same amplitude of vibration led to the generation of a level of vibration magnitude at 25 Hz that exceeded the recommended A(8) value. But we believe that subjects' posture on the platform with flexed knees caused partial reduction of the mechanical energy of WBV transmitted to the body through the feet [6].

In our study, WBV generated at 20 and 25 Hz caused an increase in SBF both during and after the exposure, and the responses under these two conditions were significantly greater than that observed under the 15 Hz exposure condition. However, the peak vibration magnitude exceeded the recommended safe exposure limit at 25 Hz. Therefore, the findings provide evidence for the practical applicability and also the efficacy of exposure to WBV at 20 Hz as a simple, safe, and feasible noninvasive modality for increasing SBF of the lower extremity in the elderly.

Our observation of no significant vibration-induced change in ST is in line with the current literature [1]. This may be due to the fact that we measured ST at the dorsal skin which is thermally more stable as it lacks arteriovenous anastomoses and less responsive to external stimuli than the glabrous skin.

Aging is associated with changes in ANA with reduced HRV, and the latter is associated with the development of adverse health outcomes [7]. Therefore, WBV intervention should not cause any adverse effects on the ANA. As we observed in

our study, applied WBV did not cause any significant change in the HRV indicating that no cardiovascular stress was caused by the WBV intervention used in this study.

5 Conclusion

Acute exposure to WBV within the ISO-recommended limit appears to be able to induce improvements in peripheral SBF without exerting any negative effects on the ANA in the elderly. For this purpose, exposure with a vibration frequency of 20 Hz and peak-to-peak displacement of 4 mm producing an A(8) value of 1.12 m/s^2 r.m.s. was found to be effective.

Acknowledgments This research was supported by a Grant-in-Aid for Scientific Research (no.16K09132) from the Japan Society for Promotion of Science (JSPS).

References

1. Mahbub, M.H., Hiroshige, K., Yamaguchi, N., Hase, R., Harada, N., Tanabe, T.: A systematic review of studies investigating the effects of controlled whole-body vibration intervention on peripheral circulation. Clin. Physiol. Funct. Imaging. **39**(6), 363–377 (2019). https://doi.org/10.1111/cpf.12589
2. International Organization for Standardization. Mechanical vibration and shock – Evaluation of human exposure to whole-body vibration - Part 1: General requirements. International Standard, ISO 2631–1 (1997)
3. European Union: Directive 2002/44/EC of the European Parliament and of the Council of 25 June 2002 on the minimum health and safety requirements regarding the exposure of workers to the risks arising from physical agents (vibration). Off. J. Eur. Communities. **L177**, 13–19 (2002)
4. Eger, T., Thompson, A., Leduc, M., et al.: Vibration induced white-feet: overview and field study of vibration exposure and reported symptoms in workers. Work. **47**(1), 101–110 (2014). https://doi.org/10.3233/WOR-131692
5. Murata, K., Araki, S., Okajima, F., Nakao, M., Suwa, K., Matsunaga, C.: Effects of occupational use of vibrating tools in the autonomic, central and peripheral nervous system. Int. Arch. Occup. Environ. Health. **70**(2), 94–100 (1997)
6. Abercromby, A.F.J., Amonette, W.E., Layne, C.S., McFarlin, B.K., Hinman, M.R., Paloski, W.H.: Vibration exposure and biodynamic responses during whole-body vibration training. Med. Sci. Sports Exerc. **39**(10), 1794–1800 (2007)
7. Reardon, M., Malik, M.: Changes in heart rate variability with age. Pacing Clin. Electrophysiol. **19**(11 Pt 2), 1863–1866 (1996)

Effects of Vibration on Seated Human Drowsiness/Alertness

K. Zou, M. Fard, J. L. Davy, and S. R. Robinson

1 Introduction

The Australian National Highway Traffic Safety Administration estimated that in 2013 alone, drowsy driving was responsible for 72,000 crashes, 44,000 injuries, and 800 deaths, and these numbers are trending upwards. Drowsy driving has cost the economy at least $3 billion every year since 2000 [15]. Driver's drowsiness has become a challenging problem for modern transport safety [1, 14].

Alertness is a state of consciousness in which drivers have a clear mental condition and can make the judgment quickly and accurately. On the other hand, when drivers are drowsy, their response time becomes longer, and the accuracy of their judgments deteriorates. Alertness is influenced by the degree of activation of two parts of the autonomic nervous system. The sympathetic nervous system (SNS) is more active during periods of stress or arousal, while the parasympathetic nervous system (PNS) is more active when we are feeling calm, relaxed, and sleepy. These two systems exist in a dynamic equilibrium [2]. For example, as people feel increasingly relaxed while they drive, the PNS becomes more dominant, but then as they fight to stay alert, the SNS is activated in short bursts, in an attempt to arouse from drowsiness. The relative amount of activation of the SNS and PNS at a given time can be estimated by examining the heartbeat. It turns out that when we are

K. Zou (✉) · M. Fard
School of Engineering, RMIT University, Melbourne, VIC, Australia
e-mail: s3459679@student.rmit.edu.au

J. L. Davy
School of Science, RMIT University, Melbourne, VIC, Australia

S. R. Robinson
School of Health and Biomedical Sciences, RMIT University, Melbourne, VIC, Australia

Institute for Breathing and Sleep, Austin Health, Heidelberg, VIC, Australia

S. Oberst et al. (eds.), *Vibration Engineering for a Sustainable Future*,
https://doi.org/10.1007/978-3-030-46466-0_51

stressed, the heartbeat is more rapid and regular, whereas when we are relaxed, the heartbeat is slower and less regular [3, 5, 7].

Variation in sympathetic and parasympathetic activity can be estimated by analyzing the heart rate variability (HRV). There are two principal components to the variable duration between heartbeats [4]. Beat-to-beat variability is called "high-frequency" (HF) variability (0.15–0.4 Hz) and is primarily due to the activity of the PNS, while periodic variations in the heart rate over periods of 10 seconds or more (0.04–0.15 Hz) are called low-frequency" (LF) variability and are more strongly influenced by the SNS (but not exclusively, see [6]). Thus, the LF/HF ratio can be used to identify periods of relaxation and decreased alertness: as we become drowsy, the PNS starts to dominate, and the LF/HF ratio decreases. However, if the person becoming drowsy is driving at the time, they will struggle to stay awake, and in these situations, the LF/HF ratio fluctuates erratically, as the stress involved in staying alert results in strong but brief activations of the SNS.

Another way to assess driver drowsiness is to ask them to rate their subjective sleepiness on the *Karolinska sleepiness scale (KSS)* [9]. The KSS describes an individual's current state of alertness on a scale of 1 to 10. Level 1 means that the participant feels extremely alert, and level 10 means that the participants are extremely sleepy or cannot keep awake. The ratings obtained on the KSS can be used to validate conclusions reached from measures of HRV. Both of these measures were employed in the present study.

2 Methodology

2.1 Participants

Ten normal male subjects aged 20–25 volunteered for this study. The ages, weights, heights, and daily routine of all subjects were recorded. Any subjects with a history of neurological disease or sleep disturbances were excluded from this study. The study was approved by the RMIT University Human Ethics Committee. All subjects were asked to go to bed before 10 pm on the day before testing and to have at least 7 hours sleep.

2.2 Experimental Procedure

Due to the requirements of experimental repeatability and driver safety, all experiments were conducted in a laboratory-based driving simulator. This simulator was designed and built at RMIT University. The simulator system includes a 2.5 m*2.5 m*3 m semi-open cabin, a 32-inch monitor in the front of this cabin, a

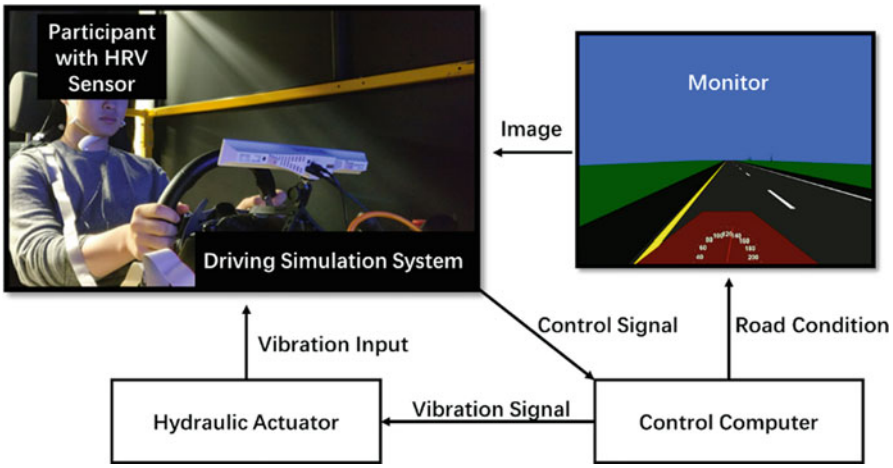

Fig. 1 Schematic view of the experimental setup [8, 12]

metal vibration platform in the center of the room, a mid-size sedan car seat mounted on the platform, and a steering wheel fixed between the monitor and the seat (Fig. 1). The experimental laboratory has a stable temperature at 24 °C, and lighting is dimmed to simulate evening driving conditions. Driving simulation software (York Driving Simulator: York Computer Technologies Inc., Kingston, ON, Canada) was used to simulate the highway driving conditions. In the experiment, the participants were asked to sit in a comfortable posture in the driver's seat, which is located about 1.5 m from the video monitor. The driving simulator software displayed a scenic two-way straight highway road view with two lanes in each direction to simulate the monotonous highway driving condition. The participants were instructed to do their best to drive safely and to keep the vehicle in the center of the left lane by using the steering wheel.

Each run of the experiment lasted 60 minutes. Every participant needed to complete two simulated driving tasks (two test runs): one involved no vibration, and the other involved exposure to whole-body vibration. The order in which these conditions were presented was randomized between participants. The vibration of the platform was powered by a computer-controlled hydraulic actuator. This actuator can apply a virtually multiaxial (x-, y-, z-axis) input vibration to the seat to provide a real-world driving perception of the vibration. The vibration input was adjusted to provide a 0.2 m/s^2 r.m.s total multiaxial vibration to the driver's body over a range of 4–7 Hz in Gaussian random input. This range corresponds to the frequency band of theta brainwaves that are associated with the onset of drowsiness [10].

Table 1 Average KSS score for both the control and vibration conditions

	Control condition	Vibration condition
KSS before the test run (mean ± SEM)	5.3 ± 0.33	5.0 ± 0.33
KSS after the test run (mean ± SEM)	6.2 ± 0.36	7.7 ± 0.42

2.3 Data Processing

The participants were asked to rate their subjective sleepiness scale via KSS at the beginning and end of each test run for both the control condition and vibration condition. Two-tailed paired t-test was used to assess the statistical significance ($p < 0.05$). Standard error of the mean (SEM) is displayed in Table 1.

A Polar H7 heart rate monitor was used to collect HRV data. The RR intervals data (the temporal differences between successive R-wave occurrence times) were collected by the heart rate monitor and saved by the smartphone application "Elite HRV" as .txt files. The time resolution for each RR interval is 1 ms (precisely 1/1024s). The HRV was processed by "Kubios HRV Premium 3.1.0." In this software, the artifact correction, data window, and trend components can be set up for data processing. The time window is 180 s, so the 60 minutes of HRV data were divided into 20 parts.

The following frequency-domain features of the HRV data were calculated from the power spectral density (PSD) [11, 13]:

LF = The power in low-frequency range (0.04–0.15 Hz) in the PSD reflects SNS activity combined with some PNS activity.
HF = The power in high-frequency range (0.15–0.4 Hz) in the PSD reflects mainly PSN activity.
LF/HF = Indicated the approximate balance between SNS and PNS activity.

To aid comparison between subjects and runs, the average values of the LF/HF ratio at the 6 minutes is calculated as the benchmark point. All the raw data will be shifted to the same point at 6 minutes for each run, and it is recalibrated to 1.5.

3 Results

3.1 Subjective Sleepiness Scale

The average of KSS values of all the volunteers before and after the test run are shown in Table 1. The table shows that the subjective sleepiness scale of the volunteers before and after the test run changed significantly ($p < 0.05$), especially under the vibration condition ($p < 0.0001$). The comparison of the averaged KSS values between the vibration and control condition after test the run suggests that

the exposure to vibration has a significant influence on the onset of drowsiness ($p < 0.05$). This result means that volunteers became more tired after the vibration has been applied to driver's body.

3.2 The LF/HF Ratio

The LF/HF ratio is the objective index of the participant sleepiness level. Compared with the LF/HF ratio in the control condition, the trend lines in the vibration condition display significantly more variability.

The standard deviations for both the control condition and the vibration condition are calculated and shown in Table 2. The two-tailed paired t-test result shows that the difference between these two conditions is significant ($p < 0.05$). This means that the SNS and PNS have a stronger antagonism effect under the vibration condition.

The averaged LF/HF ratio trend lines for all ten participants are shown in Fig. 2. The mean standard deviation value for the vibration condition is 0.65, and the mean for the control condition is 0.44. Previous research [12] shows that higher SD values are interrelated to higher drowsiness level. It is believed that the subjects feel drowsier due to the low-frequency vibration. The data in both conditions trends upwards over time, indicating that both sets of conditions activated the SNS, presumably in an attempt to combat drowsiness. However, the lines for the vibration condition exhibited larger fluctuations than the lines for the control condition, consistent with the greater effort required to fight drowsiness in the vibration condition.

Table 2 Standard deviation of the LF/HF ratio

Standard deviation of LF/HF ratio		
	Vibration condition	Control condition
Subject #1	0.83	0.57
Subject #2	1.69	1.09
Subject #3	2.40	1.55
Subject #4	0.71	0.22
Subject #5	0.99	0.88
Subject #6	3.09	0.58
Subject #7	0.81	0.50
Subject #8	1.16	0.98
Subject #9	2.40	1.54
Subject #10	0.89	0.40
Average	1.50	0.83

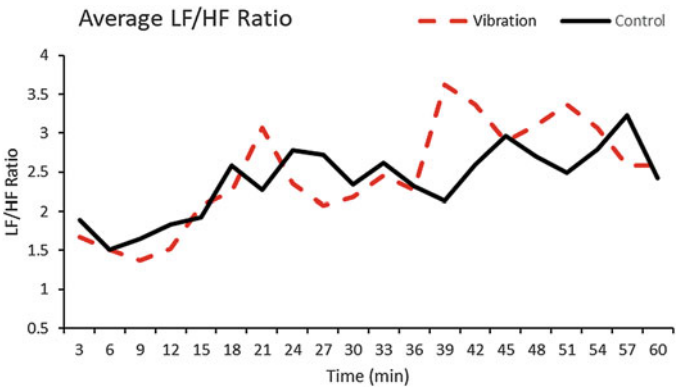

Fig. 2 The averaged data of all participants for control condition and vibration condition

4 Discussion

This study investigated the relationship between whole-body vibration and driver drowsiness. Currently, relatively little is known about the relationship between physical vibration and the human response. The present results have shown that under controlled conditions, vibration transmitted through the driver's seat for a period of 60 minutes increases the subjective sense of drowsiness when compared to a no-vibration condition. An objective measure of drowsiness, the LF/HF ratio, indicated that over the 60 minutes period, all drivers experienced an increase in mean SNS activation, which was of similar magnitude in both conditions. However, the vibration condition was associated with significantly greater variability in the LF/HF ratio, which is consistent with these drivers having to exert a greater amount of mental effort to remain alert throughout the driving task.

It is evident from Table 2 that there was a wide range of variability in individual responses to the vibration condition, with some subjects exhibiting large standard deviations in the LF/HF ratio (indicative of bursts of SNS activity) and others exhibiting relatively small standard deviations. This heterogeneity might reflect individual differences in susceptibility to drowsiness while driving. It is notable, however, that every one of the ten participants exhibited a larger standard deviation while in the vibration condition than when in the control condition, indicating that all participants were affected to some degree by the vibration.

While these results were obtained within the controlled environment of a driving simulator, the range and magnitude of vibrations experienced by the participants were consistent with that experienced by drivers on normal Australian highways, and therefore the results should have relevance to real-world driving conditions. The previous research of Zhang et al. [12] demonstrated that whole body vibration significantly enhances the perception and experience of drowsiness during a simulated highway driving task. These findings raise the interesting possibility that by

suppressing drowsiness-inducing vibrational frequencies in motor vehicles, it may be possible to reduce the incidence of motor vehicle accidents.

References

1. Chen, L.L., Zhao, Y., Zhang, J., Zou, J.: Automatic detection of alertness/drowsiness from physiological signals using wavelet-based nonlinear features and machine learning. Expert Syst. Appl. **42**, 7344–7355 (2015)
2. Eckberg, D.L.: Sympathovagal balance: a critical appraisal. Circulation. **96**, 3224–3232 (1997)
3. Lombardi, F.: Clinical implications of present physiological understanding of HRV components. Card. Electrophysiol. Rev. **6**, 245–249 (2002)
4. Michail, E., Kokonozo, A.,Chouvarda.: EEG and HRV markers of sleepiness and loss of control during car driving, 30th Annual international IEEE EMBS conference, 2008
5. Vicente, J., Laguna, P., Bartra, A., Bailon, R.: Detection of Driver's drowsiness by means of HRV analysis. Comput. Cardiol. **38**, 98–92 (2011)
6. Shaffer, F., Ginsberg, J.P.: An overview of heart rate variability metrics and norms. Front. Public Health. **5**, Article 258 (2017)
7. Shinar, Z., Akselrod, S., Dagan, Y., Baharav, A.: Autonomic changes during wake-sleep transition: a heart rate variability based approach. Auton. Neurosci. Basic Clin. **130**, 17–27 (2006)
8. Kawamura, R., Bhuiyan, M.S., Kawanaka, H., Oguri, K.: Simultaneous stimuli of vibration and audio for in-vehicle driver activation (2011)
9. Karolinska Sleepiness Scale (KSS): In: Shahid, A., et al. (eds.) STOP, THAT and One Hundred Other Sleep Scales. © Springer Science+Business Media, LLC (2012). https://doi.org/10.1007/978-1-4419-9893-4_47
10. Dustman, R.E., Boswell, R.S., Porter, P.B.: Beta brain waves as an index of alertness. Science. **137**(3529), 533–534 (1962)
11. Rosenberg, W., Chanwimalueang, T., Adgei, T., Jaffer, U., Goverdovsky, V., Mandic, D.P.: Resolving Ambiguities in the LF/HF Ratio: LF-HF scatter plots for the categorization of mental and physical stress from HRV, viewed on 20th March 2018. (2017) https://www.frontiersin.org/articles/10.3389/fphys.2017.00360/full
12. Zhang, N., Fard, M., Bhuiyan, M.H.U., Verhagen, D., Azari, M.F., Robinson, S.R.: The effects of physical vibration on the heart rate variability as a measure of drowsiness. Ergonomics. **61**(9), 1259–1272 (2018)
13. Jiao, K., Li, Z., Chen, M.: Effect of different vibration frequencies on heart rate variability and driving fatigue in healthy drivers. Int. Arch. Occup. Environ. Health. **77**, 205–212 (2004)
14. Ahn, I., Bae, M.J.: A study on warning sound for drowsiness driving prevention system. Int. J. Appl. Eng. Res.. ISSN 0973-4562. **12**(24), 14088–14094 (2017)
15. Fatigue Statistic.: Transport Accident Commission Victoria, viewed on 3rd January (2019). http://www.tac.vic.gov.au/road-safety/statistics/summaries/fatigue-statistics

Author Index

S. Oberst et al. (eds.), *Vibration Engineering for a Sustainable Future*,
https://doi.org/10.1007/978-3-030-46466-0

Subject Index

S. Oberst et al. (eds.), *Vibration Engineering for a Sustainable Future*,
https://doi.org/10.1007/978-3-030-46466-0